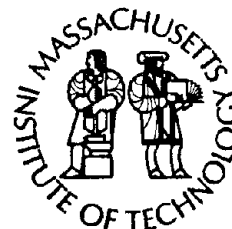


# Woods Hole Oceanographic Institution Massachusetts Institute of Technology



Joint Program  
in Oceanography  
and  
Oceanographic Engineering



---

DOCTORAL DISSERTATION

Variations in Structure and Tectonics  
Along the Mid-Atlantic Ridge, 23°N and 26°N

by

Laura S. L. Kong

June 1990



WHOI-90-28

**Variations in Structure and Tectonics  
Along the Mid-Atlantic Ridge, 23°N and 26°N**

by

Laura S. L. Kong

Woods Hole Oceanographic Institution  
Woods Hole, Massachusetts 02543

and

The Massachusetts Institute of Technology  
Cambridge, Massachusetts 02139

June 1990

**Doctoral Dissertation**

Funding was provided by the National Science Foundation.

Reproduction in whole or in part is permitted for any purpose of the  
United States Government. This thesis should be cited as:  
Laura S. L. Kong, 1990. Variations in Structure and Tectonics  
Along the Mid-Atlantic Ridge, 23°N and 26°N. PhD Thesis.  
MIT/WHOI, WHOI-90-28.

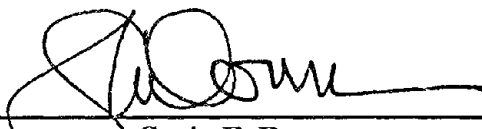
Approved for publication; distribution unlimited.

**Approved for Distribution:**



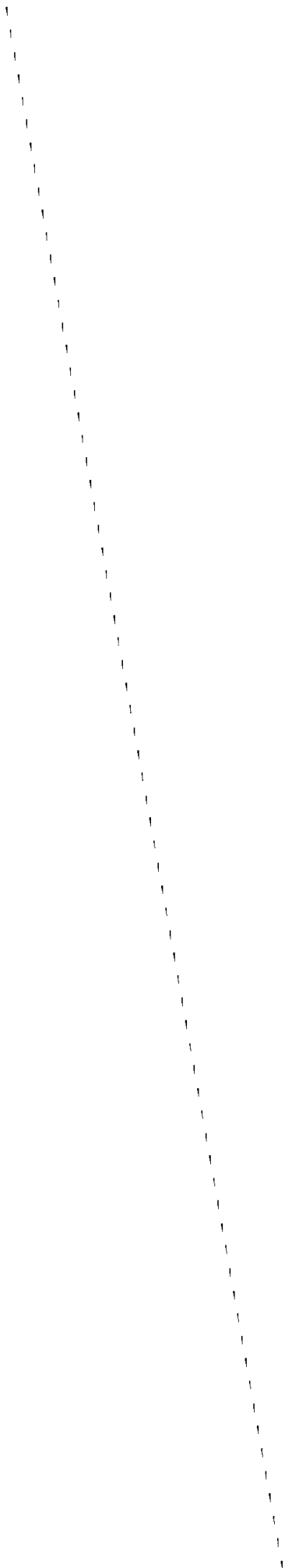
---

**David A. Ross, Chairman**  
Department of Geology and Geophysics



---

**Craig E. Dorman**  
Acting Dean of Graduate Studies



VARIATIONS IN STRUCTURE AND TECTONICS  
ALONG THE MID-ATLANTIC RIDGE, 23°N AND 26°N

by

LAURA SAU LIN KONG  
Sc. B., 1983, Brown University

SUBMITTED IN PARTIAL FULFILLMENT  
OF THE REQUIREMENTS FOR THE DEGREE OF  
DOCTOR OF PHILOSOPHY

at the

MASSACHUSETTS INSTITUTE OF TECHNOLOGY

and the

WOODS HOLE OCEANOGRAPHIC INSTITUTION

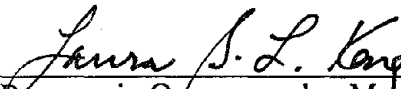
June, 1990

© Laura S. L. Kong, 1990

NTIS is authorized to reproduce and sell this report. Permission for further reproduction must be obtained from the copyright owner.

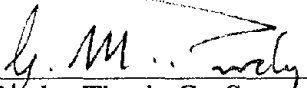
The author hereby grants to MIT and WHOI permission to reproduce and distribute copies of this thesis document in whole or in part.

Signature of Author



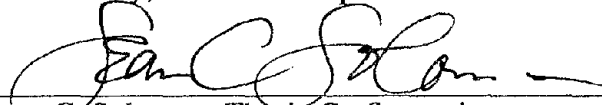
Joint Program in Oceanography, Massachusetts Institute of Technology and Woods Hole Oceanographic Institution, and the Department of Earth, Atmospheric, and Planetary Sciences, Massachusetts Institute of Technology, March, 1990.

Certified by



G. M. Purdy, Thesis Co-Supervisor

Certified by



Sean C. Solomon, Thesis Co-Supervisor

Accepted by



Chairman, Joint Committee for Marine Geology and Geophysics,  
Massachusetts Institute of Technology / Woods Hole Oceanographic Institution



VARIATIONS IN STRUCTURE AND TECTONICS  
ALONG THE MID-ATLANTIC RIDGE, 23°N AND 26°N

by

Laura Sau Lin Kong

Submitted to the Department of Earth, Atmospheric, and Planetary Sciences  
Massachusetts Institute of Technology

and

the Department of Geology and Geophysics  
Woods Hole Oceanographic Institution

on March 19, 1990

in partial fulfillment of the requirements  
for the degree of Doctor of Philosophy

**ABSTRACT**

The variation in the depth and width of the median valley along the Mid-Atlantic Ridge (MAR) suggests that the formation of ocean crust at slow spreading centers is not a simple two-dimensional process in which crustal accretion occurs uniformly both along the ridge axis and with time. Rather, it has been proposed that the ridge axis can be divided into a number of distinct segments or spreading cells. This thesis investigates the segmentation model by studying the variability in the structure and tectonics within spreading cells at 23°N and 26°N along the MAR. The results support the segmentation model in which accretion varies along the ridge, evolving as independent spreading cells or segments, with different portions of the ridge system being in different stages of volcanic and tectonic evolution.

Chapter 2 presents an overview of morphologic and tectonic variations along a 100-km-length of the MAR south of the Kane Fracture Zone (MARK area). Sea MARC.I side scan sonar data and multi-beam Sea Beam bathymetry are used to document the distribution of crustal magmatism and extensional tectonism near 23°N. The data indicate a complex median valley composed by two distinct *en echelon* spreading cells which overlap in a discordant zone that lacks a well-developed rift valley or neovolcanic zone. The northern cell, immediately south of the fracture zone, is dominated by a large constructional volcanic ridge and is associated with active high-temperature hydrothermal activity. In contrast, the southern cell is characterized by a NNE-trending band of small fissured and faulted volcanos that are built upon relatively old, fissured and sediment-covered lavas; this cell is inferred to be in a predominantly extensional phase with only small, isolated volcanic eruptions. Despite the complexity of the MARK area, volcanic and tectonic activity appears to be confined to the 10-17 km wide inner rift valley. Small-offset normal faulting along near-vertical planes begins within a few kilometers of the ridge axis and appears to be largely completed by the time the crust moves out of the median valley. Mass-wasting and gullying of scarp faces, and sedimentation which buries low-relief seafloor features, are the major geological processes occurring outside the rift valley.

In Chapters 3 and 4, the microearthquake characteristics and P wave velocity structure beneath the median valley of the Mid-Atlantic Ridge near 26°N are studied; this ridge segment is characterized by a large high-temperature hydrothermal field situated within the inner floor at the along-axis high. Chapter 3 explores the tectonic variations within the crust as evidenced from the distribution and source mechanisms of microearthquakes observed by a network of seven ocean bottom hydrophones and two ocean bottom seismometers over a three week period in 1985. Hypocenters were determined for 189 earthquakes, with good resolution of focal depth obtained for 105 events. Almost all events occurred at depths between 3 and 7 km beneath the seafloor, with earthquakes occurring at shallower depths beneath the along-axis high (< 4 km). The distribution of hypocenters and the diversity of faulting associated with earthquakes beneath the inner floor and walls suggests a spatially variable tectonic state for the ridge segment at 26°N. These variations are presumably a signature of lateral heterogeneity in the depth region over which brittle failure occurs, and are a consequence of along-axis changes in the thermal structure and state of stress.

We suggest that at present the hydrothermal activity and deposition of massive sulfides is being sustained by heat generated by a recent magmatic intrusion. A consequence of this scenario is that thermal stresses play a dominant role in controlling the distribution of earthquakes and nature of faulting. Such a hypothesis is consistent with an apparent lack of seismicity beneath the hydrothermal field, the location of hypocenters around the low velocity zone (Chapter 4), attenuation of P wave energy to instruments atop the high (Chapter 4), the higher b-values associated with the along-axis high region, and the occurrence of high-angle (or very low angle) normal faulting and reverse faulting, as well as the variability in nodal plane orientations, associated with inner floor events beneath the along-axis high and the volcano.

In Chapter 4, we report results from the explosive refraction line and from the tomographic inversion of P wave travel time residuals for seismic velocity structure in the vicinity of the hydrothermal field. The two-dimensional along-axis P wave structure beneath the inner floor indicates that young oceanic crust cannot be adequately characterized by a simple, laterally homogeneous velocity structure, but that one-dimensional structures are at least locally valid (at 5-10 km length scales). The shallowmost crust (upper 1-2 km) beneath an axial volcano and the along-axis high is characterized by significantly higher velocities (by more than 1 km/s) than are associated with the upper crust in the deepest portions of the median valley. The variation is inferred to be a consequence of more recent magmatic and volcanic activity in the along-axis high region, as compared with the along-axis deep where tectonic fissuring has created a highly porous crust characterized by lower seafloor velocities. The crust beneath the along-axis deep appears to be typical of normal young oceanic crust, with a mantle velocity of 8.25 km/s observed at 5 km depth.

A low velocity zone centered beneath the along-axis high and extending under an axial volcano is imaged from 3 to 5 km depth (7.2 km/s to 6.0 km/s); the velocity decrease is required to satisfy the travel time residual data and to explain the severe attenuation in compressional wave energy to instruments atop the along-axis high. The presence of an active high-temperature hydrothermal field atop the along-axis high, together with the observations of lower P wave velocities, the absence of microearthquake activity greater than 4 km in depth, and the propagation of S waves through the crust beneath the volcano and along-axis high (Chapter 3), suggest that the volume corresponds to a region of hot



rock with no seismically-resolvable pockets of partial melt. The shallow velocity gradients describing the low velocity volume ( $< 0.6 \text{ s}^{-1}$ ) appear to be a common characteristic of inferred zones of magmatic intrusion on the MAR. Comparison of the depth to the velocity inversion with the depths determined in other seismic studies at locally high regions along the MAR, the Juan de Fuca Ridge, and the East Pacific Rise reveals a correlation between lid thickness and spreading rate, suggesting that the amount of magma available at each location is spatially variable, or that the differences in lid thickness are describing the temporal evolution of magmatic intrusions beneath mid-ocean ridges.

In Chapter 5, the first direct measurement of upper mantle P- and S-wave delay times beneath an oceanic spreading center is presented. Two independent estimates of the epicenters and origin times are made for each of two earthquakes in a 1985 earthquake swarm near  $25^{\circ}50'N$  on the Mid-Atlantic Ridge using local and teleseismic arrival time data. Comparison indicates a 14-20 km northward bias in the epicenters teleseismically located using a *Herrin* [1968] Earth model. The bias is due to departures of the actual velocity structure from that implicit in the travel time tables used for the locations, combined with unbalanced station distribution. The comparison of origin times for the best-located event, after correction for the epicentral bias and for an oceanic crustal thickness, shows there to be only slightly lower velocities than a *Herrin* [1968] upper mantle; the P-wave delay is  $+0.3 \pm 0.9 \text{ s}$  ( $+0.2 \pm 0.9 \text{ s}$  and  $-2.4 \pm 0.9 \text{ s}$  relative to the isotropic Preliminary Earth Reference Model (PREM) and the *Jeffreys-Bullen* [1940] (JB) travel time tables, respectively). The lack of a resolvable P-wave delay suggests that the *Herrin* [1968] model is a good approximation to the average upper mantle velocity beneath this segment of the MAR.

Measurement of the S-wave delay for the same MAR swarm event shows there to be a positive delay ( $+3.1 \pm 2.0 \text{ s}$ ), or larger travel times and slower velocities compared to the JB S-wave tables ( $+3.9 \pm 2.0 \text{ s}$  relative to the isotropic PREM S-wave model). In contrast to the larger P-wave delays found in other MAR studies, the lack of a significant seismic anomaly near  $26^{\circ}N$  indicates that sizeable regions of low velocity material do not presently exist in the upper few hundred kilometers of mantle beneath this section of the ridge. This evidence argues for substantial along-axis variations in the active upwelling of mantle material along the slowly-spreading Mid-Atlantic Ridge. In order to explain the observation of a smaller than expected P wave delay in a region where the S delay suggests significant temperature anomalies (low velocities), we propose a model for mantle upwelling in which the decrease in travel time is due to an anisotropic P wave structure (fast direction vertical); the anisotropy results from the reorientation of olivine crystals parallel to the ascending flow and balances the travel time delay due to a region of low velocities.

Thesis Co-Supervisors: Dr. G. Michael Purdy  
Senior Scientist, WHOI

Dr. Sean C. Solomon  
Professor of Geophysics, MIT



## ACKNOWLEDGEMENTS

This thesis is dedicated to my parents whose unwithering patience and support I have treasured over the last decade spent pursuing an education not only of scholarly knowledge but also of experience in the gamut of life. And now as I compose these words, reminiscing about the eastern side of the world as I sit far to the west in a land of foreign culture and tongue, I hope that they will understand yet another of my sojourns to a faraway destination.

To Mike and Sean, quite a twosome, my heartfelt appreciation and thanks for silently enduring those extended homeleaves in Hawaii and for your advice and support especially through the last six months of this thesis and as March 31st neared. Your scientific intuition, intellect, and professionalism (and I don't mean your tie, Mike...) are without equals.

I would like to acknowledge the many people who have devoted more than a passing interest in my Ph. D. endeavors. Don Forsyth gave me the opportunity to work on OBS microearthquake data way back when, and Clyde Nishimura was always good for words of brotherly wisdom (and friendly sarcasm). Neil Frazer arranged for that fateful first cruise, and Tom Brocher and John Mutter gave me my first introduction to the scientific process. Special acclaims go to Joe Cann and Hans Schouten for the many inspiring (and random) discussions on mid-ocean ridges, and to Henry Dick and Niall Slowey for many diversionary hours of procrastination. I can't thank enough the efforts, both large and small, tedious, simple, or uninterpretable, of David DuBois (I'll take care of whatever whenever) and Lee Gove (Obladi, Oblada, life goes on...) of the WHOI seismology group, and Warren Sass (the night owl) and Chan Hilliard (yes, your slides will be ready this afternoon) of IPC. Along the way, Donna Blackman, Barbara Braatz, John Collins, Marty and Robin Dougherty, Cindy Ebinger, Karen Fischer, Tanya Furman, Sarah Little, Barbara Marsh, Peter Meyer, Mark Murray, Margaret and Jacek Sulanowska, Doug Toomey, Will Wilcock, Beecher and Chris Wooding, and Carolyn Zehnder made the long hours and frustrations of graduate school palatable. My kudos go to Faith Hampshire, Marie Senat, and Katherine Ware for taking care of the details in those last hectic months. The night guards at Clark provided cheerful anecdotes and opened many a locked door in the wee hours of the night. To the staff and students at Woods Hole and MIT; it has been a wonderful experience, one of much pleasure (and some agony) and one that I will not ever forget.

Without Jake Pierson, Mary Athanis, and Abbie Jackson of the Education Office to fund many an AGU trip to San Francisco and to Lamont, and without their unrelenting willingness to guide me through that maze of dissertation etiquette, I would never have reached the time for writing this prose. Many thanks to the other members of my thesis committee, Bill Bryan, Jason Phipps-Morgan, Debbie Smith, and Dick Von Herzen, for their encouragement and advice.

My gratitude is extended to all the non-science persons who would not let me forget that a big, wide world existed outside of WHOI and MIT. To the few of you from Punahou, who I manage to write to once a year and yet can bridge those lapses of time with only a moments thought, I savor the true friendships which will embrace us for the rest of our lives. To the women athletes at Brown, who brought to me a network of comradeship

and adventure, and where time passed by all too quickly amid laughter and drink, I hope that we can continue to cherish the ways, and means, by which we were first united.

And finally, to Kevin, we have helped in the labors of many and rejoiced in the fortunes of few, but always I shall remember the quiet pleasures we shared. My words could not ever express the emotional and physical strength you have nurtured in me over the last year. Although the yearning for a place where the tradewinds purr softly amidst the lap of a gentle surf, and island guitars sing mellow under the amber glow of the setting sun, is steadfast in our hearts, I know that, wherever we may be, the love which became a part of our lives as we strove toward common goals will only grow stronger with the years to come.

This thesis was funded in part by grants EAR-8407798, EAR-8407745, and EAR-8817173 from the National Science Foundation.

## TABLE OF CONTENTS

ABSTRACT	3
ACKNOWLEDGEMENTS	7
CHAPTER 1. INTRODUCTION	13
References	15
CHAPTER 2. THE MORPHOLOGY AND TECTONICS OF THE MARK AREA FROM SEA BEAM AND SEA MARC I OBSERVATIONS (MID-ATLANTIC RIDGE 23°N)	17
Introduction	19
Regional Setting and Related Work	20
Data Collection	21
Morphology of the Ridge Axis from Sea Beam	22
Outer Rift Valley / Rift Mountains	27
Rift Valley	28
Fine Scale Structural Relationships within the Rift Valley	29
Sea MARC I Data: Acoustic Textures	29
Across-axis Rift Valley Structure	30
Along-axis Rift Valley Structure	34
Northern Spreading Cell	34
Southern Spreading Cell	44
Discordant Zone	45
Discussion	47
Conclusions	50
References	50
CHAPTER 3. MICROEARTHQUAKES BENEATH THE MEDIAN VALLEY OF THE MID-ATLANTIC RIDGE NEAR THE TAG HYDROTHERMAL FIELD, 26°N	53
Introduction	53
Background - The Mid-Atlantic Ridge at 26°N	55
Seismic Network - Experiment Description	57

Instrument Relocation	58
Hypocentral Location	60
Arrival Time Data	61
One-dimensional Crustal Velocity Structure	63
Starting Trial Parameters	64
Solution Quality	65
Dependence on S Wave Time, $V_p/V_s$ Ratio, and 1D Velocity Model	66
Epicentral and Focal Depth Distribution	67
Inner Floor Seismicity	68
Eastern and Western Wall Seismicity	69
Earthquake Location by RMS Grid Search	70
Effect of Crustal Heterogeneity on Hypocenters	72
Focal Mechanisms	75
Effect of Crustal Heterogeneity on Focal Mechanisms	77
Earthquake Source Parameters	79
Discussion	83
Fault Geometry	83
Along-strike Variation in Focal Depth	85
Hydrothermal Circulation at the Along-axis High	87
The 26°N Spreading Cell	89
Conclusions	90
References	94
Figure Captions	102
Tables	114
Figures	127

<b>CHAPTER 4.</b>	
<b>TWO-DIMENSIONAL VELOCITY STRUCTURE ALONG THE</b>	
<b>MID-ATLANTIC RIDGE NEAR THE TAG HYDROTHERMAL FIELD, 26°N</b>	<b>175</b>
Introduction	175
Experiment location	177
Data Reduction	177
Refraction Line Analysis	179
Southern Limb of Refraction Line	180
Amplitude Modelling - Median Valley South of Along-Axis High	182
Summary of Refraction Analysis	185

Tomographic Inversion for P Wave Velocity Structure	185
Input Parameters	187
Average 2D Median Valley Structure	190
Tests of Robustness	191
Effect of Earthquake Mislocation on Model Estimate	195
Minimization of 3D Effects - Inner Floor 2D Model	198
Summary of Tomographic Inversions for 2D Structure	201
Discussion	202
Variability of Seismic Layer 2 - Seafloor Velocities	202
Variability in Depth to Layer 3	205
Low Velocity Zone	206
Along-axis Structural Variations in Crustal Accretion	209
Conclusions	210
Appendix. Seismic Tomography Method and Theory	212
Hypocentral Partial Derivatives	212
Estimation of Velocity Perturbations	214
Evaluation of Solution Quality	219
References	221
Figure Captions	228
Tables	240
Figures	246

<b>CHAPTER 5.</b>	
<b>UPPER MANTLE P AND S WAVE DELAYS BENEATH THE</b>	
<b>MID-ATLANTIC RIDGE NEAR 26°N</b>	<b>293</b>
Introduction	293
July 1985 Earthquake Swarm	295
Local Data and Hypocentral Determination	295
Local Velocity Model	296
Initial Hypocentral Parameters	297
Hypocentral Uncertainties	298
Teleseismic Data and Hypocentral Determination	298
Comparison of Hypocentral Estimates	301
P Wave Delay	302
S Wave Delay	304
Discussion	305

Comparison with Other Studies	305
Along-axis Variation in Upper Mantle Velocities?	307
Anisotropic Mantle Upwelling Beneath Mid-Ocean Ridges?	309
Summary and Conclusions	311
References	312
Figure Captions	317
Tables	322
Figures	324
CHAPTER 6.	
CONCLUSIONS	339
References	341



## CHAPTER 1. INTRODUCTION

As increasing amounts of geophysical and geological data are collected, it is becoming apparent that magmatism at mid-ocean ridges is not a simple two-dimensional process in which oceanic crust is accreted continuously both along the ridge axis and with time. Along the slow-spreading Mid-Atlantic Ridge (MAR), high resolution bathymetric studies indicate wide variations in the depth and width of the median valley. This topographic variability suggests that different portions of the ridge system are in different stages of volcanic and tectonic evolution. A model in which the MAR is divided into distinct segments or spreading cells, each less than 100 km in length along axis and each characterized by different proportions of active magmatism and tectonism over distances of less than 100 km, now appears to describe more appropriately the accretionary process [e.g., *Francheteau and Ballard*, 1983; *Schouten et al.*, 1985; *Langmuir et al.*, 1986; *Macdonald*, 1986; *Kong et al.*, 1988; *Sempere et al.*, 1989].

According to this segmentation model, each cell is bounded at its distal ends by an along-axis depth maximum and is approximately centered on an intervening along-axis depth minimum. Within a given segment, the model predicts that the region of most vigorous volcanism and hydrothermal activity, and thus elevated temperatures, should be situated at the along-axis high, and that away from this zone the crust should be significantly cooler and more tectonically disrupted by fissuring and faulting, and volcanism less energetic. In this thesis, I investigate the tectonic and structural variability over tens of kilometers within spreading cells at two locales, 23°N and 26°N, along the Mid-Atlantic Ridge.

Chapter 2 presents an overview of morphologic and tectonic variations along a 100-km-length of the MAR south of the Kane Fracture Zone. Sea MARC I (SMI) side scan sonar data and multi-beam Sea Beam bathymetry collected in 1984 and 1985 as part of the site survey for Ocean Drilling Program Legs 106 and 109 are used to document the distribution of crustal magmatism and extensional tectonism. The focus of the chapter is on the description and interpretation of the SMI data and integration with the Sea Beam observations. The study documents a complex median valley morphology consisting of two distinct *en echelon* spreading cells, each displaying different types and amounts of volcanism and tectonic fissuring. The two cells are separated by a discordant zone which lacks a well-developed rift valley or neovolcanic zone.

In Chapters 3 and 4, I investigate the seismic velocity and earthquake characteristics beneath the median valley of the Mid-Atlantic Ridge near 26°N, where a large active high-temperature hydrothermal field has been mapped. Chapter 3 explores the tectonic

variations within the crust as evidenced from the distribution and source mechanisms of microearthquakes observed by a network of seven ocean bottom hydrophones and two ocean bottom seismometers over a three week period in 1985. Hypocenters were determined for 189 earthquakes, with good resolution of focal depth obtained for 105 events. Almost all events occurred at depths between 3 and 7 km beneath the seafloor. The lack of seismic activity near the hydrothermal field, the diversity of faulting geometries indicated by first motions, and higher b-values associated with the along-axis high region are consistent with the hypothesis that thermal stresses play an important role in determining where and how microearthquakes occur beneath the inner floor of this region. When integrated with the two-dimensional velocity structure determined in Chapter 4, I am able to document systematic along-axis variations in both the seismic structure and microearthquake characteristics; the observations indicate that the most recent magmatic activity within the 26°N spreading cell occurred in the region of the along-axis high.

Chapter 4 documents the seismic evidence for along-axis structural heterogeneity beneath the median valley. This evidence includes the travel time and amplitude patterns from a refraction line collected in 1985 and the tomographic inversion of P wave travel time residuals from shots and earthquakes for two-dimensional structure along the ridge axis. The dependence of the tomographic solution on the model parameterization and source/receiver configuration, and on the assumptions imposed in the analysis, is evaluated. The two-dimensional structure includes higher velocities within the shallowmost crust in the region of the along-axis high and a low velocity zone at depths greater than 3 km beneath an axial volcano and the along-axis high.

In Chapter 5, average upper mantle P and S delays beneath the MAR are determined. The simultaneous characterization of an earthquake swarm near 25°50'N by local and global seismic networks offered the opportunity to measure directly the travel time delays beneath the ridge from the comparison of two independently-estimated origin times for the best-located large earthquake. The comparison of origin times, after correction of the global time for the epicentral bias and for an oceanic crustal thickness, shows there to be only slightly lower velocities than the *Herrin* [1968] upper mantle P wave model, and larger S wave travel times than the *Jeffreys-Bullen* [1940] S wave model. The small P delay, when compared with that which would be predicted from the S delay, may be evidence for compressional wave anisotropy (fast velocity direction vertical); the anisotropy is proposed to result from the realignment of crystals in a direction parallel to the vertically-ascending mantle beneath the ridge axis. Comparison with other travel time residual studies reveals a long-wavelength ( $\geq 1000$  km) variation, with a minimum at 26°N, in the P

and S wave delays along the ridge, suggesting that active mantle upwelling may vary spatially and/or temporally along strike.

Finally, in Chapter 6 important observations and ideas from the previous chapters are brought together and the segmentation model for a slow spreading mid-ocean ridge environment is discussed. The documentation of the locations of recent crustal magmatism and tectonism at two locales on the MAR supports the prediction of the segmentation model that locally shallow regions along the ridge axis represent the most likely locales at which to find elevated crustal temperatures.

The multi-authored paper constituting Chapter 2 acknowledges the many scientists who participated in the collection of the Sea Beam and Sea MARC I data. Since the focus of the paper is on the description and interpretation of the sonar data (which represents my contribution), the paper was written primarily by me; sections directly applying to the Sea Beam data were contributed by R. S. Detrick and P. J. Fox. This chapter was published in *Marine Geophysical Researches* in 1988. Work in Chapter 5 was done in collaboration with E. A. Bergman of the Massachusetts Institute of Technology, who provided the estimate of origin time and the P and SH waveform inversion solution for the source centroid used to estimate the teleseismic S wave arrival time.

## REFERENCES

- Francheteau, J., and R. D. Ballard, The East Pacific Rise near 21°N, 13°N and 20°S: Inferences for along strike variability of axial processes at mid ocean ridges, *Earth Planet. Sci. Lett.*, *64*, 93-116, 1983.
- Herrin, E. (Chairman), 1968 seismological tables for P phases, *Bull. Seismol. Soc. Am.*, *58*, 1193-1241, 1968.
- Jeffreys, H., and K. E. Bullen, *Seismological Tables*, British Association, London, 1940.
- Kong, L. S. L., R. S. Detrick, P. J. Fox, L. A. Mayer, and W. B. F. Ryan, The morphology and tectonics of the MARK area from Sea Beam and Sea MARC I observations (Mid-Atlantic Ridge 23°N), *Mar. Geophys. Res.*, *10*, 59-90, 1988.
- Langmuir, C. H., J. F. Bender, and R. Batiza, Petrological and tectonic segmentation of the East Pacific Rise, 5°30'-14°30'N, *Nature*, *322*, 422-429, 1986.
- Macdonald, K. C., The crest of the Mid-Atlantic Ridge: Models for crustal generation processes and tectonics, in *The Western North Atlantic Region, Geology of North America, Vol. M.*, edited by P. R. Vogt and B. E. Tucholke, Geol Soc. Amer., Boulder, Colo., pp. 51-68, 1986.
- Schouten, H., K. D. Klitgord and J. A. Whitehead, Segmentation of mid-ocean ridges, *Nature*, *317*, 225-229, 1985.

Sempere, J.-C., G. M. Purdy, and H. Schouten, The segmentation of the Mid-Atlantic Ridge between the Kane and Atlantis fracture zones (abstract), *Eos Trans. AGU*, 70, 455, 1989.

**CHAPTER 2.**

**THE MORPHOLOGY AND TECTONICS OF THE MARK AREA  
FROM SEA BEAM AND SEA MARC I OBSERVATIONS  
(MID-ATLANTIC RIDGE 23°N)**



# The Morphology and Tectonics of the Mark Area from Sea Beam and Sea MARC I Observations (Mid-Atlantic Ridge 23° N)

LAURA S. L. KONG

*MIT/WHOI Joint Program in Oceanography, Woods Hole Oceanographic Institution, Woods Hole, MA 02543, U.S.A.*

ROBERT S. DETRICK and PAUL J. FOX

*Graduate School of Oceanography, University of Rhode Island, Kingston, RI 02881, U.S.A.*

LARRY A. MAYER

*Department of Oceanography, Dalhousie University, Halifax Nova Scotia B3H 4J1*

and

W. B. F. RYAN

*Lamont-Doherty Geological Observatory, Palisades, NY 10964, U.S.A.*

(Received 2 November, 1987)

**Key words:** Mid-Atlantic Ridge, seafloor spreading, rift valley, oceanic crust.

**Abstract.** High-resolution Sea Beam bathymetry and Sea MARC I side scan sonar data have been obtained in the MARK area, a 100-km-long portion of the Mid-Atlantic Ridge rift valley south of the Kane Fracture Zone. These data reveal a surprisingly complex rift valley structure that is composed of two distinct spreading cells which overlap to create a small, zero-offset transform or discordant zone. The northern spreading cell consists of a magnetically robust, active ridge segment 40–50 km in length that extends from the eastern Kane ridge-transform intersection south to about 23°12' N. The rift valley in this area is dominated by a large constructional volcanic ridge that creates 200–500 m of relief and is associated with high-temperature hydrothermal activity. The southern spreading cell is characterized by a NNE-trending band of small (50–200 m high), conical volcanos that are built upon relatively old, fissured and sediment-covered lavas, and which in some cases are themselves fissured and faulted. This cell appears to be in a predominantly extensional phase with only small, isolated eruptions. These two spreading cells overlap in an anomalous zone between 23°05' N and 23°17' N that lacks a well-developed rift valley or neovolcanic zone, and may represent a slow-spreading ridge analogue to the overlapping spreading centers found at the East Pacific Rise. Despite the complexity of the MARK area, volcanic and tectonic activity appears to be confined to the 10–17 km wide rift valley floor. Block faulting along near-vertical, small-offset normal faults, accompanied by minor amounts of back-tilting (generally less than 5°), begins within a few km of the ridge axis and is largely completed by the time the crust is transported up into the rift valley walls. Features that appear to be constructional volcanic ridges formed in the

median valley are preserved largely intact in the rift mountains. Mass-wasting and gullying of scarp faces, and sedimentation which buries low-relief seafloor features, are the major geological processes occurring outside of the rift valley. The morphological and structural heterogeneity within the MARK rift valley and in the flanking rift mountains documented in this study are largely the product of two spreading cells that evolve independently to the interplay between extensional tectonism and episodic variations in magma production rates.

## 1. Introduction

The Mid-Atlantic Ridge (MAR) rift valley south of the Kane Fracture Zone known as the MARK (*Mid-Atlantic Ridge at Kane*) area, was recently the site of a major crustal drilling effort by the Ocean Drilling Program (ODP) on Legs 106 and 109 (Detrick, Honnorez, Bryan, Juteau *et al.*, 1988). In preparation for the drilling in this area, a joint United States/Canadian research team, including investigators from the University of Rhode Island, Lamont-Doherty Geological Observatory, Dalhousie University, and Woods Hole Oceanographic Institution, carried out a predrilling site survey using two state-of-the-art seafloor mapping instruments: Sea Beam, a high-resolution, multibeam echo sounder, and Sea MARC I, a mid-range, deeply-towed, side-scan

sonar (Detrick *et al.*, 1984; Mayer *et al.*, 1985). The combination of these two complimentary tools, focussed on a ~100-km-long segment of the Mid-Atlantic Ridge, provide a truly exceptional data set with which to study the morphology and tectonics of a ridge-transform-ridge system along a slowly accreting plate boundary.

In this paper we describe the Sea Beam and Sea MARC I results from the median valley. Companion papers present results from the Kane Transform (Pockalny *et al.*, 1988), the Kane Fracture Zone transverse ridge (Abrams *et al.*, 1988), and an analysis of magnetic data across the rift valley (Schulz *et al.*, 1988). These studies, together with the drilling results and a subsequent submersible investigation (Karson *et al.*, 1987; Brown and Karson, 1988), document significant along-axis changes in median valley morphology, volcanic activity, tectonic extension and crustal structure in the MARK area.

## 2. Regional Setting and Related Work

The Mid-Atlantic Ridge in the MARK area has been the site of numerous marine geological and geophysical investigations dating back to the late 1960s (van Andel and Bowin, 1968; Miyashiro *et al.*, 1969; Purdy *et al.*, 1978; Bryan *et al.*, 1981; Karson and Dick, 1983; Toomey *et al.*, 1985; Purdy and Detrick, 1986). Regional bathymetric maps compiled from conventional, wide-beam echo sounding profiles show the Kane Transform offsets the MAR rift valley about 150 km in a left-lateral sense near 23°30' N (Fox *et al.*, 1969; Fox, 1972; Rabinowitz *et al.*, 1977; Purdy *et al.*, 1979). The transform is associated with a broad zone of disturbed topography, 15–20 km in width, that trends about 100°, nearly orthogonal to the adjacent MAR rift valley (Pockalny *et al.*, 1988). On a regional scale, the rift valley south of the Kane Transform is a broad, linear ridge segment with no major transform offsets for a distance of at least 100 km (Purdy *et al.*, 1978; Cormier *et al.*, 1984). The median valley is shallowest 70–80 km south of the Kane Transform and broadens and deepens northward into a large nodal basin at the ridge-transform intersection.

Despite the along-strike continuity of the MARK rift valley on a regional scale, interpretations of surface magnetic data indicate this portion of the

Mid-Atlantic Ridge has been composed of two misaligned spreading cells that have created an offset in the magnetic anomaly pattern near 23°15' N, 40–50 km south of the Kane Transform (Schouten *et al.*, 1985; Schulz *et al.*, 1988). This present-day segmentation of spreading in the MARK area has evolved over the last few million years from an earlier ridge-transform-ridge geometry through a series of small (~10 km), eastward ridge jumps. These small ridge jumps, which were probably caused by a relocation of the neovolcanic zone within the median valley, have resulted in an overall pattern of asymmetric spreading with faster rates to the west (14 mm yr<sup>-1</sup>) than to east (11 mm yr<sup>-1</sup>) over the past 3 Ma (Schulz *et al.*, 1988).

The crustal structure of the median valley in the MARK area has been determined from a single 130-km-long explosive seismic refraction line shot along the rift valley from just south of the Kane Transform to about 22°30' N (Purdy and Detrick, 1986). These data yield a well-constrained two-dimensional model for the seismic structure of the median valley including: (1) the existence of seismically mature oceanic crust beneath much of the rift valley (22°30' N–23°15' N) characterized by a well-defined Moho transition zone, ~8 km s<sup>-1</sup> upper mantle velocities and a total crustal thickness of 6–7 km; (2) anomalously low seismic velocities in the lower crust centered beneath the median valley topographic high between 23°15' N and 23°30' N that are attributed to the most recent phase of magmatism; and (3) a major seismic discontinuity near 23°15' N separating the relatively normal crustal structure present to the south from a 30-km-long zone of relatively thin (3–4 km) crust with no distinct layering which abuts the Kane Transform to the north. No seismic evidence was found for a crustal magma chamber along this refraction line and, in general, the results from this experiment indicate that the crust within the central and southern parts of the MARK rift valley has cooled sufficiently since its last major magmatic episode to have taken on most of the seismic characteristics of 'normal' oceanic crust. These results are consistent with microearthquake foci and source mechanism in the southern part of the MARK area (22°45' N) which indicate that the rift valley is presently undergoing active extension with brittle failure occurring to depths of at least 7–8 km (Toomey *et al.*, 1985; 1988).



The magnetic and seismic data described above provide the regional tectonic and structural framework on which we base our interpretation of the Sea Beam and Sea MARC I data. Our interpretation is also aided by very detailed, submersible-based geological mapping and sampling at the eastern ridge-transform intersection (Karson and Dick, 1983), and along four east-west transects across the rift valley located 30, 40, 60 and 80 km south of the Kane Transform (Karson *et al.*, 1987; Brown and Karson, 1988). Additional 'ground-truthing' of our results comes from the camera surveys and drilling at ODP sites 648, 649 and 670 in the median valley (Detrick, Honnorez, Bryan, Juteau *et al.*, 1988). The submersible studies and drilling results have documented, on a local scale, the structural and tectonic heterogeneity of the MARK area. The Sea Beam and

Sea MARC I data presented in this paper provide a set of intermediate scale ( $10^{-2}$  to  $10^2$  km) observations that help relate these observations to the time-integrated magmatic and tectonic evolution of accretionary processes in the MARK area.

### 3. Data Collection

The Sea Beam, Sea MARC I and bottom photographic data discussed in this paper were collected on two cruises: the Sea Beam data on R/V *Conrad* Leg 25-11 in September of 1984, and the Sea MARC I and camera data on the CSS *Hudson* Leg 85-010 in May of 1985.

Sea Beam was used to map an area of nearly 20 000 km<sup>2</sup> including the entire Kane Transform, both ridge-transform intersections (RTI), and a

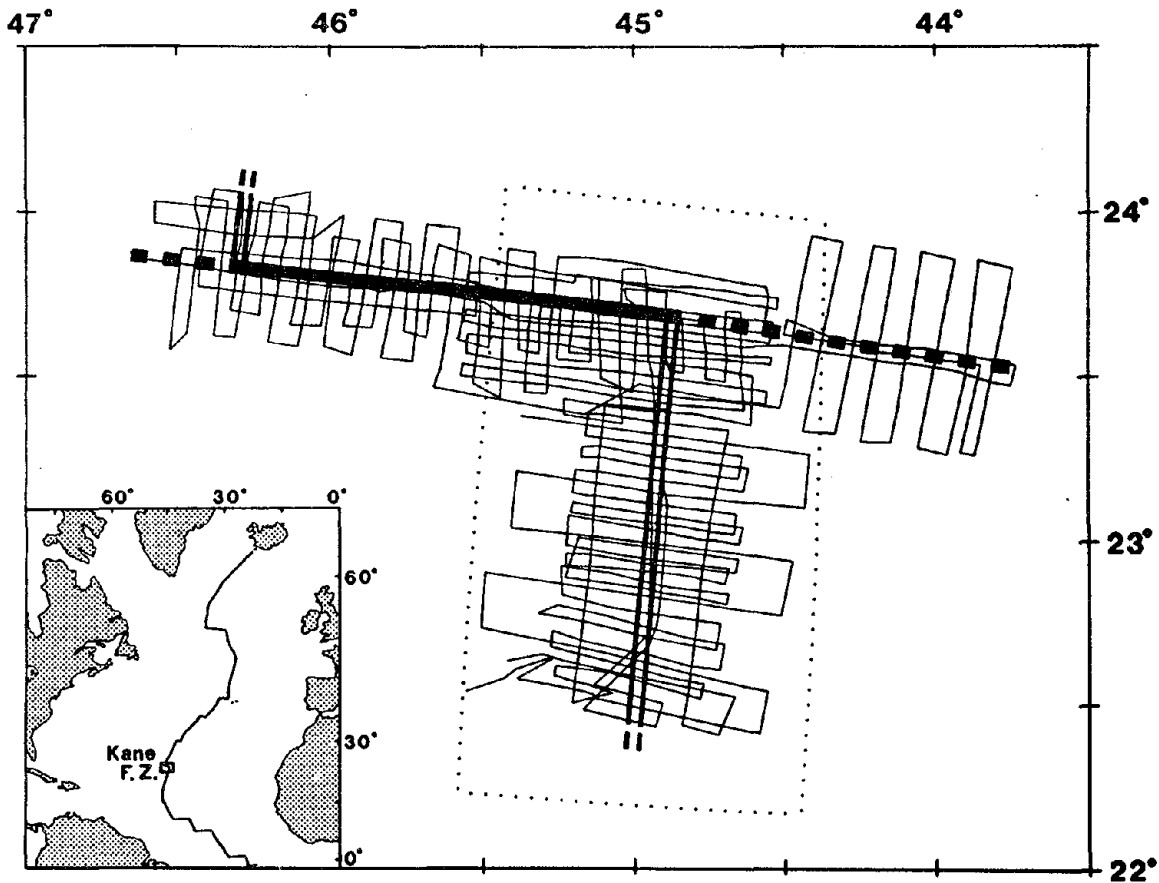


Fig. 1. Simplified tectonic map of the MARK area showing the Kane Transform (thick solid line), the Mid-Atlantic Ridge (MAR) rift valley (double line), and the aseismic extension of the Kane Fracture Zone east and west of the ridge crest (dashed line). Superimposed on this map is the track coverage obtained during the 1984 Sea Beam survey. The dotted line shows the location of the map in Figure 2.

100-km-long section of the MAR rift valley south of the Kane Transform (Figure 1). Sea Beam is a hull-mounted, multi-narrow beam 12 kHz echo sounder consisting of 16 beams ( $2.66^\circ \times 2.66^\circ$ ) which insonify a swath of seafloor with a width equal to approximately 75% of the water depth (Renard and Allenou, 1979; de Moustier and Kleinrock, 1986). The system has a nominal vertical resolution of 1–5 m, but in the rough topography associated with the Mid-Atlantic Ridge the vertical resolution decreases to 10–20 m. Lateral resolution depends on the water depth, but is about 100–200 m at the Mid-Atlantic Ridge.

Sea Beam line spacing was typically 3–4 km with a separation of about one swath width. Lines were run both parallel and perpendicular to the regional topographic trends in order to provide cross-track references. Navigation was by a combination of Global Positioning System (GPS) satellites, transit satellites and dead reckoning. GPS was typically available only 8–9 hours each day so the GPS-navigated lines were carefully laid out to 'tie-in' lines collected during non-GPS intervals. Post-cruise processing involved determining the final ship navigation by constraining the transit satellite-navigated swaths to fit with the GPS-navigated swaths where they intersected or overlapped. A color bathymetry map of the MARK area including the rift valley and its eastern intersection with the Kane Transform is shown in Figure 2. The Sea Beam data have also been interpolated onto an equally spaced 250-m grid using a biharmonic cubic spline technique in order to produce the three-dimensional perspective view of the rift valley shown in Figure 3.

Using the Sea Beam data as a basemap, *CSS Hudson* returned to the MARK area with the Sea MARC I side-scan vehicle in order to obtain higher resolution images of the seafloor and select sites suitable for 'barerock' drilling. Sea MARC I, developed by International Submarine Technology Ltd. and Lamont-Doherty Geological Observatory, is a deeply-towed vehicle consisting primarily of a bilateral 27/30 kHz side-looking sonar, a 4.5 kHz sub-bottom profiler and associated vehicle attitude and depth sensors (Chayes, 1983; Kosalos and Chayes, 1983). It is typically towed at speeds of 1.5–2.0 knots at an altitude of 200–300 m above the bottom, insonifying a swath approximately 5 km in width (on a processed image).

Highly reflective surfaces (e.g., fresh basalts, fault scarps) appear as dark grey to black sonar images; more subdued, smoother terrain (e.g., sediment covered areas) appear as lighter greys; and acoustic shadows are white. A 250 m wide swath directly beneath the vehicle is not insonified and thus always appears white on the sonar image. The sonar system can typically resolve vertical features 3–4 m in height; lateral resolution is more variable, being strongly dependent on the local relief, but can be taken to be on the order of tens of meters. The vertical and lateral resolution of the subbottom profiles in rough topography are estimated to be a few meters and a few tens of meters, respectively.

On *Hudson* 85-010, approximately 350 km of 5 km swath Sea MARC I data were obtained in the median valley from about  $22^\circ 44'$  N northward to the eastern Kane RTI (Figure 4). The data were collected in three ridge-parallel (N–S) transects and two oblique (NW–SE) crossings of the median valley resulting in the nearly complete insonification of the inner rift valley. Higher-resolution, 2-km-swath data were also collected along 70 km of the rift axis in order to provide more detailed images of potential drill sites. Navigation for the survey was provided by GPS when available (6–7 hr per day), and standard transit satellites and dead reckoning between GPS windows. The position of the Sea MARC I vehicle behind the ship was calculated from slant-range and altimeter data, and the processed side-scan images located along the vehicle track and adjusted to fit the Sea Beam bathymetry and overlapping side-scan data.

The final data set contributing to our analyses are seafloor photographs collected in the three areas selected as potential drill sites (Figure 4). The camera system was typically towed 1–12 m above the bottom at speeds of 0.5–1 knot, yielding sharp color photos of the bottom with 2–5 m (across) fields of view (Farre *et al.*, 1983). Like the Sea MARC I track, camera positions are estimated by slant-range determinations and referenced to Sea Beam bathymetry.

#### 4. Morphology of the Ridge Axis from Sea Beam

The high-resolution Sea Beam bathymetry data acquired during the site survey reveal the rift valley and flanking rift mountains in the MARK area to be surprisingly complex at all scales, both along- and across-strike (Figures 2 and 3).

## THE MORPHOLOGY AND TECTONICS OF THE MARK AREA FROM SEA BEAM AND SEA MARC I OBSERVATIONS

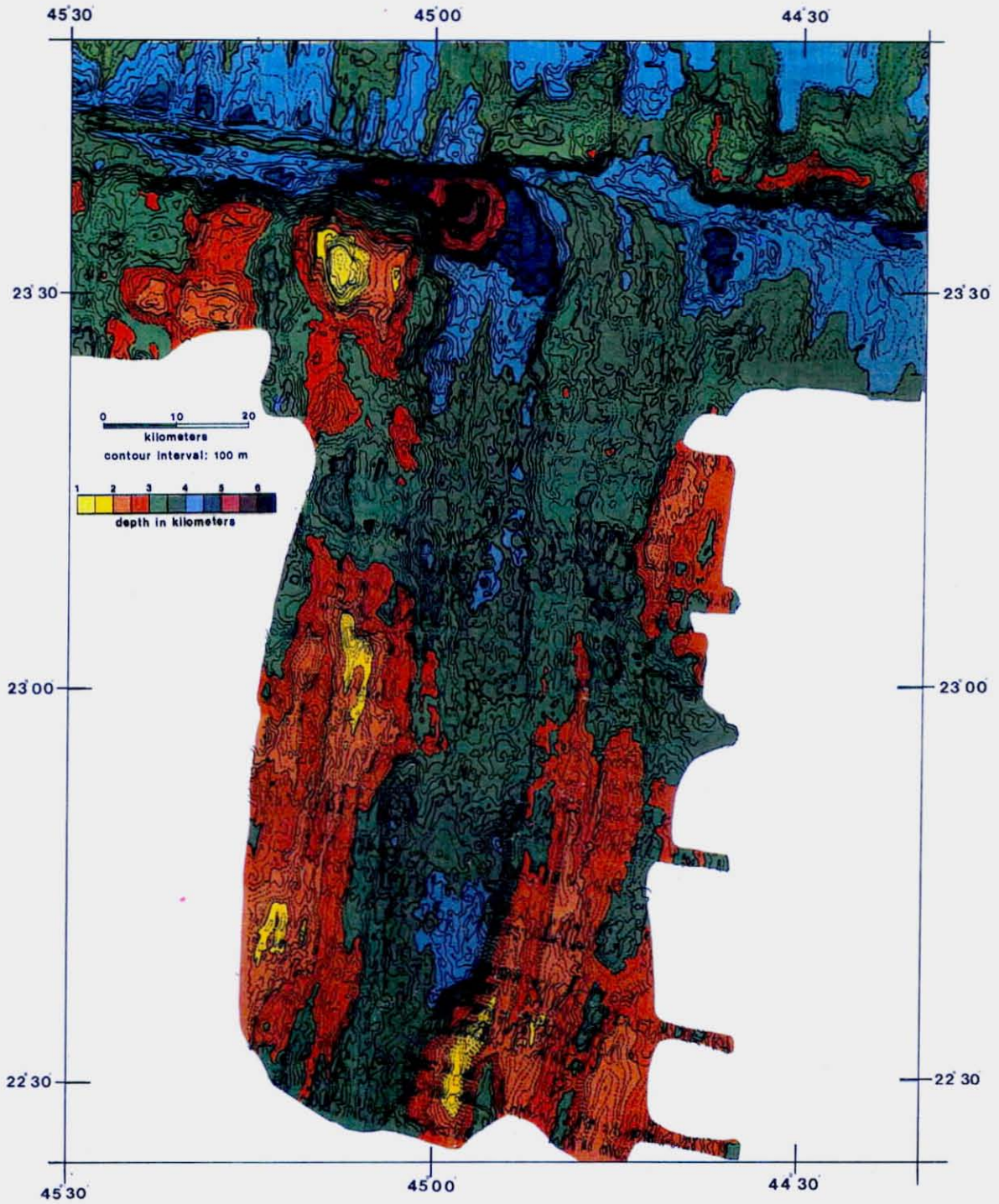


Fig. 2. Sea Beam bathymetry map of the median valley in the MARK area and the eastern Kane Transform. The map is contoured at a 100-m interval with color changes every 500 m. Dashed contours indicate interpolated values.



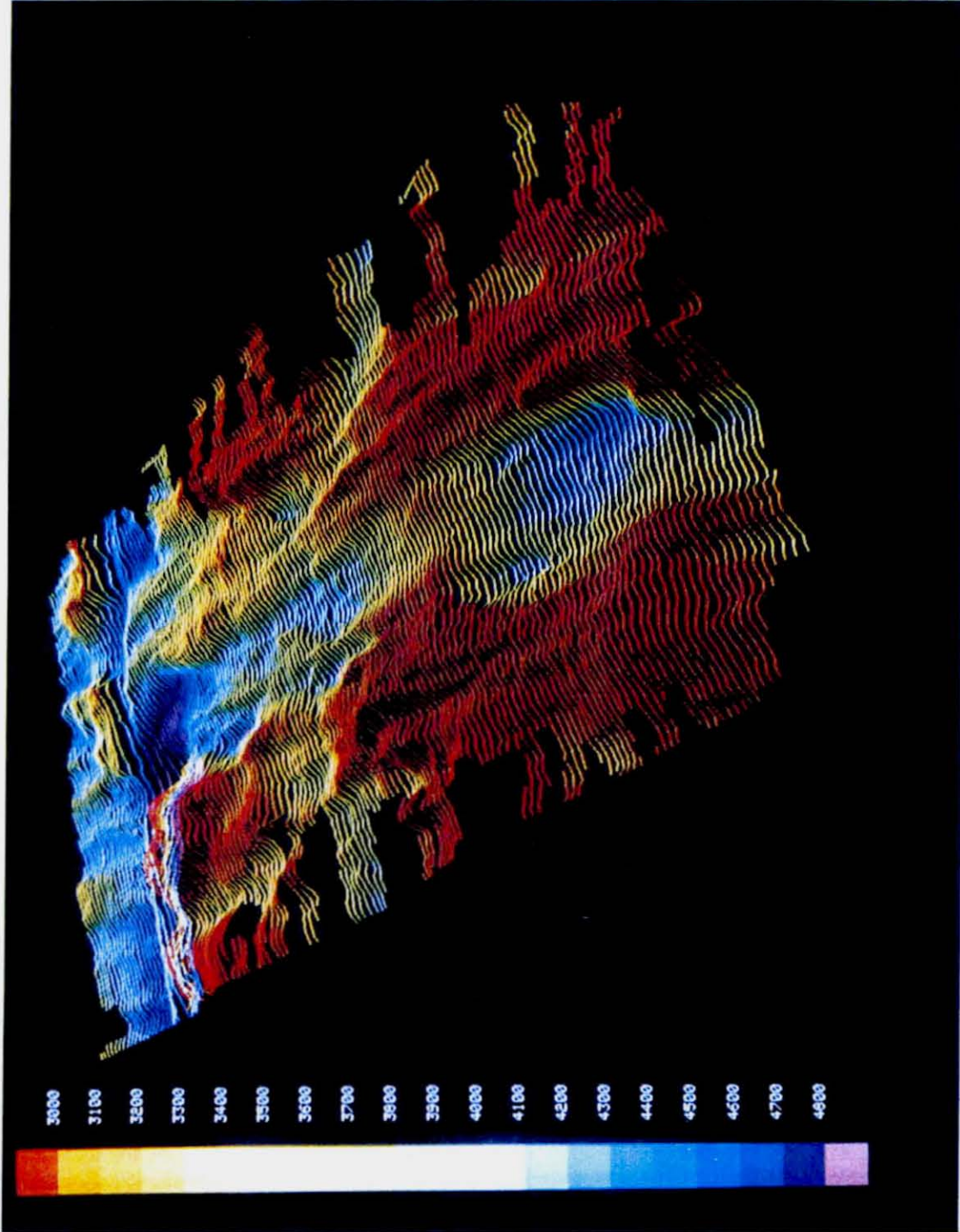


Fig. 3. Three-dimensional perspective view of the MARK rift valley using Sea Beam data that has been interpolated onto a 1 km grid. View is from the western rift mountains looking northeast. Vertical exaggeration is 3 x.



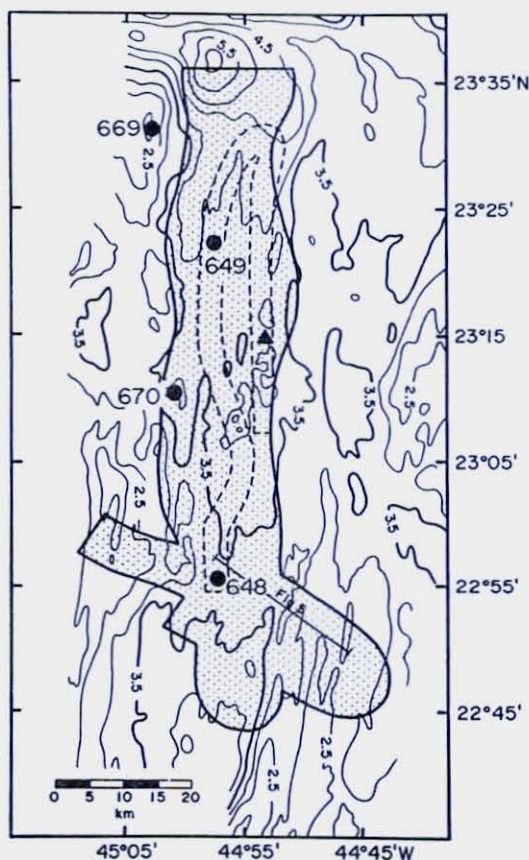


Fig. 4. Sea MARC I track coverage superimposed on a simplified bathymetry map of the MARK area. Stippled area shows coverage of 5 km swath data; dashed lines indicate location of higher resolution 2 km swath data. Location of ODP drill sites is shown for reference. Bottom photographs were obtained on the Sea MARC I leg at Sites 648 and 649, and at a third site indicated by the solid triangle.

#### 4.1. OUTER RIFT VALLEY/RIFT MOUNTAINS

Typically, the rift mountains in the MARK area rise between 1500 and 2000 m above the rift valley floor. The western rift mountains are comprised of two broad (15–20 km), shallow (<3000 m) plateaus that are separated by a U-shaped saddle between 23°12' N and 23°20' N. The plateaus display a distinctive structural grain consisting of narrow (<5 km wide), axis-parallel ridges that are approximately 500 m high and continuous along-strike over distances of several tens of kilometers. The ridges are shallowest midway along their length, deepening and tapering towards each end, with generally steeper

valley-facing scarps. Morphologically, these ridges are very similar to the median volcanic ridge that is forming today in the northern part of the MARK rift valley and the co-linear, fault-bounded volcanic ridge that extends to the south (discussed below). These features thus appear to be volcanic constructional ridges that formed on the median valley floor and that have subsequently been uplifted, without significant dismemberment by faulting, into the rift mountains (Pockalny *et al.*, 1988).

Near the U-shaped saddle in the western rift mountains between 23°12' N and 23°20' N these ridges abruptly plunge, taper and bend sharply to the west mimicking the shape of the ridges that abut the Kane Fracture Zone 40 km to the north (Figures 2 and 3; also see Pockalny *et al.*, 1988). The saddle area is characterized by depths intermediate between those of the flanking rift mountains and the median valley floor, and is associated with short (5 to 10 km), axis-parallel ridges and troughs. This anomalous portion of the western rift mountains occurs at the same latitude as the major structural discontinuity reported by Purdy and Detrick (1986) and correlates with the position of the small ridge axis discontinuity documented in the magnetics by Schulz *et al.* (1988). However, the lack of pronounced transform-parallel topographic trends in the rift mountains at this latitude indicates this is a discordant zone that has not been characterized by normal strike-slip transform tectonism during at least the past 1–2 Ma.

The western rift mountains reach their shallowest depth (<1500 m) immediately south of the Kane Transform, adjacent to the ridge-transform intersection nodal deep (Figure 2). This 'inside-corner high', which is found near RTIs at most slowly slipping transforms (Fox and Gallo, 1984; Servighaus and Macdonald, 1986), is characterized by second-order, ridge-axis parallel terrain elements that are truncated by the exceptionally steep (~20° regional slope), 3000 m high, transform-parallel slope that defines the southern wall of the Kane Transform valley. Submersible investigations of the escarpments on the east-facing rift valley wall using ALVIN (Karson and Dick, 1983; Karson *et al.*, 1987) reveal the routine exposure of variably deformed and metamorphosed gabbroic rocks up the face of this steep slope with minor occurrences of basalts and diabases.

The eastern rift mountains in the MARK area are also characterized by a series of axis-parallel, asymmetrical ridges that plunge and taper along-strike (Figures 2 and 3). The highest and steepest mountains are found in the southern part of the area, near 22°30' N, where the rift valley bends sharply to the west. Northward, the broad, lineated ridges perched atop this shallow plateau deepen and taper forming a series of narrow, finger-like extensions near 23°00' N where a prominent ESE-trending trough offsets the axis of minimum depth along the rift mountains by ten kilometers to the east. The intersection of this oblique-trending trough with the rift valley coincides with the anomalous saddle area in the western rift mountains.

Between 23°00' N and the Kane Fracture Zone, a broad (15–20 km wide) and relatively deep (3–4 km) terrace separates the rift valley floor and the shallowest portions of the eastern rift mountains. This terrace is associated with two remarkable cusped ridges that plunge and taper toward the Kane Fracture Zone (Figures 2 and 3). These ridges are approximately 10 km across at their base, 300 to 500 m high with a steeper valley-facing slope, and extend along-strike for a distance of more than 40 km. They bend sharply to the west at the Kane Fracture Zone mimicking the shape of the median ridge in the present rift valley as it curves around the eastern edge of the nodal basin (Pockalny *et al.*, 1988). The ridges have apparently experienced relatively minor faulting and, in contrast to the western rift valley walls, only basalts have been recovered from these escarpments (Karson and Dick, 1983; Karson *et al.*, 1987). The similarity in the shape of these ridges with the present neovolcanic zone in the RTI area led Pockalny *et al.* (1988) to propose that they are volcanic constructional features that were formed within the median valley and then transported laterally to their present position without extensive faulting.

#### 4.2. RIFT VALLEY

The rift valley floor in the MARK area is shallowest (slightly less than 3200 m) 70–80 km south of the Kane Transform (near 22°50' N) and deepens both to the south and north of this area, plunging to depths of 5000–6000 m at the eastern Kane RTI (Figures 2 and 3). South of the Kane Transform two opposing, approximately N–S trending steep slopes

(10°–20°), typically about 500 m high, define the borders of the rift valley floor that ranges in width from 10–17 km. Between 23°05' N and 23°30' N the rift valley floor is remarkably linear and of nearly constant width (15–17 km). At 23°05' N the valley floor narrows because of the development of a several kilometer wide and 20-km-long terrace along the western rift valley wall (Figure 2). South of this feature which is located near the sill depth for this valley segment, the rift valley floor widens and develops depths in excess of 4000 m along the base of the eastern rift valley wall. Microseismic activity is concentrated in this basin at depths of 4–8 km below the seafloor and Toomey *et al.* (1985; 1988) have proposed that this basin has formed by block faulting and tilting of the rift valley floor over the past 10<sup>4</sup> yr.

The terrain of the rift valley floor and flanking walls is very complex and quite variable along-strike. The central and northern parts of the rift valley are dominated by two colinear ridges that stand up to several hundred meters high and trend obliquely (010°) to the regional N–S strike of the rift valley (Figures 2 and 3). The southern ridge, which is located on the terrace mentioned above, can be traced northward from about 22°50' N until it disappears in a zone of complex, non-lineated topography between 23°12' N and 23°17' N. It is shallowest (<3000 m) and widest (~7 km wide at the 3500 m isobath) near 23° N, deepening and narrowing both to the north and south. The northern ridge can be traced from 23°17' N along the axis of the rift valley into the eastern RTI. It reaches a minimum depth of 3400 m at 23°22' N and deepens and narrows toward the RTI, bending around the eastern edge of the nodal basin. The northernmost extension of this feature consists of a series of small, 20–100 m high conical peaks that terminate against the northern transform valley wall (Pockalny *et al.*, 1988). The along-strike continuity of this feature, the abundant exposure of fresh, sediment-free basalts, and the discovery of hydrothermal activity on this ridge about 25 km south of the RTI all suggest this ridge is the most likely location of the neovolcanic zone in the northern part of the rift valley (Karson and Dick, 1983; Kong *et al.*, 1985, Leg 106 Scientific Party, 1986).

The linear ridges in the northern part of the MARK rift valley are flanked by marginal lows.



Associated with these lows are numerous circular topographic highs that the Sea MARC I survey and bottom topography revealed to be of volcanic origin (see below). The marginal lows deepen systematically toward the Kane RTI, although several elongate basins deeper than 4000 m are present along the eastern side of the rift valley between 23°05' N and 23°20' N. The remainder of the rift valley floor is associated with small-scale topographic variability with wavelengths of a few kilometers and amplitudes of up to a few hundred meters that is superimposed on the longer-wavelength, along-axis topographic high near 22°50' N. This terrain, which is a manifestation of on-going volcanic and tectonic processes occurring along the rift valley floor, was investigated using the high-resolution side-scan images obtained during the Sea MARC I portion of the site survey.

## 5. Fine Scale Structural Relationships within the Rift Valley

### 5.1. SEA MARC I DATA: ACOUSTIC TEXTURES

The growing collection of Deep Tow, Sea MARC I, photographic, and submersible observations of ridge crest topography provide a valuable database to aid in the sometimes difficult task of interpreting side-scan sonar observations. While the nature of a sonar return is strongly dependent on the altitude of the vehicle, as well as the range and orientation of the target, a number of characteristic textural and reflectivity patterns are apparent in Sea MARC I records that can confidently be correlated with specific geological features. In the MARK area these include: faults and fissures, constructional pillow terrain, volcanos, sediment-covered areas, and debris flows.

Faults and fissures are among the more easily identified sonar targets. These features are typically observed on sonar records as sharp, narrow lineaments with a crisp and highly reflective texture (Figure 5). Many of these features, most of which cannot be resolved on Sea Beam maps, can be traced for long distances (up to 9 km) in the median valley. It is often difficult to distinguish between faults and fissures or small grabens, but the latter can often be identified by a thin linear acoustic shadow near the vehicle closely coupled with a linear acoustic target slightly farther away. In contrast, those features that are characterized by linear acoustic shadows or

acoustic targets are interpreted as scarps (Kastens *et al.*, 1986). Where the Sea MARC I vehicle crosses one of these features, the subbottom profiler can be used to determine the vertical offset (Figure 5). The majority of lineaments imaged within the MARK rift valley have vertical offsets of less than 20 m. Bottom photographs also reveal numerous cracks or fissures generally less than 1 m wide exposing broken and sheared pillow lavas. These small-scale features are not individually resolvable on the side-scan images, although the general trend of groups of closely-spaced fissures often can be determined.

The dominant sonar texture in the median valley in the MARK area is a distinctive hummocky texture that has been shown by photographic and visual observations to represent constructional volcanic pillow lava flows (Figure 5a). This texture is characterized by numerous, overlapping subcircular lobes (50–500 m in diameter, a few meters relief) on the Sea MARC I image. While the sonar texture has the appearance of discrete pillows, the crescent-shaped targets actually represent the steep-sided flow front built by a series of downslope prograding pillow flows. Only rarely can sheet flows be unambiguously identified on sonar images (they appear as a smooth grey sonar texture), although bottom photos revealed some crenelated sheet flows associated with small axial volcanos (see below).

Individual volcanos are recognized on the side-scan image as circular or semi-circular targets casting a distinctive acoustic shadow (Figure 6a, b). The uniform surficial texture of the volcanos varies from highly reflective (black) to grey. Many of the volcanos in the rift valley show a clearly defined circular shadow at their summit indicating a collapsed summit crater. Sediment cover reduces the seafloor reflectivity and results in softer grey tones on the side-scan images. This effect provides a useful, though sometimes risky (because of the other factors controlling reflectivity), means of estimating relative ages. With all other factors held constant, a sediment-covered feature will appear lighter and more uniform in texture than its younger, unconsolidated equivalent. This association was substantiated by bottom photographs that revealed the lighter grey targets (particularly some volcanos) to be sediment-covered while the highly reflective targets showed unconsolidated, fresh surfaces. Finally, lobate reflectivity patterns associated with steep scarps, such as found

LAURA S. I. KONG ET AL.

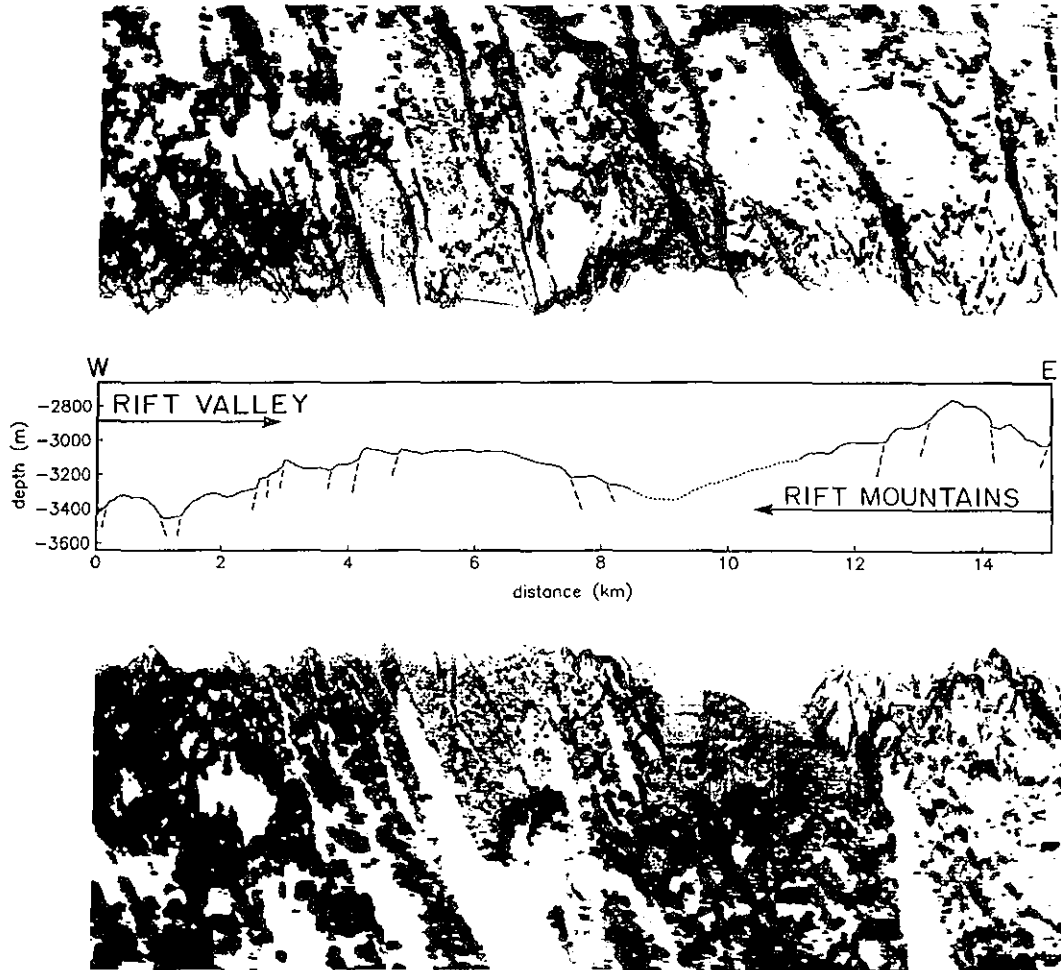


Fig. 5. (a) Sea MARC I profile across the eastern half of the median valley and up into the rift mountains southeast of Site 648 (see Figure 4 for location). Depths are from the subbottom profiler mounted on the Sea MARC I vehicle (solid) and Sea Beam bathymetry (dashed). (a) median valley showing high (left) and moderate (right) reflectivity zones; note the first occurrence of block faulting near the edge of the high reflectivity zone and the moderate tile ( $\sim 5^\circ$ ) of most of the fault blocks.

in the flanking rift mountains (Figure 5b), are indicative of talus or debris flows formed by mass wasting.

Figure 7 shows a tectonic map of the MARK rift valley constructed from Sea MARC I mosaics using the associations between sonar textures and geomorphologic features described above. Our interpretation of the Sea MARC I images is discussed in more detail in the following sections.

## 5.2. ACROSS-AXIS RIFT VALLEY STRUCTURE

Two long, oblique Sea MARC I swaths cross the

MAR rift valley between  $22^\circ 53' N$  and  $22^\circ 57' N$  (Figure 4), about 70 km south of the Kane Fracture-Zone, near the shallowest part of the median valley. This crossing is at approximately the same latitude as Transect 5 of Karson *et al.* (1987). The Sea MARC I mosaic constructed from these two profiles, along with the associated Sea Beam topography and an interpretive tectonic map is shown in Figure 8. Coverage extends from the crest of the western rift mountains, across the rift valley to the crest of the opposing eastern rift mountains. These data define

## THE MORPHOLOGY AND TECTONICS OF THE MARK AREA FROM SEA BEAM AND SEA MARC I OBSERVATIONS

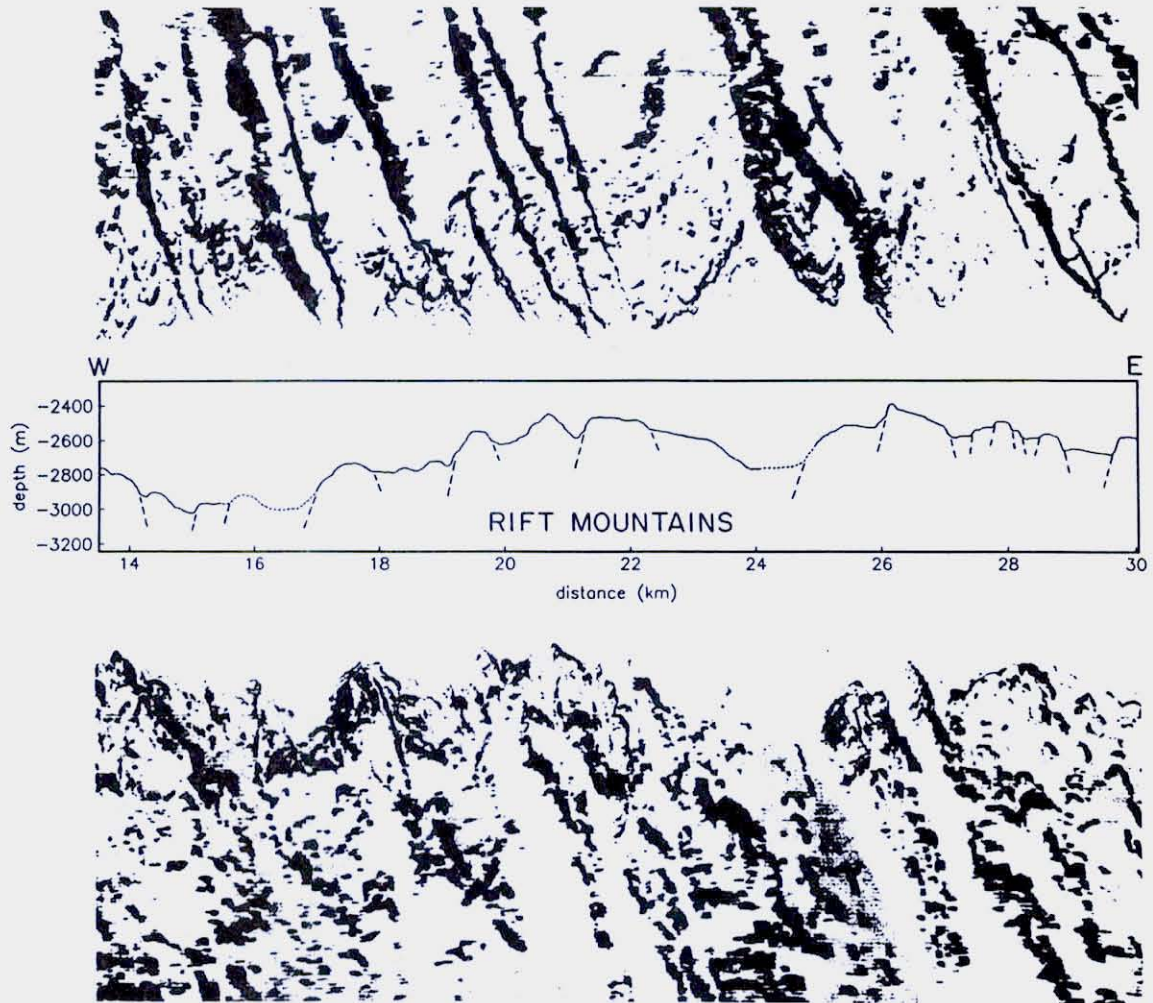


Fig. 5. (b) Rift mountains showing low reflectivity zone; note mass wasting and gullying of the scarp faces.

the structures of the rift valley and provide constraints on the processes which transform the terrain of the rift valley floor into the terrain of the rift mountains.

A high-reflectivity zone about 7 km wide, interpreted as the site of most recent volcanism, is located near the center of the rift valley floor. It is characterized by a hummocky sonar texture typical of pillow lava terrain and numerous small volcanic edifices, both of which are cut by valley-parallel faults and fissures (Figures 5a and 8b). Direct submersible observations have revealed a highly variable sediment

cover in this zone and relatively weathered basalts suggesting this part of the ridge is in a predominately tectonic phase with only minor recent volcanic activity (Brown and Karson, 1988). This high-reflectivity area is flanked by two distinct bands of less reflective, presumably older seafloor, on both sides. The inner zone of lower reflectivity, characterized by light and dark grey acoustic images, is 4–5 km wide and is associated with the walls of the rift valley, while a light grey to white outer band is located in the rift mountains beyond the main rift valley scarps (Figures 5b and 8b). The boundary between the central

LAURA S. L. KONG ET AL

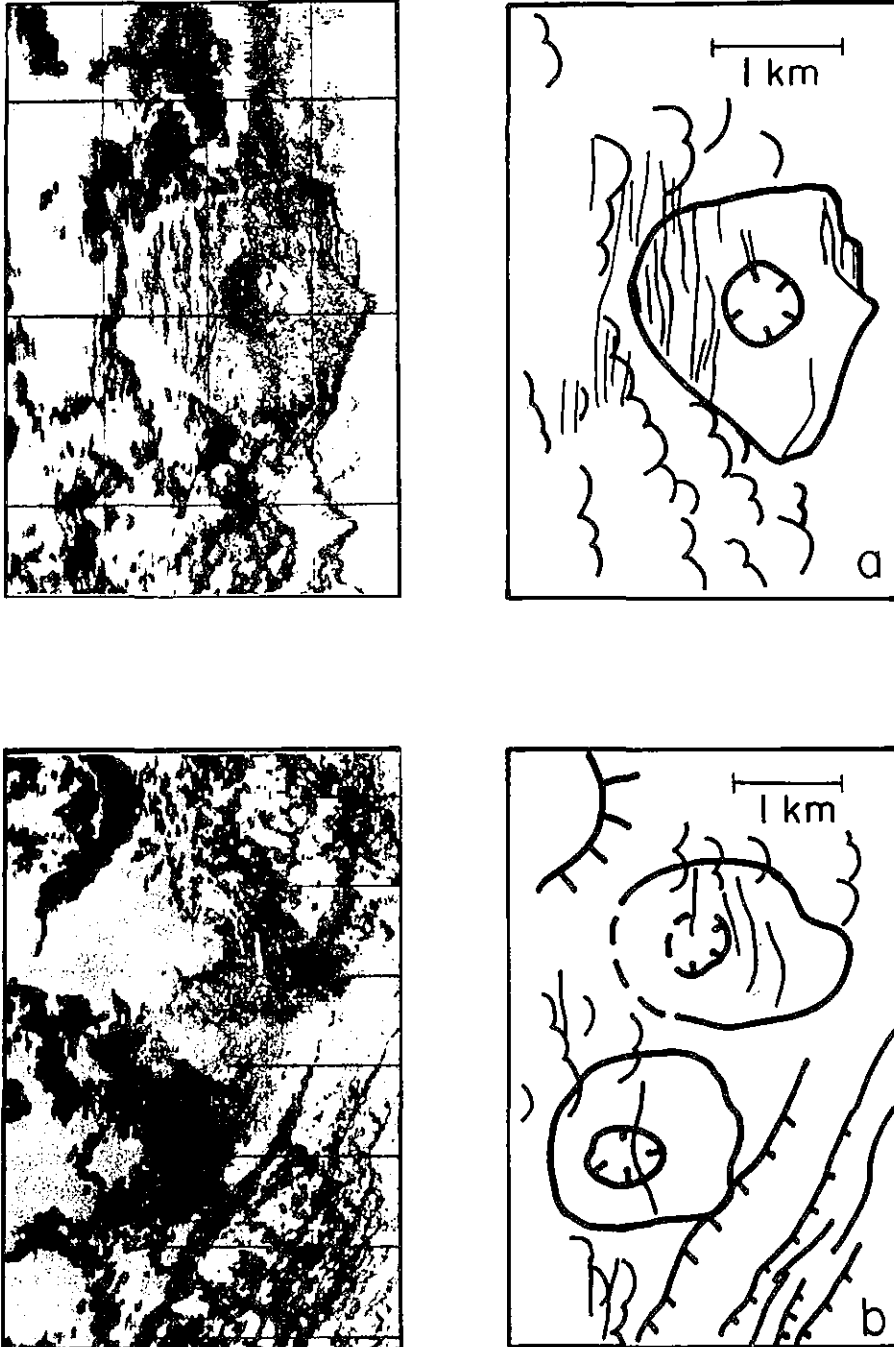


Fig. 6. (a) Sea MARS I image and interpretive line drawing of Serocki Volcano drilled at ODP Site 684, (b) Sea MARS I images and interpretive line drawings of two volcanoes from the MARK rift valley near 23°09' N.

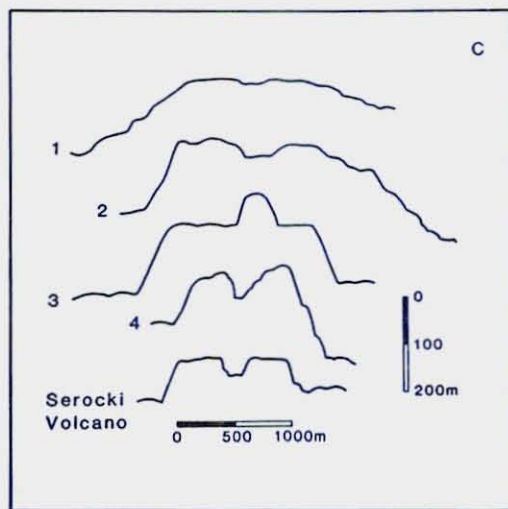


Fig. 6. (c) Representative volcano shapes based on subbottom profiler data (Serocki volcano is the lowermost profile). The volcanos typically stand 50–200 m high and are generally associated with a broad, flat summit plateau and a 10–60 m deep central crater. Vertical exaggeration is  $5\times$  (see Figure 10 for locations).

high-reflectivity zone and the flanking bands of lower reflectivity is quite distinct and approximately corresponds (to within 1 km) to the first appearance of tilted fault blocks which mark the boundary between the rift floor and walls (Figure 5a, from 3–5 km). A series of backtilted blocks ( $\sim 5^\circ$  tilt) with steeply dipping, valley-facing slopes are seen on both the eastern and western flanks of the rift walls (Figures 5b and 8c). The fault blocks are characterized by steep, inward-facing slopes and hummocky backsides. The sonar images reveal the widespread occurrence of fan-shaped bodies located along the base of inward facing slopes which are interpreted to represent talus and debris shed by active mass wasting processes. The ubiquitous distribution of erosional debris on the rift valley walls has been confirmed by direct observation (Karson *et al.*, 1987; Brown and Karson, 1988).

Structural dismemberment of the volcanic constructional terrain begins on the floor of the inner rift valley within the high-reflectivity zone. A compilation of fault/fissure spacing and associated scarp heights on these cross-axis profiles (Figure 9) reveals that fissures and faults are both more closely spaced ( $0.32 \pm 0.25$  km,  $N = 32$ ) and have smaller throws ( $48 \pm 47$  m,  $N = 32$ ) within the high-reflectivity zone on the rift valley floor than in the adjacent zones of

moderate and low reflectivity outside the central rift valley (spacing:  $0.95 \pm 0.80$  km,  $N = 24$ ,  $0.84 \pm 0.62$  km,  $N = 39$ , height:  $137 \pm 110$  m,  $N = 23$ ,  $120 \pm 86$  m,  $N = 33$ , respectively). The large scatter in these values is probably a reflection of the heterogeneous nature of the brittle crust and the local stress field. The increase in scarp height and spacing toward the flanks of the rift valley suggests that the sites of active faulting become localized and that most of the smaller faults and fissures observed in the center of the valley are buried by mass-wasting processes or post-tectonic volcanism.

A plot of cumulative fault throw with distance from the ridge axis (defined by an imaginary central line drawn between the inward facing scarps that mark the edge of the rift valley floor) reveals that, except at the rift floor/wall interface where a series of large throw faults create an abrupt step in the across-strike profile, normal fault (inward-facing) relief accrues at a relatively constant rate (Figure 9c). Outward-facing scarps account for only a minor amount of the total throw. The summed fault relief accumulated out into the rift mountains from the ridge axis exceeds the morphological depth difference (between that at the axis and that about 17 km from the axis) by about 700 m, implying that the undulating topography created by constructional ridges must, in part, be preserved and transported up into the rift flanks. That this is the case is demonstrated in Figure 5, where the height discrepancy is resolved by including the relief of the unfaulted backsides (eastern) of the rift mountains.

Closer examination shows that all relief within the high-reflectivity zone (about 250 m) can be achieved by normal faulting, but that beginning in the moderate-reflectivity zone, motion on faults becomes localized and grows at variable rates. The growth rates again become constant in the low-reflectivity rift mountains, which suggests that large-scale active faulting has largely ceased, or that all faults now grow at similar rates. Since average scarp spacing and heights do not indicate dramatic increases in normal faulting in the low-reflectivity zone (in fact, there is a slight decrease), we favor the former hypothesis. Furthermore, it seems intuitively unlikely that growth rates outside the valley would be identical along all three transects given the variability observed in the adjacent reflectivity zone. The constant slope also suggests that extreme amounts of rotation and back-tilting, or reverse faulting, both of which would show

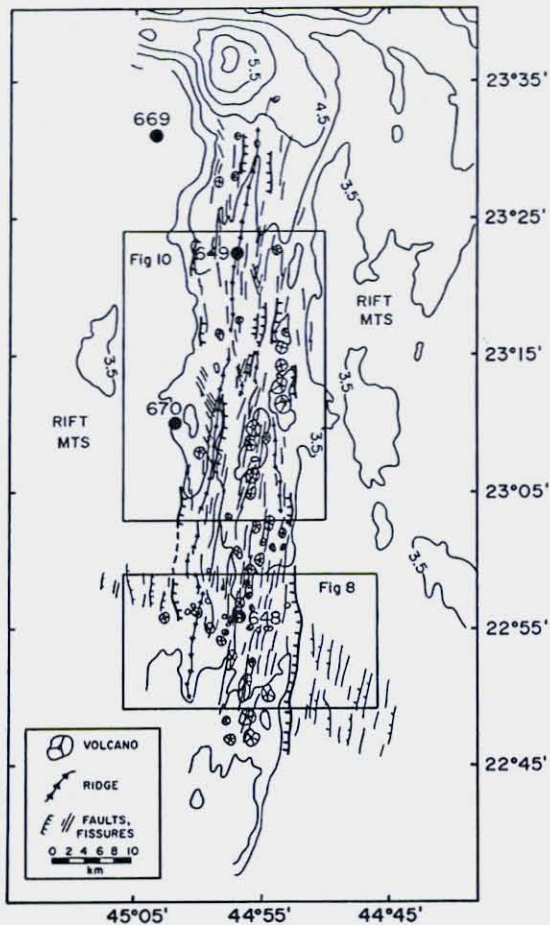


Fig. 7. Summary tectonic map of MARK rift valley based on our interpretation of the Sea MARC I data presented in this paper. Stippled area indicates the approximate location of the northern and southern ridge segments described in the text. Locations of Sea MARC I mosaics, 20-m Sea Beam maps and interpretive tectonic maps are shown for reference.

decreases in fault throw with distance, are not occurring over the first 10 km of flank topography.

The inference that faults are not reactivated during the subsequent uplift of the crust into the flanking rift mountains (which reach depths of <2000 m) is consistent with ALVIN observations that few of the scarps in the rift mountains appear to be tectonically active (Karson *et al.*, 1987). In addition no evidence was found in the Sea MARC I data for secondary volcanism in the rift mountains. Instead, the sonar images suggest that mass-wasting and gullying of scarp faces, and the resultant sedimentary products

which bury low-relief seafloor features, are the major geologic processes occurring on the walls of the rift valley and the flanking rift mountains.

### 5.3. ALONG-AXIS RIFT VALLEY STRUCTURE

The rift valley in the MARK area is segmented into two en-echelon spreading cells each displaying marked differences in morphology, volcanism, and tectonism, which are separated by a small zero-offset transform or discordant zone 40–50 km south of the Kane Fracture Zone (Figure 7). The northern spreading cell is dominated by a large constructional volcanic ridge, parts of which are magmatically and hydrothermally active. In contrast, the southern spreading cell appears to be in a predominantly extensional phase and is characterized by a NNE-trending band of small, fissured and faulted axial volcanos of various ages. These two ridge segments overlap creating a discordant zone between 23°05' N and 23°17' N that lacks a well-developed rift valley or neovolcanic zone.

#### 5.3.1. Northern Spreading Cell

A 20-m Sea Beam map, Sea MARC I mosaic and interpretive tectonic map of part of the northern spreading cell is shown in Figure 10. The linear ridge, which is the dominating structure of the rift valley floor north of 23°17' N, is characterized by highly reflective, hummocky acoustic textures that are indicative of fresh, unsedimented pillow lavas and/or pillow breccia (Figures 10b and 11a). In general, the ridge is undisrupted by the extensive faulting and fissuring that is associated with the surrounding seafloor, and in a few locations it is clear that the ridge has been constructed on top of this older tectonized crust (Figure 11a). These observations, together with bottom photographs and ALVIN dives in this area (Karson *et al.*, 1987; Brown and Karson, 1988), are all consistent with this being a constructional volcanic feature that has formed very recently by voluminous fissure eruptions along a 20–30-km-long, NNE-trending rift zone in the median valley.

This is the largest single constructional volcanic feature ever found in the Mid-Atlantic Ridge rift valley, dwarfing Mt. Venus and Pluto in the FAMOUS area (Ballard and van Andel, 1977). It is, however, similar in scale and shape to the tapered ridges identified on the Sea Beam maps in the flanking rift mountains (see above discussion). It rises up

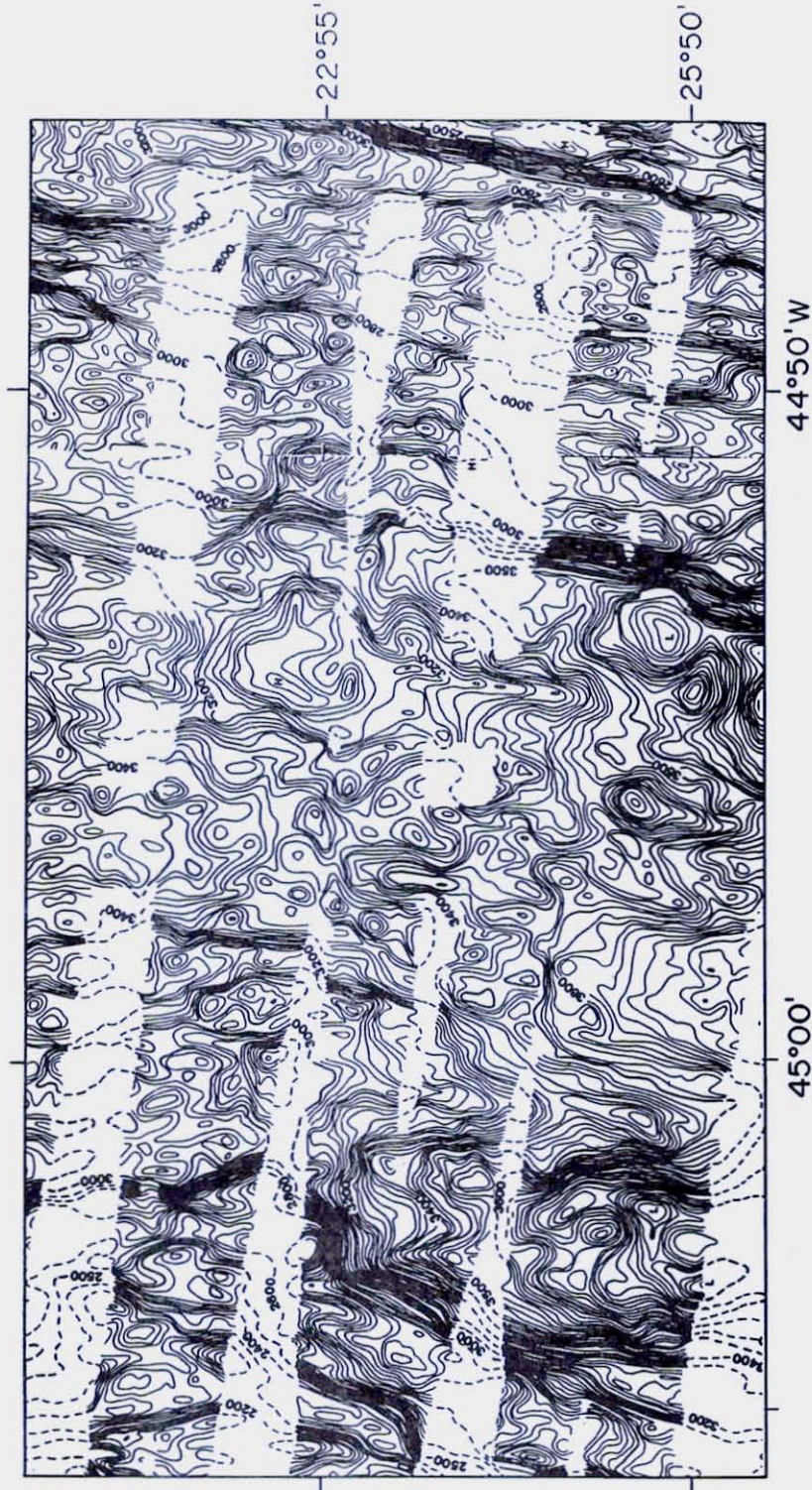


Fig. 8. (a) Sea Beam map of a section across the rift valley near  $22^{\circ}55' N$ , near Site 648 (see Figure 7 for location).

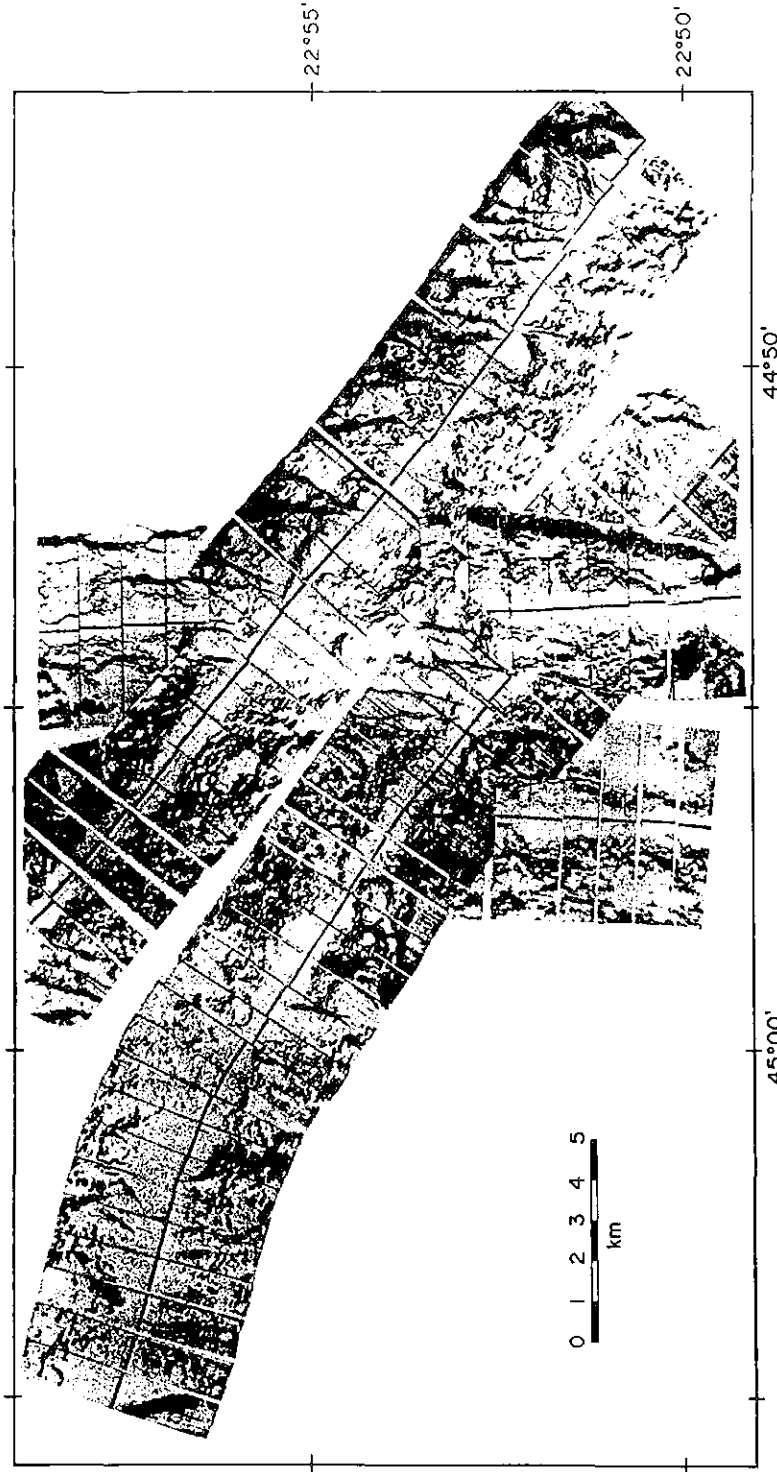


Fig. 8. (b) Sea MARC 1 mosaic of the area shown in Fig. 8(a).



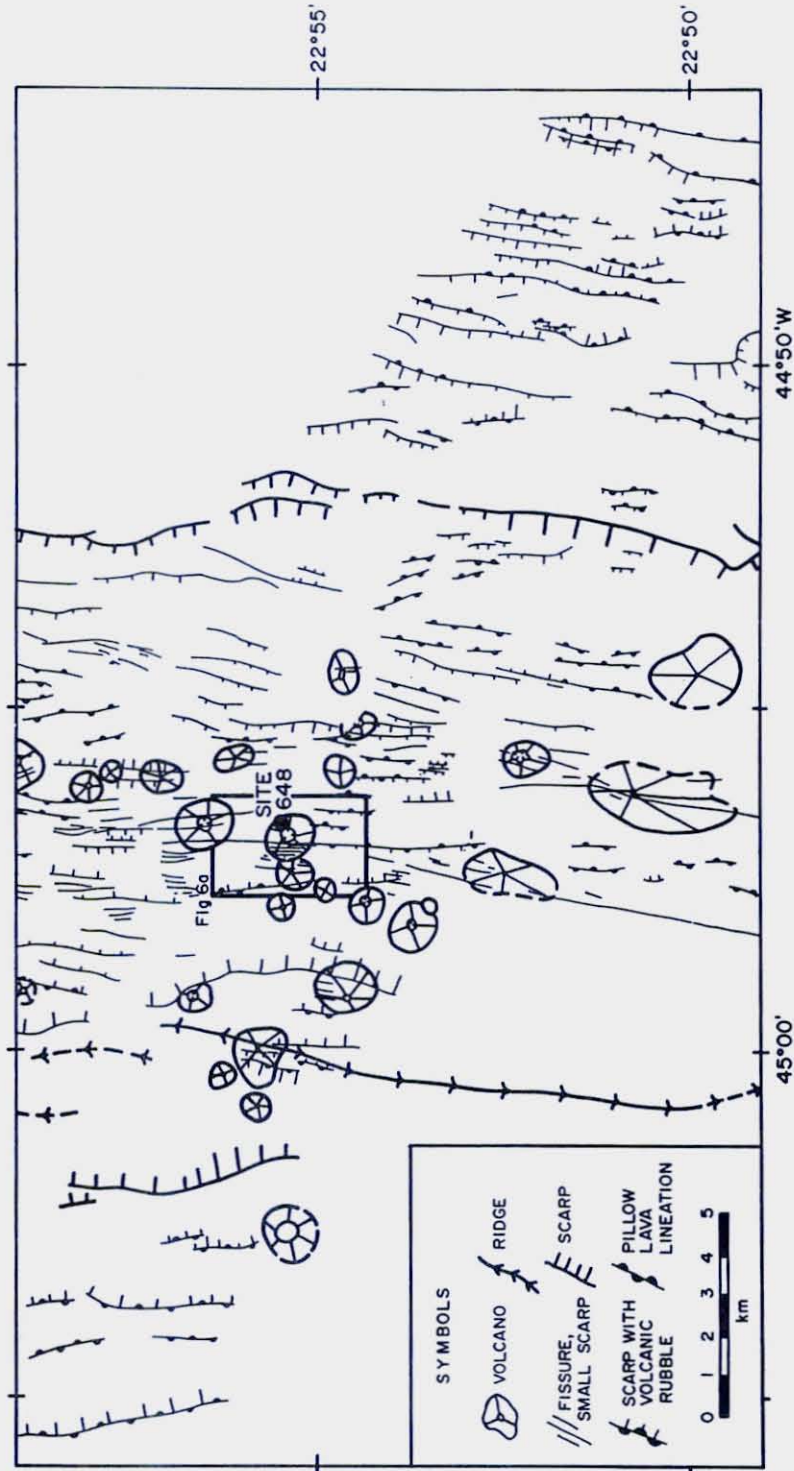


Fig. 8 (c) Interpretive tectonic map of the area shown in Figure 8(a).

LAURA S. L. KONG ET AL.

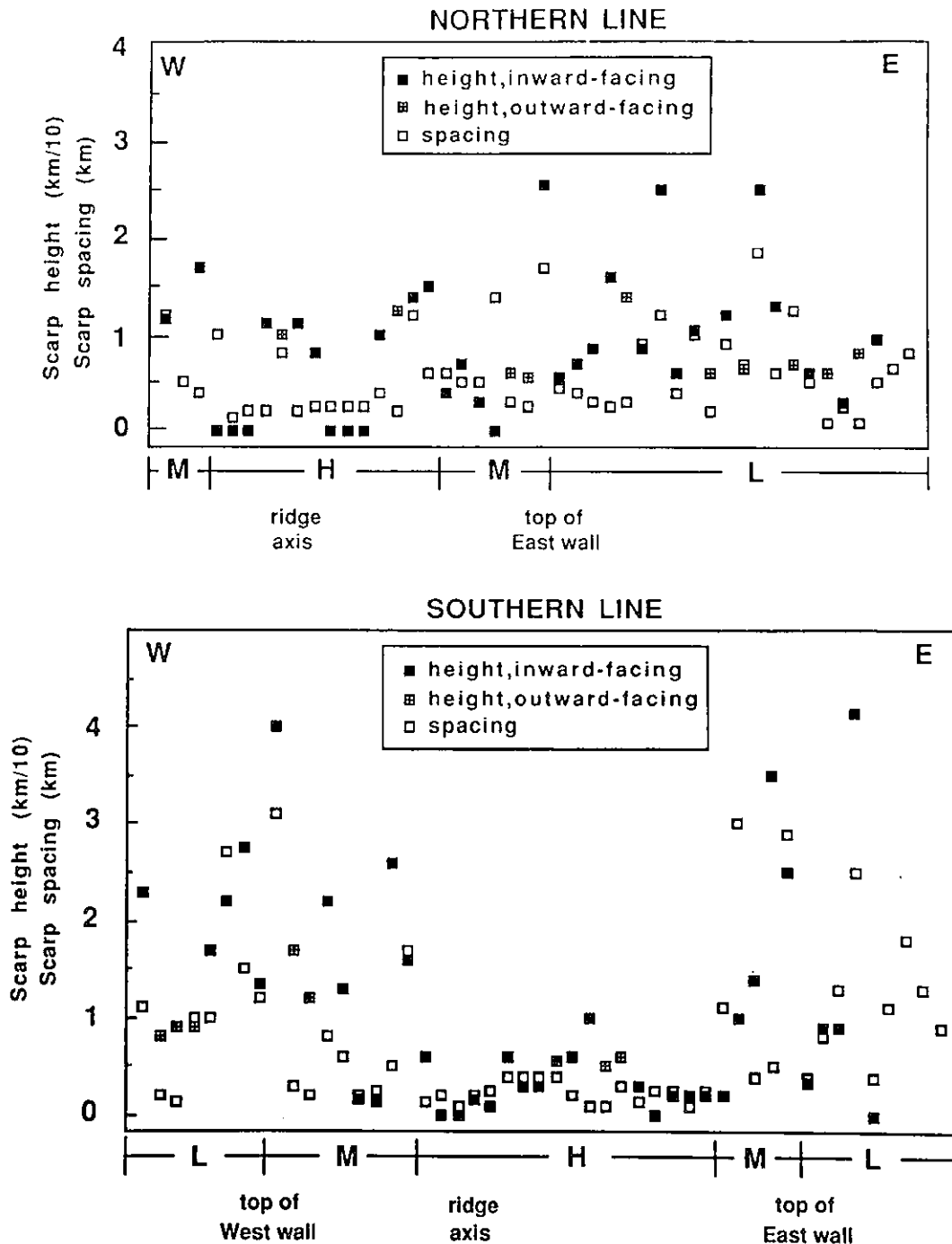
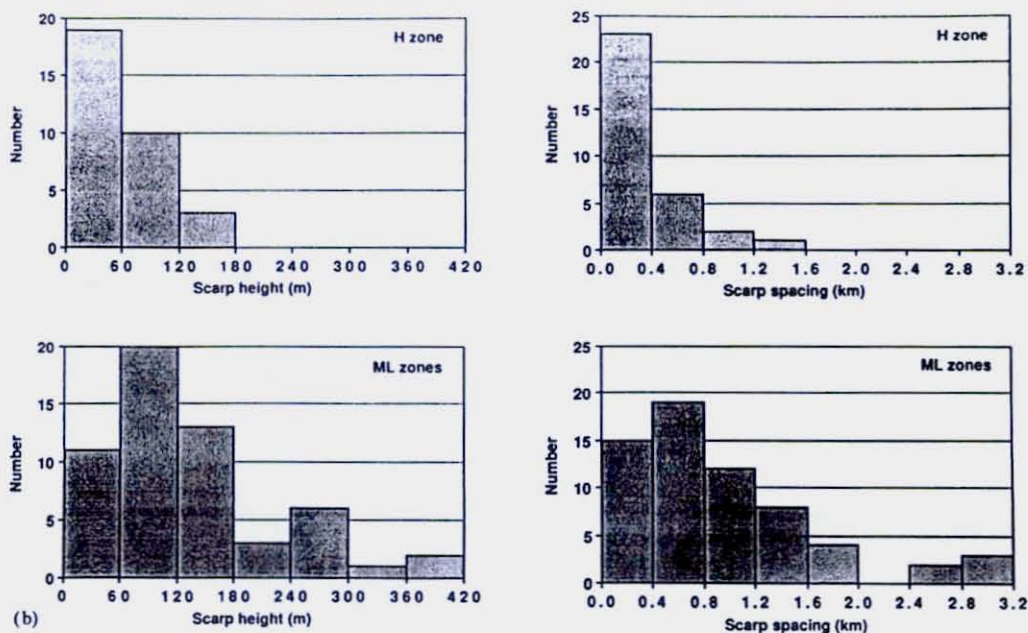
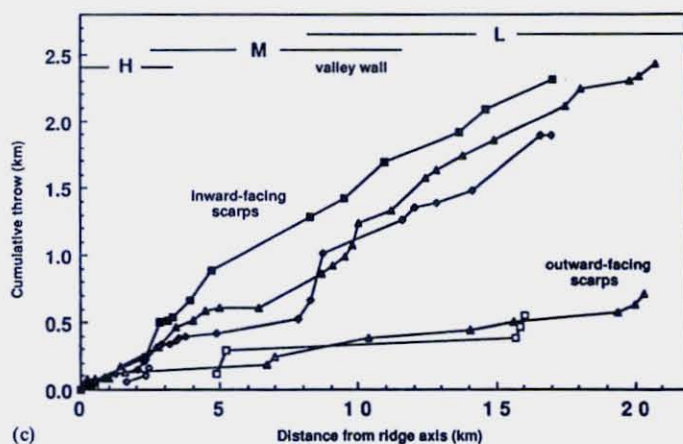


Fig. 9. (a) Scarp height and spacing vs. scarp number across the median valley near 22°55' N. H, M, and L refer to zones of high, medium, and low reflectivity discussed in the text. Fissures are plotted with zero height, and unmeasurable scarp heights are not plotted. Estimated reading errors in spacing and heights are 100–200 m and 20–30 m, respectively, with height data probably underestimated due to talus debris at the base of scarps. Transect lengths are 38 km (South) and 21 km (North).

## THE MORPHOLOGY AND TECTONICS OF THE MARK AREA FROM SEA BEAM AND SEA MARC I OBSERVATIONS



(b)



(c)

Fig. 9. (b) Compilation (height and spacing) of all inward and outward-facing scarps within H and ML zones across the median valley near  $22^{\circ}55' N$ . Larger spacing and greater heights of scarps are observed in the M and L zones than in the H zone (inspection of (a) indicates that H, ML grouping is most appropriate). This observation is insensitive to bin spacing and heights, (c) compilation fault throw vs. distances from ridge axis for the three sub-transects (southwest - squares, southeast - diamonds, northeast - triangles) near  $22^{\circ}55' N$ . Each point represents individual spacing/height pair as shown in (a). Overlap of H, M, L zones show variability in width of zones. See text for discussion.

LAURA S. L. KONG ET AL.

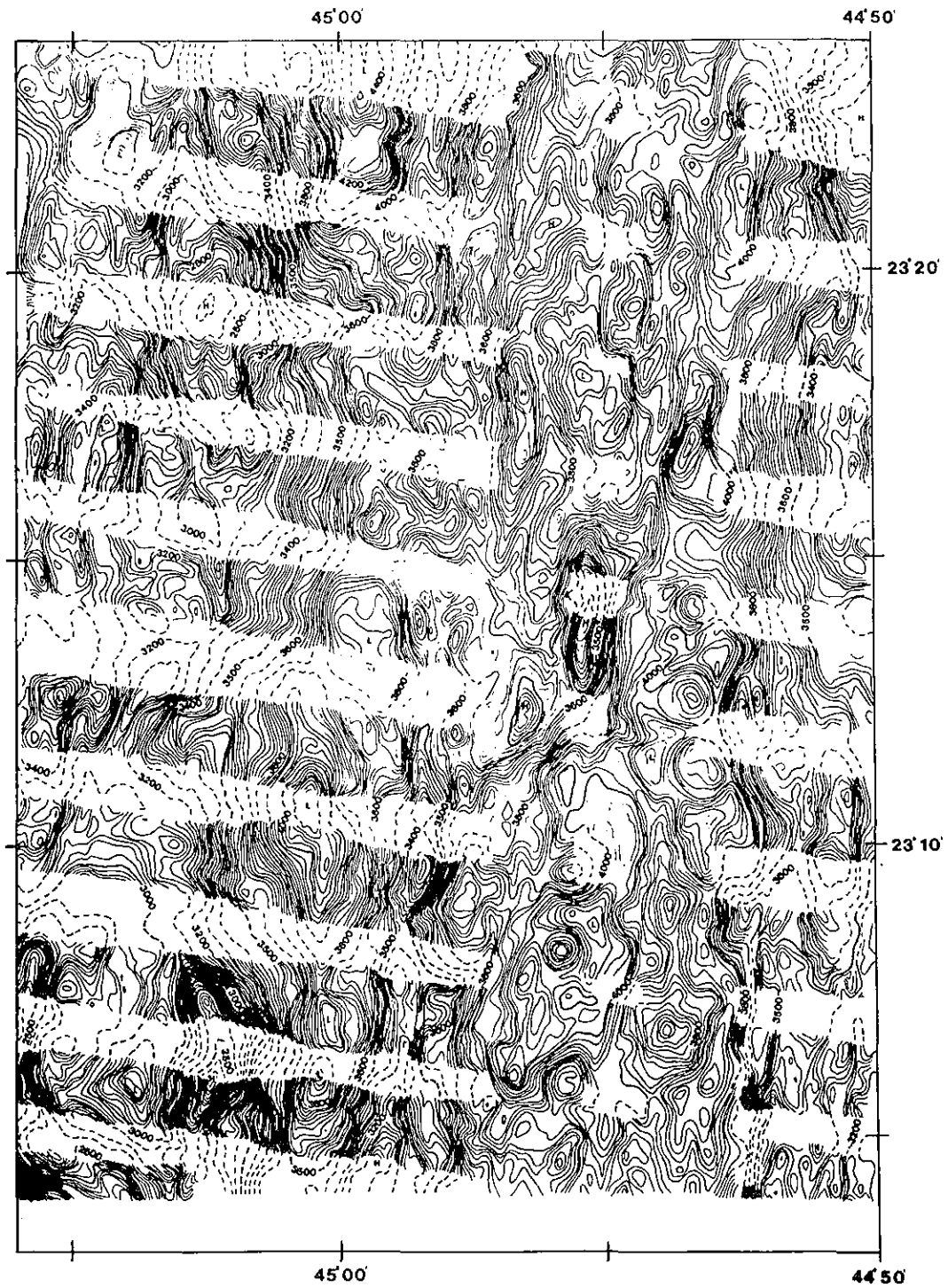


Fig. 10. (a) Sea Beam map of the inner rift valley between 23°03' N and 23°24' N (see Figure 7 for location).

## THE MORPHOLOGY AND TECTONICS OF THE MARK AREA FROM SEA BEAM AND SEA MARC I OBSERVATIONS

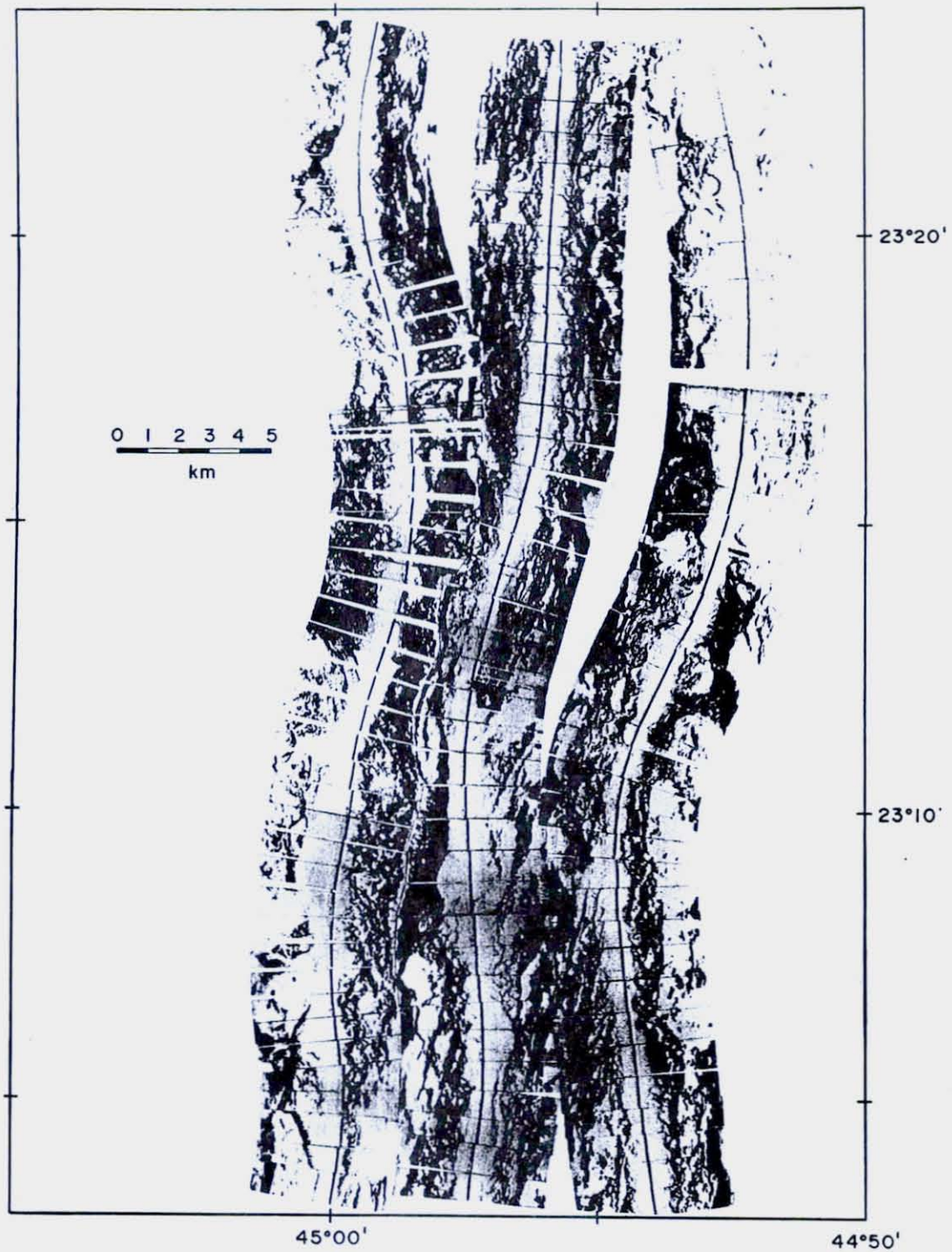


Fig. 10. (b) Sea MARC I mosaic of the area shown in Figure 10(a).

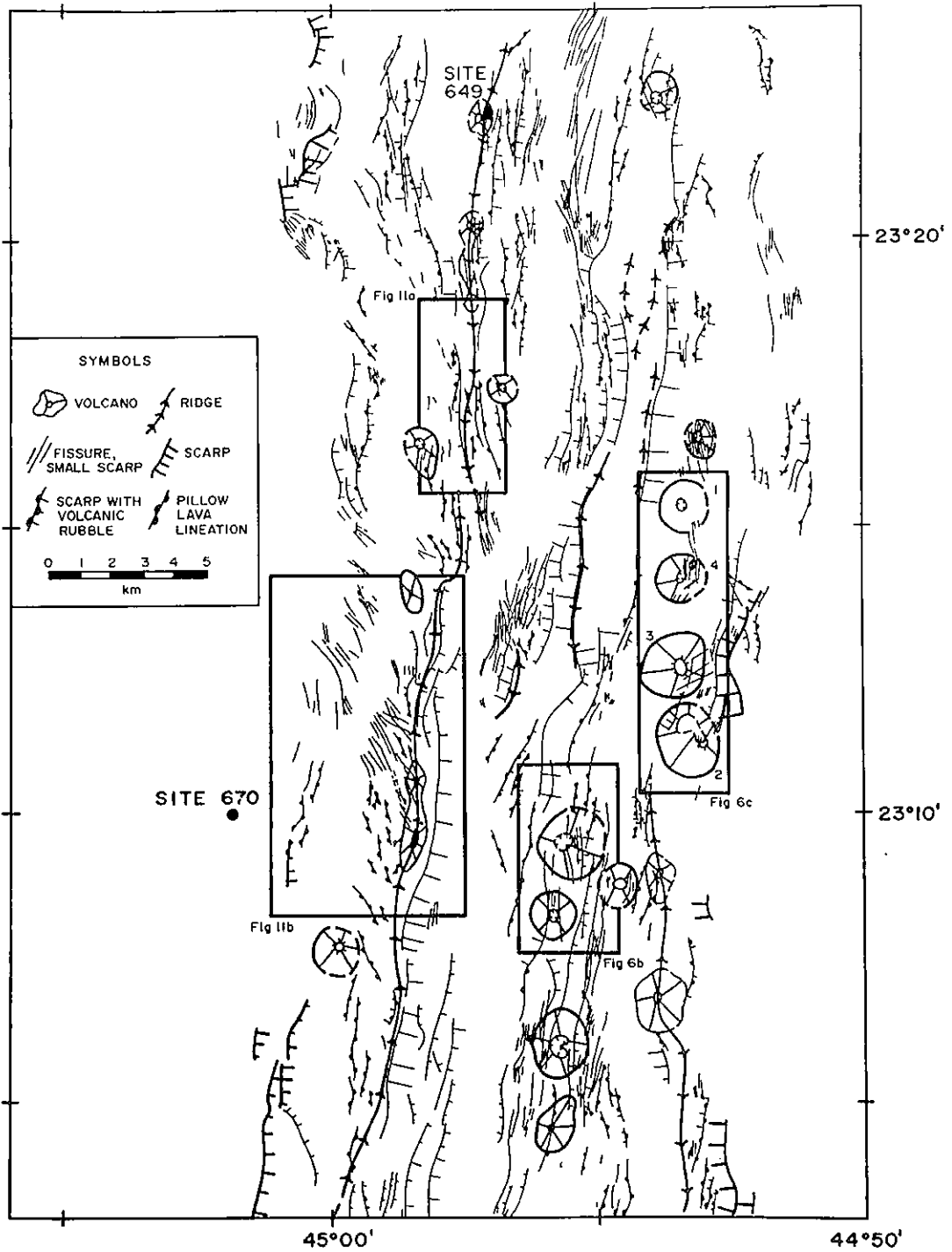


Fig. 10. (c) Interpretive tectonic map of the area shown in Figure 10(a).

## THE MORPHOLOGY AND TECTONICS OF THE MARK AREA FROM SEA BEAM AND SEA MARC I OBSERVATIONS

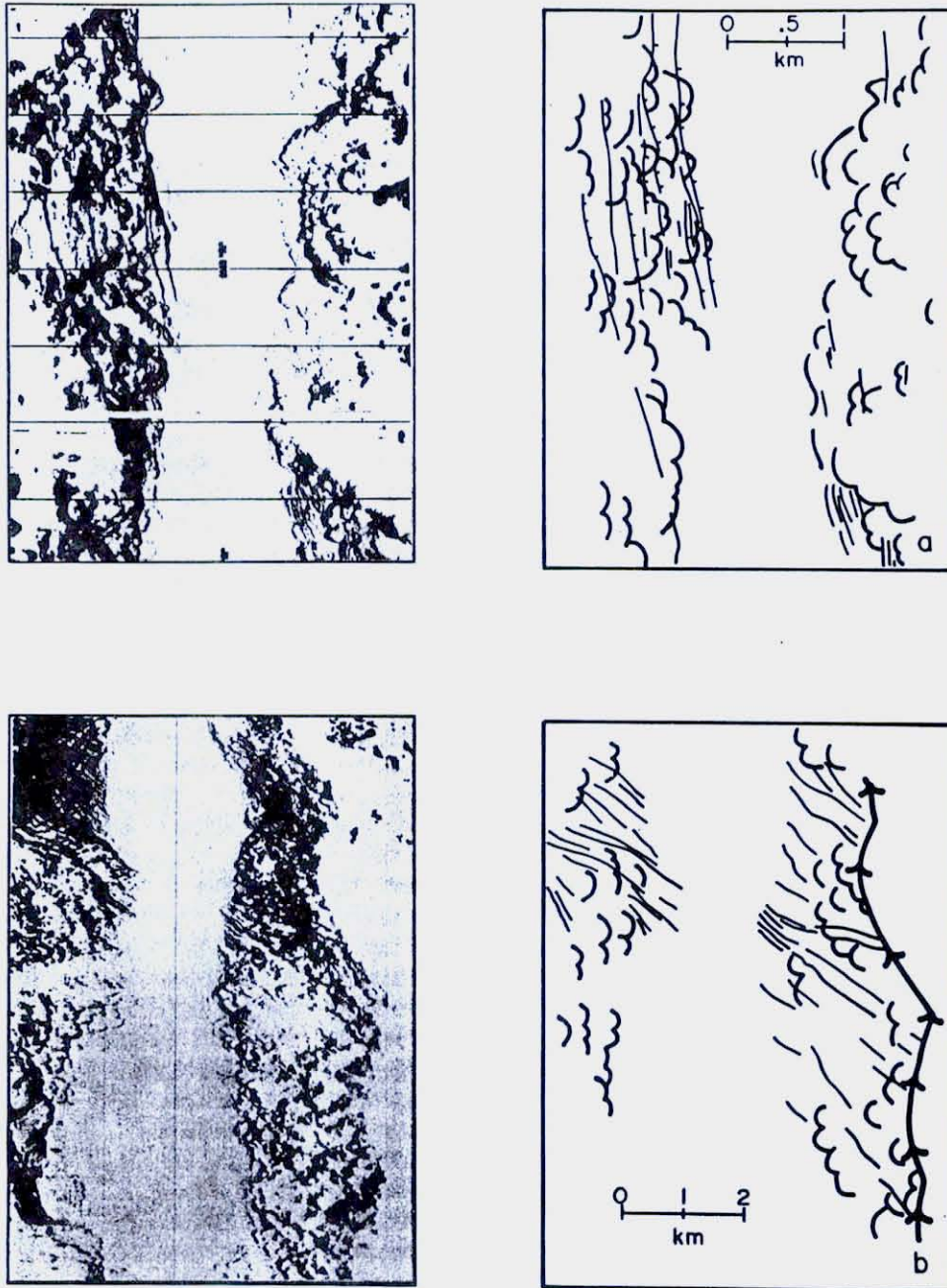


Fig. 11. Sea MARC I images and interpretive line drawings showing: (a) the young flows of the median volcanic ridge built on older, fissured crust along the northern ridge segment, and (b) oblique structural lineations in the discordant zone that separates the northern and southern spreading cells near  $23^{\circ}15' N$  (see Figure 10c for locations).

to 600 m above the surrounding seafloor and, at its widest, is more than four kilometers across at its base. Several individual bathymetric peaks spaced 2–4 km apart can be identified along the ridge in the Sea Beam and Sea MARC I records. The largest of these is located near 23°22' N where evidence for hydrothermal activity was first discovered during the site survey (Kong *et al.*, 1985), and an active, high-temperature vent field was subsequently discovered and drilled at Site 649 (Leg 106 Scientific Party, 1986). This vent field, known as the Snake Pit hydrothermal area, consists of at least six massive sulfide mounds, two of which are hydrothermally active. The mounds are composed of active and inactive black smoker chimneys and sulfide debris deposits covering at least 0.16 km<sup>2</sup> (Leg 106 Scientific Party, 1986; Thompson *et al.*, in press; Brown and Karson, 1988). Karson *et al.* (1987) report large Mn anomalies at depths of about 3500 m in this area, suggesting the presence of additional, still undiscovered, vents at greater water depths.

South of 23°20' N this volcanic ridge becomes older-looking and more subdued, finally losing its topographic expression near 23°15' N (Figure 10a). Farther south another, nearly colinear, ridge emerges that can be traced southward along the western rift valley wall for more than 40 km (Figure 3). It is characterized by a highly reflective eastern side, interpreted to be a major valley-facing fault scarp or scarps, and a western side with lower reflectivity and hummocky acoustic texture (Figure 10b). An ALVIN traverse across this area revealed the valley-facing slope to be composed of a series of steep fault scarps and talus ramps, while the outward-facing western slope is less steep and composed of moderately sedimented pillow lavas (Karson *et al.*, 1987; Brown and Karson, 1988).

Brown and Karson (1988) have interpreted this ridge as an uplifted and rotated fault block that is in the process of being incorporated into the rift mountains. They view this feature as being unrelated to the younger, colinear volcanic ridge that dominates the northern rift valley floor, and place the boundary between the northern and southern spreading cells near 23°15' N. However, Schulz *et al.* (1988) have shown that the magnetization high associated with the northern volcanic ridge is continuous across this zone and can be traced, albeit with lower magnetizations, south to about 23° N along this feature. The

tapering of this ridge north and south of its shallowest point near 23° N (note the 3500 m contour in Figure 3) is strikingly similar in shape, size, and relief to the present shape of the median volcanic ridge now forming in the northern rift valley, indicating to us that this ridge is also a constructional volcanic feature, although older, that has been truncated by faulting on its eastern side as it has been uplifted into the western rift mountains.

### 5.3.2. Southern Spreading Cell

The spreading cell in the southern part of the MARK area is characterized by a NNE-trending (010°) band of small axial volcanos that can be traced from the along-axis topographic high, 80 km south of the Kane Transform, northward along the eastern side of the median valley to where they intersect the eastern rift valley wall near 23°15' N (Figure 7). Representative sonar images of two of those volcanos are shown in Figure 6a, b; bathymetric profiles across several volcanos are plotted in Figure 6c. They typically stand 50–200 m above the surrounding seafloor and are generally associated with a broad, flat summit plateau bounded by steep scarps along their outer rim and a 10–60 m deep central crater. The volcanos are generally circular in shape, range from 1–3 km in diameter, and display a simple linear relationship between volcano height and diameter (Figure 12). Bottom photographs of Serocki Volcano, drilled at ODP Site 648 (Figure 6a), show that the summit plateau is composed of moderately sedimented bulbous and elongate pillow lavas, 1–2 m in diameter with only isolated sheet flows outcropping near the rim of the central crater (Humphris *et al.*, 1986). The crater floor is filled with highly fractured basaltic rubble.

The Sea MARC I images clearly show that these volcanos have been constructed on older, fissured and faulted seafloor and are not all of the same age (Figure 6). Some of the volcanos are dissected by numerous faults and fissures suggesting that they are old enough to have experienced a significant amount of tectonism, while others are more pristine. In the case of Serocki volcano, several different episodes of volcanism and tectonism can be identified (Figure 6a). In the first phase, the volcano was constructed on seafloor that had already been extensively fissured and faulted. These earlier fissures have been buried by the volcano, but are still seen in the surrounding



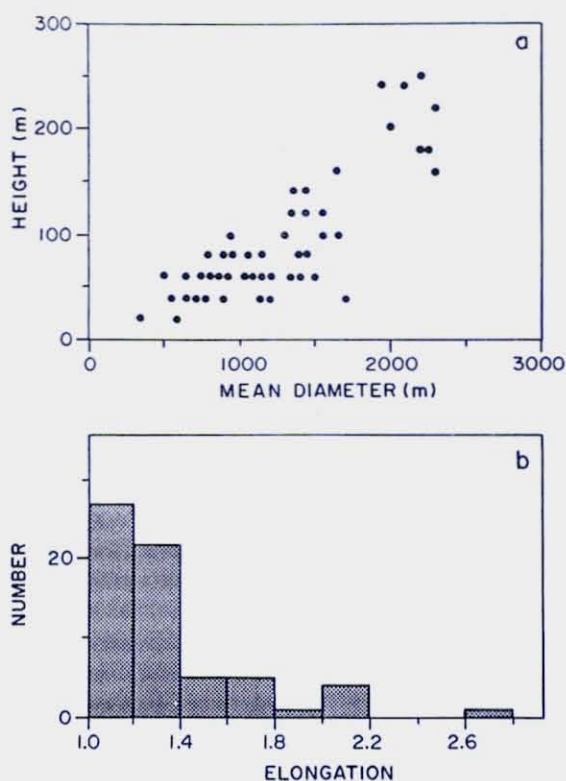


Fig. 12. Compilation of size and shape statistics for small axial volcanos found in the MARK rift valley: (a) plot of height vs mean diameter, (b) elongation (length/width ratio) histogram.

seafloor. Extensional tectonism continued after the volcano was formed, disrupting the western half of Serocki Volcano with a series of valley-parallel faults and fissures. Finally, a few younger lava flows with very high reflectivities have buried older lavas east of the summit plateau. Karson *et al.* (1987) report dredge samples from one of these areas near Serocki Volcano recovered the freshest basalt yet sampled from the MARK area.

The age of these volcanos is difficult to estimate with any accuracy, but the extensive amount of tectonism they have experienced, the absence of any known hydrothermal activity, and the relatively heavy sediment cover on the summit plateaus of many of the volcanos indicates some could be at least several tens of thousands of years old (Karson *et al.*, 1987). The source (or sources) of the volcanism forming these features is unknown. Many of the

'older' volcanos are located within or near the highly-reflective neovolcanic zone in the southern spreading cell, suggesting they are post-tectonic eruptions associated with a primarily extensional phase of spreading.

The location of a zone of recent volcanism in the rift valley south of  $22^{\circ}45'$  N is enigmatic (Figure 13). The bathymetric data indicate that the rift valley floor is broad (20 km), anomalously deep along its eastern margin, and devoid of any linear or circular features that would be suggestive of volcanic constructional edifices. In the southwestern corner of the MARK rift valley there is an elongate ridge that is morphologically similar to the volcanic ridge of the northern cell (Figure 13). However, it is located on a terrace that sits almost 1000 m above the rift valley floor and we interpret this ridge to be an extinct eruptive fissure that is now being transported intact away from the plate boundary zone and out of the rift valley. Given these characteristics and the seismicity in this area (Toomey *et al.*, 1985; 1988), we suggest that this portion of the southern cell is dominated by extensional tectonism and has been devoid of significant volcanism in the recent past.

### 5.3.3. Discordant Zone

The boundary between the northern and southern spreading cells appears to lie in a complex transition zone between  $23^{\circ}05'$  N and  $23^{\circ}17'$  N. The rift valley in this area is poorly developed, lacking the high flanking rift mountains that are present elsewhere in the MARK area. The rift valley floor also lacks a well-defined neovolcanic zone on Sea MARC I records, and the topography of the rift valley floor is dominated by a series of rugged, fault-bounded, axis-parallel ridges and troughs (Figure 10). Brown and Karson (1988) report that the western and central portions of the median valley floor in this area are blanketed by a fairly thick sediment cover (about 0.5 m) and display no evidence of recent volcanic activity. A line of five conical volcanos lies near the foot of the eastern rift valley wall between  $23^{\circ}10'$  N and  $23^{\circ}17'$  N (Figure 10c). These volcanos, which appear to be the northernmost extension of the volcanos that have formed along the southern spreading cell, are not extensively faulted, but are associated with a fairly thick sediment cover indicating an age of several tens of thousands of years (Karson *et al.*, 1987).

LAURA S. L. KONG ET AL.

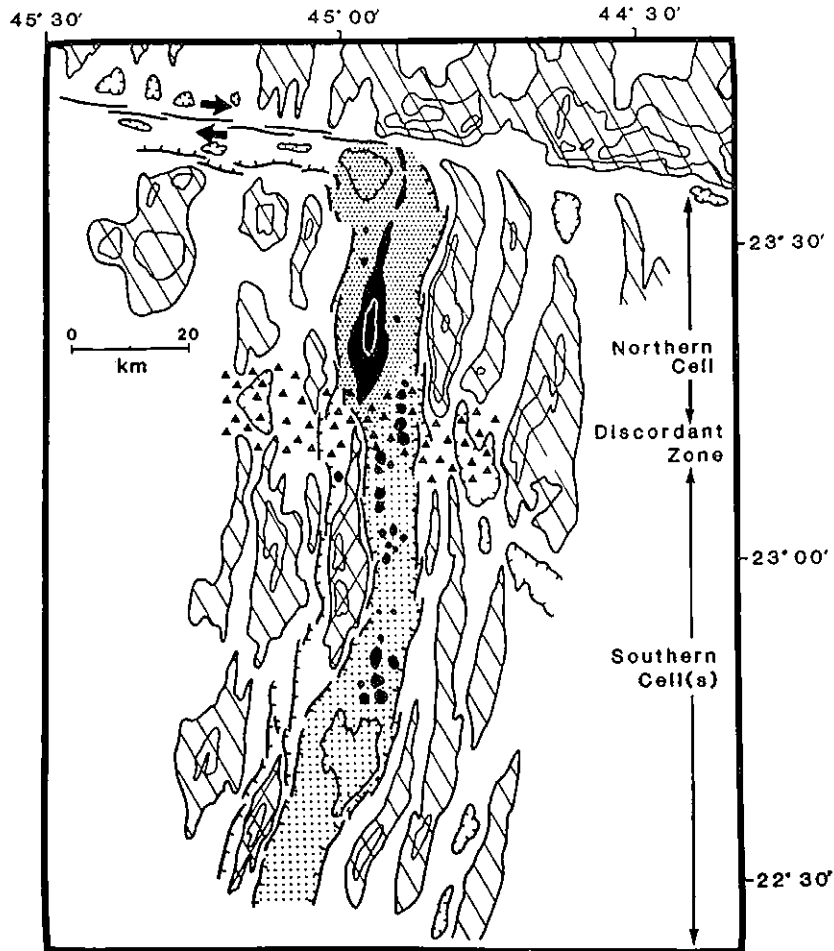


Fig. 13. A map outlining the major morphotectonic elements of the MARK arc. The across-strike limits of the rift valley floor are defined by a braided network of opposing scarps. The rift valley floor is made up of at least two spreading cells separated by a broad discordant zone (marked by triangles) between 23° N and 23° 17' N. The volcanic constructional edifices most recently created along each cell are shown in black. Elongate ridges which flank the plate boundary are identified as terraces along the western rift valley wall (double diagonal lines) or as rift mountains (diagonal lines). We propose that these flanking ridges are extinct volcanic constructional edifices that were created along the floor of the rift valley during a waxing phase of magmatism. Subsequent to construction these volcanic ridges were partitioned by faulting to one plate boundary or the other and rafted up and out of the rift valley largely intact.

This part of the median valley is characterized by generally low crustal magnetizations (Schulz *et al.*, 1988) and was found by Purdy and Detrick (1986) to mark the boundary between relatively normal seismic crustal thicknesses and velocities to the south and thinner crust with no distinct seismic layering to the north. Outcrops of serpentinized peridotites and greenstones were found by submersible along the western edge of the rift valley (Casey, 1986; Karson

*et al.*, 1987). Subsequent drilling at ODP Site 670 by the R/V JOIDES RESOLUTION penetrated over 100 m of serpentinite (Detrick, Honnorez, Bryan, Juteau *et al.*, 1988). The serpentinites show evidence of progressive retrograde alteration at very high temperatures, ductile deformation and subsequent hydration at progressively lower temperatures (Casey, 1986). The presence of these serpentinites suggests uplift of hydrated mantle beneath an

anomalously thin crustal section and/or diapirism of the serpentinites along major faults (Brown and Karson, 1988).

Schouten *et al.* (1985) have suggested the presence of a small ( $\sim 10$ – $15$  km), left-lateral transform at this latitude based on offsets of magnetic anomalies preserved in the older crust flanking the rift valley. Schulz *et al.* (1988) demonstrated that the magnetization high associated with the central magnetic anomaly is also offset left-laterally about 8 km between  $23^\circ$  N and  $23^\circ 05'$  N indicating a small offset still exists in the zone of accretion within the present median valley south of  $23^\circ 15'$  N. However, despite the evidence for an offset in the magnetics at this latitude, there is no indication of time-averaged, strike-slip motion along this boundary. Sea MARC I data show that within the present inner rift valley most tectonic lineaments retain their north-northeasterly orientation across this zone; transform-parallel trends are not observed (Figure 10c). The only features that could be related to strike-slip faulting are a series of sub-parallel, oblique lineations observed near  $23^\circ 10'$  N on the western flank of the median volcanic ridge (Figure 10c). These lineations, which may be fissures formed by the influence of a right-lateral shear couple on the regional extensional stress field, are observed on the western slope of the southern volcanic ridge and curve to the northwest ( $295^\circ$ ) toward the western edge of the rift valley (Figure 11b). The overprinting of these fissures by the volcanic ridge indicates they predate the formation of this feature, which itself is at least several tens of thousands of years old. The absence of transform-parallel trends and high magnetization values to the east of the southern ridge may imply that the accretionary axis has jumped very recently leaving the NW-trending lineaments as a record of past shear couple.

## 6. Discussion

The most remarkable aspect of the Sea Beam and Sea MARC I data described in this paper is the complexity of the rift valley structure in the MARK area. Based on previous work in the FAMOUS (Ballard and van Andel, 1977; Macdonald and Luyendyk, 1977) and AMAR (Crane and Ballard, 1981; Stakes *et al.*, 1984) rifts on the Mid-Atlantic Ridge, we had expected a simpler, symmetrical rift

valley structure in cross-section with a narrow (1–3 km wide) neovolcanic zone in the center of the median valley, flanked by marginal lows with uplifted and block-faulted terraces on the walls of the rift valley. We also expected systematic variations along the rift valley toward the Kane Transform such as those proposed by Francheteau and Ballard (1983). Their model predicted that the most recent volcanism, the most fluid lavas and the greatest hydrothermal activity would be associated with the median valley topographic high 70–80 km south of the Kane Fracture Zone, while a decrease in magmatic budget and an increase in the relative importance of faulting and fissuring were expected in those portions of the rift valley nearest the fracture zone.

The results described in this paper, and the submersible observations reported by Karson *et al.* (1987) and Brown and Karson (1988), indicate a complex, segmented rift valley with major changes in magmatic budget, tectonic style and hydrothermal activity along-axis at a 100-km-scale that are quite different than the results from these earlier studies of shorter ridge segments would have predicted. The median valley topographic high at  $22^\circ 55'$  N in the MARK area is actually a relatively old feature which is heavily fissured and faulted, with only minor, recent volcanic activity. The most voluminous volcanism, and the only evidence of hydrothermal activity in the MARK area, is found along a portion of the rift valley only 20–30 km from the Kane Fracture Zone. These results suggest that the long-wavelength (40–100 km) decrease in the depth of the rift valley floor that is associated with increasing distance from the large age-offset Kane Transform is a reflection of deep seated patterns of mantle flow and melt generation. This long wavelength signal clearly cannot be used to predict where, at any given time, recent volcanism and/or hydrothermal activity may be located along the plate boundary.

The neovolcanic zone in the MARK rift valley is discontinuous along-strike and appears to be associated with two NNE-trending, en-echelon spreading cells, each displaying a distinct volcanic style, and each striking obliquely across the floor of the rift valley. While a central constructional volcanic ridge with marginal lows characterizes the northern rift valley, recent volcanic activity in the southern portion of the MARK area is associated with a band of small volcanos of varying ages that spread, in some

cases, across the entire width of the rift valley (e.g. 22°55' N–23°15' N). The most anomalous feature discovered is a discordant zone 40–50 km south of the Kane Fracture Zone which lacks a well-developed neovolcanic zone and flanking rift mountains, and which is associated with outcrops of serpentinized peridotite on the western rift valley floor.

Three major factors appear to be responsible for the structural and tectonic complexity of the MARK area. The first is the segmentation of spreading in this area into two distinct spreading cells. This segmentation is clearly manifested in the regional bathymetry and structural fabric of the rift valley, but is also recorded in the flanking magnetic anomalies which indicate that the relative positions and dimensions of the spreading cells have remained similar along this part of the Mid-Atlantic Ridge for tens of millions of years (Schouten *et al.*, 1985; Schulz *et al.*, 1988). The differences observed in volcanic and tectonic activity within the MARK area may thus reflect, in part, spreading cells in different stages of a magmatic/tectonic cycle (Macdonald, 1983; Pockalny *et al.*, 1988) or relative differences in the importance of magmatism and tectonism within adjacent ridge segments (Karson *et al.*, 1987). We favor the first explanation since we can recognize a similarity in the terrain elements developed in these two contiguous spreading cells with morphological patterns repeated off-axis that mimic the shape and dimensions of features found within the rift valley.

A second factor which may have contributed to the tectonic complexity of the MARK area is the pattern of asymmetric spreading that characterizes this portion of the Mid-Atlantic Ridge (Schouten *et al.*, 1985; Schulz *et al.*, 1988). Over at least the past 3 Ma this asymmetric spreading has been caused by a series of small (~10 km), eastward ridge jumps resulting in faster spreading rates to the west (14 mm yr<sup>-1</sup>) than to the east (11 mm yr<sup>-1</sup>). Since the present rift valley floor is only 10–17 km wide, these jumps probably occurred by a relocation of the neovolcanic zone within the rift floor. This episodic relocation of the neovolcanic zone will lead to a complex overprinting of volcanic and tectonic patterns and could partially explain the structural and topographic heterogeneity of the rift valley.

Finally, the structure of the MARK rift valley is complicated by the presence of a small ridge-axis discontinuity between 23°07' N and 23°17' N. This

boundary separates crust with distinctly different seismic structures (Purdy and Detrick, 1986) and magnetic signatures (Schulz *et al.*, 1988), and is itself associated with a zone of very anomalous bathymetry, seismic properties and geologic structure (Purdy and Detrick, 1986; Karson *et al.*, 1987). There are, however, no structural relationships defined in the Sea Beam and Sea MARC I data to suggest that this kind of ridge axis discontinuity has behaved in a rigid fashion (e.g., a transform). Ridge-axis-parallel structures (e.g., ridges, troughs, scarps) within the rift valley do not terminate against cross-cutting structures that strike at a high angle to the plate boundary. Rather, terrain elements exhibit continuity into and, in some cases, across the discordant zone indicating it is not a boundary but an area across which magmatic and tectonic events associated with the opposing spreading cells episodically cross. Terrain relationships exhibited in the rift mountains that flank the discordant zone indicate that this type of discontinuity has persisted for at the least one to two million years. Magnetics data, however, indicate that the magnitude of this offset was larger at some time in the past and may have behaved rigidly accommodating strike-slip strains along a narrow boundary parallel to the opening direction (Schulz *et al.*, 1988).

This discordant zone may be analogous to those non-transform offsets recently described on the fast-spreading East Pacific Rise. The scale of the offset (~8 km), the overlap in the ridge segments and their associated magnetization highs, and the absence of any evidence of strike-slip tectonism all suggest that this 'zero-offset' transform or discordant zone is a reasonable slow-spreading ridge analogue to the overlapping spreading centers found on the East Pacific Rise (Macdonald and Fox, 1983; Lonsdale, 1983).

Another interesting observation of this investigation is the remarkable similarity of the terrain in the rift valley floor with the flanking ridges of the rift mountains. The most striking morphotectonic feature of the northern portion of the MARK rift valley is the long (several 10s of km), 300–800 m high ridge that lies along the center of the valley. This ridge, which is known to be a volcanic constructional edifice (Karson *et al.*, 1987), has the distinctive shape of a biconvex lens in plan view. At approximately the midpoint, the ridge is at its maximum width and its

width diminishes towards either end. An along-strike depth profile shows that the ridge is shallowest near its midpoint with depths increasing steadily towards the ends of the ridge. This distinctive morphology is likely to be the product of a fissure eruption where melt has been delivered to a shallow level reservoir located beneath the central portion of the ridge. Once emplaced at shallow levels, some melt moves laterally away from the eruption center along extensional fissures. The distinctive biconvex shape of the ridge reflects the fact that, in a time-averaged sense, less melt is delivered to the distal ends of the eruptive fissure.

Once created, such an eruptive construct can follow one of two evolutionary paths: it can be dismembered by normal faults with small slivers of the edifice incrementally rafted up the rift valley walls (see review of these models by Macdonald, 1983); or can be rafted up and out of the rift valley largely intact without significant structural dismemberment by faulting. We favor the latter process based on the morphologic and structural relationships defined in our Sea Beam and Sea MARC I data. Sea Beam data show, for example, that the terrain of the western rift valley wall (e.g., the two terraces located at 23°00' N and 22°35' N), and the rift mountains that flank the MARK rift valley, are made up of broad (across-axis) and convex (along-strike) axis-parallel ridges that plunge and taper at each end. These features are remarkably similar in shape and dimensions to the neovolcanic ridge presently forming in the floor of the rift valley in the northern part of the MARK area. Detailed shape analysis indicates that the sides of these ridges which face the plate boundary are steeper by several degrees than the outward-facing slopes suggesting some fault control (Pockalny *et al.*, in preparation). Sea MARC I data also show that significant amounts of uplift are located along the base of the rift valley wall where parcels of crust are uplifted off the rift floor (Figure 9). As crust moves from the base of the rift valley wall up into the rift mountains there is little differential motion between crustal parcels. This focusing of tectonism along the base of the rift is confirmed by direct observations in the MARK area (Karson *et al.*, 1987) as well as other rift valley segments (Stroup and Fox, 1981, OTTER, 1984). Sea MARC I bottom profile records do indicate that there is some modification of the distinctive

volcanic terrain since minor amounts of backtilting of crustal parcels (usually less than 5°) are documented to occur as parcels are uplifted along near-vertical, small-offset normal faults.

The striking similarity between the volcanic constructional terrain along the ridge axis with flanking topography has been noted at other spreading centers localities by other investigators (East Pacific Rise South of Tamayo-Lewis, 1979; Juan de Fuca Ridge-Kappel and Ryan, 1986; Kane Fracture Zone-Pockalny *et al.*, 1988). Following these investigators, we propose that the distinctive ridge flank terrain is the product of a temporally variable magma supply superimposed on a more steady-state extensional stress regime associated with the separation of two large lithospheric plates. The spacing of the ridges (~5–10 km) suggests an episodicity in major phases of magma production rates on the order of a few hundred thousand years. The presence of intact constructional volcanic edifices preserved on terraces on the flanks of the rift valley (23° N; 22°35' N) and in the rift mountains indicates the axis of accretion must periodically relocate within the 10–17 km wide inner rift valley, rafting these features flankward on one plate or the other. This observation is consistent with the overall pattern of asymmetric spreading, and the evidence for duplicate magnetic anomalies in the MARK area reported by Schulz *et al.* (1988).

The intact character of the extinct eruptive volcanic ridges that are found off-axis indicate that during a magmatic phase, extensional tectonism is largely muted by the intrusion of magma along fissures that form in the brittle carapace overlying the plate boundary. Consequently, the large amounts of extension and crustal stretching that Karson (in press) has argued for to explain the exposure of plutonic rocks are not applicable to this phase of plate boundary evolution. During a prolonged waning phase of magmatism, however, extensional tectonism could disrupt and dismember a thin crustal assemblage along the lines suggested by Karson (in press). The documented morphologic and lithologic spatial heterogeneity along the MARK rift valley and flanking rift mountains is thus largely the product of two spreading cells that evolve independently in response to the interplay between extensional tectonism and the episodic variations in magma production rates.

## 7. Conclusions

The combination of high-resolution bathymetric surveying and sidescan sonar imagery focussed on a ~100-km long segment of the Mid-Atlantic Ridge has provided an exceptional data set with which to study the morphology and tectonics of a portion of this slowly accreting plate boundary. These data, along with interpretations of magnetic anomalies and submersible observations in this area, document a surprisingly complex rift valley structure characterized by two distinct spreading cells separated by a small, zero-offset transform or discordant zone 40–50 km south of the Kane Fracture Zone. The northern spreading cell, immediately south of the Kane Transform, is characterized by a young, hydrothermally active, constructional volcanic ridge located near the center of the median valley. The southern spreading cell, in contrast, is in a predominantly extensional phase with only small, isolated volcanic eruptions that have formed a NNE-trending band of fissured and faulted, small axial volcanos. These two spreading cells are separated by a tectonically and structurally anomalous zone between 23°05' N and 23°17' N that may be a slow-spreading ridge analogue to the overlapping spreading centers and other non-transform offsets found on the East Pacific Rise. Despite the complexity of the MARK area, volcanic and tectonic activity appears to be confined to the 10–17 km wide inner rift valley. Block faulting along near-vertical, small-offset normal faults, accompanied by minor amounts of back-tilting (generally less than 5°), begins within a few km of the ridge axis and appears largely to cease as the crust moves out of the rift valley. Most of these faults do not appear to be reactivated during the subsequent uplift of the crust into the flanking rift mountains, leaving constructional volcanic ridges formed along the rift valley floor preserved largely intact in the rift mountains. The observed cumulative fault relief is consistent with the presence of non-fault-related topography, such as constructional volcanic ridges, in the rift mountains. Mass-wasting and gullying of scarp faces, and sedimentation which buries low-relief seafloor features, are the major geological processes occurring outside of the inner rift valley.

## Acknowledgements

This work was supported by a contract (67-84) from

Joint Oceanographic Institutions Inc. to the University of Rhode Island, with subcontracts to L-DGO, Dalhousie University and Woods Hole Oceanographic Institution, for a pre-drilling site survey of the MARK area. We thank the officers, crew and scientific personnel of *Conrad 25-11* and *Hudson 85-010* for help collecting these data. We also acknowledge the assistance of R. Tyce and the staff of the NECOR/Sea Beam Development Center at URI in producing the Sea Beam maps shown in this paper. Nancy Adams, John Madsen, Rob Pockalny, Norb Schulz assisted with various aspects of this work. L.K. thanks J. Cann for many inspiring discussions on mid-ocean ridge. R.S.D. and P.J.F. thank C. Sherman for skillful word processing and proofing of this manuscript.

## References

- Abrams, L. J., Detrick, R. S., and Fox, P. J., 1988, Morphology and Crustal Structure of the Kane Fracture Zone Transverse Ridge, *J. Geophys. Res.* **93**, 3195–3210.
- Ballard, R. D. and van Andel, T. H., 1977, Morphology and Tectonics of the Inner Rift Valley at Latitude 36°50' N on the Mid-Atlantic Ridge, *Geol. Soc. Amer. Bull.* **88**, 507–530.
- Brown, J. R. and Karson, J. A., 1989, Variations in Axial Processes on the Mid-Atlantic Ridge: the Neovolcanic Zone of the MARK Area, *Mar. Geophys. Res.* (in press).
- Bryan, W. B., Thompson, G., and Ludden, J. N., 1981, Compositional Variation in Normal MORB from 22–25° N; Mid-Atlantic Ridge and Kane Fracture Zone, *J. Geophys. Res.* **86**, 11815–11836.
- Casey, J. F., 1986, Ultramafic Rocks from the MAR at 23° N: Evidence for High Temperature Hydration and High Temperature–low to Moderate Stress Deformation of Mantle Tectonites beneath the Median Valley, *EOS (Trans. Amer. Geophys. Union)* **67**, 1214.
- Chayes, D. N., 1983, Evolution of Sea MARC I, *IEEE Proceedings of the 3rd Working Symposium on Oceanographic Data Systems*, IEEE Computer Society, 103–108.
- Cornier, M. H., Detrick, R. S., and Purdy, G. M., 1984, Anomalous Thin Crust in Oceanic Fracture Zones: New Constraints from the Kane Fracture Zone, *J. Geophys. Res.* **89**, 10249–10266.
- Crane, K. and Ballard, R. D., 1981, Volcanics and Structure of the FAMOUS Narrowgate Rift: Evidence for Cyclic Evolution: AMAR I, *J. Geophys. Res.* **86**, 5112–5124.
- de Moustier, C. and Kleinröck, M. C., 1986, Bathymetric Artifacts in Sea Beam Data: How to Recognize Them and What Causes Them, *J. Geophys. Res.* **91**, 3407–3424.
- Detrick, R. S., Fox, P. J., Kastens, K., Ryan, W. B. F., Mayer, L., and Karson, J., 1984, A Sea Beam Survey of the Kane Fracture Zone and Adjacent Mid-Atlantic Ridge Rift Valley, *EOS (Trans. Amer. Geophys. Union)* **65**, 1006.
- Detrick, R., Honnorez, J., Bryan, W. B., Juteau *et al.*, 1988, *Proc. ODP Init. Repts. (Pt. A)*, 106/109, College Station, TX (Ocean Drilling Program).
- Farre, J. A., Ryan, W. B. F., Koch, W., and Brosius, A. M., 1983, Applying Thyristor Technology to Deep Sea Photography, *Functional Photography*, March/April, 16–21.

- Fox, P. J., 1972, The Geology of Some Atlantic Fracture Zones, Caribbean Escarpments and the Nature of Oceanic Basement and Crust, [Ph.D. dissertation], Columbia University, New York.
- Fox, P. J. and Gallo, D.: 1984, A Tectonic Model for Ridge-Transform-Ridge Boundaries: Implications for the Structure of Oceanic Lithosphere, *Tectonophysics* **104**, 205-242.
- Fox, P. J., Pitman, W. C., III, and Shepard, F., 1969, Crustal Plates in the Central Atlantic: Evidence for a Least two Poles of Rotation, *Science* **165**, 487-489.
- Francheteau, J. F. and Ballard, R. D., 1983, The East Pacific Rise near 21° N, 13° N and 20° S: Inferences for Along-strike Variability of Axial Processes of the Mid-Ocean Ridge, *Earth Planet. Sci. Lett.* **64**, 93-116.
- Humphris, S. E. and Bryan, W. B., 1986, Anatomy of Serocki Volcano, *EOS (Trans. Amer. Geophys. Union)* **67**, 1213.
- Kappel, E. S. and Ryan, W. B. F., 1986, Volcanic Episodicity and a Non-Steady State Rift Valley along Northeast Pacific Spreading Centers: Evidence from Sea MARC I, *J. Geophys. Res.* **91**, 13,925-13,940.
- Karson, J. A., 1988, Seafloor Spreading on the Mid-Atlantic Ridge: Implications for the Structure of Ophiolites and Oceanic Lithosphere Produced in Slow-Spreading Environments, *Proceedings of the Symposium on Ophiolites and Oceanic Lithosphere-TROODOS 87*, (in press).
- Karson, J. A. and Dick, H. J. B., 1983, Tectonics of Ridge-Transform Intersections at the Kane Fracture Zone, *Mar. Geophys. Res.* **6**, 51-98.
- Karson, J. A., Thompson, G., Humphris, S. E., Edmond, J. M., Bryan, W. B., Brown, J. R., Winters, A. T., Pockalny, R. A., Casey, J. F., Campbell, A. C., Klinkhammer, G., Palmer, M. R., Kinzler, R. J., and Sulanowska, M. M., 1987, Along-Axis Variations in Seafloor Spreading in the MARK Area, *Nature* **328**, 681-685.
- Kastens, K. A., Ryan, W. B. F., and Fox, P. J., 1986, The Structural and Volcanic Expressions of a Fast-Slipping Ridge. Transform-Ridge Plate Boundary: Sea MARC I and Photographic Surveys at the Clipperton Transform Fault, *J. Geophys. Res.* **91**, 3469-3488.
- Kong, L., Ryan, W. B. F., Mayer, L., Detrick, R., Fox, P. J., and Manchester, K., 1985, Bare-Rock Drill Sites, OPD Legs 106 and 109: Evidence for Hydrothermal Activity at 23° N on the Mid-Atlantic Ridge, *EOS (Trans. Amer. Geophys. Union)* **66**, 936.
- Kosalos, J. G. and Chayes, D. N., 1983, A Portable system for Ocean Bottom Imaging and Charting, *Proceedings of Offshore Technology Conference*, Houston, TX, 649-656.
- Leg 106 Scientific Party, 1986, Drilling the Snake-Pit Hydrothermal Sulfide Deposit on the Mid-Atlantic Ridge, lat 23°22' N, *Geology* **14**, 1004-1007.
- Lewis, B. T. R., 1979, Periodicities in Volcanism and Longitudinal Magma Flow on the East Pacific Rise at 23° N, *Geophys. Res. Lett.* **6**, 753-756.
- Lonsdale, P., 1983, Overlapping Rift Zones at the 5.5° Offset of the East Pacific Rise, *J. Geophys. Res.* **88**, 9393-9406.
- Macdonald, K. C., 1983, Crustal Processes at Spreading Centers, *Rev. Geophysics*, **21**, 1441-1454.
- Macdonald, K. C. and Fox, P. J., 1983, Overlapping Spreading Centers: New Accretion Geometry on the East Pacific Rise, *Nature* **302**, 55-57.
- Macdonald, K. C. and Luyendyk, B. P., 1977, Deep-Tow Studies of the Structure of the Mid-Atlantic Ridge Crest near lat. 37° N, *Geol. Soc. Amer. Bull.* **88**, 621-636.
- Mayer, L. A., Ryan, W. B. F., Detrick, R. S., Fox, P. J., Kong, L., and Manchester, K., 1985, Structure and Tectonics of the Mid-Atlantic Ridge South of the Kane Fracture Zone Based on Sea MARC I and Sea Beam Site Surveys, *EOS* **66**, 1092.
- Miyashiro, A., Shido, F., and Ewing, M., 1969, Composition and Origin of Serpentinites from the Mid-Atlantic Ridge, 24° and 30° N, *Contrib. Mineral. Petrol.* **32**, 38-52.
- OTTER, 1984, The Geology of the Oceanographer Transform: The Ridge-Transform Intersection, *Marine Geophys. Res.* **6**, 109-141.
- Pockalny, R. A., Detrick, R. S., and Fox, P. J., 1987, A Comparison of Off-Axis Sea Beam Data Collected at Slow, Intermediate and Fast Spreading Center, *EOS (Trans. Amer. Geophys. Union)* **68**, 1491.
- Pockalny R. A., Detrick, R. S., and Fox, P. J., 1988, The Morphology and Tectonics of the Kane Fracture Zone from Sea Beam Bathymetry Data, *J. Geophys. Res.* **93**, 3179-3193.
- Pockalny, R. A., Fox, P. J., and Detrick, R. S., in preparation, Morphological Comparison of the Abyssal Hills Located on the Flanks of Slow, Intermediate and Fast Spreading Mid-Ocean Ridges.
- Purdy, G. M. and Detrick, R. S., 1986, the Crustal Structure of the Mid-Atlantic Ridge at 23° N from Seismic Refraction Studies, *J. Geophys. Res.* **91**, 3739-3762.
- Purdy, G. M., Rabinowitz, P. D., and Schouten H., 1978, The Mid-Atlantic Ridge at 23° N: Bathymetry and Magnetics, in W. C. Melson et al. (eds.), *Initial Reports of the Deep Sea Drilling Project*, **45**, pp. 119-128.
- Purdy, G. M., Rabinowitz, P. D., and Veltrop, J. J. A., 1979, The Kane Fracture Zone in the Central North Atlantic, *Earth Planet. Sci. Lett.* **45**, 429-434.
- Rabinowitz, P. D., Purdy, G. M., and Veltrop, J. J. A., 1977, The Kane Fracture Zone in the Central North Atlantic Ocean, *EOS (Trans. Amer. Geophys. Union)* **58**, 511.
- Renard, V. and Allenou, 1979, Sea Beam Multibeam Echosounding in Jean Charcot: Description, Evaluation and First Results, *Int. Hydrog. Rev.*, **56**, 35-67.
- Schouten, H. and White, R. S., 1980, Zero Offset Fracture Zones, *Geology* **8**, 175-179.
- Schouten, H., Cande, S. C., and Klitgord, K. D., 1985, Magnetic Anomaly Profiles South (22° N to 28° N), in *Ocean Margin Drilling Program Regional Data Synthesis Series, Atlas 11, Mid-Atlantic Ridge between 22° and 38° N*, Marine Science International, Woods Hole.
- Schulz, N. J., Detrick, R. S., and Miller, S. P., 1988, Two and Three Dimensional Inversions of Magnetic Anomalies in the MARK Area (Mid-Atlantic Ridge 23° N), *Mar. Geophys. Res.* **10**, 41-57 (this issue).
- Severinghaus, J. and Macdonald, K. C., 1986, High Inside Corners at Ridge Transform Intersections, *EOS (Trans. Amer. Geophys. Union)* **67**, 1232.
- Stakes, D. S., Shervais, J. W., and Hopson, C. A., 1984, The Volcano-Tectonic Cycle of the FAMOUS and AMAR Valleys, Mid-Atlantic Ridge (36°47' N): Evidence from Basalt Glass and Phenocryst Variations for a Steady-State Magma Chamber Beneath Valley Mid-Sections, AMAR 3, *J. Geophys. Res.* **89**, 6995-7028.
- Stroup, J. B. and Fox, P. J., 1981, Geologic Investigations in the Cayman Trough: Evidence for Thin Crust along the Mid-Cayman Rise, *J. Geol.* **89**, 395-420.
- Thompson, G., Humphris, S. E., Schroeder, B., Sulanowska, M., and Rona, P., 1988, Hydrothermal Mineralization on the Mid-Atlantic Ridge, *Canadian Mineralogist*, Special Publication, (in press).

LAURA S. L. KONG ET AL.

- Toomey, D. R., Solomon, S. C., and Purdy, G. M., 1988; Microearthquakes Beneath the Median Valley of the Mid-Atlantic Ridge near 23° N: Tomography and Tectonics, *J. Geophys. Res.* 93, 9093-9112.
- Toomey, D. R., Solomon, S. C., Purdy, G. M., and Murray, M. H., 1985, Micro-Earthquakes beneath the Median Valley of the Mid-Atlantic Ridge near 23° N: Hypocenters and Focal Mechanisms, *J. Geophys. Res.* 90, 5443-5458.
- van Andel, T. J. and Bowin, C. O., 1968, Mid-Atlantic Ridge between 22° and 23° North Latitude and the Tectonics of Mid-Ocean Rises, *J. Geophys. Res.* 73, 1279-1298.



### CHAPTER 3. MICROEARTHQUAKES BENEATH THE MEDIAN VALLEY OF THE MID-ATLANTIC RIDGE NEAR THE TAG HYDROTHERMAL FIELD, 26°N

#### INTRODUCTION

A knowledge of the interplay between volcanism and tectonism within the median valley is central to the understanding of the crustal accretionary process at slow-spreading centers. Deep-towed sonar surveys, bottom photography, and submersible studies have shown the rift valley to be dominated by ridge-parallel fissuring and faulting, but rarely reveal the presence of fresh, unsedimented basalts [Ballard and van Andel, 1977; Macdonald and Luyendyk, 1977; Karson et al., 1987; Kong et al., 1988]. Focal mechanism studies have shown that faulting occurs at depths extending throughout the crust [Toomey et al., 1985, 1988; Huang et al., 1986; Huang and Solomon, 1988]. In contrast to the East Pacific Rise where recent studies indicate that a shallow magma chamber may exist beneath a large fraction of the ridge system [Detrick et al., 1987], experiments to date along the Mid-Atlantic Ridge (MAR) have found no evidence for a continuous or steady-state magmatic feature. The discovery of active high-temperature, hydrothermal vents at two locations (23°N and 26°N) along the MAR [Kong et al., 1985; Detrick et al., 1986; Rona, 1985; Rona et al., 1986], however, requires there to be heat sources within the shallow crust at least locally along parts of the ridge. The dimensions, shapes, and temporal character of such thermal anomalies, and their effects on tectonism and the state of stress within the rift valley, are as yet unknown.

As increasing amounts of geological and geophysical data are collected, it is becoming apparent that the accretionary process at mid-ocean ridges varies temporally and spatially along-strike. A model in which the ridge axis is segmented into distinct spreading cells, each characterized by varying proportions of active volcanism and tectonism and each with an along-axis length of less than about 100 km, now appears to be appropriate [e.g., Francheteau and Ballard, 1983; Schouten et al., 1985; Langmuir et al., 1986; Macdonald, 1986; Kong et al., 1988; Sempere et al., 1989]. Each segment is bounded at its distal ends by an along-axis depth maximum and shoals away from the deep toward a local along-axis minimum. The model predicts that within a given cell, the region of most recent volcanism and hydrothermal activity, and thus elevated isotherms, should be located beneath the local depth minimum, and that away from this zone the crust should be cooler and more tectonized, and volcanism less voluminous.

Bathymetric surveys over large areas of the Mid-Atlantic Ridge have revealed the median valley to vary remarkably at all scales in width, depth and roughness. This topographic variability is probably an indication that different segments along the ridge system are in different stages of volcanic and tectonic evolution. If we are to draw any conclusions about accretionary processes at slow-spreading centers we must therefore study a number of ridge segments, each of which may characterize an important and distinct stage in the transformation of magma into ocean crust. In particular, determination of earthquake epicenters, focal depths, and the nature of faulting along several contrasting segments of the Mid-Atlantic Ridge can provide important constraints on the thermal and mechanical structure of the crust.

To this end, several microearthquake surveys have been conducted along the MAR [Francis and Porter, 1973; Francis *et al.*, 1977; Lilwall, 1980; Lilwall *et al.*, 1977, 1978, 1980; Murray *et al.*, 1984; Toomey *et al.*, 1985, 1988]. Most however, have lacked a large enough network of instruments to constrain hypocenters well. A study of microearthquakes beneath the median valley at 23°N using 10 ocean bottom hydrophones and seismometers has so far provided the best estimates of focal depth and mechanisms [Toomey *et al.*, 1985, 1988]. In the context of the spreading cell model, the survey at 23°N was carried out within an along-axis deep at the southern distal end of a cell [Kong *et al.*, 1988]. The distribution and source mechanisms of microearthquakes implied that no magma chamber was present and that the entire crust beneath this portion of the median valley had cooled to temperatures within the brittle field of behavior. Such an inference is consistent with predictions that the distal end of cells are less likely to experience active volcanism.

In order to investigate further the spreading cell model in the context of a slow-spreading mid-ocean ridge environment, we have collected a microearthquake and seismic refraction data set in the vicinity of an active hydrothermal field on the MAR near 26°N (Figure 1). In contrast to the magmatically quiescent, cool crust beneath the along-axis deep at 23°N, the ridge segment at 26°N is characterized by high-temperature, black-smoker chimneys on the eastern inner floor at the along-axis high [Rona, 1985; Rona *et al.*, 1986] (Figures 2, 3). The geological framework at 26°N makes this an excellent locale at which to study the relationships between volcanism, tectonism, and hydrothermal circulation.

In this chapter, we present the results of the microearthquake survey. Hypocenters for 189 earthquakes are estimated, initially using a one-dimensional (1D) velocity model with station corrections, and focal mechanism solutions are constructed for spatially and/or temporally clustered events. The effect of lateral heterogeneity on the results is then evaluated by comparing these locations and mechanisms with those obtained with a two-

dimensional (2D) velocity model determined from earthquake and shot travel times. Seismic moments, source dimensions, and recurrence rates are also estimated. Finally, these observations are compared with results from microearthquake studies at other locations along the Mid-Atlantic Ridge.

## BACKGROUND - THE MID-ATLANTIC RIDGE AT 26°N

A recent Sea Beam survey of the Mid-Atlantic Ridge from 24-31°N indicates that the ridge can be divided into a number of *en echelon* segments, each 30-50 km in length trending ~N25°E and separated by 5-25 km wide, non-transform offsets [Sempere *et al.*, 1989]. Along the ridge from 25°25'N to 26°20'N, three *en echelon* ridge segments can be identified, each varying in width and depth along its strike. The area has experienced a number of teleseismically observed earthquakes over the past 25 years, including a swarm of five events, located by the International Seismological Centre (ISC) ( $m_b = 4.5 - 5.1$ ), that occurred while our seismic network was in operation (Chapter 5). These events, two of which have centroid moment tensor solutions indicating normal faulting [Dziewonski *et al.*, 1986], were located within the median valley ~20 km south of the network.

At 26°N, a considerable quantity of background geological and geophysical data is available in the literature from the initial Trans-Atlantic Geotraverse (TAG) Project [Scott *et al.*, 1974; Rona *et al.*, 1976, 1986; McGregor *et al.*, 1977; Temple *et al.*, 1979; Jenkins *et al.*, 1980; Rona, 1980;], as well as most recently from Sea Beam [Purdy *et al.*, 1989; Sempere *et al.*, 1989], magnetic [Tivey *et al.*, 1989a, b], geochemical [Shearman *et al.*, 1983; Thompson *et al.*, 1985, 1988; Lalou *et al.*, 1990], water sample [Klinkhammer *et al.*, 1986; Rona and Speer, 1989], and near-bottom camera and submersible investigations [Karson and Rona, 1982, 1989; Rona, 1985; Rona *et al.*, 1986; Campbell *et al.*, 1988; Eberhart *et al.*, 1988; Zonenshain *et al.*, 1989]. Spreading over the last 10 My has been asymmetric, with half-rates of 1.3 cm/yr to the east and 1.1 cm/yr to the west [Lattimore *et al.*, 1974; McGregor *et al.*, 1977].

The median valley at 26°N has an hourglass shape, narrowing at the along-axis bathymetric minimum (26°09'N) with a pronounced widening and deepening of the valley to the north and south (Figure 2). The walls of the median valley display a high degree of asymmetry, with the gentler-sloping western flank composed of a series of back-tilted (5-10°) fault terraces and steeply-dipping (60°) fault scarps ranging in height from 50 to 200 m [Zonenshain *et al.*, 1989]. Because the westward transition from inner floor to valley wall is gradual at the along-axis high, we define for ease of discussion the boundary

between the inner floor and western wall to be the 3.5 km contour by extrapolation from the more abrupt transition to the south (25°05' - 07'N, 44°54.5'W).

In contrast, the much steeper and higher eastern valley wall is characterized by large amounts of mass wasting and a steplike ascent upwards with fault scarps and back-tilted (up to 30°) terraces hundreds of meters high and wide [Temple *et al.*, 1979; Karson and Rona, 1982, 1989]. The terraces are themselves composed of numerous smaller fault blocks. During submersible and near-bottom photographic transects up the eastern wall, Zonenshain *et al.* [1989] documented the exposure of gabbros, vertically-oriented sheeted dikes, and horizontally-lying pillow lavas in vertical succession from seafloor depths of 3.0 to 2.4 km, and with little or no in situ deformation. These workers suggested that large-scale vertical uplift was responsible for the topography. No mention however, was made of such an exposure of a significant fraction of a crustal section in other studies of the eastern wall [e.g., Rona, 1980; Rona *et al.*, 1976]. Historically, the TAG hydrothermal field was the term initially applied to the region of the eastern wall adjacent to the along-axis high, where low-temperature hydrothermal solutions seep out along linear fault zones resulting in the deposition of manganese oxides, enrichment of metals in sediments, and anomalies in temperature and <sup>3</sup>He in the near bottom waters [Rona, 1980]. Since 1985, the TAG hydrothermal field has come to describe the active, high-temperature vent field situated in the inner floor ~2 km to the east of the neovolcanic zone at the along-axis high (Figure 3) [Rona, 1985; Rona *et al.*, 1986].

Within the inner floor in the region of the along-axis high, the neovolcanic zone is characterized by a series of small volcanic edifices forming a ridge along the axis of the rift valley [Zonenshain *et al.*, 1989], including a 200-m-high elliptical feature at the southern end of the along-axis high (Figure 3). We will use the term "volcano" to denote this feature; this interpretation is based on the resemblance in height and shape of the edifice with seafloor volcanos mapped within the MAR median valley at 23°N [Kong *et al.*, 1988]. In the analysis of the microearthquake data to follow and in Chapter 4, we note that this axial volcano appears to be significant as marking the southern terminus of along-axis variations in structural and tectonic characteristics attributed to the median valley depth minimum.

Near-bottom observations in the high-temperature hydrothermal field document massive sulfides and active black-smoker vents (water exit temperatures > 321°C, Campbell *et al.*, 1988) atop the 55-m-high, 250-m-wide inner hydrothermal mound. If the mound is composed entirely of hydrothermal precipitates, this volume makes it comparable in size (~4 million tons) to the large sulfide ore bodies found sub-aerially, e.g., in Cyprus [Costantinou and Govett, 1973]. An outer mound ~580-m wide is composed of fractured

basalt talus interspersed with hydrothermal sediments and pillow lavas [Rona *et al.*, 1986]. Submersible dives, dredges, and piston coring in the area have been used to document at least two prior stages of volcanism and hydrothermal activity, with the most recent basalts (1000 - 5000 years old based on the glassy character of the basalts and lack of sediment) observed near the base of the hydrothermal mound [Zonenshain *et al.*, 1989].

Analysis of sea surface magnetic data show that the area of the high-temperature hydrothermal vent field is associated with a magnetic anomaly low (Figure 3) [Rona, 1980; McGregor *et al.*, 1977; Tivey *et al.*, 1989a,b]. A three-dimensional inversion of the data shows an elongated region of reduced magnetization paralleling the eastern wall at the along-axis high [Tivey *et al.*, 1989a,b]. The crustal anomaly has been suggested to result from chemical demagnetization caused by the progressive alteration of magnetic minerals by hydrothermal fluids, or from thermal demagnetization resulting from slight increases in temperature within the magnetic source layer which raise the rock above its Curie point.

Along with the microearthquake experiment, a 75-km-long refraction line was shot along the median valley axis from 25°54'N to 26°28'N. The inversion of the shot and earthquake travel time residuals for 2D velocity structure beneath the median valley is presented in Chapter 4. Higher velocities are associated with the uppermost 1-2 km of crust at the along-axis high than are present in the deeper portions of the median valley, and velocities appear to decrease below 3 km depth in the vicinity of the ridge-axis volcano and the along-axis high. These observations are interpreted as the seismic expression of a cooling magmatic intrusion beneath the along-axis high (Chapter 4).

## SEISMIC NETWORK - EXPERIMENT DESCRIPTION

During the summer of 1985, prior to the discovery of the active high-temperature vent field, a seismic network consisting of seven ocean bottom hydrophones (OBHs) from the Woods Hole Oceanographic Institution (WHOI) and three ocean bottom seismometers (OBSs) from the Massachusetts Institute of Technology (MIT) was deployed for a three-week period to record earthquake activity at 26°N. The 20 x 10 km network straddled the median valley and eastern wall from the along-axis high southward and was configured to provide coverage of the known low-temperature hydrothermal field on the eastern wall [Rona *et al.*, 1980], as well as the along-axis high at 26° 09'N and the 4500-m bathymetric deep to the south. Coverage of the deep was judged important because the majority of activity at 23°N was located beneath an equivalent morphological feature [Toomey *et al.*, 1985, 1988].

The combination of the continuously-recording analog WHOI OBHs [Koelsch and Purdy, 1979], which provide complete records of the seismicity over the deployment period, with the event-triggered, high dynamic range (108 dB) digital OBSs [Mattaboni and Solomon, 1977; Duschenes *et al.*, 1981] has proven to be very successful in obtaining well-resolved hypocentral parameters in a previous experiment [Toomey *et al.*, 1985, 1988]. The three orthogonal seismometers (vertical and two horizontals) contained in the OBS geophone package permit the identification of S waves which are important in reducing the uncertainty in the focal depth [Duschenes *et al.*, 1983]. Because the OBH package floats ~3 m off the bottom, it can be deployed in areas of rugged topography. It is able to record impulsive P wave arrivals, but has a smaller total dynamic range (60 dB) than the MIT OBS. Both the OBH and OBS records for the July 13, 1985, swarm of teleseismically-located earthquakes were saturated beyond the P wave arrival, however.

During the 23-day deployment, over 1600 distinct events were detected, and over 400 events were well-recorded by more than 5 instruments (Figure 4). All instruments except one OBS recorded data of high quality. Average numbers of events well-recorded on the continuously-recording OBHs ranged from 8 to 24 events/day. The OBHs deployed within the inner floor (OBHs 1, 2, 3, 6) recorded considerably more activity than the OBHs (4, 5, 8) and OBSs (31, 33), which were deployed on the eastern wall (Figures 4, 5). Typical examples of the high-quality hydrophone and seismometer data are shown in Figure 6. We believe this data set to be the largest, well-constrained microearthquake data set ever to have been collected on a slow-spreading ridge. By far the most active period corresponded to that of the teleseismically-located earthquake swarm (Figure 5, day 19). Unfortunately, these data are complicated by noise generated by the coincidental arrival in this area of the NOAA research vessel R/V *Researcher* to begin camera and CTD work that resulted in the discovery of the black-smoker vent field [Rona *et al.*, 1985].

## INSTRUMENT RELOCATION

Because lateral trajectories of the free-fall instrument packages are not known, and instrument mislocation directly affects the quality of the estimated hypocentral parameters, we have used the method of Creager and Dorman [1982], as applied to microearthquake networks by Toomey *et al.* [1985], to relocate our instruments. This technique utilizes acoustic ranging of shots to fixed instruments to solve simultaneously for the locations and depths of the instruments and the locations of the ranging shots. Initial ranging shot and instrument drop locations were given by the GPS navigation system ( $\pm 40$  m error), and instrument depths were read from 12 kHz echo-sounding records ( $\pm 100$  m error). A

single water layer, with an average sound velocity of 1.5137 km/sec determined from a conductivity/temperature/depth cast at 24°N, was assumed. One-way travel times were read on the OBHs from a filtered (0.15 - 2 kHz) and rectified hydrophone channel and on the OBSs vertical channel (2 - 50 Hz sensitivity). While the arrival times on both instruments can be picked to within 10 ms, there is greater uncertainty in identifying the correct arrival of the water wave on the OBSs due to interference effects that can occur at the seafloor.

Water wave arrivals with travel times greater than 12 s and five shots having low signal-to-noise ratios or suspected phase misidentifications were excluded from this analysis. In addition, for the OBSs we have attempted to retain an even azimuthal distribution of shots by excluding some data along the N25°E refraction line which arrive from only a small range of azimuths. A total of 213 observations (154 travel times, 25 initial shot locations, 9 initial instrument depths) were used to estimate 77 parameters (9 final instrument locations and depths, 25 final shot locations). A comparison of the least squares estimate of  $\chi^2$  with that expected for a system with 136 degrees of freedom provided an *a posteriori* check of the statistical estimates. With the assumption that the ranging shot locations and instrument depths were better known than the uncertainty in travel times, we obtained a travel time picking error of 15 ms ( $\chi^2 = 125$ ), consistent with our *a priori* estimate.

The final locations of the instruments and the shot locations are shown in Figure 2 and given with their 1- $\sigma$  formal confidence limits in Table 1. Since most of the instruments move laterally only about 150 m from their initial drop positions, we conclude that the instrument descent through the water column was nearly vertical. Furthermore, if high-precision navigation (such as GPS) is used during the instrument deployment, then it appears that instrument relocation results in little improvement in the locations of shots and instruments. The average change in latitude and longitude for the shots was 300 m with 1- $\sigma$  errors ranging from 20 - 60 m. For the instruments, the largest change in position (450 m) corresponded to the northernmost instrument (OBH 4) located on the eastern valley wall. This instrument was deployed using Transit satellite navigation, and its drop location could be expected to have a larger error. The 1- $\sigma$  errors in latitude and longitude of the instruments ranged from 15 - 30 m with 1- $\sigma$  errors in depth between 8 and 80 m; the root mean square (rms) travel time residual was after relocation was 9 ms.

Most of the uncertainty in instrument position is in the depth of the instrument. Comparison of the relocated depths with depths from the Sea Beam bathymetry collected over the area [Rona *et al.*, 1986; Sempere *et al.*, 1989], referenced to a 1.5 km/s sounding velocity, show an rms difference of 115 m and a maximum difference of 380 m. Both

figures are significantly larger than the formal errors in Table 1. Explanations for this discrepancy could be (1) that the steep topography associated with some instrument locations results in the underestimation of the true errors, since a small change in position corresponds to a large change in depth (for instance, a 1 km shift in longitude would correspond to over a 500 m increase in depth for OBS 33); (2) offsets in latitude and/or longitude of the Sea Beam map, which result from the merging of several bathymetric data sets collected principally by Transit satellite fixes and dead reckoning; although the mean lateral shift in swaths was 200 m, shifts of up to 1.5 km were used (R. Pockalny, pers. comm., 1988); (3) uncertainties in the identification of the water wave arrival on the OBSs may have led to inaccuracies in the instrument depth determination; previous experiments have observed a consistent bias (locating to deeper depths) when using the ocean bottom seismometer vertical channel to read the water wave arrival; (4) systematic errors in travel times to a particular instrument may be present; and (5) vertical or lateral velocity variations in the water column may be present; use instead of the Matthews Tables [1939] sounding velocity for 26°N, 45°W shows only a 10 m/s difference in velocity compared with the CTD estimate from 24°N, a difference which is much smaller than the 60 m/s increase required for a 150 m increase in depth. Because station delays are determined prior to earthquake location, the uncertainty in instrument depths should not affect hypocentral locations.

## HYPOCENTRAL LOCATION

The hypocentral parameters were determined using the HYPOINVERSE computer program [Klein, 1978] which solves the non-linear hypocentral estimation problem through linear approximation and iteration until convergence. The algorithm performs a singular value decomposition of the travel time partial derivative matrix with respect to latitude, longitude, depth, and origin time, and then determines the generalized inverse. As a result, quantifiable error estimates that take into account the uncertainties in the travel times can be determined from the calculation of the resolution and covariance matrices; parameter adjustments in poorly-constrained directions are damped between iterations to prevent solutions and errors from becoming unstable. The program assumes a one-dimensional, plane-layered velocity structure, and allows for the individual weighting of phases and specification of individual trial hypocenters.



## Arrival Time Data

Instrument clocks were corrected to Universal Time (UT) with the assumption of linear drift rates. Individual clock offsets were less than 0.03 s, with drift rates ranging from 0.002 - 0.033 s/day. The master clocks of both instrument types were rated relative to WWV and found to be stable over the 3-week deployment period. The timing incorporated a leap second on July 1, 1985.

Clear P wave arrival times on the OBHs and OBSs could often be read to within 0.02 s, and S wave arrivals on the OBSs to within 0.05 s (Figure 6). S waves were read from unoriented horizontal seismometers on the OBSs; repicking of the SH phase on the transverse horizontal seismometer for 21 events representative of the seismicity over the deployment indicates that the average difference between the two picks (SH versus earliest S on the two unoriented channels) is about 0.07 s, though differences of up to 0.2 s were observed. We will see below that for well-recorded events picking errors of this magnitude do not bias the estimate of the hypocenter. Individual phases were assigned relative weights of 1, 0.75, 0.50, and 0.25, corresponding to picking errors of < 0.02 s, 0.02 - 0.05 s, 0.05 - 0.10 s, and 0.10 - 0.25 s, respectively. To compensate for the greater uncertainty in the S arrival time, but the greater importance of the phase in determining a hypocenter, shear arrivals were further downweighted by a factor of 0.75 compared with the P arrivals. Arrival times with large residuals (> 0.5 s), presumably associated with an incorrect phase identification or a travel path through poorly-constrained portion of the velocity model, were not used. The number of arrivals for individual events ranged from 4 to 11.

Because the addition of S wave information results in better-constrained hypocentral estimates, especially for events outside the network, we investigated whether later-arriving phases on the OBHs could be utilized. Initial examination of a number of seismograms showed the common presence of a phase arriving at a time consistent with an S wave which was converted to a P wave (SP) at the seafloor near the instrument (see Figure 6a, OBHs 2-5; Figure 6b, OBHs 4,5). Comparison of predicted S - P travel times with the observed SP - P time, however, revealed that this phase does not always arrive at the S wave time expected for a constant  $V_p/V_s$  (Figure 7b). In contrast to the travel time residuals (observed minus calculated S - P time) for OBS 31, which are small ( $0.06 \pm 0.09$  s), average residuals using SP phases picked on the OBHs are larger and exhibit much scatter, ranging from  $0.17 \pm 0.16$  s on OBH 5 to  $0.38 \pm 0.24$  s on OBH 1. The larger differential travel times for the OBHs could correspond to a converted P waves exiting the subsurface at some distance from the instrument and propagating the remaining distance

through the water column. The variability in the observed OBH SP - P times (i.e., not a linear increase with range) may in part result from a locally heterogeneous velocity structure near the seafloor.

Comparisons with data from other experiments recorded simultaneously by an OBS and a hydrophone have also shown that the shear arrival observed on the horizontal could not be consistently correlated with the arrival of a phase on the hydrophone channel [e.g., Francis *et al.*, 1977; Rowlett and Forsyth, 1984]. We thus conclude that the phase observed on the hydrophone does not generally correspond to an S-to-P conversion at the seafloor beneath the OBH (though it may in some instances), and consequently that shear wave arrivals cannot be confidently picked on the hydrophone with sufficient accuracy to warrant their use in hypocentral estimation.

Station delays were initially calculated by referencing the instrument to a common datum of 3.3 km below sea level. The initial delay was taken to be,  $t = \Delta h / v$ , where  $\Delta h$  is the difference between the instrument depth and the reference datum and  $v$  is the average P wave velocity within the upper crust (6.5 km/s); this term represents the travel time residual due to the presence or absence of crustal material between the station and the datum. In order to account for crustal heterogeneities beneath the receiver, in addition to uncertainties and differences in receiver elevation with respect to the datum, final station corrections are determined iteratively by locating 19 well-recorded events (all with at least one S time) and adjusting the delays until the mean travel time residual for each instrument was close to zero. This calculation resulted in an average epicentral shift of 1 km and a 50% reduction in the mean travel time residual. Station corrections ranged from -0.08 s to +0.10 s (Figure 8). The effect of S wave arrival time reading errors (from picking the S phase on the transverse horizontal channel as opposed to the earliest S phase on an unoriented horizontal seismometer, which arrived on average 0.07 s earlier) on the calculation of station corrections was estimated for 21 events, all with at least one S wave arrival; absolute changes in station corrections were no greater than 0.01 s. Generally smaller delays are associated with inner floor instruments, implying larger travel times (or lower velocities) for paths to stations situated at greater seafloor depths; however, the observed variability implies that marked crustal heterogeneity exists. The smallest delays are associated with OBHs 2 and 4, which were located within the low magnetization region [Tivey *et al.*, 1989a] and near the active vent field (OBH 2).

In computing the covariance matrix, HYPOINVERSE utilizes a user-specified "picking error" which encompasses the total error introduced during the playback and picking of phases, correction of clocks to UT, instrument relocation, and station delay calculation. On the assumption that errors are uncorrelated, the total estimated error, or

"picking error", was 0.05 s. The *a posteriori* determination of the mean rms travel time residuals for the 105 best-located events (with focal depth resolved) was  $0.02 \pm 0.01$  s. This value is much less than the picking error (0.05 s) because of the small number of degrees of freedom in many hypocentral estimates and implies that the true errors are greater than the formal errors given by HYPOINVERSE.

### One-dimensional Crustal Velocity Structure

Along the Mid-Atlantic Ridge, only a few refraction studies have been conducted within the median valley [Whitmarsh, 1975; Fowler, 1976, 1978; Fowler and Keen, 1979; Bunch and Kennett, 1980; Purdy and Detrick, 1986]. In an analysis of travel time residuals from refraction lines across the median valley at 37°N, Whitmarsh [1975] found a 2-3 km wide axial region characterized by anomalously low layer-2 velocities and widespread lower velocities in layer 3. From travel time data and waveform modelling of additional data, Fowler [1976] proposed that the MAR inner floor at 37°N is characterized by a 3-km-thick crust underlain by anomalously low upper mantle velocities, and that the crust thickens to 6-7 km within 10 km of the ridge axis. The structure at 45°N obtained from synthetic seismogram modelling is similar to that at 37°N, and includes a high velocity layer 3B to the west of the ridge axis [Fowler and Keen, 1979] and an anomalously low upper mantle velocity at ~6 km depth beneath the axis, with normal mantle evolving within a few million years to the east of median valley [Fowler, 1978]. No evidence for a sizeable low velocity zone beneath the inner floor was found at 37°N or at 45°N. Bunch and Kennett [1980] documented a small velocity inversion (6.8 to 6.6 km/s) at 4 km depth on the Reykjanes Ridge at 60°N from the analysis of a reversed refraction line. In the most complete and best-constrained median valley seismic study to date, Purdy and Detrick [1986] found the structure at 23°N to be homogeneous over tens of kilometers and typical of simple, mature ocean crust. They observed no evidence for a magma chamber, but they did detect a zone of slightly lower layer-3 velocities beneath the along-axis high, which they interpreted as the seismic remnants of the most recent magmatic pulse along the 120-km-long section of the ridge sampled by the refraction line.

On the strength of the well-constrained 23°N experiment, we adopted as our preferred model a plane-layered compressional velocity structure derived from the Purdy and Detrick [1986] results (Figure 9). The use of this 1D structure, which was also used to locate microearthquakes at 23°N [Toomey *et al.*, 1985, 1988], facilitates the direct comparison of seismicity and tectonism between these studies. It is clear, however, from the analysis of the travel time and amplitude data from the refraction line also collected at

26°N (Chapter 4) that the crustal structure is not laterally homogeneous. In a later section, we evaluate the adequacy of the 1D model, with station corrections, by examining the effect of a 2D structure (Figure 9) on the earthquake locations and fault plane solutions. We will show that the distribution of epicenters and nature of faulting remain essentially unchanged (but the absolute depths are dependent on the velocity model). We will conclude that, for well-recorded earthquakes, the 1D model with station corrections can satisfactorily account for known lateral heterogeneity.

In order to constrain the shear wave velocity structure, we have utilized the technique of *Francis* [1976] to examine the average  $V_p/V_s$  ratio within the crust. A least squares fit to six differential S - P wave arrival times results in a  $V_p/V_s$  ratio of  $1.84 \pm 0.07$  (Figure 7a); the data sample the crust and upper mantle over a 5 - 40 km range. While the ratio is consistent with laboratory results indicating  $V_p/V_s$  ratios of 1.81 - 1.91 (Poisson's ratio of 0.28 - 0.31) for crustal layers 2 and 3 [*Hyndman*, 1979], and within the range of values (1.78 - 2.08) from previous MAR microearthquake studies [*Francis et al.*, 1977; *Lilwall et al.*, 1977, 1978], the ratio at 26°N is not well-constrained and may vary laterally and vertically throughout the region. The high  $V_p/V_s$  ratio of  $2.08 \pm 0.10$  determined by *Francis et al.* [1977] for 37°N has been attributed to a highly porous upper crust (due to high fissure and crack density), and could explain the low layer-2 velocities observed by *Whitmarsh* [1975] in this area. With an increase in pressure these cracks close, thereby decreasing the  $V_p/V_s$  ratio to average values (1.73 - 1.77) found elsewhere along the Mid-Atlantic Ridge.

### Starting Trial Parameters

A standard trial epicenter corresponding to the nearest station, with a trial origin time of 2 s prior to the earliest arrival time and an initial focal depth of 5 km beneath the datum (3.3 km below sea level), was used as the initial solution for HYPOINVERSE. To avoid improper convergence of the algorithm on local minima, all events were located using starting focal depths of 5, 8 and 10 km and the results were evaluated for consistency. In most cases, the hypocenters for one starting depth were within the 95% confidence interval of the others.

For events near or within the network for which solutions did not converge with starting depths of 5, 8, and 10 km (a total of 32 events), we fixed the depth at a value between 4 and 7 km equal to the average depth of nearby events. Some events northwest of the network on the western wall, and northeast of the network on the eastern wall, converge to the same solution (within 95% confidence limits) from starting depths of 5 and

8 km, but to an erroneously deep solution with a larger rms residual using a 10 km starting depth; for these events, we used the solution with an initial depth of 5 km. Events far to the north and south of the network (Figure 10), for which standard trial parameters gave solutions showing large negative S wave travel time residuals and near-zero eigenvalues, were located with a fixed focal depth of 8 km below the 3.3-km datum and a starting trial epicenter for events to the south midway between the ISC locations for the two largest teleseismically-determined earthquakes; events associated with the July 13, 1985, swarm used a starting location given by the teleseismically-relocated hypocenter (Chapter 5). For events in the median valley to the north, two iterations for location were done, first using the standard trial solution and second using the epicenter taken from the previous iteration of HYPOINVERSE.

### Solution Quality

Epicentral and depth resolution has been shown for a network of 3 or 4 stations spaced 10 km apart to be best both within and just outside the network [*Lilwall and Francis, 1978; Duschene et al., 1983*]. Resolution degrades for events located farther than about one focal depth in horizontal range from the nearest recording station. Of a total of 189 earthquakes located, 105 were within or sufficiently near the network to allow their focal depths to be independently resolved. Figure 11 shows a comparison of the rms travel time residuals obtained for a series of locations at fixed depths for events within and far outside the network; rms minima are clearly observed for well-recorded events (solid symbols and lines), but depth is not resolvable for the earthquake far to the south (open symbols and dashed line).

An estimate of the uncertainties in the earthquake hypocenter can be obtained from the calculated hypocenter error ellipsoid. In Table 2, the  $1-\sigma$  vertical error (erz) represents the largest value of the three semi-principal axes when projected onto a vertical line through the hypocenter, and the  $1-\sigma$  horizontal error (erh) represents the largest value when the error ellipsoid is projected onto a horizontal plane. 95% confidence error estimates were calculated by multiplying erh by 2.45 (for a system with 2 degrees of freedom) and erz by 1.96 (for a system with one degree of freedom). Actual uncertainties may be about twice the formal errors since the mean rms travel time residual (0.02 s) for the 105 events with good depth resolution is artificially low due to the small number of degrees of freedom in many hypocentral estimates, being about one-half the estimated error (0.05 s) in the reading of arrival times. Figure 12 shows histograms summarizing the distribution of residuals and errors for events with free and fixed focal depths.

### Dependence on S Wave Time, $V_p/V_s$ Ratio, and 1D Velocity Model

A subset of 26 microearthquakes with at least one S wave arrival was used to investigate the effect of errors in picking S arrival times (on an unoriented horizontal channel versus on the rotated transverse component) and the dependence of the earthquake location of the S wave observation; the events chosen are representative of the seismicity during the deployment. As mentioned earlier, repicking of the S wave time after rotation of the horizontal seismometers to radial and transverse components revealed up to 0.2 s differences between the SH pick and that from the earliest S arrival on an unoriented channel. Relocation of the events using the new SH arrival times, with station corrections re-estimated beforehand, however, showed only small changes in hypocenter (less than 350 m average change in epicenter and depth, and less than 0.02 s in origin time). These hypocentral changes are less than the estimated formal errors (Figure 12). We thus conclude that the use of S wave arrival times picked from unoriented horizontal channels on the OBSs does not result in biased estimates in hypocenter.

This subset of 26 earthquakes was also used to determine the importance of the S wave observations for events within and near the network. Hypocenters determined with only the P wave data were on average within 400 m in epicenter and depth of the locations obtained with both P and S wave observations, implying that good hypocentral estimates of well-recorded events can be obtained using only P wave data. These results also suggest that an estimate of the error made in picking the S wave on unoriented horizontal seismometers can be determined by examining the S wave travel time residual after hypocentral location. For earthquakes recorded by OBS 31, we find that the residuals for events within the inner floor range between 0.04 s and -0.10 s, which is consistent with the time difference (mean of -0.07s) in the picks made on the oriented and unoriented horizontal channels.

For 49 well-constrained events, each located with at least one S wave arrival time, we also investigated the effect of different 1D velocity structures on the resulting hypocenters. The inclusion of S with P arrivals decreases the uncertainty in focal depth but has little effect on the hypocenter itself (above). In order to test the influence of the shear velocity structure on the resulting locations, we have relocated the events with  $V_p/V_s$  ratios of 1.75 and 1.95. The value of the specific ratio results in hypocentral changes that are smaller than the 95% error estimates for events within the network; average changes in epicenter, depth, and origin time were 1 km, 0.5 km, and 0.11 s, respectively. For events outside the array, the primary effect is to move the epicenters farther ( $V_p/V_s = 1.75$ ) or

closer ( $V_p/V_s = 1.95$ ) to the network; the magnitude of the shift increases with the distance of the event to the nearest recording station. The maximum change was 3 km for earthquakes south of the array.

The effect of the compressional velocity structure was tested by relocating the events using a 1D velocity model determined for the Mid-Atlantic Ridge at 37°N [Fowler, 1976] and a  $V_p/V_s$  ratio of 1.84; station delays were recalculated before earthquake location. This model, which is characterized by a thinner crust and lesser upper mantle velocities, results in poorly-resolved focal depths for events outside the network, but for events within the network hypocentral changes are less than the 95% confidence estimates (average epicenter, depth, and origin time changes of 0.5 km, 0.7 km, and 0.04 s); although epicentral locations were insensitive to which was P wave model was used, smaller formal errors in focal depths were obtained using the structure from 23°N. Hence, we believe that the hypocentral parameters of the well-recorded events in this study are independent of the specific 1D velocity model.

## EPICENTRAL AND FOCAL DEPTH DISTRIBUTION

Hypocenters for 189 earthquakes (an average of 8.5 earthquakes/day, Figure 13) occurring over a 23-day period are shown in Figure 10 and tabulated in Table 2. These results show that there was a high level of activity beneath the median valley walls and inner floor to the south of the along-axis depth minimum, but that no earthquakes occurred immediately beneath the high-temperature hydrothermal field (Figures 3, 14). Figure 15 reveals that the focal depths of well-resolved events cluster between 3 and 7 km beneath the seafloor, with shallower depths associated with events beneath the along-axis high (Figure 16). Shear wave arrivals were used to locate 85 of the 189 earthquakes. Well-constrained hypocenters located with only P arrival time data have comparable depth distributions and rms fits to the data but have slightly larger horizontal and vertical errors ( $0.89 \pm 0.40$  km vs.  $0.51 \pm 0.22$  km,  $0.75 \pm 0.40$  vs  $0.50 \pm 0.10$  km, respectively, Figure 12). The mean rms residual for all events was  $0.04 \pm 0.04$  s; for 105 events with focal depth a free variable the rms residual was  $0.02 \pm 0.01$  s, and for 84 events with focal depth held fixed the rms residual of  $0.07 \pm 0.05$  s (Table 3, Figure 12). Earthquakes (both with free and fixed depth) located with S arrivals had a rms residual of  $0.05 \pm 0.03$  s and those located with only P arrivals had an rms residual of  $0.04 \pm 0.05$ s. The average travel time residual to all instruments for all events was  $0.01 \pm 0.18$  s ( $n=1,111$ , Figure 12), with the residuals for events with good focal depth resolution clustered tightly around zero ( $0.00 \pm 0.06$  s,  $n=662$ ).

The earthquake activity can be grouped into seven regions (Figure 10): (1) 27 events occurring beneath the inner floor at the along-axis high (H); (2) 11 events located beneath a local elliptical bathymetric high (volcano) at the ridge axis (V); (3) 15 events associated with the along-axis inner floor depth maximum (D, seafloor depths > 4.1 km); (4) 28 events occurring beneath the steeper eastern valley wall (E); (5) 56 events associated with the western inner floor/wall transition zone (W); (6) 15 events located to the south of the network in the area of the July 1985 teleseismically observed earthquake swarm (S); and (7) 18 events located to the north of the network (N). In general, no temporal correlation in seismicity was observed, though several swarm sets (typically 2-4 events within an hour) were located.

### **Inner Floor Seismicity**

Microearthquake hypocenters for events occurring beneath the inner floor of the median valley, defined nominally as events within 2 - 2.5 km of the ridge axis (seafloor depths ~3.7 km at the along-axis high and depths > 4.1 km to the south, Figure 14), show considerable variations in their spatial characters. In general, locatable activity defines an approximately linear trend parallel to the N25°E trend of the ridge axis. The variation in focal depth along the ridge axis from the seafloor depth minimum southward into the deeper portions of the median valley is shown in Figure 17. From this figure, we can see that the maximum depths of earthquakes beneath the inner floor appear to progressively increase as seafloor depth increases. A series of cross-axis sections at the locations of the along-axis high, volcano, and along-axis deep is shown in Figure 18.

#### *Inner Floor at Along-axis High*

The shallowmost recorded activity occurred beneath the along-axis high region (26°09'N) (Figure 17). Focal depths range from 2.2 to 5.8 km below the seafloor (Figure 16). Well-resolved depths between 2.2 and 3.4 km were obtained for five earthquakes (two at 26°09'N, average depth =  $2.6 \pm 0.5$  km; a swarm of three to the south at 26°07'N, average depth =  $3.3 \pm 0.2$  km) using S wave arrival times. No locatable events occurred in the immediate vicinity of the high-temperature hydrothermal vent field (Figure 3); the closest events were located within the inner floor about 3.5 km to the southwest (July 1, 2341UT) and about 3 km to the southeast beneath the base of the eastern wall (July 10, 1325UT), at depths of 5.8 km and 5.2 km, respectively. 86% of the events with good depth resolution were located at depths  $\leq 3.5$  km.



The profusion of earthquakes located only with P wave arrival times, events recorded primarily by only those OBHs located within the median valley, suggests that a comparatively large number of small earthquakes characterize the along-axis high area. This is also supported by the larger numbers of events that were detected by OBHs 2 and 3 (1660 events, 74 events/day; 1496 events, 70 events/day, respectively) located atop the high than by OBHs 1 and 6 in the deeper portions of the median valley (1187 events, 56 events/day; 1323 events, 64 events/day, respectively),

#### *Inner Floor at Ridge Axis Volcano*

A cluster of 11 earthquakes, including a swarm of seven events within 1.5 hours (July 10, 0212UT - 0333UT, average depth =  $5.5 \pm 1.0$  km), occurred almost directly beneath the ridge-axis volcano (Figures 3). Six of the swarm events (with epicenters < 1km in horizontal range from OBH 1) have well-resolved focal depths between 5.5 and 5.9 km below the seafloor, and 9 of 10 events (one event was located with a fixed focal depth) have depths from 4.8 to 6.7 km (Figures 17, 18b). The similarity of the waveforms and S - P times of two other events recorded by OBS 33 within the swarm time period, as well as a peak in the total number of events recorded per day on OBH 1 (Figure 5, day 15), suggest that the located earthquakes are but a small part of the swarm population.

#### *Inner Floor at Along-axis Deep*

Earthquakes located south of  $26^{\circ}05'N$  in the along-axis deep define a linear trend approximately parallel to the  $N25^{\circ}E$  trend of the median valley (Figure 14). Focal depths average  $5.4 \pm 1.0$  km, and range from 3.7 to 7.3 km below the seafloor (Figures 16, 17, 18c). The focal depths for the three shallowest events located farthest to the south (Figure 17) are not reliable and were excluded from the average estimate because both are located outside the network and have spuriously small vertical errors compared with errors for closer events.

#### **Eastern and Western Wall Seismicity**

Considerable activity, defining trends generally parallel to the ridge axis, is associated with both median valley walls adjacent to the along-axis high (Figure 14). Focal depths range from 3.5 to 6.8 km below the seafloor.

### *Eastern Wall*

Along the eastern wall within the network (Figure 14), the 12 well-constrained events adjacent to the along-axis high have focal depths from 4.4 to 6.2 km (Figure 18a, b), and two events near OBS 33 (July 10, 1904UT; July 16, 0456UT) have depths of 5.8 and 6.3 km (Figure 18c). Earthquake hypocenters do not appear to define a single fault plane with depth. Although significant topographic relief is present so that no one plane-layered structure is adequate, we believe that these events are well-resolved because they occurred within the network and appropriate station corrections have been applied. Of the 10 other earthquakes to the north of the network along the eastern wall, only four have depths that can be independently constrained. Changes in the local velocity structure in this area outside the network and north of the along-axis high may be the cause of the poor resolution of focal depth.

### *Western Inner Floor / Wall Transition*

The most active region during the 3-week deployment was on the western portion of the inner floor and beneath the adjacent walls. Of the 56 events within this region, good focal depth resolution was obtained for 40 earthquakes, including 17 events located with an S arrival. Events along the gentler sloping western wall in the along-axis high region were primarily located within 5 km of OBH 3 (instrument at high,  $x=10$  km, Figure 18a), and have depths of 3.5 to 5.7 km. Those closer than 3.5 km to the ridge axis appear to have occurred at shallower depths ( $4.0 \pm 0.3$  km) than those farther away ( $4.8 \pm 0.4$  km) (Figure 18a). Three events (July 6, 1029UT; July 7, 1723UT; July 8, 1503UT) were located at distances more than 2 km greater than their estimated focal depths, and their depths therefore have large uncertainties.

## **EARTHQUAKE LOCATION BY RMS GRID SEARCH**

The determination of earthquake locations and the construction of error ellipsoids from the rotated covariance matrix in HYPOINVERSE can give misleading results, especially with the use of sparse seismic networks in regions with locally heterogeneous velocity. In order to investigate whether the non-linearity is severe, we have used an rms travel-time-residual, grid-search technique [Rowlett and Forsyth, 1984] to determine earthquake hypocenters and rms residual confidence maps showing more realistic patterns of the true error volume (Figure 19). Rms residuals, weighted by the quality of the arrival

time readings as used in the HYPOINVERSE locations, are calculated at 1 km intervals in latitude and longitude for a 30 x 30 horizontal grid at eight depth levels (1 to 8 km at 1-km intervals) using the plane-layered model adopted in the previous section. Station corrections are included to account for station elevation and uncertainties in velocity structure and travel times. The best estimate of the hypocenter corresponds to the location of the smallest rms travel time residual in the grid volume.

Comparison of hypocentral parameters estimated by the inversion of the travel time data, with those determined by the rms grid-search method show that most epicenters and depths differ by less than the grid spacing ( $1.1 \pm 0.8$  km and  $0.7 \pm 0.6$  km respectively, Figure 20). Figure 19 shows an example of the distribution of rms residuals for two earthquakes using first the observed arrival time data and then noise-free, synthetic data calculated by assuming the HYPOINVERSE hypocenter. The virtually identical locations of the rms minima, as well as the general agreement between the orientations of the residual contours and the HYPOINVERSE error ellipse, demonstrate that the two methods are providing equally acceptable solutions. Because the network is fairly regular in instrument spacing, and iteratively-estimated station corrections have been used to account for travel time anomalies beneath the instruments, we conclude that problems with non-linearity in the estimation of realistic error ellipses appear to be negligible.

Location uncertainties can be estimated by considering confidence contours of the rms residual, though the statistically-estimated level of confidence lacks a true physical correspondence [Rowlett and Forsyth, 1984]. The residual associated with the  $\gamma\%$  contour can be written as

$$R_{\gamma} = R_{\text{MIN}} \left[ 1 + \left( \frac{N}{M-N} \right) F \left( N, M-N, 1 - \frac{\gamma}{100} \right) \right]^{1/2}$$

where  $R_{\text{MIN}}$  is the minimum weighted rms residual within the grid,  $N$  is the number of free parameters,  $M$  is the number of observations, and  $F$  follows the  $F$  distribution. Statistically, we can write the expected value for  $R_{\text{MIN}}$  for  $N$  parameters and  $M$  observations as  $[(M-N) / N]^{1/2}$ , but this appears to give 95% confidence contours that are too large ( $\pm 7$  km for  $R_{95\%} = 0.17$  s, event June 27, 0758UT in Figure 19) since instrument spacing ( $\sim 5$  km) would be less than the estimated error. We therefore take  $R_{\text{MIN}}$  to be the minimum calculated rms residual from the forward modelling when we compute the estimated error in the hypocenter.

The use of a probability representation of the error has the advantage of permitting both the seismicity and associated error to be quantitatively described by a single parameter

[Rowlett and Forsyth, 1984; Cessaro and Hussong, 1986]. By simply assigning a probability of occurrence per unit area, based on the 50% and 95% confidence levels for the rms residual (0, 0.50, or 0.95 depending on whether the grid space lies outside, or within the 50% or 95% contour), and then summing over all grid squares, we can graphically contour the level of seismicity taking into account the magnitude of error associated with the travel time data, station geometry, and crustal structure. Figure 21 shows the epicentral distribution for our experiment calculated for a fixed focal depth of 5 km using only events with more than 5 observations. The contours represent values of the summed probability for each non-zero grid square normalized by the total probability for the area. A comparison with the distribution of grid search and HYPOINVERSE epicenters shows that values of the summed probability  $> 7.4$ , describing regions with 0.05 events/km<sup>2</sup>, correspond to regions with well-resolved hypocenters or high levels of activity, and conversely, areas with values between 2 (0.01 events/km<sup>2</sup>) and 7.4 are regions in which a lower level of seismicity is present, or resolution of hypocentral parameters is poor.

## **EFFECT OF CRUSTAL HETEROGENEITY ON HYPOCENTERS**

In order to assess the adequacy of using a 1D velocity model with iteratively-determined station corrections to estimate hypocenters, we have relocated all well-resolved earthquakes using a 2D velocity structure derived in Chapter 4. Our primary goal is to evaluate whether the patterns of seismicity during the experiment, particularly the apparently shallower focal depths beneath the along-axis high and the lack of recorded earthquakes beneath the hydrothermal field, are robust with respect to uncertainties in crustal structure.

The model we use is derived from the tomographic inversion of travel time residuals from 32 shots and 57 earthquakes to seven instruments and encompasses the median valley from the along-axis high southward to the deep (Chapter 4). Velocity is parameterized at three nodal columns along axis (high, volcano, deep); in each column velocity is specified at depths of 0, 1, 3, and 5 km below a 3.6 km datum. The major features of this model (Figures 9, 22) are (1) significantly higher velocities within the shallowmost crust beneath the volcano and along-axis high region than beneath the deep, where low seafloor velocities characteristic of young oceanic crust are observed; (2) a decrease in velocity by more than 1.5 km/s from 3 to 5 km depth beneath the ridge-axis volcano; and (3) a complete crustal section (including a Moho) constrained only for the crust beneath the deep, where a crustal thickness of  $\sim 5$  km is observed. Because some

events occur at depths greater than 5 km beneath the inner floor high and valley walls where velocities are unconstrained, we consider two simple models: one in which velocities in the halfspace below 5 km jump discontinuously to 8.33 km/s beneath the volcano and high (model A), and a second in which velocities at 5 km are extended to depth (model B). Hypocenters located with these models should thus represent the two extremes of mislocation since we expect that velocities likely increase with depth below the volcano and high, but a step increase to mantle velocities is not probable. Use of model A results in minimum and model B in maximum changes in focal depth, or later and earlier origin times, respectively, for events greater than 5 km in depth. In addition, we assume that the median valley velocity structure extends beneath the eastern wall. Errors in the travel times and hypocenters of this approximation, which we know to be untrue from the comparison of P wave travel times from shots to instruments in the median valley and atop the eastern wall, are minor since typically only one or two arrival times are affected for the median valley events (our primary focus), and the travel time increase is probably at most only  $\sim 0.2$  s for ranges up to 15 km (Chapter 4); relocation of several earthquakes in which P wave travel times to OBH 5 and OBS 31, located on the crest of the wall furthest from the ridge axis, are increased 0.2 s (0.35 for S wave times) results in epicentral and depth changes ( $< 1$  km) that are within the 95% confidence limits of the hypocenters obtained with models A and B.

The method we use to invert the P and S wave travel times for hypocenter employs a generalized inverse method and involves the singular value decomposition of the hypocentral partial derivative matrix. The program utilizes an algorithm and weighting scheme similar to that of HYPOINVERSE. Quantitative estimates of the solution quality are obtained from the covariance matrix, and the simplified horizontal (erh) and vertical (erz) errors, as defined by HYPOINVERSE, are determined so that results are directly comparable. Travel times were calculated using a computationally-efficient, approximate ray tracer [Thurber, 1981] for a velocity structure parameterized by a set of grid points arbitrarily spaced in the x, y, and z directions; the velocity at any point along the ray path is determined by the linear average of the eight surrounding nodes weighted by the point's proximity to the node. S wave travel times were calculated using a  $V_p/V_s$  ratio of 1.84, as determined earlier. Station corrections were not used since travel times are computed with respect to the instrument's elevation above the datum and for a laterally-varying structure.

The changes in epicenter and depth upon relocation of the 105 earthquakes with good focal depth resolution using the 2D structure are shown for models A and B in Figures 23 and 24. In general, the patterns of seismicity remain unaltered, implying that a one-dimensional structure which includes station corrections provides an adequate measure

of the hypocentral distribution of well-recorded earthquakes at 26°N. Figures 23 and 24 show that the seismicity can still be characterized according to source location (as was done in Figures 10, 16, 17, and 18). Most importantly, from the examination of the along-axis depth distribution (Figure 24, top panels), we conclude that the observation of an increase in maximum focal depth with the deepening and widening of the median valley is independent of the assumed structure, and from Figure 23 that the crust in the immediate vicinity of the hydrothermal area remains free of activity. Note also that although these general patterns of seismicity are robust, the absolute depths of the events are dependent on the structure. Variations in structure with distance from the ridge axis, which are not accounted for by the 2D along-axis model, result in hypocentral biases for events on the periphery of the network and beneath the eastern wall. A consistent translation in hypocenters can be expected for events on the periphery of the network since azimuthal coverage is incomplete. Because the 2D model contains regions of higher velocities than the 1D structure, the translation of events beneath the western median valley is toward the network. Well-recorded events beneath the eastern wall are also translated eastward toward the wall-deployed instruments. This shift is likely not real, but arises because the true crustal velocities (as suggested by the travel times from shots to instruments on the wall, Chapter 4, and those used in the 1D model) are lower than those used in this 2D model.

The average change in epicenter and focal depth using models A and B was  $1.7 \pm 1.0$  km and  $1.6 \pm 0.7$  km (both eastward), and  $0.1 \pm 1.1$  km (shallower) and  $-1.21 \pm 1.6$  km (deeper), respectively (Table 3). These changes are comparable to the 95% confidence errors in horizontal and vertical position from the solutions obtained with the 1D model. The average change in origin time was  $0.2 \pm 0.2$  s (earlier) and  $0.0 \pm 0.2$  s using models A and B, respectively. Since most of the events are located within the upper 5 km of crust, hypocenters using models A and B are determined by the same crustal structure (generally higher velocity than that at 23°N, Figure 9) and result in increases in focal depth (with origin time unchanged, model B) or earlier origin times (with depth unchanged, model A). For earthquakes below 5 km, simple calculations show the percentage of travel time contributed by rays travelling within the half-space to be small (10-20% for a 6-km deep event 12 km from the receiver). The hypocentral differences illustrate the tradeoff between origin time and focal depth implicit in the algorithm for locating earthquakes; in our experiment, a 0.2-s change in origin time maps into a 1.2 km change in focal depth.

Closer examination of the median valley hypocentral distribution reveals that the largest changes in earthquake depth occur beneath the along-axis deep (1.6 - 1.8 km deeper for the 2D models, Table 4, Figure 24); in this region, velocities are greater than those assumed in the 1D model. Overall, the cluster beneath the ridge axis volcano remains, but

it moves ~1 km to the east and ~500 m deeper (using model B, Figure 24b). Events near the western inner floor-wall transition show the largest change in epicenter, a 2-km eastern shift toward the network and inner floor (Figures 23, 24). Events beneath the eastern wall move upward (Figure 24a, model A), which is opposite in sense to all other focal depth changes. These observations result from our assumption that velocities within the inner floor extend indefinitely off axis, which is not likely since travel times from shots within the inner floor to instruments on the wall show measurable differences (Chapter 4).

## FOCAL MECHANISMS

Individual and composite double-couple focal mechanisms were constructed from impulsive first motion observations of well-recorded events. The polarities of the OBHs and the vertical components of the OBSs were determined from the water wave arrivals of the closest ranging shots to the instruments. For OBH 5 and 8, both located on the valley walls, the impulsive high-amplitude first motion water arrivals from shots centered within the median valley were used since arrivals from the closest ranges shot "downslope" to the instrument appeared to be contaminated by refracted energy. The angles of emergence and azimuths from the source to the receivers determined by HYPOINVERSE were used to plot the first motions on an equal-area projection of the lower focal hemisphere. Orthogonal fault planes were determined by finding the best fitting set of nodal planes, judged visually, which maximized the placement of small amplitude arrivals ("x" symbol in focal sphere plots) near nodal planes and impulsive first motions centrally within compressional and dilatational quadrants. Figure 25 shows the locations of events used in the construction of selected composite fault plane solutions for the inner floor and flanking walls (Figures 26-31); Table 5 gives the event times and nodal plane orientations for the composite mechanisms.

Figure 32 summarizes the diversity of fault mechanisms derived from the construction of double-couple fault plane solutions for spatially-clustered events. Beneath the inner floor, normal faulting on near-vertical or sub-horizontal planes striking parallel to the ridge axis is suggested. In addition, reverse or thrust faulting appears to be associated with a swarm of events beneath the axial volcano. A number of inconsistent first motions, presumably due to a 90° phase shift at a reflecting boundary within the crust, however, attest to the complexity of the inner floor faulting. In a later section, we will demonstrate that these fault plane solutions appear to be robust with respect to uncertainties in the velocity structure.

## Inner Floor

Composite focal mechanisms for three groups of events (H1, H2, H3) within the inner floor near the along-axis high indicate faulting along steeply dipping, or sub-horizontal, planes trending approximately parallel, N12°E to N35°E, to the median valley (Figure 26). Although most arrivals are dilatations, impulsive dilatational first motions located centrally on the focal sphere (see for example H2, OBHs 2 and 3), coupled with compressional arrivals at the periphery, suggest that a near-vertical and sub-horizontal set of focal planes is appropriate. Later analysis of the effects on the takeoff angle and azimuth of a two-dimensional structure shows that the nodal plane orientations are reasonably well-constrained with respect to variations in structure.

Focal mechanism solutions for eight events beneath the volcano can be divided into two groups, with the difference resulting from a phase reversal for arrivals at OBH 2, situated near the active, high-temperature hydrothermal vents (Figure 27). Compressional arrivals at OBH 1 rule out normal faulting mechanisms. Four events can be fit with a reverse faulting mechanism (V1), with planes trending N28°E, parallel to the ridge. In contrast, because arrivals to OBH 2 are dilatational instead of compressional, we cannot fit any double couple mechanism to the other four events (V2). However, if we ignore the OBH 2 observations, two of which have small amplitude first motions, then the same thrust mechanism can be fit to these events.

In the along-axis deep, although good azimuthal coverage exists, there is uncertainty as to whether reverse faulting or normal faulting on either near-vertical or sub-horizontal planes characterizes the region (Figure 28, D1, D2). Compressional arrivals at OBHs 1 and 6 preclude a conventional normal faulting mechanism. Construction of composite and single event mechanisms for other events in this region also result in non-unique sets of nodal planes. Consideration of ray incidence angles using a heterogeneous velocity structure (below) does not resolve the ambiguity in the faulting mechanism.

## Eastern and Western Valley Walls

Two composite focal mechanism solutions (Figure 29, E1, E2) are consistent with normal faulting beneath the eastern valley wall. For three events within 2 km of each other at the base of the eastern wall near OBH 2 (depths of 4.5 and 5.2 km, E2), the preferred mechanism is consistent with normal faulting along a plane dipping ~50° towards the valley and striking N53°E. Similarly, normal faulting along a plane striking N42°E and dipping 60° to the NW characterizes three other events at the base of the eastern wall (Figure 29,



E1), but a reverse faulting mechanism cannot be excluded by the available data. For the normal faulting mechanisms, the strikes of both sets of focal planes are subparallel to the local trend of the eastern wall.

First motion observations for earthquakes beneath the western portions of the inner floor and adjacent wall near the along-axis high are consistent with normal faulting (Figure 30). The profusion of consistent, unambiguous first motion data suggests a common mechanism for large subsets of the events from this area (W1). On the western portion of the inner floor along-axis high, two sets of fault planes can be fit equally well to the first motion observations (W2, W3). The north-south striking planes, rather than those trending northwest-southeast, are preferred because of their consistency with the trend of the seismicity. For all three composite mechanisms, we suggest that it is the high-angle plane dipping toward the axis, rather than the low-angle plane dipping away, that is the actual fault plane for these events. The limited azimuthal coverage and the lack of knowledge about the local velocity structure specific to the earthquake source area, however, contributes to an uncertainty in the ray takeoff angles, and thus in nodal plane orientations, that is larger than for events within the network.

The close similarities in the first motion data for earthquakes at the western wall/inner floor transition zone (Figure 30, W1, and possibly W2 and W3) with fault plane solutions for inner floor events at the along-axis high (Figure 26, H1, H2, H3) suggests a consistent faulting mechanism (normal faulting along planes dipping steeply toward the valley) for earthquakes beneath the median valley in the along-axis high region. In contrast, normal faulting along moderately dipping planes striking N50°E (Figure 31, WD) is suggested by a composite solution for three events at the base of the western valley wall in the region of the along-axis depth maximum (26°04'N, 44°54'W).

## **EFFECT OF CRUSTAL HETEROGENEITY ON FOCAL MECHANISMS**

To evaluate the effect of earthquake mislocation on the focal mechanism solutions for the major groups of activity, we have determined changes in the positions of first motion observations on the focal sphere when the earthquakes are relocated with 2D models A and B. Note that our test models represent extremes bracketing the probable structure at depths greater than 5 km, and thus the probable magnitude and sense of change lies somewhere between those obtained with these models. In addition, in order to evaluate more easily the robustness of each fault plane solution, we have also plotted along with the relocated data the preferred set of nodal planes determined from the locations and ray parameters obtained with the 1D structure.

The reanalysis of the first motion data with a 2D structure results in no major changes in the nature of faulting (Figures 33-37). The eastward and downward translations of the hypocenters do cause the first motion observations to move to the east and toward the center of the focal sphere, resulting in most cases only in changes in fault dip ( $\leq 20^\circ$ ), but the type of faulting (normal, reverse) appears robust because the locations of diagnostic first motion observations (dilatational or compressional first arrivals to instruments located above the sources) do not change substantially.

Examination of Figures 33-37 reveals that no change in either the type of double-couple mechanism or in the orientations of the nodal planes is required for first motion data mapped onto the focal sphere with 2D model A (8.33 km/s velocity within the halfspace below 5 km). This is because the changes in focal depth (Figure 24a), which influence the steepness of the ray takeoff angle from the source, are small. Although the mapping of first motion data from earthquakes beneath the western median valley and walls to OBHs 1, 2, and 3 show translations of up to  $30^\circ$  to the southeast (Figures 33, 37), the sense of movement serves only to confirm that the mechanisms are characterized by normal faulting (dilatational arrivals are now more centrally located within the focal sphere).

First motion observations for earthquakes located with 2D model B, characterized by slower velocities beneath the volcano and high at depths of 5 km and greater, show larger changes in their mapped positions due to the greater focal depths (Figure 24b), but these changes are still not sufficient to alter the type of faulting inferred from the solutions obtained with the 1D model. A shoaling in the dip of the high-angle nodal planes by  $\sim 20^\circ$  for mechanisms beneath the along-axis high (Figure 33) and ridge-axis volcano (Figure 34) is suggested, however, because of the eastward movement of the epicenters.

To summarize, in general we find that faulting beneath the along-axis high is characterized by normal faulting along near-vertical, or sub-horizontal, planes striking parallel to the ridge (Figure 33). Reverse or thrust faulting remains associated with the swarm of events beneath the volcano, since compressional arrivals at OBH 1 move insignificantly (Figure 34); a mechanism constructed using model B requires changes in fault plane dip by  $\sim 20^\circ$ . The type of faulting describing activity beneath the inner floor deep remains ambiguous, although a compressional arrival at OBH 1 continues to rule out normal faulting along moderately dipping planes (Figure 35); the larger uncertainties in the hypocentral estimates (larger and more variable changes in hypocenter are seen upon relocation, Figures 23, 24, Table 4) result in a number of inconsistent first motions, and as a consequence we cannot confidently fit a pair of orthogonal nodal planes to the data.

Faulting beneath the eastern wall is also still consistent with normal faulting (Figure 36), but the orientations of the nodal planes are not well-constrained because only one set

of compressional arrivals is observed (OBH 5). On the basis of the consistency among composite mechanisms constructed for events beneath the eastern wall, we believe that normal faulting characterizes this region. However, we note that these solutions lack the conclusive evidence (clear dilatational arrivals located centrally within the focal sphere) to establish this inference firmly.

Although the events beneath the western wall / inner floor transition lie outside the network, and are thus susceptible to location biases resulting from the limited azimuthal range of the arrival time data, the observation of dilatational arrivals near the center of the focal sphere (OBHs 1, 2, 3 in Figure 37a; OBH 3 in Figure 37b) strongly suggests normal faulting beneath this region. However, the orientations of the nodal planes for mechanisms W2 (and also W3) remain uncertain. The similarity in mechanisms for events in Figure 37 with those characterizing the inner floor (Figure 33) suggests that all of these events reflect normal faulting along relatively high-angle inward-facing, or near-horizontal outward-facing, planes. The first motion data using model A (Figure 37a) can be better fit with a high-angle nodal plane that dips less steeply by perhaps  $10^\circ$ .

## EARTHQUAKE SOURCE PARAMETERS

Estimates of the seismic moment  $M_0$ , source radius  $r$ , average fault slip  $u$ , and average stress drop  $\Delta\sigma$ , using the seismic source theory of *Brune* [1970, 1971] were calculated from the low-frequency spectral level  $\Omega_0$  and corner frequency  $f_0$  read from OBS and OBH amplitude spectra. *Hanks and Wyss* [1972] have shown in a comparison of source parameters determined from teleseismic P and S wave data and field observations that the Brune model spectra can be used to obtain reliable estimates for these quantities from P waveforms. *b*-values describing the size distribution of microearthquakes were determined from the seismic moments of well-constrained events within or near the network.

### Low-frequency Spectral Level and Corner Frequency

Displacement spectra for P and S waves recorded on the vertical seismometer by OBSs 31 and 33, both of which showed good coupling characteristics to the seafloor, were calculated by correcting for instrument response and waveform attenuation following *Trehu and Solomon* [1983]. Computation of OBH water displacement spectra, accomplished by correcting for instrument response and attenuation and assuming P waves incident as plane waves at the seafloor, followed *Toomey et al.* [1988]. The P and S spectra were calculated

using 1- and 2-s time windows starting at 0.1 and 0.2 s before the phase arrival time, respectively. No dependence of  $f_0$  on slant range from the source to receiver, and no difference between estimates from P and S waveforms, was observed, suggesting that the assumption of a constant attenuation factor ( $Q_p = Q_s = 500$ ) is adequate. To minimize the Q uncertainty however, we picked  $f_0$  only on the instrument closest to the source (OBHs 1, 2, or 6), since the high-frequency content is maximized for closer instruments. An example of the amplitude spectrum for an event recorded by OBH 2, along with the  $\Omega_0$  and  $f_0$  estimates, is shown in Figure 38. Average  $\Omega_0$  values could usually be picked to within a factor of 2 to 3 for the 26°N data. The far-field displacement spectra show properties typically predicted by earthquake rupture models [e.g., *Aki, 1966; Haskell, 1969; Brune, 1970*], with amplitudes which are constant at low frequencies ( $< f_0$ ) and decay at  $f^{-2}$  at higher frequencies ( $> f_0$ );  $f_0$  was picked as the frequency corresponding to the intersection of the  $\Omega_0$  level and the line with a slope of  $f^{-2}$  at higher frequencies.

events within the network was observed.

### Seismic Moments

In order to investigate possible correlations with earthquake location (high, deep, volcano, valley walls) and/or instrument, and to obtain the best estimate, through averaging, of the earthquake size for each event, we examined spectra for all earthquakes recorded on OBHs 1, 2, and 6, and for all earthquakes located with an S arrival recorded on OBHs 3 and 5, in addition to P and S spectra on OBSs 31 and 33. This resulted in a very large data set (492  $M_0$  estimates) describing 170 earthquakes.

Seismic moments were calculated from the formula [*Brune, 1970, 1971*]

$$M_0 = \frac{4 \pi \rho V^3 x \Omega_0}{K R}$$

where  $\rho$  and  $V$  are the density and wave velocity at the source, respectively,  $x$  is the distance from the source to the receiver, and  $\Omega_0$  is the low frequency spectral amplitude. The quantities  $\rho$  and  $V$  were taken to be average values for density (2.9) and velocity ( $V_p = 6.5$  km/s,  $V_p/V_s = 1.84$ ) within the crust.  $K$ , a correction factor for the interaction of a plane wave at the seafloor [*Ergin, 1952*], was calculated for a typical range of incidence angles (20° to 30°) using plausible velocities and densities logged from ODP Leg 106 and 109 drill cores at 23°N [*Shipboard Scientific Party, 1988*], and taken to be 1.6 and 0.8 for P and S waves, respectively.  $R$  is the radiation pattern correction factor, varying from 0 to

1, for an observation on a given instrument assuming a double-couple fault mechanism [Aki and Richards, 1980]. Because of the uncertainty in the precise orientations of the nodal planes, we used general mechanisms which describe the nature of faulting associated with each epicenter (normal or reverse faulting on steeply dipping ( $\delta = 70^\circ$ ) or moderately dipping ( $\delta = 50^\circ$ ) planes); the strike is constrained to be N25°E, parallel to the median valley. Exceptions were events to the south of the array, which were assigned a normal faulting mechanism ( $\phi_s = N01^\circ E$ ,  $\delta = 46^\circ$ , and  $\lambda = 248^\circ$ ) based on the Harvard moment tensor solution for the large earthquake at 1854UT on July 13, 1985 [Dziewonski *et al.*, 1986]; no correction ( $R = 1$ ) was made for events to the north of the network since their locations and mechanisms are poorly constrained, resulting in a minimum estimate of  $M_0$ . Moments were not estimated from near-nodal records ( $R \leq 0.05$ ).

In order to arrive at an objective estimate of the size of an event, especially in an area of crustal heterogeneity, we calculate an average value for  $M_0$ , weighted by the quality of the  $\Omega_0$  estimate; weights of 1, 0.5, and 0.33, corresponding to reading errors of 0.2, 0.5, and 1.0 log units, respectively, were assigned to each  $\Omega_0$  pick. The number of data for a single event ranged from 1 to 9. Although a few estimates for a single event differ by more than a factor of 10, probably due to incorrect radiation pattern corrections, most  $M_0$  estimates are within a factor of 3 to 5 of each other (Figure 39). Comparison of  $M_0$  estimates using different instruments revealed no correlation with receiver, suggesting that the best objective estimate of  $M_0$  is obtained by taking an average.

Moments for 170 earthquakes ranged from  $4 \times 10^{17}$  to  $6 \times 10^{22}$  dyn cm, with 75% of the earthquakes between  $2 \times 10^{18}$  and  $6 \times 10^{19}$  dyn cm (Figure 40a, Table 6). Examination of the earthquake size distribution by location (Figure 40b) showed that the largest events were those to the south of the network, associated with the July 13, 1985, teleseismically-recorded earthquake swarm. The figure also shows that moments for earthquakes recorded only by the OBHs (P wave times only), of which the majority occurred beneath the along-axis high and western wall (see also seismicity in Figures 3 and 14), to be generally smaller than those events recorded by OBS 31 atop of the eastern wall. Comparison reveals also that no significant correlation of  $M_0$  with source location for events within the network was observed.

### Source Dimension, Fault Slip, and Stress Drop

Using the Brune model we estimated a source dimension by calculating the radius of an equivalent circular source from the formula

$$r = \frac{cV}{f_0}$$

where  $V$  is the P wave velocity at the source,  $f_0$  is the corner frequency, and  $c$  is a constant equal to about 0.2 [Sato and Hirasawa, 1973].

Several other source parameters were calculated from the estimates of  $M_0$  and  $r$ . Brune [1970, 1971] derived the expression for the average stress drop  $\Delta\sigma$  to be

$$\Delta\sigma = \frac{7}{16} \frac{M_0}{r^3}$$

Also,  $M_0$  can be related to the average slip across a fault by

$$u = \frac{M_0}{\mu A}$$

where  $\mu$  is the shear modulus, and  $A$  is the fault area [Keilis-Borok, 1959; Aki, 1966], here taken to be  $\pi r^2$ .

Source dimensions, stress drops, and fault slip magnitudes for 27 well-constrained events (for which confident estimates of  $f_0$  could be obtained) that were used in the construction of focal mechanisms (events in Figures 26-31), ranged from 0.1 - 0.3 km, 0.1 - 5 bar, and 0.02 - 0.4 mm, respectively (Table 6). Events beneath the inner floor at the along-axis high and the western inner floor/wall transition tended to have smaller moments (average  $9.6 \times 10^{18}$  dyn cm) and were characterized by smaller stress drops ( $< 2$  bar) and fault displacements ( $< 0.2$  mm) than were calculated for events beneath and near the volcano, along-axis deep, and eastern wall (average  $8.6 \times 10^{19}$  dyn cm).

### **b-values**

The distribution of events by seismic moment is shown by plotting the logarithmic cumulative number  $N$  of earthquakes greater than  $M_0$  versus  $M_0$  for 136 earthquakes located within or near the network. The slope of a linear fit to the data then yields the so-called "b-value," described by the relation  $\log N(M_0) = a - bM_0$ . Higher b-values indicate larger numbers of small events and fewer large ones; studies have suggested that high b-values describe volcanic environments where small earthquakes may accompany the injection of magma or result from thermal-contraction-induced cracking of a cooling intrusion [Minakami, 1960; Scholz, 1968; Wyss, 1973; Brandsdottir and Einarsson, 1979;

*Foulger and Long*, 1984]. For events within or near the network with  $M_0 \geq 10^{18.5}$  (so as to avoid a bias resulting from incomplete sampling of small earthquakes), linear regression gives a b-value of  $1.02 \pm 0.08$  (Figure 41a). Closer examination of b-values associated with earthquakes in particular source regions indicates, however, a variation ranging from 0.6 to 1.5 (Figure 41b). Earthquakes beneath the inner floor depth minimum and adjacent walls appear to be associated with higher b-values (H:  $1.1 \pm 0.1$ ,  $n = 27$ ; W:  $1.5 \pm 0.1$ ,  $n = 54$ ; E:  $1.2 \pm 0.1$ ,  $n = 28$ ) than events beneath the deeper portions of the inner floor to the south (V:  $0.9 \pm 0.1$ ,  $n = 11$ ; D:  $0.6 \pm 0.1$ ,  $n = 15$ ). We believe the effect of earthquake mislocation on  $M_0$  and b is likely to be minor overall because most events with measured moments occurred within or near the network. Since a 1 km change in epicenter and focal depth (such as might occur using the model B structure) results in a consistent increase in  $M_0$  (on average by a factor of 3 to 4), which is within the estimated error, we believe the b-values estimated with the 1D model to be insensitive to earthquake mislocation.

## DISCUSSION

The distribution of hypocenters and the diversity of fault types associated with earthquakes beneath the inner floor and walls suggest a spatially variable tectonic state for the ridge segment at  $26^\circ\text{N}$ . These variations are presumably a signature of the depth region over which brittle failure occurs and are a consequence of along-axis changes in the thermal structure and state of stress. In the following discussion we compare the observations  $26^\circ\text{N}$  with results of other microearthquake studies and attempt to place the seismic observations in the context of a kinematic spreading cell model describing accretionary variations in the vicinity of a ridge-crest hydrothermal field.

### Fault Geometry

The observation of source mechanisms suggesting high-angle or sub-horizontal faulting beneath the inner floor high at  $26^\circ\text{N}$  (Figure 32), as well as at  $35^\circ\text{N}$  [*Murray et al.*, 1984] and  $45^\circ\text{N}$  [*Lilwall*, 1980], implies that the geometry of faulting beneath portions of the inner floor may be fundamentally different from that which describes earthquake activity a few kilometers off-axis. Although normal faulting associated with the valley walls may be responsible for the rift flank topography, microearthquakes within the inner floor, especially beneath the along-axis high, may in contrast result from other processes, including thermal stresses induced by the cooling of hot rock, or hydraulic fracture (cracking) resulting from hydrothermal circulation or magma migration. The presence of an

active high-temperature hydrothermal field strongly suggests that thermal stresses may be important, especially in the region of the along-axis high. The observation of dilatational, rather than compressive first motions (which would be expected for an expanding fluid-filled crack, *Chouet and Julian, 1985*), to instruments atop the high suggests that fracture induced by the recent intrusion of a sizeable magma body is unlikely, and the propagation of shear waves across the median valley (e.g., Figure 42) also appears to preclude the existence of a large zone of molten material.

When interpreted together with normal faulting at more conventional dip angles beneath the eastern wall, near-horizontal fault planes beneath the central inner floor might suggest listric faulting along fault planes which become less steep toward the ridge axis (to the west). The presence of a shallow heat source, whose roof lies sub-parallel to the seafloor, may produce horizontal slip near the brittle-ductile transition [*Byerlee, 1968*]. Alternatively, an interpretation of the mechanisms in terms of high-angle normal faulting might suggest that faulting beneath the inner walls is at lower dip angles because of subsequent rotation of fault blocks away from the axis during extension [*Angelier and Colletta, 1983*]. The observation of back-tilted fault terraces with dip angles of up to 30° atop the eastern wall [*Karson and Rona, 1982, 1989*] is permissive of both interpretations. We lack an independent measure to ascertain which of these mechanisms is more likely.

The reverse fault mechanisms of events beneath the ridge axis volcano at 26°06'N, 44°51.5'W (Figure 32) cannot be explained by extension along the ridge axis. These mechanisms and aspects of the distribution of seismic activity, however, can be qualitatively explained by the release of thermal stress formed by the juxtaposition of hot and cool rock. In Figure 43, we superimpose the seismic structure determined in Chapter 4 on the along-axis profile of earthquake focal depths. The inferred low velocity zone beneath the volcano and the along-axis high (stippled area in Figure 43), based on the seismic observations from this chapter and Chapter 4, is comparatively aseismic but is limned by regions of high rates of seismicity. Tensional crack formation resulting from the thermal contraction of a cooling intrusive body has been used to explain anomalous focal solutions for small magnitude earthquakes beneath the Hengill geothermal field in Iceland [*Foulger and Long, 1984*]. If we assume the most recent intrusion at 26°N occurred laterally from the high (rather than by vertical ascent), then the lateral contraction upon cooling would lead to tension cracking or normal faulting within the region of greatest volume change but would put the overlying and underlying material (e.g., beneath the volcano) under horizontal compression, leading to reverse faulting.

Microearthquake studies of active rifting and eruptive episodes in Iceland [*Klein et al., 1977, Brandsdottir and Einarsson, 1979*], where subaerial mapping of fissures can



often be used to infer a preferred fault plane, reveals a hypocentral distribution and range of faulting characteristics broadly similar to the results from 26°N. During a deflation episode of the Krafla volcano in 1977, *Brandsdottir and Einarsson* [1979] found hypocenters of well-resolved events to cluster between 3- and 4-km depth near the top of the inferred magma chamber [*Einarsson*, 1978]; composite fault plane solutions suggested normal or reverse faulting along steeply dipping planes with fault plane strikes that were more variable than suggested by the trends of surface fissures and faults. In a study of a large earthquake swarm along the Reykjanes Peninsula in 1972, *Klein et al.* [1977] document a number of anomalous events near a region of low seismicity characterized by nonorthogonal nodal planes. The mechanisms constructed for individual events have reduced dilatational quadrants and were located very close to earthquakes described by steeply-dipping normal faults, suggesting that either a non-double-couple seismic source (such as from dike injection) or small-scale velocity heterogeneities were present. The conclusions of both studies imply that earthquake swarm activity in association with active tectonism and volcanism results in a diversity of faulting types because of the presence of a locally variable thermal structure that is superimposed on an extensional environment [*Mogi*, 1963]. By analogy, we note that a similar diversity of faulting types might also be expected at 26°N, especially in the vicinity of the hydrothermal field where local variations in pore pressure and rock strength are apt to be large.

### Along-strike Variation in Focal Depth

The apparent deepening of microearthquake hypocenters southward from the along-axis high into the deeper portions of the median valley compares similarly with the depth distributions from two well-constrained microearthquake studies which were carried out within a morphological along-axis depth maximum (23°N, [*Toomey et al.*, 1985, 1988]) and minimum (35.3°N, [*Murray et al.*, 1984]) (Figure 44). Microearthquakes beneath the inner floor at 23°N were in general located between 4 and 8 km below the seafloor and were characterized by normal faulting along planes dipping at 30° or more. This region is characterized by a velocity structure and crustal thickness typical of normal young ocean crust [*Purdy and Detrick*, 1986] and was interpreted by *Toomey et al.* [1985, 1988] as a volcanically quiescent region that has experienced continuous extension without magmatic intrusion for at least  $10^4$  years. In addition, b-values for earthquakes beneath the along-axis deep in both this study and at 23°N are comparable ( $0.6 \pm 0.1$  and  $0.8 \pm 0.2$ , respectively). On the basis of the similarity in focal depth distribution, b-values, and velocity structure at 23°N with those observed beneath the deeper portions of the median

valley at 26°N, we speculate that the crust beneath the inner floor deep at 26°N is presently characterized by ongoing extension and lacks recent sizeable intrusions of magma.

Although two instruments were located less than 10 km from the along-axis depth minimum during the experiment at 23°N, only one poorly-constrained event was located there, suggesting a paucity of tectonic faulting beneath the along-axis high region. The generally low activity during the experiment was consistent with the interpretation that this region represented the locus of the most recent magmatic injection, as suggested by the zone of lower layer-3 velocities found by *Purdy and Detrick* [1986]. From a microearthquake survey centered about the inner floor, along-axis high near 35.3°N, *Murray et al.* [1984] suggested a thinner seismogenic zone. The preferred composite fault plane solution and hypocentral locations for a swarm of 11 events at 3-5 km depth indicated high-angle or very low angle normal faulting, although reverse faulting was possible. Both the depth distribution and the type of faulting found at 35°N are similar to the inner floor activity observed beneath the along-axis high at 26°N. These results suggest that along-axis highs may be characterized by generally shallower seismic activity than along-axis deeps. Such an inference is in accord with generally higher temperatures beneath the axial highs. The maximum depth of earthquakes along axis likely marks the transition from brittle fracture to more ductile behavior; crust below this zone deforms aseismically at temperatures in excess of about 400°C [*Chen and Molnar*, 1985]. Substantiation of such a working hypothesis will require much longer deployments and investigation of a number of other ridge segments, however, since microearthquake observations over only a two- to three-week period may not characterize the long-term behavior of the ridge.

In addition, the presence of an active, high-temperature, black-smoker field atop the along-axis high at 26°N is an indicator that the thermal structure probably plays a major role in determining the spatial distribution of hypocenters and thus the extent of brittle failure. Along the faster-spreading East Pacific Rise (EPR), the general aseismicity and the shallow depths inferred for the few locatable ridge-axis microearthquakes [*Riedesel et al.*, 1982; *Lilwall et al.*, 1981] have been used as evidence supporting the existence of only a thin brittle zone overlying the inferred magma chamber. From multichannel seismic profiling [*Detrick et al.*, 1987] and tomographic imaging [*Burnett et al.*, 1989; *Toomey et al.*, 1989] of a zone of low velocities along the EPR between 9 and 13°N, this lid could be as thin as 1.5 km. Over a period of 3 weeks, *Riedesel et al.* [1982] reported the occurrence of only 11 small earthquakes ( $M_0 \sim 10^{17}$  dyn cm), with maximum depths of 2-3 km, located in the vicinity of the black-smoker field at 21°N on the EPR. Along the MAR at 26°N, the lack of seismic activity beneath the hydrothermal field, and the shallowness of the earthquake activity beneath the along-axis high during our experiment, bears some resemblance to the

observations on the EPR at 21°N. We interpret the volume lacking seismic activity beneath the hydrothermal field at 26°N as a region of hot, unfractured rock which is predominantly solid but may still possess small pockets of melt.

### Hydrothermal Circulation at the Along-axis High

No clear consensus presently exists as to the maximum depth of hydrothermal circulation along mid-ocean ridges, or the conduits along which the water travels or the efficiency of cooling. The discrepancy between measured values of the conductive heat flow at the ridge crest and those predicted by thermal models for the cooling of the oceanic lithosphere imply that the contribution of hydrothermal convection to cooling is substantial. In a numerical simulation of convective cooling at a slow-spreading ridge environment, *Fehn and Cathles* [1979] found that the presence of high permeability zones, such as created by faults and fissures, would greatly increase the rate at which hot rock cools. *Strens and Cann* [1982, 1986] and *Lowell and Rona* [1985] have modelled the formation of large sulfide bodies using upflow and downflow zones of faults and sets of fractures. Large metallic sulfide bodies, such as might be found at 26°N [*Rona et al.*, 1986], could only be generated by the deep circulation of water through hot rock (not a magma chamber) under a favorable geometry of fault-controlled conduits, or by the tapping of additional heat from a magma body [*Strens and Cann*, 1986]. These studies suggest that the intensity of high-temperature hydrothermal activity is a function of the ability of seawater to tap the heat source beneath the seafloor, and that locations favorable for the efficient penetration of water would be along faults. Their inferences are consistent with the occurrence of high-temperature vent fields in conjunction with fissures along the East Pacific Rise [e.g., *Hekinian et al.*, 1984; *RISE Project Group*, 1980] and Mid-Atlantic Ridge [*Detrick et al.*, 1986].

Analysis of oxygen isotope data from the Samail Ophiolite in Oman suggests that two hydrothermal convective systems, each independent of the other, must have existed during the time of crustal accretion [*Gregory and Taylor*, 1981]. The upper system was characterized by high water / rock ratios (i.e., a large amount of water is required to produce a given amount of the  $\delta^{18}\text{O}$  isotope) and operated with open seawater circulation within the upper 3 km of the crust over the ridge-axis magma chamber, while the lower one developed at the periphery of the chamber interacting with the layered gabbros at depth under high temperatures ( $>400^\circ\text{C}$ ) and in a closed system (low water / rock ratios). The two systems only come into contact at the edges of the chamber where solidified rock can fracture, thereby permitting pathways for the interaction of  $\delta^{18}\text{O}$ -depleted, deep water with

$\delta^{18}\text{O}$ -enriched, pillow lava water and formation of the intermediary waters describing the mid-level sheeted dikes. The depletion of  $\delta^{18}\text{O}$  in the gabbros relative to  $\delta^{18}\text{O}$  values of primary magmas, which can result from high-temperature hydrothermal alteration, represents evidence that seawater penetrated to depths greater than 5 km into the 8 km crustal section.

In the context of the high-temperature vent field at 26°N, we suggest that the formation of the field near the base of the eastern wall is a direct consequence of water movement along fault planes formed by the dip-slip faulting that characterizes microearthquake activity beneath the wall (Figure 43b). The normal faults, which strike subparallel to the ridge axis and dip at  $\sim 50^\circ$  toward the inner floor, provide permeable pathways along which heated water (perhaps  $> 400^\circ\text{C}$  according to *Gregory and Taylor* [1981]) can return rapidly and efficiently to the surface, where it exits at still high temperatures from black-smoker chimneys and fissures. The penetration of water into hot rock can result in the substantial extraction of heat since thermal contraction provides an efficient mode of tapping the thermal energy from the rock by producing a rapidly advancing crack front [*Lister*, 1977, 1983]. This scenario is essential for the formation of high-temperature vent fields, for at slower upflow rates (such as through a randomly-cracked crust), mineral precipitation and clogging of the discharge zone results in lower temperature alteration [*Sleep*, 1983]. The low-temperature hydrothermal activity observed on the eastern wall [*Rona et al.*, 1976] would also be consistent with this scenario since in general the discharge zones (faults) on the wall are located farther from the inner floor heat source.

The occurrence of earthquake activity, albeit only two events, at depths  $> 5$  km within  $\sim 3$  km of the mapped vent field suggests that faults could extend to these levels and thus allow water to penetrate to depths consistent with those inferred from the  $\delta^{18}\text{O}$  values of gabbros in the Samail ophiolite [*Gregory and Taylor*, 1981]. Such a setting for hydrothermal activity, in which the major conduits for water flow are along faults, would account for the low values of magnetization associated with the crust beneath the eastern wall and hydrothermal field (either through the alteration of magnetic minerals upon contact with the hot water or by raising the temperature of the source volume above the Curie point [150-200 °C, *Irving*, 1970; *Johnson and Atwater*, 1977] for remanent magnetization) observed by other authors [*Rona*, 1980; *McGregor et al.*, 1977; *Tivey et al.*, 1989a, b].

## The 26°N Spreading Cell

The variation in focal depth along the axis and the reasonable inference of a heat source beneath the along-axis high suggests that the ridge segment at 26°N may, to a first approximation, fit the spreading cell model first proposed to describe along-axis variations in accretionary processes by *Francheteau and Ballard* [1983]. This model attempted to explain topographic, volcanic, tectonic, and hydrothermal variations in ridge crest processes relative to distances from major ridge-axis discontinuities (in the original case, transform faults). Based on observations along the East Pacific Rise, Galapagos Spreading Center, and Mid-Atlantic Ridge, the authors proposed that the most likely site for the presence of an axial magma chamber and the profuse effusion of fluid lavas with a minimum of surficial fissures, is at the along-axis topographic high. This high would be found at some distance from the cooling effects of transform faults and other discontinuities. Where the magma chamber is best developed, isostatic uplift by the buoyant magma is the greatest, and the crustal lid is expected to be the thinnest, thus resulting in the greater likelihood that water could tap into the heat from the magma chamber to form high-temperature, black-smoker vent fields.

The immense increase in geophysical surveys, principally the collection of high-resolution Sea Beam bathymetry, of the Earth's mid-ocean ridge system over the last 10 years has resulted in the recognition of shorter-wavelength spatial and temporal variations in the volcanic and tectonic morphologies along the ridge axis [e.g., *Macdonald et al.*, 1984, 1988; *Schouten et al.*, 1985; *Langmuir et al.*, 1986; *Kong et al.*, 1988; *Kuo and Forsyth*, 1988]. Along the slowly-spreading Mid-Atlantic Ridge, a number of recent investigations have documented an *en echelon* segmentation of the ridge into individual spreading cells up to 90 km in length from regional geophysical (seismic, magnetic, gravity) and morphological (Sea MARC I, Sea Beam) surveys of extended lengths of ridge (100 - 1000 km) [*Purdy and Detrick*, 1986; *Brown and Karson*, 1988; *Kong et al.*, 1988; *Kuo and Forsyth*, 1988; *Schulz et al.*, 1988; *Lin et al.*, 1990; *Sempere et al.*, 1989]. These detailed studies have led to only modest changes to the model proposed by *Francheteau and Ballard* [1983].

In the current version of the spreading cell model for slow spreading ridges, the most likely locale in which to find elevated crustal and/or mantle temperatures is at locally high regions of the inner floor. While thermal considerations appear to preclude the steady-state existence of magma chambers at slow spreading rates [*Sleep*, 1975], several seismic studies have found anomalous velocities, possibly related to recent intrusive episodes, beneath the along-axis high region of the median valley inner floor [*Whitmarsh*, 1975;

*Fowler, 1976; Purdy and Detrick, 1986; Chapter 4]. Gravity studies suggest that mantle preferentially upwells in discrete plumes centered within each spreading cell (or that crustal thickness decreases significantly from sites of gravity anomaly minima toward the ridge-axis discontinuities) [Kuo and Forsyth, 1988; Lin et al., 1990].*

We suggest additionally that the microearthquake evidence, especially when integrated with the available geological and geophysical data for 26°N, provide an exceptionally detailed documentation of along-axis variations in the accretionary processes within a distinct spreading cell along a slow spreading, mid-ocean ridge. With the caveat that microearthquake focal depths observed over short time intervals give only an instantaneous view of the state of stress, we speculate that the along-axis variation in the maximum depth extent of microearthquake activity is mapping a brittle/ductile transition zone, and that its shallowest point occurs at the along-axis inner floor high. The presence of an active high-temperature hydrothermal field, beneath which the crust appears aseismic, the finding of lower seismic velocities (Chapter 4), and requirement of a heat source to effectively erase the normally-polarized crustal magnetization beneath the vent field, are consistent with the hypothesis that the along-axis high, situated approximately midway between two ridge-axis discontinuities [*Sempere et al.*, 1989], represents the most likely site for recent volcanism along this spreading segment. In addition, higher b-values, which are often correlated with active volcanic environments [e.g., *Minakami, 1960; Brandsdottir and Einarsson, 1978*], were obtained for earthquakes in this region. Away from the high, to the south, earthquake focal depths increase to depths extending to the base of the crust. We contend, by analogy with the volcanically-quiet ridge segment centered at 22°45'N [*Toomey et al.*, 1988], that this region is characterized primarily by crustal extension devoid of significant magmatic activity.

## CONCLUSIONS

Over a period of 23 days, over 500 events were recorded by a 20 x 10 km network of OBHs and OBSs in the median valley of the Mid-Atlantic Ridge at 26°N. Hypocenters were determined for 189 earthquakes of that set (for an average of 8.5 earthquakes/day); good resolution of focal depth was obtained for 105 of these events. The high seismicity level translates to 0.2 events/km<sup>2</sup> for a 30 x 20 km area centered about the ridge axis. Almost all events occurred at depths between 3 and 7 km beneath the seafloor (average of  $4.7 \pm 1.1$  km). Seismic moments ranged from  $10^{17}$  to  $10^{22}$  dyn cm with 75% of the events between  $2 \times 10^{18}$  and  $6 \times 10^{19}$  dyn cm. Source radii, stress drops, and fault displacements for well-constrained events used in the construction of focal mechanisms

ranged from 0.1 - 0.3 km, 0.1 - 5 bars, and 0.02 - 0.4 mm, respectively; inner floor events beneath the along-axis high and the western inner floor and wall tended to have smaller moments, stress drops ( $< 2$  bar), and displacements ( $< 0.2$  mm) than events beneath the volcano, along-axis deep, and eastern wall. A b-value for seismic moment of 1.0 was found for all earthquakes near the network. From the determination of hypocenters and source parameters for major groups of earthquakes beneath the median valley and adjacent walls, we can identify several primary characteristics of the observed microearthquake activity at 26°N:

- (1) None of the locatable microearthquakes occurred beneath the high-temperature, hydrothermal field at 26°08'N, 44°49'W. The closest events were 3 - 3.5 km away at depths greater than 5 km below the seafloor.
- (2) Within the inner floor, events located beneath the along-axis high region occurred at shallower focal depths (18 of 21 earthquakes have depths  $< 3.5$  km) than those beneath the along-axis deep 15 km to the south (average  $5.4 \pm 1.0$  km with none less than 3.7 km depth). Near the along-axis high, focal mechanism solutions suggest near-vertical or sub-horizontal faulting along planes striking parallel to the median valley. In addition, reverse or thrust faulting is suggested for a swarm of earthquakes ( $M_0 = 3 \times 10^{18} - 3 \times 10^{20}$  dyn cm) located in a cluster 5-6 km beneath a 200-m-high volcanic edifice.
- (3) Seismicity along the valley walls defines a broad zone of activity trending parallel to the ridge axis. This zone was widest adjacent to the along-axis high during our experiment. First motion observations are consistent with normal faulting along inward-dipping planes trending subparallel to the local trend of the valley walls.
- (4) A higher b-value (1.1 - 1.5) was associated with events beneath the along-axis high and the adjacent eastern valley walls than for events to the south beneath the along-axis, inner floor deep (0.6). The high b-values result from the high level of small earthquake activity characterizing the transition from the inner floor to the western walls, which was by far the most active region during the experiment. .

The distribution of hypocenters and the diversity of fault types associated with earthquakes beneath the inner floor and walls suggests a spatially variable tectonic state for the ridge segment at 26°N. In particular high-angle or sub-horizontal faulting beneath the inner floor high imply that faulting at the ridge axis in this region is fundamentally different from that which describes earthquake activity a few kilometers off-axis. The variations are presumably a signature of heterogeneity in the depth region over which brittle failure occurs, and are a consequence of along-axis changes in the thermal structure and state of stress. The presence of an active high-temperature hydrothermal field strongly suggests that thermal stresses may be dominant, especially in the region of the along-axis high.

We suggest that at present the hydrothermal activity and deposition of massive sulfides is being sustained by heat generated by a recent magmatic intrusion (not a large molten body). The inference is based on the lack of seismicity beneath the black smoker field, the shallow focal depths (< 4 km) of inner floor seismicity, higher b-values associated with the along-axis high events, the presence of a low velocity zone 3 km beneath the along-axis high region (Chapter 4), the anomalous faulting mechanisms including reverse faulting associated with an earthquake swarm below the low velocity region, and severe attenuation of the first-arriving compressional energy for shots whose ray paths traverse the high below 3 km depth (Chapter 4). The apparent lack of seismicity of the hydrothermal area is also consistent with the hypothesis that the crust there may be locally hotter, perhaps due to more recent volcanism, than the neovolcanic zone at the ridge axis.

We interpret the along-axis variation in the maximum depth extent of microearthquake activity as mapping the variability in the depth to the brittle/ductile transition zone. The presence of an active high-temperature hydrothermal field, the lack of seismic activity beneath the vent field, the finding of a body of low seismic velocity (Chapter 4), and the requirement of a heat source to reduce the magnetization of the crust beneath the vent field, are consistent with the hypothesis that the along-axis high is the site of most recent magmatism along this spreading segment. Away from the high, to the south, earthquake focal depths increase to depths extending to the base of the crust. From the similarity in focal depth distribution, b-values, and velocity structure at 23°N with those observed beneath the deeper portions of the median valley at 26°N, we speculate that the crust beneath the inner floor deep at 26°N is presently characterized by ongoing extension and lacks recent sizeable intrusions of magma.

In the context of the high-temperature vent field at 26°N, we suggest that the formation of the field near the base of the eastern wall is a direct consequence of water movement along normal faults that characterize microearthquake activity beneath the wall.



The normal faults provide permeable pathways along which heated water can return rapidly and efficiently to the surface, where it exits at still high temperatures from black-smoker chimneys and fissures.

## REFERENCES

- Aki, K. Generation and propagation of G waves from the Niigata earthquake of June 16, 1964. Part 2. Estimation of earthquake moment, released energy, and stress drop from the G-wave spectrum, *Bull. Earthq. Res. Inst. Tokyo Univ.*, *44*, 73-88, 1966.
- Aki, K., and P. G. Richards, *Quantitative Seismology, Theory and Methods*, W. H. Freeman, San Francisco, CA, 932 pp., 1980.
- Angelier, J., and B. Colleta, Tension fractures and extensional tectonics, *Nature*, *301*, 49-51, 1983.
- Ballard, R. D., and Tj. H. van Andel, Morphology and tectonics of the inner rift valley at lat 36°50'N on the Mid-Atlantic Ridge, *Geol. Soc. Amer. Bull.*, *88*, 507-530, 1977.
- Brandsdottir, B., and P. Einarsson, Seismic activity associated with the September 1977 deflation of the Krafla central volcano in northeastern Iceland, *J. Volcanol. Geotherm. Res.*, *6*, 197-212, 1979.
- Brown J. R., and J. A. Karson, Variations in axial processes on the Mid-Atlantic Ridge: The median valley of the MARK area, *Mar. Geophys. Res.*, *10*, 109-138, 1988.
- Brune, J. N., Tectonic stress and the spectra of seismic shear waves from earthquakes, *J. Geophys. Res.*, *75*, 4997-5009, 1970. (Correction, *J. Geophys. Res.*, *76*, 5002, 1971.)
- Bunch, A. W. H., and B. L. N. Kennett, The crustal structure of the Reykjanes Ridge at 59°30'N, *Geophys. J. R. Astron. Soc.*, *61*, 141-166, 1980.
- Burnett, M. S., D. W. Caress, and J. A. Orcutt, Tomographic image of the magma chamber at 12°50'N on the East Pacific Rise, *Nature*, *339*, 206-208, 1989.
- Byerlee, J. D., Brittle-ductile transition in rocks, *J. Geophys. Res.*, *36*, 4741-4750, 1968.
- Campbell, A. C., M. R. Palmer, G. P. Klinkhammer, T. S. Bowers, J. M. Edmond, J. R. Lawrence, J. F. Casey, G. Thompson, S. Humphris, P. Rona and J. A. Karson, Chemistry of hot springs on the Mid-Atlantic Ridge, *Nature*, *335*, 514-519, 1988.
- Cessaro, R. K., and D. M. Hussong, Transform seismicity at the intersection of the Oceanographer Fracture Zone and the Mid-Atlantic Ridge, *J. Geophys. Res.*, *91*, 4839-4853, 1986.
- Chen, W.-P., and P. Molnar, Focal depths of intracontinental and intraplate earthquakes and their implications for the thermal and mechanical properties of the lithosphere, *J. Geophys. Res.*, *88*, 4183-4214, 1983.
- Chouet, B., and B. R. Julian, Dynamics of an expanding fluid-filled crack, *J. Geophys. Res.*, *01*, 13967-13992, 1986.
- Costantinou, G. and G. J. S. Govett, Genesis of sulfide deposits, ochrem and umber of Cyprus, *Trans. Inst. Mining Metall.*, *81*, B34-B46, 1973.
- Creager, K. C., and L. M. Dorman, Location of instruments on the seafloor by joint adjustment of instrument and ship positions, *J. Geophys. Res.*, *87*, 8379-8388, 1982.

- Detrick, R. S., J. Honnorez, and Leg 106 Scientific Party, Drilling the Snake Pit hydrothermal sulfide deposit on the Mid-Atlantic Ridge, lat. 23°22'N, *Geology*, 14, 1004-1007, 1986.
- Detrick, R. S., P. Buhl, E. Vera, J. Muttet, J. Orcutt, J. Madsen, and T. Brocher, Multichannel seismic imaging of a crustal magma chamber along the East Pacific Rise, *Nature*, 326, 35-41, 1987.
- Duschenes, J. D., T. W. Barash, P. J. Mattaboni and S. C. Solomon, On the use of an externally deployed geophone package on an ocean bottom seismometer, *Mar. Geophys. Res.*, 4, 437-450, 1981.
- Duschenes, J., R. C. Lilwall, and T. J. G. Francis, The hypocentral resolution of microearthquake surveys carried out at sea, *Geophys. J. R. Astron. Soc.*, 72, 435-451, 1983.
- Dziewonski, A. M., J. E. Franzen, and J. H. Woodhouse, Centroid-moment tensor solutions for July-September 1985, *Phys. Earth Planet. Inter.*, 42, 205-214, 1986.
- Eberhart, G. L., P. A. Rona, and J. Honnorez, Geologic controls of hydrothermal activity in the Mid-Atlantic Ridge rift valley: Tectonics and volcanics, *Mar. Geophys. Res.*, 10, 233-259, 1988.
- Einarsson, P., S wave shadows in the Krafla caldera in NE Iceland, evidence for a magma chamber in the crust, *Bull. Volcanol.*, 43, 1-9, 1978.
- Ergin, K., Energy ratio of the seismic waves reflected and refracted at a rock-water boundary, *Bull. Seismol. Soc. Am.*, 42, 349-372, 1952.
- Fehn, U., and L. M. Cathles, Hydrothermal convection at slow-spreading mid-ocean ridges, *Tectonophysics*, 55, 239-260, 1979.
- Foulger, G., and R. E. Long, Anomalous focal mechanisms: Tensile crack formation on an accreting plate boundary, *Nature*, 310, 43-45, 1984.
- Fowler, C. M. R., Crustal structure of the Mid-Atlantic ridge crest at 37°N, *Geophys. J. R. Astron. Soc.*, 47, 459-491, 1976.
- Fowler, C. M. R., The Mid-Atlantic Ridge: Structure at 45°N, *Geophys. J. R. Astron. Soc.*, 54, 167-183, 1978.
- Fowler, C. M. R., and C. E. Keen, Oceanic crustal structure - Mid-Atlantic Ridge at 45°N, *Geophys. J. R. Astron. Soc.*, 56, 219-226, 1979.
- Francheteau, J., and R. D. Ballard, The East Pacific Rise near 21°N, 13°N and 20°S: Inferences for along strike variability of axial processes at mid ocean ridges, *Earth Planet. Sci. Lett.*, 64, 93-116, 1983.
- Francis, T. J. G., The ratio of compressional to shear velocity and rock porosity on the axis of the Mid-Atlantic Ridge, *J. Geophys. Res.*, 81, 4361-4364, 1976.
- Francis, T. J. G., and I. T. Porter, Median valley seismology: The Mid-Atlantic Ridge near 45°N, *Geophys. J. R. Astron. Soc.*, 34, 279-311, 1973.

- Francis, T. J. G., I. T. Porter, and J. R. McGrath, Ocean-bottom seismograph observations on the Mid-Atlantic Ridge near lat 37°N, *Geol. Soc. Am. Bull.*, 88, 664-677, 1977.
- Gregory, R. T. and H. P. Taylor, Jr., An oxygen isotope profile in a section of cretaceous oceanic crust, Samail Ophiolite, Oman: Evidence for  $\delta^{18}\text{O}$  buffering of the oceans by deep (> 5 km) sea water - hydrothermal circulation at mid-ocean ridges, *J. Geophys. Res.*, 86, 2737-2755, 1981.
- Hanks, T. C., and M. Wyss, The use of body-wave spectra in the determination of seismic-source parameters, *Bull. Seismol. Soc. Am.*, 62, 561-589, 1972.
- Harding, A. J., J. A. Orcutt, M. E. Kappus, E. E. Vera, J. C. Mutter, P. Buhl, R. S. Detrick, and T. M. Brocher, Structure of young oceanic crust at 13°N on the East Pacific Rise from expanding spread profiles, *J. Geophys. Res.*, 94, 12163-12196, 1989.
- Haskell, N. A., Elastic displacements in the near-field of a propagating fault, *Bull. Seismol. Soc. Am.*, 59, 865-908, 1969.
- Hekinian, R., V. Renard, and J. L. Cheminee, Hydrothermal deposits on the East Pacific Rise near 13°N: Geological setting and distribution of active sulfide chimneys, in *Hydrothermal Processes at Seafloor Spreading Centers*, edited by P. A. Rona, K. Bostrom, L. Laubier, and K. L. Smith, Jr., Plenum Press, New York, pp. 571-594, 1983.
- Hyndman, R. D., Poisson's ratio in the oceanic crust - a review, *Tectonophysics*, 59, 321-333, 1979.
- Huang, P. Y., and S. C. Solomon, Centroid depths of mid-ocean ridge earthquakes: Dependence on spreading rate, *J. Geophys. Res.*, 93, 13445-13477, 1988.
- Huang, P. Y., S. C. Solomon, E. A. Bergman, and J. L. Nabelek, Focal depths and mechanisms of Mid-Atlantic Ridge earthquakes from body waveform inversion, *J. Geophys. Res.*, 91, 579-598, 1986.
- Irving, E., The Mid-Atlantic Ridge at 45°N, XIV. Oxidation and magnetic properties of basalt; review and discussion, *Can. J. Earth Sci.*, 7, 1528, 1970.
- Jenkins, W. J., P. A. Rona, and J. M. Edmond, Excess  $^3\text{He}$  in the deep water over the Mid-Atlantic Ridge at 26°N: Evidence of hydrothermal activity, *Earth Planet. Sci. Lett.*, 49, 39-44, 1980.
- Johnson, H. P., and T. Atwater, Magnetic study of basalts from the Mid-Atlantic Ridge, lat 37°N, *Geol. Soc. Amer. Bull.*, 88, 637, 1977.
- Karson, J. A., and P. A. Rona, Structure of the eastern median valley wall, MAR 26°N (abstract), *Eos Trans. AGU*, 36, 1103, 1982.
- Karson, J. A., and P. A. Rona, Block-tilting, transfer faults, and structural control of magmatic and hydrothermal processes in the TAG area, *Geol. Soc. Amer. Bull.*, submitted, 1989.

- Karson, J. A., G. Thompson, S. E. Humphris, J. M. Edmond, W. B. Bryan, J. R. Brown, A. T. Winters, R. A. Pockalny, J. F. Casey, A. C. Campbell, G. Klinkhammer, M. R. Palmer, R. J. Kinzler, and M. M. Sulanowska, Along-axis variations in seafloor spreading in the MARK area, *Nature*, 328, 681-685, 1987.
- Keilis-Borok, V. I., On estimation of the displacement in an earthquake sources and of source dimensions, *Ann. Geofis.*, 12, 205-214, 1959.
- Klein, F. W. Hypocenter location program HYPOINVERSE, 1, User's guide to versions 1,2, 3, 4, *U. S. Geol. Surv. Open File Report*, 78-694, 103 pp., 1978.
- Klein, F. W., P. Einarsson, and M. Wyss, The Reykjanes Peninsula, Iceland, earthquake swarm of September 1972 and its tectonic significance, *J. Geophys. Res.*, 82, 865-888, 1977.
- Klinkhammer, G., H. Elderfield, M. Greaves, P. Rona, and T. Nelsen, Manganese geochemistry near high-temperature vents in the Mid-Atlantic Ridge rift valley, *Earth Planet. Sci. Lett.*, 80, 230-240, 1986.
- Klitgord, K. D., and H. Schouten, Plate kinematics in the Central Atlantic Ocean, in *The Western North Atlantic Region, The Geology of North America, Vol. M.*, edited by P. R. Vogt and B. E. Tucholke, Geol. Soc. Am., Boulder, Colo., pp. 351-358, 1986.
- Koelsch, D. E. and G. M. Purdy, An ocean bottom hydrophone instrument for seismic refraction experiments in the deep ocean, *Mar. Geophys. Res.*, 4, 115-125, 1979.
- Kong, L., W. B. F. Ryan, L. Mayer, R. Detrick, P. J. Fox and K. Manchester, Bare-rock drill sites, ODP Legs 106 and 109: Evidence for hydrothermal activity at 23°N in the Mid-Atlantic Ridge (abstract), *Eos Trans. AGU*, 66, 936, 1985.
- Kong, L. S. L., R. S. Detrick, P. J. Fox, L. A. Mayer, and W. B. F. Ryan, The morphology and tectonics of the MARK area from Sea Beam and Sea MARC I observations (Mid-Atlantic Ridge 23°N), *Mar. Geophys. Res.*, 10, 59-90, 1988.
- Kuo, B.-Y., and D. W. Forsyth, Gravity anomalies of the ridge-transform system in the South Atlantic between 31 and 34.5°S: Upwelling centers and variations in crustal thickness, *Mar. Geophys. Res.*, 10, 205-232, 1988.
- Lalou, C., G. Thompson, M. Arnold, E. Bricquet, E. Druffel, and P. Rona, Geochronology of TAG and Snake Pit Hydrothermal Fields, Mid-Atlantic Ridge: Witness to a long and complex hydrothermal history, *Earth Planet. Sci. Lett.*, in press, 1990.
- Langmuir, C. H., J. F. Bender, and R. Batiza, Petrological and tectonic segmentation of the East Pacific Rise, 5°30'-14°30'N, *Nature*, 322, 422-429, 1986.
- Lattimore, R. K., P. A. Rona, and O. E. DeWald, Magnetic anomaly sequence in the central North Atlantic, *J. Geophys. Res.*, 79, 1207-1209, 1974.
- Lilwall, R. C., Fault mechanisms and sub-crustal seismic velocities on the Mid-Atlantic Ridge, *Geophys. J. R. Astron. Soc.*, 60, 245-262, 1980.
- Lilwall, R. C. and T. J. G. Francis, Hypocentral resolution of small ocean bottom seismic networks, *Geophys. J. R. Astron. Soc.*, 54, 721-728, 1978.

- Lilwall, R. C., T. J. G. Francis, and I. T. Porter, Ocean-bottom seismograph observations on the Mid-Atlantic Ridge near 45°N, *Geophys. J. R. Astron. Soc.*, 51, 357-370, 1977.
- Lilwall, R. C., T. J. G. Francis, and I. T. Porter, Ocean-bottom seismograph observations on the Mid-Atlantic Ridge near 45°N - further results, *Geophys. J. R. Astron. Soc.*, 55, 255-262, 1978.
- Lilwall, R. C., T. J. G. Francis, and I. T. Porter, Some ocean-bottom seismograph observations on the Reykjanes Ridge near 59°N, *Geophys. J. R. Astron. Soc.*, 62, 321-328, 1980.
- Lilwall, R. C., T. J. G. Francis, and I. T. Porter, A microearthquake survey at the junction of the East Pacific Rise and the Wilkes (9°S) Fracture Zone, *Geophys. J. R. Astron. Soc.*, 66, 407-416, 1981.
- Lin, J., G. M. Purdy, H. Schouten, J. C. Sempere, and C. Zervas, Evidence from gravity data for focused magmatic accretion along the Mid-Atlantic Ridge, *Nature*, 344, 627-632, 1990.
- Lister, C. R. B., Qualitative models of spreading-center processes, including hydrothermal penetration, *Tectonophysics*, 37, 203-218, 1977.
- Lister, C. R. B., The basic physics of water penetration into hot rock, in *Hydrothermal Processes at Seafloor Spreading Centers*, edited by P. A. Rona, K. Bostrom, L. Laubier, and K. L. Smith, Jr., Plenum Press, New York, pp. 141-168, 1983.
- Lowell, R. P., and P. A. Rona, Hydrothermal models for the generation of massive sulfide ore deposits, *J. Geophys. Res.*, 90, 8769-8783, 1985.
- Macdonald, K. C., Mid-ocean ridges: Fine scale tectonic, volcanic, and hydrothermal processes within the plate boundary zone, *Ann. Rev. Earth Planet. Sci.*, 10, 155-190, 1982.
- Macdonald, K. C., The crest of the Mid-Atlantic Ridge: Models for crustal generation processes and tectonics, in *The Western North Atlantic Region, Geology of North America, Vol. M.*, edited by P. R. Vogt and B. E. Tucholke, Geol. Soc. Amer., Boulder, Colo., pp. 51-68, 1986.
- Macdonald, K. C., and B. P. Luyendyk, Deep-tow studies of the structure of the Mid-Atlantic Ridge crest near lat 37°N, *Geol. Soc. Amer. Bull.*, 88, 621-636, 1977.
- Macdonald, K. C., J.-C. Sempere, and P. J. Fox, East Pacific Rise from Siqueiros to Orozco Fracture Zones: Along-strike continuity of axial neovolcanic zone and structure and evolution of overlapping spreading centers, *J. Geophys. Res.*, 89, 6049-6069, 1984.
- Macdonald, K. C., P. J. Fox, L. J. Perram, M. F. Eisen, R. M. Haymon, S. P. Miller, S. M. Carbotte, M.-H. Cormier, and A. N. Shor, A new view of the mid-ocean ridge from the behavior of ridge-axis discontinuities, *Nature*, 335, 217-225, 1988.
- Mattaboni, P. J. and S. C. Solomon, MITOBS: A seismometer system for ocean-bottom earthquake studies, *Mar. Geophys. Res.*, 3, 87-102, 1977.

- Matthews, D. J., *Tables of the Velocity of Sound in Pure Water and Sea Water for Use in Echo-sounding and Sound-ranging*, British Admiralty, Hydrgr. Dept., London, 1939.
- McGregor, B. A., C. G. A. Harrison, J. W. Lavelle, and P. A. Rona, Magnetic anomaly pattern on the Mid-Atlantic Ridge crest at 26°N, *J. Geophys. Res.*, 82, 231-238, 1977.
- Minakami, T., Fundamental research for predicting volcanic eruptions, *Bull. Earthq. Res. Inst. Tokyo Univ.*, 38, 497-544, 1960.
- Mogi, K., Some discussions on aftershocks, foreshocks, and earthquake swarms, the fracture of a semi-infinite body caused by an inner stress origin and its relation to the earthquake phenomena, 3, *Bull. Earthq. Res. Inst., Tokyo Univ.*, 41, 615-658, 1963.
- Murray, M.H., L. Kong, D.W. Forsyth, S.C. Solomon and D.M. Hussong, An OBS study of microearthquakes in the median valley on the Mid-Atlantic Ridge near 35°N (abstract), *Eos Trans. AGU*, 65, 1009, 1984.
- Purdy, G. M., and R. S. Detrick, Crustal structure of the Mid-Atlantic Ridge at 23°N from seismic refraction studies, *J. Geophys. Res.*, 91, 3739-3762, 1986.
- Purdy, G. M., H. Schouten, M. A. Tivey, and J.-C. Sempere, High-resolution central magnetic anomaly field along the Mid-Atlantic Ridge between 24°N and 31°N (abstract), *Eos Trans. AGU* 70, 468, 1989.
- Riedesel, M. J. A. Orcutt, K. C. Macdonald, and J. S. McClain, Microearthquakes in the black smoker hydrothermal field, East Pacific Rise at 21°N, *J. Geophys. Res.*, 87, 10613-10623, 1982.
- RISE Project Group, Hot springs and geophysical experiments on the East Pacific Rise, *Science*, 207, 1421-1433, 1980.
- Rona, P. A., TAG hydrothermal field: Mid-Atlantic Ridge crest at latitude 26°N, *J. Geol. Soc. Lond.*, 137, 385-402, 1980.
- Rona, P. A., Black smokers and massive sulfides at the TAG hydrothermal field, Mid-Atlantic Ridge 26°N (abstract), *Eos Trans. AGU*, 66, 936, 1985.
- Rona, P. A., and K. G. Speer, An Atlantic hydrothermal plume: Trans-Atlantic Geotraverse (TAG) area, Mid-Atlantic Ridge crest near 26°N, *J. Geophys. Res.*, 94, 13879-13893, 1989.
- Rona, P. A., R. N. Harbison, B. G. Bassinger, R. B. Scott, and A. J. Nalwalk, Tectonic fabric and hydrothermal activity of Mid-Atlantic Ridge crest (lat 26°N), *Geol. Soc. Amer. Bull.*, 87, 661-674, 1976.
- Rona, P. A., G. Klinkhammer, T. A. Nelsen, J. H. Trefry, and H. Elderfield, Black smokers, massive sulfides and vent biota at the Mid-Atlantic Ridge, *Nature*, 321, 33-37, 1986.
- Rowlett, H., and D. W. Forsyth, Recent faulting and microearthquakes at the intersection of the Vema Fracture Zone and the Mid-Atlantic Ridge, *J. Geophys. Res.*, 89, 6079-6094, 1984.

- Sato, T., and T. Hirasawa, Body wave spectra from propagating shear cracks, *J. Phys. Earth*, 21, 415-431, 1973.
- Scholz, C. H., The frequency-magnitude relation of microfracturing in rock and its relation to earthquakes, *Bull. Seismol. Soc. Am.*, 58, 399-415, 1968.
- Schouten, H., K. D. Klitgord and J. A. Whitehead, Segmentation of mid-ocean ridges, *Nature*, 317, 225-229, 1985.
- Schulz, N. J., R. S. Detrick, and S. P. Miller, Two and three-dimensional inversions of magnetic anomalies in the MARK area (Mid-Atlantic Ridge 23°N), *Mar. Geophys. Res.*, 10, 41-57, 1988.
- Scott, S. D., P. A. Rona, B. A. McGregor, and M. R. Scott, The TAG hydrothermal field, *Nature*, 251, 301-302, 1974.
- Sempere, J.-C., G. M. Purdy, and H. Schouten, The segmentation of the Mid-Atlantic Ridge between the Kane and Atlantis fracture zones (abstract), *Eos Trans. AGU*, 70, 455, 1989.
- Shearme, S., D. S. Cronan, and P. A. Rona, Geochemistry of sediments from the TAG hydrothermal field, Mid-Atlantic Ridge at latitude 26°N, *Mar. Geol.*, 51, 269-291, 1983.
- Shipboard Scientific Party, Site 648, in *Proc. ODP Init. Repts. (pt. A)*, 106, edited by R. Detrick, J. Honnorez, et al., Ocean Drilling Program, College Station, Tex., pp. 35-134, 1988.
- Sleep, N. H., Formation of oceanic crust: Some thermal constraints, *J. Geophys. Res.*, 80, 4037-4042, 1975.
- Sleep, N. H., Hydrothermal convection at ridge axes, in *Hydrothermal Processes at Seafloor Spreading Centers*, edited by P. A. Rona, K. Bostrom, L. Laubier, and K. L. Smith, Jr., Plenum Press, New York, pp. 71-82, 1983.
- Strens, M. R., and J. R. Cann, A model of hydrothermal circulation in fault zones at mid-ocean ridge crests, *Geophys. J. R. Astron. Soc.*, 71, 225-240, 1982.
- Strens, M. R., and J. R. Cann, A fracture-loop thermal balance model of black-smoker circulation, *Tectonophysics*, 122, 307-324, 1986.
- Temple, D. G., R. B. Scott, and P. A. Rona, Geology of a submarine hydrothermal field, Mid-Atlantic Ridge, 26°N latitude, *J. Geophys. Res.*, 84, 7453-7466, 1979.
- Thompson, G., M. J. Mottl, and P. A. Rona, Morphology, mineralogy, and chemistry of hydrothermal deposits from the TAG area, 26°N, Mid-Atlantic Ridge, *Chem. Geol.*, 49, 243-257, 1985.
- Thompson, G., S. E. Humphris, B. Shroeder, M. Sulanowska, and P. Rona, Active vents and massive sulfides at 26°N (TAG) and 23°N (Snake Pit) on the Mid-Atlantic Ridge, *Can. Min.*, 26, 697-711, 1988.
- Thurber, C. H., Earth structure and earthquake locations in the Coyote Lake area, central California, Ph.D. thesis, 332 pp., Mass. Inst. of Technol., Cambridge, 1981.



- Tivey, M. A., H. Schouten, J. C. Sempere, and A. Wooldridge, Implications of the three-dimensional structure of the TAG magnetic anomaly on the Mid-Atlantic Ridge (abstract), *Eos Trans. AGU*, 70, 455, 1989a.
- Tivey, M. A., H. Schouten, J. Lin, J.-C. Sempere, and A. Wooldridge, Predictions of hydrothermal fields on the Mid-Atlantic Ridge based on magnetic anomalies (abstract), *Eos Trans. AGU*, 70, 455, 1989b.
- Toomey, D. R., S. C. Solomon, G. M. Purdy, and M. H. Murray, Microearthquakes beneath the median valley of the Mid-Atlantic Ridge near 23°N: Hypocenters and focal mechanisms, *J. Geophys. Res.*, 90, 5443-5458, 1985.
- Toomey, D. R., S. C. Solomon, G. M. Purdy, Microearthquakes beneath median valley of Mid-Atlantic Ridge near 23°N: Tomography and tectonics, *J. Geophys. Res.*, 93, 9093-9112, 1988.
- Toomey, D. R., G. M. Purdy, and S. C. Solomon, Three-dimensional seismic structure of the East Pacific Rise at 9°30'N (abstract), *Eos Trans. AGU*, 70, 1317, 1989.
- Trehu, A. M., and S. C. Solomon, Earthquakes in the Orozco transform zone: Seismicity, source mechanisms, and tectonics, *J. Geophys. Res.*, 88, 8203-8225, 1983.
- Whitmarsh, R. B., Axial intrusion zone beneath the median valley of the Mid-Atlantic Ridge at 37 degrees N detected by explosion seismology, *Geophys. J. R. Astron. Soc.*, 42, 184-215, 1975.
- Wyss, M., Towards a physical understanding of the earthquake frequency distribution, *Geophys. J. R. Astron. Soc.*, 31, 341, 1973.
- Zonenshain, L. P., M. I. Kuzmin, A. P. Lisitsin, Yu. A. Bogdanov, and B. V. Baranov, Tectonics of the Mid-Atlantic rift valley between the TAG and MARK areas (26-24°N): Evidence for vertical tectonism, *Tectonophysics*, 159, 1-23, 1989.

## FIGURE CAPTIONS

- Figure 1. Location of the TAG area at 26°N on the Mid-Atlantic Ridge. Also shown is the MARK area near 23°N south of the Kane Fracture Zone that was the subject of studies by *Purdy and Detrick* [1986] and *Toomey et al.* [1985, 1988]. Tectonic framework from *Klitgord and Schouten* [1986].
- Figure 2. Sea Beam bathymetric chart of the experiment area at 0.25 km contour interval, from *Sempere et al.* [1989]. The locations of ranging shots used for instrument relocation and of refraction shots are shown by triangles. The seismic network consisted of seven ocean bottom hydrophones (circles) and two ocean bottom seismometers (squares). The shape of the median valley (nominally seafloor depths > 3.5 km) varies along axis, widening and deepening south and north of the vicinity of the active high-temperature hydrothermal field (hourglass).
- Figure 3. Detailed Sea Beam bathymetry of the inner floor at the along-axis high; depths greater than 3.5 km (inner floor) are contoured at an interval of 0.02 km and depths shallower than 3.5 km (valley walls) are contoured at 0.10 km intervals. The 200-m-high inferred volcano (cross-hatched area) is located on the axis of the neovolcanic zone (dashed line). Stippled area delineates the region of low magnetization, with heavy stippling showing the lowest values [*Tivey et al.*, 1989a]. Microearthquake epicenters within the inner floor are indicated by closed circles and triangles, with larger symbols representing events with good focal depth resolution. The crust in the vicinity of the high-temperature hydrothermal field was inactive over the deployment period. The circular distribution of epicenters beneath the volcano may not be real because 1- $\sigma$  errors in epicenters for individual events are 0.3 km.
- Figure 4. Cumulative number of events detected by more than four instruments over the deployment period. Median valley receivers (OBHs 1, 2, 3, 6) recorded much higher levels of activity than instruments deployed on the walls (OBHs 4, 5, 8; OBSs 31, 33). The smaller numbers of events detected by the OBSs are in part due to the event detection scheme (OBSs were

triggered and recorded digitally while the analog OBHs recorded continuously). See Figure 2 for instrument locations.

- Figure 5. Histograms showing the total numbers of events recorded per day (dashed lines) on each instrument during the deployment. The levels of seismicity are comparable to those observed at 23°N on the MAR by *Toomey et al.* [1985, 1988]. Solid line histogram indicates events that were located (Figure 10).
- Figure 6. Examples of seismograms for two earthquakes. Vertical bars indicate the arrival times of impulsive P waves on the OBH and OBS vertical components, and of the S waves on the OBS horizontal components. For each event, seismograms (water pressure on the OBHs and ground displacement on the OBSs) are scaled to the same maximum amplitude. Compressional arrivals have upward first motions, and dilatational first motions are down for all instruments except OBH 4, whose polarity is reversed. Event time is given in Julian day, hour, and minute (UT).
- Figure 7. (a) Differential S wave arrival times versus differential P wave arrival times for events simultaneously recorded by both OBSs. The slope of the linear regression fit to these points gives an estimate of the  $V_p/V_s$  ratio. S wave times were picked on the transverse horizontal component after rotation. (b) SP - P times (picked on the OBHs) and S - P times (from OBS 31, using the transverse horizontal component to identify the S wave arrival) versus range. Large residuals and a high degree of scatter for the OBH data, as compared with the OBS data, imply that the most prominent SP phase on the OBH does not always correspond to an S-to-P conversion immediately beneath the OBH. The solid line shows the calculated S - P time for a uniform  $V_p/V_s$  ratio of 1.84.
- Figure 8. Iteratively-determined station delays used in the estimation of hypocentral parameters with the 1D velocity model. The variability is not a simple function of instrument depth and is an indication of the magnitude of crustal heterogeneity. Note that the delays for OBHs 2 and 4, which are located near the active black-smoker field and region of anomalously low magnetization, are negative, implying that lesser travel times are required.

The dashed line corresponds to the datum used for instrument and earthquake locations.

Figure 9. Velocity models used in the location of earthquakes at 26°N. The 1D model for 23°N is shown as a bold solid line, and the 2D model for 26°N (parameterized at three nodal columns along-axis, with nodes at depths of 0, 1, 3, and 5 km below a 3.6-km datum) is shown with symbols and light solid lines. Two 2D models were considered, one in which velocities at 5 km extend downward indefinitely (solid line), and one in which velocities jump discontinuously to 8.33 km/s below 5 km (dashed line).

Figure 10. Distribution of located seismicity. Solid circles represent earthquake epicenters, with the larger symbols representing events for which focal depths could be resolved. Open circles show the locations of the OBHs, open squares show OBSs, and the hourglass indicates the location of the black-smoker field. Epicenters of large earthquakes determined teleseismically by the ISC for the period 1964-1989 are plotted as crossed hexagons. A pie diagram (lower right) shows the percentage of events that were located in each region. Abbreviations for regions in figure correspond to those used in Table 2. Box outlines area shown in Figure 14. Locations of many of the events well to the south (S) of the network are poorly constrained (e.g., those aligning along an azimuth of N315°E) since only P arrival times were used.

Figure 11. Rms travel time residuals for earthquake locations at various fixed depths. Whereas clear minima are associated with events with good depth resolution (solid lines and symbols), the focal depth for an event far outside the network cannot be constrained because no clear minima are identifiable. Event time is given in Julian day, hour, and minute. Region codes are from Figure 10.

Figure 12. Distribution of residuals and errors, divided into events for which focal depth was independently resolvable (FR) and ones for which depth was fixed (FIXD), for the 189 earthquakes located during the deployment. In general, events with fixed depths are characterized by larger rms residuals and epicentral errors. Vertical errors for events located with an S wave

arrival (FRPS) were on average less than those in which only P wave data (FRP) were used.

- Figure 13. Summary of the number and cumulative number of earthquakes located per day. Over the deployment period, the daily number of locatable events varied from 1 to 12, averaging 8.5 events per day.
- Figure 14. Distribution of microearthquake epicenters located using a 1D velocity model with station corrections (from Table 2). Events are divided into those with at least one S wave observation (P + S) and those with only P wave times (P). Good resolution of focal depth (larger solid circles and triangles) was obtained for almost all of the earthquakes near or within the network. Sea Beam bathymetry is contoured at an interval of 0.1 km. Major groups of activity discussed in the text are epicenters beneath (1) the inner floor topographic high (seafloor depths  $\sim 3.7$  km, events within 2.5 km of depth minimum at  $26^{\circ}09.25'N$ ,  $44^{\circ}51'W$ ); (2) an inferred ridge-axis volcano (delineated by the 4.0 km contour at  $26^{\circ}06'N$ ,  $44^{\circ}51.5'W$ ); (3) the inner floor deep (seafloor depths  $> 4.1$  km); and (4) the western and eastern median valley walls outside the inner floor (seafloor depths  $< 3.7$  km). See Figure 3 for details of the seismicity in the along-axis high region (area within dashed lines). Solid lines show locations of along- and cross-axis sections (Figures 17 and 18).
- Figure 15. Distribution of focal depth, subdivided into events located with at least one S wave arrival and those located with only P arrivals, for 105 earthquake hypocenters estimated with a 1D velocity model. The mean and standard deviation of focal depth was  $4.7 \pm 1.1$  km. Sea Beam bathymetry was used to correct the focal depth below a 3.3-km datum to depth below the seafloor. Almost all events occurred between 3 and 7 km beneath the seafloor.
- Figure 16. Focal depth (with respect to seafloor) distribution according to earthquake source location (see Figure 10 for categorization). Beneath the inner floor (high, volcano, deep), the shallowest events occurred beneath the along-axis high region. The error shown represents the average value for all earthquakes with resolvable depths.

- Figure 17. Distribution of focal depths for events along the axis of the median valley inner floor south of the inner floor high. See Figure 14 for location of profile A-AA. Epicenters within 2 km of A-AA are included. Hypocenters, along with their 95% error bars, are projected onto a vertical plane for events located with at least one S wave time (solid circles) and those located with only P wave times (open circles). The uncertainties in the depths of the three shallowest events beneath the deep may be considerable since the events occurred outside the network. Squares show the locations of inner floor instruments projected onto the section.
- Figure 18. Focal depth variation across-axis at three locations corresponding to (a) the along-axis median valley high, (b) the ridge-axis volcano, and (c) the along-axis deep. Events with epicenters up to 3 km from the profile are included. Symbols are as explained in Figure 17. See Figure 14 for locations of profiles B-BB, C-CC, and D-DD.
- Figure 19. Rms travel time residual maps versus latitude and longitude for two microearthquakes. The focal depth for each is fixed at the depth estimated by HYPOINVERSE. On the left are residuals computed from the observed arrival time data, and on the right are residuals determined from noise-free synthetic data at the same station locations as the observations. Latitude and longitude values are in kilometers from an arbitrary origin. The minima obtained from real data show little difference from HYPOINVERSE solutions (which are at (41 km, 48 km) for an event on June 27, 0758UT, and (34 km, 39 km) for an event on July 2, 0145UT). The concentric nature of the elliptical contours implies that for well-recorded events in this study, non-linearity of the location problem is not a major source of uncertainty, and the error ellipses from HYPOINVERSE are good approximations to the true epicentral uncertainty.
- Figure 20. Magnitudes of hypocentral differences for all events with resolved focal depths computed from HYPOINVERSE and the 1D velocity model with station corrections with those obtained with the rms grid-search method (1-km grid spacing). Minimal differences imply that the two methods are giving equally acceptable solutions. The largest differences in epicenter are

for events to the west of the network.  $DX$  is the horizontal distance between the two epicenters, and  $DZ$  is the difference in focal depth.

- Figure 21. Probability distribution of seismicity at  $26^{\circ}N$ . The rms grid-search technique permits the assignment of a probability of occurrence to all grid squares, thus giving a quantitative measure of not only the level of seismicity but also the quality of the estimated hypocenter. Values of the summed probability greater than 7.4 correspond to areas of high activity or well-constrained epicenters. See text for further explanation. The seismic network (solid symbols: circles-OBHs; squares-OBSs) is shown for reference. A star shows the location of the hydrothermal field.
- Figure 22. Two-dimensional velocity model used to evaluate the robustness of the hypocenters obtained with a 1D structure. Velocity is parameterized at 12 nodes arranged in three columns along the ridge axis; the vertical structure at each nodal column is shown in Figure 9.
- Figure 23. Changes in epicenters of 105 events upon relocation with 2D models A (8.33 km/s half-space) and B (velocities at 5 km depth extend indefinitely downwards) for all earthquakes for which focal depth was a free parameter. Locations of the OBHs and OBSs are indicated by solid squares. Epicenters relocated with the 2D model are plotted with open circles, with a line tracing the change from the location obtained with the 1D model. The hydrothermal field is located at  $26^{\circ}8.5'N$ ,  $44^{\circ}49.5'W$ . The ridge axis volcano is located at  $26^{\circ}06'N$ ,  $44^{\circ}51.5'W$ . See text for discussion.
- Figure 24. Changes in focal depth for 105 events relocated with (a) model A and (b) model B are shown projected onto a vertical plane along (top) and across (bottom) the median valley. Symbols are as in Figure 23. Changes in focal depth with model A are small because most of the effect is assigned to changes in the origin time, whereas those from model B are larger because origin times remain the same. The depths shown are with respect to a datum at 3.3 km depth below sea level. The locations of activity discussed in the text are: ridge axis ( $\sim 10$  km across-axis); along-axis high (19-24 km

along-axis); volcano (15 km along-axis); along-axis deep (<13 km along-axis).

- Figure 25. Locations of events used in the construction of selected composite focal mechanisms (Figures 26-31, 33-37). Earthquake symbols as in Figure 14, except for the events occurring in a swarm beneath the volcano where closed (V1) and open (V2) symbols are used to differentiate between mechanisms. H1, H2, and H3 are groups of events beneath the inner-floor along-axis high, D1 and D2 are groups of events beneath the along-axis deep, E1 and E2 are groups of eastern wall events, W1, W2, and W3 are groups of events near the western wall at the along-axis high, and WD are events near the western wall adjacent to the inner floor deep. Large open symbols denote OBH (circles) and OBS (square) instruments, and the hourglass symbol shows the location of the hydrothermal field.
- Figure 26. Composite focal mechanisms for events beneath the inner floor at the along-axis high (H1, H2, H3). See Figure 25 for event locations. Open circles correspond to dilatational arrivals, solid circles to compressions, and "x" symbols denote small-amplitude arrivals (interpreted as arrivals near nodal directions or showing high attenuation). Smaller symbols indicate less certain observations. Solid lines show the orientations of the preferred set of nodal planes, and dashed lines show equally plausible solutions. Numbers on the focal sphere denote instruments recording key groups of observations (as discussed in text). Normal faulting along either near-vertical or sub-horizontal planes is indicated. Event times and nodal plane orientations are given in Table 5.
- Figure 27. Composite focal mechanisms for a swarm of events occurring beneath the ridge axis volcano (V1, V2). Compressional arrivals at OBH 1 suggest reverse or thrust faulting (V1), but a phase reversal (from compression to dilatation) for rays arriving at OBH 2 near the hydrothermal field is required for the four events in the V2 group in order to fit a similar thrust mechanism. See Figure 25 for event locations and Figure 26 for explanation of symbols. Event times and nodal plane orientations are given in Table 5.



- Figure 28. Composite focal mechanisms for events beneath the inner floor deep (D1, D2). Both normal (solid) and reverse (dashed) fault planes can be fit, but neither solution offers a perfect fit to the data. Although good azimuthal coverage exists, there is ambiguity in the determinations of the mechanism. See Figure 25 for event locations and Figure 26 for explanation of symbols. Event times and nodal plane orientations are given in Table 5.
- Figure 29. Composite focal mechanisms for events beneath the eastern valley wall (E1, E2) at the along-axis high. Events are consistent with normal faulting, but a reverse fault can be fit to the data comprising mechanism E1. Compressional arrivals at OBH 5 are crucial for constraining the geometry of one plane. See Figure 25 for event locations and Figure 26 for explanation of symbols. Event times and nodal plane orientations are given in Table 5.
- Figure 30. Composite focal mechanisms for events associated with the western median valley walls (W1, W2, W3). Normal faulting along planes parallelling the ridge are suggested, though northwest-trending nodal planes are possible (W2, W3). See Figure 25 for event locations and Figure 26 for explanation of symbols. Event times and nodal plane orientations are given in Table 5.
- Figure 31. A composite focal mechanism for events associated with the western wall adjacent to the along-axis deep (WD) suggests normal faulting along moderately dipping planes. See Figure 25 for event locations and Figure 26 for explanation of symbols.
- Figure 32. Summary of observed types of faulting inferred from focal mechanisms obtained with the 1D velocity model. Beneath the inner floor, high-angle (or sub-horizontal) normal faulting is suggested, but reverse faulting is seen beneath the axial volcano and normal faulting along planes dipping near 45° characterizes events beneath the eastern wall.
- Figure 33. Changes in first motion observations for events beneath the along-axis high upon relocation with 2D models A and B (mechanism H2). Only the preferred set of nodal planes obtained with the 1D structure is shown for simplicity (solid lines). Event locations are shown in Figure 25, and

symbols are as in Figure 26. Dotted lines connect the locations on the focal sphere obtained with the 2D model (circles) with those obtained with the 1D model. Observations at OBHs 2, 3, and 4 move toward the center of the focal sphere upon relocation and make the dip of the high-angle nodal planes less steep by  $\sim 20^\circ$ . Event times and nodal plane orientations are given in Table 5.

Figure 34. Changes in first motion observations for events beneath the volcano upon relocation with 2D models A and B. Compressional arrivals still preclude normal faulting. The movement of observations toward the east on the focal sphere for mechanism V1 results in the shoaling of the eastward-dipping plane and steepening of the westward-dipping plane (by  $\sim 20^\circ$  for each plane). Event locations are shown in Figure 25 and symbols are the same as in Figures 26 and 33. Event times and nodal plane orientations are given in Table 5.

Figure 35. Changes in first motion observations for events (D2) beneath the along-axis deep upon relocation with 2D models A and B. No double couple mechanism can fit all of the observed data. The nature of faulting, while suggestive of high-angle normal or reverse faulting, remains ambiguous even after event relocation. Compressional arrivals at OBH 1 (at azimuth  $\sim 280^\circ$ ) and 6 preclude normal faulting along moderately dipping planes. Chain dash lines show an alternate set of fault planes. Event locations are shown in Figure 25 and symbols are the same as in Figures 26 and 33. Event times and nodal plane orientations are given in Table 5.

Figure 36. Changes in first motion observations for events beneath the eastern wall upon relocation with 2D models A and B (mechanism E2). Although normal faulting along planes parallelling the local bathymetry is consistent with the data, the availability of only one set of compressional arrivals precludes well-constrained orientations of the nodal planes. Event locations are shown in Figure 25 and symbols are the same as in Figures 26 and 33. Event times and nodal plane orientations are given in Table 5.

Figure 37. (a) Changes in first motion observations for events beneath the western wall at the southern end of the along-axis high upon relocation with 2D models A

and B (mechanism W1). OBH 1 dilatational arrivals move eastward, making the inference of normal faulting more robust. (b) Changes in first motion observations of western inner floor/wall events upon relocation with 2D models A and B (mechanism W2). High-angle normal faulting on inward facing faults is suggested, but the preferred orientations of the nodal planes (north-south or northwest trending) remains uncertain even after event relocation. Chain dash lines show an alternate set of fault planes. Event locations are shown in Figure 25 and symbols are the same as in Figures 26 and 33. Event times and nodal plane orientations are given in Table 5.

- Figure 38. Example of an amplitude spectrum corrected for instrument response and attenuation recorded by the OBH 2 for an event beneath the eastern wall on July 10, 1325UT; the seismogram for this event is shown in Figure 6b. Conversion of pressure to equivalent seafloor displacement is described in the text. The low-frequency spectral level  $\Omega_0$  and the  $f^{-2}$  decay at higher frequencies ( $> f_0$ ) are shown by the solid lines.
- Figure 39. (a) Differences in  $M_0$  estimated from P and S waves at OBS 31. (b) Differences in  $M_0$  between the average value determined from the OBHs and that from P waves at OBS 31. The  $M_0$  ratio is the ratio of the larger  $M_0$  estimate divided by the smaller  $M_0$  determination.
- Figure 40. (a) Distribution of seismic moment  $M_0$  for 170 earthquakes located with the 1D model. (b) Distribution of  $M_0$  according to source location. The 86 earthquakes located with only P wave data possess smaller  $M_0$  values than the 84 events located with both P and S wave data.
- Figure 41. (a) Plot of the cumulative number of events greater than a given  $M_0$ . A linear fit to the data ( $\log_{10} M_0 > 18.5$ , open circles) yields a b-value of  $1.02 \pm 0.08$  for 136 events within or near the network (events far to the north and south of the network are excluded). (b) b-value by earthquake source location. Higher b-values are associated with the along-axis high (open symbols: inner floor - H; western floor/wall transition - W; eastern wall - E) than with events beneath the deeper portions of the median valley (stippled circles: volcano - V, solid squares: inner floor deep - D).

Figure 42. Seismograms from shots on the western side of the median valley to OBSs 31 and 33 located atop the eastern wall. The rays from these shots sample the upper 1-2 km of the low velocity region imaged by delay time tomography. Shear wave arrivals can be clearly identified, implying that large regions of partial melt are not present. Seismograms are scaled to a common maximum amplitude. Event time is given as Julian day, hour, and minute (UT).

Figure 43. Cartoon showing possible relationships between tectonic and volcanic processes operating beneath the median valley near 26°N. Earthquake hypocenters are from Figures 17 (with the addition of three swarm events located at 26°07'N, 44°52.25'W and exclusion of the shallowmost two events within the deep) and 18, and the two-dimensional P-wave velocity structure (solid lines, 1 km/s contour interval) is from Chapter 4. Stippled area shows the location of the low velocity region. Question marks represent portions of the model that are not constrained by the seismic data.

(a) Along-axis within the inner floor. Brittle failure at 3 and 6 km depths beneath the volcano suggest a thinning of the low velocity zone away from the high, with cooling of this intrusive body contributing compressive thermal stress to the over- and underlying regions of cooler pre-existing crust. Earthquake activity within the inner floor deep to the south may extend to the base of the crust.

(b) Across-axis in the vicinity of the inner floor high. The lack of seismic activity in the crust beneath the hydrothermal field and the shallow seismicity at the high, together with the identification of a region of lower velocities and severe attenuation of waveform amplitudes beneath the volcano and along-axis high, suggest the presence of a recent magmatic intrusion, but efficient shear wave propagation through the low velocity zone (Figure 42) and the occurrence of microearthquakes within this region implies that large portions cannot be molten. The across-axis extent of the intrusion is constrained by the locations of seismicity beneath the walls and the observation of impulsive P wave energy at all ranges for rays sampling the eastern inner floor and wall to OBH 4 (see Figure 5 in Chapter 4). Much of the microearthquake activity near the high may result from rapid cooling at the top of the high-temperature body; the cooling is a

consequence of hydrothermal circulation through the 3-4 km of crust in this region. The black-smoker vent field (hourglass symbol) is inferred to result from the rapid upflow of heated water from depth along fault-controlled conduits.

Figure 44. Cross section of inner floor hypocenters along-axis (from Figure 17) with the range of reported focal depths (stippled areas) found for inner floor events at 23°N [*Toomey et al.*, 1985, 1988] and 35°N [*Murray et al.*, 1984]. The latter two studies, which were conducted at an along-axis deep and an along-axis high, respectively, show good agreement with the depth distribution observed beneath their along-axis counterparts in the median valley at 26°N.

TABLE 1. Relocated Instrument and Shot Positions

Instr	Latitude °N	Longitude °W	Location Error Ellipse (1- $\sigma$ )			Depth km	Depth Error km	Station Delay, s
			min, km	maj, km	azimaj,°			
1	26 5.54	44 51.71	0.015	0.020	111.3	3.666	0.012	0.00
2	26 7.76	44 49.41	0.015	0.022	120.7	3.509	0.020	-0.08
3	26 9.40	44 50.23	0.016	0.024	107.4	3.647	0.017	0.04
4	26 9.72	44 46.91	0.016	0.028	128.4	3.046	0.021	-0.08
5	26 5.65	44 47.31	0.015	0.022	150.4	2.234	0.026	0.04
6	26 1.49	44 52.90	0.015	0.026	117.0	4.335	0.008	0.00
8	26 4.05	44 54.29	0.016	0.019	113.3	3.670	0.016	0.06
31	26 7.57	44 45.68	0.027	0.030	156.2	2.394	0.076	0.08
33	26 3.47	44 48.75	0.021	0.028	164.5	3.328	0.028	0.10

Shot	Latitude °N	Longitude °W	Location Error Ellipse (1- $\sigma$ )		
			min, km	maj, km	azimaj,°
2323	26 8.86	44 53.43	0.019	0.024	58.6
1	26 6.83	44 54.42	0.020	0.026	173.9
15	26 4.89	44 55.48	0.021	0.029	154.9
32	26 2.38	44 55.49	0.017	0.030	143.8
47	26 0.90	44 53.56	0.017	0.033	114.8
109	26 1.55	44 50.02	0.017	0.024	90.5
135	26 4.09	44 46.62	0.020	0.024	15.6
151	26 6.11	44 44.84	0.019	0.030	169.6
207	26 8.23	44 43.83	0.023	0.036	165.0
230	26 10.39	44 46.49	0.019	0.038	131.0
254	26 10.47	44 50.36	0.019	0.030	99.8
313	26 7.93	44 50.31	0.018	0.025	120.3
327	26 5.79	44 50.73	0.018	0.026	129.9
332	26 5.06	44 51.01	0.017	0.025	134.0
337	26 4.32	44 51.37	0.017	0.025	133.6
342	26 3.60	44 51.73	0.017	0.025	122.7
347	26 2.87	44 52.15	0.017	0.026	118.7
352	26 2.16	44 52.53	0.017	0.025	118.7
357	26 1.42	44 52.94	0.017	0.028	115.4
402	26 0.68	44 53.31	0.018	0.033	112.5
407	25 59.97	44 53.73	0.019	0.036	112.0
412	25 59.23	44 54.14	0.017	0.039	113.7
417	25 58.51	44 54.54	0.018	0.042	113.4
422	25 57.77	44 54.87	0.019	0.053	106.6
427	25 57.03	44 55.22	0.021	0.058	103.9
432	25 56.32	44 55.68	0.096	0.520	298.3
437	25 55.60	44 56.07	0.096	0.583	298.3
442	25 54.85	44 56.47	0.115	0.644	298.3
447	25 54.16	44 56.85	0.115	0.745	298.3
1706	26 10.58	44 49.35	0.151	0.203	299.6
1711	26 11.39	44 48.87	0.097	0.223	299.6
1716	26 12.17	44 48.34	0.097	0.223	299.6
1726	26 13.72	44 47.30	0.086	0.233	299.6
1731	26 14.05	44 46.48	0.086	0.284	299.6
1736	26 14.10	44 45.53	0.086	0.406	299.6
1741	26 14.18	44 44.55	0.086	0.477	299.6
1746	26 14.62	44 43.84	0.097	0.714	299.6
1751	26 15.40	44 43.39	0.097	0.611	299.6
1756	26 16.24	44 42.92	0.097	0.652	299.6
1801	26 17.03	44 42.47	0.097	0.734	299.6
1811	26 18.63	44 41.56	0.097	0.814	299.6
1816	26 19.36	44 41.15	0.097	1.038	299.6
1821	26 20.15	44 40.70	0.116	1.017	299.6

1826	26 20.90	44 40.27	0.097	0.835	299.6
1831	26 21.65	44 39.85	0.077	0.915	299.6
1836	26 22.39	44 39.43	0.095	1.147	299.6
1841	26 23.09	44 39.02	0.129	1.375	299.6
1846	26 23.85	44 38.60	0.170	1.555	299.6
1851	26 24.59	44 38.17	0.095	1.171	299.6
1856	26 25.31	44 37.76	0.118	1.318	299.6
1901	26 26.02	44 37.36	0.095	1.196	299.6
1906	26 26.72	44 36.97	0.095	1.170	299.6
1911	26 27.46	44 36.54	0.077	1.079	299.6
1916	26 28.37	44 36.03	0.271	0.484	299.6
2040	26 18.06	44 41.89	0.116	0.936	299.6
2131	26 12.74	44 47.57	0.086	0.192	299.6

TABLE 2. Earthquake Hypocenters

YR	MDA	HRMIN	SEC	REGION	LAT (N)	LONG (W)	DBD km	SF km	DBSF km	NOR S	MAG deg	DCS km	RMS sec	ERH km	ERZ km
85	626	752	46.78	H	26	9.22	44 51.04	3.49	3.76	3.0	4 0 248	1.4	0.00	0.7	0.6
85	626	846	13.04	W	26	11.68	44 51.31	5.27	3.52	5.1	6 1 325	4.7	0.02	0.9	0.5
85	626	1048	43.39	H	26	9.40	44 51.24	3.75	3.76	3.3	7 0 237	1.7	0.04	0.5	0.3
85	626	1230	40.57	W	26	10.67	44 51.86	5.00	—	—	5 0 305	3.6	0.03	1.2	PDC
85	626	1249	27.81	W	26	9.34	44 53.17	5.23	3.58	5.0	6 0 255	4.9	0.03	0.9	0.8
85	626	1255	43.33	S	25	52.61	45 1.29	8.00	—	—	6 0 345	21.6	0.08	1.7	PDC
85	626	1438	34.69	W	26	9.22	44 52.43	5.95	3.54	5.7	4 0 275	3.7	0.01	1.8	1.0
85	626	1443	19.76	W	26	9.25	44 53.19	5.54	3.60	5.2	6 0 256	4.9	0.02	0.9	0.5
85	626	1447	26.88	W	26	8.94	44 52.79	5.40	3.66	5.0	11 2 243	4.3	0.03	0.3	0.6
85	626	1525	24.66	W	26	9.03	44 52.74	5.31	3.64	5.0	11 2 245	4.2	0.04	0.3	0.6
85	626	2215	1.07	W	26	8.20	44 52.95	5.05	3.83	4.5	4 0 245	5.0	0.00	1.0	1.2
85	626	23 2	23.56	W	26	7.56	44 53.38	5.04	3.80	4.5	8 1 224	4.7	0.03	0.4	0.6
85	626	2318	12.64	W	26	10.05	44 51.95	4.79	3.52	4.6	8 1 273	3.1	0.04	0.6	0.5
85	627	758	45.21	E	26	7.93	44 48.27	4.76	3.56	4.5	10 2 149	2.0	0.06	0.2	0.4
85	627	820	21.76	W	26	11.04	44 51.02	4.38	3.68	4.0	6 0 279	3.4	0.02	1.2	0.5
85	627	851	34.34	W	26	11.75	44 52.18	5.00	—	—	4 0 298	5.5	0.02	2.5	PDC
85	627	930	39.20	W	26	4.40	44 53.96	5.92	3.87	5.4	6 0 174	0.8	0.03	0.8	0.5
85	627	14 9	58.04	D	26	3.51	44 52.55	5.00	—	—	4 0 190	3.8	0.04	2.4	PDC
85	627	16 0	6.48	W	26	7.65	44 53.38	5.11	3.74	4.7	5 0 243	4.8	0.02	0.7	0.7
85	627	1625	26.23	E	26	7.21	44 48.41	5.23	3.56	5.0	8 1 68	2.0	0.03	0.2	0.6
85	627	1829	41.16	E	26	9.86	44 45.48	5.00	—	—	8 1 281	4.3	0.08	0.9	PDC
85	627	1855	57.43	H	26	6.98	44 52.17	3.80	3.96	3.1	8 1 182	2.8	0.03	0.3	0.6
85	627	1913	4.11	W	26	8.88	44 52.28	5.00	—	—	4 0 272	5.2	0.11	1.6	PDC
85	627	1925	27.68	H	26	6.93	44 52.03	4.15	4.02	3.4	11 2 177	2.7	0.04	0.2	0.5
85	627	1945	54.88	E	26	10.00	44 45.27	5.00	—	—	5 1 286	4.6	0.06	1.0	PDC
85	627	1950	11.56	H	26	7.02	44 52.33	4.07	3.96	3.4	9 1 187	3.0	0.03	0.3	0.5
85	627	1959	46.45	E	26	10.08	44 45.01	5.00	—	—	7 1 292	4.8	0.10	0.9	PDC
85	627	20 8	25.90	W	26	10.79	44 53.86	5.00	—	—	4 0 307	10.4	0.14	0.5	PDC
85	627	2258	58.54	W	26	4.67	44 54.09	7.00	—	—	4 0 232	1.1	0.02	0.8	PDC
85	628	148	50.78	H	26	8.51	44 51.57	3.67	3.80	3.2	6 0 205	2.8	0.01	0.4	0.7
85	628	251	47.71	H	26	9.52	44 51.01	3.34	3.76	2.9	7 1 252	1.3	0.02	0.7	0.6
85	628	1156	41.58	H	26	9.21	44 50.99	3.45	3.76	3.0	5 0 243	1.3	0.01	0.6	0.4
85	628	1449	4.13	W	26	7.64	44 52.96	5.05	3.93	4.4	4 0 235	4.5	0.00	1.2	0.8
85	628	15 1	18.87	E	26	5.86	44 49.05	6.23	3.36	6.2	5 0 193	3.5	0.01	0.8	0.8
85	628	1820	27.36	N	26	16.41	44 40.31	8.00	—	—	6 0 345	16.6	0.13	2.2	PDC
85	628	1942	58.10	N	26	14.96	44 45.23	8.00	—	—	9 1 325	10.1	0.15	0.9	PDC
85	628	2034	21.44	S	25	53.35	45 2.30	8.00	—	—	6 0 346	21.8	0.17	1.7	PDC
85	628	2358	0.06	E	26	6.45	44 48.50	5.00	—	—	4 0 125	2.5	0.05	0.3	PDC
85	629	013	25.70	N	26	15.46	44 51.29	8.00	—	—	4 0 322	11.4	0.03	0.8	PDC
85	629	1849	48.04	D	26	4.06	44 52.89	6.66	4.16	5.8	7 1 118	2.3	0.03	0.4	0.7
85	629	2139	25.48	S	25	52.52	45 1.19	8.00	—	—	6 0 349	21.6	0.06	2.3	PDC
85	629	2154	11.93	S	25	51.72	45 0.18	8.00	—	—	6 0 350	21.8	0.07	2.3	PDC
85	629	2228	22.24	N	26	15.72	44 51.27	8.00	—	—	5 0 323	11.9	0.08	0.9	PDC
85	630	143	11.79	W	26	11.62	44 51.32	5.00	—	—	4 0 319	4.6	0.03	2.4	PDC
85	630	4 7	8.13	W	26	9.32	44 53.45	5.62	3.58	5.3	9 1 258	5.3	0.04	0.7	0.3
85	630	621	35.16	W	26	10.60	44 51.57	4.70	3.63	4.4	5 0 279	3.2	0.02	1.5	0.6
85	630	643	15.64	H	26	10.34	44 51.14	5.00	—	—	4 0 273	2.4	0.00	1.0	PDC
85	630	1048	19.10	E	26	9.27	44 46.03	5.00	—	—	5 1 257	3.3	0.04	0.8	PDC
85	630	1052	27.39	N	26	17.84	44 41.98	8.00	—	—	9 1 336	17.1	0.13	1.2	PDC



85 630 1133 4.10	N	26 14.63	44 45.07	8.00	-	-	4 0 331	12.9 0.07	1.0	PDC
85 630 1142 42.13	N	26 14.88	44 44.71	8.00	-	-	5 0 347	13.7 0.16	2.1	PDC
85 630 1523 16.76	W	26 11.33	44 51.23	4.30	3.60	4.0	8 1 286	4.0 0.02	1.0	0.5
85 630 1656 35.84	H	26 8.72	44 51.67	5.56	3.70	5.2	4 0 234	2.7 0.01	0.9	0.7
85 630 1837 0.81	N	26 16.29	44 48.21	8.00	-	-	5 0 338	13.3 0.16	1.2	PDC
85 630 2044 22.08	S	25 53.63	45 2.79	8.00	-	-	4 0 348	22.0 0.07	2.6	PDC
85 630 2144 4.15	D	26 3.92	44 53.56	4.50	4.10	3.7	7 0 117	1.2 0.02	0.4	0.5
85 630 2318 22.85	E	26 7.82	44 46.53	3.91	2.78	4.4	5 1 161	1.5 0.01	0.6	0.9
85 701 0 9 10.69	E	26 10.00	44 44.66	5.00	-	-	8 1 298	3.8 0.05	0.6	PDC
85 701 229 16.10	W	26 6.27	44 54.14	5.81	3.88	5.2	9 1 224	4.1 0.03	0.5	0.3
85 701 628 54.88	N	26 15.71	44 43.02	8.00	-	-	5 1 339	15.8 0.12	1.5	PDC
85 701 8 9 19.57	S	25 52.48	45 1.08	8.00	-	-	7 0 344	21.6 0.05	1.5	PDC
85 701 1125 15.25	H	26 9.21	44 51.27	3.39	3.76	2.9	6 0 231	1.8 0.01	0.9	1.2
85 701 2341 13.44	H	26 7.45	44 50.57	6.45	3.90	5.8	5 0 161	2.0 0.01	0.4	1.2
85 702 1 2 11.93	H	26 9.47	44 50.72	3.43	3.70	3.0	6 0 234	0.9 0.01	0.6	0.3
85 702 145 38.33	D	26 2.88	44 52.67	6.49	4.41	5.4	9 1 129	2.6 0.04	0.5	0.5
85 702 333 9.24	D	26 2.33	44 53.35	8.60	4.66	7.2	8 1 182	1.7 0.04	0.6	0.8
85 702 513 5.16	W	26 12.34	44 50.83	5.00	-	-	4 0 296	5.6 0.02	0.5	PDC
85 702 1022 29.11	S	25 50.96	44 58.91	8.00	-	-	4 0 350	22.0 0.06	2.1	PDC
85 702 1038 20.64	W	26 10.72	44 51.88	4.89	3.52	4.7	9 1 264	3.7 0.03	0.6	0.2
85 702 1059 13.37	W	26 10.53	44 51.31	5.00	-	-	5 0 272	2.8 0.03	1.0	PDC
85 702 1536 49.91	W	26 9.91	44 51.65	4.03	3.68	3.7	9 1 250	2.5 0.02	0.4	0.4
85 702 1759 7.08	D	26 1.25	44 53.30	7.00	-	-	6 0 288	0.9 0.02	0.5	PDC
85 702 1819 15.78	H	26 9.41	44 50.62	3.32	3.70	2.9	6 0 232	0.7 0.01	0.5	0.3
85 702 1921 43.82	S	25 53.12	45 1.98	8.00	-	-	6 0 346	21.7 0.08	1.8	PDC
85 703 440 30.72	W	26 9.01	44 52.55	4.79	3.62	4.5	5 0 256	3.9 0.01	0.8	0.7
85 703 721 5.53	W	26 7.72	44 53.31	5.20	3.74	4.8	8 1 224	4.9 0.04	0.4	0.7
85 703 1342 11.02	H	26 9.52	44 51.01	3.54	3.76	3.1	5 0 254	1.4 0.01	0.8	0.4
85 703 1637 5.25	W	26 9.64	44 51.38	4.29	3.77	3.8	5 0 258	2.0 0.01	1.0	0.4
85 703 1825 59.85	W	26 4.58	44 56.76	5.00	-	-	4 0 293	4.3 0.10	0.4	PDC
85 703 2143 54.08	S	25 54.90	45 4.59	8.00	-	-	7 0 344	23.0 0.07	1.7	PDC
85 703 2251 42.01	D	26 4.02	44 52.46	6.80	4.34	5.8	6 0 202	3.0 0.00	0.7	0.8
85 703 2337 37.20	N	26 15.80	44 48.47	8.00	-	-	6 0 331	11.6 0.08	0.8	PDC
85 703 2341 48.73	E	26 9.09	44 44.89	5.00	-	-	6 1 276	3.2 0.06	0.7	PDC
85 704 120 48.19	H	26 8.77	44 51.31	3.54	3.70	3.1	6 0 207	2.1 0.03	0.5	0.6
85 704 140 48.79	W	26 8.27	44 53.47	5.23	3.66	4.9	5 0 239	5.8 0.02	1.0	1.4
85 704 9 4 37.97	W	26 9.86	44 52.42	4.87	3.48	4.7	9 1 255	3.8 0.03	0.6	0.2
85 704 1041 0.17	E	26 9.95	44 45.21	5.50	2.92	5.9	7 1 288	2.9 0.02	0.8	0.4
85 704 1322 19.92	W	26 10.13	44 52.40	5.29	3.43	5.2	6 0 271	3.9 0.02	1.1	0.5
85 704 1526 59.64	W	26 9.09	44 53.07	4.60	3.63	4.3	6 0 250	4.8 0.02	0.7	0.6
85 704 1555 24.25	E	26 7.05	44 47.32	3.50	2.78	4.0	9 1 111	2.6 0.03	0.2	0.6
85 704 1917 40.96	H	26 9.18	44 50.44	2.70	3.73	2.3	6 0 226	3.2 0.02	0.4	0.7
85 704 1928 27.36	W	26 10.08	44 52.66	4.86	3.42	4.7	9 1 259	4.3 0.03	0.6	0.3
85 704 1934 18.16	W	26 10.33	44 52.22	5.11	3.40	5.0	8 1 260	3.8 0.02	0.5	0.4
85 705 536 0.45	V	26 6.20	44 51.94	3.69	4.02	3.0	4 0 224	1.4 0.01	0.9	0.4
85 705 617 5.72	V	26 5.74	44 51.83	6.36	3.90	5.8	9 1 148	0.5 0.02	0.3	0.6
85 705 638 10.33	N	26 13.29	44 49.76	8.00	-	-	5 1 328	8.2 0.12	1.2	PDC
85 705 16 4 51.08	W	26 7.44	44 53.19	4.91	3.94	4.3	6 0 216	4.3 0.02	0.6	0.4
85 705 1718 27.08	W	26 10.10	44 52.16	5.00	-	-	4 0 308	6.3 0.05	0.5	PDC
85 705 1828 27.50	E	26 5.96	44 48.86	6.04	3.30	6.0	7 1 117	2.6 0.02	0.4	0.6
85 706 018 37.39	E	26 7.14	44 46.86	5.00	-	-	4 0 197	2.9 0.01	0.5	PDC
85 706 131 40.23	N	26 17.09	44 52.45	8.00	-	-	5 0 330	18.1 0.09	1.0	PDC
85 706 343 48.47	H	26 9.55	44 51.29	4.00	-	-	4 0 261	4.6 0.01	1.1	PDC

85 706	542	10.51	S	25	53.32	45	5.40	8.00	-	-	7	1	349	25.8	0.06	1.9	PDC
85 706	6 6	11.67	S	25	53.29	45	5.06	8.00	-	-	8	1	347	25.4	0.05	1.7	PDC
85 706	615	54.38	S	25	53.75	45	4.86	8.00	-	-	8	2	346	24.6	0.07	1.5	PDC
85 706	626	14.95	S	25	53.86	45	2.92	8.00	-	-	5	0	351	21.9	0.06	2.4	PDC
85 706	642	52.73	S	25	51.23	45	3.84	8.00	-	-	8	1	348	26.4	0.05	2.0	PDC
85 706	756	57.62	E	26	5.56	44	47.14	5.45	2.58	6.2	4	0	268	0.3	0.00	1.1	1.2
85 706	935	7.53	H	26	9.90	44	50.78	5.00	-	-	4	0	303	1.4	0.01	0.8	PDC
85 706	1029	28.58	W	26	12.52	44	50.54	3.96	3.56	3.7	9	1	288	5.8	0.03	0.8	0.3
85 706	1310	35.19	E	26	6.28	44	47.74	5.21	2.78	5.7	8	1	138	1.4	0.04	0.3	0.6
85 706	2038	19.98	N	26	14.10	44	45.65	8.00	-	-	8	1	319	8.4	0.07	0.8	PDC
85 706	2048	13.73	E	26	6.71	44	47.38	5.14	2.74	5.7	5	0	170	2.0	0.01	0.5	1.0
85 707	053	16.88	S	25	44.84	45	10.90	8.00	-	-	9	1	352	43.0	0.10	2.4	PDC
85 707	234	58.24	E	26	10.26	44	45.70	3.77	3.28	3.8	6	1	281	2.3	0.03	0.8	0.4
85 707	432	23.01	N	26	14.40	44	51.76	8.00	-	-	5	1	331	9.7	0.14	1.1	PDC
85 707	731	53.67	D	26	4.61	44	52.62	7.00	-	-	4	0	152	2.3	0.09	0.8	PDC
85 707	843	57.97	H	26	9.51	44	51.01	2.70	3.76	2.2	8	1	237	4.2	0.05	0.4	0.9
85 707	1114	28.79	D	26	1.81	44	54.66	4.47	4.28	3.5	6	0	309	4.3	0.03	1.6	0.5
85 707	1723	59.14	W	26	10.88	44	51.22	3.75	3.74	3.3	8	1	264	6.6	0.01	0.5	0.5
85 707	1957	49.91	S	25	53.61	45	2.65	8.00	-	-	6	0	347	21.9	0.07	1.8	PDC
85 707	21 2	57.65	H	26	8.76	44	51.75	5.00	-	-	5	0	236	2.8	0.02	0.6	PDC
85 708	035	32.21	W	26	8.41	44	53.40	5.43	3.65	5.1	4	0	284	6.1	0.00	2.5	1.1
85 708	249	39.87	D	26	0.23	44	54.37	5.07	4.43	3.9	8	1	312	3.4	0.04	0.8	0.3
85 708	529	25.35	W	26	10.10	44	51.46	5.00	-	-	5	0	266	2.5	0.03	0.9	PDC
85 708	714	51.07	W	26	8.04	44	52.73	5.72	3.82	5.2	4	0	237	4.8	0.01	1.0	1.3
85 708	847	11.14	H	26	9.87	44	50.37	4.76	3.60	4.5	5	0	256	0.9	0.00	0.8	0.6
85 708	929	4.79	D	26	1.39	44	54.41	6.22	4.30	5.2	9	1	277	2.5	0.03	0.7	0.4
85 708	957	14.32	D	25	59.47	44	55.54	4.61	4.20	3.7	8	1	323	5.8	0.03	0.6	0.2
85 708	1357	5.19	E	26	6.26	44	48.86	5.71	3.33	5.7	6	0	104	2.8	0.03	0.3	0.7
85 708	15 3	11.53	W	26	11.01	44	52.01	5.86	3.48	5.7	7	1	268	8.8	0.02	0.8	0.3
85 708	2225	58.82	S	25	52.36	45	0.90	8.00	-	-	4	0	344	21.6	0.03	2.1	PDC
85 709	051	39.25	W	26	9.89	44	51.72	4.22	3.64	3.9	6	0	250	2.7	0.02	0.9	0.4
85 709	327	37.01	H	26	10.63	44	49.50	4.00	-	-	5	0	263	2.6	0.20	0.7	PDC
85 709	524	59.75	H	26	8.75	44	50.69	5.00	-	-	4	0	197	1.4	0.01	0.9	PDC
85 709	1023	40.38	W	26	7.83	44	52.79	5.00	-	-	4	0	235	4.7	0.01	0.9	PDC
85 709	1044	4.58	S	25	48.42	45	10.09	8.00	-	-	8	1	351	37.5	0.04	3.0	PDC
85 709	11 1	22.48	S	25	51.09	44	59.88	8.00	-	-	6	0	348	22.6	0.09	2.8	PDC
85 709	22 3	28.75	E	26	10.37	44	46.21	4.60	3.44	4.5	8	1	275	1.7	0.03	0.7	0.3
85 710	023	34.21	W	26	10.86	44	51.08	4.22	3.74	3.8	6	0	276	3.1	0.02	1.2	0.5
85 710	120	4.11	S	25	54.67	45	4.39	8.00	-	-	7	0	344	23.0	0.07	1.4	PDC
85 710	212	10.44	V	26	6.03	44	51.63	6.40	3.92	5.8	9	1	149	0.9	0.01	0.3	0.5
85 710	223	56.06	V	26	5.99	44	51.65	6.36	3.94	5.7	9	1	149	0.9	0.02	0.3	0.5
85 710	229	21.22	V	26	5.67	44	51.38	5.45	3.90	4.8	7	1	132	0.6	0.05	0.3	0.6
85 710	233	45.67	V	26	5.96	44	51.65	6.55	3.94	5.9	8	1	148	0.8	0.01	0.3	0.5
85 710	240	18.25	V	26	5.98	44	51.52	6.38	3.94	5.7	11	2	145	0.9	0.02	0.2	0.5
85 710	245	47.42	E	26	5.32	44	50.42	5.00	-	-	4	0	191	2.2	0.02	0.9	PDC
85 710	252	51.29	V	26	5.89	44	51.36	6.46	3.90	5.9	7	1	157	0.9	0.03	0.3	0.4
85 710	333	8.20	V	26	5.85	44	51.35	6.13	3.90	5.5	6	0	153	0.9	0.02	0.7	0.5
85 710	7 5	39.20	W	26	3.80	44	54.11	7.35	3.90	6.8	7	0	179	0.6	0.02	0.9	1.0
85 710	1150	22.70	H	26	9.79	44	50.82	3.99	3.76	3.5	5	0	258	1.3	0.03	0.9	0.3
85 710	1325	49.66	E	26	7.29	44	48.94	5.56	3.66	5.2	9	1	79	1.1	0.03	0.3	0.6
85 710	1525	23.53	E	26	9.60	44	44.87	5.46	2.80	6.0	7	1	286	3.4	0.03	0.8	0.4
85 710	1648	0.31	N	26	14.30	44	42.41	8.00	-	-	4	0	342	11.3	0.09	1.9	PDC
85 710	1654	57.05	D	26	3.00	44	51.50	6.98	4.16	6.1	6	0	166	3.6	0.02	0.5	1.4
85 710	17 1	23.14	W	26	9.67	44	53.42	5.18	3.42	5.1	9	1	261	5.3	0.02	0.5	0.7
85 710	1816	47.63	W	26	8.24	44	52.71	5.58	3.78	5.1	4	0	240	4.7	0.01	1.1	1.7

85 710	19 4	11.55	E	26	3.24	44 49.49	6.53	3.56	6.3	9 1	171	1.3 0.03	0.5	0.4
85 711	733	34.58	S	25	53.25	45 2.18	8.00	-	-	7 0	346	21.8 0.14	1.7	PDC
85 711	1037	9.10	W	26	9.88	44 51.38	3.96	3.78	3.5	9 1	247	2.2 0.01	0.6	0.2
85 711	15 3	0.75	W	26	8.20	44 52.50	5.43	3.76	5.0	4 0	255	4.3 0.00	1.2	1.6
85 711	1523	56.16	D	26	5.02	44 52.98	5.90	4.12	5.1	8 1	158	2.4 0.02	0.5	0.3
85 711	1542	48.64	D	26	3.16	44 53.07	6.78	4.42	5.7	8 1	136	2.6 0.05	0.3	0.6
85 711	18 6	34.79	N	26	16.02	44 45.10	8.00	-	-	6 0	336	12.1 0.23	1.1	PDC
85 712	334	33.77	S	25	56.90	44 58.51	8.00	-	-	8 1	340	12.7 0.07	1.3	PDC
85 712	959	6.64	H	26	9.52	44 51.15	3.70	3.76	3.2	7 0	239	1.6 0.02	0.5	0.3
85 712	1450	42.78	W	26	9.43	44 53.73	5.33	3.47	5.2	7 0	261	5.8 0.02	0.8	0.8
85 712	1956	12.83	V	26	5.98	44 51.96	7.46	4.02	6.7	5 0	233	0.9 0.01	1.4	1.9
85 712	2051	43.55	V	26	6.01	44 51.44	6.40	-	-	4 0	172	1.0 0.01	1.1	PDC
85 713	332	51.24	S	25	48.47	44 57.13	8.00	-	-	5 0	349	25.1 0.11	2.3	PDC
85 713	732	18.89	E	26	9.32	44 46.74	5.65	3.00	6.0	6 1	171	0.8 0.02	0.7	1.0
85 713	813	29.09	W	26	9.29	44 52.68	5.00	-	-	4 0	281	4.1 0.02	1.1	PDC
85 713	14 5	37.74	W	26	9.82	44 51.78	4.45	3.62	4.1	8 1	264	2.7 0.01	0.8	0.4
85 713	1520	13.90	E	26	8.53	44 48.04	5.48	3.40	5.4	7 1	162	2.8 0.02	0.3	0.6
85 713	1627	43.12	S	25	53.27	45 2.35	8.00	-	-	4 0	351	22.0 0.07	2.9	PDC
85 713	1819	13.21	S	25	51.53	45 0.05	8.00	-	-	6 0	347	22.0 0.08	2.2	PDC
85 713	1848	17.77	S	25	48.77	45 2.67	8.00	-	-	6 1	351	36.0 0.03	0.4	PDC
85 713	1854	14.89	S	25	46.27	45 3.19	6.40	-	-	8 1	350	33.0 0.08	3.6	PDC
85 713	19 7	2.93	S	25	50.31	45 3.53	6.40	-	-	8 1	349	27.3 0.06	3.2	PDC
85 713	1939	12.88	S	25	49.51	45 3.10	6.40	-	-	7 1	351	28.0 0.11	2.6	PDC
85 713	2032	8.68	S	25	49.42	44 59.55	8.00	-	-	6 1	348	25.0 0.10	2.5	PDC
85 713	2049	55.11	S	25	51.00	45 3.15	8.00	-	-	8 1	348	25.9 0.05	2.1	PDC
85 714	042	29.95	S	25	52.95	45 2.68	8.00	-	-	7 1	351	22.8 0.06	2.5	PDC
85 714	214	35.73	S	25	55.10	45 4.73	8.00	-	-	6 1	351	29.1 0.04	2.6	PDC
85 714	1327	15.64	H	26	10.06	44 51.16	3.87	3.76	3.4	5 0	269	2.0 0.01	1.2	0.4
85 714	1347	24.60	S	25	50.86	45 4.81	8.00	-	-	7 1	352	28.0 0.05	2.8	PDC
85 715	1120	6.28	N	26	16.12	44 42.55	8.00	-	-	5 1	333	13.9 0.10	1.3	PDC
85 715	1321	20.42	N	26	15.86	44 41.63	8.00	-	-	6 1	342	16.8 0.08	1.4	PDC
85 716	456	59.33	E	26	2.99	44 49.72	6.47	4.00	5.8	5 1	287	5.7 0.02	1.0	0.5

REGIONS: E = EASTERN WALL  
W = WESTERN INNER FLOOR/WALL  
H = INNER FLOOR, ALONG-AXIS HIGH  
D = INNER FLOOR, ALONG-AXIS DEEP  
V = INNER FLOOR, VOLCANO  
S = SOUTH OF ARRAY  
N = NORTH OF ARRAY

DBD : DEPTH BELOW DATUM (3.3 km)  
SF : SEAFLOOR DEPTH (USING SEA BEAM BATHYMETRY)  
DBSF : DEPTH BELOW SEAFLOOR  
NOR : NUMBER OF WEIGHTED ARRIVALS (P+S,S)  
MAG : MAXIMUM AZIMUTHAL GAP  
DCS : DISTANCE TO CLOSEST STATION  
RMS : ROOT MEAN SQUARE TRAVEL TIME RESIDUAL  
ERH : HORIZONTAL ERROR (FROM 1-SIGMA ERROR ELLIPSOID)  
ERZ : VERTICAL ERROR (FROM 1-SIGMA ERROR ELLIPSOID)  
PDC : POOR DEPTH CONTROL

TABLE 3. Earthquake Location Residuals and Errors

	All, 1D Depth free, 1D <u>Depth fixed, 1D</u>	Depth free, 2D (8.33 km/s halfspace) <u>Model A</u>	Depth free, 2D (velocities extend below 5 km) <u>Model B</u>
Number of earthquakes	189 105 84	105	105
rms, s	0.04 ± 0.04 0.02 ± 0.01 0.07 ± 0.05	0.06 ± 0.04	0.06 ± 0.05
erh, km <sup>1,2</sup>	1.05 ± 0.72 0.69 ± 0.37 1.48 ± 0.73	0.76 ± 0.90	0.70 ± 0.73
erz, km <sup>1,2</sup>	0.62 ± 0.33	0.63 ± 0.55	0.78 ± 0.56
Δ Epicenter, km <sup>3</sup>	-	1.74 ± 1.04	1.64 ± 0.73
Δ Depth, km <sup>3</sup>	-	0.10 ± 1.08	-1.19 ± 1.57
Δ Origin time, s <sup>3</sup>	-	0.19 ± 0.18	0.02 ± 0.17

1 Errors are  $1\sigma$

2 erh = Horizontal error, erz = Vertical error

3 Δ = Difference in hypocentral estimates between solutions with 1D and 2D structures

TABLE 4. Hypocentral Changes for Major Groups of Activity with the 2D Structure relative to the 1D Model

<u>Earthquake Location</u>	<u>Velocity Model</u>	<u>Number of Events</u>	<u><math>\Delta</math> Epicenter, km</u>	<u><math>\Delta</math> Depth, km</u>	<u><math>\Delta</math> Origin Time, s</u>
High	A	21	$1.51 \pm 0.55$	$0.02 \pm 0.49$	$0.23 \pm 0.07$
	B	21	$1.50 \pm 0.61$	$-0.84 \pm 1.15$	$0.12 \pm 0.14$
Volcano	A	10	$1.10 \pm 0.53$	$0.11 \pm 0.58$	$0.20 \pm 0.04$
	B	10	$1.28 \pm 0.45$	$-0.61 \pm 0.71$	$0.01 \pm 0.13$
Deep	A	8 <sup>a</sup>	$1.03 \pm 1.16$	$-1.79 \pm 0.87$	$0.00 \pm 0.12$
	B	9 <sup>b</sup>	$1.95 \pm 1.09$	$-1.68 \pm 2.30$	$-0.01 \pm 0.31$
Eastern Wall	A	18 <sup>c</sup>	$1.41 \pm 0.92$	$1.12 \pm 0.79$	$0.08 \pm 0.13$
	B	18 <sup>c</sup>	$1.64 \pm 0.72$	$0.16 \pm 1.15$	$-0.05 \pm 0.13$
Western Median Valley / Wall	A	42 <sup>d</sup>	$2.13 \pm 0.94$	$-0.02 \pm 0.92$	$0.26 \pm 0.17$
	B	43	$1.71 \pm 0.72$	$-2.03 \pm 1.07$	$0.02 \pm 0.15$

<sup>a</sup> Excludes events 7/7/1114UT and 7/8/0249UT ( $erh > 2$  km), 7/8/0957UT ( $erh, erz > 2$  km), 7/10/1654UT ( $erz > 2$  km).

<sup>b</sup> Excludes events 7/3/2251UT ( $erz > 2$  km), 7/7/1114UT ( $erh > 2$  km), 7/8/0957UT ( $erh, erz > 2$  km).

<sup>c</sup> Excludes event 7/16/0456UT ( $erz > 2$  km).

<sup>d</sup> Excludes event 6/26/0846UT ( $erh > 2$  km).

TABLE 5. Focal Mechanism Events and Nodal Plane Orientations

Focal Mechanism	Events Used Month, day, origin time (UT)	Nodal Plane Orientation
H1	6/28 0251, 7/02 0102, 7/02 1819, 7/04 1917, 7/07 0843	N12°E 0°E
H2	6/26 0752, 6/26 1048, 6/28 0148, 6/28 0251, 6/28 1156, 7/01 1125, 7/02 0102, 7/02 1819, 7/03 1342, 7/04 0120, 7/04 1917, 7/07 0843, 7/12 0959	N17°E 80°SE, N26°E 10°NW N12°E 0°E
H3	6/27 1855, 6/27 1925, 6/27 1950	N35°E 10°NW, N35°E 80°SE
V1	7/10 0212, 7/10 0223, 7/10 0229, 7/10 0252	N28°E 24°NW, N28°E 66°SE
V2	7/05 0617, 7/10 0233, 7/10 0240, 7/12 1956	N28°E 24°NW, N28°E 66°SE
D1	7/02 0145, 7/03 2251, 7/11 1542	N42°E 28°SE, N62°E 65°NW N02°E 20°W, N50°E 75°SE
D2	7/02 0145, 7/08 0929, 7/11 1542	N46°E 70°NW, N46°E 20°SE N40°E 60°SE, N52°E 32°NW
W1	6/26 2215, 6/26 2302, 6/27 1600, 6/28 1449, 7/03 0721, 7/04 0140, 7/05 1604, 7/08 0035, 7/08 0714, 7/10 1816, 7/11 1503	N02°E 65°SE, N12°E 25°W
W2	7/02 1536, 7/09 0051, 7/11 1037, 7/13 1405	N36°E 65°SE, N48°E 25°NW N75°W 40°SW, N05°W 70°NE
W3	6/26 1438, 6/26 1443, 6/26 1447, 6/26 1525	N05°W 64°E, N30°E 28°NW N48°W 30°SW, N32°W 60°NE
E1	6/28 1501, 7/05 1828, 7/08 1357	N42°E 60°NW, N48°E 30°SE N04°E 30°W, N35°E 62°SE
E2	6/27 0758, 6/27 1625, 7/10 1325	N53°E 50°NW, N79°E 42°S
WD	6/27 0930, 6/29 1849, 7/10 0705	N36°E 55°NW, N50°E 35°SE

TABLE 6. Seismic moments and Source Dimensions

Origin time Yr, mo, day, hr, min, s	Region	$M_0$ , dyn cm	$f_0$ , Hz	$r$ , km	$\Delta\sigma$ , bar	$u$ , mm	Instr
85 626 752 46.78	H	$3.0 \times 10^{-19}$	8	0.16	0.3	0.03	2
85 626 846 13.04	W	$2.0 \times 10^{-19}$					
85 626 1048 43.39	H	$9.1 \times 10^{-18}$	9	0.14	0.4	0.03	2
85 626 1230 40.57	W	$4.3 \times 10^{-18}$					
85 626 1249 27.81	W	$2.7 \times 10^{-19}$					
85 626 1438 34.69	W	$1.5 \times 10^{-18}$					
85 626 1443 19.76	W	$3.2 \times 10^{-19}$					
85 626 1447 26.88	W	$8.4 \times 10^{-18}$					
85 626 1525 24.66	W	$2.7 \times 10^{-19}$					
85 626 2215 1.07	W	$6.1 \times 10^{-18}$	5	0.26	0.1	0.02	1
85 626 2302 23.56	W	$2.0 \times 10^{-20}$					
85 626 2318 12.64	W	$1.1 \times 10^{-19}$					
85 627 758 45.21	E	$3.3 \times 10^{-19}$	10	0.13	5.0	0.4	2
85 627 820 21.76	W	$3.3 \times 10^{-19}$					
85 627 851 34.34	W	$9.8 \times 10^{-18}$					
85 627 930 39.20	W	$5.0 \times 10^{-18}$					
85 627 1409 58.04	D	$8.3 \times 10^{-18}$					
85 627 1600 6.48	W	$2.2 \times 10^{-19}$	10	0.13	2.0	0.1	1
85 627 1625 26.23	E	$2.1 \times 10^{-19}$	10	0.13	2.0	0.2	2
85 627 1829 41.16	E	$3.0 \times 10^{-19}$					
85 627 1855 57.43	H	$2.1 \times 10^{-20}$	9	0.14	4.0	0.3	1
85 627 1913 4.11	W	$1.8 \times 10^{-19}$					
85 627 1925 27.68	H	$4.5 \times 10^{-19}$	10	0.13	3.0	0.2	1
85 627 1945 54.88	E	$1.5 \times 10^{-19}$					
85 627 1950 11.56	H	$7.8 \times 10^{-19}$	10	0.13	4.0	0.3	1
85 627 1959 46.45	E	$3.0 \times 10^{-19}$					
85 627 2008 25.90	W	$1.4 \times 10^{-19}$					
85 627 2258 58.54	W	$2.8 \times 10^{-18}$					
85 628 148 50.78	H	$3.5 \times 10^{-18}$	10	0.13	0.5	0.04	2
85 628 251 47.71	H	$2.1 \times 10^{-19}$					
85 628 1156 41.58	H	$3.5 \times 10^{-18}$	8	0.16	0.4	0.04	2
85 628 1449 4.13	W	$8.1 \times 10^{-18}$	10	0.13	1.0	0.1	1
85 628 1501 18.87	E	$9.4 \times 10^{-18}$	10	0.13	2.0	0.1	2
85 628 1820 27.36	N	$8.9 \times 10^{-18}$					
85 628 1942 58.10	N	$1.4 \times 10^{-19}$					
85 628 2358 0.06	E	$2.7 \times 10^{-18}$					
85 629 13 25.70	N	$2.1 \times 10^{-18}$					
85 629 1849 48.04	D	$8.7 \times 10^{-19}$	11	0.12	4.0	0.3	6
85 629 2228 22.24	N	$2.0 \times 10^{-18}$					
85 630 143 11.79	W	$2.4 \times 10^{-18}$					
85 630 407 8.13	W	$4.8 \times 10^{-19}$					
85 630 621 35.16	W	$8.5 \times 10^{-18}$					
85 630 643 15.64	H	$4.3 \times 10^{-18}$					
85 630 1048 19.10	E	$8.7 \times 10^{-18}$					
85 630 1052 27.39	N	$2.2 \times 10^{-19}$					

85 630 1133 4.10	N	$1.6 \times 10^{-18}$					
85 630 1142 42.13	N	$7.2 \times 10^{-18}$					
85 630 1523 16.76	W	$6.5 \times 10^{-19}$					
85 630 1656 35.84	H	$1.7 \times 10^{-18}$					
85 630 1837 0.81	N	$3.6 \times 10^{-18}$					
85 630 2144 4.15	D	$7.0 \times 10^{-18}$					
85 630 2318 22.85	E	$2.6 \times 10^{-18}$					
85 701 9 10.69	E	$3.1 \times 10^{-19}$					
85 701 229 16.10	W	$5.4 \times 10^{-19}$					
85 701 628 54.88	N	$1.1 \times 10^{-19}$					
85 701 1125 15.25	H	$1.6 \times 10^{-19}$	8	0.16	2.0	0.2	2
85 701 2341 13.44	H	$2.8 \times 10^{-18}$					
85 702 102 11.93	H	$9.1 \times 10^{-18}$					
85 702 145 38.33	D	$2.7 \times 10^{-19}$					
85 702 333 9.24	D	$5.5 \times 10^{-19}$					
85 702 513 5.16	W	$1.4 \times 10^{-19}$					
85 702 1038 20.64	W	$4.3 \times 10^{-19}$					
85 702 1059 13.37	W	$4.3 \times 10^{-18}$					
85 702 1536 49.91	W	$3.3 \times 10^{-19}$					
85 702 1759 7.08	D	$8.8 \times 10^{-18}$					
85 702 1819 15.78	H	$9.7 \times 10^{-18}$	8	0.16	1.0	0.1	2
85 703 440 30.72	W	$6.5 \times 10^{-18}$					
85 703 721 5.53	W	$6.2 \times 10^{-18}$					
85 703 1342 11.02	H	$2.5 \times 10^{-18}$					
85 703 1637 5.25	W	$4.5 \times 10^{-18}$					
85 703 1825 59.85	W	$2.7 \times 10^{-18}$					
85 703 2143 54.08	S	$1.7 \times 10^{-20}$					
85 703 2251 42.01	D	$7.7 \times 10^{-18}$					
85 703 2337 37.20	N	$1.7 \times 10^{-18}$					
85 703 2341 48.73	E	$1.0 \times 10^{-18}$					
85 704 120 48.19	H	$6.2 \times 10^{-18}$	7	0.19	0.3	0.03	2
85 704 140 48.79	W	$1.1 \times 10^{-19}$	10	0.13	1.0	0.1	1
85 704 904 37.97	W	$1.3 \times 10^{-19}$					
85 704 1041 0.17	E	$1.1 \times 10^{-19}$					
85 704 1322 19.92	W	$1.4 \times 10^{-19}$					
85 704 1526 59.64	W	$9.2 \times 10^{-18}$					
85 704 1555 24.25	E	$1.5 \times 10^{-19}$					
85 704 1917 40.96	H	$1.3 \times 10^{-19}$					
85 704 1928 27.36	W	$5.6 \times 10^{-19}$					
85 704 1934 18.16	W	$4.1 \times 10^{-19}$					
85 705 536 0.45	V	$1.9 \times 10^{-18}$					
85 705 617 5.72	V	$3.8 \times 10^{-20}$					
85 705 638 10.33	N	$2.6 \times 10^{-18}$					
85 705 1604 51.08	W	$5.6 \times 10^{-18}$					
85 705 1718 27.08	W	$3.5 \times 10^{-18}$					
85 705 1828 27.50	E	$9.0 \times 10^{-18}$	11	0.12	2.0	0.2	2
85 706 18 37.39	E	$1.8 \times 10^{-18}$					
85 706 131 40.23	N	$5.1 \times 10^{-18}$					
85 706 343 48.47	H	$3.9 \times 10^{-19}$					
85 706 542 10.51	S	$4.2 \times 10^{-20}$					
85 706 606 11.67	S	$1.2 \times 10^{-20}$					
85 706 615 54.38	S	$7.9 \times 10^{-20}$					
85 706 642 52.73	S	$1.8 \times 10^{-20}$					



85 706	756	57.62	E	$5.6 \times 10^{-17}$					
85 706	935	7.53	H	$2.3 \times 10^{-18}$					
85 706	1029	28.58	W	$4.9 \times 10^{-19}$					
85 706	1310	35.19	E	$5.0 \times 10^{-18}$					
85 706	2038	19.98	N	$2.2 \times 10^{-19}$					
85 706	2048	13.73	E	$9.9 \times 10^{-17}$					
85 707	53	16.88	S	$4.1 \times 10^{-20}$					
85 707	234	58.24	E	$1.1 \times 10^{-19}$					
85 707	432	23.01	N	$3.0 \times 10^{-18}$					
85 707	731	53.67	D	$2.7 \times 10^{-18}$					
85 707	843	57.97	H	$3.7 \times 10^{-19}$					
85 707	1114	28.79	D	$2.8 \times 10^{-19}$					
85 707	1723	59.14	W	$1.7 \times 10^{-20}$					
85 707	2102	57.65	H	$7.6 \times 10^{-18}$					
85 708	35	32.21	W	$1.8 \times 10^{-19}$					
85 708	249	39.87	D	$1.2 \times 10^{-20}$					
85 708	529	25.35	W	$3.6 \times 10^{-18}$					
85 708	714	51.07	W	$1.7 \times 10^{-18}$					
85 708	847	11.14	H	$4.0 \times 10^{-18}$					
85 708	929	4.79	D	$2.0 \times 10^{-20}$	9	0.14	3.0	0.3	6
85 708	957	14.32	D	$3.2 \times 10^{-19}$					
85 708	1357	5.19	E	$4.7 \times 10^{-18}$					
85 708	1503	11.53	W	$2.6 \times 10^{-19}$					
85 709	327	37.01	H	$1.6 \times 10^{-19}$					
85 709	524	59.75	H	$1.4 \times 10^{-18}$					
85 709	1023	40.38	W	$1.8 \times 10^{-18}$					
85 709	1044	4.58	S	$1.3 \times 10^{-20}$					
85 709	2203	28.75	E	$1.8 \times 10^{-19}$					
85 710	120	4.11	S	$1.7 \times 10^{-19}$					
85 710	212	10.44	V	$9.5 \times 10^{-19}$					
85 710	223	56.06	V	$1.4 \times 10^{-20}$	10	0.13	2.0	0.2	1
85 710	229	21.22	V	$7.0 \times 10^{-18}$					
85 710	233	45.67	V	$2.7 \times 10^{-20}$	10	0.13	3.0	0.2	1
85 710	240	18.25	V	$6.5 \times 10^{-19}$					
85 710	245	47.42	E	$4.2 \times 10^{-18}$					
85 710	252	51.29	V	$5.2 \times 10^{-18}$	10	0.13	0.4	0.03	1
85 710	333	8.20	V	$3.1 \times 10^{-18}$					
85 710	705	39.20	W	$4.9 \times 10^{-18}$	10	0.13	1.0	0.09	6
85 710	1150	22.70	H	$2.7 \times 10^{-18}$					
85 710	1325	49.66	E	$1.7 \times 10^{-19}$	10	0.13	3.0	0.2	2
85 710	1525	23.53	E	$1.0 \times 10^{-19}$					
85 710	1648	0.31	N	$2.3 \times 10^{-18}$					
85 710	1654	57.05	D	$8.6 \times 10^{-18}$					
85 710	1701	23.14	W	$9.3 \times 10^{-19}$					
85 710	1816	47.63	W	$2.5 \times 10^{-18}$	9	0.14	0.5	0.04	2
85 710	1904	11.55	E	$8.2 \times 10^{-18}$					
85 711	1037	9.10	W	$2.5 \times 10^{-19}$					
85 711	1503	0.75	W	$2.2 \times 10^{-18}$	7	0.19	0.2	0.02	1
85 711	1523	56.16	D	$2.2 \times 10^{-20}$					
85 711	1542	48.64	D	$6.6 \times 10^{-18}$					
85 711	1806	34.79	N	$5.8 \times 10^{-18}$					
85 712	334	33.77	S	$5.4 \times 10^{-20}$					
85 712	959	6.64	H	$2.0 \times 10^{-19}$					
85 712	1450	42.78	W	$3.3 \times 10^{-19}$					

85 712	1956	12.83	V	$2.5 \times 10^{-18}$
85 712	2051	43.55	V	$2.5 \times 10^{-18}$
85 713	732	18.89	E	$6.7 \times 10^{-20}$
85 713	813	29.09	W	$3.2 \times 10^{-18}$
85 713	1405	37.74	W	$2.7 \times 10^{-19}$
85 713	1520	13.90	E	$1.2 \times 10^{-19}$
85 713	1848	17.77	S	$2.6 \times 10^{-20}$
85 713	1854	14.89	S	$5.5 \times 10^{-22}$
85 713	1907	2.93	S	$5.4 \times 10^{-21}$
85 713	1939	12.88	S	$4.5 \times 10^{-21}$
85 713	2049	55.11	S	$4.2 \times 10^{-20}$
85 714	42	29.95	S	$1.9 \times 10^{-20}$
85 714	214	35.73	S	$3.1 \times 10^{-20}$
85 714	1327	15.64	H	$1.5 \times 10^{-19}$
85 714	1347	24.60	S	$2.8 \times 10^{-21}$
85 715	1120	6.28	N	$1.4 \times 10^{-19}$
85 715	1321	20.42	N	$1.3 \times 10^{-19}$
85 716	456	59.33	E	$6.6 \times 10^{-19}$

Region : See Table 2 for explanation  
 $M_0$  : Moment  
 $f_0$  : Corner frequency  
 $r$  : Fault radius  
 $\Delta\sigma$  : Stress drop  
 $u$  : Fault displacement  
 Instr : Instrument number on which corner frequency read

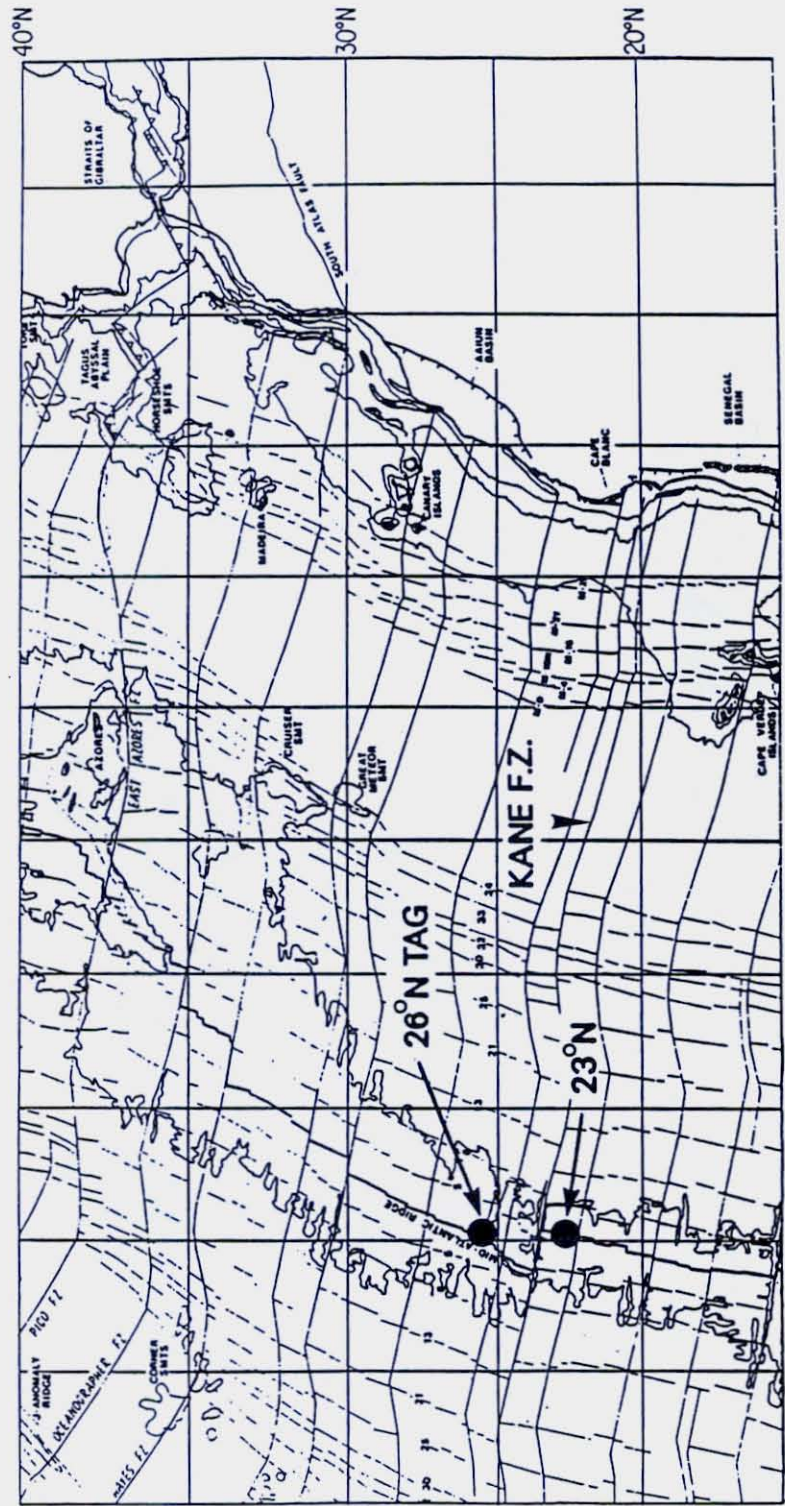


Figure 1

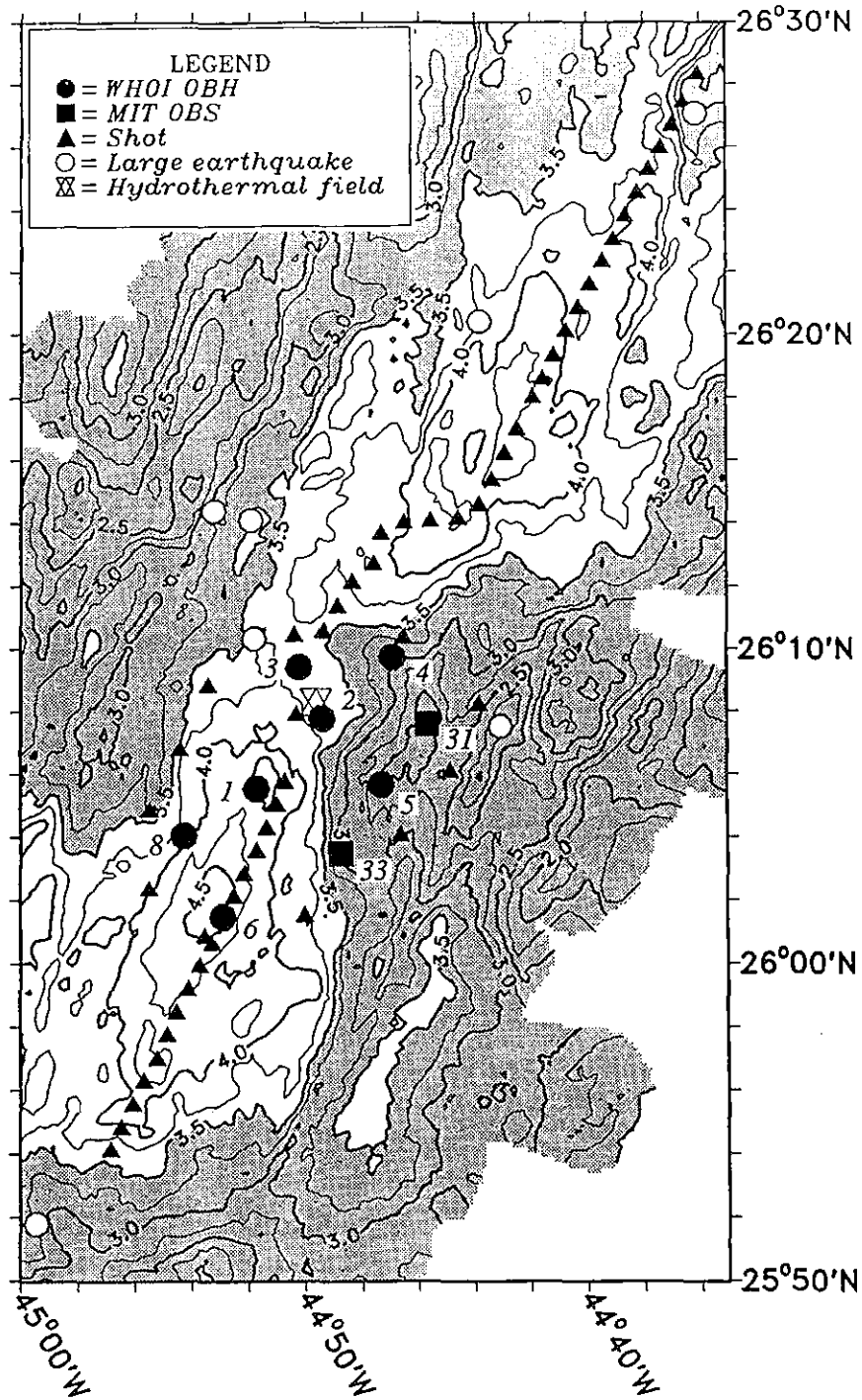


Figure 2

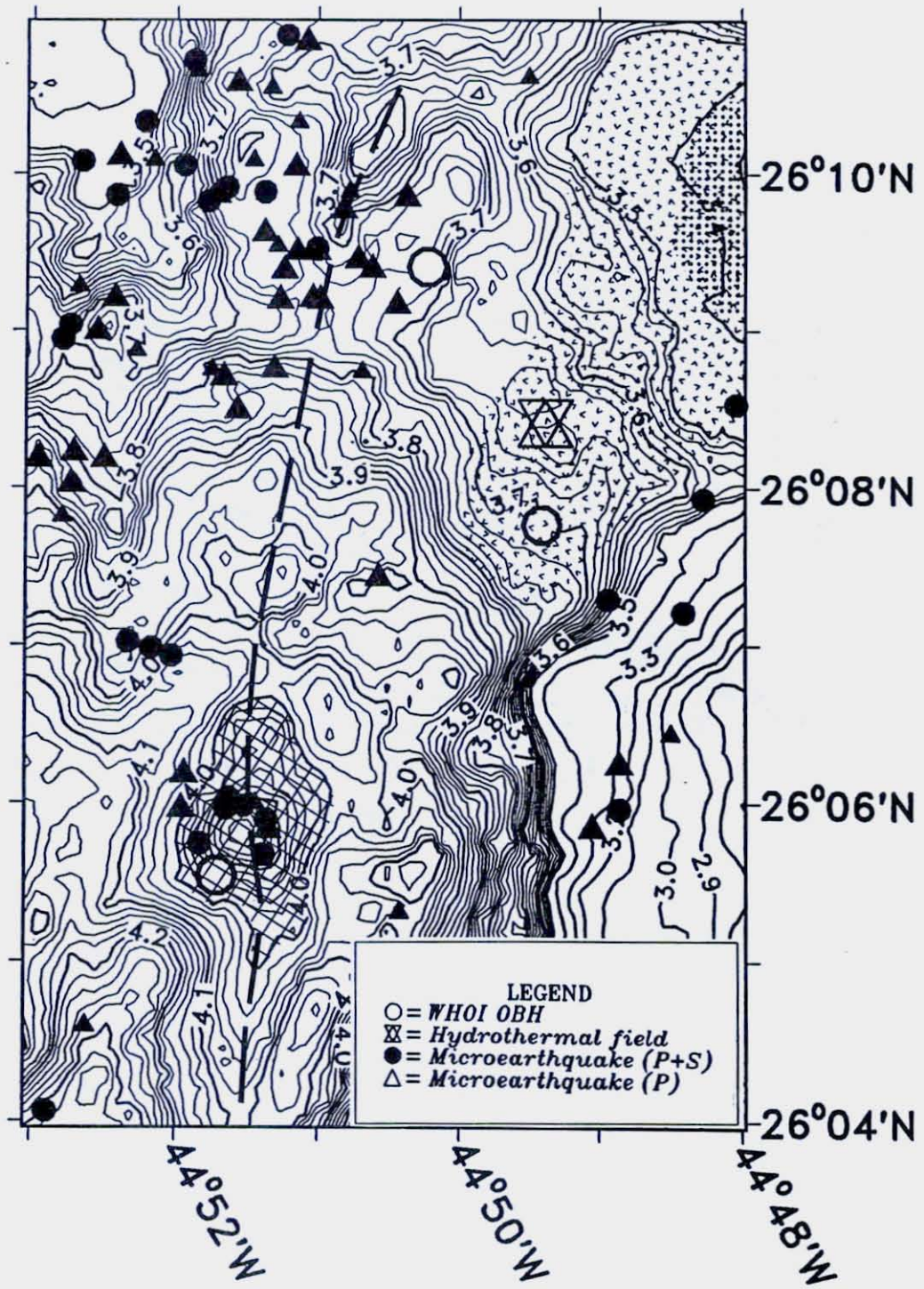


Figure 3

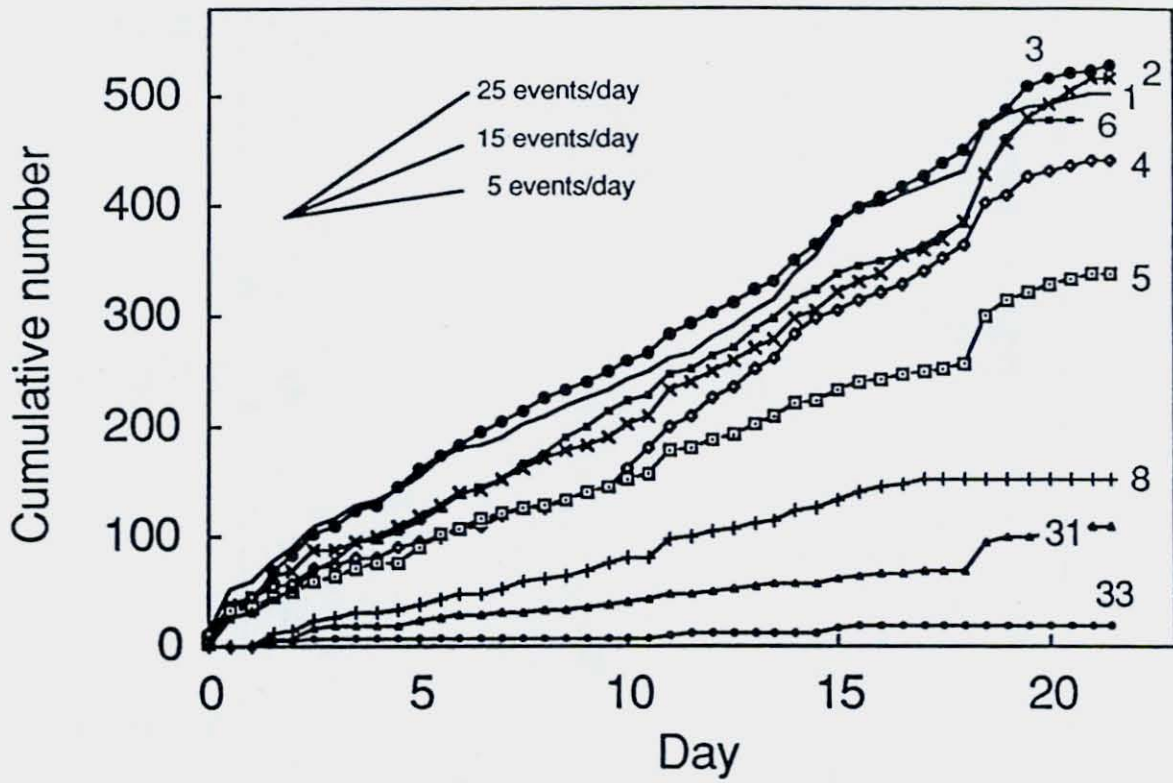
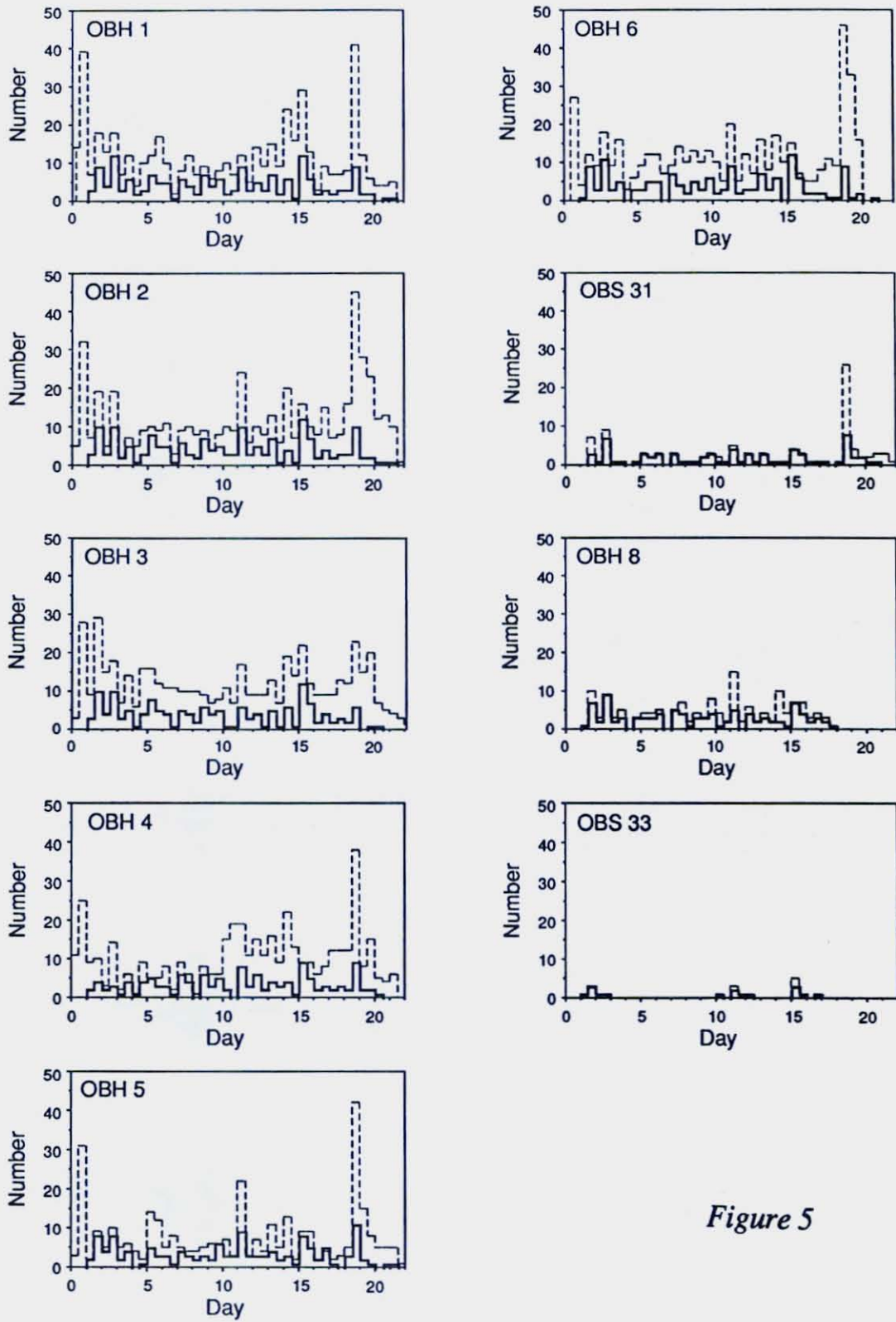


Figure 4

*Figure 5*

Event 1910240 - volcano

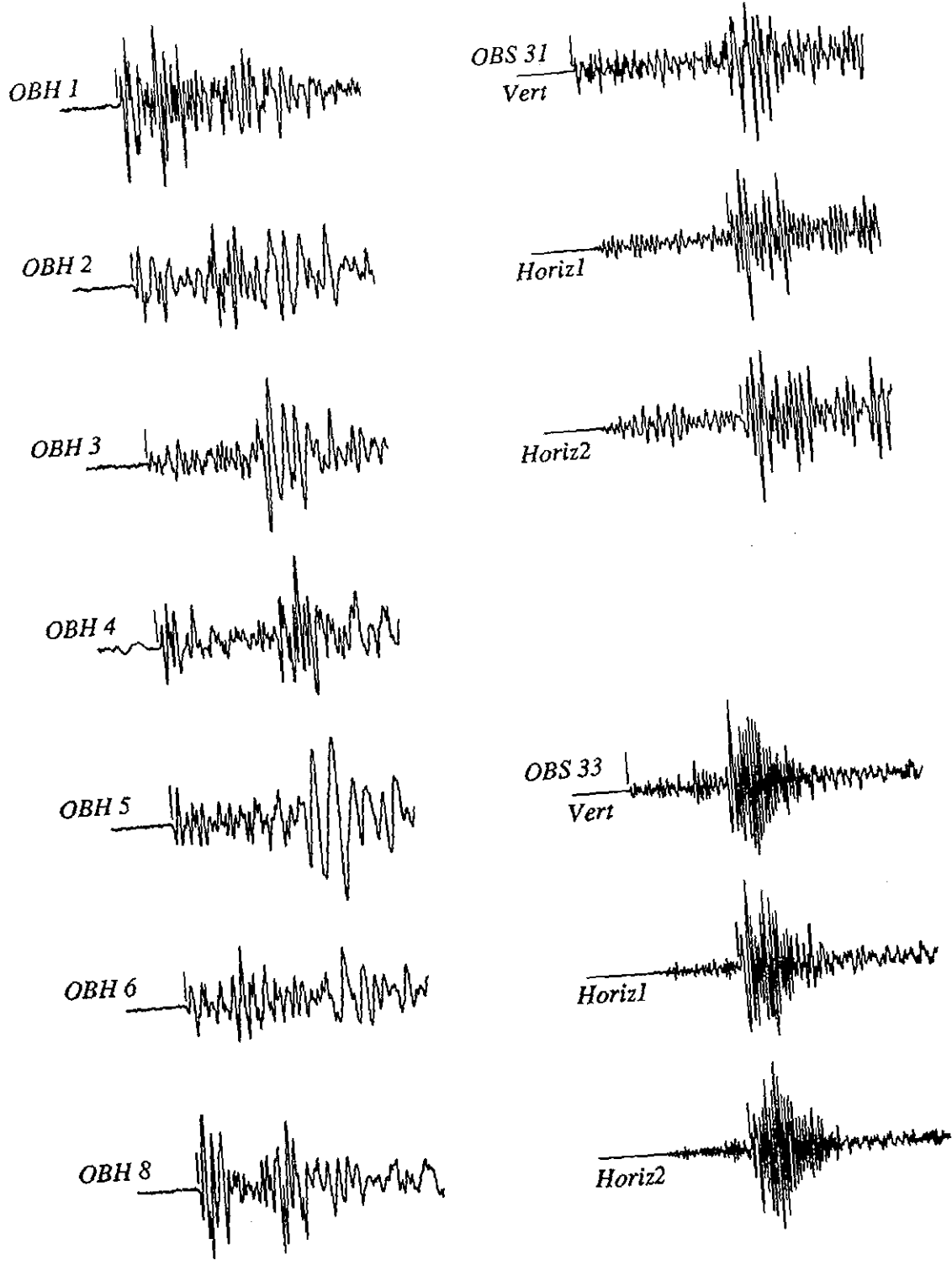


Figure 6 a

----- 2 s -----



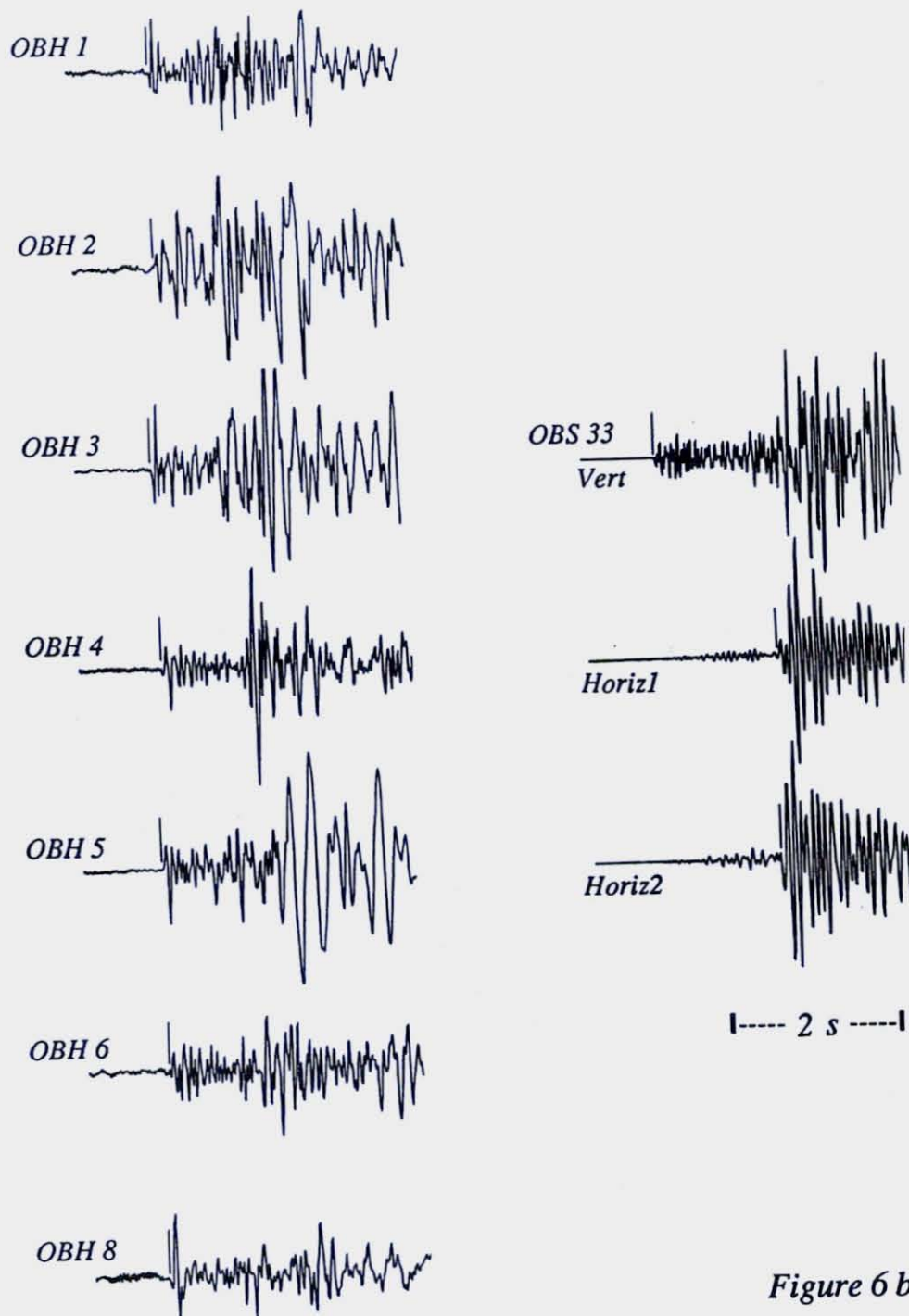
*Event 1911325 - eastern wall*

Figure 6 b

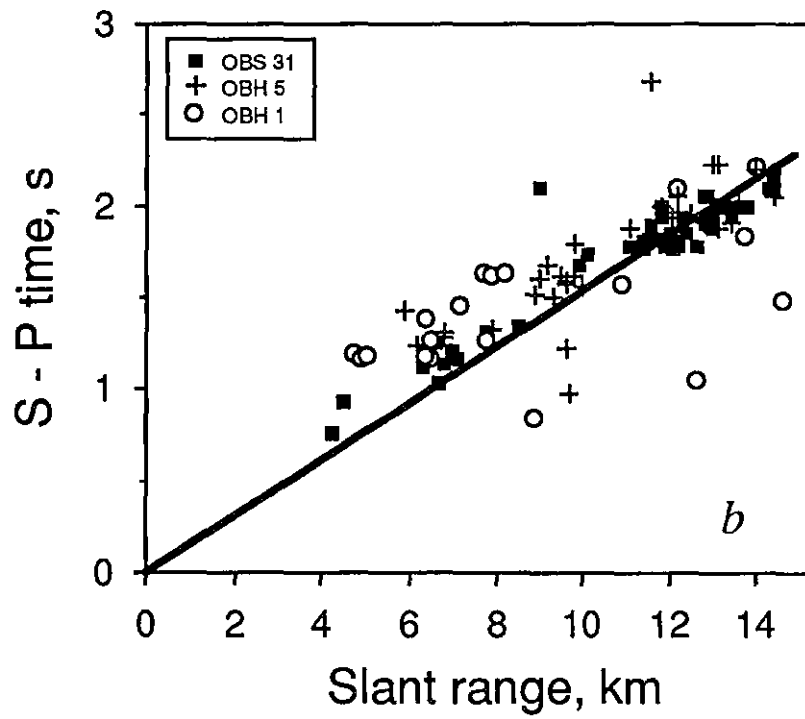
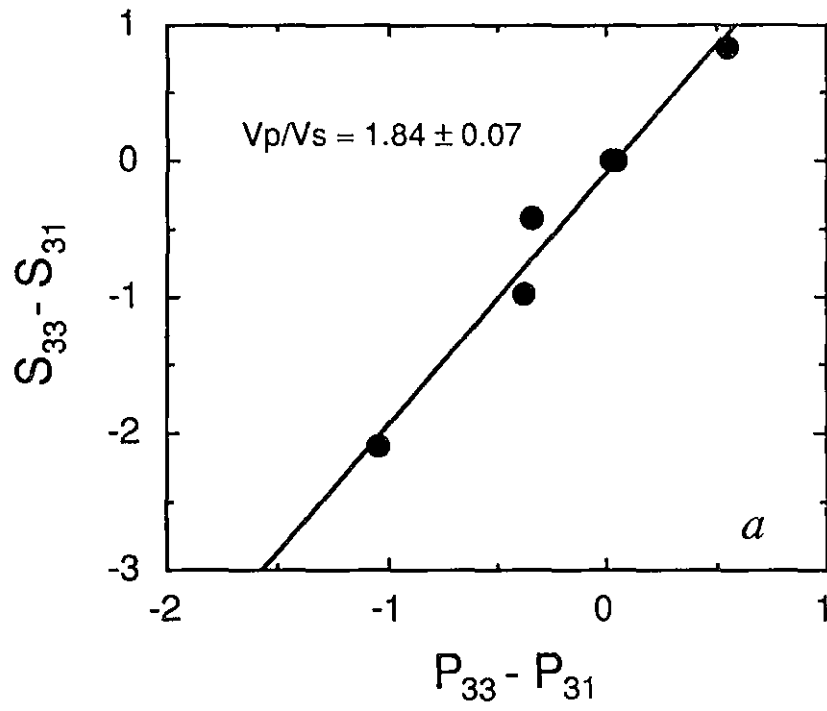
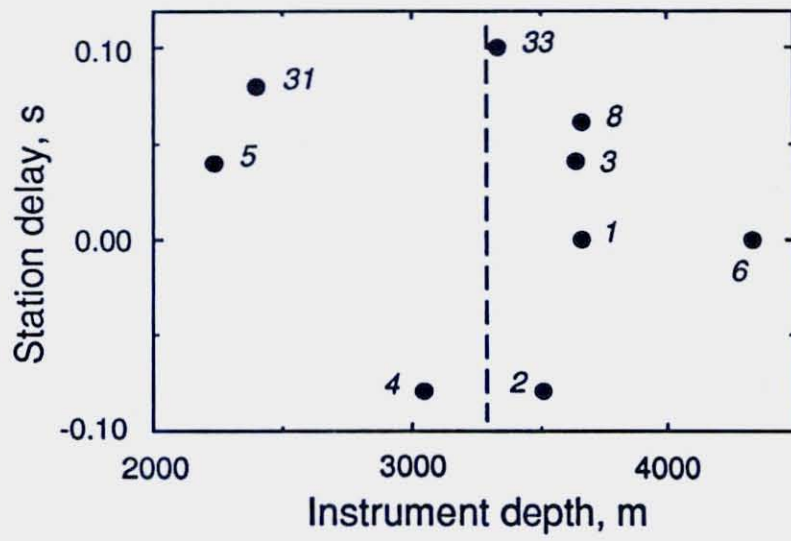
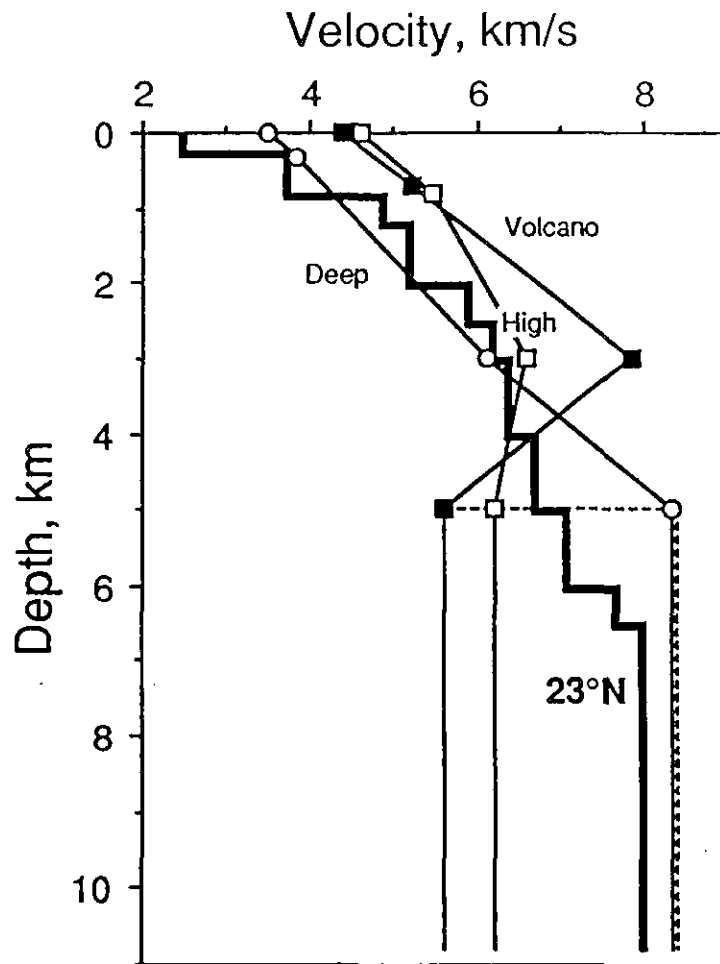


Figure 7

*Figure 8*

*Figure 9*

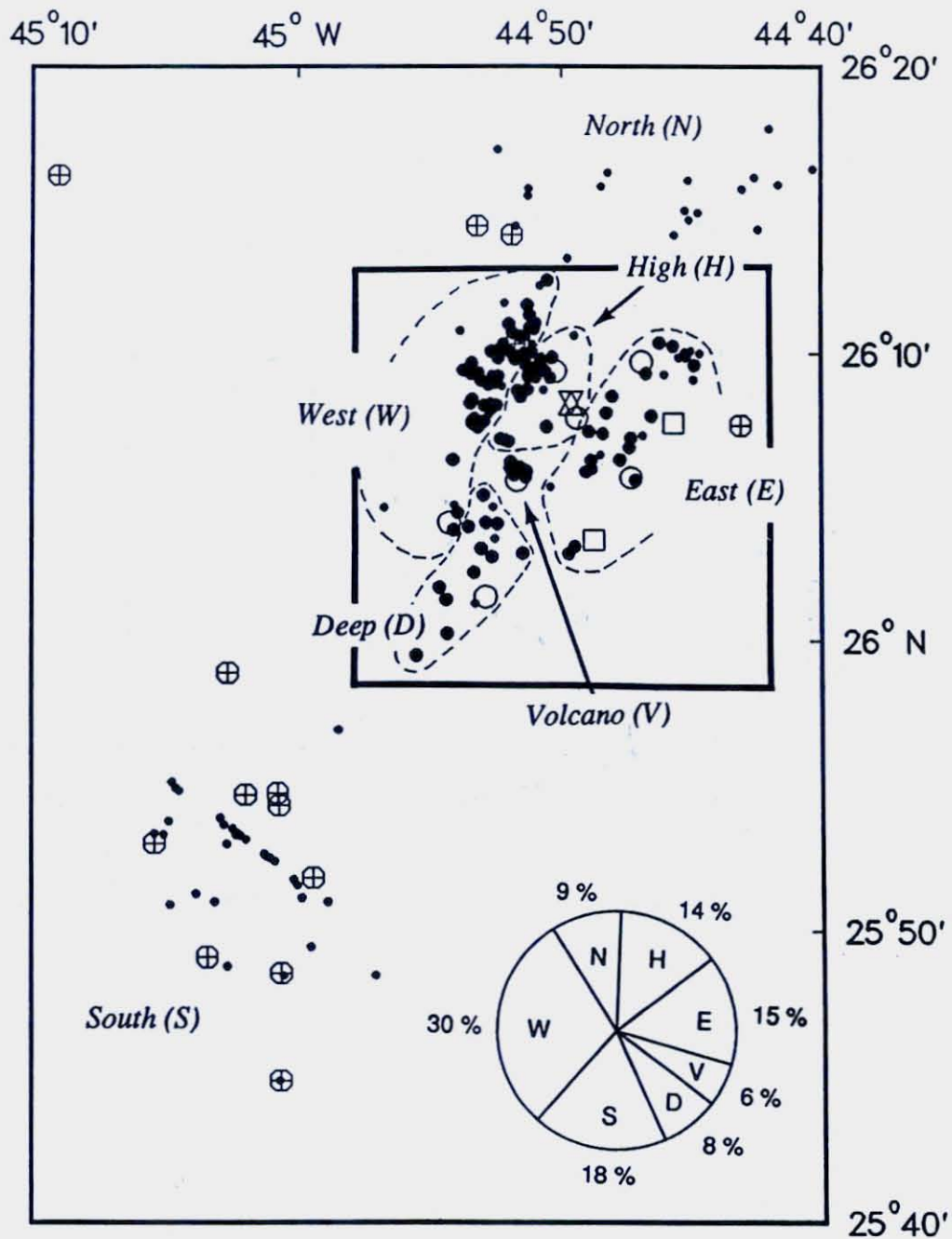
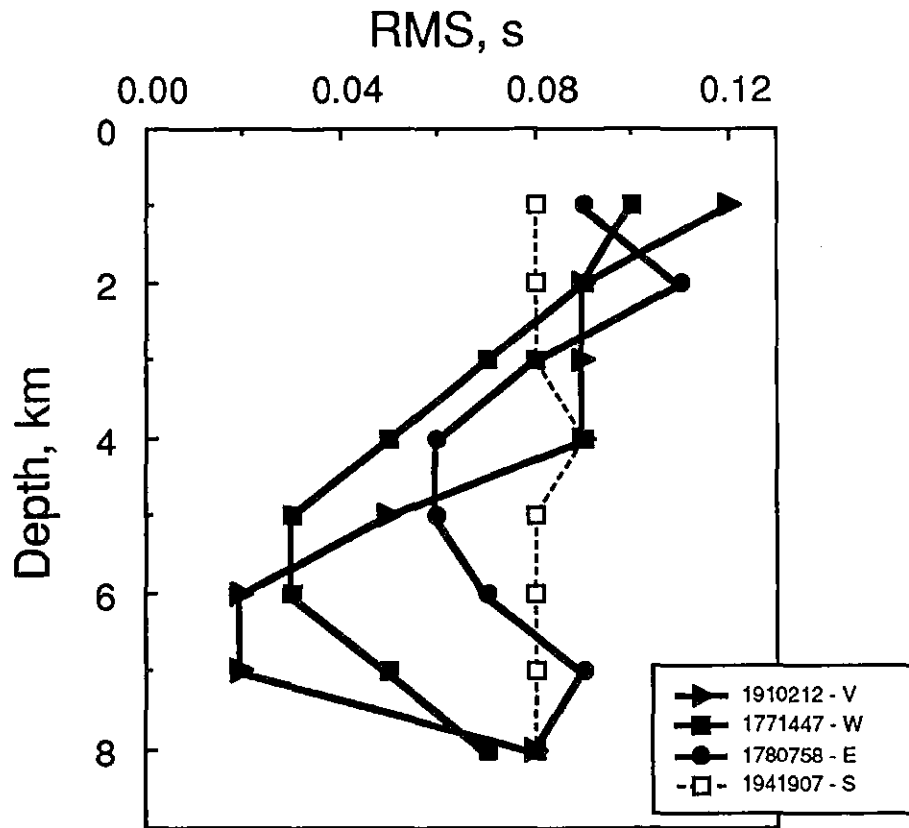


Figure 10

*Figure 11*

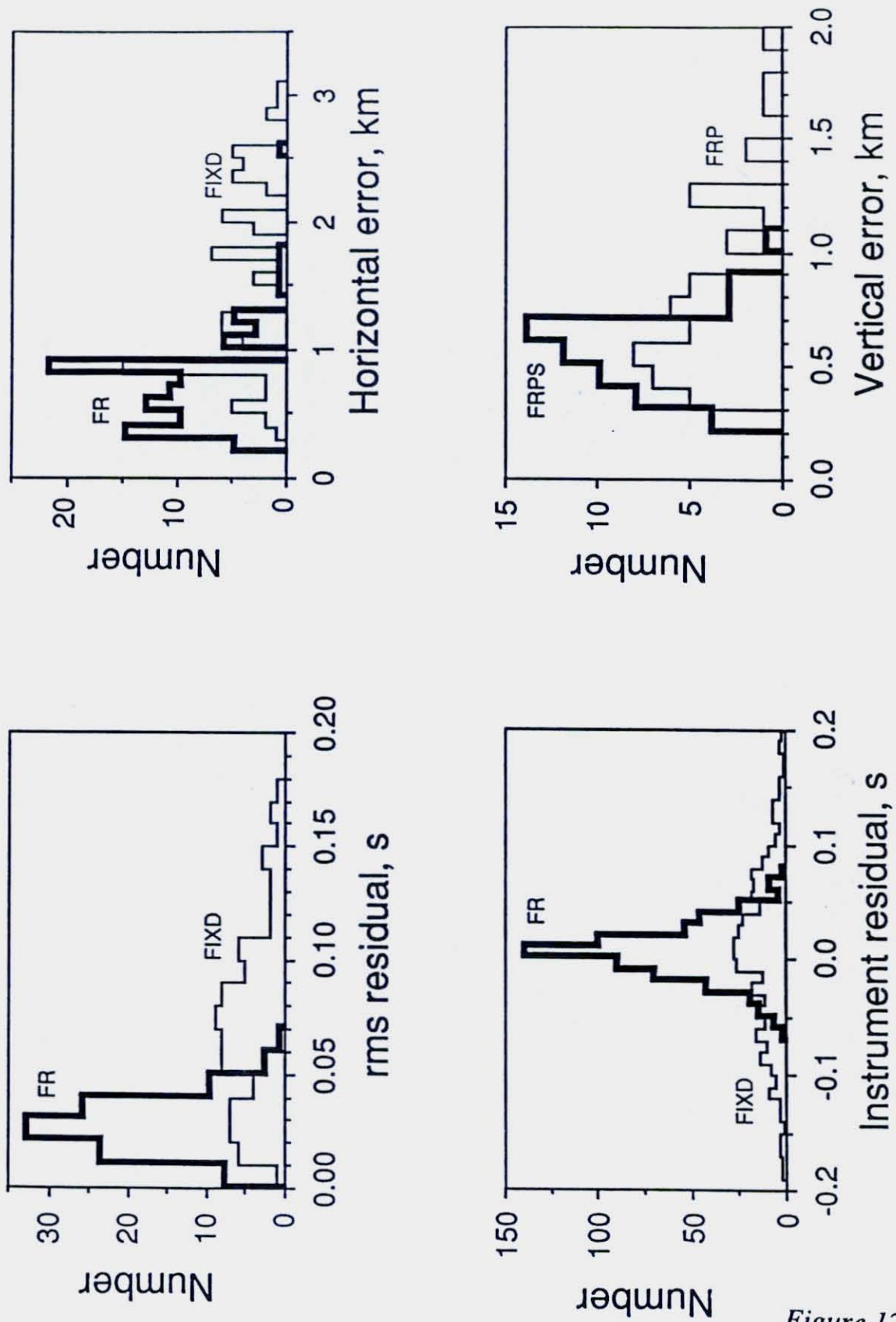


Figure 12

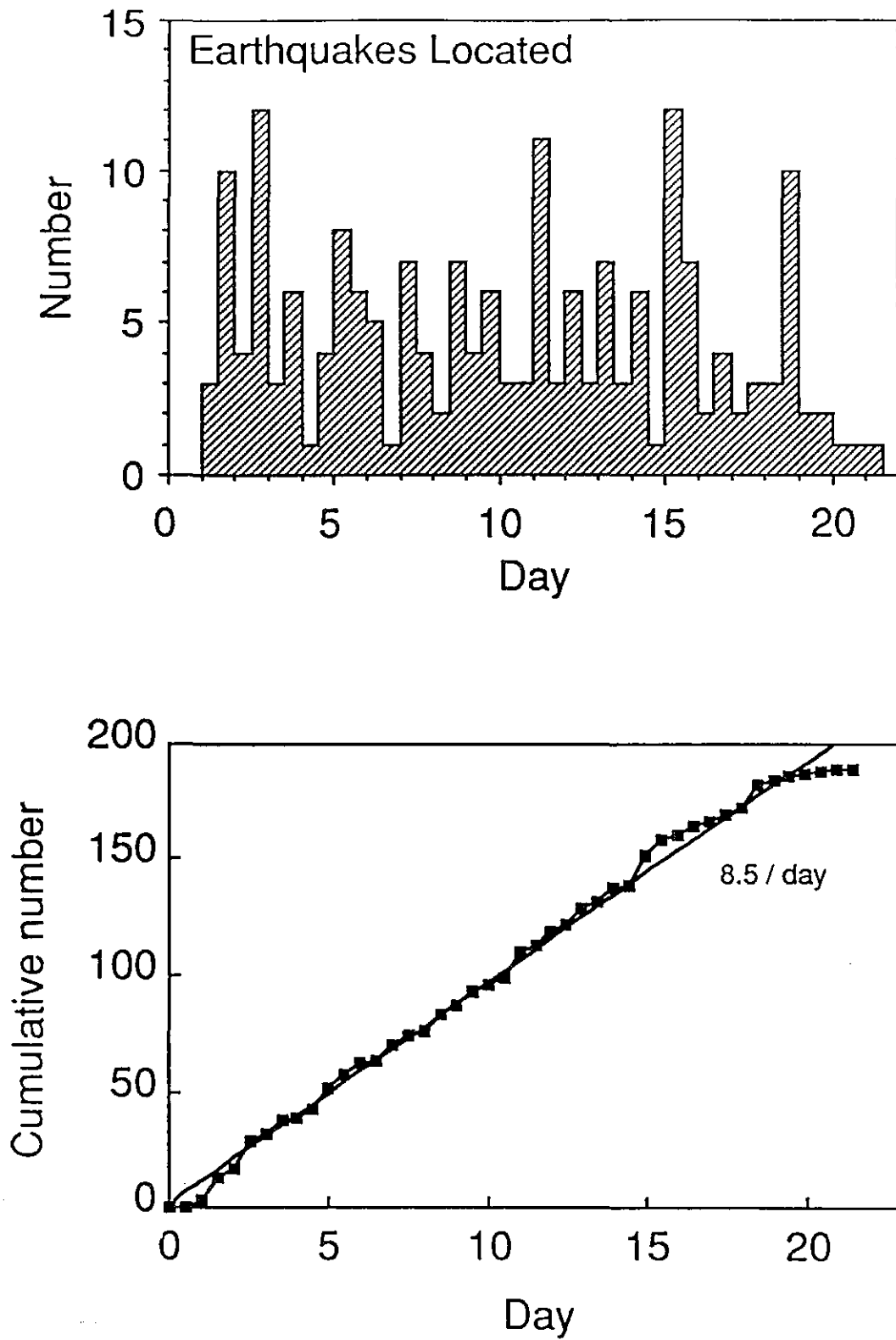


Figure 13



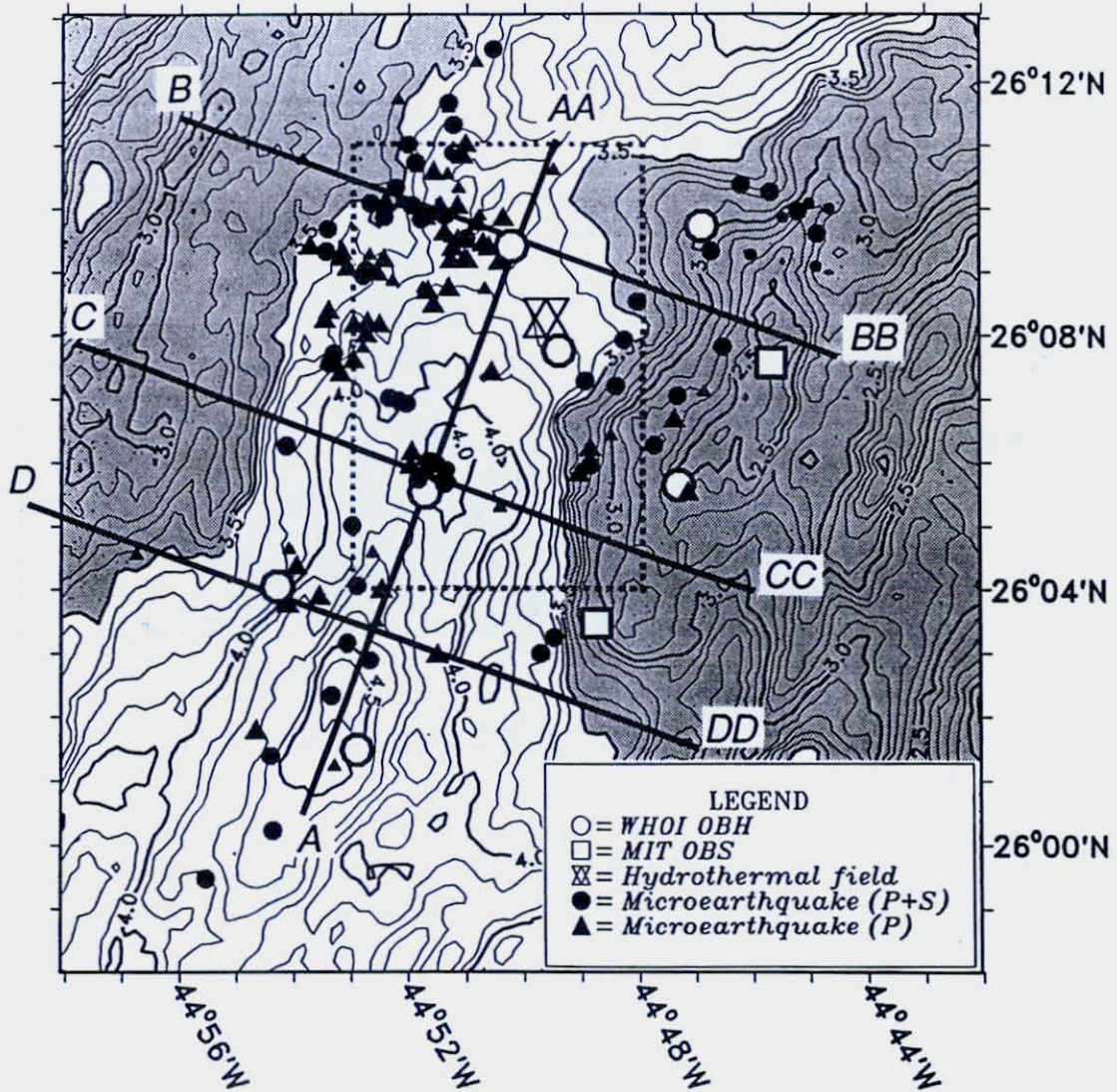
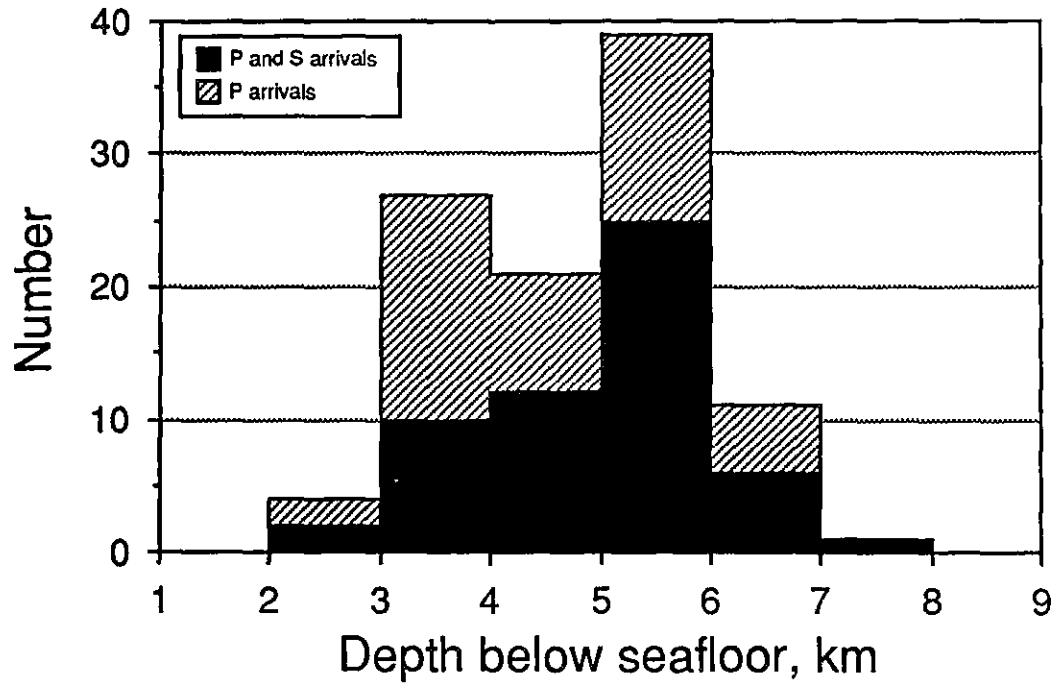
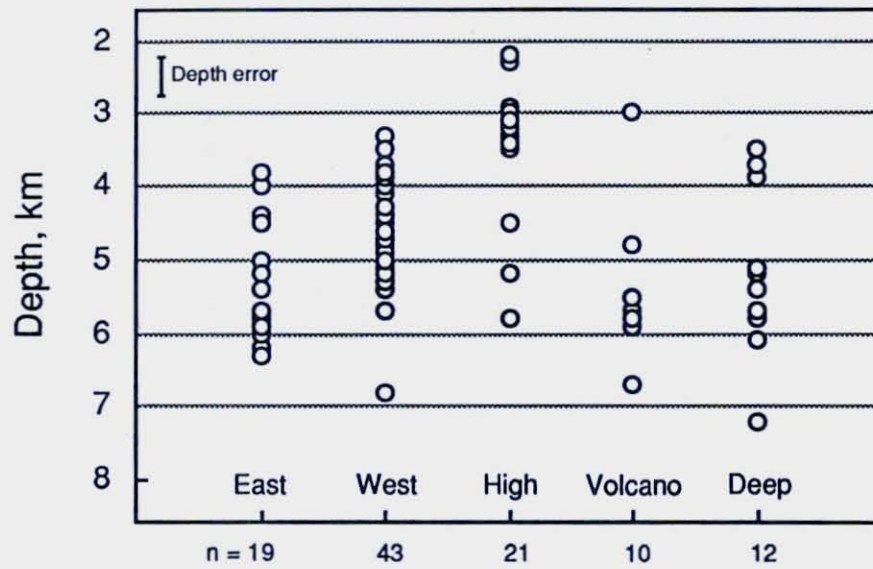


Figure 14



*Figure 15*



*Figure 16*

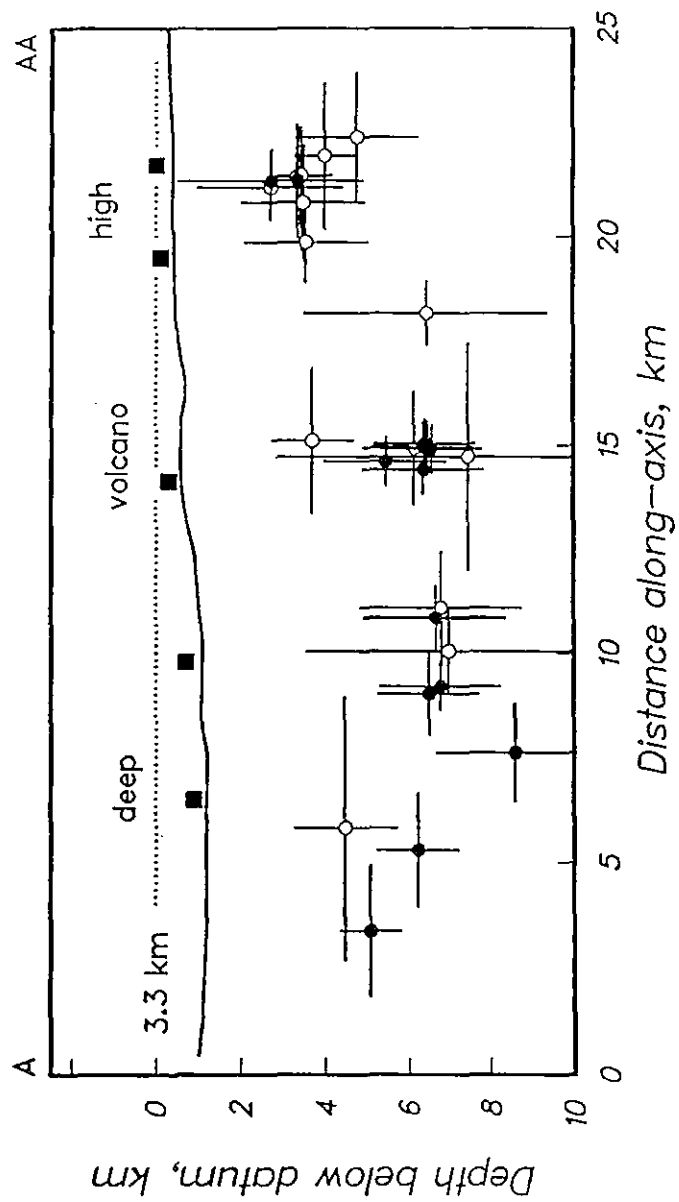


Figure 17

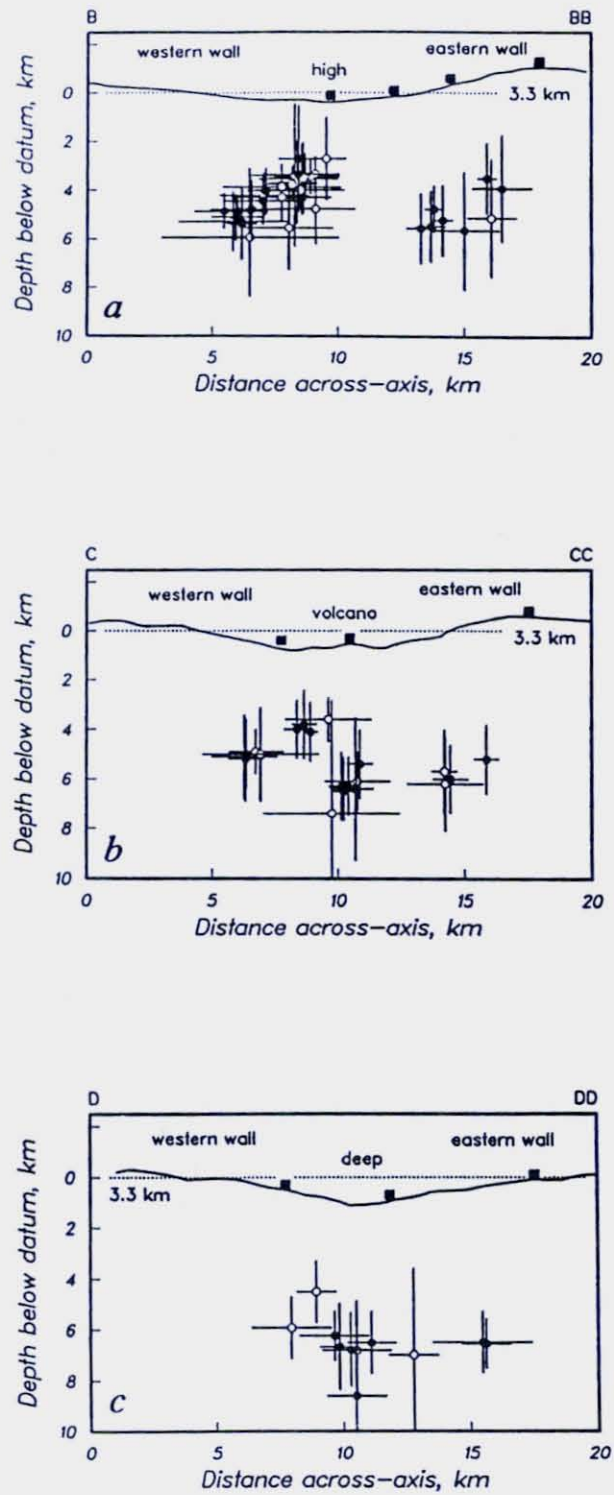


Figure 18

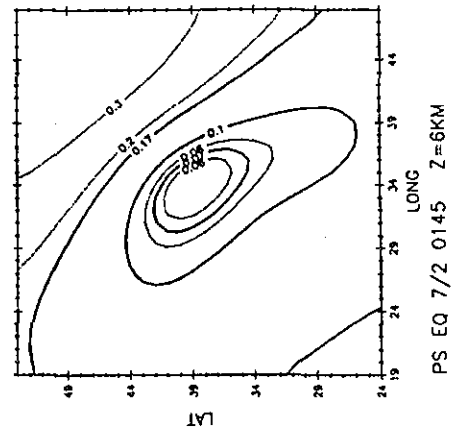
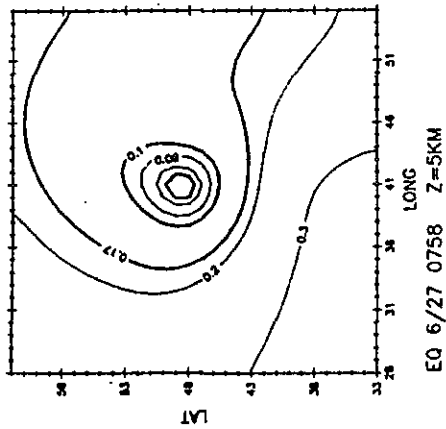
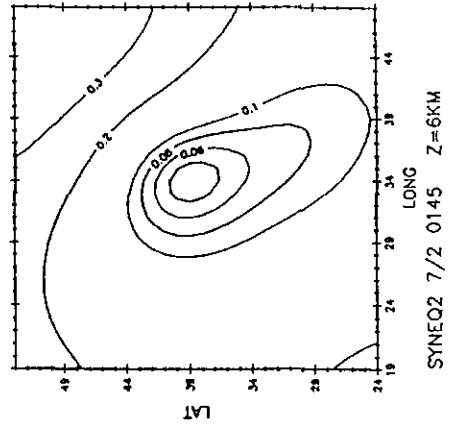
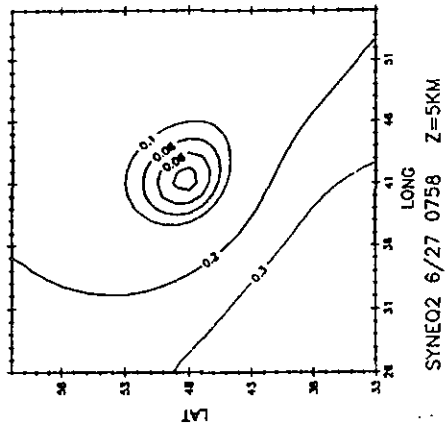
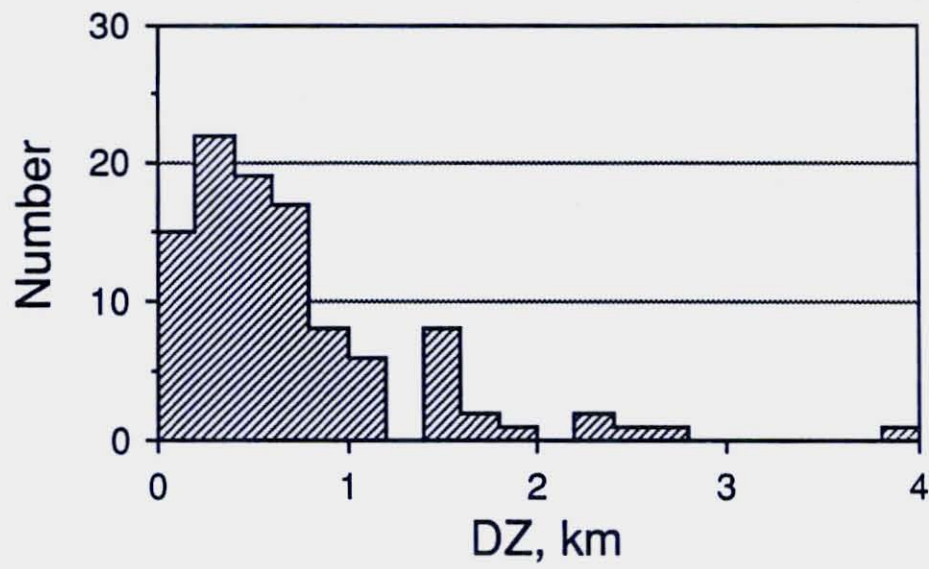
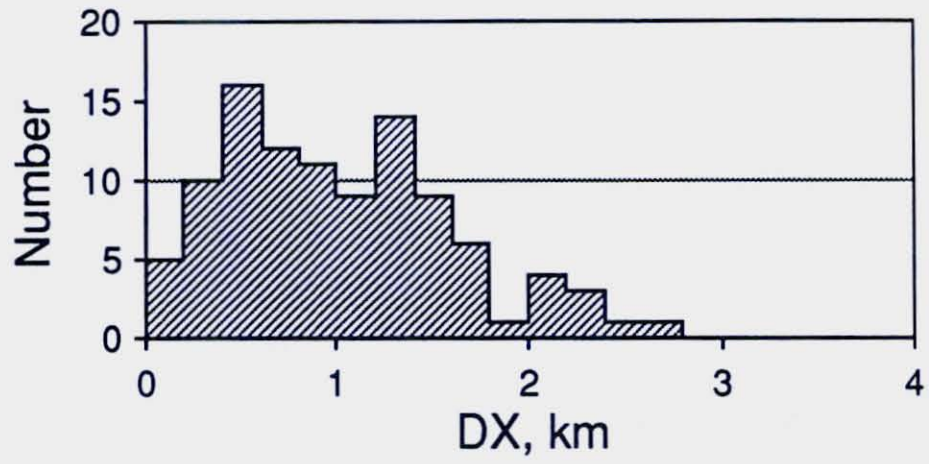
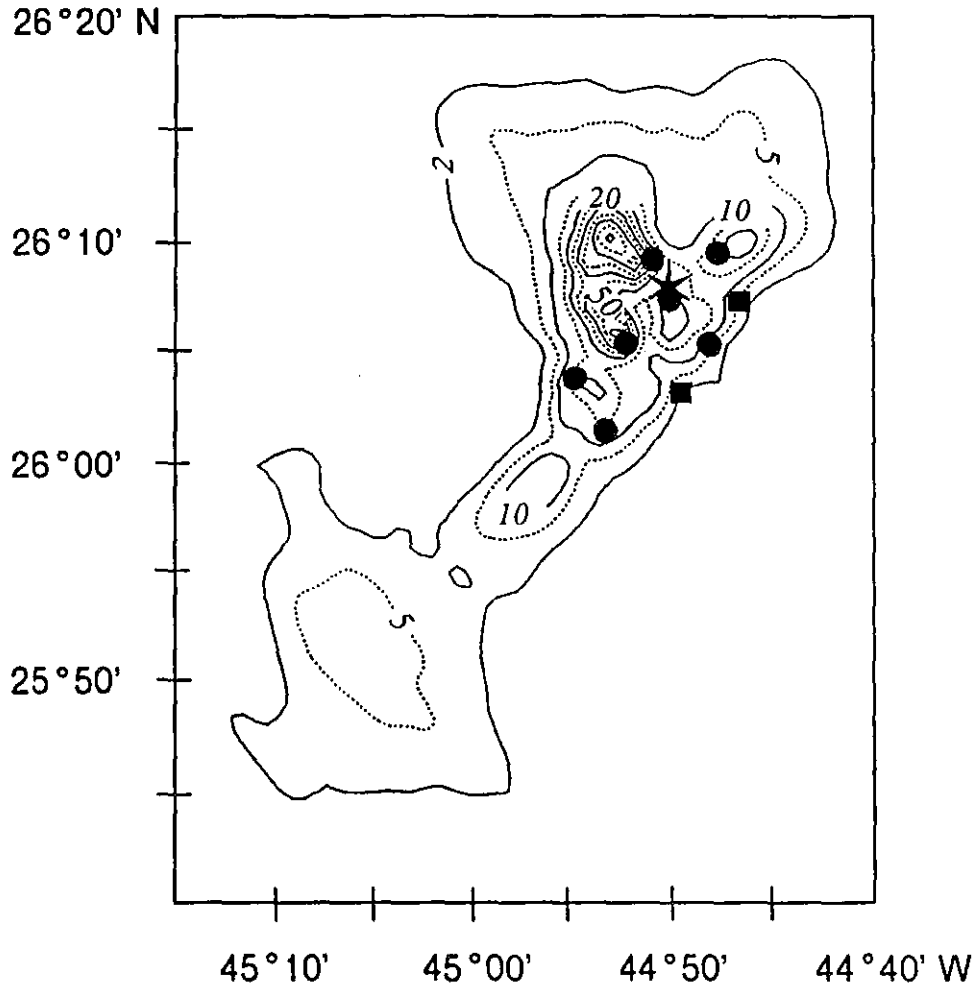


Figure 19

*Figure 20*



*Figure 21*



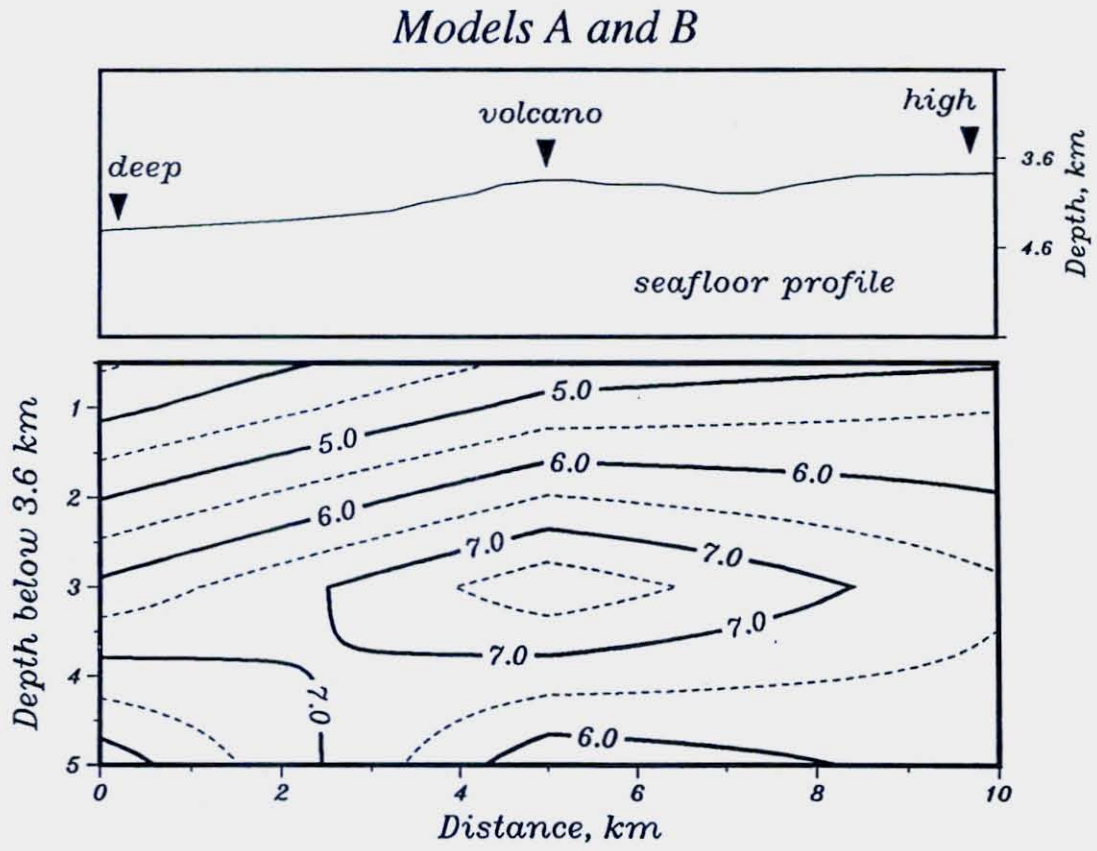


Figure 22

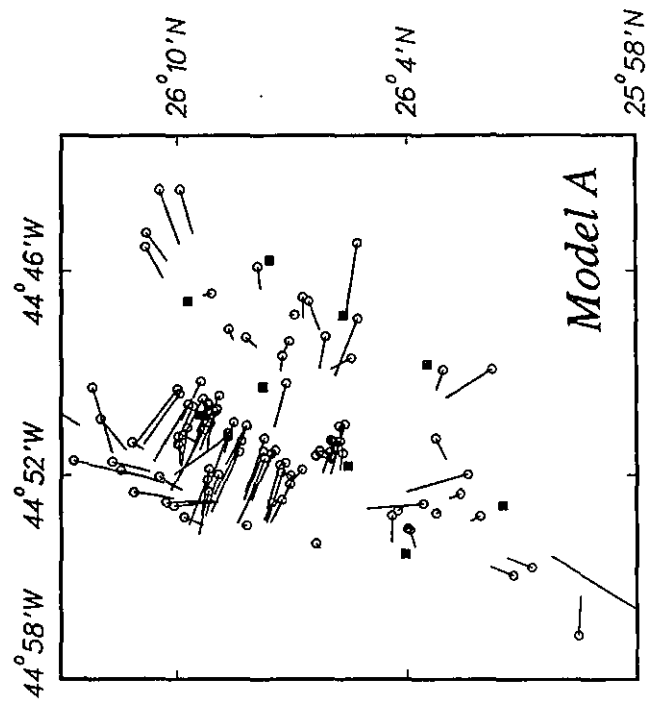
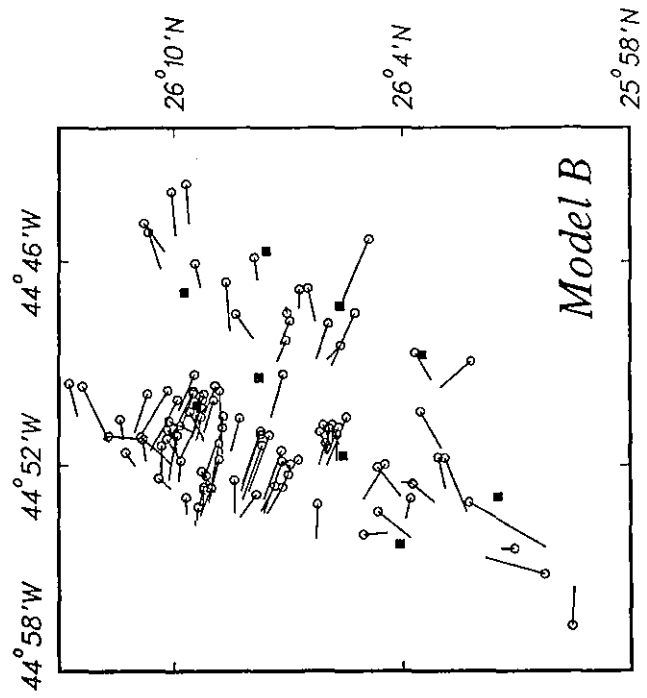
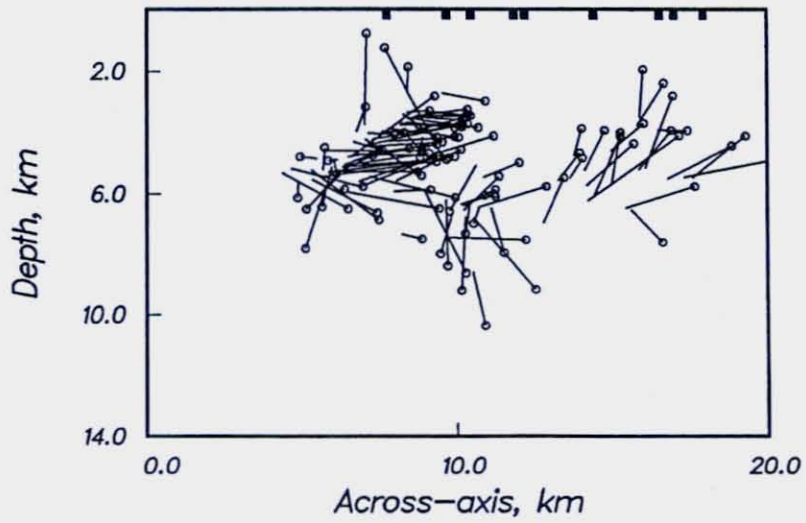
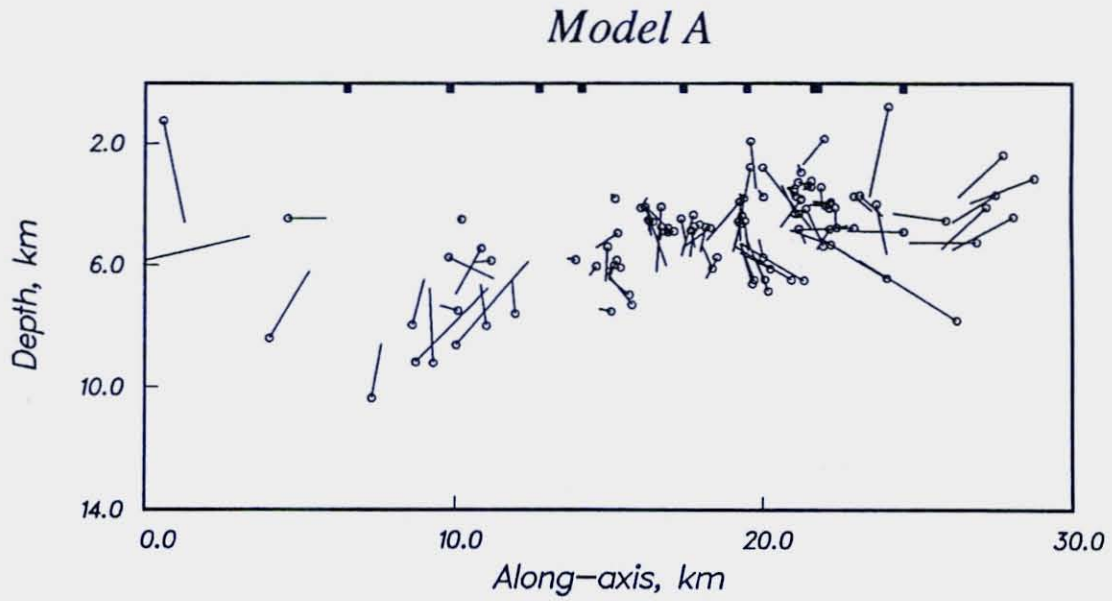
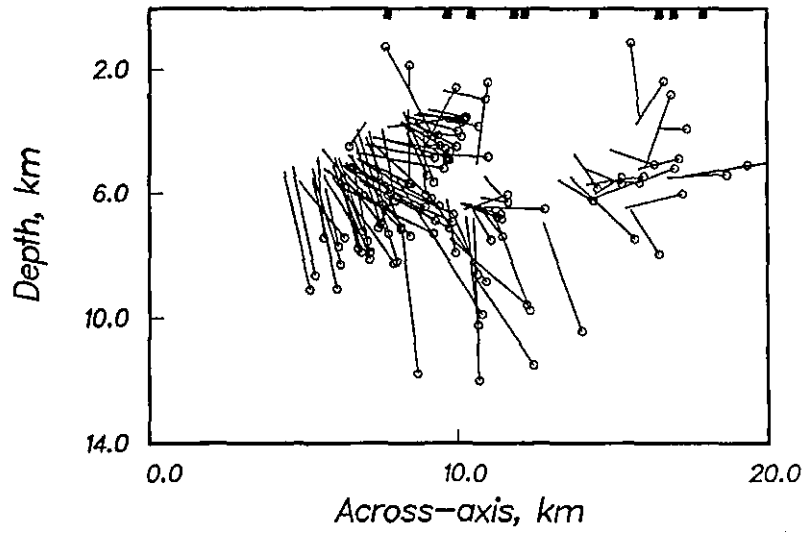
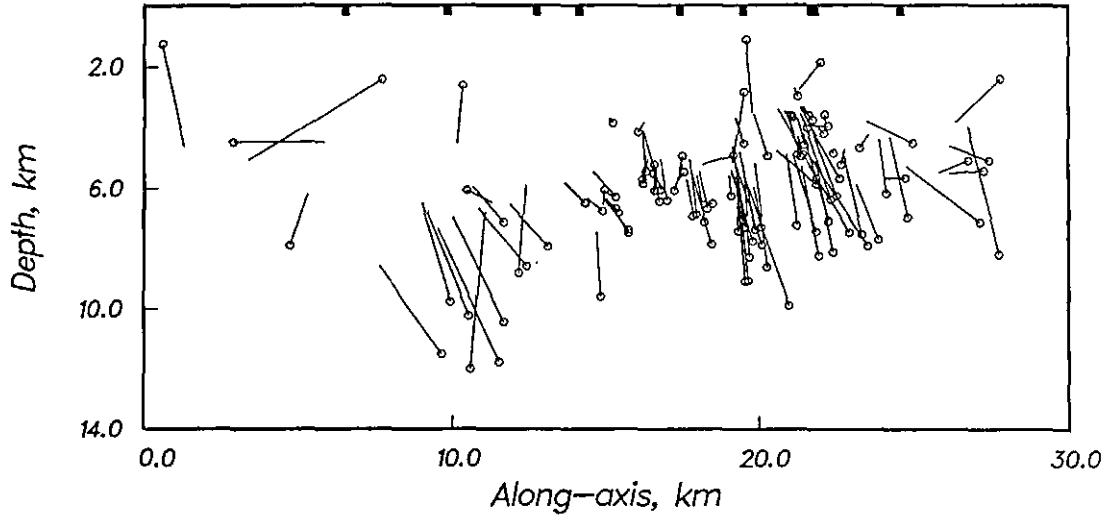


Figure 23

*Figure 24a*

*Model B*



*Figure 24 b*

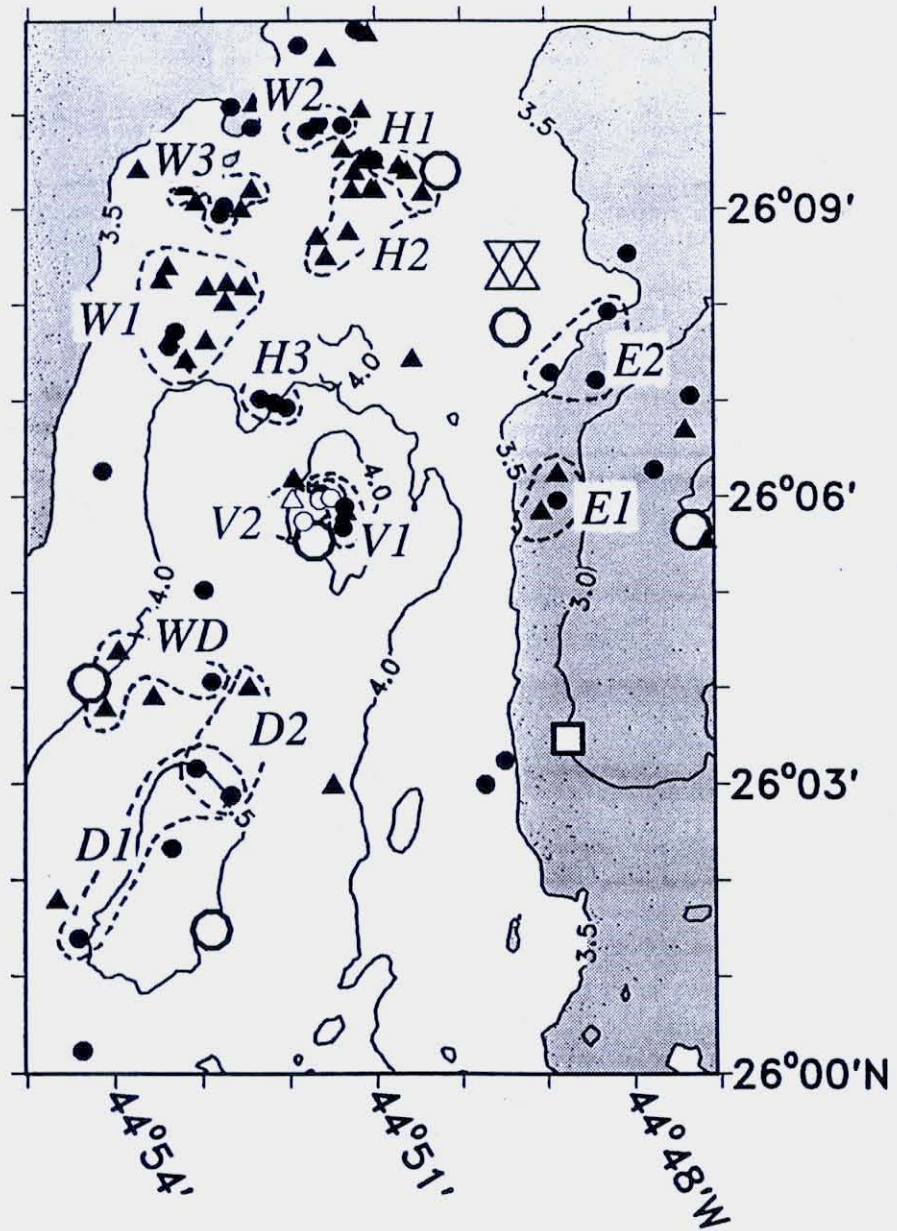


Figure 25

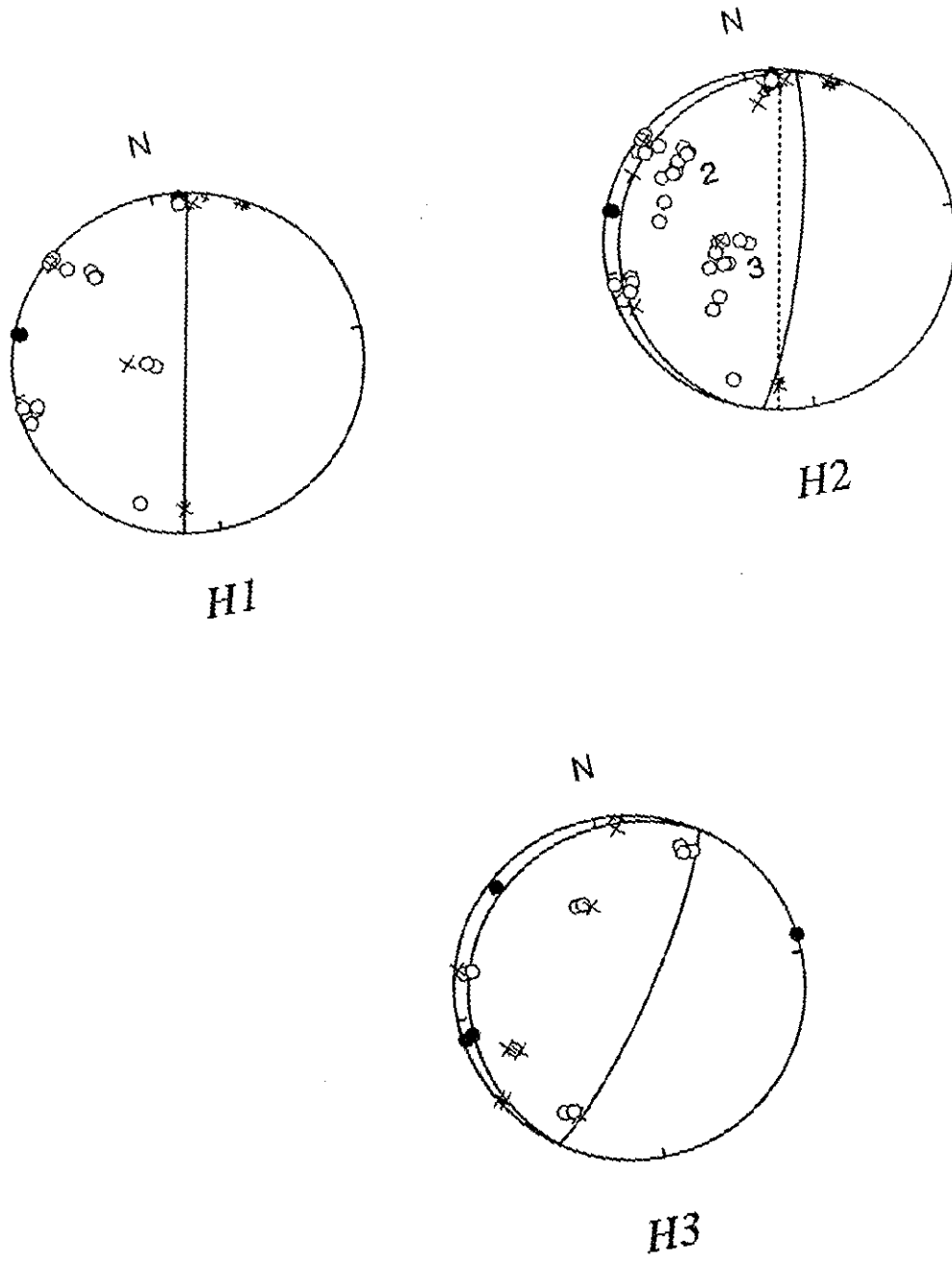


Figure 26

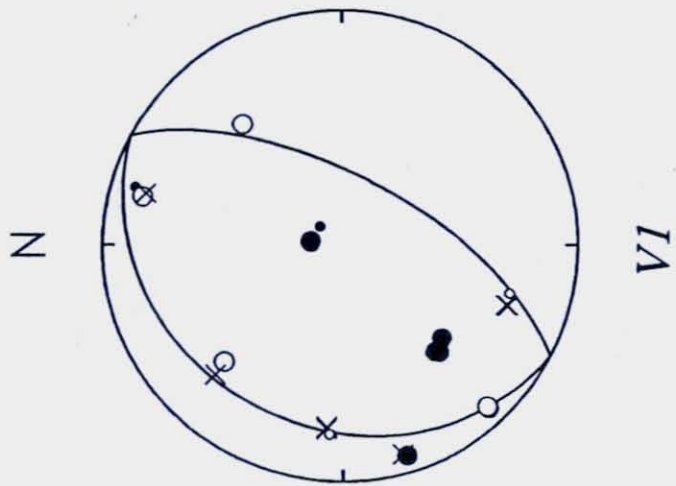
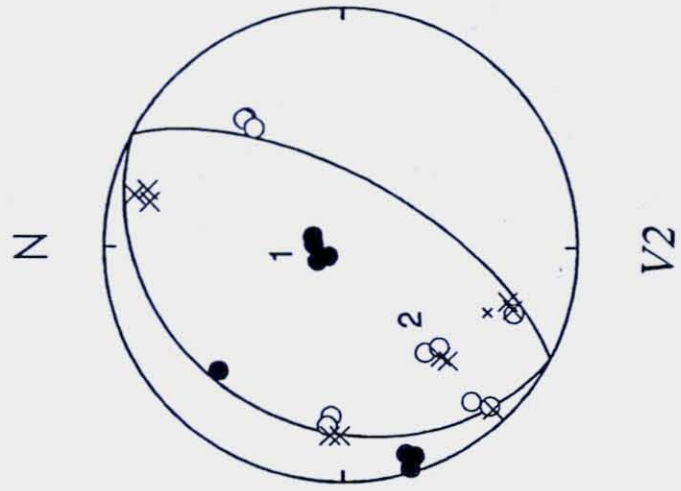
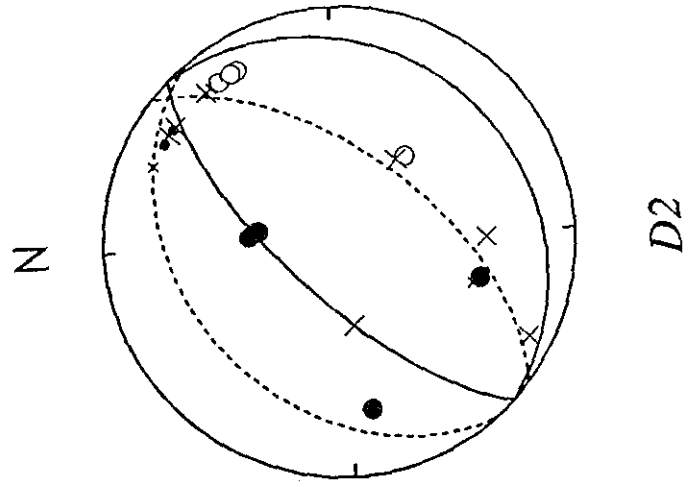
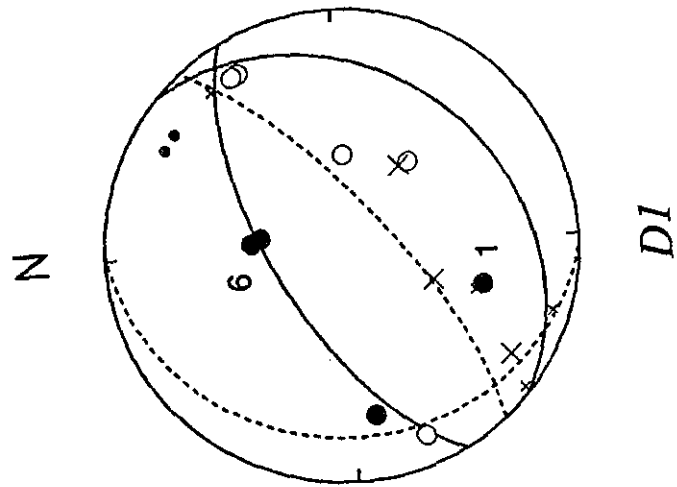


Figure 27



D2



D1

Figure 28



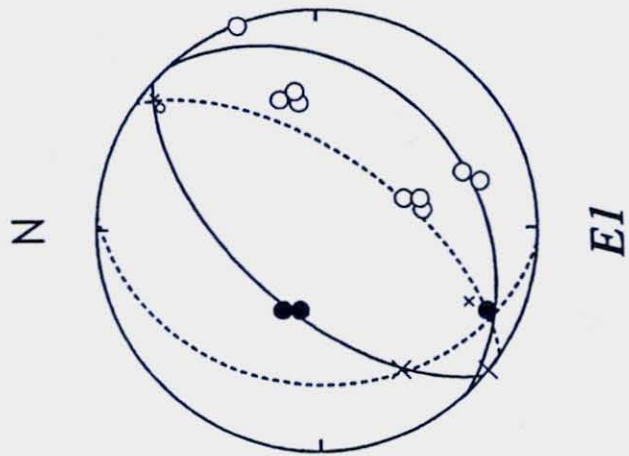
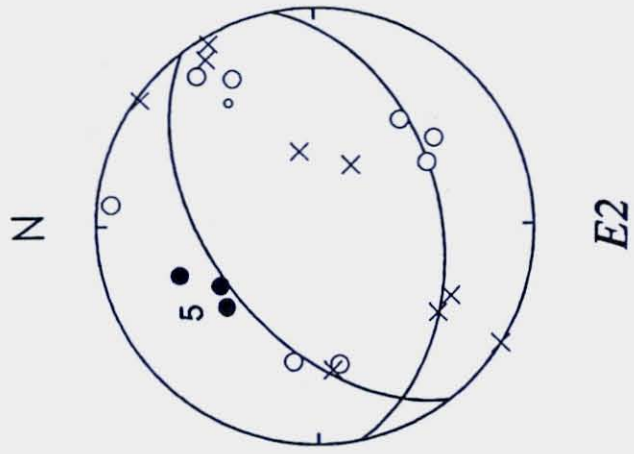


Figure 29

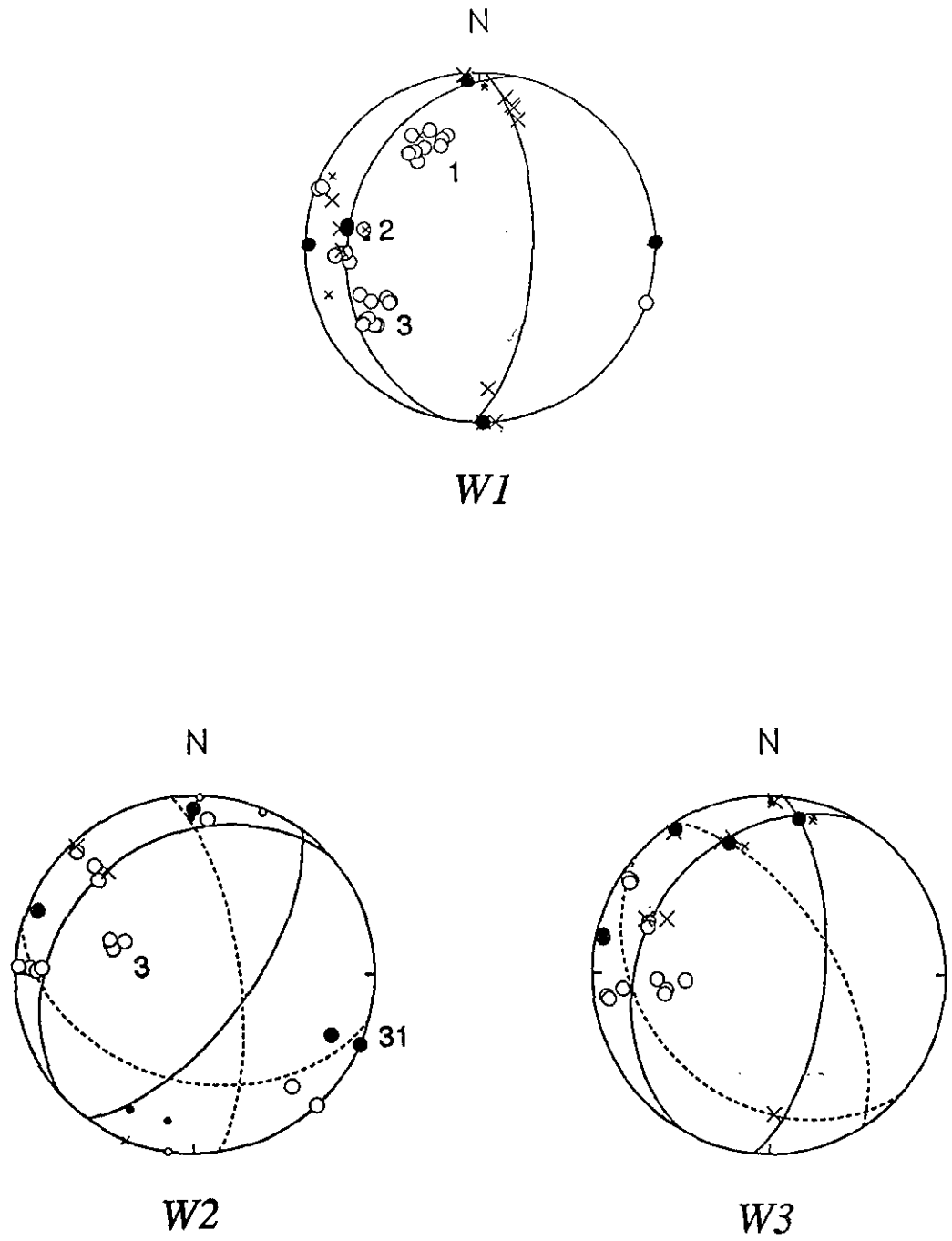
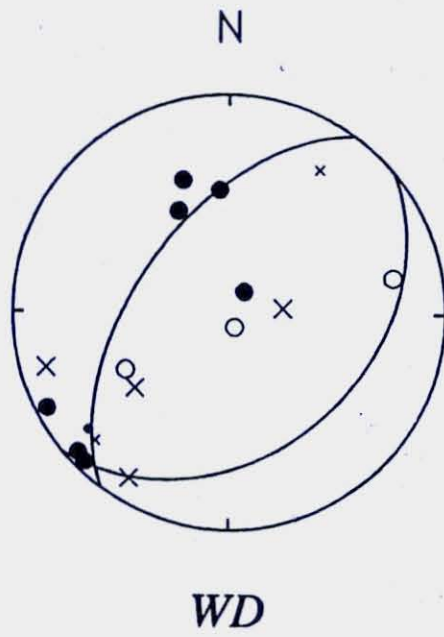


Figure 30



*Figure 31*

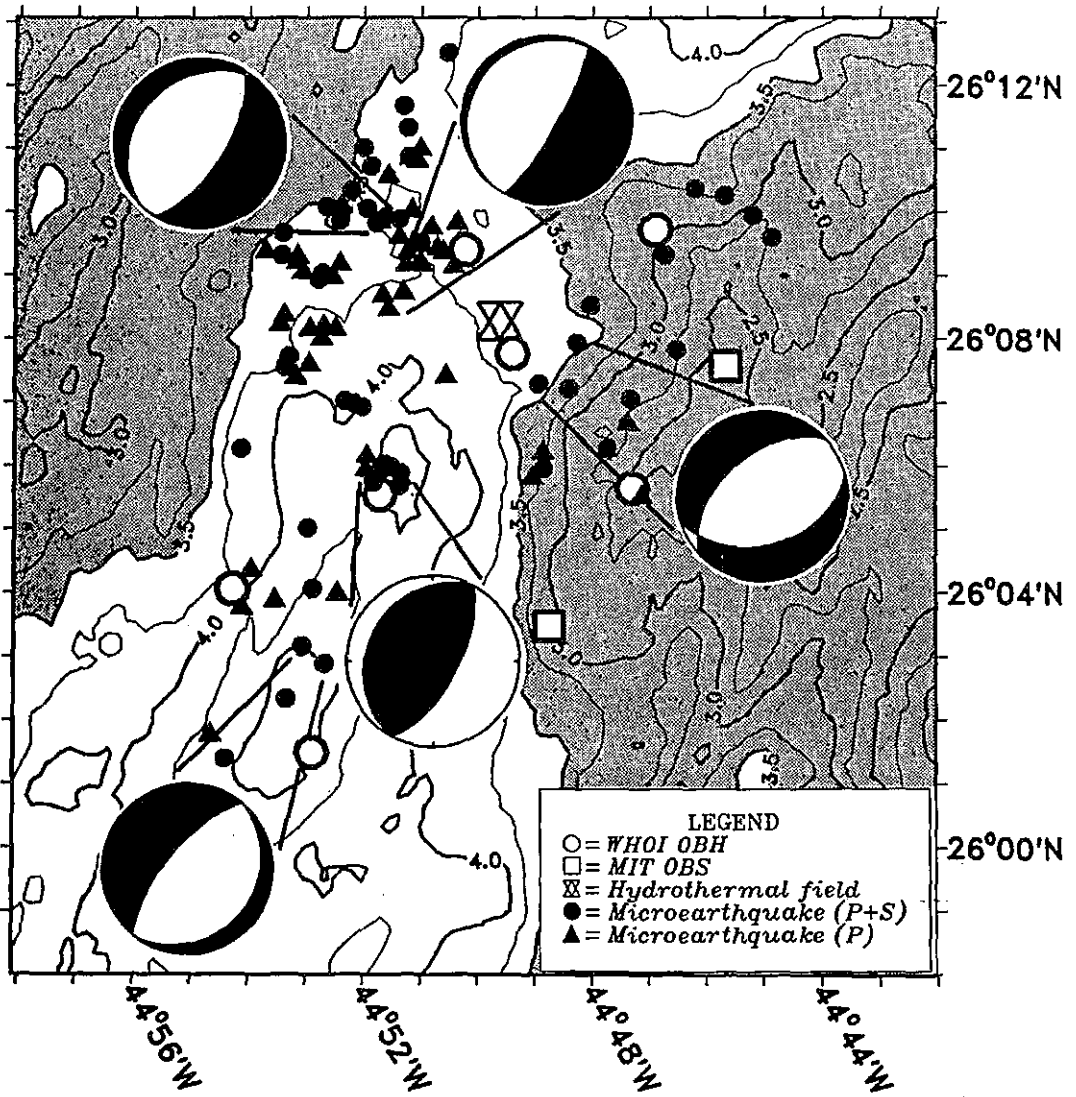
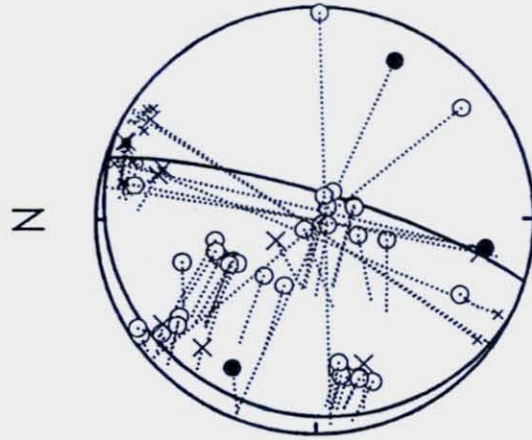
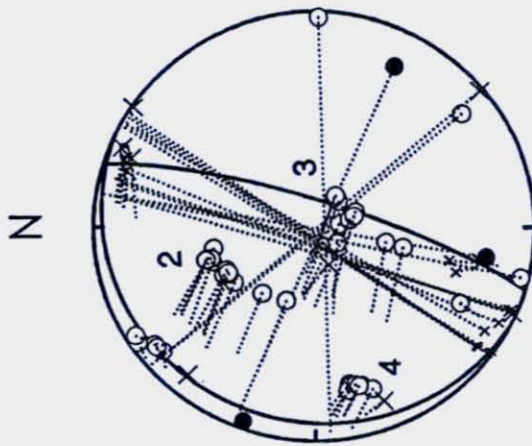


Figure 32

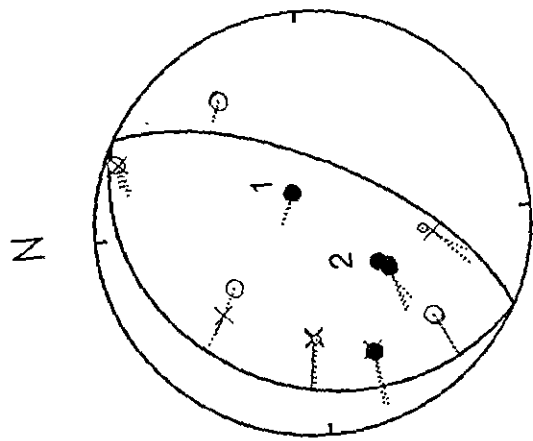


*H2 - model B*

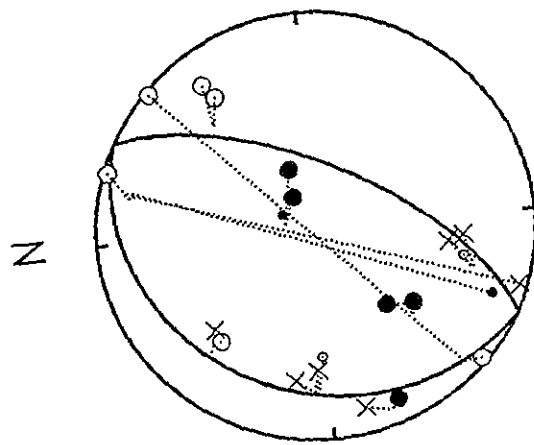


*H2 - model A*

*Figure 33*

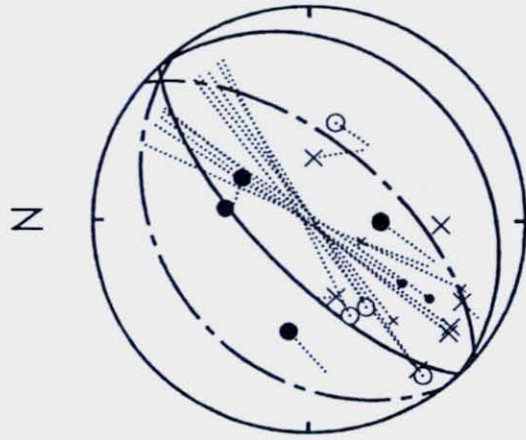


VI - model B

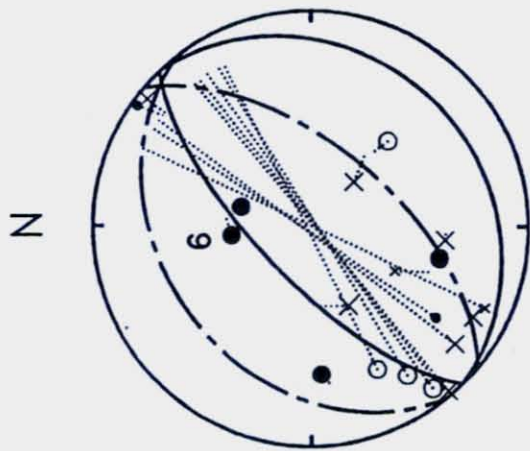


VI - model A

Figure 34

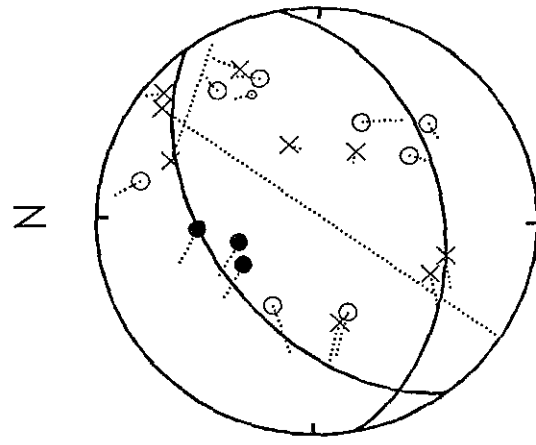


*D2 - model B*

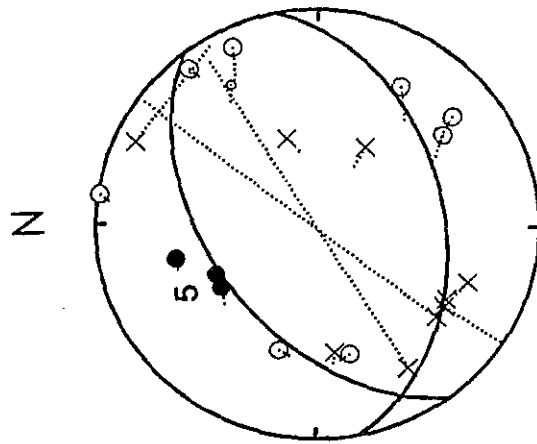


*D2 - model A*

*Figure 35*



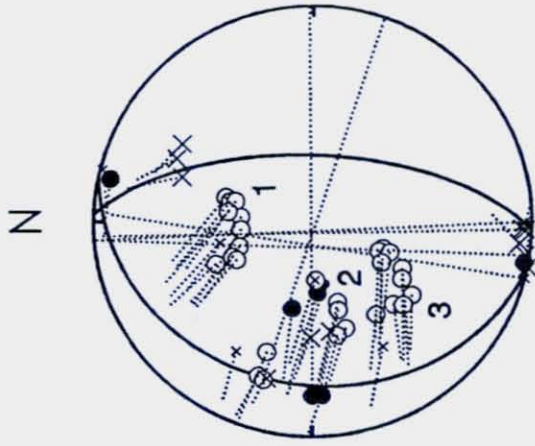
*E2 - model B*



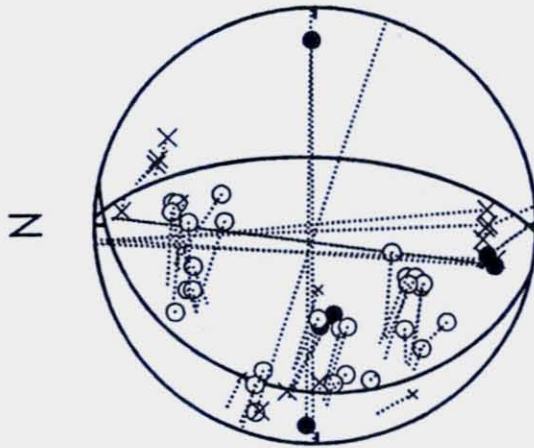
*E2 - model A*

*Figure 36*





*W1 - model B*



*W1 - model A*

*Figure 37a*

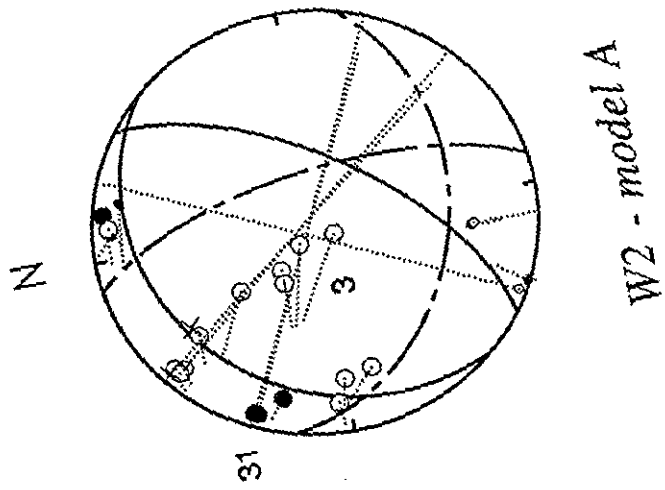
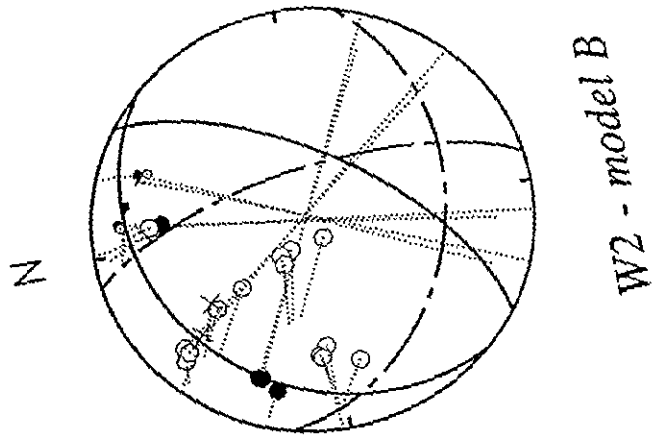


Figure 37 b

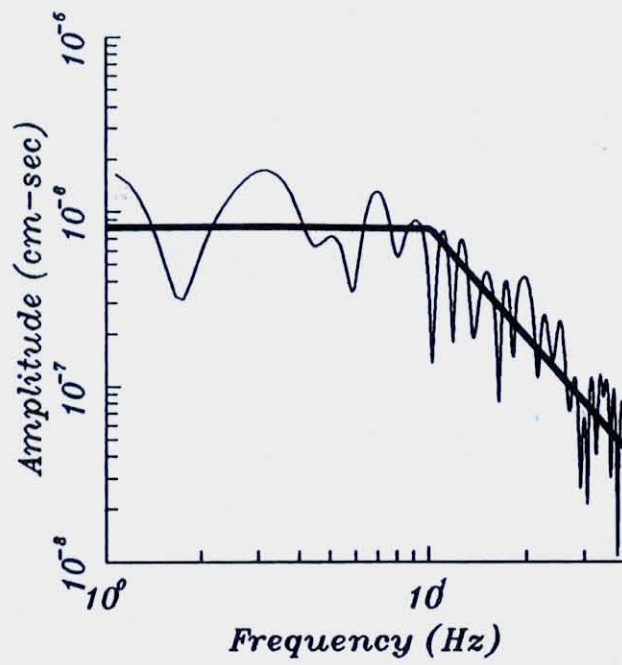


Figure 38

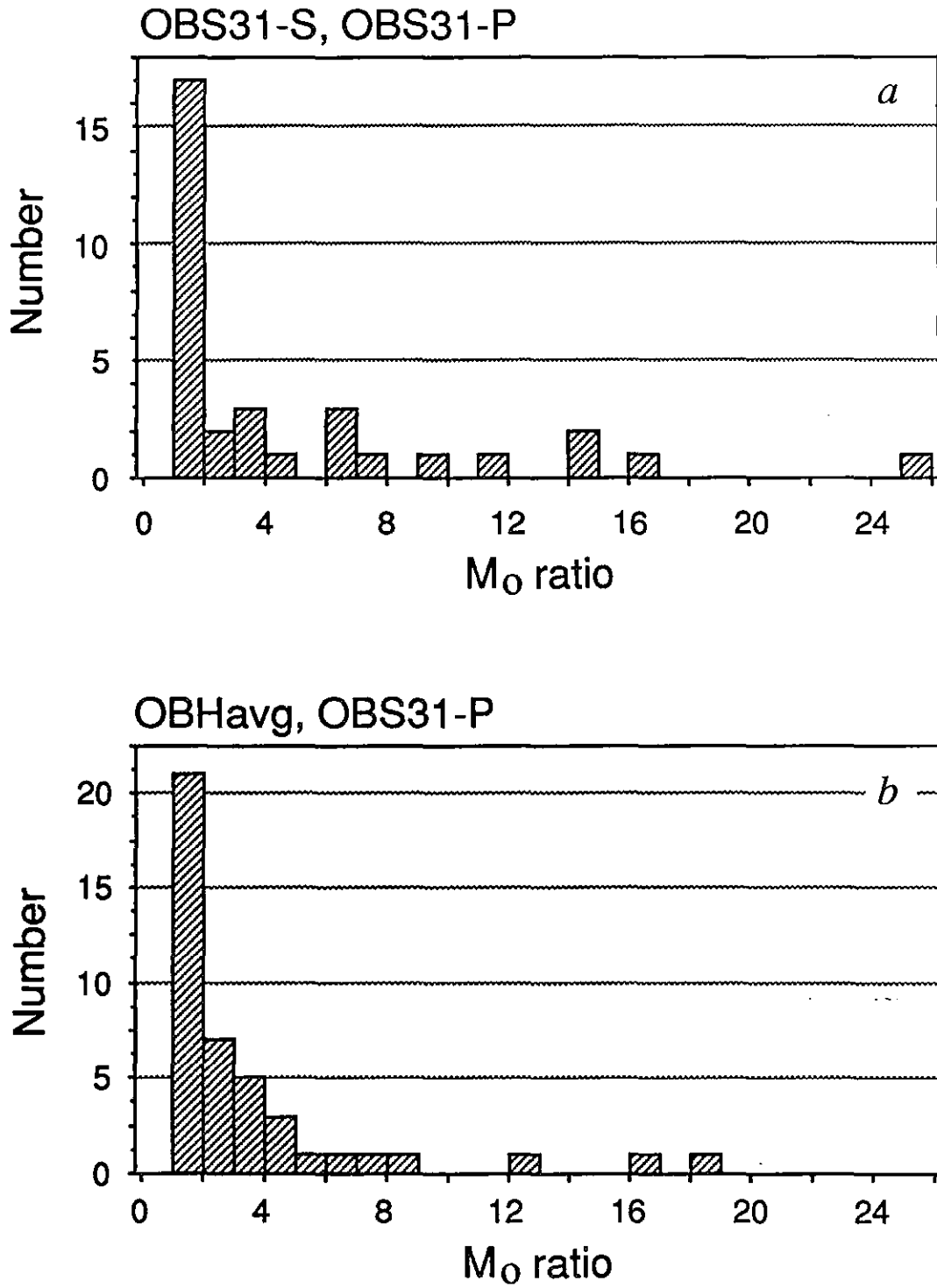


Figure 39

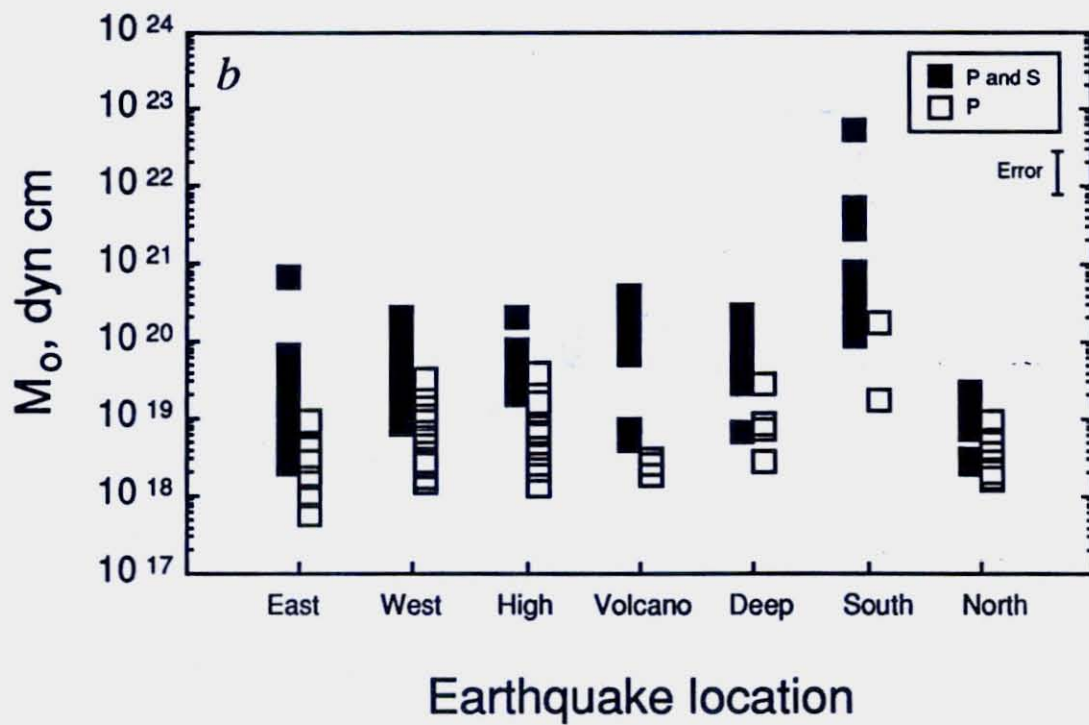
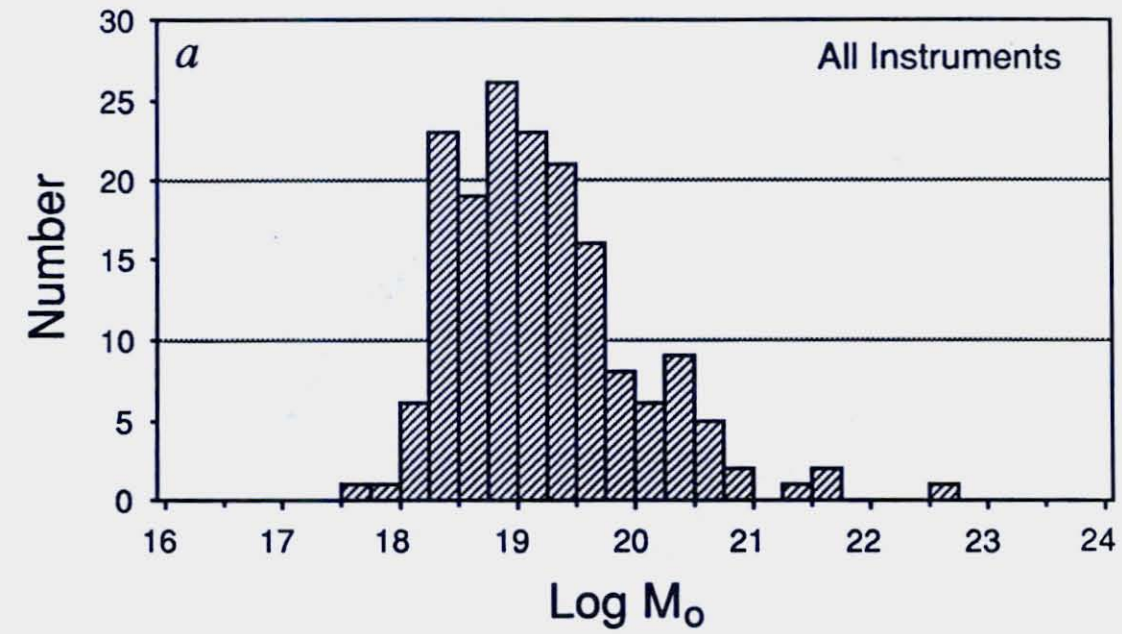


Figure 40

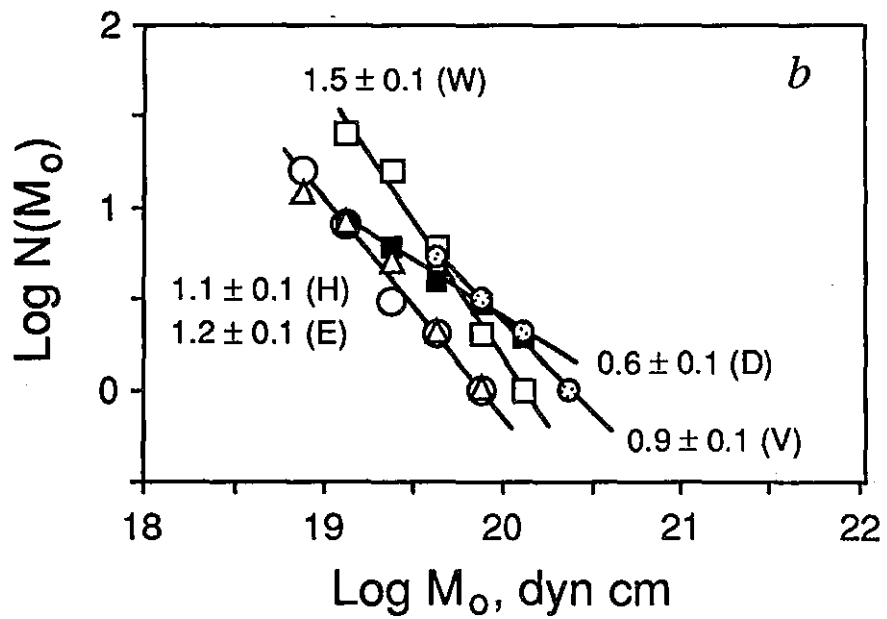
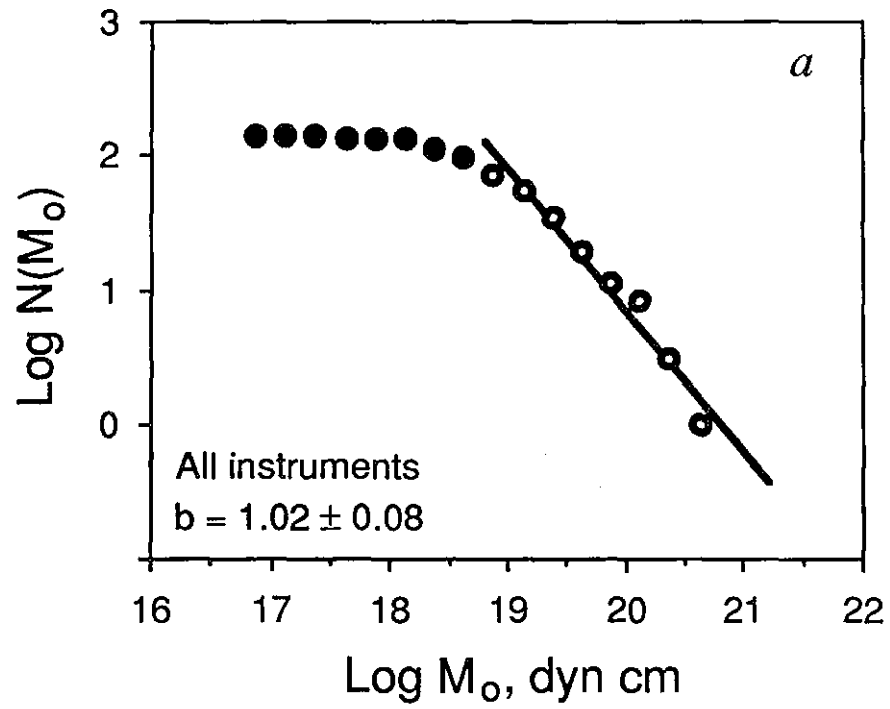


Figure 41

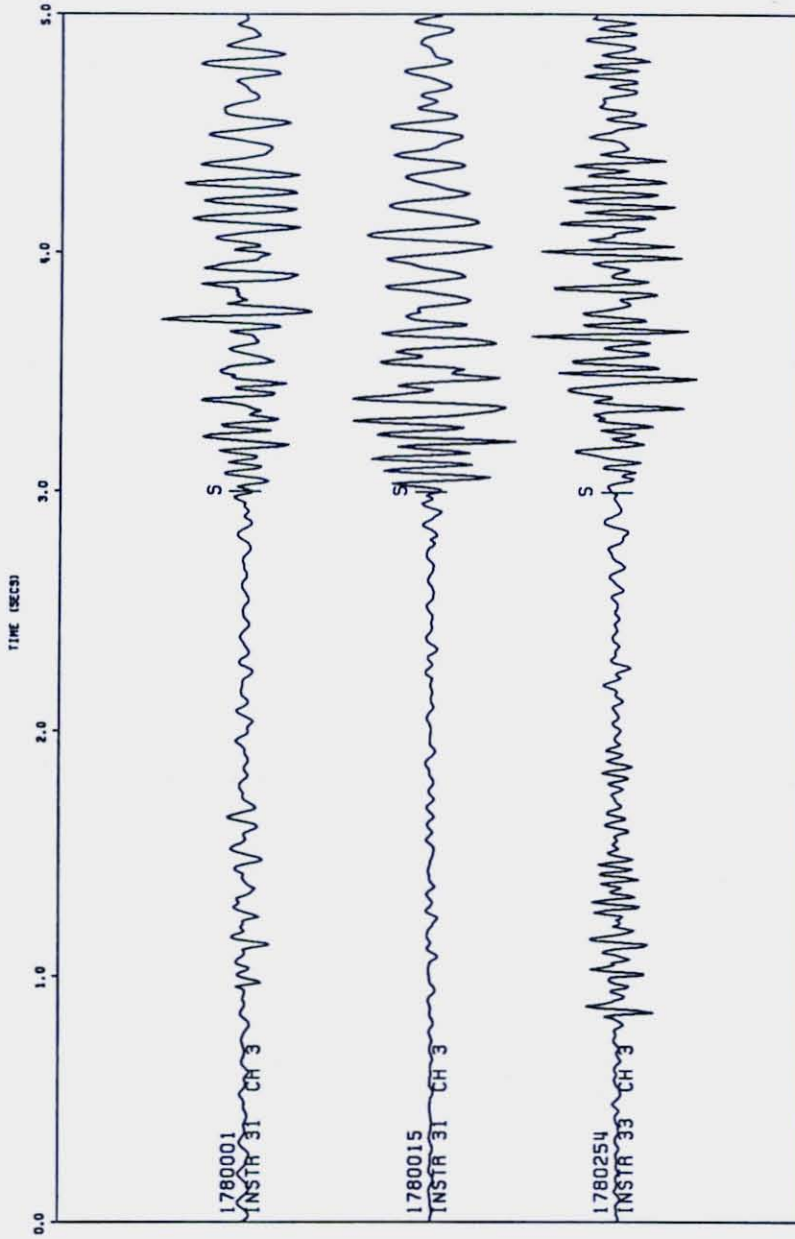


Figure 42

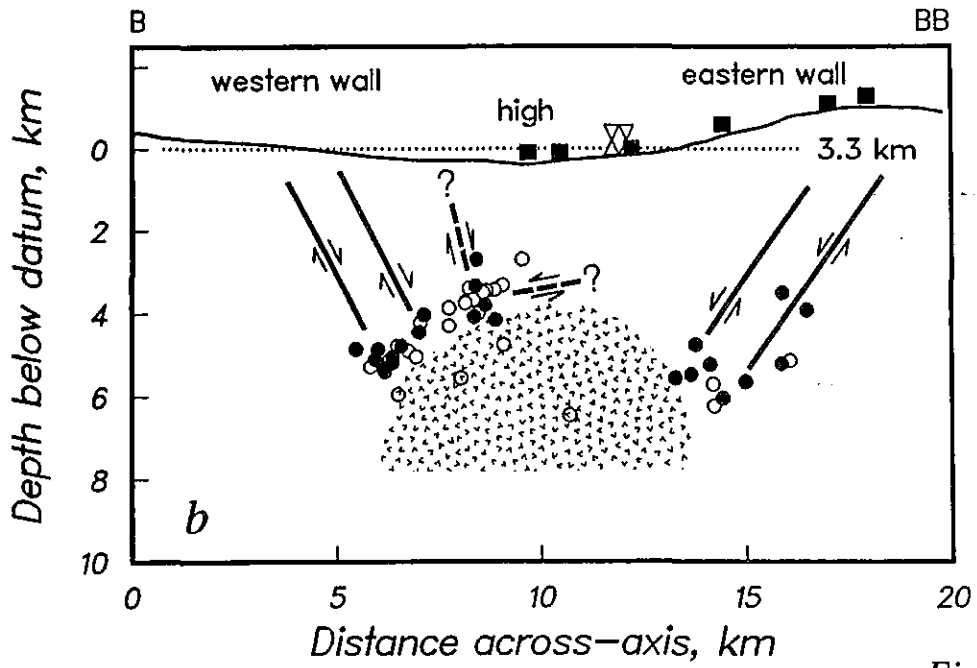
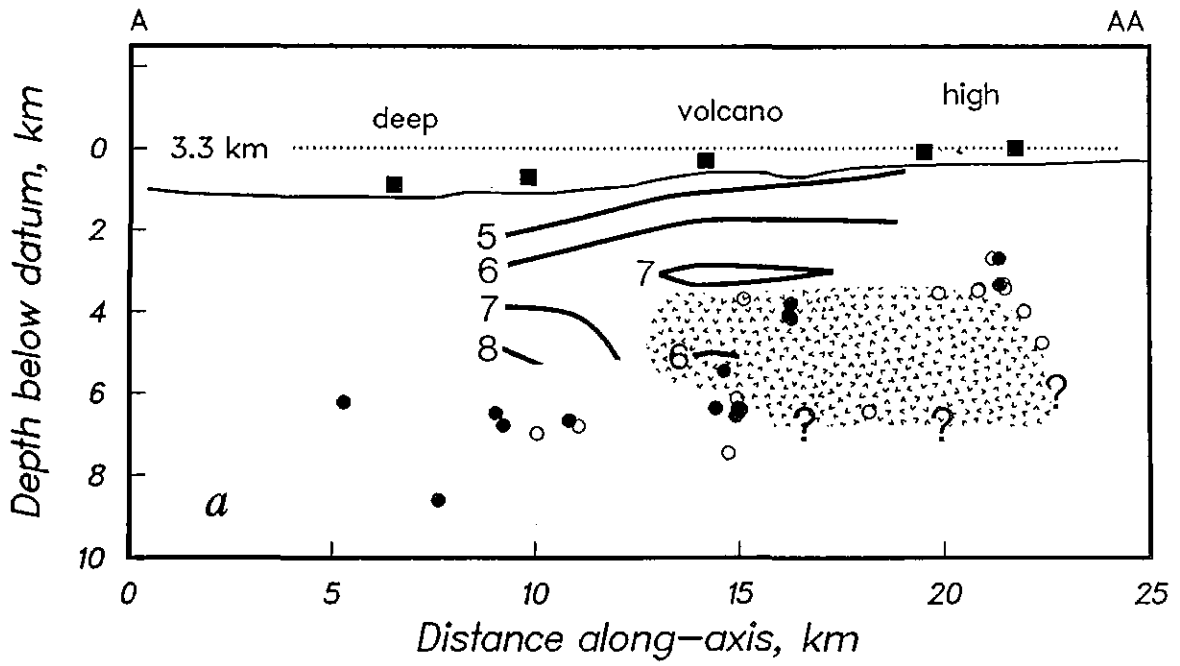


Figure 43



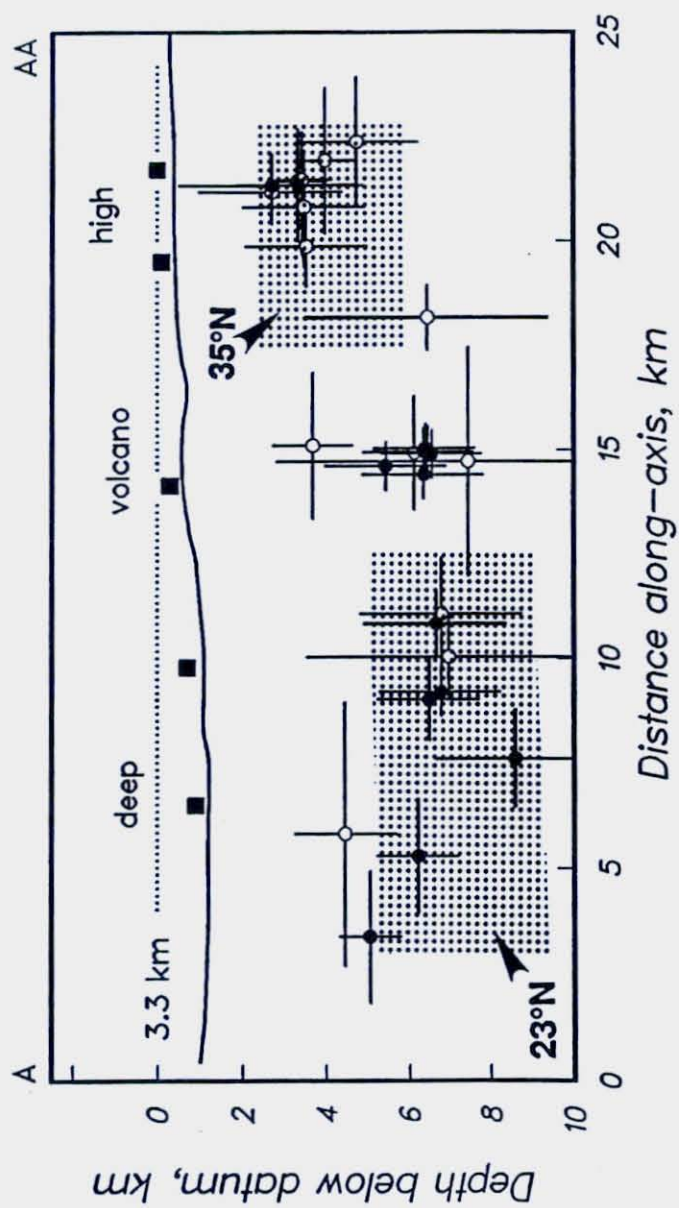
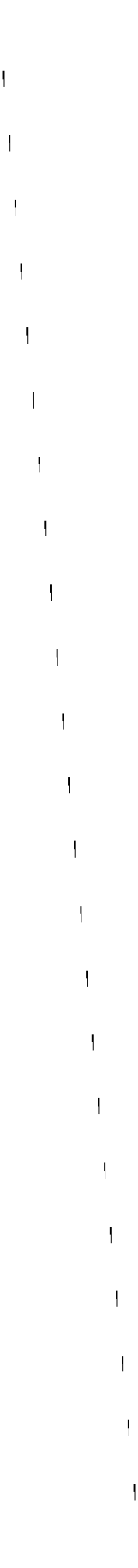


Figure 44



CHAPTER 4. TWO-DIMENSIONAL VELOCITY STRUCTURE  
ALONG THE MID-ATLANTIC RIDGE  
NEAR THE TAG HYDROTHERMAL FIELD, 26°N

INTRODUCTION

A fundamental issue in understanding mid-ocean ridge processes is to resolve the manner by which upwelling mantle material is transformed into ocean crust at the ridge axis. The creation of oceanic lithosphere, which appears petrologically variable along-axis, from mantle source material that is presumably homogeneous, requires spatial and temporal variability in the accretion process. A common explanation for the petrological and geochemical signatures of basalts dredged from the ocean floor includes the presence of a shallow crustal magma chamber where low-pressure fractionation can occur. The mid-ocean ridge magma chamber, while also supported by analogies with subaerial volcanos and ophiolitic assemblages, has nonetheless escaped direct seismic detection until recently [e.g., East Pacific Rise, *McClain et al.*, 1985; *Detrick et al.*, 1987]. Questions as to its dimensions, along-axis continuity, and temporal longevity, especially at slow spreading centers, remain largely unanswered.

The discovery within the last few years of high-temperature hydrothermal vent fields on the slow-spreading Mid-Atlantic Ridge [*Kong et al.*, 1985; *Rona et al.*, 1985] implies that heat sources must be present at least locally in order to fuel the high heat flux of black smoker vents. *Strens and Cann* [1982, 1986] have evaluated the conditions under which shallow hydrothermal circulation at active black smoker systems can form large volcanogenic ore deposits, such as are inferred at 26°N and are found in Cyprus; their model, based on lateral heat conduction and turbulent heat extraction along fault-controlled conduits, requires the presence of an underlying heat source, such as a magma chamber, to sustain the circulation and precipitation of sulfides.

Along the Mid-Atlantic Ridge (MAR), only a few seismic studies have focussed exclusively on the axis of accretion, and of these none have unambiguously imaged a crustal magma chamber [*Whitmarsh*, 1975; *Fowler*, 1976, 1978; *Fowler and Keen*, 1979; *Bunch and Kennett*, 1980; *Purdy and Detrick*, 1986]. Because of the 1-2 km seismic wavelengths and poor spatial sampling that characterize these studies, however, small zones of low velocity or high attenuation beneath the median valley would not be resolvable. *Whitmarsh* [1975] used travel time residuals from two refraction lines across

the median valley as evidence for a 2-3 km wide, axial low velocity zone (3.2 km/s) situated within the upper 2.5 km of crust at 37°N, while *Fowler* [1976] proposed a 3-km-thick crust underlain by anomalously low upper mantle velocities (7.2 km/s) from travel time data and synthetic seismogram modelling of refraction data, also at 37°N. At 45°N, the propagation of shear waves across the median valley precluded the existence of a sizeable zone of high attenuation [*Fowler*, 1978; *Fowler and Keen*, 1979]. *Bunch and Kennett* [1980], using synthetic seismograms, documented a small velocity inversion (6.8 to 6.6 km/s) at 4 km depth on the Reykjanes Ridge at 60°N. In the best-constrained study of median valley seismic structure to date, *Purdy and Detrick* [1986] found the axial structure at 23°N to be homogeneous over tens of kilometers and typical of simple, relatively mature ocean crust. They observed no evidence for a steady state magma chamber, but they did image a zone of slightly lower layer-3 velocities beneath an along-axis bathymetric high, which they interpreted as the seismic remnants of the most recent magma pulse along the 120-km-long section of ridge sampled by the refraction line. Tomographic inversion of shot and earthquake travel time residuals for two-dimensional, across-axis median valley structure beneath a morphological deep south of the along-axis high showed a narrow zone (less than 10 km wide, 1-5 km depth) of slightly lower velocities (by several percent) centered at the ridge axis [*Toomey et al.*, 1988]; the low velocities were interpreted as the seismic expression of the most recent site of magma injection within the inner floor deep.

During the summer of 1985, a combined microearthquake and seismic refraction experiment was carried out in the median valley of the Mid-Atlantic Ridge at 26°N (Figure 1) with the intent of investigating the mechanical and structural properties of young ocean crust at a hydrothermally-active, slow spreading center. The geologically well-studied ridge segment at 26°N [e.g., *Rona et al.*, 1976, 1986; *McGregor et al.*, 1977; *Rona*, 1980; *Karson and Rona*, 1989; *Thompson et al.*, 1985; *Zonenshain et al.*, 1989] provides an excellent locale at which to investigate the relationships between tectonism, volcanism, and hydrothermal circulation, and the effect of these processes on the seismic velocity structure beneath the median valley. The presence of high-temperature black-smoker vents also establishes this area as one of the more probable sites identified to date (along with the hydrothermal field at 23°22'N) at which to find a seismically-detectable magma chamber at a slow spreading center.

In this chapter, we report results from the explosive refraction line and from the tomographic inversion of P wave travel time residuals for seismic velocity structure in the

vicinity of the hydrothermal field. The analysis of the microearthquake data was presented in Chapter 3. In the first part of this chapter, we document the travel time and amplitude evidence for seismic heterogeneity beneath the median valley. This is followed by one-dimensional (1D) travel time inversion and amplitude modelling of the refraction data south of the along-axis inner floor high to explore plausible plane-layered structures associated with the different receivers. The second part of this chapter presents laterally-varying P wave velocity models of median valley structure obtained from the tomographic inversion of P wave travel time residuals from shots and earthquakes. These results are evaluated in light of the data resolution and spread in the resolving kernel and the assumptions imposed in the analysis, and then interpreted in terms of models of crustal accretion.

## EXPERIMENT LOCATION

The 75-km refraction line was shot along the axis of the median valley between 25°54'N and 26°28'N to a 20 x10 km network of seven ocean bottom hydrophones [OBHs, *Koelsch and Purdy, 1979*] and two ocean bottom seismometers [OBSs, *Mattaboni and Solomon, 1977; Duschenes et al., 1981*]. The network encompassed the high-temperature black-smoker field at the along-axis depth minimum, as well as the deeper portions of the inner floor to the south (Figure 1). In total, 44 charges (27 kg, ~ 1.5 km shot spacing) were shot along the northern and southern limbs of the refraction line, and an additional 13 ranging shots (7 kg) were detonated in the vicinity of the network. The mean detonation depths were 10.4 m and 6.1 m for the 27 kg and 7 kg shots, respectively.

In addition to the travel time and amplitude analysis of the refraction line for P wave velocity structure beneath the inner floor south of the along-axis high, we used travel time residuals from refraction and ranging shots within and close to the network, along with travel time residual data from the microearthquakes (Chapter 3), to tomographically invert for two-dimensional, along-axis structure.

## DATA REDUCTION

Shot instant corrections, which account for the fact that shot times are recorded by a hydrophone towed 50 m behind the ship, were typically ~ 0.2 s. Receiver clock corrections were calculated assuming linear drift rates (0.002 - 0.033 s/day) from pre- and post-deployment time checks against ship clocks. All times, including a leap

second on July 1, 1985, were corrected to Universal Time (UT). Most crustal arrivals could be picked to within 0.02 s (2 samples) on the low frequency (2-40 Hz), high gain hydrophone channels on the OBHs or the vertical channel on the OBSs. The overall reading error for both water waves and crustal first arrivals, including uncertainties introduced by the playback and picking of phases, clock correction to UT, and instrument location, was estimated to be 0.04 s.

Instrument and shot locations near the network were determined by the formal inversion method of *Creager and Dorman* [1982] using Global Positioning System (GPS) navigation fixes and direct water wave travel times (Chapter 3). The technique utilizes acoustic ranging of shots at a range of azimuths to fixed instruments to solve simultaneously for the locations and depths of the instruments and the locations of the ranging shots. Final shot and instrument locations have formal one-standard-deviation errors of  $\pm 30$  m.

In order to improve upon the locations of the remaining explosive shots, which are little constrained by the above inversion method because of their long ranges and narrow range of azimuths, we employed a grid search technique using the available direct water wave data to estimate the best location for each shot by minimization of the root mean squared (rms) travel time residual. Direct water wave arrivals were read on the OBHs from a filtered (0.15 - 2 kHz) and rectified hydrophone channel digitized at 100 Hz, and on the OBSs from the vertical channel (1 - 60 Hz sensitivity) sampled at 120 Hz. A constant water velocity layer (a sounding velocity of 1.5137 km/s computed from a CTD water sampling cast at 24°N) was assumed. Because of the rugged topography, direct water wave arrivals were not observed on all instruments from all shots.

Two iterations for shot location were carried out, the first using a 3-km-wide square grid (100-m spacing) centered around the GPS or Transit satellite location of the shot, and the second employing a smaller, 1.5-km grid (50-m spacing) centered around the location from the first iteration. In the final step, an additional constraint, imposed on the farthest shots for which rms residuals did not yield a robust location in the northwest-southeast direction (Figure 2), was that all shots for each line occurred along the same azimuth, defined as follows. For the south line the azimuth (N28.3°E) was determined by a least squares fit through the locations obtained with the *Creager and Dorman* [1982] method, while for shots north of 26°15'N the azimuth (N29.6°E) was obtained by a fit to the small-grid relocations. Uncertainties in shot locations, from the

0.04-s travel time error for the water waves, were estimated from spline fits to the rms residuals versus position along azimuths parallel and perpendicular to the shot line direction. The average error in shot location along the azimuth of the refraction line was 119 m.

The substantial effects of seafloor topography on crustal P wave travel times were removed by computing travel time and range corrections for each shot to each receiver using an improved version of the water path method described by *Purdy* [1982]. Estimates of the range dependence of the ray parameter were utilized to correct both the range and travel time of each data point to the seafloor. The ray parameter was estimated from a cubic spline fit to the travel time data for the refraction lines, and from the average shot-receiver range and corresponding estimated velocity at the ray turning depth for the remaining ranging shots. A ray parameter uncertainty of 0.03 s/km was determined from an examination of the travel time curves and consideration of reasonable ray parameters (velocities) at ray turning points.

Because of the distribution of receivers and the large topographic variations in the study area (over 1 km of relief), ray entry points beneath the shots can in some cases be offset by more than 2 km from the ship track. This renders the conventional one-dimensional bathymetry recorded by the shooting ship inadequate for the determination of accurate topographic corrections. To overcome the two-dimensionality of the shot-receiver configuration, we have used the complete three-dimensional representation of the seafloor topography provided by the Sea Beam bathymetry [*Sempere et al.*, 1989], gridded at 150-m spacing with linear interpolation between data points, to determine the ray entry point along the shot-receiver azimuth for the estimated ray parameter. Typical corrections were 2.5 - 3.0 s in travel time, with an estimated error of 0.07 s assuming a  $\pm 0.03$  s/km uncertainty in the ray parameter.

## REFRACTION LINE ANALYSIS

In this section, we present amplitude and travel time evidence for crustal heterogeneity beneath the median valley in the vicinity of our experiment site (Figure 1). A plot of all water-path-corrected times from shots to the south of the along-axis high to instruments in the network shows a wide scatter (up to 0.8 s) in the water-path-corrected travel times (Figure 3), indicating that substantial variations in velocity are

required beneath the median valley. Figure 4 reveals that P-waves traversing the region of the along-axis high (to OBHs 2 and 3) have reduced travel times at 5 - 15 km range that are up to 0.4 s less than those to instruments in the deeper portions of the median valley to the south (OBHs 1, 6, and 8) or atop the eastern wall (OBH 5; OBSs 1 and 3). At these ranges, rays turn within the topmost 3-4 km of crust, implying that higher velocities are associated with the upper crust in the region of the along-axis high. Amplitudes of compressional first arrivals beyond 19 km range at receivers located atop the along-axis high (OBHs 2 and 3; Figures 5a,b, 6) are severely attenuated, suggesting a decrease in velocity at depths greater than about 4 km. The observation of high-amplitude arrivals at comparable ranges at an instrument deployed on the eastern wall only 5 km to the east (OBH 4; Figures 5c, 6) indicates that the heterogeneity may be local in nature and confined to the inner floor.

Examination of the water-path-corrected, reduced travel times from the northern limb of the refraction line show travel time variations of up to 0.6 s out to ranges of 25 km (Figure 7a). These variations, which correspond to systematically larger travel times to OBHs 1 and 6 compared to times to OBHs 2 and 4 (Figure 7b), are consistent with lower velocities within the uppermost 3 km of crust beneath the along-axis deep region to OBH 6, and north of the along-axis high to OBH 1. Northern limb seismograms to OBHs 1 and 6, as compared to OBHs 2 and 4, also display significantly smaller P wave amplitudes out to 20 km range (Figure 8). Although these variations are qualitatively consistent with the inferences made from data from the southern limb, shot locations (and thus topographic correction calculations) and travel times (because of the lower signal to noise ratio of the P waves at far ranges) have larger uncertainties. For these reasons, we have chosen not to examine in detail variations observed from the northern limb data.

## **Southern Limb of Refraction Line**

### *Record Sections - Amplitude Observations*

The seismograms to OBH 4, located on the eastern wall just to the north of the along-axis high region, display high signal to noise ratios at all ranges (Figure 5c). The amplitude-range variations are similar to those observed within the MAR median valley at 23°N by *Purdy and Detrick* [1986], which is characterized by steep layer-2



velocity gradients underlain by shallow layer-3 gradients and a distinct mantle transition zone. OBH 4 seismograms show lower amplitudes at 17-18 km due to slightly increasing velocities at mid-crustal depths and high amplitudes, suggestive of a Moho triplication, from 20-25 km range (Figure 5c). The amplitude patterns, which are consistent with a normal oceanic crustal column only a few kilometers off the ridge axis, constitute evidence that oceanic crust evolves to a relatively mature structure within 0.4 My at this latitude on the MAR. The observation of high-amplitude first arrivals extending to ranges beyond 25 km is not typical of normal oceanic crust, and suggests the presence of heterogeneities at depth.

In contrast, rays which traverse the median valley to OBHs 2 and 3, located atop the shallower portions of the along-axis high where the high-temperature hydrothermal field is situated, show low signal to noise ratios, and are severely attenuated beyond 18-19 km range (Figures 5a,b, 6). No consistent refracted arrival times could be picked over these ranges (Figure 5a), and certainly no Moho triplication is observed (Figure 5a,b). The low amplitude, emergent phases contrast sharply with the impulsive arrivals at OBH 4, which is located less than 5 km to the east.

The data recorded by OBHs 1 and 8, located within the along-axis inner floor deep, show high signal to noise ratios with high amplitudes out to 15 km, characteristics typical of steep layer-2 velocity gradients within the upper crust (Figures 6, 9). Both record sections show the appearance of lower crustal or upper mantle velocities ( $\sim 8$  km/s) at relatively short ranges ( $\sim 15$  km).

### *Travel Time Patterns*

Compilation of the refracted wave travel time data indicates that substantial, and systematic, seismic heterogeneity exists within the crust at 26°N (Figure 3). That consistency is seen among travel times of shots to spatially-clustered receivers (Figure 4) implies, however, that some lateral heterogeneity in structure may exist at length scales of 5 km or less. Cubic splines, constrained so that slopes decrease with increasing range, can be fit to the data groups shown in Figure 4 with rms deviations of 0.10 s (along-axis high), 0.06 s (along-axis deep), and 0.08 s (eastern wall). Within the median valley, velocity-depth functions were obtained for OBHs 1 and 3 from the inversion of the spline-fit travel time curves (Figure 10). The simple plane-layered models, which serve only as starting models for the amplitude modelling in the

next section, are shown in Figure 11. Velocities in the uppermost crust were approximated by a linear gradient using the method of *Ewing and Purdy* [1982]. Because of the scatter in the travel times at ranges > 21 km to OBH 3 (see Figure 4), the velocity-depth function below 3 km is unconstrained.

Comparison of the travel times (Figure 4) and velocities (Figure 11) reveals three first order observations: (1) Travel times associated with paths traversing the crust beneath the inner floor along-axis high (OBHs 2, 3) are significantly less than the times for rays which sample the crust beneath the deeper portions of the median valley to the south (OBHs 1, 6, 8). The variations, up to 0.4 s for travel times of ~ 1 s in the 5-15 km range to instruments a few kilometers apart, indicate that systematic differences in velocities exist along the median valley axis. At these ranges, rays turn in the topmost 3-4 km of crust, suggesting much higher average velocities exist in the upper crust beneath and to the north of OBH 1. It is worthwhile to mention at this time that OBH 1 is located on a 200 m conical feature situated within the neovolcanic zone (see Figure 3 in Chapter 3 for location). The coincidence of this edifice, probably a small volcano, with the mapped velocity anomaly will be discussed in more detail later. (2) No mantle phases (~ 8 km/s) are observed in the travel time data (Figure 4), or waveform data (Figures 5a,b), to OBHs 2 and 3 out to 30 km range. In the next sections, we will show that a velocity decrease with depth near OBH 1 is required to explain the lack of strong, coherent P wave arrivals beyond 19 km range to OBHs 2 and 3, as well as the travel time observations to instruments within the inner floor. (3) Travel times to OBHs 2 and 3 atop the along-axis high are also resolvably shorter than those to instruments on the eastern wall (Figure 4b), though the contrast is not as striking as with the structure beneath the along-axis inner floor deep.

### **Amplitude Modelling - Median Valley South of Along-Axis High**

In this section, we present WKB seismograms [*Wiggins, 1976; Chapman, 1978*] that satisfactorily fit both the amplitude patterns and P wave travel time data observed by OBH 3 (Figures 4a, 5a) and OBH 1 (Figures 4a, 9a). The plane-layered models, which represent average velocity structures, are significantly different even though their ray paths sample crustal volumes only a few kilometers apart. In determining the models, our goal was to find the simplest structures (hence with only 2 or 3 layers, Figure 12, Table 1)

consistent with the major amplitude - range patterns in each record section; because of the known heterogeneity and limited spatial sampling ( $\sim 1.5$  km), as well as topographically-induced focussing and partial detonation uncertainties, no attempt was made to match shot-to-shot amplitude variations. For each instrument, two possible models are presented, one in part derived from the inversion of travel times from each refraction line (models 1A-1d; 3A,3B-1d), and the second motivated by the results of the two-dimensional tomographic inversions of shot and earthquake travel time residuals (models 1A-2d, 3A-2d). We introduce the results from the tomographic inversions in order to explore the effects of a low velocity zone on the travel times and amplitudes, and to compare the structure estimated from the analysis of travel times to a single instrument with that independently estimated from the inversion of travel time residuals from a number of sources to a number of receivers.

### *OBH 3*

The important features modelled for the OBH 3 record section are the sharp cutoff in amplitude beyond 19 km (Figures 6, 13b) and the lack of Moho velocities out to 30 km; the amplitude maximum at  $\sim 14$  km was not modelled since it is observed only on a single shot. The travel times and high-amplitude first arrivals can be matched by a two or three layer upper crust which has positive velocity gradients to 2.7-3.1 km depth (Figure 13a). Relatively steep velocity gradients ( $\sim 1.3$  s $^{-1}$ ) in the upper kilometer of crust and gentler gradients (layer 2/3, 0.3 - 0.7 s $^{-1}$ ) down to 3 km depth are required to fit the curvature of the travel time curve; the shallower layer 2/3 gradients act to decrease the amplitudes with range (3B-1d model, Figure 13b). Below these depths, however, velocities cannot increase since this results in significant amounts of energy in the 20-30 km range (3A-1d model, Figure 13b).

The introduction of a low velocity layer would further decrease the amount of first-arriving energy. This hypothetical model, 3A-2d, is instructive in predicting the magnitude of travel time delay that might be expected from a layer of lower velocities. Figure 13c shows the calculated travel time curve, WKB seismograms, and ray paths for a 7 km crust containing a 2.7 km thick low velocity layer from 3.1 to 5.8 km depth. Because of the positive velocity gradient which is introduced below 5 km (1.2 s $^{-1}$ ), rays turn at increasingly shorter ranges with decreasing ray parameter resulting in high amplitude, refracted arrivals delayed 0.3 - 0.4 s over the 20 - 25 km range. The synthetic

seismograms in Figure 13c show only the major features, as the WKBJ approximation breaks down in the presence of sharp velocity gradients and in shadow zones [Wiggins, 1976; Chapman, 1978]. Examination of the observed travel times to OBHs 2 and 3 (Figures 4a) clearly shows that such a delay may exist, though the shot to shot arrival time variations over this range suggest that heterogeneity is present. The lack of a coherent set of delayed phases also implies that a layer of low velocities cannot extend continuously along-axis and, furthermore, that the along-axis extent of the low velocity is probably not more than 5-10 km since Figure 13c shows that coherent phases can be generated from a low-velocity layer with an along-axis continuity of < 10 km (i.e., coherent arrivals in the 20 -28 km range). This inference is confirmed by the higher velocities found at depth to the south from the refraction analysis of travel time data at OBH 1, and the two-dimensional velocity variations resolved by the tomographic inversions.

### *OBH 1*

The primary characteristics of the structure south of OBH 1, which describes the average crust beneath the deeper portions of the median valley, are the greater travel times (than to OBH 3) to 20 km range (Figure 4a), the appearance of lower crustal or mantle velocities at ~ 15 km range (Figure 10b), and the generally high amplitudes throughout (Figure 9a). While the amplitude - range pattern is similar to that observed at OBH 3, the distinguishing feature of the OBH 1 data is the much lower velocities over the upper 3 km of crust required to match the travel times (Figure 12).

The two models, again based on synthetic seismogram modelling using starting velocity models from the refraction-line travel time inversion (1A-1d, Figure 14b) and from the tomography inversions (1A-2d, Figure 14c), both require much lower velocities in the upper 2.2 -2.5 km of crust than were needed by the OBH 3 data. Model 1A-1d contains a  $1.7 \text{ s}^{-1}$  velocity gradient in the upper kilometer followed by successively shallower gradients ( $1.1 \text{ s}^{-1}$ ,  $0.7 \text{ s}^{-1}$ ) to 5.2 km. Model 1A-2d, which used the tomographic results as a starting base, includes higher velocities within the uppermost 0.7 km of crust in order to satisfy the travel time data. The one-dimensional structure obtained from the refraction line data is consistent with the travel time data and mean velocity structure found by Purdy and Detrick [1986] for the upper 2.5 km within the median valley at 23°N (Figure 11). The low seafloor velocity, and the steep gradient in the upper kilometer of crust, in contrast with a more gradual increase in velocity to 6 km/s over the next 1 - 1.5 km (Figure 12),

appear to be common characteristics of layer 2 structure in young oceanic crust [see Figure 9 in *Spudich and Orcutt, 1980a; Bratt and Purdy, 1984; Purdy and Detrick, 1986*].

Both models require velocities in excess of 7.4 km/s (maximum velocity estimated by the refraction line travel time inversion, Figure 11) in order to match the travel times and curvature of the T-X curve. The generally high-amplitude refracted arrivals to OBH 1, rather than an amplitude minimum at ~ 15 km that would result from gentle layer 3 gradients [*Purdy and Detrick, 1986*], are consistent with a steady increase in velocity with depth ( $0.7 \text{ s}^{-1}$ ) below 2.5 km depth.

### Summary of Refraction Analysis

The comparison of data from the southern limb of the refraction line to receivers located within the median valley at 26°N reveals that young oceanic crust cannot be adequately characterized by a simple, laterally homogeneous velocity structure. The consistency in amplitude and travel time patterns among spatially-clustered instruments does suggest, however, that some degree of homogeneity exists and that one-dimensional structures are at least locally valid (at 5-10 km length scales). These observations imply that the variations are systematic, and possibly related to the crustal accretion processes responsible for the formation of the active hydrothermal field.

The most striking feature of the refraction data set is an along-axis variation in the structure of the crust beneath the inner floor. Substantially lesser travel times, or higher velocities, appear to be associated with the uppermost 3 km of crust at the along-axis high. The structure at this locality requires a decrease in velocity at depth to explain the lack of coherent energy over the 19 - 30 km range to OBHs 2 and 3. Travel times (OBH 5, OBS 31) and amplitudes (OBH 4) to instruments a few kilometers to the east on the valley wall do not show such a variation, implying that the seismic structure varies perpendicular to, as well as along the ridge axis. The upper crust beneath the deeper portions of the inner floor is characterized by steep gradients in the upper kilometer and appears to be typical of young oceanic crust found at many mid-ocean ridge locales.

### TOMOGRAPHIC INVERSION FOR P WAVE VELOCITY STRUCTURE

In order to explore further the nature of the inferred along-axis seismic heterogeneity, we have carried out formal tomographic inversions for two-dimensional

(2D) P-wave velocity structure beneath the median valley at 26°N. By enlarging our source data set to include both the southern limb and portions of the northern limb of the refraction line and the ranging shots, as well as travel time residuals from microearthquakes, we are able to resolve along-axis variations in velocity.

The technique we use to solve for the velocity structure employs travel time residual data from shots and earthquakes whose locations are fixed throughout the inversion [Toomey *et al.*, 1988], and is a modification of a simultaneous earthquake relocation and velocity inversion method first developed by Thurber [1981, 1983, 1984]. The procedure incorporates an approximate three-dimensional ray tracer (ART2), enabling efficient computation of travel times for a velocity structure parameterized by an arbitrary distribution of grid values. The use of fixed earthquake hypocenters as sources is motivated by the limited number of explosive shots (up to 35) and receivers (up to 7); a simultaneous earthquake and velocity inversion would not be possible since at most only three travel time observations could be used to constrain the velocity structure after hypocentral estimation. As a consequence, the underlying assumption throughout, which later analysis shows is reasonable, is that the earthquake locations we use are "close" to their true locations so that travel time variations due to source mislocation are independent of small velocity perturbations. A review of the solution technique, including methods used to evaluate solution quality, is presented in the Appendix.

We begin this section with a discussion of the input parameters to the tomographic inversion, including the selection of an appropriate configuration of sources and receivers and parameterization of the velocity model. Using this source/receiver configuration, we present a 2D velocity model describing the average crustal structure beneath the median valley south of the along-axis high. Evaluation of the contribution of each source type and the effects that different source and receiver combinations have on the solution show, however, inconsistencies among some well-resolved nodal velocity estimates. Examination of the effects of earthquake source mislocation on the solution indicate that the spurious values result from tradeoffs in velocity estimates with changes in hypocenter caused by unmodelled structural variations at depths below that resolvable by the shot data alone, or out of the crustal volume described by the 1D model with station corrections. The inversions indicate that the best crustal model, the one which is most consistent with the velocities estimated from the shot data and which results in the highest reduction in data variance and best travel time fit, is obtained by using only the centermost events along the ridge axis and earthquake hypocenters relocated with a 2D structure which better

approximates the true structure. Because of the likely presence of heterogeneity in three dimensions, velocities may still be biased by hypocentral errors.

## **Input Parameters**

### *Travel Time Data Set*

Figure 15 shows the source (32 shots, 69 earthquakes) and receiver (7 instruments) distribution for the tomographic inversions (a total number of 532 observations) used in the following discussion. The explosive source data set, which consists of accurately-located ranging and refraction shots for which P wave arrivals could often be picked to within 0.02 s, includes only shots whose ray paths sample the inner floor; these include median valley shots up to 10 km to the north and south of the network. Tests show that the inclusion of shots at farther ranges helps to constrain the crustal structure at depth, but does not significantly affect the velocity estimates at shallow depths.

The earthquake sources (Figures 15 and 16) are those events with the best constrained locations. Hypocenters were independently calculated using a plane-layered structure with station corrections determined iteratively from a subset of well-recorded events (Chapter 3). The 69 earthquakes were culled from the full data set (185 events) by eliminating those events (1) whose ray paths sampled the rift mountains; (2) whose focal depths could not be resolved by the network - these events often were located outside the network; and (3) whose change in epicenter and depth, after relocation with only the inner floor network, was larger than the average one-standard-deviation ( $1-\sigma$ ) errors using the full 9-station network. For the 7-station configuration of Figure 15, the earthquake locations have nominal  $1-\sigma$  formal errors of  $0.85 \pm 0.40$  km in the horizontal direction and  $0.73 \pm 0.42$  km in the vertical direction. We will see in a later section that these hypocenters can be taken as "close" estimates of the true locations, and that for the given model parameterization, the resulting Earth model is independent of source mislocation.

A vertical cross section along the axis (Figure 16) suggests a general shoaling of earthquake focal depths toward the along-axis high and a relative paucity of shallow crustal events. Qualitatively, such a distribution means that the earthquake sources by themselves will not resolve the shallow structure since all rays will sample this volume to a comparable degree. The inclusion of explosive sources, which can independently resolve the uppermost crust, are thus crucial for a meaningful inversion for velocity structure.

### *Velocity Model Parameterization*

On the basis of the available source and receiver configurations for the experiment, including features constrained by the refraction line (above), we opt to solve for the along-axis, median valley crustal structure. In a later section we assess the effects of a three-dimensional structure on the solution. We seek a configuration of velocity nodes that can satisfactorily represent the velocity heterogeneity beneath the median valley at 26°N. Because our data set is finite and less than ideal, we want to select a set of parameters which can be resolved by the travel time observations. The 5-10 km heterogeneity length scale documented by the 1D refraction line analysis suggests that a 3-nodal-column parameterization might be appropriate. Such a model parameterization will implicitly seek to determine average anomalies beneath our instruments, and so to a first approximation the tomographic inversion will extract velocity perturbations to an initial structure from the station corrections. This is an important point because it explains why travel time residuals from fixed-location earthquakes can be used to provide independent information on the velocity structure we wish to resolve. Because the inversion uses data from a range of azimuths, information on the patterns of the structural heterogeneity not parameterized by the 1D model with station corrections can be extracted.

We use as our preferred initial model a layered structure which is approximately conformal to the seafloor (Table 2). Velocities in the upper 3 km are from inversion 0 (Table 3) which employed a one-dimensional starting model (Figure 17a) from the median valley at 23°N [Purdy and Detrick, 1986] and the 21 explosive sources within 5 km of the network; comparison of the structures obtained with the 1D and 2D starting models show that the solutions are not sensitive to the initial model, however. From structural models for young ocean crust [Spudich and Orcutt, 1980a], we fixed the nodal depths at 0, 1, 3, and 5 km beneath the seafloor in an attempt to characterize regions of high vertical gradients with a minimum number of parameters. The nodes at 0 and 1 km depth are needed to model the steep velocity gradients often found in the shallowmost crust. Using the criteria outlined below, with the above depth parameterization, we then performed a series of trial inversions with different numbers of along-axis nodal columns (Table 3, inversions 1-3) to determine an optimum horizontal node spacing.

A consideration in optimizing the model parameterization is to ensure that each parameter is not influenced by neighboring nodes, i.e., reflects a localized average. To



investigate this, we examine the resolution matrix  $\mathbf{R}$ . For an underdetermined problem, where  $m$  (number of velocity nodes) is greater than  $k$  (number of linearly independent parameters), off-diagonal elements of the resolution matrix will in general be non-zero [Wiggins, 1972]. Thus, we also seek a parameterization which results in a  $\delta$ -like resolving kernel. The node number-grid spacing (in km) map for the 3-nodal-column case is shown in Figure 18, and examples of the averaging vector for each node are shown in Figure 19 for (a) inversion 1 using earthquake and shot sources, (b) inversion 4 using shot sources only, and (c) inversion 5 using earthquake sources only.

The discussion in the Appendix suggests the optimal nodal configuration can be determined by examining plots of the derivative weight sum (DWS), spread, and resolution for a number of possible along-axis parameterizations. Figure 20 shows that the DWS and resolution decrease, and spread correspondingly increases, as the number of along-axis velocity parameters increases (see Figure 15 for nodal spacing and data distribution). From this series of plots, we can see that high resolution with minimal spread and smoothly varying DWS characterizes the 3-nodal-column parameterization (5 km spacing, A nodes in Figure 15), whereas the 5 and 7 nodal column cases (2.5 km and 1.7 km spacing, B and C nodes) are marked by progressively poorer resolution, larger spread, lower DWS, and in general increasingly larger degrees of scatter among the values.

Examination of the spread and resolution reveals a clear break, most clearly seen in the plots of resolution versus spread and DWS versus spread in Figure 20, that delineates well-resolved from poorly-estimated parameters. For the data in inversions 1-3, the threshold values for well-constrained velocity (plotted as dashed lines in the figure) were empirically taken to be 0.8 for the diagonal element of the resolution matrix, and 60 for the spread function value at a particular velocity parameter; for later inversions which use fewer data, resolution and spread threshold values will be lower and higher, respectively. In addition, evaluation of the potential number of degrees of freedom for the system (trace  $\mathbf{R}$ ) shows the percentage of linearly independent parameters ( $k/m$ ) decreases noticeably as the number of nodes increases from 12 to 28 (83% to 54%). Combined with increases in spread, this implies that a finer parameterization is not leading to a better estimate of velocities since averaging over adjacent nodes now occurs. On the basis of these results, we chose the 3-nodal-column configuration to be the optimal model parameterization; plots of the averaging vector (Figure 19a) show that these velocity parameters are well-resolved, generally-localized averages.

Trial inversions using a three-dimensional median valley parameterization (3 nodal columns along-axis, 2 across-axis) indicate that the available data do not allow the determination of meaningful solutions. This can also be qualitatively inferred from the distribution of earthquakes (Figure 15); the non-uniform arrangement results in the coupling of high and low values of resolution for some across-axis, nodal pairs. The low number of degrees of freedom (DOF,  $k=14$ ,  $m=24$ ) and large spread further suggest that such a parameterization does not add information to the model estimate.

### Average 2D Median Valley Structure

The results of the two-dimensional inversion for the along-axis velocity structure beneath the median valley in our experiment area, using 32 shots and 69 earthquakes recorded by 7 stations (total of 532 observations, Figure 15), are shown in Figures 21 and 22, and Table 3 (inversion 1). Examination of Figure 19b shows that most velocity parameters (nodes 5-10) represent localized averages and are not affected by adjacent nodes. The final rms travel time residual,  $rms_f$ , was 0.12 s after 5 iterations with a 63% reduction in variance (Table 3). Initial travel time residuals show substantial negative delays associated with the shot travel time data (Figure 23), suggesting that velocities are on average faster than in the initial model. After inversion, the mean travel time residual was  $0.02 \pm 0.12$  s. Although the shot residuals are much reduced, a slight bias is still observed; we will see later that this bias results from errors in the assumed earthquake hypocenters and that upon relocation of the events with a better estimate of the velocity structure, both shot and earthquake residuals after inversion show a zero mean with small variance.

The mean standard error in the estimation of a velocity parameter (the square root of the diagonal elements of the covariance matrix), expressed as a percent deviation from the starting model, was 2%, which corresponds to  $\sim 0.15$  km/s. In a comparison using synthetic data, *Thurber* [1981] found that the actual velocity errors were only weakly correlated with the standard error, and that the mean absolute error was nearly twice the mean standard error. From this result, we take our estimated average velocity error to be  $\sim 4\%$  or  $\sim 0.3$  km/s. As can be seen in Figure 22, the estimated velocity structure is well-resolved below a depth of 1 km, with resolution  $> 0.8$  and spread much less than 60; the smoothly varying DWS shows that the nodes are more or less uniformly sampled.

The two-dimensional model (Figures 21 and 22, Table 4) shows four major resolvable features: (1) Significantly higher velocities are associated with the shallowmost crust beneath the volcano and along-axis high than are found in the deepest portions of the median valley. (2) A region of higher velocities ( $\sim 7$  km/s,  $\Delta v = 0.6$  km/s) is located at shallower levels ( $\sim 3$  km) beneath the axial volcano than beneath the deep. (3) Beneath the axial volcano, velocities decrease directly below this level and are at least 1 km/s less than the starting model at a depth of 5 km. These lower velocities are not present beneath the along-axis deep but may extend beneath the along-axis high. The data do not constrain the thickness of the low velocity region. (4) A crustal thickness of 5 km is inferred from the observation of mantle velocities (8.1 km/s) beneath the along-axis deep.

Features 1, 2, and 4 can be resolved by the shot data alone (Figure 24, inversion 4), while feature 3, which describes patterns at depth beneath the volcano and along-axis high, is dependent on the earthquake travel times. The imaging of a velocity decrease below 3 km beneath the volcano is consistent, however, with the observed attenuation of P waves to OBHs 2 and 3 beyond 19 km range. A fifth observation, that mid-crustal velocities beneath the along-axis high appear to also be low, is inconsistent with results from inversions using only shot data (inversions 0, 4; Tables 4, 5), suggesting that the earthquake sources sampling these nodes are spuriously biasing the estimated structure. In a later section, we assess the quality of the earthquake locations, and suggest that by winnowing the source data set to those closest to the ridge axis and reestimating the hypocenters with a 2D model, we arrive at a more consistent estimate of the crustal structure.

## **Tests of Robustness**

### *Contributions of Shot and Earthquake Data*

In order to assess the contribution of the shot and earthquake sources to the inversion solution, we have compared the above solution with inversions using only shots (Figure 24, Tables 3 and 5 - inversion 4), and then only earthquake data (Figure 25, Table 3 - inversion 5). From Figure 26, which summarizes the relationships between the data and resolution, we can see that as the ray density (DWS) near a node decreases, the resolution of the parameter decreases. However, as resolution (or spread) is a function of the distribution of data, rather than its quantity, nodal parameters can be well-resolved with

a small amount of data which uniformly samples the target volume. This is demonstrated in Figure 26 by the high resolution and low spread values associated with the lower DWS for the shot data set and the 58-source subset of the data (inversion 6), and can also be inferred from the source distribution (Figures 15 and 27). Conversely, lower resolution and higher spread, resulting from highly variable ray density, characterize the inversion of earthquake travel time residuals only (inversion 5).

As reviewed above, inversion 4 using only shot data can independently resolve most of the major velocity heterogeneities. The 32 shots have an initial rms residual of 0.32 s, which is reduced to 0.13 s (83% variance reduction) after four iterations (Table 3). The tomographic inversion allows the use of a larger data set and thus estimates a two-dimensional, along-axis structure that builds upon the preliminary conclusions from the refraction analysis. We note, for future comparison, the existence of well-resolved 7 km/s velocities at 2.5 km depth beneath the volcano and along-axis high; this observation is consistent with the travel times from the southern limb of the refraction line to OBH 3. Comparison of the velocities from inversion 4 with that from inversion 1, as well as from inversions 2-3 and 7-11 which also utilize earthquake and shot sources, suggests biases in the assumed hypocenters which map into incorrect estimates for the velocity ( $< 6$  km/s) at 3 km depth beneath the high; examination of the source distribution reveals that the responsible events are those located beneath the western median valley at the along-axis high, since ray paths from these events would densely sample the upper crust in this area.

The results of inversion 5 using earthquake data illustrate the necessity of constraining the upper crustal structure with accurately-located source data (i.e., shots). Since the earthquakes occur at mid-crustal depths (Figure 16, DWS in Figure 25), all ray paths sample predominantly the same upper crustal section, thereby leading to velocity perturbations within the upper 3-4 km which are poorly constrained (see Figure 25, resolution). This can also be predicted by examining the resolving kernels of the shallow nodes (Figure 19c); the observation of significant off-diagonal components associated with nodes 1-8 implies that these parameters cannot be well-resolved. Comparison with Figure 24 shows that inversion 5 results are not consistent with those estimated by inversion 4 (slower rather than faster velocities are found). From inversion 5, we conclude that the use of a clustered set of earthquake sources will produce misleading and spurious model estimates unless independent data are incorporated to constrain crucial model parameters.

### *Source Dependence*

We also investigated the dependence of the final model on the quantity of sources used in the inversion by varying the number of shots and earthquakes used. Figure 27 shows the source distribution for each test, and Figures 28 and 29 contrast the inversion solutions utilizing only the 21 shots nearest the network and the 37 best-constrained earthquakes (originally located with an S-wave arrival, Chapter 3; Table 3 - inversion 6), with an inversion using all available earthquakes (91 events) and the 32 shots (Table 3 - inversion 7).

Qualitative comparison of the source distribution (Figures 15 and 27) and their respective DWS plots (Figures 22, 28 and 29) indicate that the addition of source data does not significantly increase the amount of independent information available for the model estimate. While the DWS is largest for inversion 7 and smallest for inversion 6, the areas of well-resolved velocities (spread  $< 60$ ) are unaltered by the inclusion or exclusion of travel time data because the ray path geometry of the target volume remains essentially unchanged. Also, initial and final rms residuals, variances, and variance reductions are comparable (Table 3 - inversions 1, 6, 7). Visual comparison of the three velocity models suggests that additional data, which in general only increases the ray path density for a given node rather than expand the spatial sampling, does not alter the patterns of velocity heterogeneity. From an examination of the spread and resolution, we see that all three models represent equally satisfactory estimates of the velocity structure beneath the median valley, but again velocities at the 3-km-deep node beneath the high are low ( $< 6.5$  km/s) compared with those inferred from the shot data ( $> 7$  km/s). Inversion 6 suggests that the use of only the best-constrained events minimizes the effects of biased hypocentral estimates on the model. We cannot determine whether the observed smoothing of variations with an increase in data is a result of better spatial sampling (and thus a truer estimate of the actual structure) or a result of increases in source uncertainty (leading to greater travel time scatter and smaller perturbations in velocity).

### *Receiver Dependence*

In order to assess the dependence of the model on the configuration of receivers, we compared inversions using shot and earthquake data recorded by five- and six-station networks (Figure 30) that excluded instruments located at the base of the eastern wall.

Earthquake sources, located with 5 or 6 OBHs (inversions 8 and 9, respectively), were culled in the same way as for the 7-instrument sources. Inversions with these data resulted in compact resolution (Figures 31 and 32) and similar reductions in variance and rms residual as for the 7-station inversions (Table 3 - inversions 1, 8, 9). The inclusion of travel time data only to five instruments yields a virtually identical velocity structure (compare Figures 21, 22 with Figure 32), resolving all features using only 372 observations (versus 532 to 7 instruments). This inversion is also characterized by a lower initial rms and variance since the travel times to eastern-wall stations with larger uncertainties are not used. Although times to the excluded instruments help to constrain the structure at depth beneath the along-axis high, this appears to be of second-order importance compared with the higher velocities at 3 km beneath the volcano and the decrease in velocity below this region. Note again the lower ( $< 6$  km/s) velocities at 3 km beneath the high.

We conclude from the above tests of robustness that the structure determined in inversion 1 is robust with respect to the configuration of sources and receivers employed. By varying the number of sources and receivers, we have shown that at well-resolved nodes the 2D model shown in Figure 21, parameterized by three along-axis nodal columns (5 km spacing), represents a valid estimate of the average variations in velocity beneath the median valley near and south of the high-temperature hydrothermal field. This result does not imply that the velocity estimates themselves are correct, only that the solution is independent of the source/receiver configuration. Biases in the hypocenters (and thus the travel time residual observations), which can result from the inability of the 1D model to adequately represent the true structure, can lead to the determination of incorrect, though well-resolved, velocities especially in seismically heterogeneous areas. In the next section, we evaluate the effect of earthquake mislocation on the model and conclude that in our study earthquake hypocentral errors do not significantly affect the model estimate, though spurious estimates for some well-resolved nodes are observed. We will argue that tradeoffs in velocity for these nodes are minimized if we use only inner floor sources within 4 km of the ridge axis, and earthquake hypocenters re-estimated with a 2D model that better describes the along-axis structure.

## Effect of Earthquake Mislocation on Model Estimate

### *Conditions for Unbiased Estimates of Hypocenters*

In an earlier discussion, we stated that implicit in the use of fixed earthquake locations for structural inversion is the assumption that the estimated hypocenters are "close" to their true locations. We saw in the Appendix that travel time variations due to small source mislocations are independent of velocity perturbations along the ray path, being a function only of the velocity and takeoff angle at the source. The definition of "small" or "close" is dependent on the model parameterization, or spacing between nodes. For instance, in the simplest case consider the determination of the velocity within a rectangular area using a single travel time observation (Figure 33a). Clearly, the velocity will be perfectly resolved as long as the observation is located within the rectangle; an observation need only be located somewhere within the rectangle to be considered "close." If now the rectangle is divided into two squares (Figure 33b), only the left square will be constrained and the right square unresolved; the size of the "close" box has been halved. For the nodal configuration in our experiment, a "small" source mislocation, or "closeness," can be defined approximately as one-half the grid dimensions (2.5 km in Y and 1 km in Z). Since partial derivatives are weighted linearly according to the ray path's distance from a node, "small" ray path or source errors will change little the proximity of the path to the node, and thus estimated velocity adjustments are not likely to change significantly.

The magnitude of source mislocation is in part a function of the adequacy of a one-dimensional model and station corrections in representing a heterogeneous structure. To the extent that travel time variations can be attributed to velocity anomalies beneath the stations rather than near the source, and that the use of well-recorded earthquakes will result in good estimates of instrument travel time corrections, errors in hypocenter should be minimal. In other words, if the velocity variations we seek through tomographic inversion (as parameterized by the spacing between nodes) are equivalent to the length scales of heterogeneity represented by the station corrections (i.e., the spacing between instruments), then the earthquake locations determined by the one-dimensional method will be "close" to the true hypocenters. In addition, if the heterogeneity is not too severe (so that station corrections do not correspond to averaging over the entire ray path), or is relatively systematic (so that errors are of similar magnitude and sense), then the patterns of

heterogeneity, at least in a two-dimensional case, are independent of source mislocation. We will see that this is the case for the earthquakes in our experiment and that the hypocenters located with a layered velocity structure are "close" to the true locations so that velocity perturbations for most of the nodes are not affected.

### *Relocation of Earthquakes*

In order to quantify the effect of velocity heterogeneity on the earthquake locations, we have relocated the events using the two-dimensional structure estimated from the tomography and refraction analysis. The inversion method incorporates the computationally-efficient ART2 ray tracer [Thurber, 1981] and gives quantitative estimates of the solution quality by performing a singular value decomposition of the partial derivative matrix. The velocity model we use is based on inversion 1 (Table 3, Figure 21); seafloor velocities within the along-axis deep and at the volcano, which were not resolved by the inversion, were estimated by linear extrapolation from the seafloor velocity atop the high assuming isovelocity contours conformal to the 5 km/s contour. In addition, the model assumes that velocities at 5 km extend downward indefinitely. Since we expect that velocities likely increase with depth below the volcano and along-axis high, focal depths of earthquakes in the halfspace may be overestimates. Station corrections were not used since travel times are now calculated with respect to stations at their correct elevations and with a 2D crustal structure.

The relocation of the 69 earthquakes indicates a systematic shift in epicenters to the east ( $1.6 \pm 1.0$  km, Figure 34a) and increases in focal depth ( $1.1 \pm 1.3$  km, Figure 35a); origin time changes were small ( $0.03 \pm 0.18$  s earlier). Changes in the travel times (Figures 35b, 36) were typically  $< 0.2$  s, [e.g.,  $-0.04 \pm 0.13$  s (OBH 6,  $n=61$ ), to  $0.08 \pm 0.20$  s (OBH4,  $n=45$ )]. The  $1-\sigma$  epicentral and depth uncertainties were  $1.1 \pm 1.1$  km and  $1.0 \pm 1.3$  km, respectively. The lack of a variation in travel time differences along axis (Figure 35b), or a significant correlation in average differences with instrument (Figure 36), results in systematic changes in location since on average all travel time observations are affected similarly. The increase in focal depth can be explained largely by the higher upper crustal velocities (see perturbations in Figure 24), which act to "push" hypocenters consistently away from the receivers (i.e., deeper). Larger epicentral shifts were associated with the deeper events since faster velocities persist throughout the crustal column beneath the deep (Figure 34b). Because we are seeking a median valley structure which varies only



along axis (and not across), the eastward translation of epicenters approximately perpendicular to the ridge axis does not significantly alter the geometry of ray paths. The observed translation implies that the relative locations of events are better known than their absolute locations, and is a manifestation of the nonuniqueness of earthquake location algorithms, especially in the presence of 3D heterogeneity.

Comparison of the earthquake hypocenters determined with the 1D model (including station corrections) with those obtained with the 2D model reveals the two estimates to be generally consistent at the 95% confidence level (horizontal and vertical errors for the 1D case are  $2.1 \pm 1.0$  km and  $1.4 \pm 0.8$  km, respectively), implying that the 1D locations represent "close" estimates of the true locations. *Eberhart-Phillips* [1986], in a comparison of northern California earthquakes located by the 3D simultaneous inversion of earthquake and refraction data using Thurber's method with locations estimated using a 1D velocity model with station corrections, found similar differences in epicenter and depth (1-2 km). Her conclusion, which was based on the evaluation of 170 earthquakes and a 64-station network, was that the 3D method would only provide more accurate estimates if the variations in velocity could be constrained over distances smaller than the spacing between stations. Since in this study we seek seismic heterogeneities at wavelengths approximating the distances between stations, our use of the 1D model to estimate hypocentral parameters of well-recorded hypocenters appears to be adequate.

#### *Relationship between Source Location and Model Estimate*

As a final exercise, we explore the effect potential errors in earthquake source location will have on the estimate of the two-dimensional velocity structure. In inversion 10, we use instead the relocated hypocenters determined above along with the 32 shots to determine the laterally-varying structure. Note that the new earthquake data set includes travel time observations which differ by up to 0.2 s (but have a zero mean), corresponding to epicentral and depth changes of typically up to 3 km. The change in hypocenters (i.e., increase in focal depth upon relocation) is attributed largely to the faster velocities over the upper 3-4 km of crust beneath the along-axis high and volcano (and the upper 5 km beneath the deep). Because much of this structure can be independently constrained by the shot data (see velocity perturbations and resolution in Figure 24), we are justified in reestimating the earthquake hypocenters with the above structure; the larger rms<sub>i</sub> and mean initial travel time residuals of the shots (0.32 s and -0.24 s, respectively) compared with those for the

earthquakes (0.11 s and -0.03 s, respectively) (Table 3, Figure 23a) also imply that the shot data contribute largely to the 2D model estimate.

Comparison of inversion 1 with inversion 10 (Figure 37, Table 3) indicates little change in the patterns of velocity heterogeneity along the ridge axis, but shows several significant differences in the estimated velocities at the 3 km depth nodes beneath the volcano and high. Although both models are equally well-resolved and show compact resolution matrices, the much higher velocities (by 0.7 km/s) at these nodes in inversion 10 demonstrate the dependence of the velocity estimate on the assumed hypocenter. The velocity inconsistencies, which result from biased hypocentral estimates for earthquake sources beneath the western median valley at the along-axis high, suggest the presence of velocity variations in three dimensions (i.e., away from the ridge axis, as well as along-axis). Because these events occurred outside the network, and as such are susceptible to travel time anomalies unaccounted for by the assumed station corrections, we must pay careful attention to which sources we use in the tomographic inversion. In the next section, we examine tomographic solutions using only the innermost earthquake sources in order to finally arrive at a 2D model that minimizes the effects of using earthquake locations that could be biased.

### **Minimization of 3D Effects - Inner Floor 2D Model**

#### *Inversion 11 - Shots and Earthquakes (obtained with 1D Model)*

In the above analyses, we suggested that the use of earthquakes to the west of the network may be biasing the velocity estimates of the node at 3 km depth beneath the high and volcano. In particular, it was noted that the bias could be due to the use of events farthest from the ridge axis, which could sample dissimilar crustal structures, or the use of biased earthquake locations, which could result from inadequacies in the 1D model used to estimate the hypocenters.

In order to explore the former scenario, we narrowed the across-axis aperture of the sampling volume, and performed an inversion using only inner floor shots and earthquakes closer to the ridge axis than 4 km (inversion 11, Table 3). The distribution of the 59 sources for this inversion is shown in Figure 38, and the results in Figure 39. Comparison with inversion 1 (Figures 21, 22), which uses 101 median valley sources, shows no change in the patterns of heterogeneity or in the estimates of velocity (all along-axis

velocities were within 0.3 km/s of each other for the nodes at 1, 3, and 5 km depth), though lower values of resolution are associated with inversion 11 because fewer data are used. Based on these results, we conclude that the travel time residuals of events to the west, as well as to the east, of the inner floor events do not introduce a bias to the model estimate.

#### *Inversion 12 - Shots and Earthquakes (obtained with 2D Model)*

The second possible cause of the velocity-hypocenter tradeoff evidenced in Figure 37 is investigated by relocating the inner floor earthquakes using a 2D structure derived from inversion 11. Unconstrained velocities at the seafloor were again replaced by extrapolating from the seafloor velocity at the along-axis high assuming velocity contours conformal to the 5 km/s contour. The earthquake source data were further culled by removing 5 events for which the relocation yielded poor convergence or little constraint on some hypocentral parameters.

Using 23 shots and 31 earthquakes with re-estimated locations, we carried out a tomographic inversion for two-dimensional structure beneath the inner floor (inversion 12). Circular reasoning is avoided because we attribute most of this 2D structure to information provided by the shot travel time residuals, which are much larger than the earthquake residuals (Figure 40a). Our hypothesis here is that by using only the centermost events, and relocating the earthquakes using a 2D structure that better describes the along-axis structure than the 1D model with station corrections, we have minimized the number of biased hypocenters and thus the number of spurious velocity estimates. That the relocated earthquakes may be less biased is suggested by the more consistent initial travel time residuals for inversion 12 (Figure 40a), as compared with those for inversion 1 where -0.2 s residuals to OBH 4 appear as outliers (Figure 23a). Hence, we argue that the inversion 12 model we compute (Figures 41, 42, Tables 3, 6) represents the best estimate of the average structure beneath the inner floor south of the along-axis high. Threshold values of 0.7 and 125 for good resolution and minimal spread, respectively, were determined from an examination of the averaging vector for each velocity parameter.

As can be seen by the comparison of Figures 24 and 41 and Tables 5 and 6, inversion 12 results in a structure that is consistent at well-resolved nodes with that estimated using the shot data (inversion 4), suggesting that hypocentral biases in at least the upper crust have been reduced. Because the shot data do not constrain the model at depths

below 3 km beneath the volcano and high, the model in these regions may still be biased, i.e., variations in three dimensions are being mapped unpredictably into two-dimensional variations; the smaller area enclosed by the 6 km/s contour at 5 km depth beneath the volcano, as compared to that found in inversion 11, for instance, suggests that tradeoffs in velocity with hypocenter are still present though the magnitude of the tradeoff is unclear. For this reason, we cannot constrain with confidence the lowest velocity attained at depth beneath the volcano, other than to say that it may be as low as 5.5 km/s (Table 4, inversion 1); the attenuation of waveform amplitudes beyond 18 km range on OBHs 2 and 3 (Figure 5a,b) constitutes independent evidence that velocities do decrease below 3 km, however.

#### *Effect of 3D Structure on Inner Floor Earthquake Locations*

Although we have attempted to minimize the effects of hypocentral bias on the model estimate by using only the innermost events closest to the ridge axis, there remains the possibility that lateral variations in structure (away from the axis) may contribute significantly to the tradeoffs in velocity observed at depth. To explore the effect of a three-dimensional velocity structure on the earthquake locations, we relocated the 36 inner floor events using hypothetical structural models, parameterized similarly by three along-axis nodal columns, in which velocities increase and/or decrease with distance from the ridge axis; velocities determined from inversion 12 were used for ridge-axis values with seafloor velocities replaced following the same criteria as in the previous relocations. In each of the three test models, the structure beneath the rift mountains was assumed to be homogeneous.

Within the inner floor, three models were considered, one in which velocities symmetrically increased away from the ridge axis, one in which velocities decreased from the axis, and a third in which velocities increased away from the ridge axis at the along-axis deep and decreased away from the axis at the locations of the volcano and along-axis high. Physically, these models would describe velocity increases with the reduction in the large-scale porosity as fissures and pore spaces become sealed within the crust, decreases in velocity as recently extruded and intruded material becomes tectonized, and a combination of the two processes which might be active beneath the inner floor south of the along-axis high. Evidence for systematic changes in velocity with distance from the ridge axis have been documented by a number of authors [e.g., *Christensen and Salisbury, 1972; McClain et al., 1985; Purdy and Detrick, 1986; Purdy, 1987; Toomey et al., 1988; Harding et al.,*

1989]. The magnitudes of the velocity changes were based on the results obtained within the MAR median valley at 23°N, where up to a 1 km/s increase in velocity over a 6-km horizontal distance from the ridge axis was resolved from a tomographic inversion of P wave travel time residuals [Toomey *et al.*, 1988]; we have used their results for the variations to the west of the axis, which are larger, since we want to investigate a limiting case scenario.

Comparison of the hypocenters obtained with these models with the locations estimated with the 2D model in the previous section, reveals epicentral and depth shifts of less than 1 km, and changes in origin time of less than 0.1 s. The differences are much less than those found from the comparison of locations estimated with the 1D and 2D models previously. By analogy with the conclusions of earlier tests, which were based on larger hypocentral changes, shifts in hypocenter observed with the 3D model should not result in significant changes in the velocity model estimate when the travel time residuals are tomographically inverted for structure. We thus conclude that for the inner floor source data set, lateral variations in structure with distance from the ridge axis will not affect the model estimate; we recognize, however, that small localized heterogeneities of significant magnitude could affect the solution, but we lack observational evidence requiring such anomalies.

### **Summary of Tomographic Inversions for 2D Structure**

After exhaustive tests to investigate the effects of the starting velocity model, source type, source/receiver configuration, and earthquake mislocation on the solution, we conclude that the best and most consistent P wave model is obtained from inversion 12. This inversion employs travel time residuals recorded by a 7-instrument network, and explosive and earthquake sources closest to the ridge axis with earthquake hypocenters located with a 2D structure, to estimate the velocity at three nodal columns situated at the along-axis deep, the ridge-axis volcano, and the along-axis high. Such a configuration minimizes the effects of hypocentral biases in the model estimate, though tradeoffs in velocity with changes in hypocenter may still be present at 5 km depth beneath the volcano and high. The source distribution results in good resolution of all velocity nodes, except the 5-km-deep node beneath the along-axis high, within the crust; because of the paucity of sources whose ray paths sample the deeper crustal levels beneath the high, the velocity

estimated for this region is not as well-constrained. Inversion 12 (Figure 41, Table 6) reveals four first order observations about the patterns of along-axis seismic heterogeneity:

- (1) The shallowmost crust (upper 1 km) beneath the volcano and along-axis high is characterized by significantly higher velocities (5.3 km/s) than are associated with the upper crust in the deepest portions of the median valley (3.7 km/s).
- (2) The depth to the 7.2 km/s velocity contour is 1 km shallower beneath the volcano (at 3 km depth) than beneath the along-axis deep to the south (at ~ 4 km depth).
- (3) Velocities beneath the volcano decrease by 1.2 km/s from 3 to 5 km depth. This low velocity region, which is characterized by shallow velocity gradients ( $0.6 \text{ s}^{-1}$ ), is not present beneath the along-axis deep but appears to extend northward under the along-axis high. The shot data are not able to constrain the depth extent of the lower velocities.
- (4) The crust beneath the along-axis deep appears to be typical of normal young oceanic crust [e.g., *Purdy and Detrick, 1986*], with a mantle velocity of 8.25 km/s observed at 5 km depth.

Observations 1, 2, and 4 can be independently resolved by the shot data alone (Figure 24, inversion 4), while observation 3, which describes patterns at depth beneath the volcano and along-axis high, is dependent on the travel time residuals from earthquakes. We note, however, that the imaging of a velocity decrease below 3 km is consistent with the attenuation of first-arriving energy from explosive shots to OBHs 2 and 3 beyond 19 km range.

## DISCUSSION

### Variability of Seismic Layer 2 - Seafloor Velocities

Seismic layer 2 is characterized by P wave velocities ranging from 2.0 km/s upwards to 5.6 km/s, and is thought to consist of pillow lavas and sheet flows underlain by

dikes with a total thickness of less than 3 km [*Basaltic Volcanism Study Project*, 1981]; laboratory-measured velocities of basalts can range up to 6.4 km/s [*Christensen and Salisbury*, 1972, 1973]. Together with lithological analogies with ophiolites [e.g., *Peterson et al.*, 1974; *Christensen and Smewing*, 1981], a number of seismic investigations [*Bratt and Purdy*, 1984; *Harding et al.*, 1989] and physical property studies of dredged or drilled rock samples [*Hyndman and Drury*, 1976; *Anderson et al.*, 1982] have led to the proposal that layers 2A, 2B, and 2C correspond to high- to low-permeability basalt extrusives that grade into sheeted dykes.

Mid-ocean ridge seismic studies have documented a wide range of seafloor velocities [e.g., *Whitmarsh*, 1975; *Spudich and Orcutt*, 1980a, b; *Ewing and Purdy*, 1982; *McClain et al.*, 1985; *Purdy and Detrick*, 1986; *Purdy*, 1987; *Burnett et al.*, 1989; *Harding et al.*, 1989], but because water wave arrivals from sea surface sources often mask refracted energy from the shallow seafloor, the description of seismic layer 2 from conventional refraction studies (such as in this study) must be viewed as an average integrated over sublayers 2A, 2B, and 2C. Several recent investigations, however, have been able to successfully resolve the nature of layer 2A. From the results of an experiment using near-bottom seismic sources (50 m shot spacing) and receivers, *Purdy* [1987] reported the presence of low seafloor velocities (2.1 km/s underlain by a  $4 \text{ s}^{-1}$  gradient over the upper 200 m) at the ridge axis of the Mid-Atlantic Ridge at  $23^\circ\text{N}$  (Ocean Drilling Program site 648), and inferred seafloor porosities of 30-50% for layer 2A from the comparison with laboratory velocity measurements of basalt recovered at the site. In a detailed study of expanding spread data (50 m sort bins for each shot) at  $13^\circ\text{N}$  on the East Pacific Rise (EPR), *Harding et al.* [1989] documented a thin layer (< 200 m) of low seafloor velocities (2.3 - 3.0 km/s), which they proposed to be correlated with the relatively permeable aquifer (bulk porosity ~ 13%) of pillow lava rubble, breccia, and fractured crust comprising layer 2A within Deep Sea Drilling Project hole 504B drilled in 6.2 My crust in the Pacific [*Anderson et al.*, 1982, *Becker et al.*, 1982].

Overall, the uppermost crust is characterized by steep velocity gradients (up to  $5.5 \text{ s}^{-1}$ ) which describe rapid increases in velocity (to > 5 km/s) over the upper kilometer of crust. The increase has been attributed to the transition into less-porous material [*Hyndman and Drury*, 1976; *Spudich and Orcutt*, 1980a]; for instance, drilling results from hole 504B suggest that the layer 2A/2B transition is characterized by a decrease in the bulk porosity (to 8%) [*Anderson et al.*, 1982]. Studies show that seismic velocities in the shallowmost crust are controlled primarily by the large-scale porosity, or extent to which low velocity

materials such as water or sediments are able to fill voids created by fracturing and cracking [O'Connell and Budiansky, 1974; Spudich and Orcutt, 1980a; Christensen, 1984; Shearer, 1988]. At the ridge axis on the fast spreading EPR, the generally high velocities ( $> 5$  km/s) characterizing the uppermost crust are suggested to correspond to regions of recent volcanism that have yet to experience the fracturing that increases porosity and lowers seafloor velocities with distance from the axis [McClain *et al.*, 1985; Harding *et al.*, 1989]. Conversely, the generally lower velocities ( $< 4$  km/s) found along the slow spreading MAR are caused by a highly fissured crust where tectonic forces dominate with fewer episodes of volcanism [Keen and Tramontini, 1970; Whitmarsh, 1975; Purdy and Detrick, 1986].

Under such a scenario, the decrease in layer 2 velocities to the south away from the along-axis high and hydrothermal field near  $26^{\circ}\text{N}$  suggests a more fractured or porous crust with low seafloor velocities beneath the inner floor deep ( $V_p = 3.73$  km/s), and a more consolidated crust with higher seafloor velocities (5.34 km/s) beneath the volcano and along-axis depth minimum. The lower velocities within the upper 1 km of crust beneath the deep ( $V_p < 4.5$  km/s) are consistent with those found along the ridge axis at  $23^{\circ}\text{N}$  [Purdy and Detrick, 1986; Purdy, 1987] (Figure 43), where no low velocity zone was observed. In contrast, the higher velocities from 0.5 - 1.2 km depth ( $V_p > 4.5$  km/s) near the active high-temperature hydrothermal field and overlying the low velocity region appear to be similar to those characterizing the EPR ridge axis at  $13^{\circ}\text{N}$  [Harding *et al.*, 1989], where an axial low velocity zone and hydrothermal activity are well-documented. If we hypothesize that the higher velocities describe recently-extruded basalts or intruded dikes (i.e., tectonic fracturing is minimal and the large-scale porosity small), then it is inferred that the most recent volcanism along the median valley at  $26^{\circ}\text{N}$  occurred in the along-axis high region. In a slow spreading environment where magmatic activity appears to be less robust, layer 2A velocities at  $26^{\circ}\text{N}$  can be thought of as indicators of the length of time since the last episode of magmatic accretion, with velocities decreasing as the proportion of tectonic fissuring and thus large-scale porosity increases (after the cessation of volcanic activity). By this view, hydrothermal circulation and cracking of young oceanic crust, which would lower velocities somewhat, has only a secondary effect on the seismic structure of the Mid-Atlantic Ridge compared with extensional tectonism.

Seismic anisotropy, in which the fast direction is perpendicular to the spreading direction, has been used to explain the sinusoidal variation with azimuth in P wave travel times and the arrival of horizontally polarized shear waves before vertically polarized shear waves for shot data sampling 6-my-old crust in the equatorial Pacific [Stephen, 1985]. The



observed anisotropy is inferred to result from the preferred orientation of large-scale fractures and fissures in upper layer 2. Because the imaged velocity structure in this study was obtained by using only the innermost well-recorded shots, most ray paths are nearly along the ridge axis. We believe that the observed velocity variations cannot, therefore, be attributed to anisotropy.

### Variability in Depth to Layer 3

Seismic layer 3 is defined as a region of shallow velocity gradients with P wave velocities ranging from 6.5 km/s to 7.5 km/s [*Basaltic Volcanism Study Project*, 1981]; integration of seismic studies, dredging programs, and laboratory measurements of rock velocities suggests that layer 3A is probably composed of gabbro, or its metamorphosed counterparts, and that velocities are relatively uniform ( $V_p \sim 7.2$  km/s), while layer 3B velocities are intermediate between laboratory velocities for gabbro and peridotite ( $V_p \sim 8.2$  km/s) and may possess higher velocity gradients [*Christensen and Salisbury*, 1975; *Hyndman and Drury*, 1976; *Spudich and Orcutt*, 1980a]. From ophiolite studies, layer 3A may encompass the transition from sheeted dikes to coarse-grained isotropic gabbros, and layer 3B may correspond to deeper-lying layered gabbros and ultramafic cumulates near the seismic Moho [*Peterson*, 1974].

The depth to the top of the low velocity zone at 26°N is about 3 km beneath the volcano and along-axis high ( $V_p = 7.2$  km/s at 3 km depth). Based on laboratory-derived velocities and typical refraction line estimates for seismic layer 3, we suggest that the lid at 3 km depth is located within the high-level gabbroic intrusives of layer 3. Since our model parameterization has nodes at depths of only 1, 3 and 5 km, we are not able to constrain the depth at which velocities first decrease, but synthetic seismogram modelling of the refraction line is consistent with a velocity inversion at about 3 km. Beneath the along-axis deep, the depth to the 7.2 km/s velocity contour is about 4 km. The 1 km shoaling toward the region of inferred most-recent volcanism (at the along-axis high) is similar to the variation observed along a 50 km section of the Northern Symmetric segment of the Juan de Fuca Ridge, where the thickness of the layer over the ridge axis low velocity zone shoals from 3.5 to 3.0 km, also toward the along-axis high [*Christeson et al.*, 1989; G. Christeson, pers. comm., 1990] (Figure 44, light dashed lines).

If we interpret the depths to low velocity zones as relative indicators of magmatic activity, then we may hypothesize that the most likely locale for the eruption of basalt onto

the seafloor would be in an area where the lid is the thinnest, i.e., where the intrusion comes closest to the seafloor; thicker lids would describe regions where magmatic activity is less recent (temporal variability), or regions where magmatic activity is less robust (spatial variability). In our experiment, the thinnest lid is found in the along-axis high region where the youngest basalts do appear to be located [*Rona et al.*, 1986; *Zonenshain et al.*, 1989], and the highest seafloor velocities are found. Similarly, the larger depth to the 7.2 km/s velocity contour beneath the along-axis deep (about 4 km) implies that magmatic activity is less recent (or not as common) and that extensional tectonism presently dominates in this region, an inference which is consistent with the conclusions of the microearthquake study (Chapter 3). Furthermore, by this scenario we would interpret the large lid thickness (4 km) and small velocity inversion observed at 59°N on a locally shallow portion of the MAR [*Bunch and Kennett*, 1980] as an area where a longer period of time (than at 26°N) has elapsed since the last magmatic intrusion (Figure 44).

The above hypothesis is reasonable if we also consider the converse, that in areas where recent extrusion has occurred, such as along the faster spreading EPR, we would expect the lid to be the thinnest. Observational evidence indicates that depths to the low velocity zone at 13°N on the EPR [*Harding et al.*, 1989] are indeed shallower (1.3 - 2.2 km below the seafloor) than those observed both along the Juan de Fuca Ridge and at 26°N and 59°N on the MAR (Figure 44).

### Low Velocity Zone

The inference from geochemical evidence that magma mixing and low-pressure fractionation are common processes [e.g., *Bryan et al.*, 1977, 1981; *Rhodes et al.*, 1979; *Langmuir et al.*, 1986], the mapping of magma chamber-like boundaries in ophiolites [*Pallister and Hopson*, 1981; *Casey and Karson*, 1981; *Nicolas et al.*, 1988], and the documentation of low velocity anomalies at depths of ~ 3 km depth beneath subaerial volcanos in Hawaii, Iceland and Oregon [*Thurber*, 1984; *Toomey and Foulger*, 1989; *Achauer et al.*, 1988, respectively] make it reasonable to propose the existence of magma chambers at volcanically-active spreading centers. The imaging of a zone of very low P-wave velocities at depths of 1.5 to 2 km below the seafloor on the fast-spreading EPR comprise the first widely accepted observations of mid-ocean ridge magma chambers [*Orcutt et al.*, 1976; *McClain et al.*, 1985; *Detrick et al.*, 1987; *Burnett et al.*, 1989; *Harding et al.*, 1989; *Toomey et al.*, 1989]. Strong reflections from the top of the chamber

at 9°N [Hale *et al.*, 1982] and at 13°N, where significant attenuation of compressional wave energy beyond 11 km is also observed [Detrick *et al.*, 1987], suggest the presence of a layer of significant melt fraction. From the analysis of expanding spread data gathered at four locations both along and up to 10 km from the ridge axis at 13°N, Harding *et al.* [1989] find a low velocity body with a half-width of at least 6 km. They infer that this body is composed almost entirely of hot rock, however, with only a thin layer of partial melt (less than 4 km in width and 1 km in thickness) at the top of the chamber required to satisfy the multi-channel reflection data of Detrick *et al.* [1987] and Mutter *et al.* [1988].

The region of lower velocities at depth beneath the volcano and along-axis high imaged in this study appears to be a robust characteristic of the seismic structure near 26°N on the slow spreading Mid-Atlantic Ridge. The severe attenuation in the first arriving energy past 19 km range to instruments atop the along-axis high is consistent with a velocity inversion below 3 km depth, but the propagation of shear waves from shots whose ray paths traverse the median valley to OBS 31 atop the eastern wall implies that large amounts of melt are not present in at least the upper portion of the low velocity zone (Chapter 3). In addition, the variability in the reduced travel times over the 19-30 km range from shots along the southern limb of the refraction line to instruments atop the along-axis high indicates that the low velocity layer is not continuous along the ridge axis. If we assume that earthquakes result from brittle failure, then we can use the distribution of focal depths to delineate regions where the crust appears to be more brittle or ductile (at least over the deployment period). The occurrence of earthquakes at 3 km depth at the top of the low velocity zone and at 6 km depth below the region of decreasing velocity constrains the maximum thickness of the low velocity zone to be about 3 km at this latitude (Chapter 3, Figure 43).

The gentle velocity gradients describing the region of low velocities beneath the volcano and along-axis high are consistent with the characteristics of seismic layer 3A [Spudich and Orcutt, 1980a], but the velocities are much lower than those conventionally measured for gabbro in the laboratory at room temperature ( $V_p \sim 7.2$  km/s). This suggests the presence of a zone of elevated temperatures, which acts as the heat source for the active high-temperature black smoker vent field. For a linear temperature dependence of velocity of  $-6 \times 10^{-4}$  km/s/°C (as measured by Christensen [1979] over 25-300°C and 3-8 kbar), a 1 km/s decrease in velocity would correspond to a nominal temperature anomaly of more than 1500°C, yielding a temperature well in excess of the solidus temperature for crustal material. The zone cannot contain substantial pockets of partial melt, however, since shear

waves appear to propagate through this region. Furthermore, if we assume that the basalts erupted on the seafloor originated from within a chamber, then we see that the observed velocities ( $V_p = 5.5 - 6.0$  km/s) are much higher than laboratory-measured velocities for basaltic melts [ $V_p < 3$  km/s, *Murase and McBirney*, 1973; *Manghnani et al.*, 1986]. One possible explanation is that the temperature derivative of P wave velocity increases significantly in magnitude as the solidus temperature approaches, but this possibility remains to be verified experimentally for oceanic gabbros.

Several other plausible lithologies are consistent with the observed velocities, but a scenario in which the low velocity region represents the seismic expression of a cooling intrusion appears to be the simplest and most reasonable interpretation. Alternatively, the velocities observed at 5 km depth could correspond to a stock of plagiogranite within layer 3 [ $V_p = 4.8 - 5.9$  km/s, *Christensen*, 1977], such as found at the uppermost levels of a chamber in ophiolites; structural mapping within ophiolites suggests a thickness of less than 1 km [*Casey and Karson*, 1981; *Christensen and Smewing*, 1981], which is thinner than that implied near 26°N. Laboratory velocities of serpentinites range from 4.5 to 6.5 km/s [*Christensen*, 1972], but are more commonly found associated with the valley walls [e.g., *Karson et al.*, 1987], which provide pathways for the interaction of seawater with peridotite, than beneath the ridge axis. Lastly, the observed velocities could correspond to a layer of basalt located deep within the crust, but no geological or structural evidence for such an occurrence exists in the literature.

Along the Mid-Atlantic Ridge, several refraction studies have presented evidence for crustal intrusive bodies, or anomalously thin crust beneath the median valley. *Fowler* [1976], using synthetic seismograms, proposed the existence of only a 3-km-thick crust underlain by an anomalously low 7.2 km/s upper mantle at the ridge axis at 37°N; the propagation of shear waves across the ridge axis, and gradual decrease in amplitudes with range beyond 20 km were used to argue that no sizeable magma chamber could be present. While the 3 km crustal thickness for 37°N is comparable to the depth of the 7.2 km/s velocity contour beneath the volcano and along-axis high at 26°N, no decrease in velocity was required at 37°N. A refraction study at 45°N [*Fowler*, 1978] yielded similar results to those found at 37°N, with an absorptive zone within the upper mantle, but again no large crustal magma chamber.

Beneath the along-axis high at 23°N on the MAR, *Purdy and Detrick* [1986] found a 15-km zone of slightly lower velocities at the base of layer 3 ( $0.5$  s<sup>-1</sup> from 3 - 6.5 km depth,  $-0.4$  s<sup>-1</sup> from 6.5 - 8.5 km depth), which they interpreted as the seismic remnants of

the last magmatic intrusion along the 120 km section of ridge south of the Kane Fracture Zone. Similarly, *Bunch and Kennett* [1980] observed a small velocity inversion (giving rise to a 6.6 km/s isovelocity layer from 4-5.6 km depth) at an along-axis high region at 59°30'N on the MAR, which they attributed to a region of elevated temperatures at the ridge axis. The results of the two experiments represent the best seismic evidence (other than this study) supporting the presence of a crustal low-velocity zone on the MAR. A comparison of the anomalous volumes with that at 26°N ( $-0.3 \text{ s}^{-1}$  from 3-5 km depth over a distance of  $\sim 12$  km) shows much similarity in the gradient structure and along-axis extent of these zones. In particular, it is suggested that shallow velocity gradients within the lower crust that extend over 10-15 km lengths of the ridge axis may seismically characterize magmatic intrusions on the slow-spreading Mid-Atlantic Ridge. Differences in velocity and depths to the anomalous zone could describe a spatially-variable distribution of active magmatism along the ridge, or alternatively a temporally-variable accretionary process in which differences are a function of the length of time since the last intrusive event.

#### **Along-axis Structural Variations in Crustal Accretion**

The determination of the seismic velocity structure along a 25-km section of the inner floor south of the along-axis high near 26°N reveals systematic changes in velocity over distances of 5 km or less. We interpret the heterogeneity as evidence that crustal accretion is not a steady-state process along slow spreading Mid-Atlantic Ridge, but varies within the inner floor. At 26°N, the seismic and geologic data document preferred regions of active crustal construction as well as locales where tectonism is most important.

Integration of the crustal structure with the results of the microearthquake survey (Chapter 3) suggests that the most recent locus of magmatic activity is concentrated at the along-axis high region where the hydrothermal field is located. The imaging of a low velocity zone, whose lid is situated at about 3 km depth, beneath the volcano and along-axis high, and an absence of microearthquake activity within this zone are consistent with the presence of a volume of hot rock (Chapter 3, Figure 43); the propagation of S waves through this region precludes the existence of a large body of partial melt (Chapter 3). If we interpret the earthquakes at 3 km depth and at 6 km depth beneath the volcano as resulting from thermal contraction at the edges of the thermal anomaly, then the low velocity zone may be thought of as a 3-km-thick cooling intrusion within seismic layer 3 (Chapter 3, Figure 43). In contrast, both the velocity structure and focal depth distribution

of earthquakes suggest the crust beneath the along-axis deep to be characteristic of normal young oceanic crust such as found beneath a similar morphological deep at 23°N by *Purdy and Detrick* [1986] and *Toomey et al.* [1985, 1988]. The low seafloor velocities indicate that the inner floor deep near 26°N is dominated at present by extension. The systematic decrease in seafloor velocities away from the inner floor high appears to describe seismically the transition from active accretion at the along-axis high to active tectonism within the inner floor deep.

## CONCLUSIONS

Results from travel time and waveform modelling analysis of the seismic refraction line and tomographic inversion of shot and earthquake travel time residuals for P wave structure show variations, over wavelengths of 5-10 km, in the along-axis seismic velocity structure. The structural variations imply that crustal accretion at slow spreading centers is not a steady state process, but appears to be localized at present beneath the shallowest along-strike portion of the inner floor.

Higher velocities (by more than 1 km/s) are associated with the upper 1-2 km of crust at the along-axis high than with the crust in the deepest portions of the median valley. It is inferred that the variation is a result of more recent volcanic activity in the along-axis high region, as compared with the along-axis deep where tectonic fissuring has created a highly porous crust characterized by lower seafloor velocities. The crust beneath the along-axis deep appears to be typical of normal young oceanic crust, and is characterized by low seafloor velocities with mantle velocities observed at 5 km depth.

Further, we image a low velocity zone centered beneath an axial volcano and extending under the along-axis high. From 3 to 5 km depth within this zone, velocities decrease from 7.2 km/s to 6.0 km/s. The presence of an active high-temperature hydrothermal field atop the along-axis high, together with the observations of lower P wave velocities, the absence of microearthquake activity greater than 4 km depth, and the propagation of S waves through the crust beneath the volcano and along-axis high (Chapter 3), suggest that the low velocity zone corresponds to a region of hot rock with no seismically-resolvable pockets of partial melt. The shallow velocity gradients describing the low velocity volume appear to be characteristic of inferred zones of magmatic intrusion on the MAR. The depth to the velocity inversion (about 3 km) is comparable to that observed along the Juan de Fuca Ridge, smaller than that found at 59°N on the MAR, but

less than that seen on the fast-spreading EPR. Such a correlation with spreading rate may imply that the amount of magma available at each location is spatially variable, or that the differences in lid thickness are describing the temporal evolution of magmatic intrusions beneath mid-ocean ridges.

## Appendix. Seismic Tomography Method and Theory

For a given set of body-wave travel times from a set of sources to receivers, we seek the Earth model which best satisfies our observations. Our goal is to determine the P-wave velocity structure which minimizes the travel time residuals and at the same time maximizes the model resolution. An observation is related to the velocity structure by the travel time functional,

$$T = \int_{\text{path}} V(\underline{r})^{-1} ds = \sum_{i=1}^N \Delta s_i / V(\underline{r}) \quad (1)$$

where  $T$  is the travel time from a source to a receiver, and  $V(\underline{r})$  is the velocity at some point  $\underline{r}(x,y,z)$ . In the discrete formulation,  $\Delta s_i$  is an element of arc length along a path described by  $N$  segments. Our convention in the Appendix will be that vectors are underlined and matrices are in bold face. In this study, the method of solution involves the inversion of travel time data from both shots and earthquakes for velocity structure. Because of the finite number of sources and receivers, we choose to hold the earthquake locations fixed throughout the inversion. This assumes that the earthquake hypocenters are sufficiently "close" to their true locations so that travel time perturbations resulting from errors in source location are small and do not affect the estimates of the velocity structure.

### Hypocentral Partial Derivatives

To understand this assertion, we use a variational argument to derive an expression for the change in travel time,  $\delta T$ , relative to the spatial hypocentral parameters for a small change in the source location. Following *Lee and Stewart* [1981] and *Thurber* [1981], we can write in general

$$\delta T = \frac{\partial T}{\partial x} \delta x + \frac{\partial T}{\partial y} \delta y + \frac{\partial T}{\partial z} \delta z \quad (2)$$

In order to find  $\partial T/\partial x$ ,  $\partial T/\partial y$ , and  $\partial T/\partial z$ , we introduce a new parameter  $q$  and reparameterize the travel time functional (1), letting  $\underline{r}$  be a function of  $q$ . An increment of the path may be written



$$ds = (\dot{x}^2 + \dot{y}^2 + \dot{z}^2)^{\frac{1}{2}} dq \quad (3)$$

where the dot represents differentiation with respect to  $q$ . Further, we can then write

$$T = \int w dq$$

where

$$w = (\dot{x}^2 + \dot{y}^2 + \dot{z}^2)^{\frac{1}{2}} / V(\mathbf{r})$$

Since Fermat's principle states that the travel time is stationary for close ray paths, the change in travel time due to a small change in hypocenter can be written

$$\delta T = \int_{\text{path}} \delta w dq = \int_{\text{source}}^{\text{receiver}} \left( \frac{\partial w}{\partial x} \delta x + \frac{\partial w}{\partial y} \delta y + \frac{\partial w}{\partial z} \delta z + \frac{\partial w}{\partial \dot{x}} \delta \dot{x} + \frac{\partial w}{\partial \dot{y}} \delta \dot{y} + \frac{\partial w}{\partial \dot{z}} \delta \dot{z} \right) dq$$

Integration by parts results in

$$\begin{aligned} &= \left[ \frac{\partial w}{\partial \dot{x}} \delta x + \frac{\partial w}{\partial \dot{y}} \delta y + \frac{\partial w}{\partial \dot{z}} \delta z \right]_{\text{source}}^{\text{receiver}} - \int_{\text{source}}^{\text{receiver}} \left( \frac{d}{dq} \frac{\partial w}{\partial \dot{x}} - \frac{\partial w}{\partial x} \right) \delta x dq \\ &\quad - \int_{\text{source}}^{\text{receiver}} \left( \frac{d}{dq} \frac{\partial w}{\partial \dot{y}} - \frac{\partial w}{\partial y} \right) \delta y dq - \int_{\text{source}}^{\text{receiver}} \left( \frac{d}{dq} \frac{\partial w}{\partial \dot{z}} - \frac{\partial w}{\partial z} \right) \delta z dq \end{aligned}$$

For a minimum time path, the integrals vanish (equating the integrands to zero gives Euler's equations), and since the receiver location is fixed, the travel time variation simplifies to

$$\delta T = \left[ \frac{\partial w}{\partial \dot{x}} \delta x + \frac{\partial w}{\partial \dot{y}} \delta y + \frac{\partial w}{\partial \dot{z}} \delta z \right]_{\text{source}} \quad (4)$$

From (2), (3), and (4), we can write the spatial hypocentral partial derivatives as

$$\frac{\partial T}{\partial x} = \left[ \frac{1}{V} \frac{dx}{ds} \right]_{\text{source}} \quad (5)$$

$$\frac{\partial T}{\partial y} = \left[ \frac{1}{V} \frac{dy}{ds} \right]_{\text{source}}$$

$$\frac{\partial T}{\partial z} = \left[ \frac{1}{V} \frac{dz}{ds} \right]_{\text{source}}$$

Note that (5) states that the travel time variation due to a small perturbation in source location is dependent only on the velocity and direction cosines at the source, and is independent of velocity anomalies along the ray path and path of integration. *Pavlis and Booker* [1980] and *Spencer and Gubbins* [1980] have used this result to justify the separation of the earthquake location problem from the velocity perturbation determination, thereby reducing the computational effort to the inversion of two much smaller matrices and making the iterative simultaneous inversion algorithm tractable.

### Estimation of Velocity Perturbations

The general procedure for estimating velocity perturbations to an initial model from observed travel time residuals is through the iterative solution of a linearized system of equations. For an assumed velocity model, travel time residuals are calculated by solving the forward problem for known source-receiver combinations. The travel time partial derivatives with respect to each velocity parameter are computed next, and linear inverse theory is used to obtain a set of parameter adjustments and a new estimate of the velocity model. This process is repeated until convergence is achieved, in this case specified by an F test of the ratio of iteration step variances to determine if reductions in variance are significant at the 95% level. Because the use of a finite set of  $n$  data to estimate a discrete set of  $m$  velocity parameters, which describe a naturally continuous function, will almost always lead to the poor resolution of some model parameters, the problem in general will be underdetermined. However, as long as  $n > m$ , the problem is also overconstrained and

no unique solution can be found. A discussion of the method of damped least squares and the tradeoff between model resolution and covariance for the underdetermined, overconstrained problem has been presented by *Wiggins* [1972] and *Jackson* [1972, 1979]. The Levenberg-Marquardt technique, which is used in this study, has been historically employed in seismic tomography studies to damp spuriously large perturbations associated with poorly constrained parameters [*Aki and Lee*, 1976; *Crosson*, 1976a,b; *Thurber*, 1983, 1984].

### *Velocity Model Parameterization and Calculation of Travel Times*

In the *Thurber* [1981] method, the Earth model is parameterized by a discrete set of velocities on a three-dimensional grid. The representation is general, i.e., nodes can be spaced irregularly, thus enabling all scales of heterogeneity to be investigated by choosing an appropriate grid size and spacing. The velocity at any position,  $\mathbf{r}$ , is defined as a linear average of the surrounding nodal velocities,

$$V(\mathbf{r}) = \sum_{i=1}^8 w_i(\mathbf{r}) v_i \quad (6)$$

where  $v_i$  represents a nodal velocity and  $w_i$  is a weighting function defined by the physical distance between the point and each node. This parameterization allows the specification of a continuous velocity field (gradient description) from the nodal velocities. In this study, the ability to specify the velocity model at three points along-axis that are of morphological and geological interest, and at depths which approximate changes in crustal gradients, makes this representation superior to the constant layer [*Crosson*, 1976a, b] and uniform block [*Aki and Lee*, 1976] parameterizations.

The problem of determining accurate travel times through a three-dimensional structure has typically been approached through three-dimensional ray tracing techniques using either an initial value [*Lee and Stewart*, 1981] or boundary value formulation [*Pererya et al.*, 1980]. Because these methods are rather time-consuming, especially in an iterative simultaneous inversion problem, *Thurber* [1981] has developed a computationally efficient and fast approximate ray tracing routine (ART2) which can calculate accurate travel times over local distances. The travel time error,  $-0.01 \pm 0.01$  s for simple ray paths at

distances < 35 km, is often much less than the estimated picking error ( $\pm 0.04$  s for shots,  $\pm 0.05$  s for earthquakes in our study). ART2 calculates the predicted time by seeking the minimum travel time from a family of times computed for a large number of arcs and semi-circular paths from the source to the receiver through the parameterized three-dimensional velocity model.

### *Velocity Partial Derivatives*

In the forward problem, travel time residuals are obtained from the calculated and observed data. To build the medium partial derivative matrix, we need an expression for the change in travel time due to a small perturbation in velocity. Following *Thurber* [1981], we define the travel time residual,  $b$ , as

$$b = T_{\text{obs}} - T_{\text{calc}} \quad (7)$$

and seek to satisfy the equation

$$T_{\text{obs}} - (T_{\text{calc}} + \Delta T_{\text{calc}, \Delta v}) = 0 \quad (8)$$

Combining (7) and (8) we have

$$b = \Delta T_{\text{calc}, \Delta v} = \sum_{j=1}^m \frac{\partial T}{\partial v_j} \Delta v_j \quad (9)$$

where  $\Delta T_{\text{calc}, \Delta v}$  depends on the sum of all travel time variations associated with each of the  $m$  nodal velocity perturbations  $\Delta v_j$ . An expression for  $\partial T / \partial v_j$  derived from the differentiation of (1) can be written as

$$\frac{\partial T}{\partial v_j} = - \int_{\text{path}} \frac{\partial V(\underline{r})}{\partial v_j} V(\underline{r})^{-2} ds \quad (10)$$

In the discrete form, we use the *Thurber* [1981] model parameterization (6) and substitute into (10) to get

$$\begin{aligned} \frac{\partial T}{\partial v_j} &= \sum_{i=1}^N -\Delta s_i / V(\mathbf{r})^2 \frac{\partial}{\partial v_j} \left[ \sum_{p=1}^8 w_p v_p \right] \\ &= \sum_{i=1}^N -\Delta s_i w_j / V(\mathbf{r})^2 \end{aligned} \quad (11)$$

where the ray path is composed of  $N$  arc length segments  $\Delta s_i$ . From (11) we can see that the travel time perturbations with respect to each velocity perturbation depend on the velocity,  $V(\mathbf{r})$ , along the ray path. In the inversion, velocity perturbations at each step are limited to 0.5 km/s to maintain the first order linearity assumption.

#### *Solving the Linear System of Equations*

In matrix form, the inverse problem can be cast in the form

$$\mathbf{A} \Delta \mathbf{x} = \mathbf{b} \quad (12)$$

where  $\mathbf{A}$  is an  $[n \times m]$  matrix of medium partial derivatives,  $\Delta \mathbf{x}$  is an  $[m \times 1]$  model vector of velocity adjustments, and  $\mathbf{b}$  is an  $[n \times 1]$  data vector of travel time residual observations. The normal equations will also include components of random (reading error, clock uncertainties) and non-random (parameterization inadequacies) error, but for simplicity they are excluded in the following discussion. We seek solutions to (12) by finding the inverse of  $\mathbf{A}$ , so

$$\Delta \mathbf{x} = \mathbf{A}^{-1} \mathbf{b} \quad (13)$$

An informative technique for determining  $\mathbf{A}^{-1}$ , which provides information on the solution stability and parameter resolution and error, is through the singular decomposition of  $\mathbf{A}$  [Lanczos, 1961]. In general,  $\mathbf{A}$  can be decomposed into

$$\mathbf{A} = \mathbf{U} \mathbf{S} \mathbf{V}^T \quad (14)$$

where  $\mathbf{U}$  and  $\mathbf{V}$  are  $[n \times n]$  and  $[m \times m]$  matrices of eigenvectors that span the data and model spaces, respectively,  $\mathbf{S}$  is an  $[n \times m]$  diagonal matrix whose diagonal elements correspond to the eigenvalues or singular values of the system, and  $\mathbf{T}$  denotes transpose. In addition,  $\mathbf{U} \mathbf{U}^T = \mathbf{V} \mathbf{V}^T = \mathbf{I}$  (identity matrix), and the eigenvectors are orthogonal to each other and of unit length. The solution,  $\underline{\Delta x}$ , is then written as

$$\underline{\Delta x} = \mathbf{U} \mathbf{S}^{-1} \mathbf{V}^T \underline{b} \quad (15)$$

where  $\mathbf{U} \mathbf{S}^{-1} \mathbf{V}^T$  is known as the generalized inverse or Moore-Penrose operator, and here the diagonal elements of  $\mathbf{S}^{-1}$  are the reciprocals of the diagonal elements of  $\mathbf{S}$ . The generalized inverse operator is equivalent to a classical least squares operator for  $n > m$ , and  $m = k$ , where  $k$  is the number of linearly independent parameters. However, since in practice the problem is underdetermined, the matrix  $\mathbf{S}^{-1}$  will not be full rank, and  $m > k$ . In this case, where near-zero or zero-valued eigenvalues exist, use of the generalized inverse will lead to spuriously large velocity adjustments for poorly constrained model parameters [Crosson, 1976a].

In order to avoid solution instability resulting from near-zero singular values [Aki and Lee, 1976], most seismic tomography studies utilizing discrete model spaces have employed the Levenberg-Marquardt method of damped least squares. By minimizing the weighted sum of travel time residuals and solution vectors, the normal system of equations and corresponding solution becomes

$$(\mathbf{A}^T \mathbf{A} + \lambda^2 \mathbf{I}) \underline{\Delta x} = \mathbf{A}^T \underline{b} \quad (16)$$

$$\underline{\Delta x} = \mathbf{V} [(\mathbf{S}^2 + \lambda^2 \mathbf{I})^{-1} \mathbf{S}] \mathbf{U}^T \underline{b} \quad (17)$$

where a damping parameter,  $\lambda$ , is now introduced [Levenberg, 1944; Marquardt, 1963]. The inclusion of  $\lambda^2$  in the inversion has the effect of modifying the eigenvalue spectrum so that small eigenvalues do not produce large perturbations, while for large eigenvalues the addition of  $\lambda^2$  changes little the magnitude of the adjustment. Wiggins [1972] has utilized a sharp eigenvalue cutoff, rather than the damping filter, with similar results.

The choice of  $\lambda$  is motivated by the desire to obtain stable solutions with reasonable variances and is often chosen by trial and error. The tradeoff between covariance and resolution is a well-known product of the damping parameter magnitude in problems where

$m > k$ . Resolution is maximized for  $\lambda = 0$  at the expense of larger covariances, while for large  $\lambda$ , travel time residuals are minimized but parameter resolution decreases. The use of a damping parameter also decreases the potential number of degrees of freedom  $k$ , since smoothing of the singular values occurs [Wiggins, 1972].

## Evaluation of Solution Quality

### *Resolution and Covariance Matrices*

The singular value decomposition technique enables one to examine the solution quality quantitatively through the construction of the resolution and covariance matrices [Wiggins, 1972; Jackson, 1972, 1979]. The matrices are functions of the data kernel and *a priori* information (not the actual data), and as such give measures of how well a model and distribution of data will be able to estimate an Earth structure. For the method of damped least squares, the resolution matrix  $\mathbf{R}$ , which examines the effect adjacent nodes have on the model parameterization, is defined as,

$$\mathbf{R} = \mathbf{V} [(\mathbf{S}^2 + \lambda^2 \mathbf{I})^{-1} \mathbf{S}^2] \mathbf{V}^T \quad (18)$$

In the ideal case,  $\mathbf{R} = \mathbf{I}$  implies that the model is perfectly resolved by the given data kernel. However, in reality the rows of the resolution matrix, or resolving kernels, never take on a  $\delta$ -like appearance. Wiggins [1972] proposes the term "compact" for  $\mathbf{R} \sim \mathbf{I}$ , and Backus and Gilbert [1967, 1968] and Menke [1984] define a scalar spread  $S(r_j)$ , or averaging vector, which quantitatively describes the compactness of the resolution matrix. The trace of the resolution matrix can be used as an estimate of the potential number of degrees of freedom (DOF) of the system. The covariance matrix is defined as

$$\mathbf{C} = \mathbf{V} [(\mathbf{S}^2 + \lambda^2 \mathbf{I})^{-1} \mathbf{S}]^2 \mathbf{V}^T \quad (19)$$

and maps the way data error affects the estimates of the model parameters. The tradeoff between resolution and covariance can be examined by following the behavior of the  $j$ th velocity parameter while varying the damping parameter.

*Derivative Weight Sum (DWS) and Spread Function*

An optimal model parameterization can be arrived at by examining the derivative weight sum (DWS) and spread function to ensure that velocity nodes are adequately sampled by the available source-receiver ray paths. The DWS gives a quantitative representation of ray density near the  $j$ th node [C. H. Thurber, pers. comm., 1988; Toomey and Foulger, 1989]

$$DWS_j = \sum_{k=1}^{NE} \sum_{p=1}^{NS} \int_{\text{path}} w_j(\mathbf{r}) ds \quad (20)$$

where  $w_j(\mathbf{r})$  is the linear weighting function defined earlier for the velocity at a point  $\mathbf{r}$ , NE is the number of events, and NS is the number of stations. For an ideal data kernel and model, the DWS, which is dependent on the incremental arc length  $ds$ , will be smooth and slowly varying. This will lead to a minimum of poorly sampled nodes and thus avoid solutions containing spurious nodes of unperturbed velocity (which are products of the damped least squares algorithm for near-zero singular values).

A quantitative measure of compactness is given by the Backus-Gilbert scalar spread function,  $S(r_j)$ , of the  $j$ th velocity node [Backus and Gilbert, 1967, 1968; Menke, 1984]

$$S(r_j) = |r_j|^{-1} \sum_{k=1}^{NN} W_{jk} R_{jk}^2 \quad (21)$$

where  $|r_j|$  is the magnitude of the  $j$ th row in  $\mathbf{R}$  (the averaging vector for the  $j$ th velocity parameter),  $R_{jk}$  is an element of the resolution matrix,  $W_{jk}$  is a weighting function that depends of the physical distance between the  $j$ th and  $k$ th nodes, and NN is the number of nodes. For a compact matrix where the contribution of velocity at neighboring nodes is minimal,  $S(r_j)$  will be small since  $S(r_j) = 0$  if  $\mathbf{R} = \mathbf{I}$ .



## REFERENCES

- Achauer, U., J. R. Evans, and D. A. Stauber, High-resolution seismic tomography of compressional wave velocity structure at Newberry volcano, Oregon Cascade Range, *J. Geophys. Res.*, *93*, 10135-10147, 1988.
- Aki, K., and W. H. K. Lee, Determination of three-dimensional velocity anomalies under a seismic array using first P arrival times from local earthquakes 1. A homogeneous initial model., *J. Geophys. Res.*, *81*, 4381-4399, 1976.
- Anderson, R. N., J. Honnorez, K. Becker, A. C. Adamson, J. C. Alt, R. Emmermann, P. D. Kempton, H. Kinoshita, C. Laverne, M. J. Mottl, and R. L. Newmark, DSDP hole 504B, the first reference section over 1 km through layer 2 of the oceanic crust, *Nature*, *300*, 589-594, 1982.
- Backus, G., and F. Gilbert, Numerical applications of a formalism for geophysical inverse problems, *Geophys. J. R. Astron. Soc.*, *13*, 247-276, 1967.
- Backus, G., and F. Gilbert, The resolving power of gross Earth data, *Geophys. J. R. Astron. Soc.*, *16*, 169-205, 1968.
- Basaltic Volcanism Study Project, *Basaltic Volcanism on the Terrestrial Planets*, Pergamon Press, Inc., New York, 1286 pp., 1981.
- Becker, K., et al., In situ electric resistivity and bulk porosity of the oceanic crust, Costa Rica Rift, *Nature*, *300*, 594-598, 1982.
- Bratt, S. R., and G. M. Purdy, Structure and variability of oceanic crust on the flanks of the East Pacific Rise between 11° and 13°N, *J. Geophys. Res.*, *89*, 6111-6125, 1984.
- Bryan, W. B., and J. G. Moore, Compositional variations of young basalts in the Mid-Atlantic Ridge rift valley near lat 36°49'N, *Geol. Soc. Amer. Bull.*, *99*, 556-570, 1977.
- Bryan, W. B., G. Thompson, and J. L. Ludden, Compositional variation in normal MORB from 22-25°N: Mid-Atlantic Ridge and Kane Fracture Zone, *J. Geophys. Res.*, *86*, 11815-11836, 1981.
- Bunch, A. W. H., and B. L. N. Kennett, The crustal structure of the Reykjanes Ridge at 59°30'N, *Geophys. J. R. Astron. Soc.*, *61*, 141-166, 1980.
- Burnett, M. S., D. W. Caress, and J. A. Orcutt, Tomographic image of the magma chamber at 12°50'N on the East Pacific Rise, *Nature*, *339*, 206-208, 1989.
- Casey, J. F., and J. A. Karson, Magma chamber profiles from the Bay of Islands ophiolite complex, *Nature*, *292*, 295-301, 1981.
- Chapman, C. H., A new method for computing synthetic seismograms, *Geophys. J. R. Astron. Soc.*, *54*, 481-518, 1978.

- Christensen, N. I., The abundance of serpentinites in the oceanic crust, *J. Geol.*, *80*, 709-719, 1972.
- Christensen, N. I., The geophysical significance of oceanic plagiogranite, *Earth Planet. Sci. Lett.*, *36*, 297-300, 1977.
- Christensen, N. I., Compressional wave velocities in rocks at high temperatures and pressures, critical thermal gradients, and crustal low-velocity zones, *J. Geophys. Res.*, *84*, 6849-6857, 1979.
- Christensen, N. I., Pore pressure and oceanic crustal seismic structure, *Geophys. J. R. Astron. Soc.*, *79*, 411-423, 1984.
- Christensen, N. I., and M. H. Salisbury, Sea floor spreading, progressive alteration of layer 2 basalts, and associated changes in seismic velocities, *Earth Planet. Sci. Lett.*, *15*, 367-375, 1972.
- Christensen, N. I., and M. H. Salisbury, Velocities, elastic moduli and weathering-age relations for Pacific layer 2 basalts, *Earth Planet. Sci. Lett.*, *95*, 461-470, 1973.
- Christensen, N. I., and M. H. Salisbury, Structure and constitution of the lower oceanic crust, *Rev. Geophys. Space Phys.*, *13*, 57-86, 1975.
- Christensen, N. I., and J. D. Smewing, Geology and seismic structure of the northern section of the Oman ophiolite, *J. Geophys. Res.*, *86*, 2545-2555, 1981.
- Christeson, G., G. M. Purdy, and K. Rohr, A seismic refraction experiment along the crest of the northern symmetric segment of the Juan de Fuca ridge (abstract), *Eos Trans. AGU*, *70*, 1160, 1989.
- Crosson, R. S., Crustal structure modeling of earthquake data 1. Simultaneous least squares estimation of hypocenter and velocity parameters, *J. Geophys. Res.*, *81*, 3036-3046, 1976a.
- Crosson, R. S., Crustal structure modeling of earthquake data 2. Velocity structure of Puget Sound region, *J. Geophys. Res.*, *81*, 3047-3054, 1976b.
- Creager, K. C., and L. M. Dorman, Location of instruments on the seafloor by joint adjustment of instrument and ship positions, *J. Geophys. Res.*, *87*, 8379-8388, 1982.
- Detrick, R. S., P. Buhl, E. Vera, J. Mutter, J. Orcutt, J. Madsen, and T. Brocher, Multichannel seismic imaging of a crustal magma chamber along the East Pacific Rise, *Nature*, *326*, 35-41, 1987.
- Duschenes, J. D., T. W. Barash, P. J. Mattaboni, and S. C. Solomon, On the use of an externally deployed geophone package on an ocean bottom seismometer, *Mar. Geophys. Res.*, *4*, 437-450, 1981.

- Eberhart-Phillips, D., Three-dimensional velocity structure in northern California Coast ranges from inversion of local earthquake arrival times, *Bull. Seismol. Soc. Am.*, 76, 1025-1052, 1986.
- Ewing, J. I., and G. M. Purdy, Upper crustal velocity structure in the ROSE area of the East Pacific Rise, *J. Geophys. Res.*, 87, 8397-8402, 1982.
- Fowler, C. M. R., Crustal structure of the Mid-Atlantic ridge crest at 37°N, *Geophys. J. R. Astron. Soc.*, 47, 459-491, 1976.
- Fowler, C. M. R., The Mid-Atlantic Ridge: Structure at 45°N, *Geophys. J. R. Astron. Soc.*, 54, 167-183, 1978.
- Fowler, C. M. R., and C. E. Keen, Oceanic crustal structure - Mid-Atlantic Ridge at 45°N, *Geophys. J. R. Astron. Soc.*, 56, 219-226, 1979.
- Hale, L. D., C. J. Morton, and N. H. Sleep, Reinterpretation of seismic reflection data over the East Pacific Rise, *J. Geophys. Res.*, 87, 7707-7717, 1982.
- Harding, A. J., J. A. Orcutt, M. E. Kappus, E. E. Vera, J. C. Mutter, P. Buhl, R. S. Detrick, and T. M. Brocher, Structure of young oceanic crust at 13°N on the East Pacific Rise from expanding spread profiles, *J. Geophys. Res.*, 94, 12163-12196, 1989.
- Hyndman, R. D., and M. J. Drury, The physical properties of oceanic basement rocks from deep drilling on the Mid-Atlantic Ridge, *J. Geophys. Res.*, 81, 4042-4052, 1976.
- Jackson, D. D., Interpretation of inaccurate, insufficient and inconsistent data, *Geophys. J. R. Astron. Soc.*, 28, 97-109, 1972.
- Jackson, D. D., The use of *a priori* data to resolve non-uniqueness in linear inversion, *Geophys. J. R. Astron. Soc.*, 57, 137-157, 1979.
- Karson, J. A., and P. A. Rona, Block-tilting, transfer faults, and structural control of magmatic and hydrothermal processes in the TAG area, *Geol. Soc. Amer. Bull.*, submitted, 1989.
- Karson, J. A., G. Thompson, S. E. Humphris, J. M. Edmond, W. B. Bryan, J. R. Brown, A. T. Winters, R. A. Pockalny, J. F. Casey, A. C. Campbell, G. Klinkhammer, M. R. Palmer, R. J. Kinzler, and M. M. Sulanowska, Along-axis variations in seafloor spreading in the MARK area, *Nature*, 328, 681-685, 1987.
- Keen, C., and C. Tramontini, A seismic refraction survey of the Mid-Atlantic Ridge, *Geophys. J. R. Astron. Soc.*, 20, 473-491, 1970.
- Koelsch, D. E. and G. M. Purdy, An ocean bottom hydrophone instrument for seismic refraction experiments in the deep ocean, *Mar. Geophys. Res.*, 4, 115-125, 1979.

- Kong, L., W. B. F. Ryan, L. Mayer, R. Detrick, P. J. Fox and K. Manchester, Bare-rock drill sites, ODP Legs 106 and 109: Evidence for hydrothermal activity at 23°N in the Mid-Atlantic Ridge (abstract), *Eos Trans. AGU*, 66, 936, 1985.
- Lanczos, D., *Linear Differential Operators*, 564 pp., Van Nostrand Reinhold, New York, 1981.
- Langmuir, C. H., J. F. Bender, and R. Batiza, Petrological and tectonic segmentation of the East Pacific Rise 5°30'-14°30'N, *Nature*, 322, 422-429, 1986.
- Lee, W. H. K., and S. W. Stewart, *Principles and Applications of Microearthquake Networks*, 293 pp., Academic Press, New York, 1981.
- Levenberg, K., A method for the solution of certain non-linear problems in least squares, *Quant. Appl. Math.*, 2, 164-168, 1944.
- Manghnani, M. H., H. Sato, and C. S. Rai, Ultrasonic velocity and attenuation measurements of basalt melts to 1500°C: Role of composition and structure in the viscoelastic properties, *J. Geophys. Res.*, 91, 9333-9342, 1986.
- Marquardt, D. W., An algorithm for least squares estimation of non-linear parameters, *J. Soc. Ind. Appl. Math.*, 11, 431-441, 1963.
- Mattaboni, P. J., and S. C. Solomon, MITOBS: A seismometer system for ocean-bottom earthquake studies, *Mar. Geophys. Res.*, 3, 87-102, 1977.
- McClain, J. S., J. A. Orcutt, and M. Burnett, The East Pacific Rise in cross section: A seismic model, *J. Geophys. Res.*, 90, 8627-8639, 1985.
- McGregor, B. A., C. G. A. Harrison, J. W. Lavelle, and P. A. Rona, Magnetic anomaly pattern on the Mid-Atlantic Ridge crest at 26°N, *J. Geophys. Res.*, 82, 231-238, 1977.
- Menke, W., *Geophysical Data Analysis: Discrete Inverse Theory*, 260 pp., Academic Press, New York, 1984.
- Murase, T., and A. R. McBirney, Properties of some common igneous rocks and their melts at high temperatures, *Geol. Soc. Amer. Bull.*, 84, 3563-3592, 1973.
- Mutter, J. C., G. A. Barth, P. Buhl, R. S. Detrick, J. Orcutt, and A. Harding, Magma distribution across ridge-axis discontinuities on the East Pacific Rise from multichannel seismic images, *Nature*, 336, 156-158, 1988.
- Nicolas, A., I. Reuber, and K. Benn, A new magma chamber model based on structural studies in the Oman ophiolite, *Tectonophysics*, 151, 87-105, 1988.
- O'Connell, R. J., and B. Budiansky, Seismic velocities in dry and saturated cracked solids, *J. Geophys. Res.*, 79, 5412-5426, 1974.

- Orcutt, J. A., B. L. N. Kennet, and L. M. Dorman, Structure of the East Pacific Rise from an ocean bottom seismometer survey, *Geophys. J. R. Astron. Soc.*, *45*, 305-320, 1976.
- Pallister, J. S., and C. A. Hopson, Samail ophiolite plutonic suite: Field relations, phase variation, cryptic variation and layering, and a model of a spreading ridge magma chamber, *J. Geophys. Res.*, *86*, 2593-2644, 1981.
- Pavlis, G. L., and J. R. Booker, The mixed discrete-continuous inverse problem: An application to the simultaneous determination of earthquake hypocenters and velocity structure, *J. Geophys. Res.*, *85*, 4801-4810, 1980.
- Pereyra, V., W. H. K. Lee, and H. B. Keller, Solving two-point seismic ray tracing problems in a heterogeneous medium, Part 1, A general adaptive finite difference method, *Bull Seismol. Soc. Am.*, *70*, 79-99, 1980.
- Petersen, J. J., P. J. Fox, and E. Schrieber, Newfoundland ophiolites and the geology of the oceanic layer, *Nature*, *247*, 194-196, 1974.
- Purdy, G. M., The correction for travel time effects of seafloor topography in interpretation of marine seismic data, *J. Geophys. Res.*, *87*, 8389-8396, 1982.
- Purdy, G. M., New observations of the shallow seismic structure of young oceanic crust, *J. Geophys. Res.*, *92*, 9351-9362, 1987.
- Purdy, G. M., and R. S. Detrick, The crustal structure of the Mid-Atlantic Ridge at 23°N from seismic refraction studies, *J. Geophys. Res.*, *91*, 3739-3762, 1986.
- Rhodes, J. M., M. A. Dungan, D. P. Blanchard, and P. E. Long, Magma mixing at mid-ocean ridges: evidence from basalts drilled near 22°N on the Mid-Atlantic Ridge, *Tectonophysics*, *55*, 35-61, 1979.
- Rona, P. A., TAG Hydrothermal field: Mid-Atlantic Ridge crest at latitude 26°N, *J. Geol. Soc. Lond.*, *137*, 385-402, 1980.
- Rona, P. A., Black smokers and massive sulfides at the TAG hydrothermal field, Mid-Atlantic Ridge 26°N (abstract), *Eos Trans. AGU*, *66*, 936, 1985.
- Rona, P. A., R. N. Harbison, B. G. Bassinger, R. B. Scott, and A. J. Nalwalk, Tectonic fabric and hydrothermal activity of Mid-Atlantic Ridge crest (lat 26°N), *Geol. Soc. Amer. Bull.*, *87*, 661-674, 1976.
- Rona, P. A., G. Klinkhammer, T. A. Nelsen, J. H. Trefry, and H. Elderfield, Black smokers, massive sulfides and vent biota at the Mid-Atlantic Ridge, *Nature*, *321*, 33-37, 1986.
- Sempere, J. C., G. M. Purdy, and H. Schouten, The segmentation of the Mid-Atlantic Ridge between the Kane and Atlantis fracture zones (abstract), *Eos Trans. AGU*, *70*, 455, 1989.

- Shearer, P. M., Cracked media, Poisson's ratio and the structure of the upper oceanic crust, *Geophys. J.*, 92, 357-362, 1988.
- Spencer, C., and D. Gubbins, Travel-time inversion for simultaneous earthquake location and velocity structure determination in laterally varying media, *Geophys. J. R. Astron. Soc.*, 63, 95-116, 1980.
- Spudich, P., and J. Orcutt, A new look at the seismic velocity structure of the oceanic crust, *Rev. Geophys. Space Phys.*, 18, 627-645, 1980a.
- Spudich, P., and J. Orcutt, Petrology and porosity of an oceanic crustal site: Results from wave form modeling of seismic refraction data, *J. Geophys. Res.*, 85, 1409-1433, 1980b.
- Stephen, R. A., Seismic anisotropy in the upper oceanic crust, *J. Geophys. Res.*, 90, 11383-11396, 1985.
- Strens, M. R., and J. R. Cann, A model of hydrothermal circulation in fault zones at mid-ocean ridge crests, *Geophys. J. R. Astron. Soc.*, 71, 225-240, 1982.
- Strens, M. R., and J. R. Cann, A fracture-loop thermal balance model of black smoker circulation, *Tectonophysics*, 122, 307-324, 1986.
- Thompson, G., M. J. Mottl, and P. A. Rona, Morphology, mineralogy, and chemistry of hydrothermal depositis from the TAG area, 26°N, Mid-Atlantic Ridge, *Chem. Geol.*, 49, 243-257, 1985.
- Thurber, C. H., Earth structure and earthquake locations in the Coyote Lake area, central California, Ph. D. thesis, 332 pp., Mass. Inst. of Technol., Cambridge, 1981.
- Thurber, C. H., Earthquake locations and three-dimensional crustal structure in the Coyote Lake area, central California, *J. Geophys. Res.*, 88, 8226-8236, 1983.
- Thurber, C. H., Seismic detection of the summit magma complex of Kilauea volcano, Hawaii, *Science*, 223, 165-167, 1984.
- Toomey, D. R., and G. R. Foulger, Tomographic inversion of local earthquake data from the Hengill-Grensdalur central volcani complex, Iceland, *J. Geophys. Res.*, 94, 17497-17510, 1989.
- Toomey, D. R., G. M. Purdy, and S. C. Solomon, Three-dimensional seismic structure of the East Pacific Rise at 9°30'N (abstract), *Eos Trans. AGU*, 70, 1317, 1989.
- Toomey, D. R., S. C. Solomon, G. M. Purdy, and M. H. Murray, Microearthquakes beneath the median valley of the Mid-Atlantic Ridge near 23°N: Hypocenters and focal mechanisms, *J. Geophys. Res.*, 90, 5443-5458, 1985.
- Toomey, D. R., S. C. Solomon, G. M. Purdy, Microearthquakes beneath median valley of Mid-Atlantic Ridge near 23°N: Tomography and tectonics, *J. Geophys. Res.*, 93, 9093-9112, 1988.

- Whitmarsh, R. B., Axial intrusion zone beneath the median valley of the Mid-Atlantic Ridge at 37 degrees N detected by explosion seismology, *Geophys. J. R. Astron. Soc.*, *42*, 184-215, 1975.
- Wiggins, R. A., The general linear inverse problem: Implications of surface waves and free oscillations for Earth structure, *Rev. Geophys. Space Phys.*, *10*, 251-285, 1972.
- Wiggins, R. A., Body wave amplitude calculations - II, *Geophys. J. R. Astron. Soc.*, *46*, 1-10, 1976.
- Zonenshain, L. P., M. I. Kuzmin, A. P. Lisitsin, Yu. A. Bogdanov, and B. V. Baranov, Tectonic of the Mid-Atlantic rift valley between the TAG and MARK areas (26-24°N): Evidence for vertical tectonism, *Tectonophysics*, *159*, 1-23, 1989.

## FIGURE CAPTIONS

- Figure 1. Location of the refraction and microearthquake experiment near 26°N. Sea Beam bathymetry is contoured at an interval of 0.25 km [*Sempere et al.*, 1989]. Locations of refraction line and ranging shots are shown by triangles, instruments by open symbols (31 and 33 are ocean bottom seismometers); instrument numbers discussed in the text are indicated, and symbols are keyed to travel times in Figures 3, 4, and 7. The shape of the median valley inner floor (nominally seafloor depths > 3.5 km) varies along axis, widening and deepening south and north of the high-temperature hydrothermal field (hourglass).
- Figure 2. Examples of direct water wave rms travel time residuals calculated at 50-m intervals, and contoured at 0.01 s intervals for values less than 0.1 s and at 0.1 s intervals for greater values. The best estimate of shot location corresponds to the minimum residual. The location of the shot on the left (a ranging shot within the network which was also located by the *Creager and Dorman* [1982] method) can be estimated with good confidence, while the location of the shot on the right (located far to the south) is poorly constrained in the northwest-southeast direction.
- Figure 3. Compilation of water-path-corrected, reduced travel times from the southern limb of the refraction line to instruments in Figure 1 (symbols correspond to the instrument recording the arrival). Errors include contributions from uncertainty in the determination of the water path correction and reading error. The observations sweep out a large swath (~ 0.8 s wide) with range, indicating that a single, simple, one-dimensional velocity model cannot describe in detail the seismic structure in this area. Closer examination shows the presence of systematic differences between spatially-clustered instruments (Figure 4).



- Figure 4. Comparison of travel times from the southern limb of the refraction line to spatially-clustered stations. Symbols are keyed to instruments recording the phases in Figure 1. (a) Travel times to instruments atop the along-axis high (OBHs 2, 3) are up to 0.4 s less than times to instruments within the deep (OBHs 1, 6, 8) in the 5-15 km range. Rays at these ranges turn in the topmost 3-4 km suggesting that the shallow crust to the north of OBH 1 is characterized by substantially higher velocities than are found at similar levels beneath the along-axis deep. (b) Travel times to instruments atop the eastern wall (OBH 5, OBS 31) are also resolvably larger than those to the instruments atop the high.
- Figure 5. Record sections (8 km/s reduction velocity) for the southern limb of refraction line to (a) OBH 3, (b) OBH 2, and (c) OBH 4. Waveform amplitudes on the low-gain, low-frequency channel are severely attenuated in the 19 - 30 km range to OBHs 2 and 3 as compared to those to OBH 4, located only 5 km to the east on the eastern wall (see Figure 1 for locations). The cutoff in first-arriving energy constitutes evidence for a decrease in velocity below 3-4 km depth (see waveform modelling and tomographic inversions for further discussion). Only the water delay correction (i.e., no range correction) has been applied for all record sections displayed in this chapter. Waveform amplitudes are scaled linearly with range. The seismograms are truncated at the arrival of the water wave.
- Figure 6. Normalized power on the low-gain, low-frequency channel versus water-path-corrected range. The power is calculated as the square of the amplitude, normalized to the largest value for each instrument, for a 0.25 s window following the P-wave arrival time (from the low gain channel). There are striking differences in the power - range trends to OBH 4 on the eastern wall compared with those to instruments within the valley (OBHs 2 - circles, 3 - triangles, 1 - squares, 6 - diamonds, and 8 - stars). The amplitude cutoff seen in Figure 5 for OBHs 2 and 3 is quite sharp and distinct.

- Figure 7. Water-path-corrected, reduced travel times from northern refraction line shots to spatially-clustered stations. Symbol types are keyed to instruments recording the phases in Figure 1. (a) The observations sweep out a large swath ( $\sim 0.6$  s wide) with range, suggesting along-axis crustal heterogeneity. (b) Travel times for rays which traverse the along-axis high to instruments within the along-axis deep (OBHs 1 - large closed circles, 6 - small closed circles) are up to 0.6 s larger than times for rays sampling the inner floor north of the along-axis high (OBHs 2, 4, open symbols) for ranges out to 20-25 km.
- Figure 8. Record sections (8 km/s reduction velocity) for northern limb of refraction line to (a) OBH 4, (b) OBH 2, (c) OBH 1, and (d) OBH 6. P wave amplitudes on the low-gain, low-frequency channel are attenuated out to a range of 19 km range to OBH 1 as compared to those to OBHs 4 and 2 (see Figure 1 for locations). The relative lack of first-arriving energy to OBH 1 could result from a velocity decrease with depth. Only seismograms from shots north of the network are displayed. See Figure 5 for plotting parameters.
- Figure 9. Record sections (see Figure 5 for plotting specifications) from southern limb shots to (a) OBH 1 and (b) OBH 8 located within the along-axis deep. The limited amount of data show high signal to noise ratios and velocities approaching 8 km/s at short ranges ( $\sim 15$  km).
- Figure 10. Cubic spline fits (constrained so that velocity increases with depth) to the travel time data recorded at (a) OBH 3 and (b) OBH 1. The water-path-corrected travel time data are plotted versus range with reduction velocities of 8 km/s. The spline fit to data of OBH 3 (range to 21 km) has an rms deviation of 0.04 s and that to OBH 1 has an rms deviation of 0.06 s. Inversions of these data for velocity versus depth are given in Figure 11.
- Figure 11. Plane-layered velocity-depth functions obtained from inversions of the splines fit to travel time data displayed in Figure 10. These functions

describe the average structure associated with arrivals to OBH 3 (along-axis high, light lines) and OBH 1 (along-axis deep, heavy line). Comparison shows that the shallow crust sampled by rays to OBH 3, corresponding to the region beneath the high and volcano, is characterized by higher velocities than those beneath the deep (to OBH 1), which compares well with the average structure for the median valley at 23°N [*Purdy and Detrick, 1986; dashed line*].

Figure 12. Velocity-depth functions which fit both the travel time and amplitude data at OBHs 1 and 3. The solid lines show the solutions based on the travel time inversion and amplitude modelling of the refraction line data. The dashed lines show the solutions derived from amplitude modelling using as starting models the velocities (at volcano, high) from the tomographic inversions. The two alternative models for each structure are very similar.

Figure 13. (a) Summary of velocity-depth functions investigated for OBH 3. The plane-layered inversion solution is shown for reference. All models to 3 km depth produce essentially identical travel times; the amplitude-range variations caused by the structure below 3 km are used qualitatively to reject model 3A-1d (b), and to predict the amount of travel time delay for a low velocity layer (3A-2d) (c). Ray tracing shows that rays turn within the upper 3 km at ranges less than 15 km.

(b) Observed waveforms (top) and WKBJ seismograms for two models derived from the travel time inversion of the refraction line. Model 3A-1d, which was based on spline-fit times to 30 km, clearly cannot match the waveforms in the 20 to 25 km range, whereas with model 3B-1d constant or decreasing velocities below 2.7 km can match the observed low amplitudes beyond 19 km. An exponentially-damped cosine function,  $\cos(2\pi ft) \exp[-(2\pi ft / \gamma)^2]$  with  $f = 6$  Hz and  $\gamma = 5$ , is used as the source time function. Waveform amplitudes are normalized to the largest trace and scaled linearly with range.

(c) Hypothetical model (3A-2d) which predicts the effect on the travel times, amplitudes, and ray path geometry for a layer of lower velocities

below 3.1 km. Travel times (solid lines) will be delayed by  $\sim 0.4$  s; stars represent the observed times. Rays entering the low velocity layer are delayed and focussed beyond 20 km (as seen in the synthetic seismograms). See (b) for WKBJ seismogram calculation procedure and display parameters.

- Figure 14. (a) Observed waveforms to OBH 1 within the median valley. The seismograms at ranges less than 10 km possess very high amplitudes, including saturation beyond the first arrival, and were excluded. (b) Model 1A-1d based on the travel time inversion of the refraction data, and (c) 1A-2d based on the tomography results, fit the observed data equally well (in part because there are so few data). (d) Ray tracing indicates that rays turn within the upper 4 km at ranges  $< 15$  km. See Figure 13b for WKBJ seismogram calculation procedure and display parameters.
- Figure 15. Distribution of sources (32 shots, 69 earthquakes) and receivers (6 OBHs, 1 OBS) used in the tomographic inversions for two-dimensional velocity structure. The solid line shows the location of the along-axis profile in Figure 16. Inversions were performed using 3 (nodes A), 5 (nodes A and B), and 7 (nodes A and C) columns of along-axis nodes spaced 5, 2.5, and 1.7 km apart, respectively (Table 3, inversions 1-3). In the 3-nodal column configuration (A, diamonds), a velocity parameter was placed within the along-axis deep, at the ridge-axis volcano (hidden by symbols for earthquake sources and an instrument), and at the along-axis high. See text for distribution of nodes with depth.
- Figure 16. Focal depth distribution for earthquake sources shown in Figure 15. All events are shown projected onto the vertical plane with  $1\text{-}\sigma$  errors. Earthquakes which were originally located with an S-wave arrival (Chapter 3) are shown with a solid circle at the hypocenter. Solid squares show the locations of instruments. Because of the lack of

shallow crustal events, travel times from earthquakes alone cannot be used to invert for the full velocity structure.

- Figure 17. Starting models for the tomographic inversions. (a) A plane-layered model from 23°N [Purdy and Detrick, 1986] was first used to determine the shallow structure using the 21 closest shots. (b) The starting model for all subsequent runs is a two-dimensional model (Table 2) which is approximately subparallel to the seafloor and constrained at shallow levels by inversion 0 using the 1D starting model and the 21 closest shots.
- Figure 18. A table of node numbers for the 3-nodal-column model parameterization versus distance along-axis (Y) and with depth (Z). Node numbers are used in Figure 19 and in the text.
- Figure 19. Pictorial representation of each row of the resolution matrix for (a) inversion 1, (b) inversion 4, and (c) inversion 5. Each perspective plot shows the magnitude of the diagonal element as well as the values at adjacent nodes. A velocity parameter is uniquely-resolved if it has a compact averaging vector (a  $\delta$ -like nodal value with near-zero adjacent values). For example, the solution from inversion 1 is well-resolved at all nodes except 1 and 2.
- Figure 20. Comparison of the DWS, resolution, and spread for inversions 1-3 (using 3, 5, and 7 along-axis nodal columns, respectively). Resolution is greatest and spread smallest for the 3-nodal column configuration (solid circles) suggesting that this represents the optimal number of columns. A threshold value for well-constrained nodal velocities can be determined by examining the behavior of the resolution, spread, DWS, and averaging vector (Figure 19) as nodal density is increased. The empirically-derived values (dashed lines) for the data from this experiment are 0.8 for resolution and 60 for the spread function.

- Figure 21. Two-dimensional velocity model determined for inversion 1. The bathymetry along-axis is shown at the top with arrowheads placed at the locations of nodal columns. Velocity is contoured at 0.5 km/s intervals. A region of higher velocities is observed at 3 km depth beneath the volcano, and velocity decreases below this depth level. Velocities within the shallowmost crust beneath the volcano and along-axis high are greater than those at similar depths within the along-axis deep.
- Figure 22. Velocity perturbations (+ = faster velocities) relative to the 2D starting model (Figure 17b, Table 2), resolution, DWS, and spread for inversion 1 in Figure 21. This model is well-resolved with compact resolution, but comparison with inversion 4 (Figure 24) shows that velocities at 3 km depth beneath the high are spurious.
- Figure 23. Instrument travel time residuals for each source (1 - 69 are earthquakes, 70 - 101 are shots): (a) relative to the starting model in Figure 17b and Table 2, and (b) upon convergence to the final velocity model in Figure 21 and Table 3. The initial skewness in residuals, especially in the shot data, is removed as the residuals map into perturbations in velocity from the initial structure. The dashed line shows the mean for all data.
- Figure 24. Inversion 4 results (Table 5) using 32 shots, 7 instruments, and 3-nodal columns (see Figure 15 for source-receiver distribution). For an 0.8 resolution cutoff value, we see that the shots alone can resolve most of the major variations in velocity (high shallow crustal velocities beneath the high and volcano with lower velocities in the deep, high velocities (> 7 km/s) at 3 km depth beneath the volcano, and a 5 km thick crust beneath the deep).
- Figure 25. Results from inversion 5 using only earthquake travel time data from 69 events, for a 3-nodal-column, 7-instrument configuration (see Figure 15 for source-receiver distribution). In contrast to Figure 24, resolution is poor throughout the imaged area and contradicts the sense of perturbations at shallow depths from inversion 4. The lack of a uniform

distribution of sources with depth (see Figure 16) does not allow any constraint on the shallow structure and leads to spurious perturbations in velocity.

- Figure 26. Variation in DWS, resolution, and spread with number and type of sources for the 7-instrument and 3-nodal column configuration. Although the number of sources is less (DWS is less) than for inversion 1 (filled circles), inversion 6 (open circles) still yields well-resolved estimates since the data distribution is uniform. This is also true for inversion 4 (crosses), but the lack of observations which sample deep into the section prevents good resolution of all velocity parameters. The 69-earthquake run (inversion 5, triangles), characterized by large spread, low resolution, and a large scatter in values, illustrates a case where the data cannot resolve the model. The empirically-derived cutoff values for good resolution are shown by dashed lines.
- Figure 27. Source and receiver (6 OBHs, 1 OBS) distributions used in the tomographic inversion for two-dimensional velocity structure using (a) 58 sources (inversion 6: 21 shots, 37 earthquakes) and (b) 123 sources (inversion 7: 32 shots, 91 earthquakes). Inversions were performed using 3 nodal columns spaced 5 km apart and different numbers of earthquakes. The source distribution shows good azimuthal coverage for both runs. Inversion results are shown in Figures 28 and 29.
- Figure 28. Inversion 6 results using a 58-source data set with a 3-nodal column, 7-instrument configuration (see Figure 27a for source-receiver distribution). The data provide good resolution with low spread. The velocity structure shows the same patterns of heterogeneity as in Figure 21 with higher absolute velocities and a more distinct high velocity body.
- Figure 29. Results from inversion 7 using 123 sources with a 3-nodal column, 7-instrument configuration (see Figure 27b for source-receiver distribution). The data result in a compact resolution matrix similar to

inversion 1 (see spread in Figure 21), and a general smoothing of the velocity variations and perturbations. However, the patterns of heterogeneity remain consistent with inversions 1 and 6.

- Figure 30. Source and receiver configurations used in the tomographic inversion for two-dimensional velocity structure parameterized by three nodal columns using (a) 5 instruments (inversion 8, 84 sources) and (b) 6 instruments (inversion 9, 97 sources). Results are shown in Figures 31 and 32.
- Figure 31. Variation in resolution and spread with the number of instruments used in the inversion for 2D structure. The plot indicates that all model estimates will be equally well-resolved. This can also be inferred from the source distributions in Figures 15 and 30, which show very little difference. The empirical threshold value is shown by the dashed line.
- Figure 32. Inversion results using 3-nodal columns and (top panels) 84 sources to 5 instruments - inversion 8, and (bottom panels) 97 sources to 6 instruments - inversion 9. See Figure 30 for source-receiver distributions. The well-resolved structure from inversion 8 is nearly identical to that from inversion 1 (Figures 21 and 22), and shows that the elimination of the instruments on the eastern wall does not significantly affect the velocity determination.
- Figure 33. Cartoon illustrating, for a simple case, the effect of source mislocation on velocity estimation. In (a), velocity will be perfectly resolved as long as the observation is within the rectangle (which defines the closeness criterion for this case). In (b), the closeness criterion has been halved to the size of the square. The effect of errors in source location on the estimate is thus dependent on the model parameterization.
- Figure 34. (a) Changes in epicenter upon relocation of the 69 earthquakes using 7 instruments and the 2D model determined tomographically (modified for unconstrained seafloor velocities in the deep and at the volcano).



Epicenters moved an average of  $1.6 \pm 1.0$  km to the southeast. The translation is a manifestation of the nonuniqueness in the earthquake location problem. Squares show the locations of receivers. Lines connect the locations obtained from the 1D model with station corrections to those obtained with the 2D model (open circles). The volcano is located at  $26^{\circ}5.9'N$  and  $44^{\circ}51.6'W$ . (b) The scalar change in epicenter DX, was typically less than 3 km, with slightly larger shifts associated with the deeper events. DX is plotted at the focal depths, relative to a 3.3 km datum, estimated with the 1D model.

- Figure 35. Hypocentral changes along the ridge axis upon relocation with 7 instruments and the 2D model. (a) Most events showed an increase in focal depth ( $1.1 \pm 1.3$  km) with the largest shifts associated with earthquakes beneath the along-axis deep and western portion of the median valley. The swarm of earthquakes beneath the volcano (at 15 km range and 7 km depth) moved only minimally. Symbol explanation given in Figure 34. (b) The change in the travel time DT to OBH 1, which was situated atop the axial volcano (mean =  $-0.03 \pm 0.18$  s, dashed line). DT, plotted at the focal depth obtained with the 1D model (3.3 km datum), does not appear to be correlated with distance along-axis, and is typically less than 0.2 s. Positive DT values correspond to larger travel times, and thus increases in focal depth.
- Figure 36. Changes in travel time versus focal depth for receivers atop the axial volcano (OBH 1, mean =  $-0.03 \pm 0.18$  s), within the deep (OBH 6, mean =  $-0.04 \pm .13$  s), atop the high (OBH 3, mean =  $-0.07 \pm 0.18$  s), and on the eastern wall to the north (OBH 4, mean =  $0.08 \pm 0.20$  s). The mean changes (dashed lines) for each instrument show a slight correlation with location, but the scatter is so large that this is not significant. DT is plotted at the focal depth, relative to a 3.3 km datum, obtained with the 1D model.
- Figure 37. Comparison of the velocity structure determined using earthquakes located with the 1D model (top panels, inversion 1) with the structure

obtained using earthquakes relocated with the 2D model (bottom panels, inversion 10). The patterns of velocity variation along the ridge axis remain the same in spite of source location shifts of up to 5 km.

- Figure 38. Source and receiver configuration used in the tomographic inversion for 2D velocity structure using only inner floor events within 4 km of the ridge axis (inversion 11: 23 shots, 36 earthquakes). Result is shown in Figure 39.
- Figure 39. Results from inversion 11 using inner floor events (23 shots and 36 earthquakes located with the 1D model). This figure should be directly compared with Figures 21 and 22. The use of only inner floor events results in little difference in the overall patterns of velocity heterogeneity in areas with good resolution; a velocity decrease with depth below 3 km beneath the volcano, higher upper crustal velocities in the along-axis high region, and normal young ocean crust beneath the along-axis deep appear to be robust characteristics of the centermost region beneath the median valley.
- Figure 40. Instrument travel time residuals for inversion 12 (1 - 31 are earthquakes, 32 - 54 are shots). (a) Residuals relative to the 2D starting model in Figure 17b and Table 2 (mean =  $-0.14 \pm 0.17$  s, dashed line). (b) Residuals upon convergence to the final 2D model in Figure 41 and Table 6 are much reduced and cluster tightly near zero (mean =  $0.01 \pm 0.09$ s, dashed line).
- Figure 41. Two-dimensional velocity model from inversion 12 using inner floor events, with earthquake locations re-estimated with the 2D model. See Figure 21 for plotting specifics. This structure is consistent with the velocities suggested by the refraction line and those estimated in inversion 4 (shot data). Higher velocities are imaged beneath the volcano with velocities decreasing below this region.

- Figure 42. Velocity perturbations relative to the 2D starting model, resolution, DWS, and spread for inversion 12 in Figure 41. The resolved structure is consistent with inversion 11 (same set of earthquakes located with the 1D structure, Figure 39), suggesting that for well-resolved regions errors in hypocentral location are independent of the estimated velocity structure. Inversion 12 is consistent with the shot data (inversion 4), but we acknowledge that tradeoffs in velocity at depth with hypocentral changes probably cause the shrinking of the area enclosed by the 6 km/s contour at 5 km depth.
- Figure 43. Comparison of seismic layer 2 velocity-depth functions from this study (1D models for deep-OBH 1 and high-OBH 3, bold solid lines) with those determined for the East Pacific Rise at 13°N [dashed lines-*Harding et al.*, 1989], and the Mid-Atlantic Ridge at 23°N [solid line-*Purdy and Detrick*, 1986; squares-*Purdy*, 1987]. Higher velocities from 0.25 km to 1.25 km depth are present both in the along-axis high region at 26°N on the MAR and at the ridge axis the EPR at 13°N. See text for discussion.
- Figure 44. Comparison of depths to the top of the low velocity zone in this study (resolved nodes at volcano-inversion 12, bold solid line), at 59°N on the MAR [light solid line-*Bunch and Kennett*, 1980], on the Juan de Fuca Ridge [light long dashed lines-at along-axis high, light short dashed lines-in deeper portions away from high, G. Christeson, pers. comm., 1990], and at 13°N on the EPR [bold dashed lines-*Harding et al.*, 1989]. The lid thickness is shallowest on the fast-spreading East Pacific Rise. See text for discussion.

Table 1. One-dimensional P Wave Velocity Models  
 Derived from the Southern Limb of the Refraction Line

OBH 3:		Model 3B - 1d		Model 3A - 2d		
<u>Layer</u>	<u>Thickness</u>	<u>V<sub>p</sub>, km/s</u>		<u>Thickness</u>	<u>V<sub>p</sub>, km/s</u>	
		<u>Top</u>	<u>Bottom</u>		<u>Top</u>	<u>Bottom</u>
1	0.80	4.30	5.40	0.90	4.30	5.45
2	1.00	5.40	6.10	2.20	5.45	6.65
3	0.90	6.10	6.40			

OBH 1:		Model 1A - 1d		Model 1A - 2d		
<u>Layer</u>	<u>Thickness</u>	<u>V<sub>p</sub>, km/s</u>		<u>Thickness</u>	<u>V<sub>p</sub>, km/s</u>	
		<u>Top</u>	<u>Bottom</u>		<u>Top</u>	<u>Bottom</u>
1	1.00	3.00	4.70	2.50	3.50	6.10
2	1.20	4.70	6.00	3.00	6.10	8.15
3	3.00	6.00	8.15			

Table 2. Starting Two-Dimensional P Wave Velocity Model  
for Tomographic Inversions

	Bounding node <u>-200 km</u>	Deep <u>0 km</u>	Volcano <u>5 km</u>	High <u>10 km</u>	Bounding node <u>200 km</u>
Bounding node -200 km	2.50	2.50	2.50	2.50	2.50
0 km	2.50	2.50	3.25	3.40	3.40
1 km	4.00	4.00	4.85	5.00	5.00
3 km	6.00	6.00	6.30	6.40	6.40
5 km	6.90	6.90	7.00	7.10	7.10
Bounding node 200 km	8.00	8.00	8.00	8.00	8.00

Table 3. Tomographic Inversion Summaries

Inversion	# instr # nodes <sup>a</sup>	# sources shot / eq	# obs	# iter	rms <sub>i</sub> (sec) rms <sub>f</sub> (sec)	s <sup>2</sup> <sub>i</sub> (sec <sup>2</sup> ) s <sup>2</sup> <sub>f</sub> (sec <sup>2</sup> )	Variance reduction (%)
0 <sup>b</sup>	7 3	21 21 / --	106	3	0.29 0.14	0.087 0.018	79
1 <sup>c</sup>	7 3	101 32 / 69 <sup>d</sup>	532	5	0.19 0.12	0.039 0.014	63
2 <sup>c</sup>	7 5	101 32 / 69 <sup>d</sup>	532	5	0.20 0.12	0.040 0.010	65
3 <sup>c</sup>	7 7	101 32 / 69 <sup>d</sup>	532	5	0.20 0.12	0.040 0.013	66
4 <sup>c</sup>	7 3	32 32 / --	169	4	0.32 0.13	0.100 0.016	83
5 <sup>c</sup>	7 3	69 -- / 69 <sup>d</sup>	363	4	0.11 0.08	0.011 0.006	50
6 <sup>c</sup>	7 3	58 21 / 37 <sup>d</sup>	314	4	0.19 0.12	0.037 0.014	62
7 <sup>c</sup>	7 3	123 32 / 91 <sup>d</sup>	645	5	0.19 0.12	0.035 0.015	57
8 <sup>c</sup>	5 3	84 32 / 52 <sup>d</sup>	372	3	0.17 0.11	0.027 0.012	56
9 <sup>c</sup>	6 3	97 32 / 65 <sup>d</sup>	480	5	0.20 0.12	0.041 0.015	63
10 <sup>c</sup>	7 3	101 32 / 69 <sup>e</sup>	532	5	0.20 0.10	0.041 0.010	77
11 <sup>c</sup>	7 3	59 23 / 36 <sup>d</sup>	316	4	0.21 0.12	0.044 0.016	64
12 <sup>c</sup>	7 3	59 23 / 31 <sup>e</sup>	291	5	0.22 0.09	0.047 0.008	83

<sup>a</sup> Number of nodal columns along-axis (3, 5, 7 nodes correspond to spacings of 5, 2.5, 1.7 km). In each column, nodes are placed at 0, 1, 3, and 5 km depth.

<sup>b</sup> 1D starting velocity model. See text for details.

<sup>c</sup> 2D starting velocity model (Table 2). See text for details.

<sup>d</sup> Earthquake hypocenters determined with 1D model and station corrections

<sup>e</sup> Earthquake hypocenters determined with 2D model

Table 4. Two-Dimensional P Wave Velocity Model from Inversion 1

	Bounding node <u>-200 km</u>	Deep <u>0 km</u>	Volcano <u>5 km</u>	High <u>10 km</u>	Bounding node <u>200 km</u>
Bounding node -200 km	2.50	2.50	2.50	2.50	2.50
0 km-v, km/s	2.50	3.73	2.23	5.40	5.40
$\Delta v$ , km/s		1.23	-1.02	2.00	
DWS		234	229	1078	
Res		0.50	0.19	0.87	
Spread		82	163	5	
1 km	4.00	3.93 -0.07 1513 0.85 47	5.31 0.46 1039 0.87 51	5.83 0.83 1999 0.92 14	5.00
3 km	6.00	6.21 0.21 1937 0.90 39	6.98 0.68 1970 0.91 17	5.74 -0.66 2046 0.90 24	6.40
5 km	6.90	8.09 1.19 1363 0.94 11	5.54 -1.46 1232 0.88 21	6.24 -0.86 842 0.82 33	7.10
Bounding node 200 km	8.00	8.00	8.00	8.00	8.00

Table 5. Two-Dimensional P Wave Velocity Model from Inversion 4

	Bounding node <u>-200 km</u>	Deep <u>0 km</u>	Volcano <u>5 km</u>	High <u>10 km</u>	Bounding node <u>200 km</u>
Bounding node -200 km	2.50	2.50	2.50	2.50	2.50
0 km-v, km/s	2.50	3.79	2.59	5.00	5.40
$\Delta v$ , km/s		1.29	-0.66	1.60	
DWS		161	91	488	
Res		0.38	0.11	0.82	
Spread		108	206	10	
1 km	4.00	3.90 -0.10 860 0.84 48	5.18 0.33 392 0.77 69	5.51 0.51 779 0.84 31	5.00
3 km	6.00	6.00 0 1114 0.87 46	7.44 1.14 680 0.80 49	7.46 1.06 659 0.83 54	6.40
5 km	6.90	8.23 1.33 968 0.93 54	6.04 -0.96 203 0.43 219	6.95 -0.15 28 0.03 329	7.10
Bounding node 200 km	8.00	8.00	8.00	8.00	8.00



Table 6. Two-Dimensional P Wave Velocity Model from Inversion 12

	Bounding node <u>-200 km</u>	Deep <u>0 km</u>	Volcano <u>5 km</u>	High <u>10 km</u>	Bounding node <u>200 km</u>
Bounding node -200 km	2.50	2.50	2.50	2.50	2.50
0 km-v, km/s	2.50	4.00	2.61	5.40	3.40
$\Delta v$ , km/s		1.50	-0.64	2.00	
DWS		172	120	549	
Res		0.55	0.14	0.84	
Spread		99	270	6	
1 km	4.00	3.73 -0.27 979 0.76 99	5.34 0.49 504 0.78 61	5.34 0.34 949 0.76 106	5.00
3 km	6.00	6.32 0.32 1401 0.86 69	7.19 0.89 1097 0.84 40	6.90 0.50 1085 0.75 124	6.40
5 km	6.90	8.25 1.35 1146 0.93 19	5.96 -1.04 690 0.77 62	6.27 -0.83 366 0.57 140	7.10
Bounding node 200 km	8.00	8.00	8.00	8.00	8.00

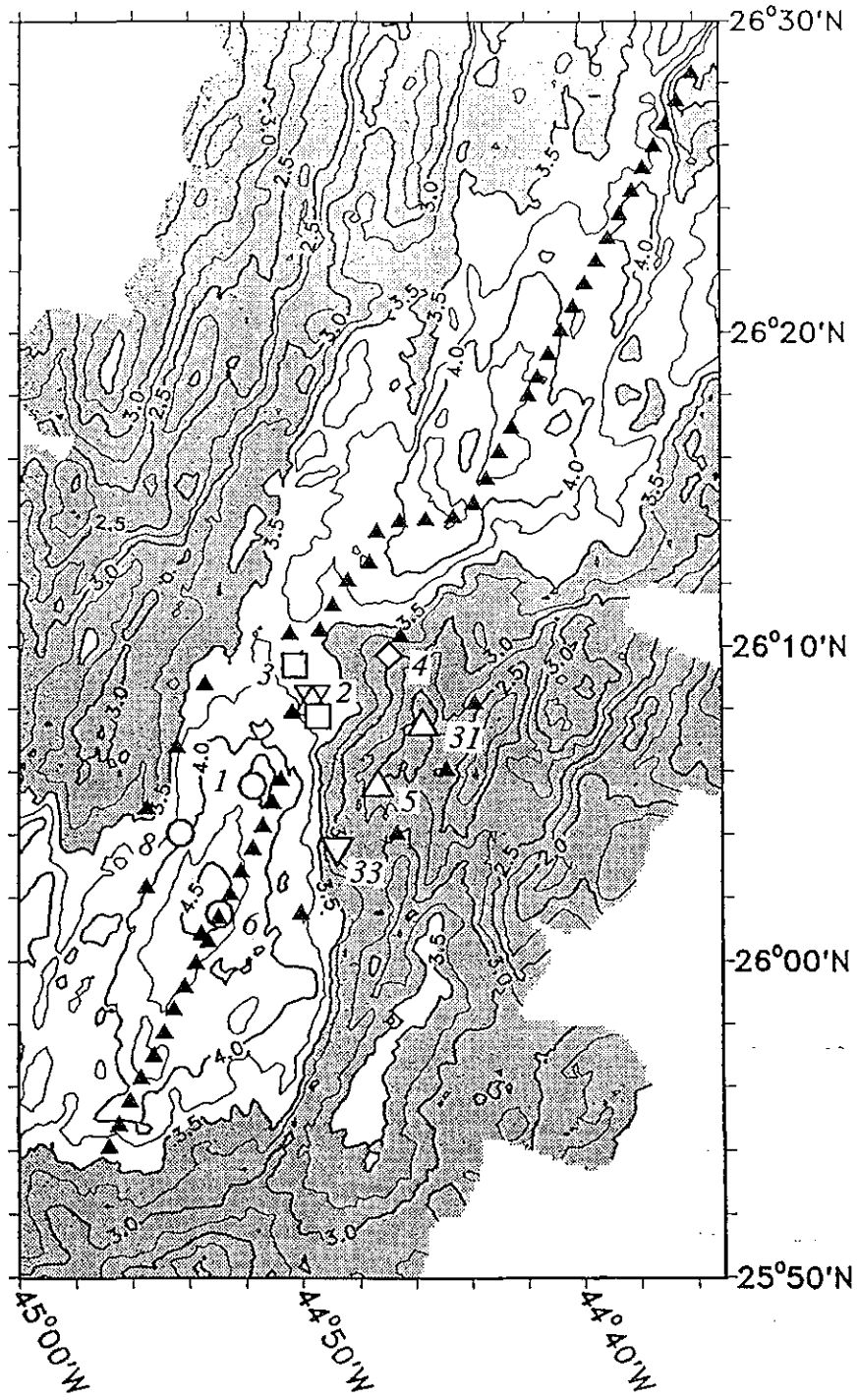


Figure 1

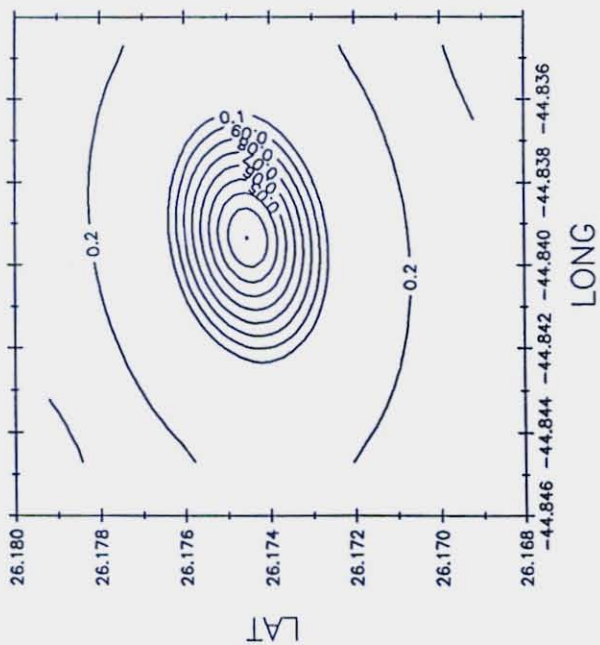
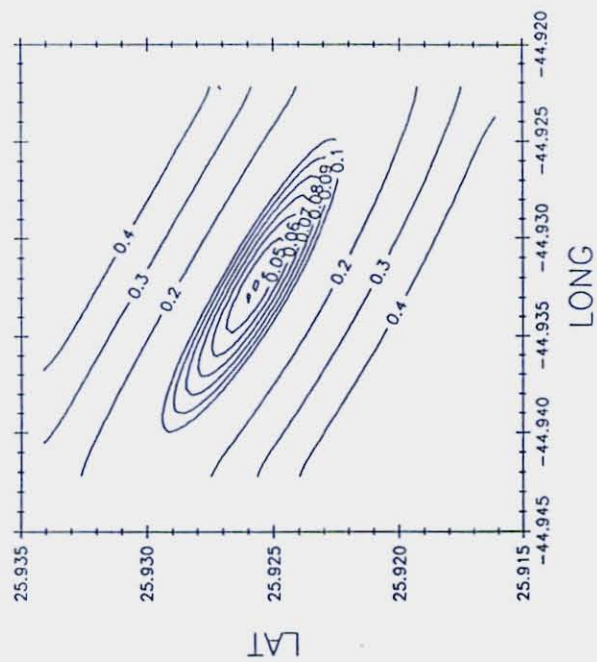


Figure 2

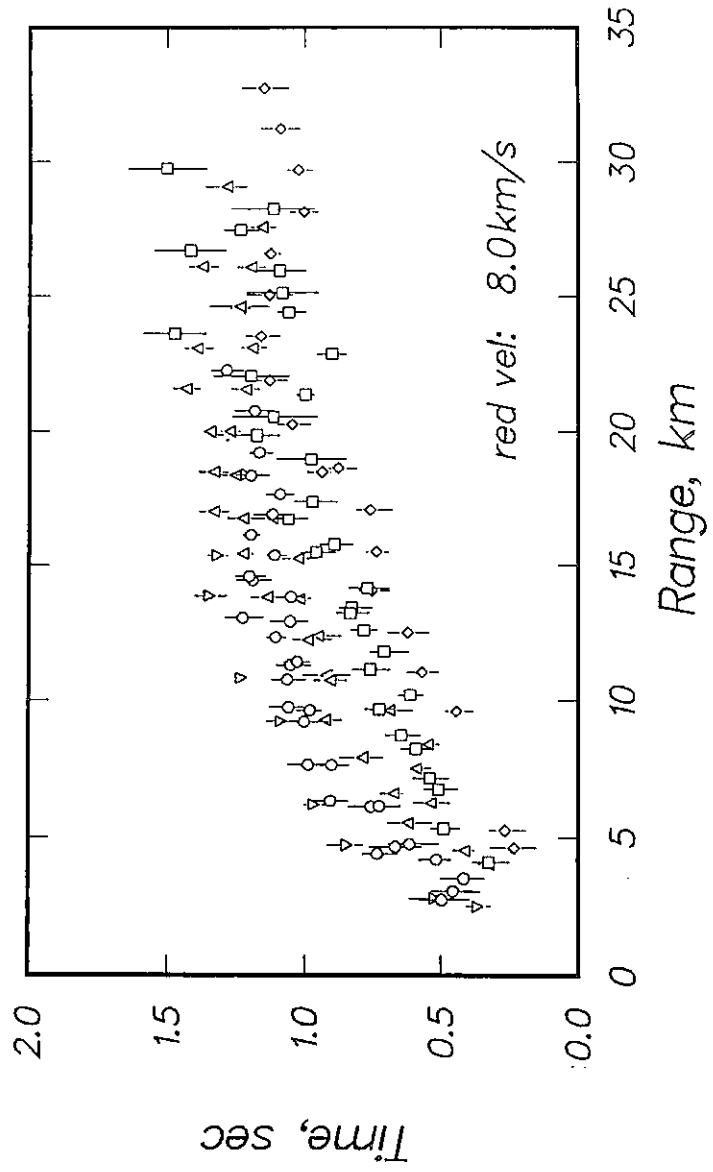


Figure 3

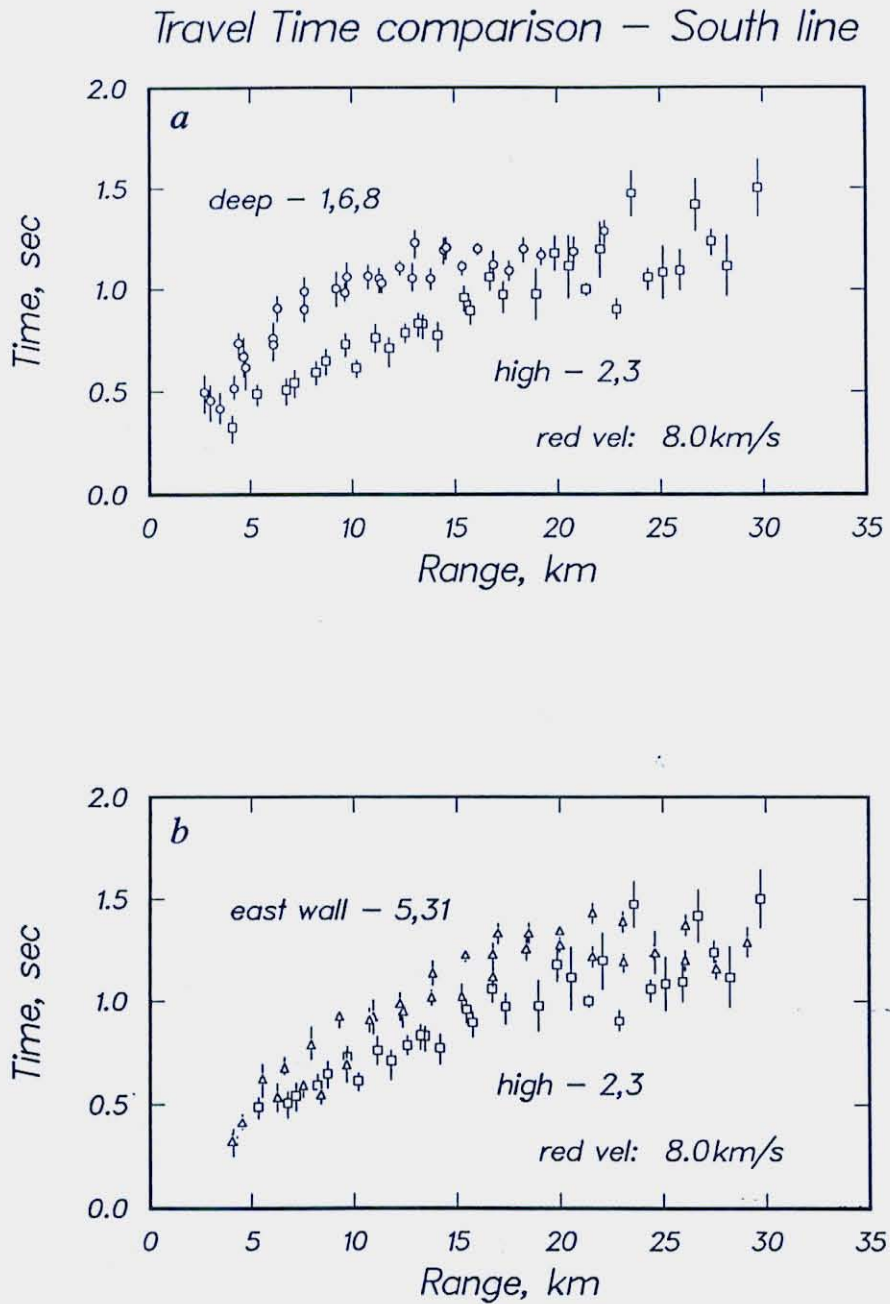


Figure 4

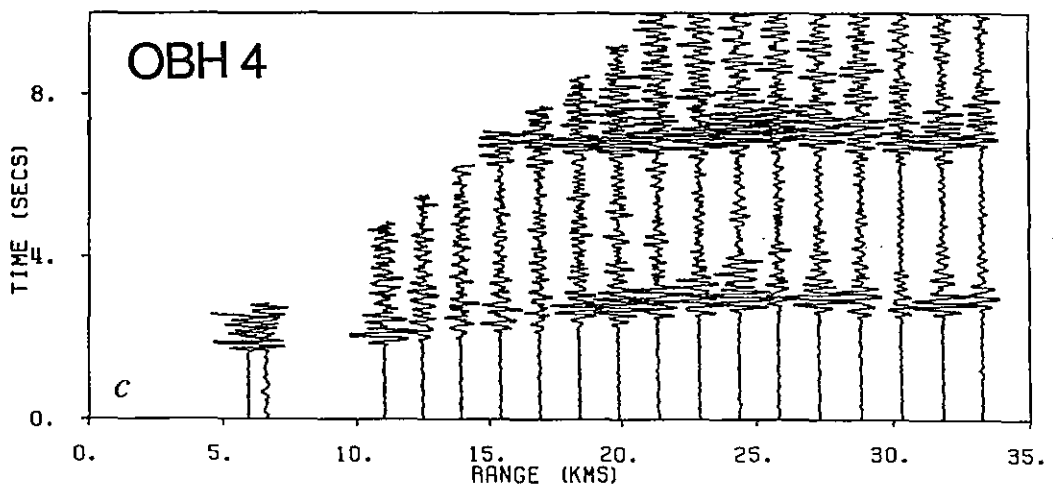
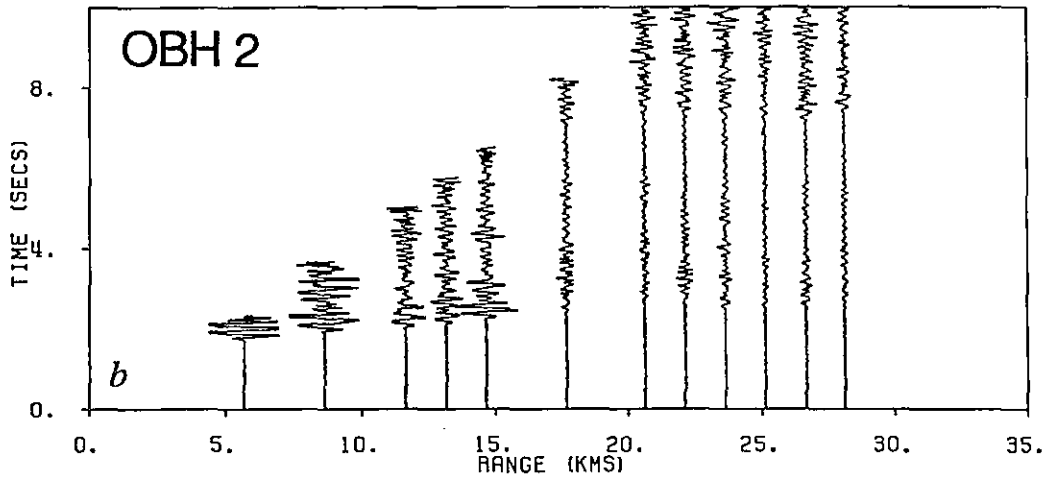
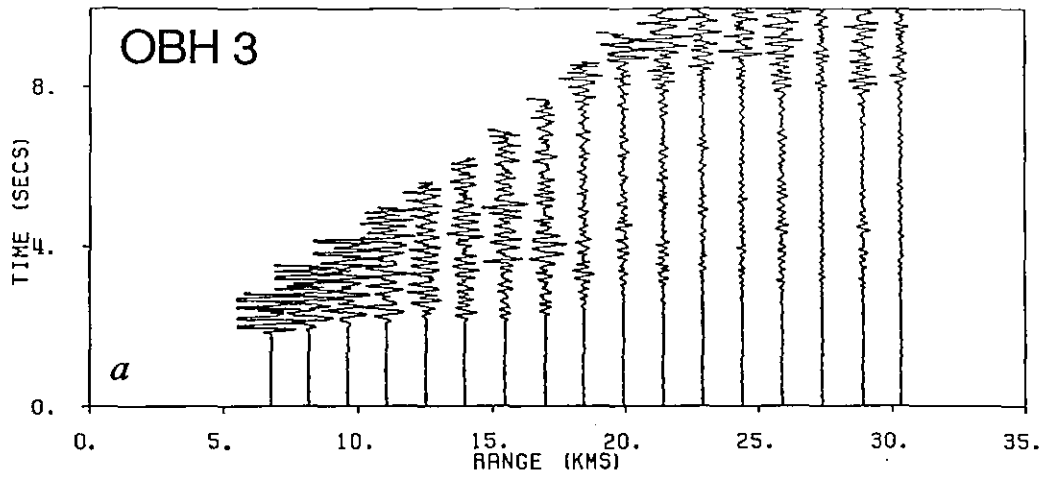


Figure 5

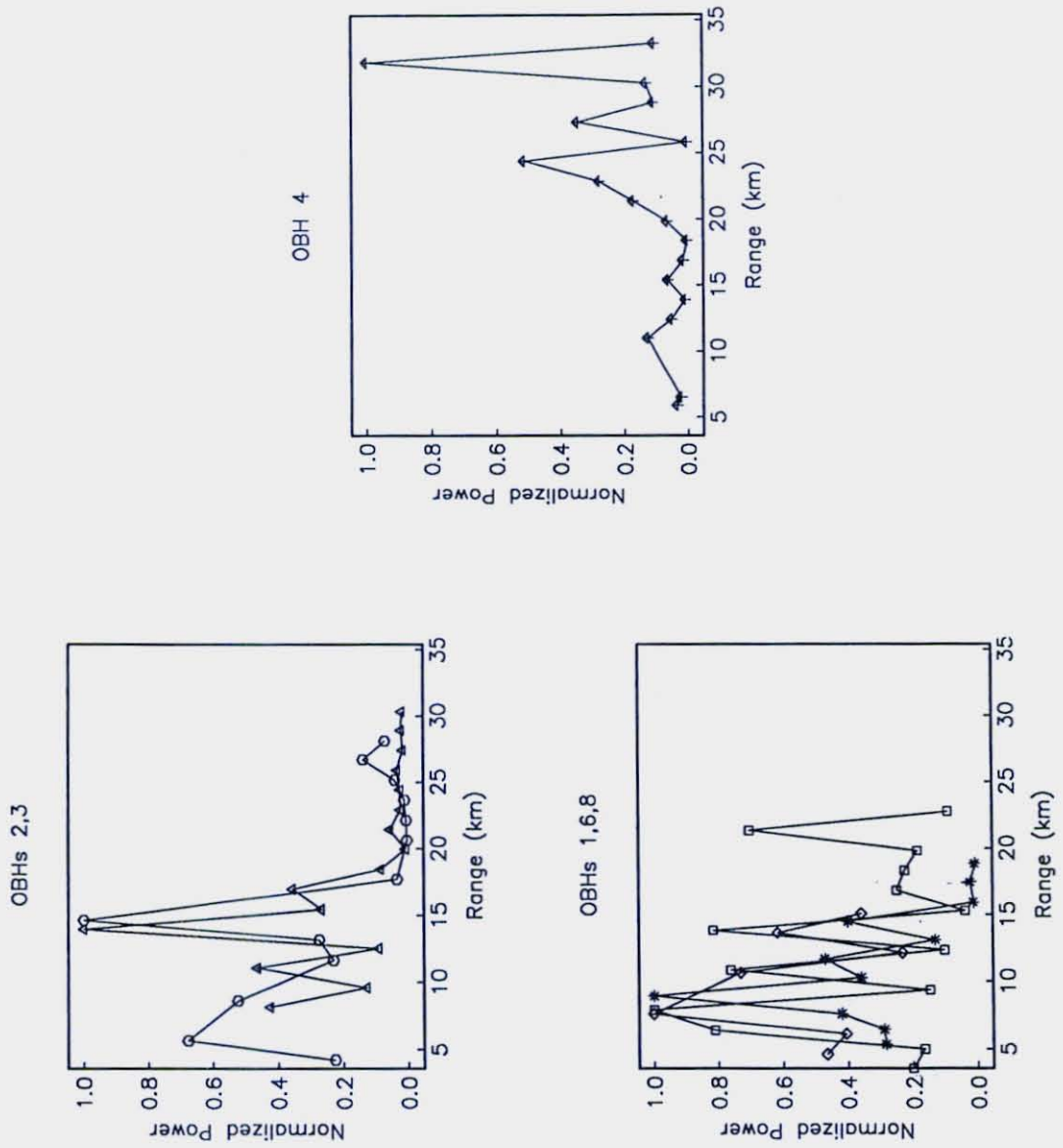


Figure 6

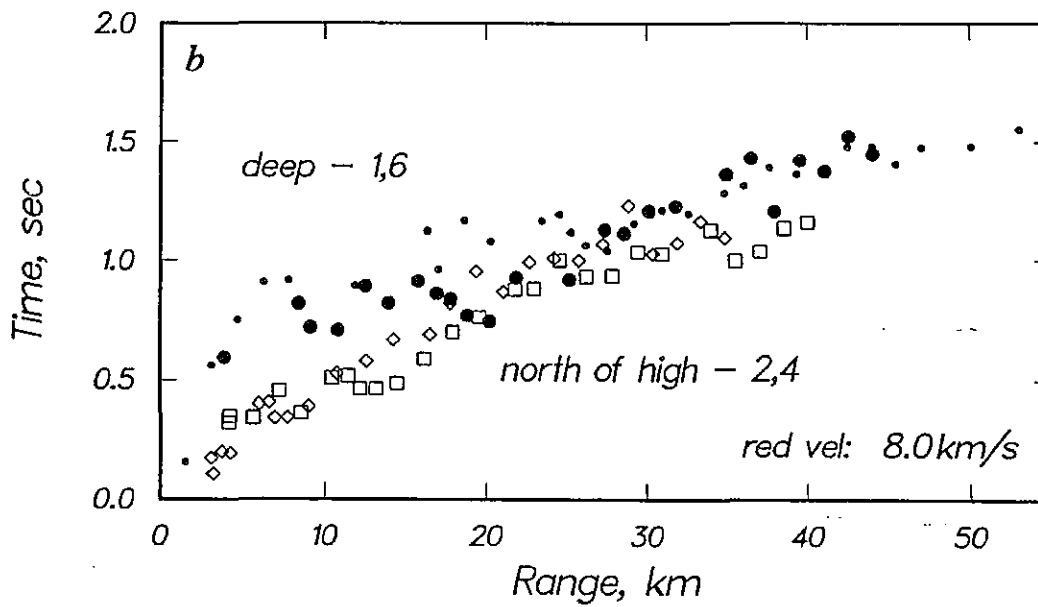
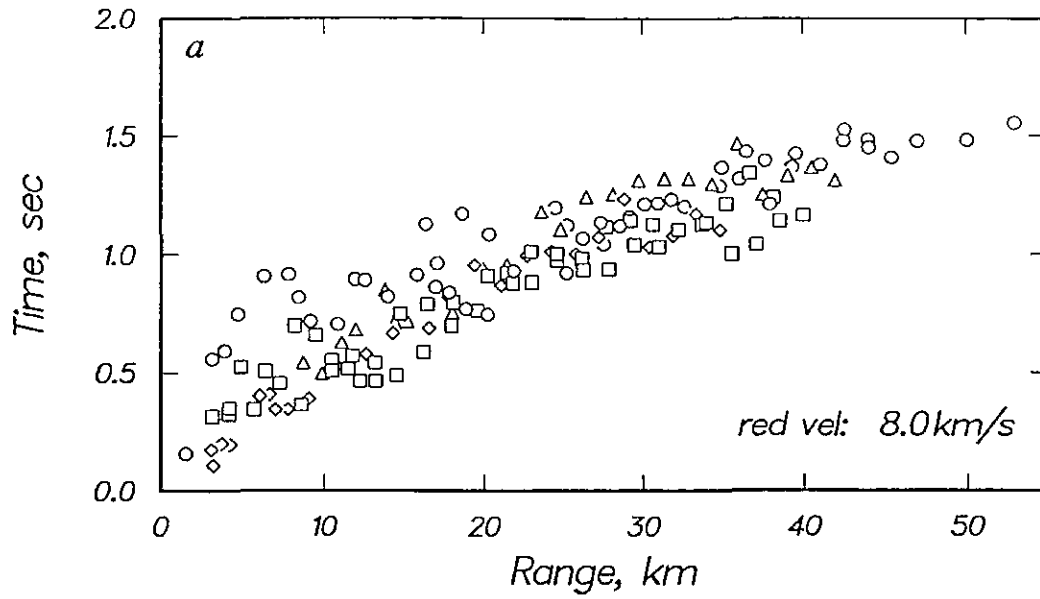


Figure 7



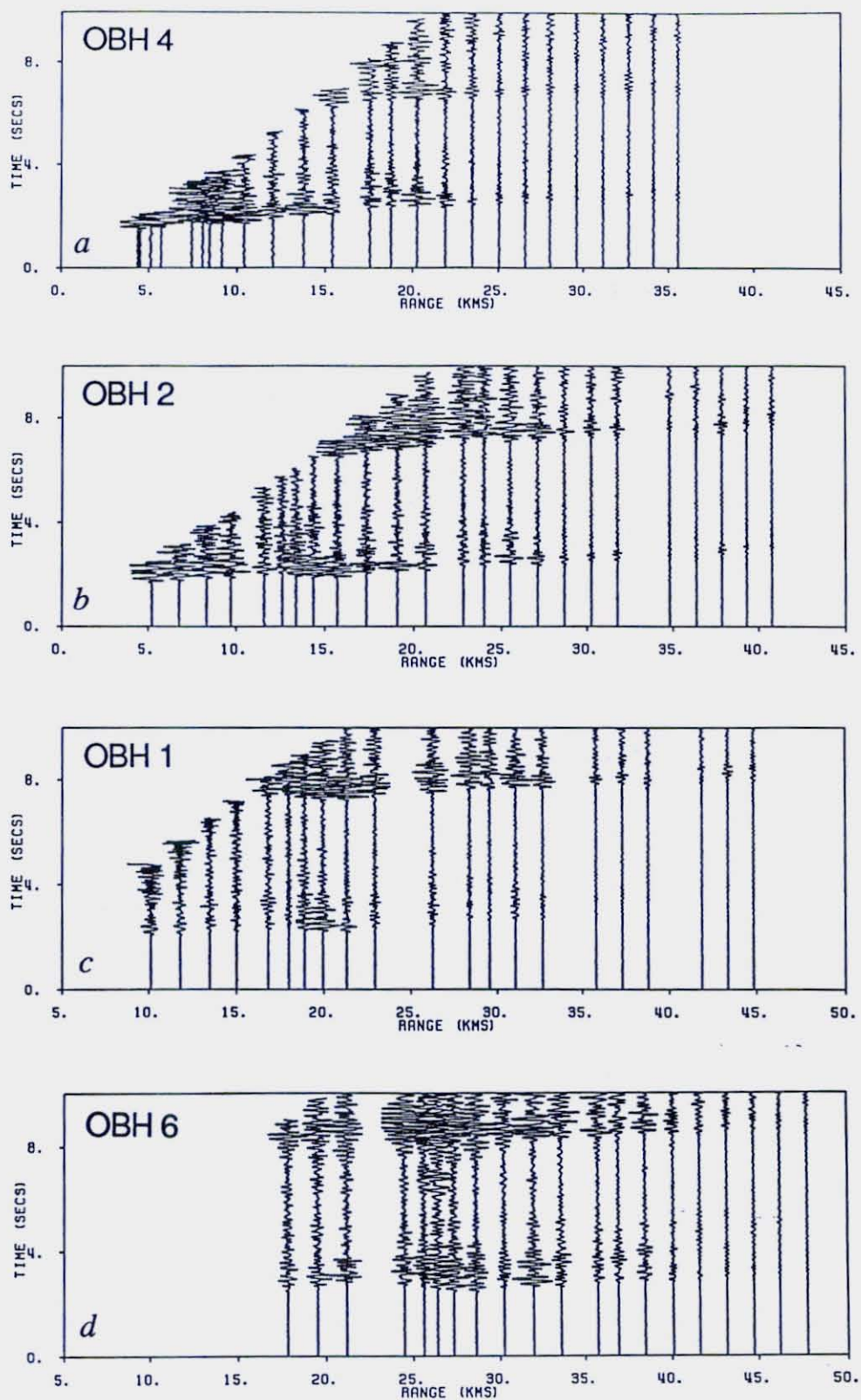
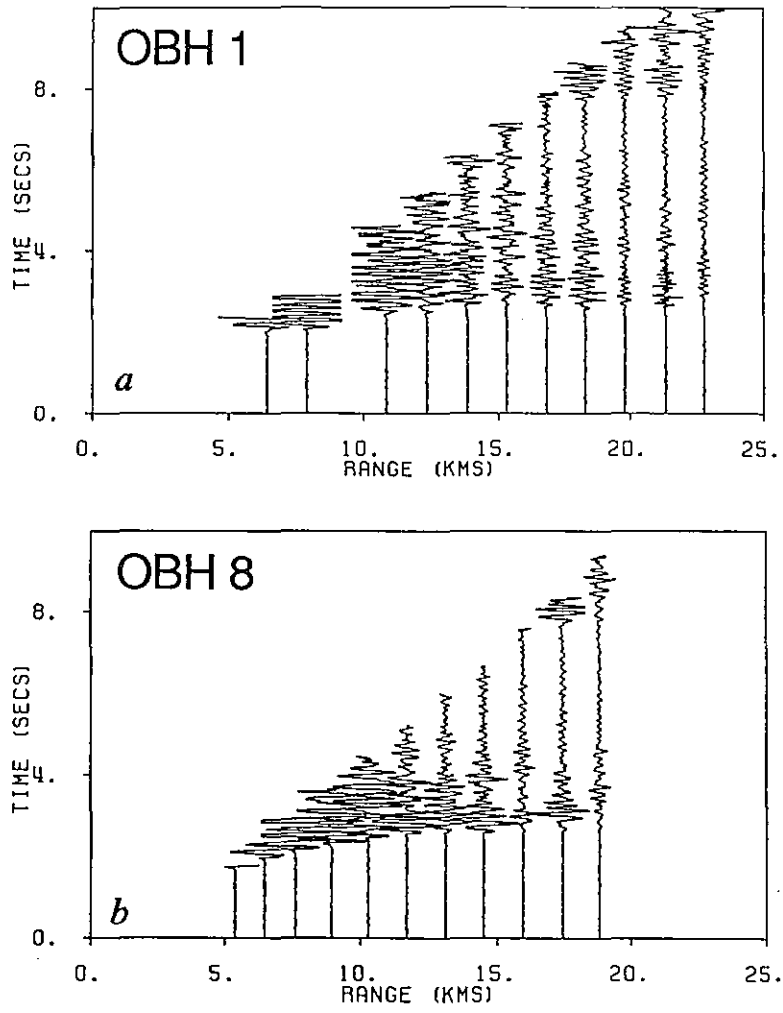
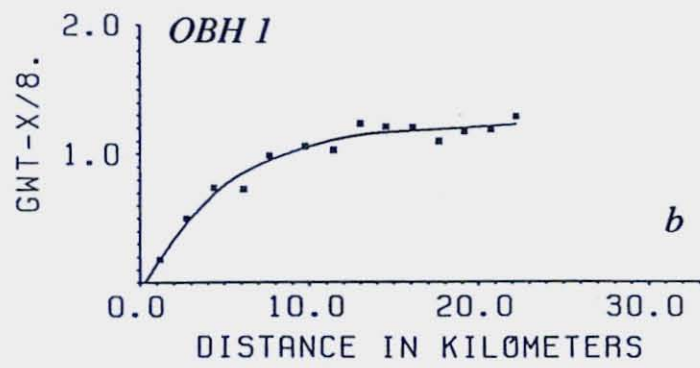
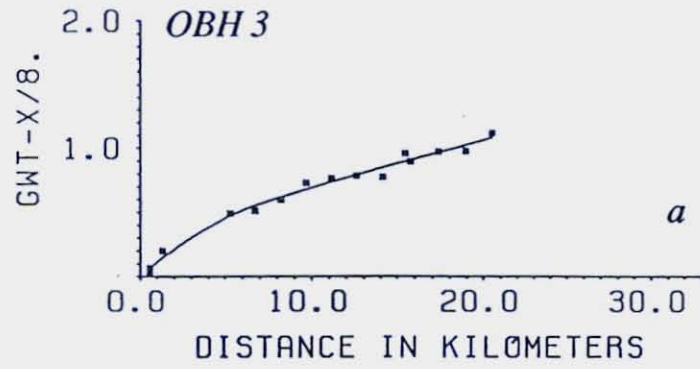
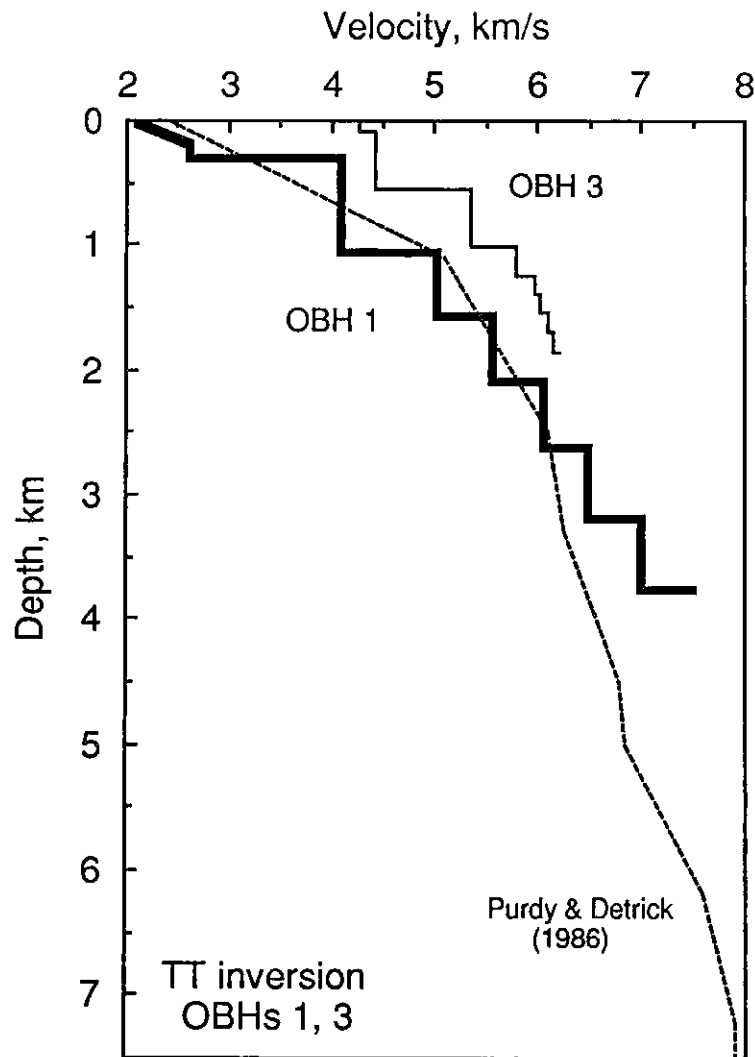
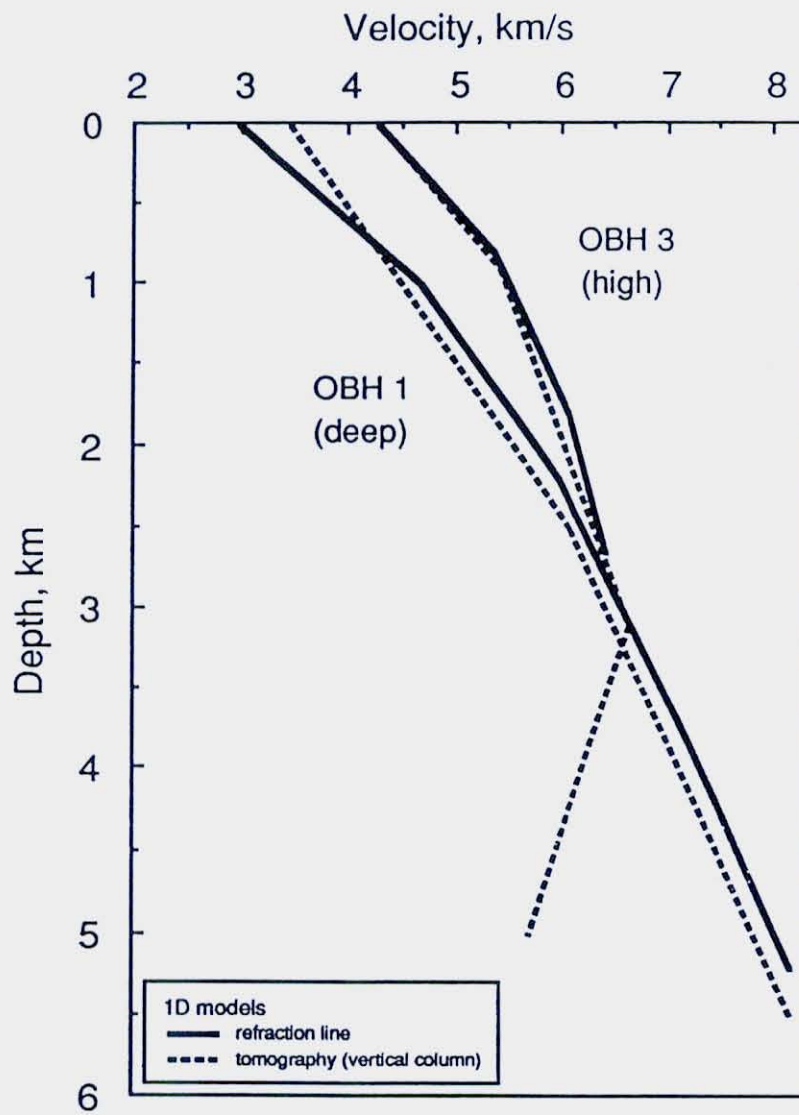


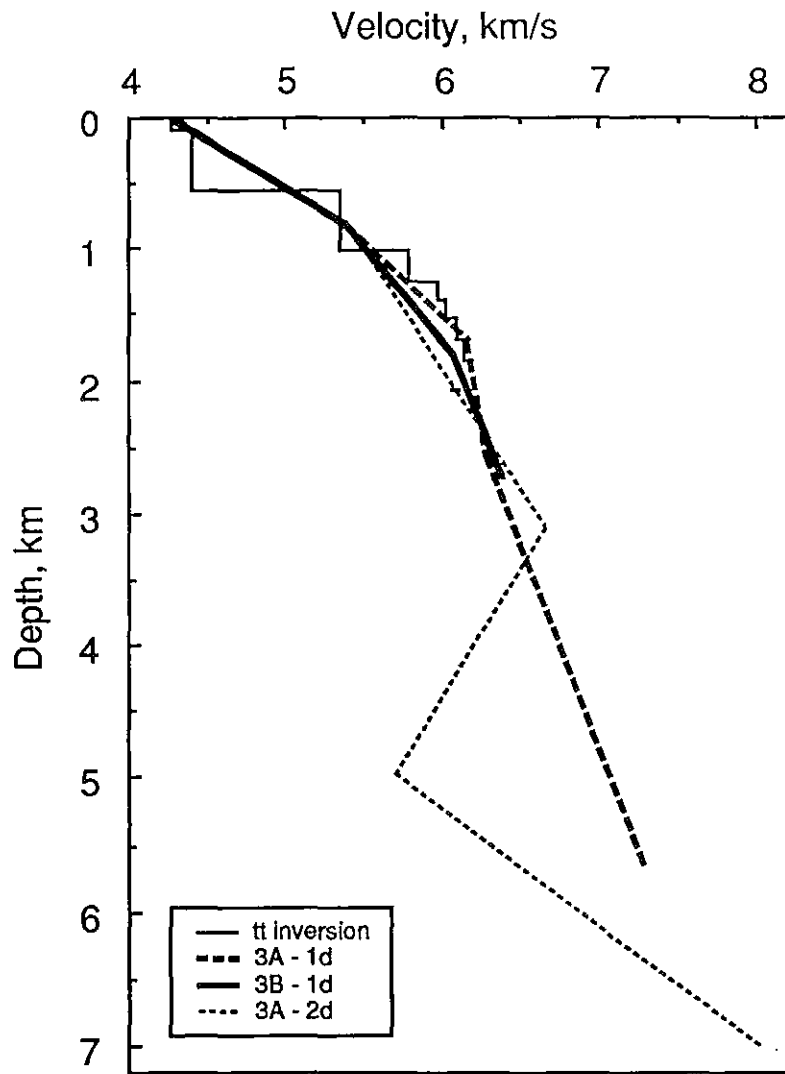
Figure 8

*Figure 9*

*Figure 10*

*Figure 11*

*Figure 12*

*Figure 13 a*

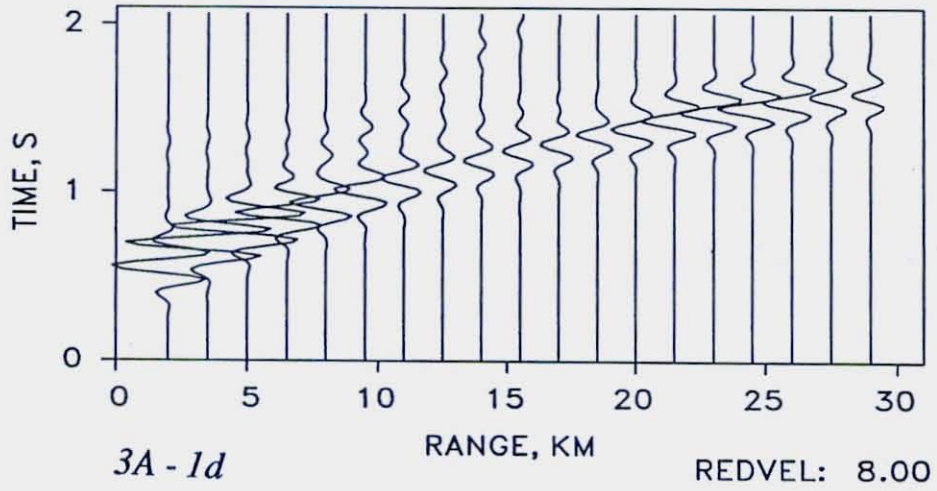
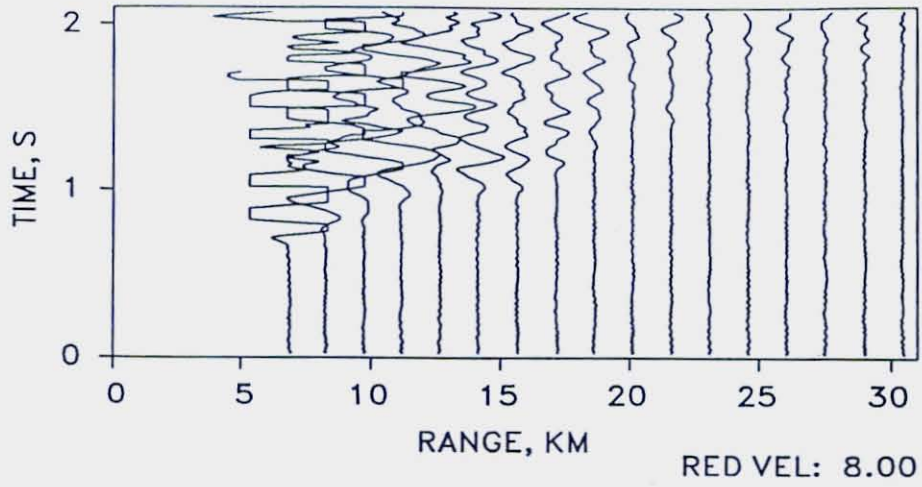


Figure 13 b

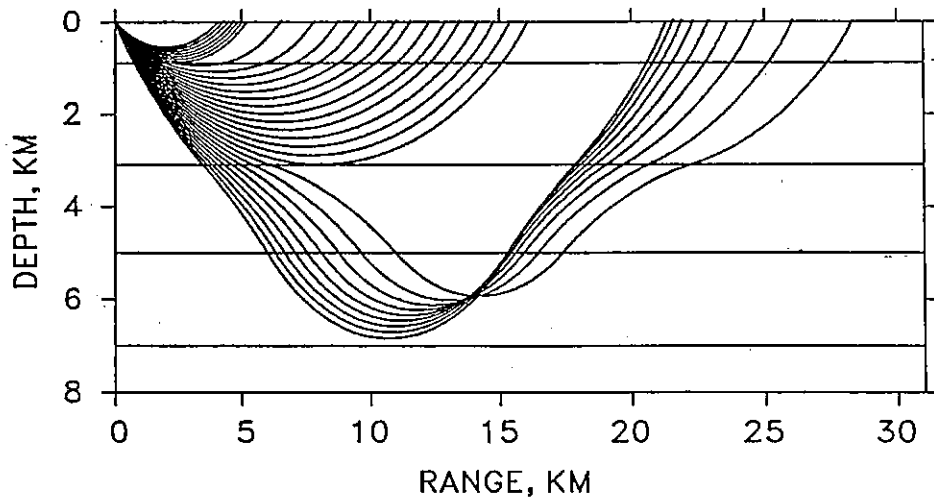
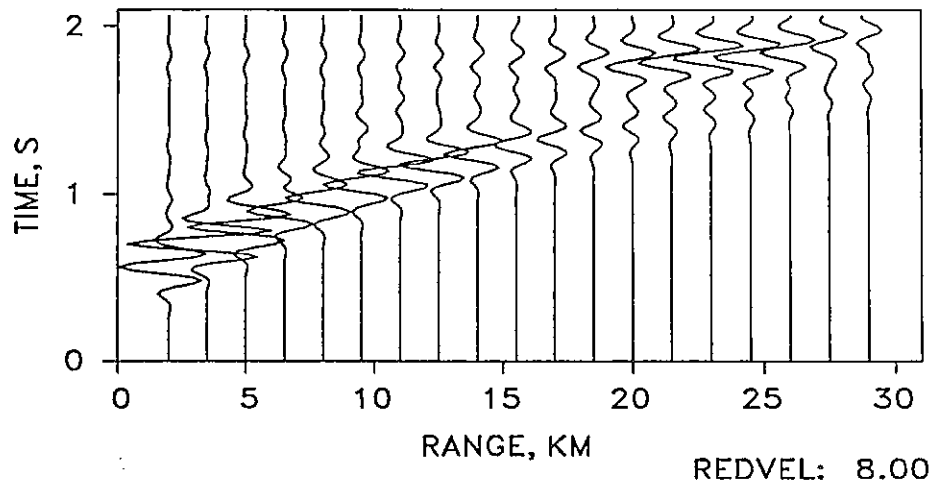
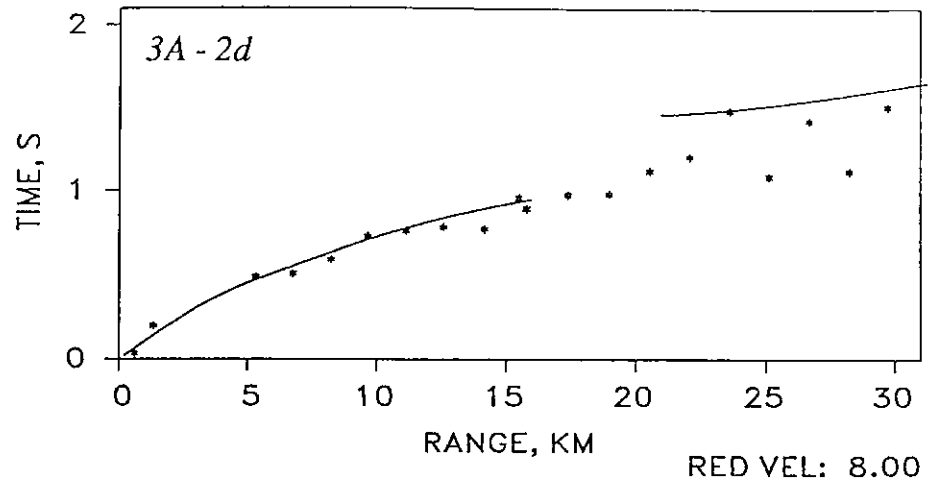


Figure 13c



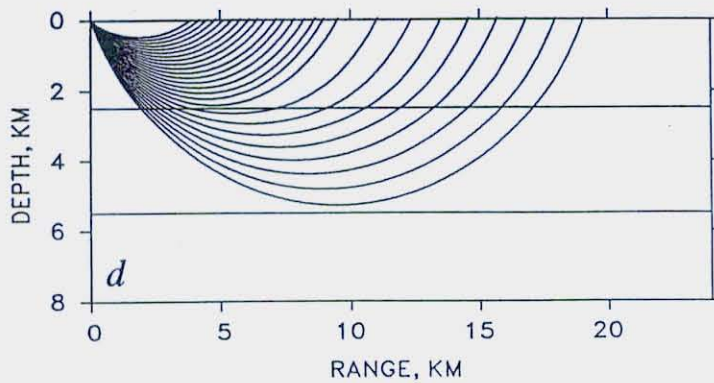
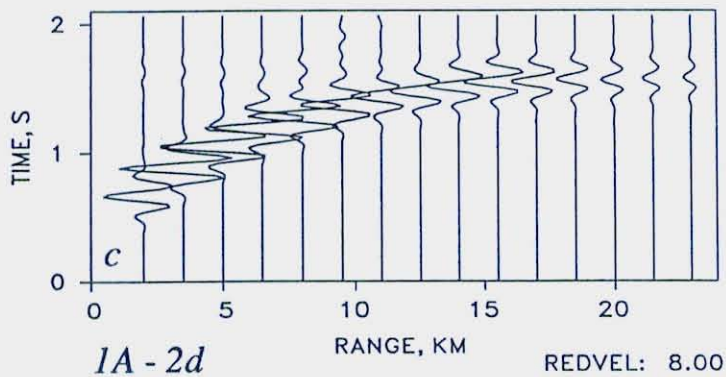
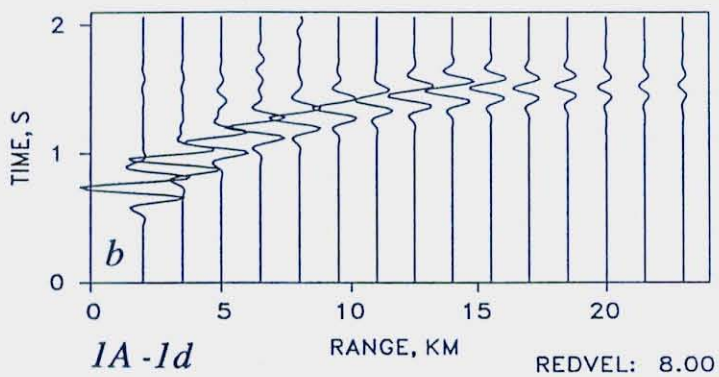
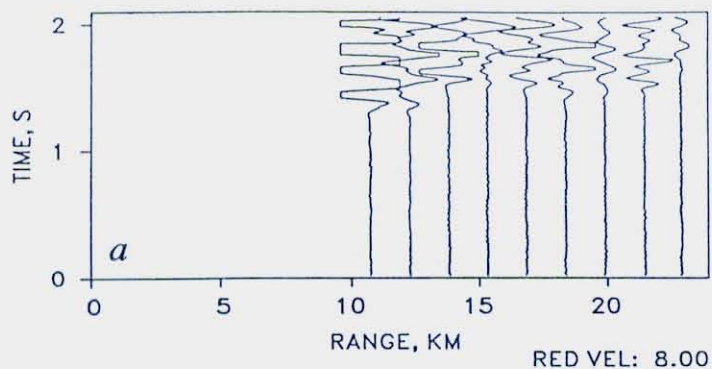


Figure 14

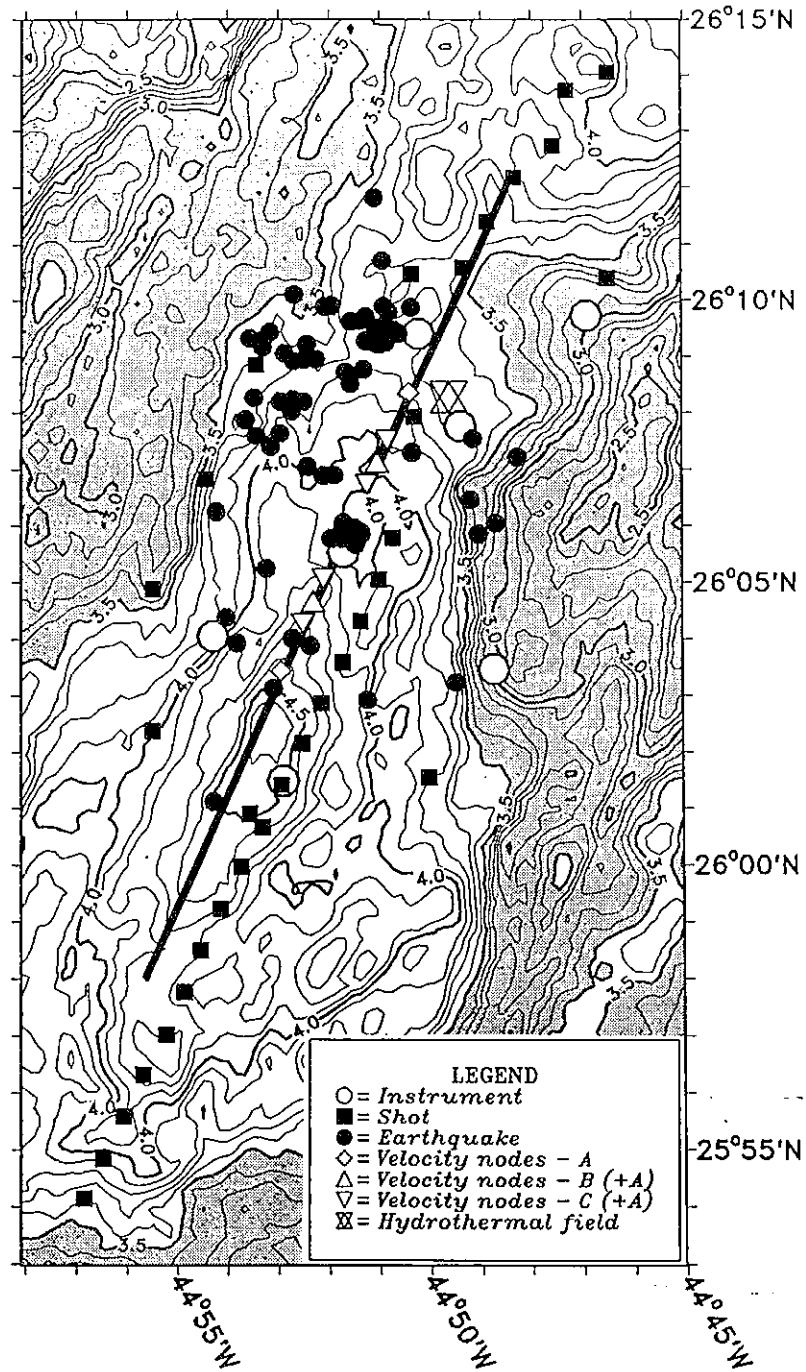


Figure 15

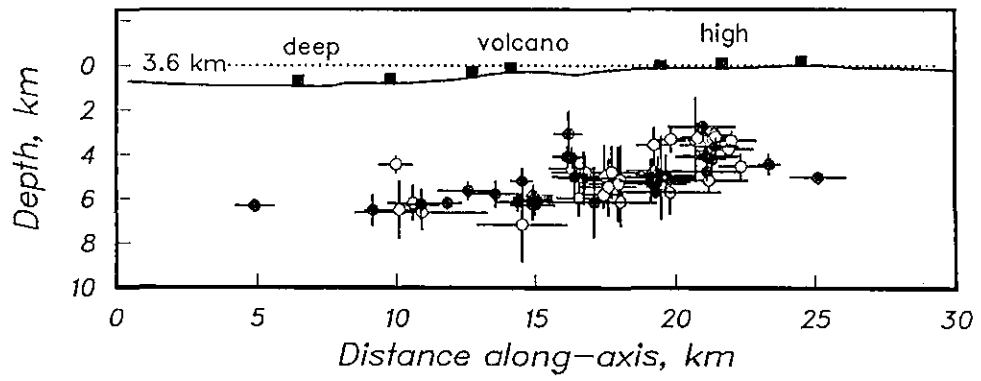


Figure 16

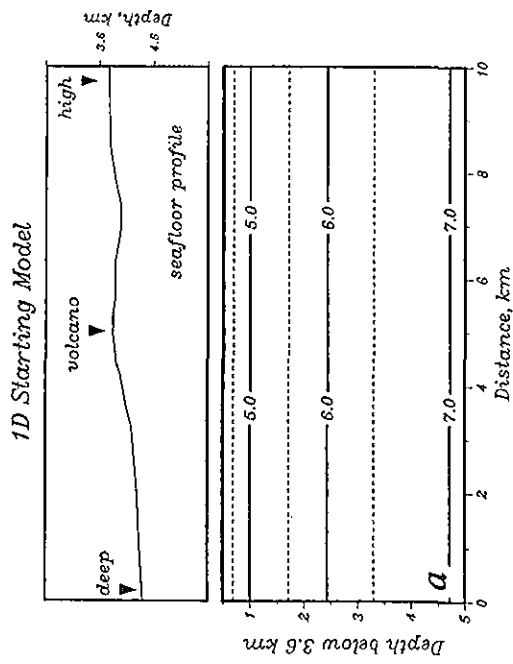
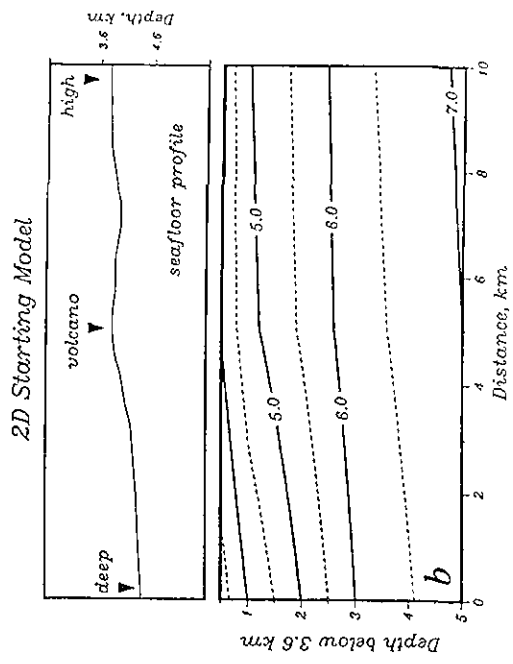
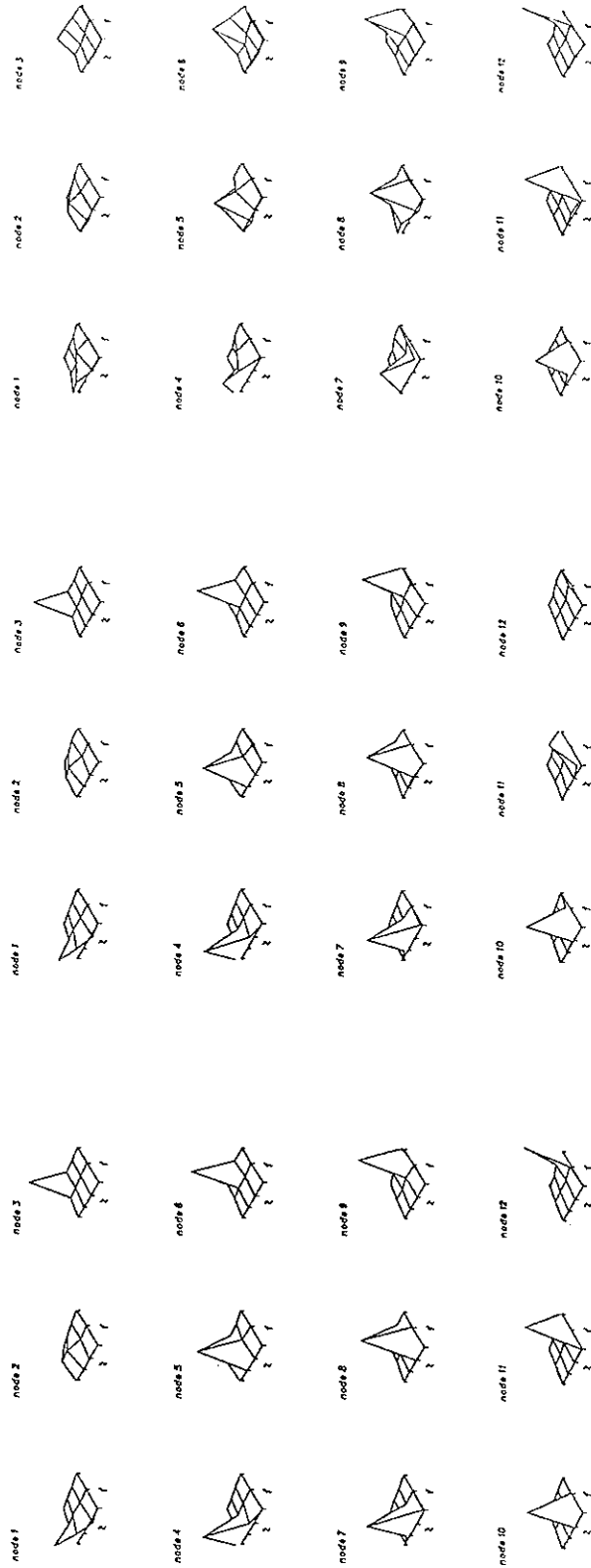


Figure 17

		Y (along - axis)		
		0 Deep	5 Volcano	10 km High
Z (depth)	0	node 1	2	3
	1	4	5	6
	3	7	8	9
	5 km	10	11	12

*Figure 18*



c

b

a

Figure 19

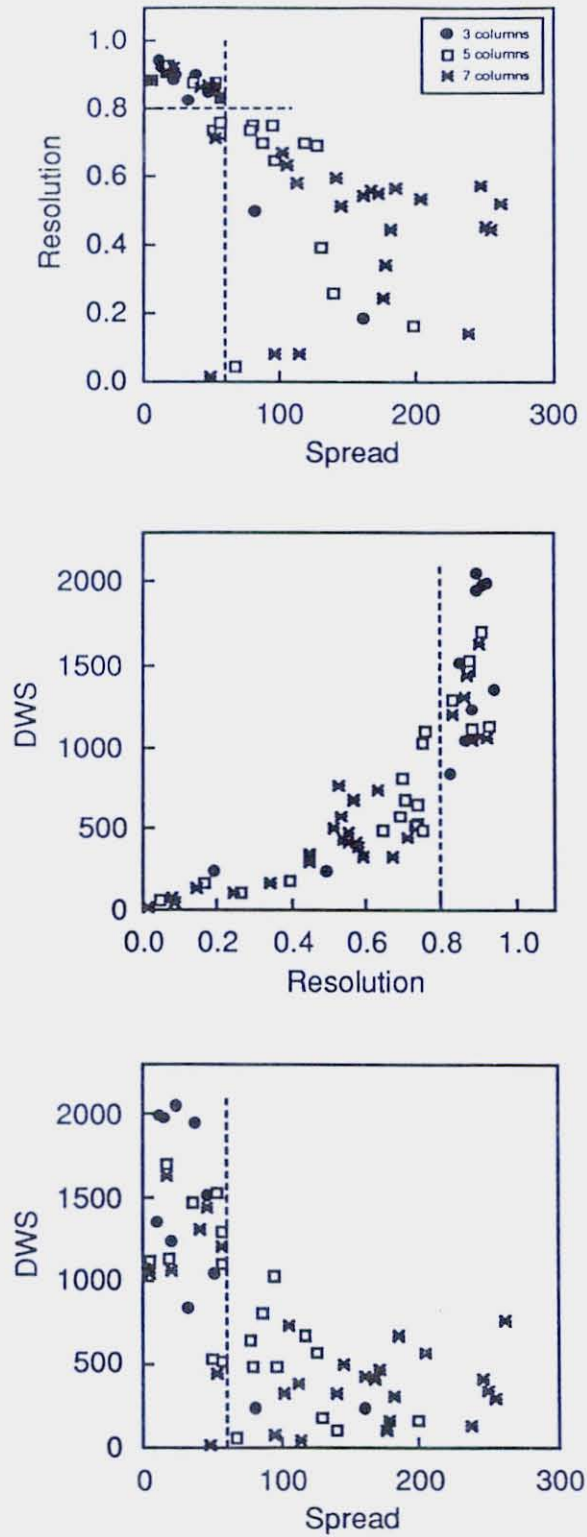
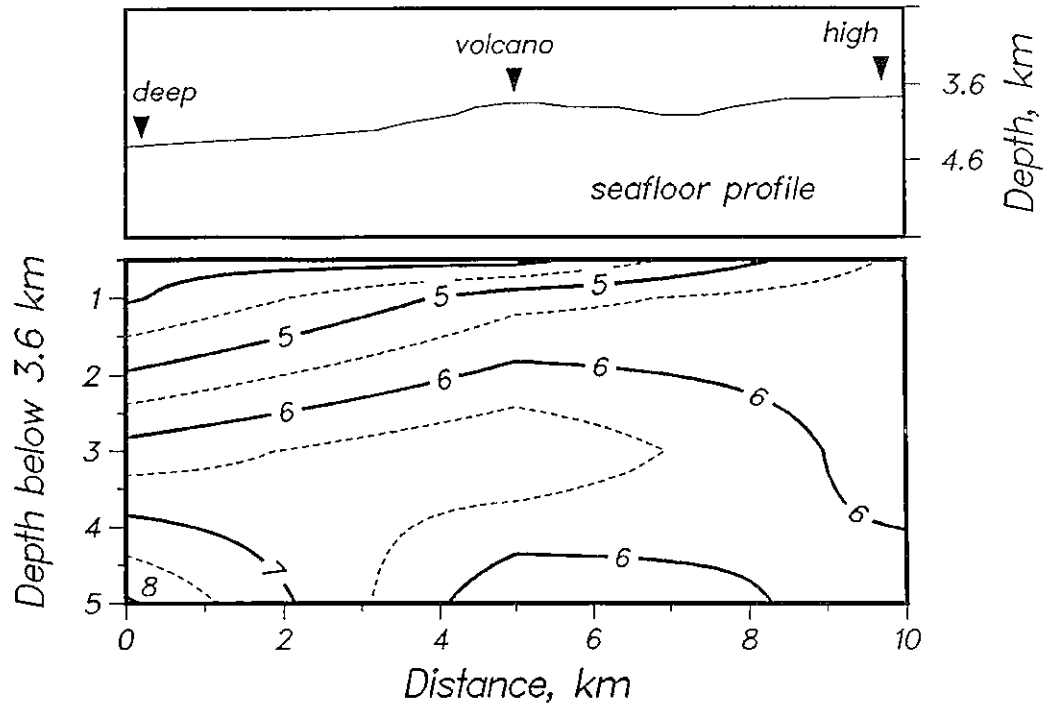


Figure 20

*Median Valley, shots and earthquakes**Figure 21*



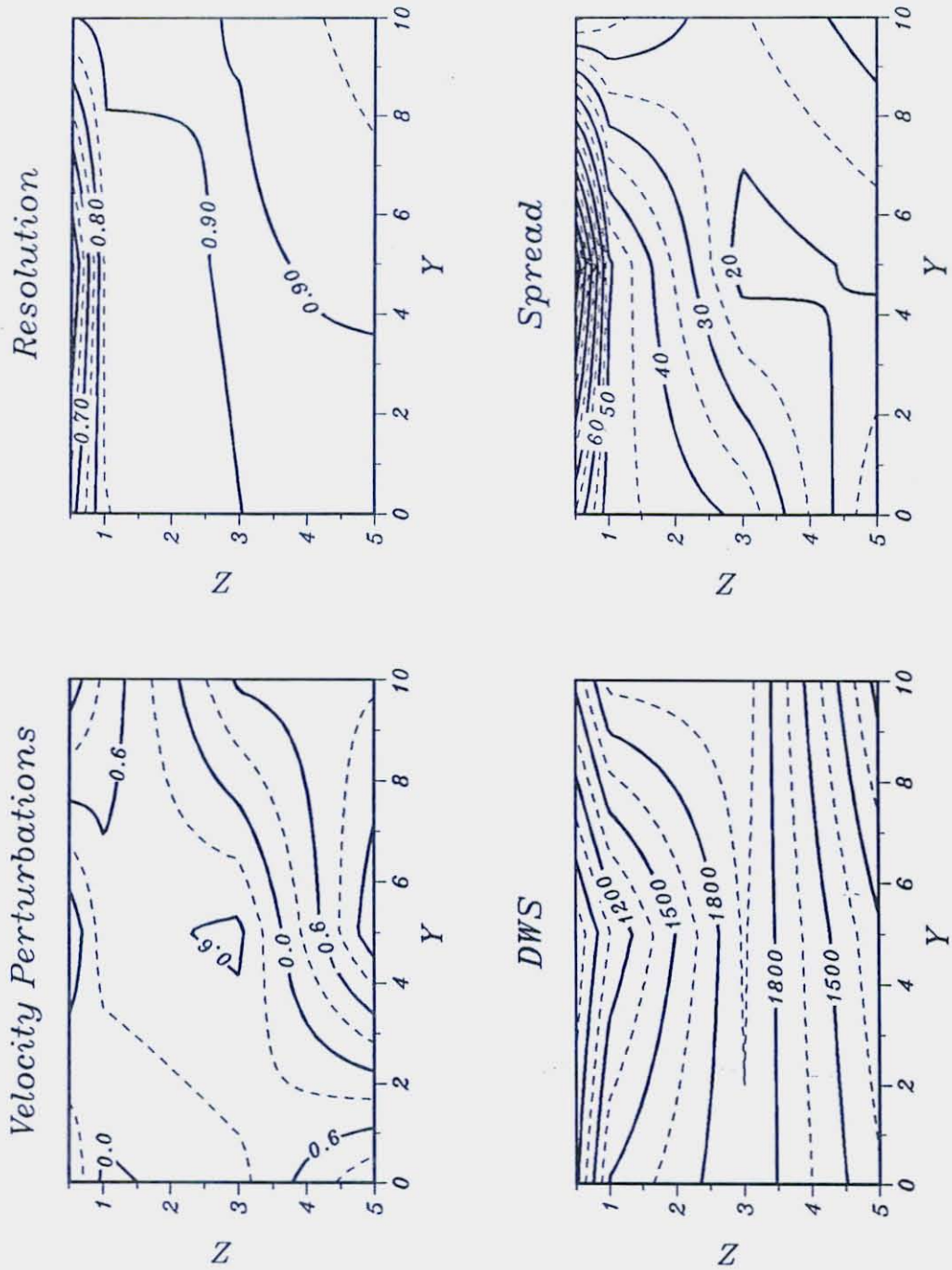
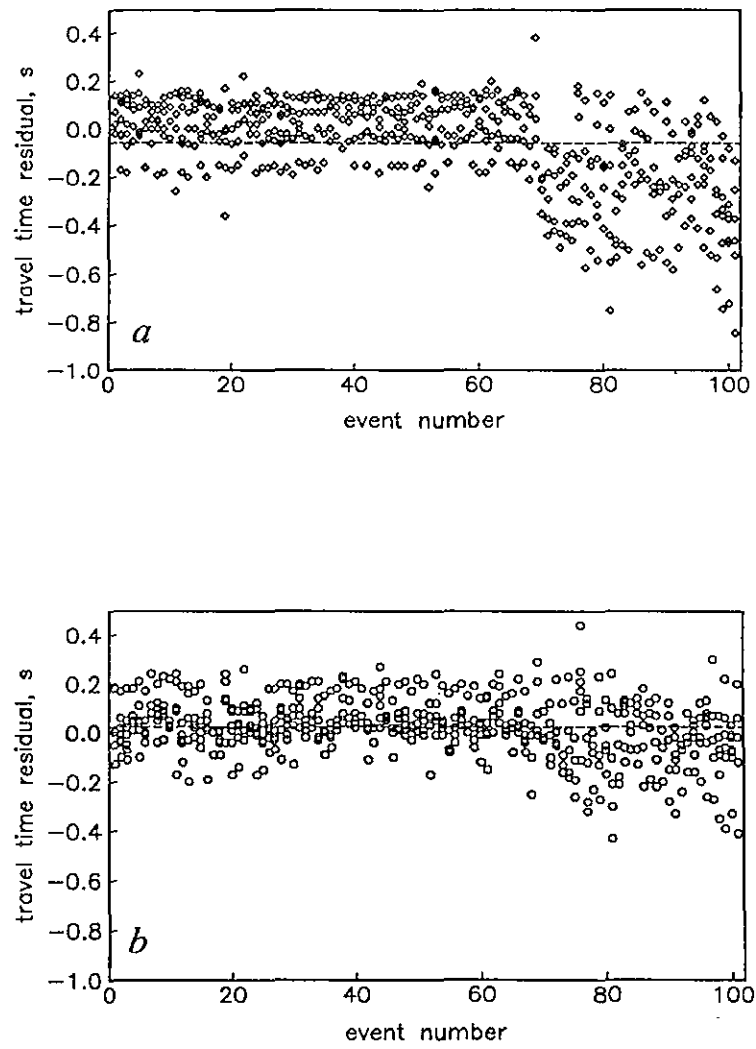


Figure 22

*Figure 23*

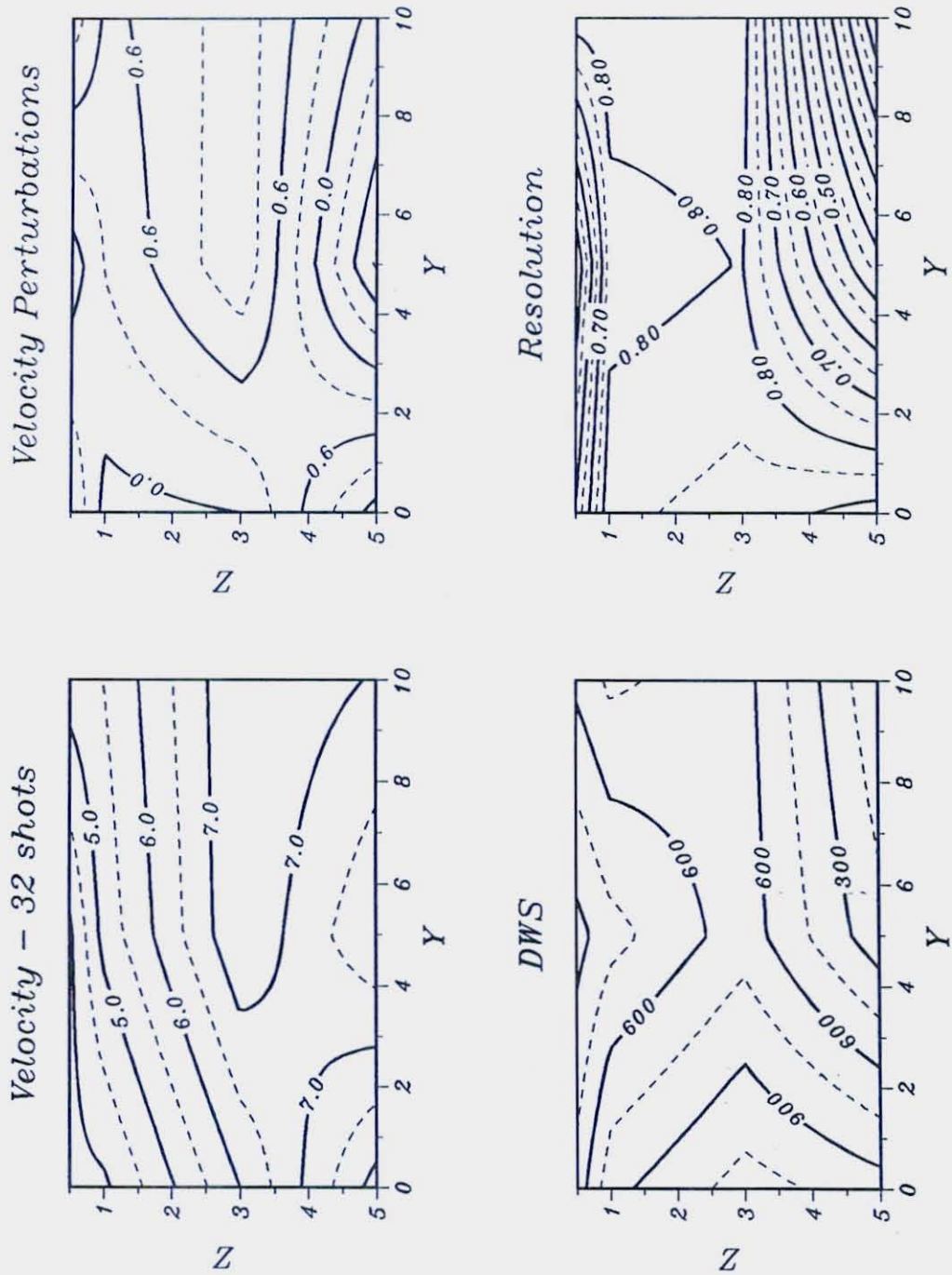


Figure 24

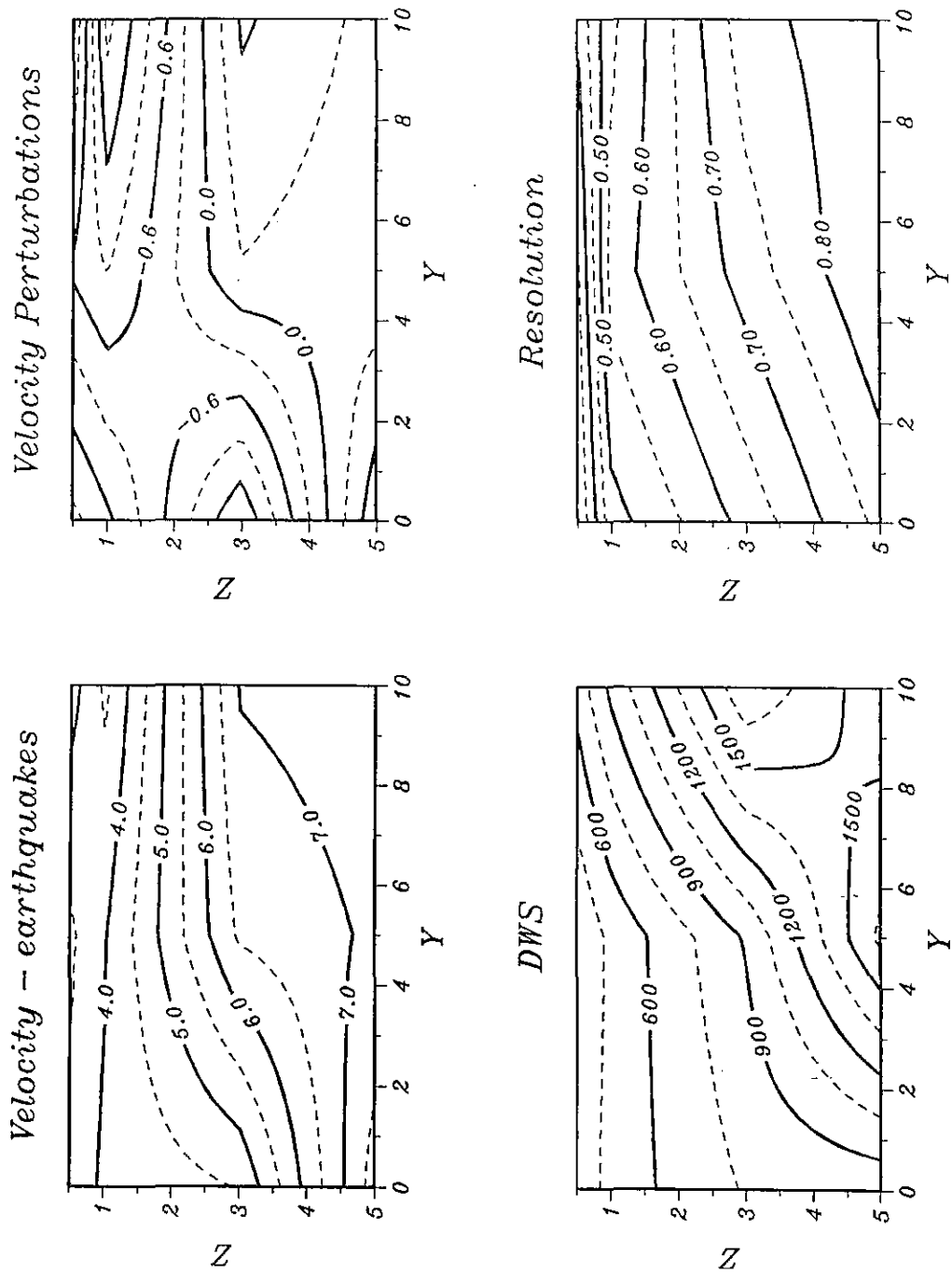
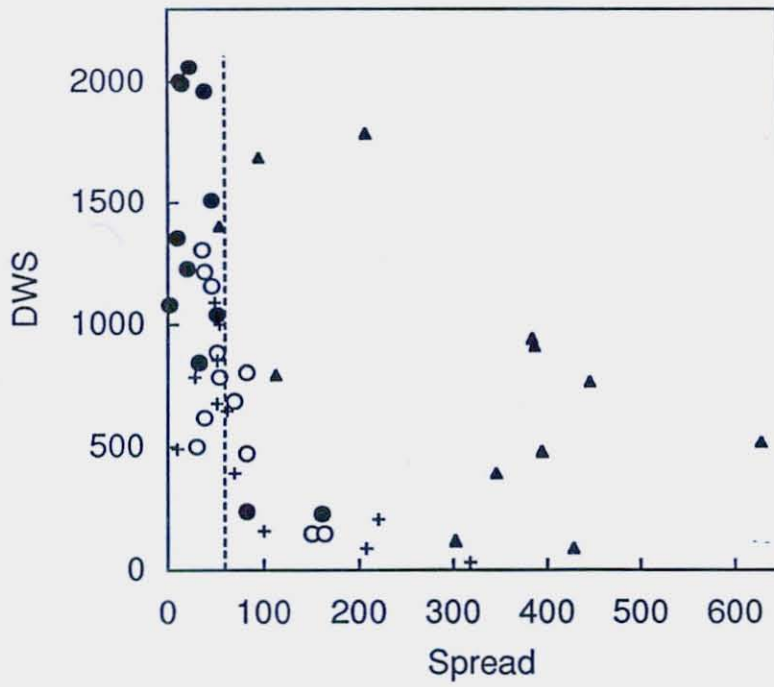
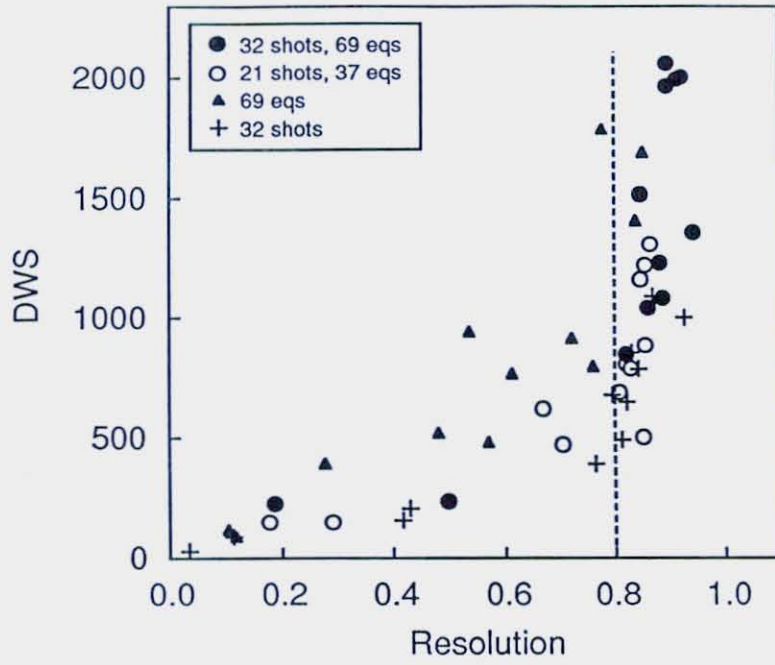


Figure 25

*Figure 26*

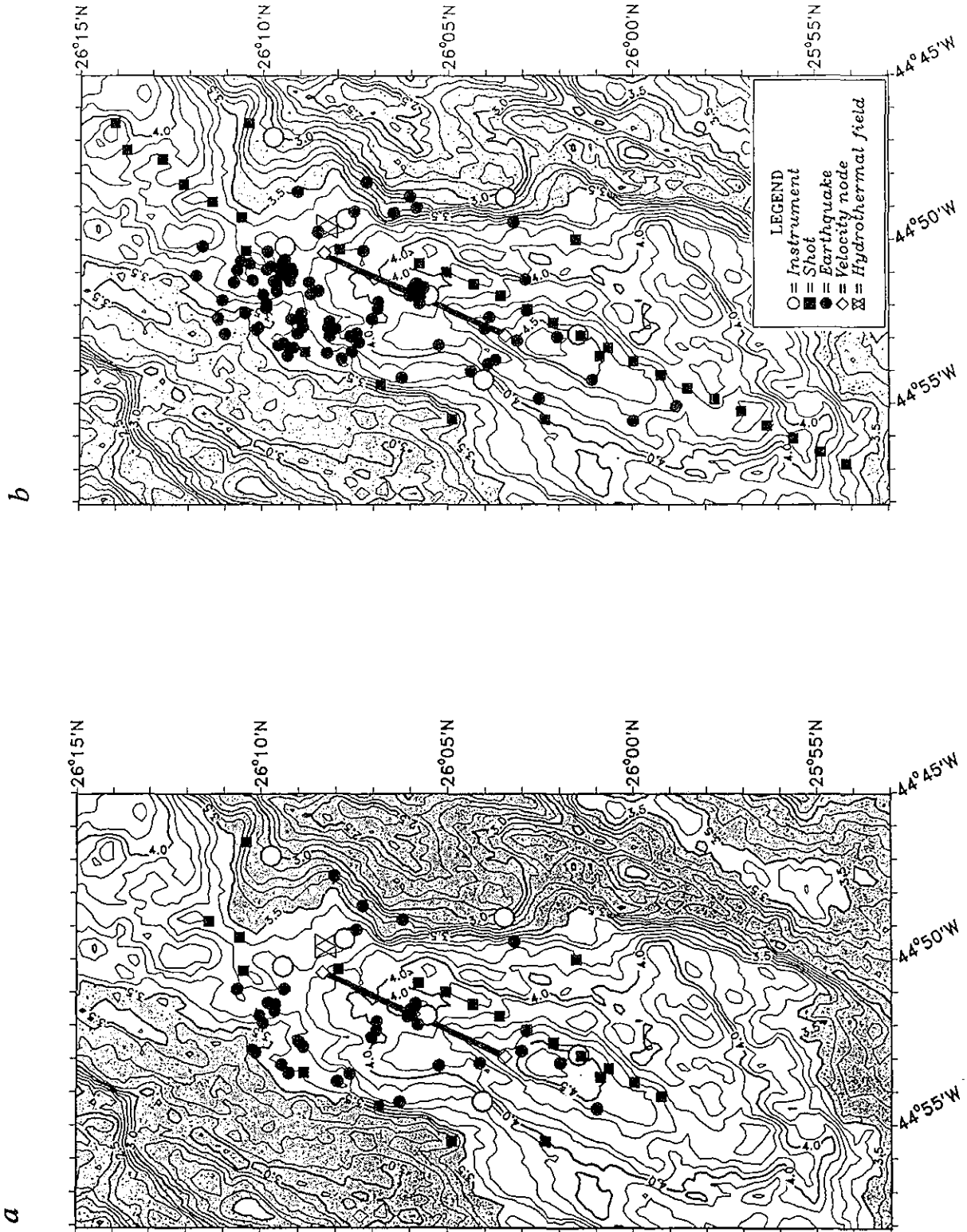


Figure 27

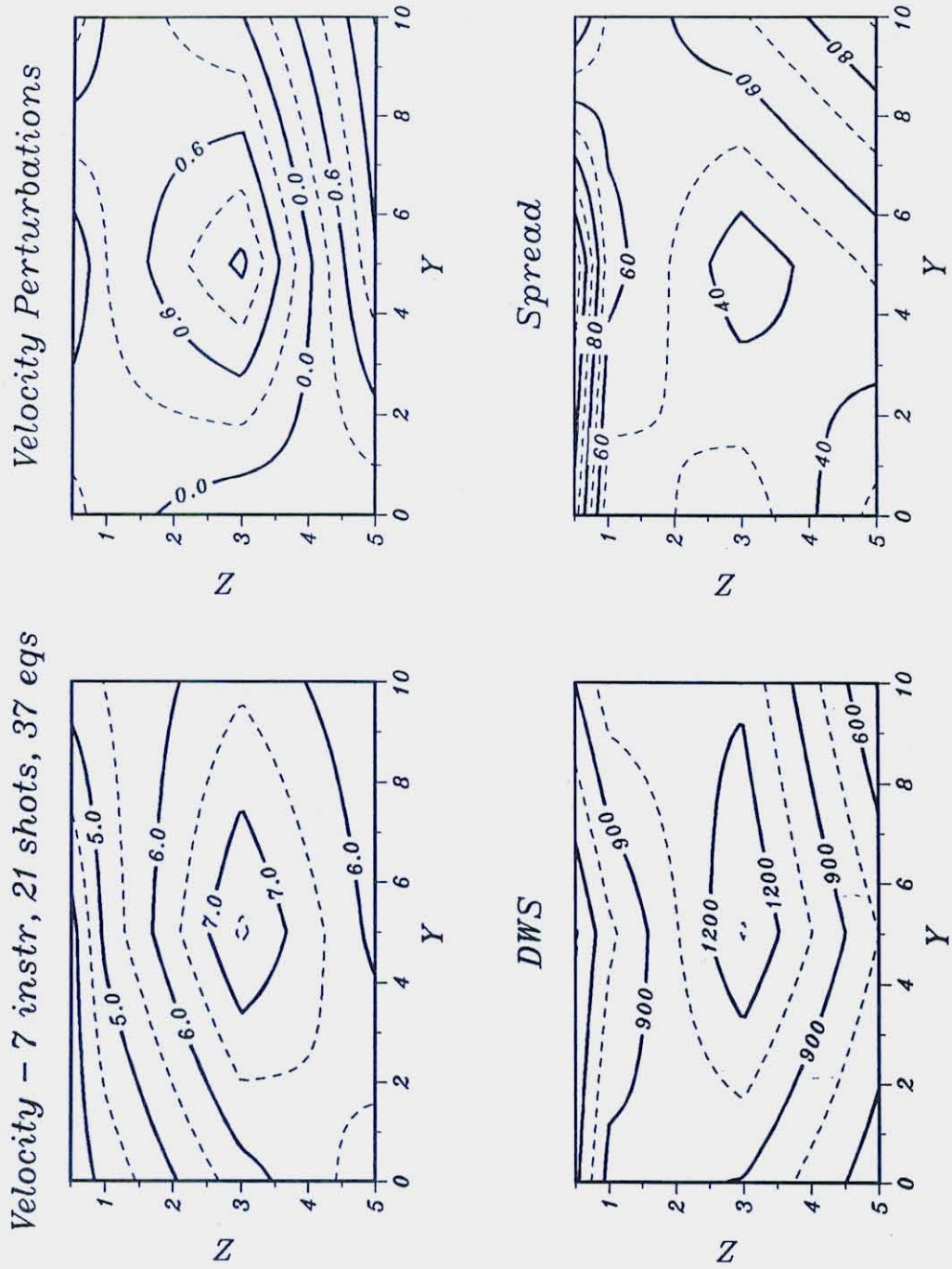


Figure 28

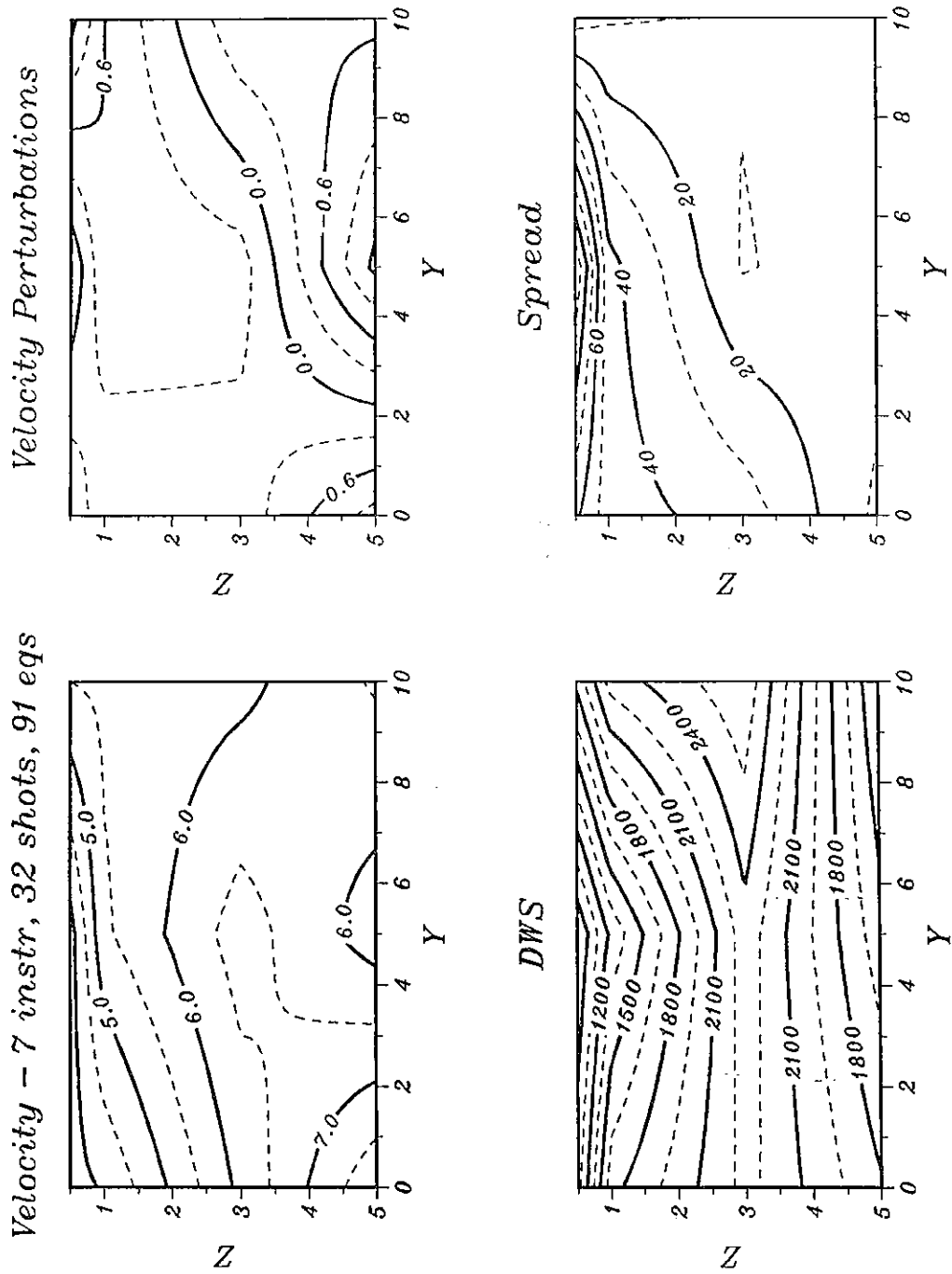
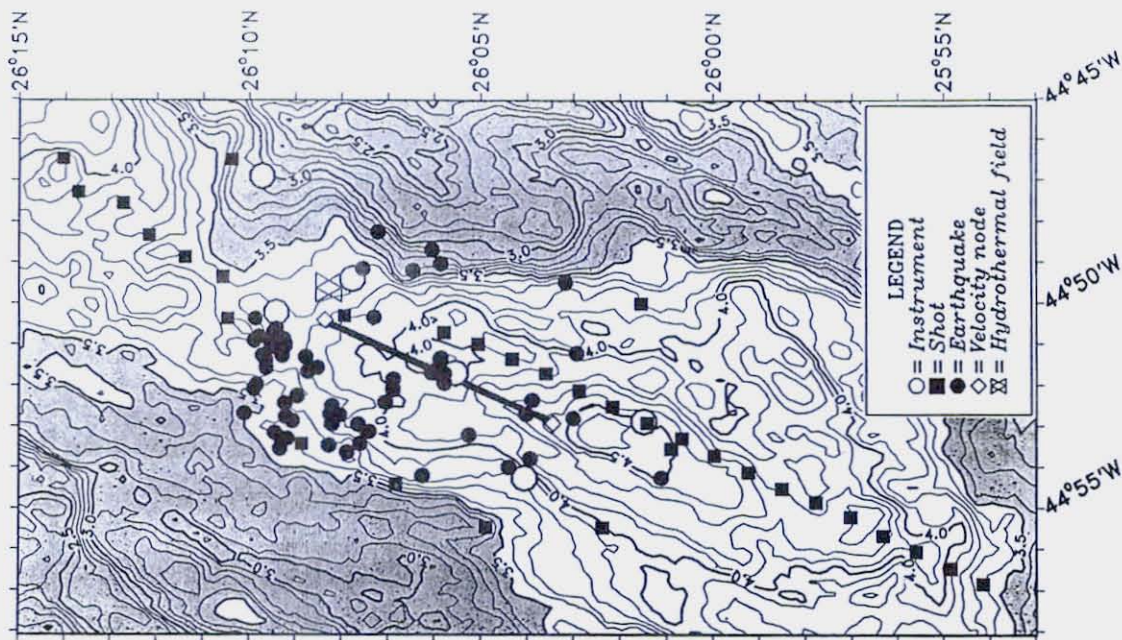
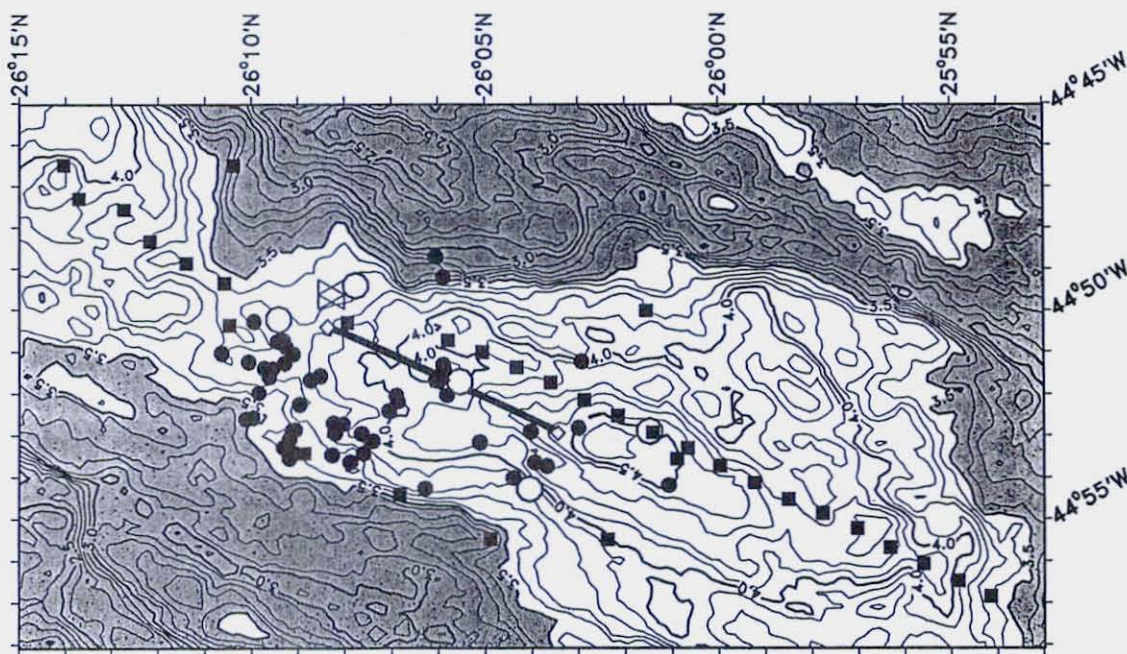


Figure 29





b



a

Figure 30

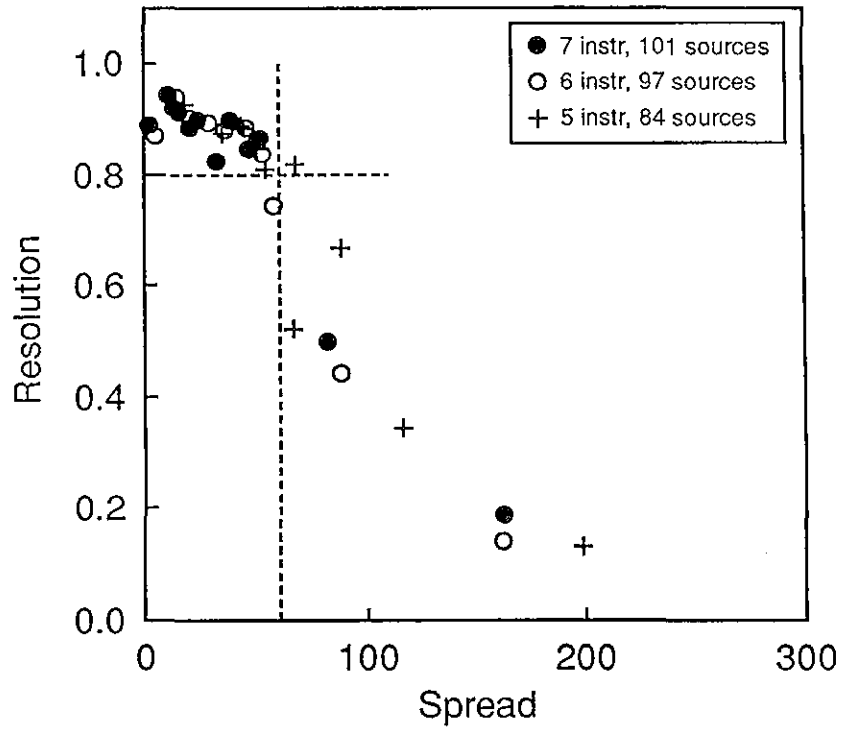


*Figure 31*

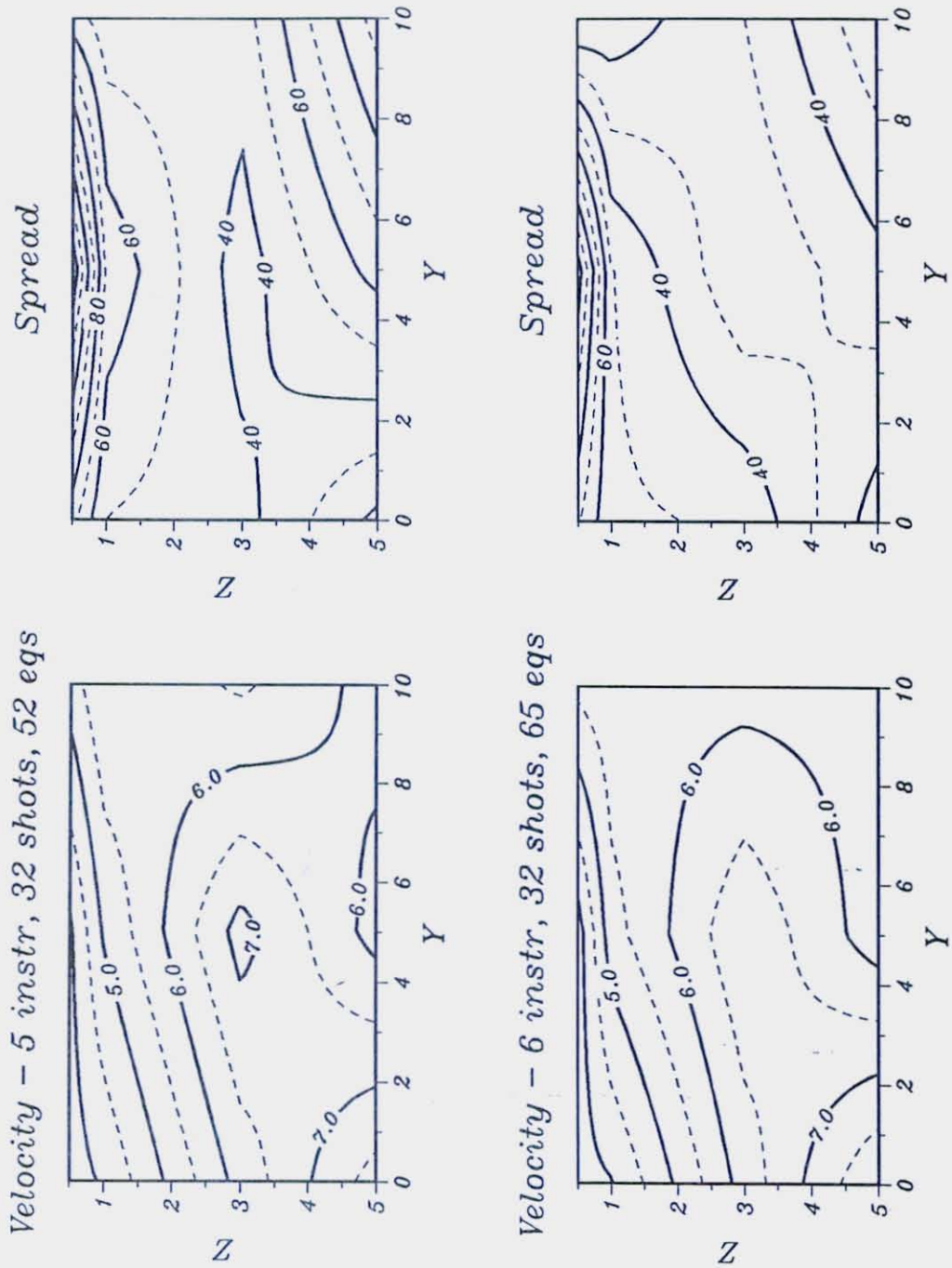
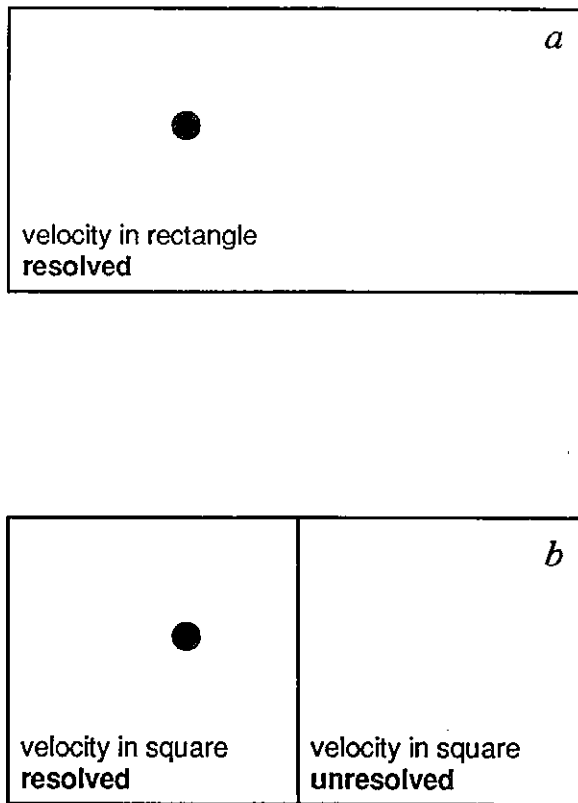


Figure 32

*Figure 33*

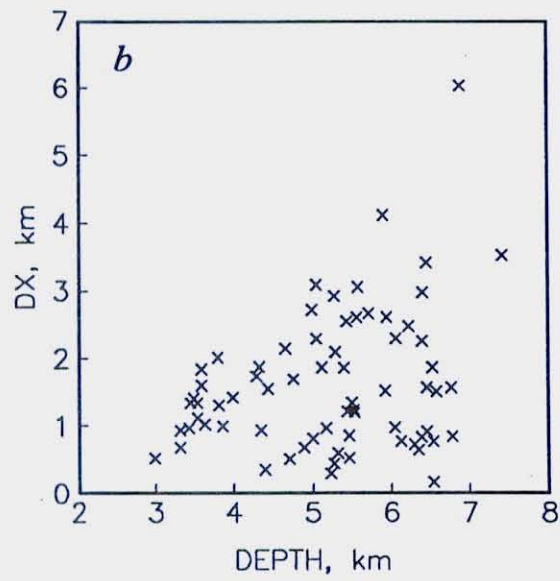
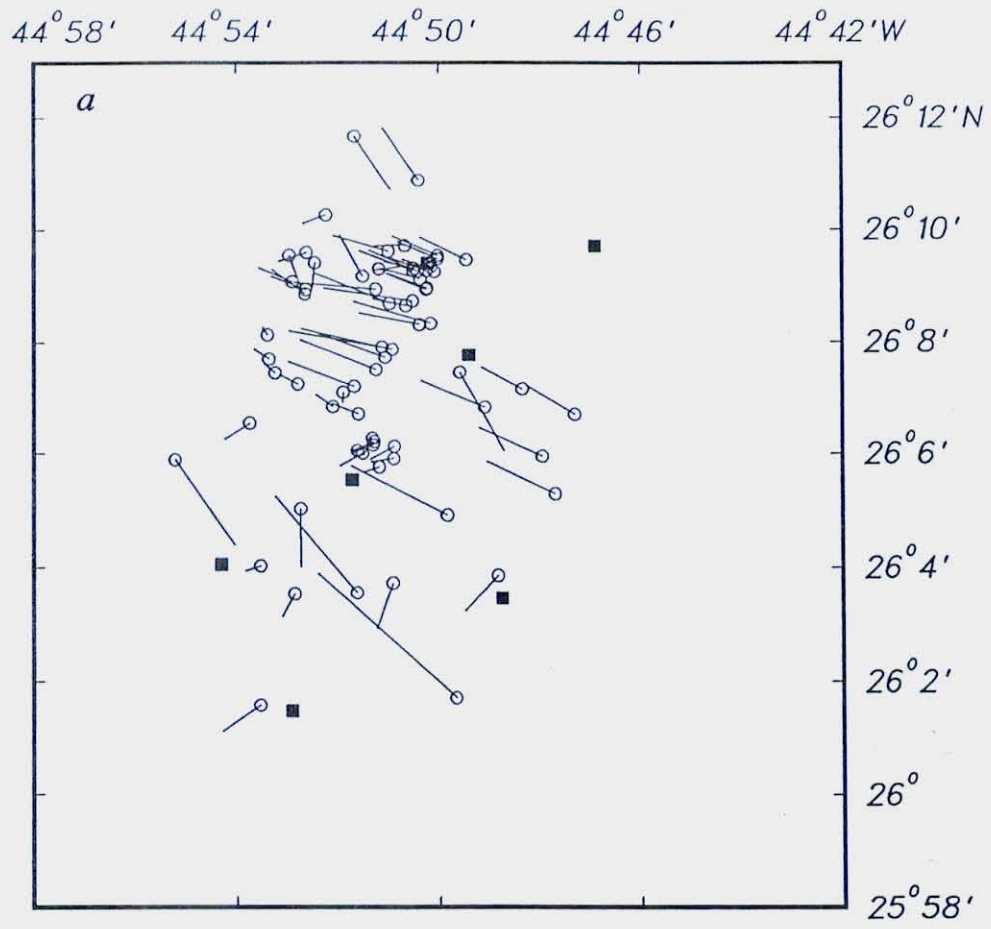


Figure 34

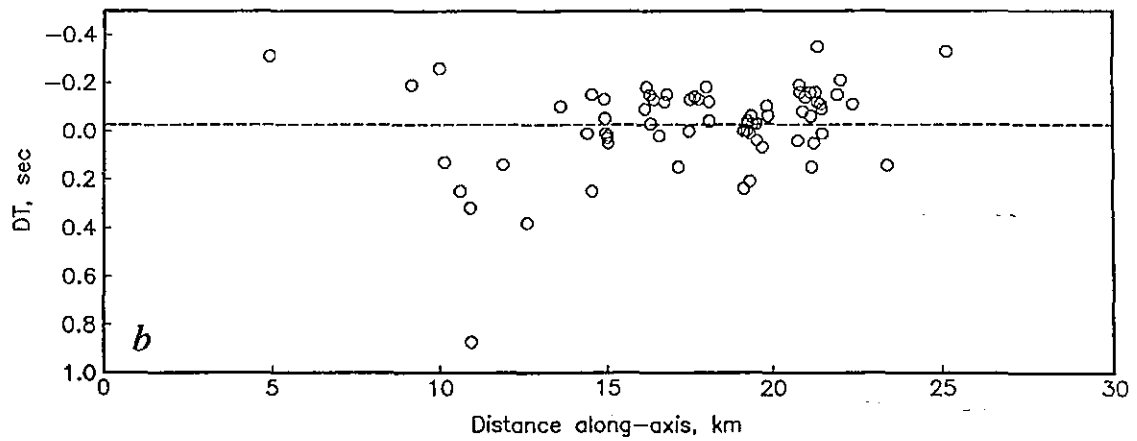
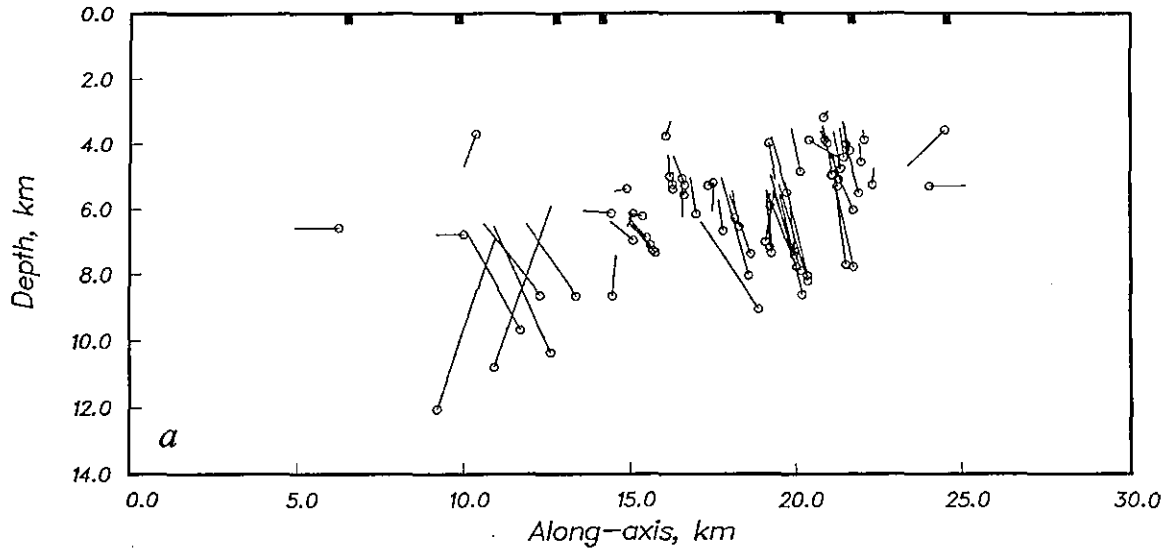


Figure 35

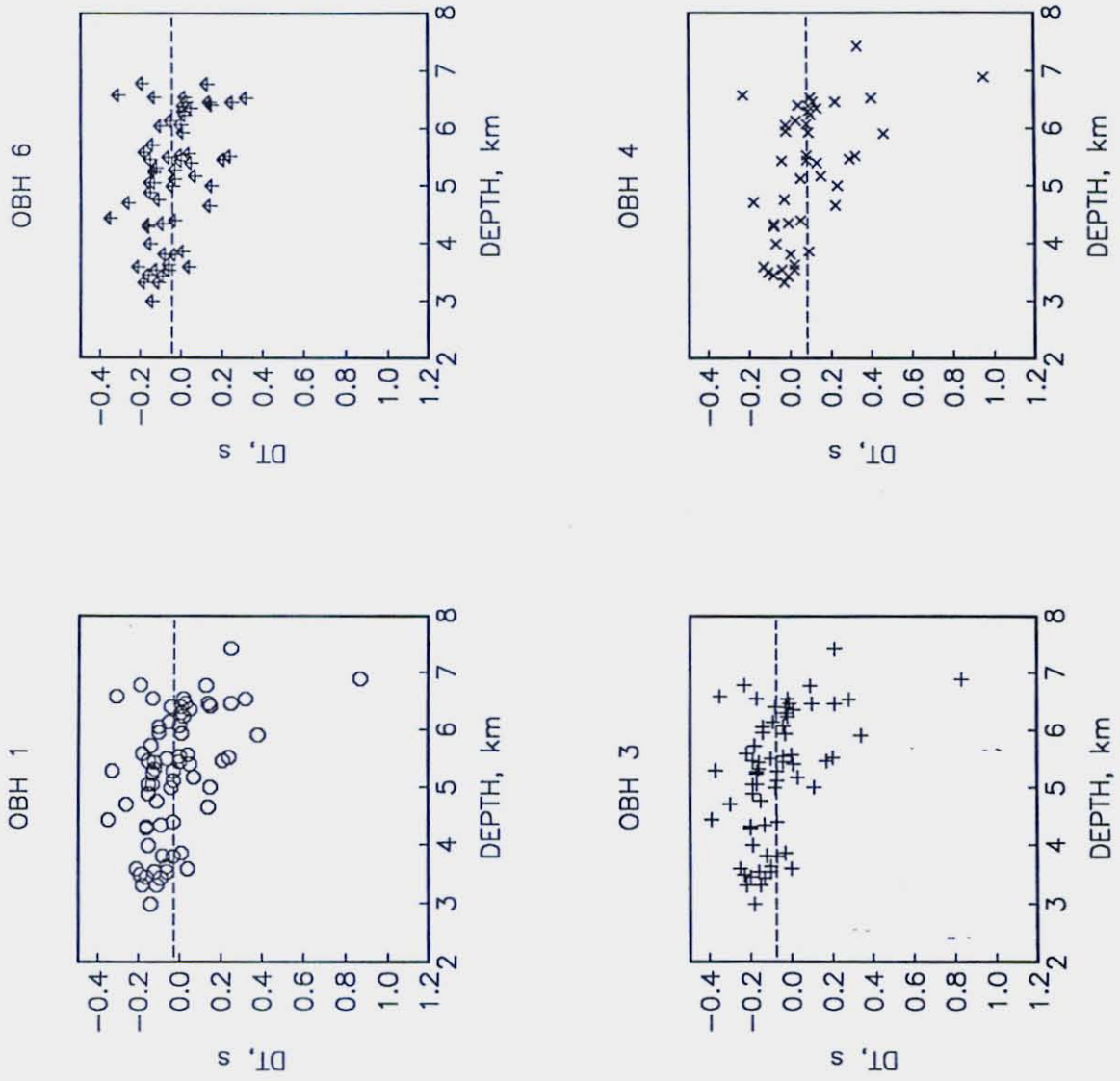


Figure 36

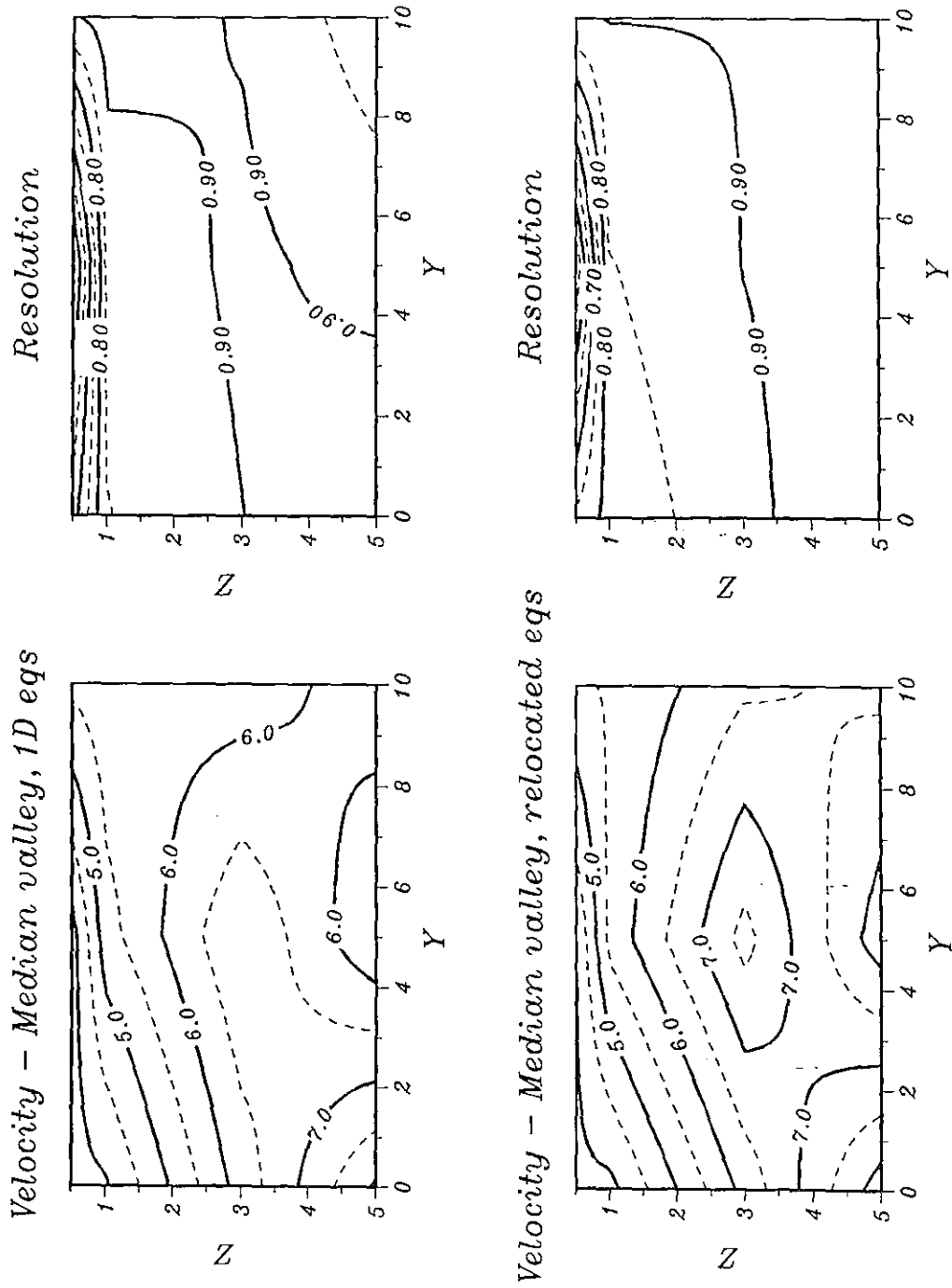


Figure 37



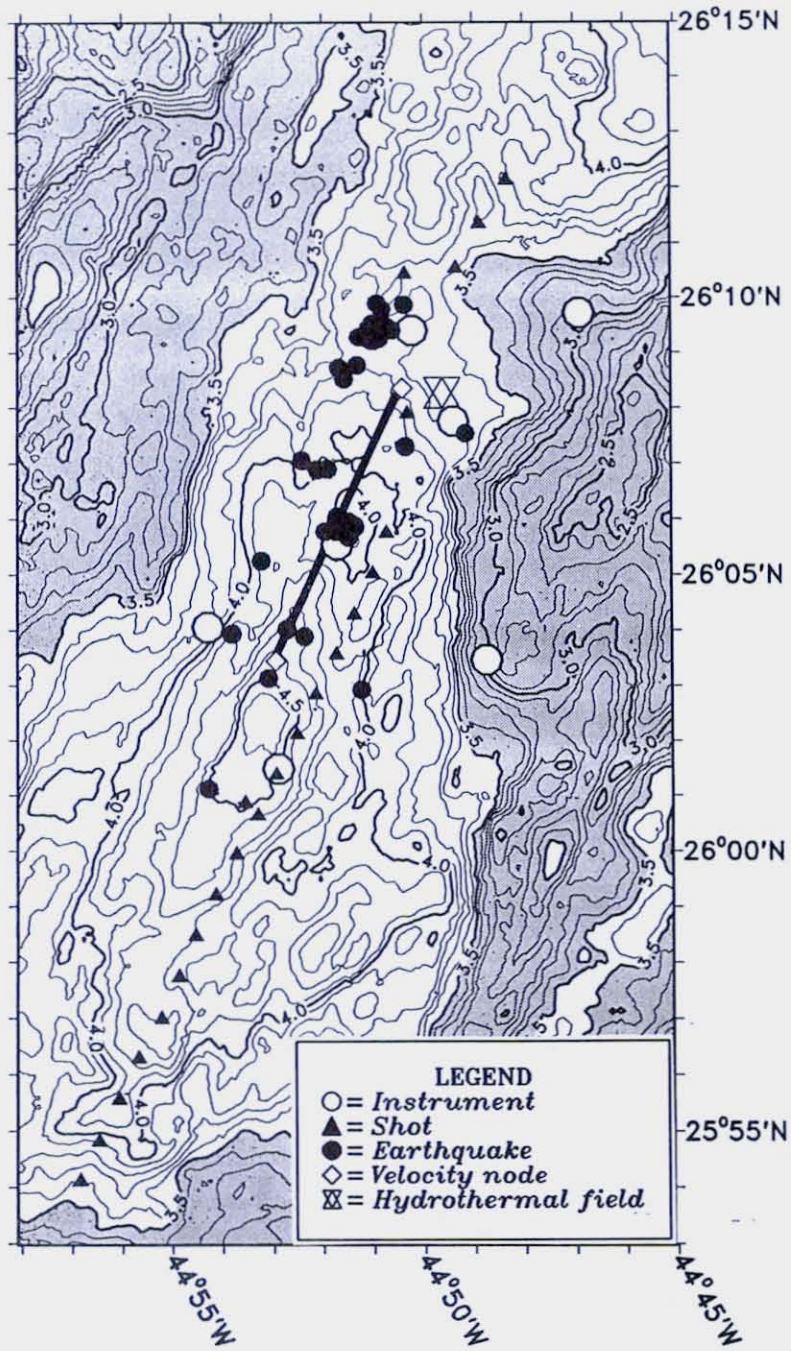


Figure 38

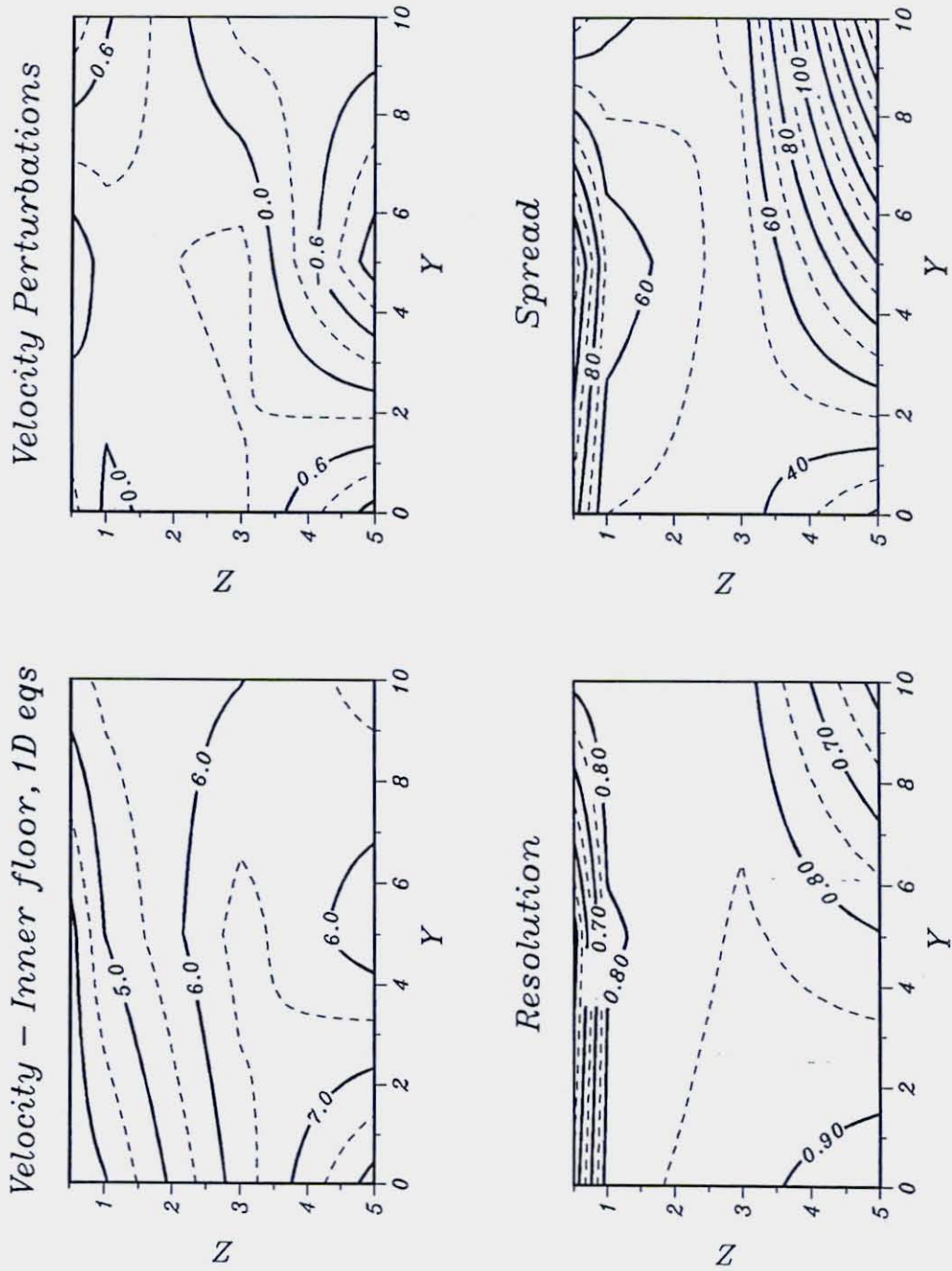
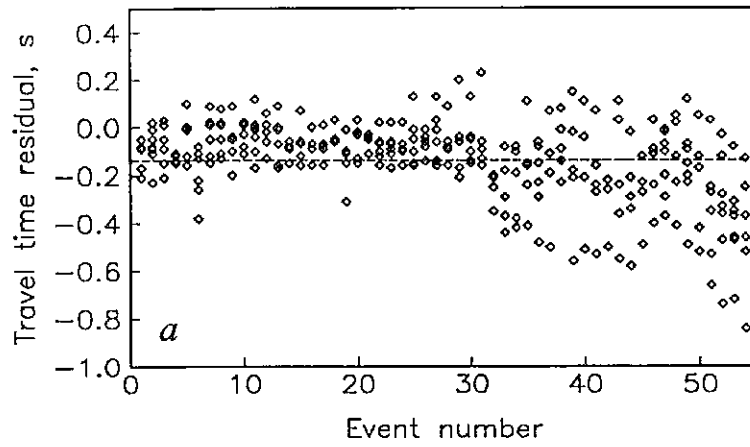


Figure 39

Residuals At Start – inner floor relocated eqs



Residuals at End – inner floor relocated eqs

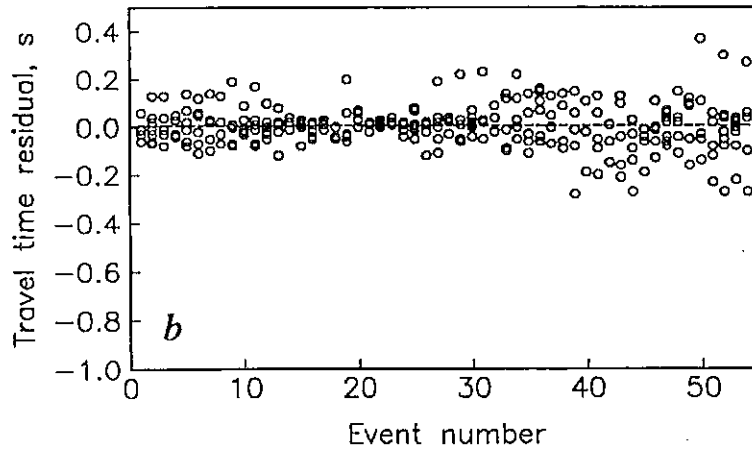
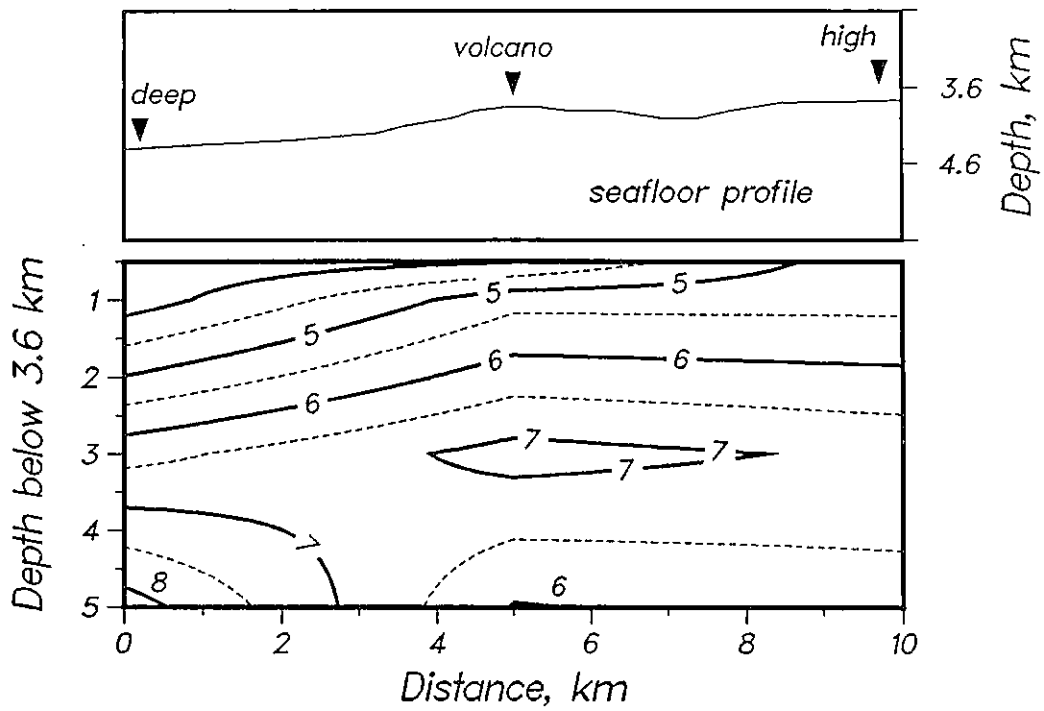


Figure 40

*Inner Floor, shots and relocated earthquakes*



*Figure 41*

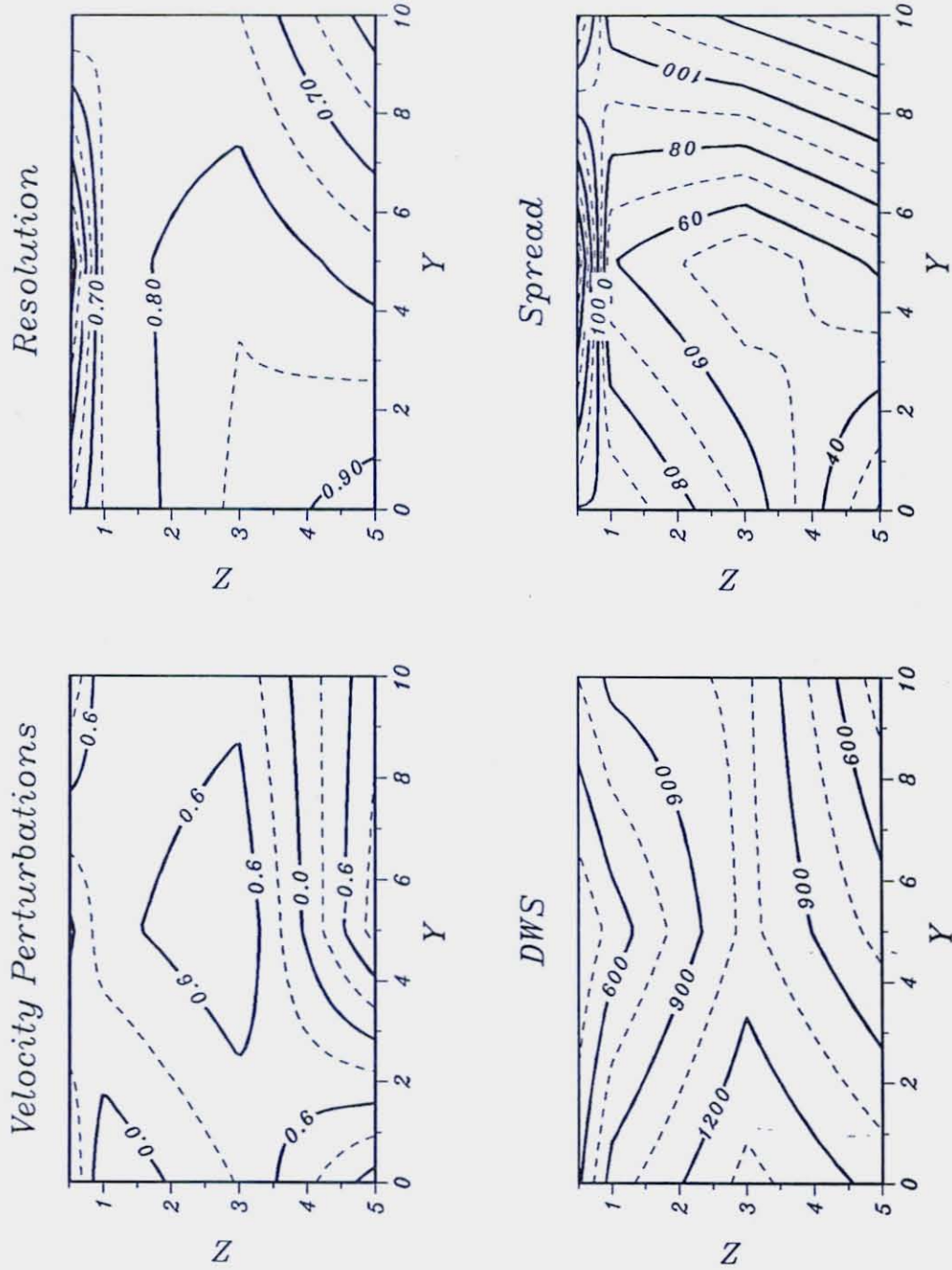


Figure 42

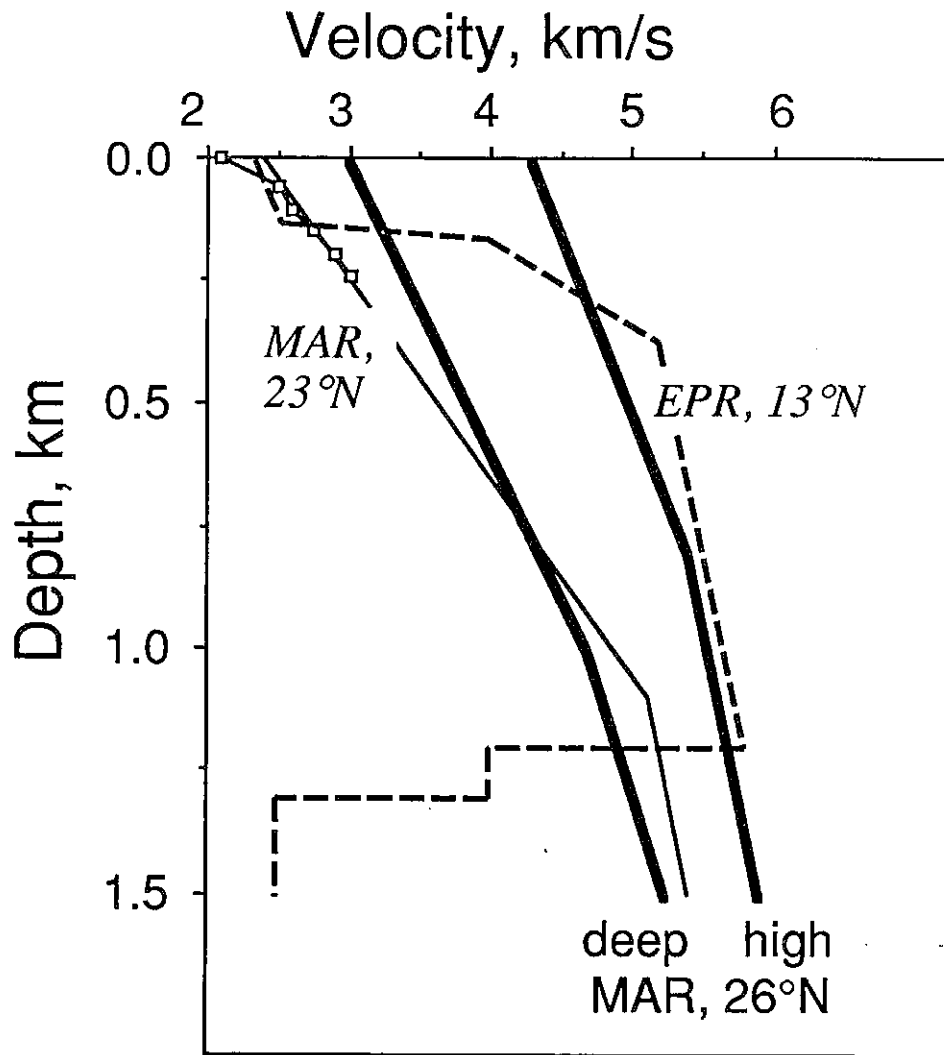


Figure 43

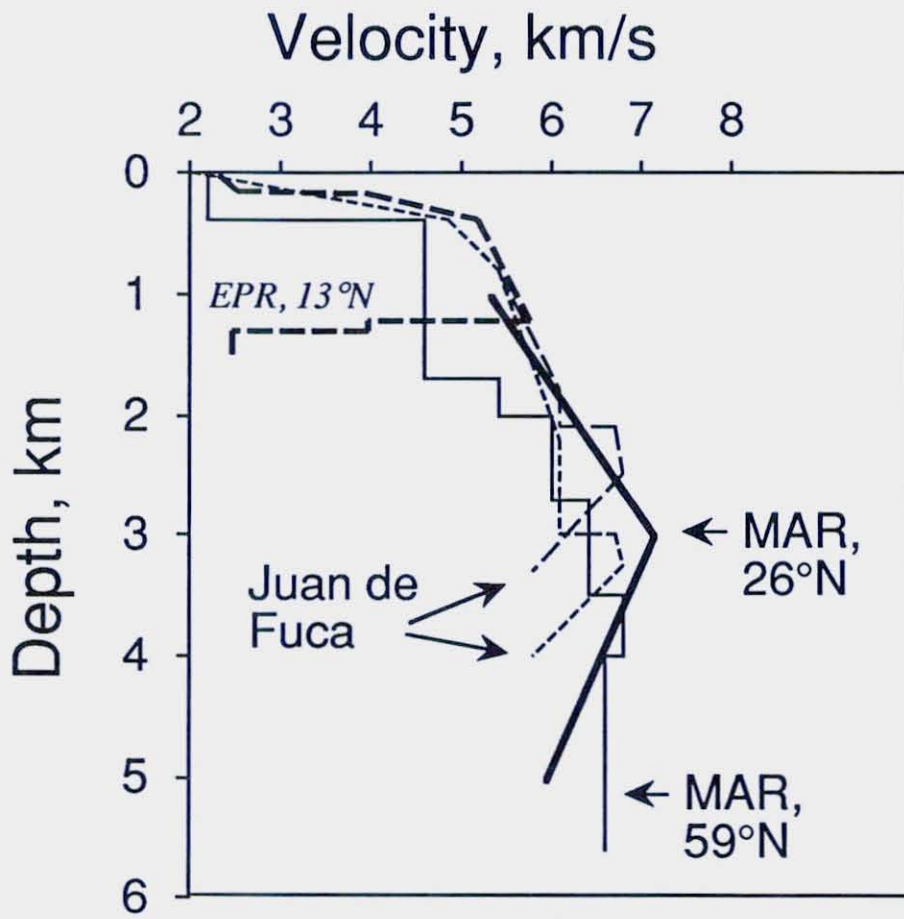


Figure 44





## CHAPTER 5. UPPER MANTLE P AND S WAVE DELAYS BENEATH THE MID-ATLANTIC RIDGE NEAR 26°N

### INTRODUCTION

Although both theoretical and petrological models for the creation of oceanic lithosphere and generation of fresh basalt on the seafloor require decompression melting of mantle material and ascent of the more buoyant melt [Green *et al.*, 1979; McKenzie, 1984; Johnson *et al.*, 1990], in general the geological and geophysical discrimination of the upwelling region along slow-spreading ridges has not been well-established. The depth and dimensions of a low velocity region which may characterize the upwelling and its spatial continuity along the ridge axis, as well as any temporal variability, are relatively poorly constrained. A temporal variation in the melt delivery process is predicted by a recently-developed mid-ocean ridge model which incorporates buoyancy and plate-driven flow to explain the observation of a narrow neovolcanic zone at the ridge axis [Scott and Stevenson, 1989]. In this model, steady-state melt generation and ascent appear to break down at slow spreading rates, thus resulting in episodic upwelling in such regions.

While published investigations attempting to measure delay times cannot unambiguously attribute their results to anomalies beneath the ridge because the seismic wavelengths (>100 km) of the teleseismic arrival time data used in the studies are much greater than, for example, the width of the median valley [e.g., ~ 20 km, Kong *et al.*, 1988], they represent the only observations which seek to calibrate average Earth travel times for a mid-ocean ridge setting. Investigations to date have found in general the slow-spreading Mid-Atlantic Ridge (MAR) to be characterized by anomalously low P and S wave velocities. Shear and surface wave studies in the vicinity of mid-ocean ridges have shown there to be zones of high-attenuation and/or low shear wave velocity beneath parts of the MAR [Girardin and Poupinet, 1974; Weidner, 1974; Dushenes and Solomon, 1977; Forsyth, 1977; Kuo *et al.*, 1987; Sheehan and Solomon, 1988, 1989; Grand, 1989]. Estimates of the extent of the anomalous velocities within the upper mantle range from a few tens of kilometers to 100 km in width at depths down to 250 km beneath the ridge crest [e.g., Solomon, 1973; Solomon and Julian, 1974; Weidner, 1974; Grand, 1989].

P wave delay studies also document positive residuals, suggesting the presence of lower velocities within the upper mantle. Differences in P-wave travel time residuals from a South American earthquake to ocean bottom seismometers in the Vema transform (11°N)

suggest the existence of a zone of lower velocities associated with the ridge [Rowlett and Forsyth, 1979]. Tryggvason [1964] and Long and Mitchell [1970], using relative travel time differences between stations, have documented positive upper mantle P-wave travel time residuals suggesting lower velocities beneath Iceland. The low velocity zone reported by Francis [1969b] from the differences in P and S-wave residuals from MAR earthquakes near Iceland to stations in Iceland and Greenland ( $\Delta \leq 22^\circ$ ) may extend to 250 km depth and to widths out to 300 km, but probably includes both a ridge upper mantle contribution and a delay due to the island and hot spot proximity.

Differential body wave travel time residuals (PP-P, SS-S), interpreted as arising from the upper mantle in the vicinity of the bounce point of the surface-reflected phase, generally indicate positive residuals and thus lower upper mantle velocities relative to older oceanic lithosphere and to average Earth models [Dorbath and Dorbath, 1981; Girardin, 1980; Kuo *et al.*, 1987; Sheehan and Solomon, 1988, 1989; Woodward and Masters, 1988, 1990]. An advantage of these studies is that travel time errors due to errors in the estimation of hypocentral parameters and to crustal and mantle heterogeneities beneath the source and receiver cancel because of the similarity of their ray paths, and thus the observed residual can be assumed to describe anomalies below the bounce point.

In this paper, we present the first direct measurement of teleseismic P and S wave delays from an earthquake on a spreading center. The simultaneous characterization of a swarm of MAR earthquakes recorded for the first time both locally by a network of ocean bottom instruments and teleseismically by land-based seismic stations provides a unique opportunity to calibrate teleseismic travel times for a mid-ocean ridge source. We have employed a multiple event relocation technique to estimate epicenters and origin times from teleseismic travel times using an average Earth model and standard station corrections. Data from the local seismic network are used to determine the true locations and origin times and to document an epicentral bias inherent in teleseismic locations for the MAR earthquakes. Corrections to the teleseismically-determined origin time for the epicentral bias and for crustal structure are then calculated, and the resulting difference in origin time is taken to represent the average P-wave upper mantle delay over the range of observed ray parameters. The absolute S-wave delay relative to an average Earth model is also measured by calculating the travel time residuals of long period SH-waves. Finally, we compare P and S-wave travel time delays at  $26^\circ\text{N}$  with the results of other delay studies along the MAR.

## JULY 1985 EARTHQUAKE SWARM

The Mid-Atlantic Ridge near 26°N where the earthquake swarm occurred is characterized by asymmetric spreading over the last 10 My, with rates faster to the east (1.3 cm/yr) than to the west (1.1 cm/yr) [Lattimore and Rona, 1974; McGregor *et al.*, 1977]. Along the ridge from 25°25'N to 26°20'N, three *en echelon* ridge segments can be identified (see Figure 1 for locations), each varying in width and depth along its strike. The variation is most pronounced south of 26°10'N, where substantial widening and deepening of the median valley occurs over distances of a few tens of kilometers. Teleseismically-located earthquake activity of the past 25 years appears to be concentrated at regular intervals (40-50 km) along the ridge axis (Figure 1).

The swarm of five earthquakes (at 1854, 1900, 1907, 1909, and 1939UT, with  $m_b = 4.4-5.0$ ) located by the International Seismological Centre (ISC) occurred near 25°50'N on the Mid-Atlantic Ridge during a one hour time span on July 13, 1985. The earthquakes appear to have occurred in the region of the along-axis depth minimum of the ridge segment (Figure 1). Centroid moment tensor solutions for two of the largest events (1854UT, 1909UT) indicate normal faulting along moderately dipping planes ( $\delta = 46^\circ$  or  $48^\circ$ , and  $22^\circ$  or  $69^\circ$ , respectively) striking subparallel to the trend of the ridge axis ( $\phi = 1^\circ$ ,  $195^\circ$ ), with  $M_0 = 1.9$  and  $2.4 \times 10^{24}$  dyn-cm, respectively, and source-time function half-durations equal to 1.9 s [Dziewonski *et al.*, 1986].

## LOCAL DATA and HYPOCENTRAL DETERMINATION

The earthquake swarm was recorded locally by an ocean bottom seismic network of seven ocean bottom hydrophones (OBHs) and one ocean bottom seismometer (OBS) in place during the summer of 1985 to study the microseismicity and style of tectonism near the TAG hydrothermal field (Chapter 3) (Figure 1). Individual instrument locations and depths ( $\sigma = \pm 25$  m) were determined acoustically using the method of Creager and Dorman [1982]. The 10 x 20 km network spanned the median valley and steeper eastern wall in the vicinity of the along-axis high and TAG hydrothermal field, and was located about 20 km to the north of the earthquake swarm (Figure 1).

Hypocentral parameters were determined for three earthquakes (1854, 1907, 1939UT) using the HYPOINVERSE algorithm [Klein, 1978]. Locations for the other events in the swarm could not be calculated because the first arrivals from those

earthquakes were buried in the long, high amplitude codas of immediately preceding events. Seismic signals from later-arriving compressional and shear phases were saturated. Individual picks were assigned relative weights based on their quality according to the criteria adopted for the microearthquake survey (Chapter 3). The total estimated error introduced during playback and picking of phases, correction of clocks to WWV, and calculation of station delays was 0.07 s for the 1854UT and 1907UT earthquakes; a 0.05 s error was assigned to the 1939UT event because of the higher signal-to-noise ratios of the first arrivals. The number of arrival time data ranged from 6 to 8. Figure 2 shows examples of seismograms recorded by the ocean bottom-network for two earthquakes associated with the swarm. The arrival of the P-wave first at OBH 6, followed later in time by arrivals at instruments farther north, establishes the earthquakes to be south of the network.

Because of the importance of the S-wave arrival in determining the earthquakes' distance from the network, we have paid special attention to the picking of the phases on the transverse horizontal component of the OBS assuming an approximate N220°E azimuth from the source to the receiver. Figure 3 shows seismograms of earthquakes associated with the 1985 swarm that were recorded by OBS 31. S-wave arrivals, easily distinguished by their high amplitudes and lower frequencies, could be unambiguously identified for almost all events, the exception being the 1854UT earthquake where the S-wave pick was based on a frequency change on the horizontal channel (due to its saturation) at a time shortly after higher amplitude SV energy arrived on the vertical channel. Consistency among the S-P times (4.9-5.8 s to OBS 31 for 13 of 16 located earthquakes) suggests that the events occurred in the same general area.

### Local Velocity Model

Earthquakes were located using the plane-layered, compressional-wave median valley structure used in Chapter 3. The model contains normal mantle velocities (8.0 km/s) and no upper mantle low velocity zone (model MAR, Figure 4). Station corrections were calculated from well-recorded earthquakes within the local seismic network. The shear velocity structure is derived from the P-wave structure using a constant ratio  $V_p/V_s$  of 1.84 (Chapter 3), obtained from data sampling the crust and upper mantle over a 5-40 km horizontal range. The ratio is consistent with laboratory results ( $V_p/V_s = 1.81-1.91$ ) for crustal layers 2 and 3 [Hyndman, 1979], and is within the range of values (1.73-2.08)

from previous MAR microearthquake studies [Francis *et al.*, 1977; Lilwall *et al.*, 1977, 1978], and the range (1.74-2.12) determined by combining sub-Moho P and/or S-wave velocities from refraction experiments and surface wave studies [Hart and Press, 1973; Weidner, 1974; Steinmetz *et al.*, 1977; Purdy and Detrick, 1986].

Because of the limited data set used in establishing the local  $V_p/V_s$  ratio (six observations, only one of which samples the upper mantle), we estimate a range of possible values in order to compute more realistic uncertainties in the hypocentral location. The range of values ( $V_p/V_s = 1.78-1.97$ ) was obtained by taking a weighted average, based on the relative percentage of ray paths in the crust (55%) and mantle (45%), of the  $V_p/V_s$  ratio at 26°N and possible mantle  $V_p/V_s$  ratios. Although the calculation of  $V_p/V_s$  ratios with P and S-wave velocities from different areas is not strictly valid, we have estimated extrema on  $V_p/V_s$  with such estimates in order to expand the range of possible values since only a few studies have yielded measures of both velocities in the mantle beneath the ridge [i.e., Fowler, 1976, 1978]. The maximum  $V_p/V_s$  was thus determined using the highest  $V_p$  and lowest  $V_s$  found along the MAR ( $V_p = 8.3$  km/s, Steinmetz *et al.* [1977];  $V_s = 3.9$  km/s, Weidner [1974]). We adopted as the minimum mantle ratio that calculated from velocities measured in peridotites sampled in the Bay of Islands ophiolite [Salisbury and Christensen, 1978], since this case corresponds to one of zero melt; the ratio,  $V_p/V_s = 1.71$ , is smaller than the smallest observed mantle  $V_p/V_s$  (1.74).

### Initial Hypocentral Parameters

Focal depth cannot be resolved because the distance between the earthquake epicenters and the nearest observing station is large compared with the network aperture (20 km). We therefore fix the focal depth to be at the base of the crust (6.4 km); shallower focal depths result in epicenters which are closer to the network (by ~0.9 km for a 1 km shallower focal depth, Figure 5a). Tests of the location procedure using different assumed starting locations, including ISC epicenters and estimates from the teleseismic relocation analysis (see below), reveal that the final epicenter is insensitive to the starting location at the 95% confidence level (Figure 5b). The epicentral confidence limits were obtained from the rotation of the covariance matrix from the inversion into the principal coordinates of the solution, and conversion of the standard error (square root of the eigenvalues) to that corresponding to a system with two degrees of freedom at the 95% level. Changes in origin time using the different starting locations were less than 0.03 s.

## Hypocentral Uncertainties

For the given P and S wave velocity structure, the largest formal errors in the locally-derived locations result from the relatively narrow network aperture (10 km in the NW-SE direction versus 20 km in the NE-SW direction) and the significant range of the network from the sources ( $> 25$  km); the least constraint is in the shortest aperture (NW-SE) of the network. Because the events occurred outside the network, the distance of earthquake from the network depends on the S wave arrival time, and as a result the epicenter is very sensitive to the  $V_p/V_s$  ratio utilized in the location algorithm. Tests show that an increase of 0.05 in the  $V_p/V_s$  ratio shifts the epicenter closer to the network by less than 3 km along the azimuth of the greatest spatial dimension of the seismic network (Figure 5c) and increases the origin time by  $\sim 0.3$  s.

We take into account below the effect this uncertainty has on the locally-derived parameters. The estimated total uncertainty in epicentral location and origin time for  $V_p/V_s = 1.78-1.97$ , including calculated formal errors, is  $\sim 16$  km along an azimuth of  $\sim N35^\circ E$  and  $\sim 1.7$  s in origin time, of which epicentral uncertainties to the northeast of the nominal location ( $V_p/V_s = 1.84$ ) are  $\sim 35\%$  larger than those to the southwest; errors in the northwest-southeast direction remain essentially constant over the entire range. For simplicity, the sample standard deviation around the mean origin time uncertainty for the adopted  $V_p/V_s$  range ( $\sim 0.6$  s), which is added to the formal standard error, is adopted as the origin time uncertainty, though we note that the true error for the adopted range in  $V_p/V_s$  is skewed.

## TELESEISMIC DATA and HYPOCENTRAL DETERMINATION

P-wave travel times from five well-recorded events published by the ISC constitute the data that were included in the teleseismic locations. Closer inspection of the ISC travel times and locally-recorded seismograms for the 1939UT event revealed the occurrence of two separate earthquakes about 5 s apart; a location for the earlier, smaller event was estimated from the local data, but could not be determined from the teleseismic data because of poor station coverage. Numbers of arrivals per event at epicentral distances greater than  $20^\circ$  ranged from 7 to 185, with good azimuthal station coverage only for the two largest events (1854UT, 1909UT).

We employed the method of *Jordan and Sverdrup* [1981] to solve for the hypocentroid (the average location of the earthquake cluster), and for the associated cluster vectors or differences between the individual event and the hypocentroid. The use of the hypocentroidal decomposition theorem allows the decoupling of the cluster vector estimation problem from the hypocentroid determination, thus maximizing use of the available data and providing a computationally-efficient algorithm for multiple-event location. The technique is especially advantageous for the analysis of small, sparsely-recorded earthquakes.

We include an additional nine events in the area (for a total number of earthquakes relocated equal to 14) in order better to estimate ray path corrections which then improve the resolution of the relative locations of the earthquakes. The epicentroid of the cluster is computed using travel time data with residuals  $\leq 3$  s ( $\leq 10$  s for the first iteration). Upon convergence, cluster vector corrections are then calculated from the path-corrected residuals, with flagged data excluded from the determination. Iteration of the process continues until residuals are normally distributed. In the analysis, 91% (946 arrival times) of the reported ISC data was used in estimating the epicentroid; the 1854UT cluster vector utilized 90% (164 times) of the reported data. In order to minimize hypocentral biases introduced by errors in theoretical travel times calculated from radially-symmetric average Earth models, we have used the *Herrin* [1968] travel time tables (Figure 4) with *Dziewonski and Anderson* [1983] azimuth-dependent station corrections for the inversion; use of station corrections is warranted for the calculation of an absolute source delay.

Choice of the azimuth-dependent corrections is based on the premise that the static corrections account for near-receiver heterogeneities in the crust and upper mantle, while the azimuthal component corrects for lower mantle heterogeneities. This assumption is in agreement with results from the redetermination of the static corrections and simultaneous estimation of lower mantle corrections by *Dziewonski* [1984]. Because the number of ridge sources used by *Dziewonski* [1984] to calculate the corrections for our study area (20-30°N) was greater than 20, we assume that the station corrections are unbiased estimates. However, it is important to note that the published corrections (typically  $< 1$  s) are probably underestimates of the actual magnitude of the heterogeneity because of the 'low-pass filtering' effect inherent in the estimation algorithm when applied to long period data. Tests in which only station elevation corrections were included show a  $\sim 5$  km southwestward epicentroid perturbation and a  $\sim 0.2$  s earlier origin time (reflecting the

magnitude of the elevation corrections), because the large positive delays beneath European stations are not accounted for.

We also computed the P-wave origin time delays relative to the isotropic Preliminary Reference Earth Model [PREM, *Dziewonski and Anderson*, 1981] and the *Jeffreys-Bullen* [1940] (JB) travel time tables. Use of the slower JB travel time tables leads to origin times  $\sim 2.6$  s earlier, and a  $\sim 3$  km northwestward epicentral shift, from the parameters estimated with the *Herrin* [1968] tables. For all Earth models, travel times are corrected for ellipticity [*Dziewonski and Gilbert*, 1976] and weighted inversely to the precision of the reported arrival time. A standard error of 0.5 s was assigned to ISC data reported to within 0.1 s, and an error of 1.0 s was assumed for times reported to the nearest second. On the basis of the maximum depth extent of MAR microearthquakes [*Toomey et al.*, 1985; Chapter 3], the centroid depths determined from body waveform studies of large MAR earthquakes [*Huang et al.*, 1986; *Huang and Solomon*, 1988], and surface wave data [*Weidner and Aki*, 1973], we fix the focal depth to be 10 km, corresponding to approximately 6-7 km below the seafloor. Relative epicentral locations are insensitive to depth errors of less than 5 km. Trial starting values for origin times and epicenters were taken from the ISC solutions.

The largest component of formal uncertainty in the teleseismically-determined locations, as represented by the azimuth of the major axis of the error ellipsoid, is generally in the NW-SE direction. This corresponds to the direction of least constraint for the given distribution of observing stations (there were very few stations to the southeast). Because of the less than ideal data coverage and inadequacies in the assumed Earth model, hypocenters determined using teleseismic P wave times may be systematically biased.

An examination of the data importance provides a quantitative estimate of the contribution of a particular travel time observation to the solution, and gives an idea of the magnitude of the random uncertainties. Because the data importance is linearly related to the partial derivative matrix, it will be greatest for an observation (or direction) in which the change in travel time with respect to the hypocentral coordinates is the greatest. Figure 6 shows that the largest contribution to the solution is from stations to the northeast of the swarm (in Europe), and that in general over 70% of the solution results from information supplied by northern hemisphere data. This is also the direction from which most of the observations come. Thus, in this case, the estimation of parameters using an uneven distribution of observing stations, combined with the existence of heterogeneities



unmodelled by the assumed travel time table and/or station corrections, results in a large northward bias of the teleseismically-estimated hypocenters.

## COMPARISON of HYPOCENTRAL ESTIMATES

Independently-determined hypocentral parameters, along with their estimated errors, are shown in Figure 7 and listed in Table 1. Also plotted are the epicenters of 16 additional earthquakes located by the local network, half of which were associated with the swarm. The relocation of the earthquakes using teleseismic data results in large shifts in epicenter ( $8.1 \pm 4.2$  km with no consistent azimuthal direction of change) and origin time ( $2.6 \pm 0.7$  s later) from the hypocenters published by the ISC (10 km focal depth). The local estimate for the best-constrained event (1854UT) is 10.8 km south of the ISC epicenter with an origin time 2.8 s earlier.

Comparison of the hypocenters estimated by both local and teleseismic networks reveals the teleseismically-determined epicenters to be located 14-20 km to the north of the locally-determined epicenters (Figure 7). We interpret the epicentral bias to be an artifact of the uneven global station distribution and departures of the actual travel times from those of the assumed Earth model, that is, we assume that the locally-determined epicenter and origin time are better estimates of the true source. A northward epicentral bias of teleseismically-located North Atlantic earthquakes has been documented by a number of authors. A recent compilation of large earthquakes along Atlantic transforms by *Bergman and Solomon* [1988] indicates that ISC locations, which utilize the JB travel time tables, are biased to the north of the transform fault zone by 5-15 km; seismic network bias maps computed by *Lilwall and Underwood* [1970] suggest an epicentral bias of similar magnitude and direction. *Phillips et al.* [1979] have demonstrated that with the use of a more realistic mid-ocean ridge velocity model, north and central Mid-Atlantic Ridge earthquakes are shifted to the southeast by ~4 km.

Further evidence for a teleseismic epicentral bias, rather than a local bias, is found by examining the OBS 31 S wave arrivals. If the bias were due to the local network estimation algorithm, S wave arrivals should be 1.5-2.0 s earlier, which is clearly not justified by the waveforms (see Figure 3). Alternatively, a  $V_p/V_s$  ratio greater than 2.20 using the arrival times adopted would be required for the bias to be locally-derived; if one attributes all the error to either the crustal or mantle  $V_p/V_s$ , then much higher P wave and lower S wave velocities (by more than 20%) are required. Although this is possible, no

observational evidence exists for such a variation in the crust or upper 5-10 km of mantle near 26°N.

The azimuthal distribution of data importance (Figure 6) also shows a smaller east-west asymmetry in that about 60% of the solution is contributed by stations located to the west of the hypocentroid, and that to the east the major concentration of stations and importance is in Europe. This would lead to a smaller westward bias in the global epicentral estimates, although this is not resolvable because of the larger uncertainties in the east-west direction of both the local and teleseismic estimates. The location by ISC of other large, well-recorded MAR earthquakes close to the ridge axis [*Huang et al.*, 1986], however, suggests that the longitudinal bias is small.

## P WAVE DELAY

To estimate a P wave delay for the upper mantle, we calculate the difference between the teleseismically-determined and true origin time, where we assume that the true epicenter is given by the local estimate. The difference in origin time represents a direct measure of the average upper mantle P-wave travel time delay, over the observed epicentral distances (seismic wavelength  $\geq 100$  km), associated with the Mid-Atlantic Ridge near 26°N. Positive delays indicate velocities slower and negative delays velocities faster than an average Earth model. In order to account for the epicentral bias and use of a continental (rather than an oceanic) crust in the teleseismic estimate, we compute corrections to the origin time. We use the first swarm earthquake (1854UT), since this is the best teleseismically-constrained event for which we also have local data. Table 2 lists the corrections which we need to make to the teleseismically-determined origin time.

The use of biased velocity model, such as the *Herrin* [1968] Earth model which contains a thicker crust, introduces a systematic error in the hypocenter which must be taken into account. The thicker crust, for shallow earthquakes, results in theoretical travel times which are larger than the actual travel times, and thus estimated origin times that are anomalously early or epicenters that are biased toward the largest concentration of seismic stations. Since the velocity structure implicit in the travel time tables of *Herrin* [1968] used to estimate the swarm epicenters from teleseismic data contains a 40-km-thick crust typical of continental regions rather than a 5-7 km thick oceanic crust [*Purdy and Detrick*, 1986], we compute a correction to the teleseismically-determined origin time for a typical thickness of oceanic crust. To do this, we replace the *Herrin* [1968] continental crust (6.00 km/s,

6.75 km/s) from the Moho to a depth of 40 km below the sea surface with *Herrin* [1968] upper mantle material (8.05 km/s). For an oceanic crustal thickness of 5-7 km with water depths of 3-5 km (average Moho depth about 10 km below sea level), the origin time correction for a ray leaving the source at a takeoff angle of  $65^\circ$  is +1.02 s, a correction which should be added to the origin time. The corrections to the PREM and JB models, each calculated by replacing crustal velocities with an upper mantle velocity over the remaining thickness of model crust, are +0.58 s and +0.90 s, respectively.

Initial comparison of the hypocentral parameters estimated by the local and teleseismic networks showed there to be little difference in origin time ( $+0.00 \pm 0.21$  s for 1854UT earthquake), but there was a 20-km northward bias in the epicenter determined from teleseismic data using the *Herrin* [1968] tables (Figure 7). To calculate the origin time correction for this bias, we fix the epicenter of the earthquake to that estimated by the local network and solve for the origin time which best fits the teleseismic arrival time data. For a 20 km northward bias, the correction to the initial origin time is  $-0.73 \pm 0.15$  s (Figure 8). Imprecise knowledge of the average  $V_p/V_s$  ratio near  $25^\circ 50'N$  will introduce uncertainties in the magnitude of the location bias. For the estimated range of probable  $V_p/V_s$  ratios (1.78-1.97, 23-12 km bias), the correction to teleseismically-determined origin time would range from -0.80 to -0.44 s, which adds an additional  $\sim 0.2$  s of uncertainty to the bias correction (making it  $-0.73 \pm 0.35$  s); note that the error in the bias correction (0.35 s) represents the sum of the formal origin time error from the inversion and the origin time uncertainty resulting from the probable  $V_p/V_s$  range since the variances are not linearly independent.

The total correction to the teleseismically-determined origin time for a *Herrin* [1968] Earth model, after correction for uneven station distribution and a more realistic crustal thickness, is  $+0.29 \pm 0.38$  s. The resulting average upper mantle P-wave origin time delay, taking into account the formal error and uncertainties in the  $V_p/V_s$  ratio used in the local-network estimate ( $\pm 0.80$  s), is  $+0.29 \pm 0.88$  s, so that corrected travel times calculated with a *Herrin* [1968] velocity structure are only slightly too long. Hence, we conclude that there is no resolvable P-wave delay associated with the upper mantle near  $25^\circ 50'N$ . The lack of a delay suggests that the *Herrin* [1968] upper mantle velocity structure, on average for arrivals over the distance range  $21^\circ$  to  $94^\circ$ , appears to be a good approximation to the average upper mantle along this segment of the Mid-Atlantic Ridge. The P-wave origin time delays relative to the isotropic PREM and the JB models are  $+0.22 \pm 0.90$  s and  $-2.39 \pm 0.91$  s, respectively.

## S WAVE DELAY

Several studies have documented a large S wave delay, perhaps in the range of +4 to +10 s relative to the JB travel time tables [*Girardin and Poupinet, 1974; Duschenes and Solomon, 1977*], in the observed shear wave arrival time with respect to the theoretical travel time. In order to investigate whether low S wave velocities are present beneath the Mid-Atlantic Ridge near 25°50'N, especially in light of the small P-wave delay found above, we have measured the shear wave travel time delays for the 1854UT event. We estimate the arrival times by modelling the SH waveforms using the method of *Nabelek [1984]*, and finding a best fit of the synthetic and observed waveforms. In addition to the arrival time, the formal waveform inversion technique also solves for the best-fitting double couple point source, which can be compared with the published moment tensor solution derived from longer period Global Digital Seismic Network (GDSN) data [*Dziewonski et al., 1986*].

Long-period P and SH-waves recorded at epicentral distances of  $\Delta = 38$  to  $65^\circ$  and azimuths of  $N38^\circ E$  to  $N311^\circ E$  by WWSSN (Worldwide Standardized Seismic Network, dominant period  $\sim 15$  s) and GDSN (dominant period  $\sim 30$  s) stations were used to invert for focal mechanism, scalar seismic moment, and source-time function, in addition to arrival time. Centroid depth was fixed at 10 km below the sea surface because of the lack of clear, unambiguous depth phases in the P waveforms. The near-source velocity structure consists of a water layer ( $V_p = 1.5$  km/s, 4.0 km thickness from bathymetric maps at  $26^\circ N$ ) and crustal layer ( $V_p = 6.40$  km/s,  $V_s = 3.70$  km/s, 6.0 km thick) over a mantle halfspace ( $V_p = 8.00$  km/s,  $V_s = 4.30$  km/s), with an attenuation parameter of  $t^* = 1.0$  and 4.0 s for the P and S waveforms, respectively. In general, formal errors in the inversion solution for ridge earthquakes are at best  $\pm 5^\circ$  in angular coordinates and  $\pm 30\%$  in seismic moment at the  $2\sigma$  (95%) confidence level [*Huang et al., 1986*].

In spite of the limited data set (3 P waveforms; 11 S waveforms), source parameters could be determined with relatively good confidence; estimates of the double couple orientation ( $\phi = 9^\circ \pm 2^\circ$ ,  $\delta = 45^\circ \pm 1^\circ$ ,  $\lambda = 281^\circ \pm 2^\circ$ ) and scalar seismic moment ( $M_0 = 1.7 \pm 0.1 \times 10^{24}$  dyn-cm) are in agreement with the published centroid moment tensor solution [*Dziewonski et al., 1986*]. The formal errors quoted above probably underestimate the true errors because of the less than ideal station distribution and signal-to-

noise ratios of some of the waveforms. Figure 9 shows a comparison of the observed and synthetic long-period SH waves for the 1854UT earthquake.

From the waveform inversion, we obtain shear wave travel time residuals between our "observed" arrival time and the theoretical arrival time. The predicted arrival time is calculated from the *Jeffreys-Bullen* [1940] S wave travel time tables, ellipticity corrections of *Dziewonski and Gilbert* [1976], and our best estimate of the hypocenter from this study. Station corrections were not applied, since published estimates show little consistency amongst each other, and precision in phase identification (for ISC S wave times) can often be comparable to the station correction. The average S wave travel time delay, with respect to the JB tables, is  $+3.1 \pm 2.0$  s for the 1854UT earthquake ( $+3.9 \pm 2.0$  s relative to the isotropic PREM S-wave model). The delay is not sensitive to hypocentral mislocation; errors in the local-network origin times resulting from uncertainties in the assumed velocity structure ( $V_p/V_s$  ratio) result in average delays which are within 0.4 s of each other.

Calculation of the JB S-wave travel time delay using 14 arrival times reported by the ISC results in a much smaller average of  $+1.0 \pm 2.2$  s ( $+1.8 \pm 2.2$  s relative to PREM). It is quite likely that the traditional "eyeball" picks of the arrival times reported to ISC correspond to the earlier-arriving SV phase, whose amplitudes are larger for normal-faulting events, leading to a smaller delay (by perhaps as much as several seconds) than that measured by the waveform-fitting method. Figure 10 shows comparison histograms of the S wave residuals, relative to the JB tables, calculated by the two methods. Because of the possible misidentification of the SH phase for arrival times reported to the ISC, we consider the S wave delay estimated from arrival times determined from the waveform inversion to be better estimates of the true delay.

## DISCUSSION

### Comparison with Other Studies

The lack of a significant P wave delay suggests that the *Herrin* [1968] upper mantle is good estimate of the average upper mantle velocity structure near  $25^{\circ}50'N$ , and furthermore, that no seismically-resolvable region (i.e.,  $> 100$  km in extent) of low P wave velocities exists in the upper mantle below the earthquake source. We find that the P delay for  $26^{\circ}N$  to be on average much smaller, by perhaps 1 s or more relative to the *Herrin* [1968] Earth model, than reported by other investigators [e.g., *Girardin*, 1980; *Dorbath*

and *Dorbath*, 1981; *Woodward and Masters*, 1990]. Although the positive S wave travel time delay indicates that lower S wave velocities than appropriate for the average Earth may be present, the small magnitude of the delay suggests that the ridge segment near 25°50'N may not be underlain by as large a low velocity anomaly as earlier studies have indicated for other regions of the MAR [e.g., *Girardin and Poupinet*, 1974; *Weidner*, 1974; *Duschenes and Solomon*, 1977; *Steinmetz et al.*, 1977; *Rowlett and Forsyth*, 1979; *Dorbath and Dorbath*, 1981; *Grand*, 1989; *Sheehan and Solomon*, 1989].

By measuring the differential residual between the direct-arriving and reflected P wave arrival, several authors have found equivalent one-way, upper mantle P wave delays (-0.8 s to +1.0 s relative to the JB tables [*Girardin*, 1980; *Dorbath and Dorbath*, 1981]) which are more than 1.5 s larger than the -2.4 s JB delay observed for 26°N (Figure 11). The use of a common datum for comparison (5 km below sea level) by *Dorbath and Dorbath* [1981] introduces an additional +0.6 s error (+0.3 s one-way) in their average value since MAR depths are typically ~3.5 km; they also use arrival times reported by the ISC, whose errors may be large. The *Girardin* [1980] delay includes corrections ( $\pm 0.4$  s) to the JB P residuals for epicentral distance. Both values plotted in Figure 11 include the above corrections to facilitate a more direct comparison with the 26°N delay. *Woodward and Masters* [1990] find an average one-way PREM delay, corrected for seafloor age at the reflection point, of  $+1.7 \pm 1.0$  s for PP-P data in the vicinity of the MAR between 20° and 30°N. Their delay, relative to the isotropic PREM model is also much larger than the +0.2 s PREM delay for 26°N (Figure 12). With similar assumptions, *Rowlett and Forsyth* [1979] have used residual differences in teleseismic P-wave delay times (JB travel time residuals from +1.3 s to +1.8 s) from an earthquake in southern Peru to ocean-bottom instruments within the Vema Transform (11°N) to argue for the existence of a narrow zone of partial melting, perhaps less than 25 km wide within the shallowmost 60 km of mantle, that might be associated with the ridge.

Results from Mid-Atlantic Ridge S wave delay studies show that larger positive travel time residuals, or lower velocities, are found beneath the ridge crest. *Woodward and Masters* [1990] find an average, one-way PREM S delay, corrected to zero age, of  $+4.1 \pm 2.2$  s for MAR SS-S reflection points between 20° and 30°N; their delay is consistent with the  $3.9 \pm 2.0$  s PREM delay for 26°N (Figure 12). In contrast to the  $+3.1 \pm 2.0$  s JB delays found at 26°N, *Girardin and Poupinet* [1974] and *Duschenes and Solomon* [1977] measure S-wave travel time residuals ranging from +4 s to +10 s using MAR earthquake sources (Figure 11). The 4.4 s average delay found by *Girardin and Poupinet* [1974] uses

ISC data whose source depths are probably too deep (by 10-30 km), leading to predicted travel times which are too short and residuals which are too large (by ~2 s for a 20 km depth error). However, because their data set includes a large number of non-ridge, transform events, the reported delay may underestimate the true ridge-mantle signature. The +8-10 s residuals reported by *Duschenes and Solomon* [1977] have estimated uncertainties of ~2 s and include station corrections, which may bias the estimate if sampling includes stations overlying very slow, or fast, crust and upper mantle. It is important to note that implicit in the S delays determined in both studies is a component of P delay since ISC epicenters determined exclusively from P-wave data were used; thus, the true S delay will be larger than the observed value, though only slightly since its magnitude is likely to be much larger than the P delay (by perhaps a factor of four [*Doyle and Hales*, 1967; *Hales and Roberts*, 1970; *Woodward and Masters*, 1988]).

#### **Along-axis Variation in Upper Mantle Velocities?**

The observation of only a small P wave delay near 25°50'N compared with those reported in other studies of the MAR suggests that active mantle upwelling (i.e., its low velocity signature) may vary spatially and/or temporally along strike. Closer examination of differential PP - P and SS - S travel time residuals between 20 and 30°N along the Mid-Atlantic Ridge shows there to be a wide scatter in the magnitudes and signs of the residuals [*Dorbath and Dorbath*, 1981; *Sheehan and Solomon*, 1989; *Woodward and Masters*, 1990], implying that a significant amount of heterogeneity may occur along the ridge. Over the latitudinal range 20-30°N ( $\Delta = 59-98^\circ$ ), age-corrected PP-P residuals collected by *Woodward and Masters* [1990] exhibit a local minimum, +0.1-0.3 s average one-way delays, at 25-27°N (Figure 12). While the scatter in their data set is often 1-2 s for bounce points that lie close to one another, the general variation in their one-way travel time residuals, ranging from +3.5 s to +0.1 s, suggests that the large scale upper mantle upwelling process may vary over length scales of at least 1000 km. SS-S travel time residuals reported by *Sheehan and Solomon* [1989], which include the *Woodward and Masters* [1990] S wave data, also exhibit a latitudinal variation with a minimum near 26°N.

Recently collected Sea Beam and gravity data along the MAR from 28-31°N indicate a correlation of mantle Bouguer gravity lows with along-axis depth minima, suggesting that low-density mantle material (~50-100 km in width) may be located beneath these locally high areas along the ridge [*Lin et al.*, 1990]. In contrast, the occurrence of the 1985

earthquake swarm in the vicinity of an along-axis high (Figure 1) suggests that that portion of the ridge is characterized by a cold, brittle oceanic crust. Thus, if the gravity anomalies at 28-31°N can be assumed to describe upper mantle processes (rather than variations in crustal thickness), then the observation of higher seismic velocities (small P-wave delay) near 26°N implies a variation in the melt generation and/or emplacement process. Unfortunately, no gravity data were collected during the Sea Beam survey from 24-28°N.

A model for melting, magma migration, and circulation due to plate spreading and density-driven flow proposed by *Scott and Stevenson* [1989] predicts that at slow spreading rates steady-state upwelling cannot exist, and behavior becomes episodic with periods of rapid magma ascent separated by times of little melting and more brittle behavior. The occurrence of teleseismically-recorded earthquakes at constant intervals along the ridge (e.g., 25°30'N, 25°50'N, and 26°10'N, Figure 1), and the lack of a large P wave anomaly beneath the earthquake swarm would be consistent with a scenario in which little melt presently exists. Moreover, if the MAR between 25 and 27°N is cooler (higher velocities), and the ridge from 28°N to 31°N is hotter due to the active upwelling of mantle material (slower velocities), then this would be qualitatively consistent with the long wavelength ( $\geq 1000$  km) variation in P-wave and S-wave delay times which *Sheehan and Solomon* [1989] and *Woodward and Masters* [1990] observe.

Long-wavelength variations in other geophysical (residual elevation, free air gravity) and geochemical parameters (major and trace element concentrations) have been suggested to arise from upper mantle temperature variations resulting from proximity to a hot spot [*Anderson et al.*, 1973; *Sclater et al.*, 1975; *Dick et al.*, 1984; *Johnson et al.*, 1990]. For example, the MAR near the Azores hot spot is anomalously shallow (by up to 1200 m) in comparison with the ridge to the south [*Sclater et al.*, 1975]. *Dick et al.* [1984] found a correlation between the geoid and an enrichment in the element Cr from dredged peridotites as the Azores hot spot is approached, and *Johnson et al.* [1990] found incompatible element depletions and compatible element enrichments in clinopyroxenes associated with the Bouvet and Marion hot spots. The spatial variations occurred over 1000-3000 km wavelengths. While our data cannot address whether a variation does occur or not, the delays for 26°N, which are lower than those found elsewhere in the Atlantic, are consistent with the latitudes at which the zero residual in elevation is seen (minimum in elevation variation) [*Sclater et al.*, 1975], and with the distances from hot spots (the MAR at 26°N is ~2000 km from the Azores) at which petrological minima/maxima have been observed [*Dick et al.*, 1984; *Johnson et al.*, 1990].



### Anisotropic Mantle Upwelling Beneath Mid-Ocean Ridges?

The observation of much smaller P wave delay, but only slightly smaller S wave delay, compared with other studies, suggests that the travel times for ray paths sampling the upper mantle beneath the ridge near 26°N may be affected by an anisotropic structure. Assuming a P wave mantle velocity of 8.1 km/s and that variations occur only within the uppermost 200 km of mantle, we find that a travel time delay of +0.3 s (26°N delay) requires only a very small decrease in velocity (< 1%); such a variation corresponds to a temperature anomaly of about 200°C [assuming  $\partial V_p/\partial T = -4 \times 10^{-4}$  km/s/°C, *Kumazawa and Anderson, 1969*]. In contrast, a +2 s P wave delay [e.g., *Woodward and Masters, 1990*; Figure 12] would require a 7% velocity decrease resulting in an unreasonably large temperature change of about 1500°C, and thus could indicate the involvement of a much greater thickness of mantle or the presence of significant amounts of partial melt. On the basis of this comparison, we would interpret the smaller P wave delay found in this study as evidence that the upper mantle near 26°N is underlain by cooler temperatures than observed along other parts of the MAR. Calculation of the temperature effect resulting from the observed S wave delay at 26°N, however, is not compatible with this conclusion since S wave delay of +3 s would require a 0.3 km/s decrease in  $V_s$  and a 1000°C nominal temperature anomaly [assuming a PREM upper mantle  $V_s$  of 4.7 km/s, and  $\partial V_s/\partial T = -3 \times 10^{-4}$  km/s/°C, *Kumazawa and Anderson, 1969*]. This paradox leads us to propose a model for mantle upwelling in which P wave anisotropy results in a smaller than expected travel time delay.

If there is indeed active and continuous upwelling beneath the MAR near 26°N, and the observed S delay is typical for the mantle along the MAR, then an alternative but more complex hypothesis is that the P-wave signature associated with the elevated temperatures and partial melting is largely erased by an anisotropic velocity structure. High-temperature, low stress laboratory experiments involving uniaxially-deformed olivine crystals and polycrystals indicate that anisotropy can result from the preferred orientation of the olivine a-axis parallel to the direction of maximum stress through subgrain rotation and grain boundary migration during syntectonic recrystallization [*Ave'Lallemant and Carter, 1970*; *Toriumi, 1984*]. Along-axis variations in the magnitude of anisotropy, however, are necessary if the long-wavelength variation in P-wave delay from 20-30°N (Figure 12) is real.

The observation of only a small P delay beneath the ridge can be explained by body wave anisotropy (with the fast direction vertical) in which olivine crystals are rotated to create a vertically-lineated mantle fabric by mantle upwelling at the ridge axis (Figure 13a). *Raleigh* [1967] has found that slip in the [100] direction along the (010) glide plane is the preferred slip mechanism at high temperatures ( $>1000^{\circ}\text{C}$ ). While *Francis* [1969a] has used this evidence to suggest that sub-horizontal mantle flow in the direction of plate-spreading away from the ridge axis can explain the P-wave anisotropy observed off-axis in the Pacific [*Morris et al.*, 1969], upwelling of mantle material at the ridge axis may also lead to a realignment of crystals parallel to the ascending flow and velocity anisotropy such that the fast direction is now oriented in a vertical plane along the ridge (Figure 13b). Moreover, because compressional wave velocities are much more dependent on the wave propagation direction than shear waves [ $\Delta V_p = 2.2$  km/s versus  $\Delta V_s = 0.2$  km/s between the fastest and slowest propagation directions, *Kumazawa and Anderson*, 1969], an anomalously small P delay, combined with a more "normal" S delay, could be a indicator of olivine anisotropy. The percentage of aligned olivine may be a gauge of the extent of anisotropy present in the upper mantle.

If we assume that a delay of  $\sim 2$  s represents the mean P wave delay along the MAR [e.g., *Woodward and Masters*, 1990; Figure 12] and that all anisotropy is confined to the upper 200 km of mantle, then we may calculate the amount of velocity anisotropy required to account for only a 0.2 s observed PREM P delay at  $26^{\circ}\text{N}$ . The calculation shows that P wave velocities would have to be 7% higher in order to seismically erase a low-velocity source anomaly. Comparison with petrofabric data from ultramafic ophiolitic assemblages reveals that this degree of compressional wave anisotropy is commonly observed in massifs with strongly-oriented olivine fabrics [*Christensen*, 1984]. A further prediction for the presence of an anisotropic upper mantle beneath the ridge would be the observation of shear wave splitting for waves propagating along or across the ridge axis; vertically-arriving SV and SH waves travel at about the same velocity and would not separate (see standard deviations about mean velocities in Figure 13b). Because ray paths from earthquakes in the swarm to OBS 31 probably do not sample deep enough into the mantle to sense such a variation, we are not able to test this prediction using particle motions of shear waves recorded by the local network.

## SUMMARY and CONCLUSIONS

A 1985 swarm of Mid-Atlantic Ridge earthquakes recorded by a local ocean-bottom seismic network has provided the first opportunity to calibrate teleseismic travel times from a mid-ocean ridge seismic source and to investigate upper mantle delay times beneath a spreading center. Using local data from a network of ocean-bottom hydrophones and seismometers centered on the ridge at 26°05' N, and teleseismic data obtained from the ISC, we have made two independent estimates of the epicenters and origin times for two of the earthquakes in the swarm. Comparison of the hypocentral estimates for two of the simultaneously-recorded events shows a 14-20 km northward epicentral bias of the teleseismically-located events. After correction for the bias and for an oceanic crustal thickness, comparison of origin times for one of the largest of the swarm earthquakes shows there to be no resolvable P wave delay ( $+0.3 \pm 0.9$  s) with respect to a *Herrin* [1968] Earth upper mantle. We interpret this to mean that the *Herrin* [1968] travel times are a good model for the average upper mantle beneath this segment of the Mid-Atlantic Ridge. A P wave origin time delay of  $+0.2 \pm 0.9$  s and  $-2.4 \pm 0.9$  s was found using the isotropic PREM and *Jeffreys-Bullen* [1940] models, respectively. Measurement of the S wave delay for the same event shows there to be a positive delay ( $3.1 \pm 2.0$  s) relative to the *Jeffreys-Bullen* [1940] travel time tables ( $3.9 \pm 2.0$  s relative to the isotropic PREM S wave model).

The lack of large origin time delays near 26°N, as has been widely observed elsewhere, indicates that substantial regions of low-velocity upper mantle material (i.e., > 100 km in extent) are not present near 26°N. The small P delay is consistent with the latitudes of differential travel time residual minima observed along the MAR between 20°N and 30°N [*Sheehan and Solomon*, 1989; *Woodward and Masters*, 1990], suggesting that the amount of low-velocity mantle material present beneath the ridge axis varies over distances of at least 1000 km. The observation near 26°N of an unexpectedly small P delay, which does not require resolvably lower velocities ("cool" upper mantle), in a region where the S delay does suggest low velocities (consistent with an upper mantle temperature anomaly of 1000°C assuming the anomaly is confined to the uppermost 200 km) can be explained by olivine compressional wave anisotropy (fast velocity direction vertical) in which crystals are realigned by an ascending mantle. The P wave anisotropy that would be required to account for the travel time discrepancy is consistent with the amounts of anisotropy documented in ultramafic sections in ophiolites.

## REFERENCES

- Anderson, R. N., D. McKenzie, and J. G. Sclater, Gravity, bathymetry and convection in the Earth, *Earth Planet. Sci. Lett.*, *18*, 391-407, 1973.
- Ave' Lallemand, H. G., and N. L. Carter, Syntectonic recrystallization of olivine and modes of flow in the upper mantle, *Geol. Soc. Amer. Bull.*, *81*, 2203-2220, 1970.
- Bergman, E. A., and S. C. Solomon, Transform fault earthquakes in the North Atlantic: Source mechanisms and depth of faulting, *J. Geophys. Res.*, *93*, 9027-9057, 1988.
- Christensen, N. I., The magnitude, symmetry and origin of upper mantle anisotropy based on fabric analysis of ultramafic tectonites, *Geophys. J. R. Astron. Soc.*, *76*, 89-111, 1984.
- Creager, K. C., and L. M. Dorman, Location of instruments on the seafloor by joint adjustment of instrument and ship positions, *J. Geophys. Res.*, *87*, 8379-8388, 1982.
- Dick, H. J. B., R. L. Fisher, and W. B. Bryan, Mineralogic variability of the uppermost mantle along mid-ocean ridges, *Earth Planet. Sci. Lett.*, *69*, 88-106, 1984.
- Dorbath, C., and L. Dorbath, Travel-time residuals of PP waves reflected under the central Atlantic Ocean, *Phys. Earth Planet. Inter.*, *25*, 121-128, 1981.
- Doyle, H. A., and A. L. Hales, An analysis of the travel times of S waves to North American stations, in the distance range 28° to 82°, *Bull. Seismol. Soc. Am.*, *57*, 761-771, 1967.
- Duschenes, J. D., and S. C. Solomon, Shear wave travel time residuals from oceanic earthquakes and the evolution of oceanic lithosphere, *J. Geophys. Res.*, *82*, 1985-2000, 1977.
- Dziewonski, A. M., Mapping the lower mantle: Determination of lateral heterogeneity in P velocity up to degree and order 6, *J. Geophys. Res.*, *89*, 5929-5952, 1984.
- Dziewonski, A. M., and D. L. Anderson, Preliminary reference Earth model, *Phys. Earth Planet. Sci. Lett.*, *25*, 297-356, 1981.
- Dziewonski, A. M., and D. L. Anderson, Travel times and station corrections for P waves at teleseismic distances, *J. Geophys. Res.*, *88*, 3295-3314, 1983.
- Dziewonski, A. M., J. E. Franzen, and J. H. Woodhouse, Centroid-moment tensor solutions for July-September 1985, *Phys. Earth Planet. Inter.*, *42*, 205-214, 1986.
- Dziewonski, A. M., and F. Gilbert, The effect of small aspherical perturbations on travel times and a re-examination of the corrections for ellipticity, *Geophys. J. R. Astron. Soc.*, *44*, 7-17, 1976.
- Forsyth, D. W., The evolution of the upper mantle beneath mid-ocean ridges, *Tectonophysics*, *38*, 89-118, 1977.

- Fowler, C. M. R., Crustal structure of the Mid-Atlantic ridge crest at 37°N, *Geophys. J. R. Astron. Soc.*, 47, 459-491, 1976.
- Fowler, C. M. R., The Mid-Atlantic Ridge: Structure at 45°N, *Geophys. J. R. Astron. Soc.*, 54, 167-183, 1978.
- Francis, T. J., Generation of seismic anisotropy in the upper mantle along the mid-oceanic ridges, *Nature*, 221, 162-165, 1969a.
- Francis, T. J. G., Upper mantle structure along the axis of the Mid-Atlantic Ridge near Iceland, *Geophys. J. R. Astron. Soc.*, 17, 507-520, 1969b.
- Francis, T. J. G., I.T. Porter, and J. R. McGrath, Ocean-bottom seismograph observations on the Mid-Atlantic Ridge near lat 37°N, *Geol. Soc. Amer. Bull.*, 88, 664-677, 1977.
- Girardin, N., Travel-time residuals of PP waves reflected under oceanic and continental platform regions, *Phys. Earth Planet. Inter.*, 23, 199-206, 1980.
- Girardin, N., and G. Poupinet, Teleseismic S travel-time delay for Mid-Atlantic Ridge earthquakes, *Phys. Earth Planet. Inter.*, 9, 306-313, 1974.
- Grand, S. P., Mantle shear structure from 30°S to 90°N and 120°W to 60°E (abstract), *Eos Trans. AGU*, 70, 389, 1989.
- Green, D. H., W. O. Hibberson, and A. L. Jaques, Petrogenesis of mid-ocean ridge basalts, in *The Earth: Its Origin, Structure, and Evolution*, edited by M. W. McElhinney, Academic Press, London, pp. 265-299, 1979.
- Hales, A. L., and J. L. Roberts, The travel times of S and SKS, *Bull. Seismol. Soc. Am.*, 60, 461-489, 1970.
- Hart, R. S., and F. Press, Sn velocities and the composition of the lithosphere in the regionalized Atlantic, *J. Geophys. Res.*, 78, 407-411, 1973.
- Herrin, E. (Chairman), 1968 seismological tables for P phases, *Bull. Seismol. Soc. Am.*, 58, 1193-1241, 1968.
- Huang, P. Y., and S. C. Solomon, Centroid depths of mid-ocean ridge earthquakes: Dependence on spreading rate, *J. Geophys. Res.*, 93, 13445-13477, 1988.
- Huang, P. Y., S. C. Solomon, E. A. Bergman, and J. L. Nabelek, Focal depths and mechanisms of Mid-Atlantic Ridge earthquakes from body waveform inversion, *J. Geophys. Res.*, 91, 579-598, 1986.
- Hyndman, R. D., Poisson's ratio in the oceanic crust - a review, *Tectonophysics*, 59, 321-333, 1979.
- Jeffreys, H., and K. E. Bullen, *Seismological Tables*, British Association, London, 1940.

- Johnson, K. T. M., H. J. B. Dick, and N. Shimizu, Melting in the oceanic upper mantle: An ion microprobe study of diopsides in abyssal peridotites, *J. Geophys. Res.*, *95*, 2661-2678, 1990.
- Jordan, T. H., and K. A. Sverdrup, Teleseismic location techniques and their application to earthquake clusters in the south-central Pacific, *Bull. Seismol. Soc. Am.*, *71*, 1105-1130, 1981.
- Klein, F. W., Hypocenter location program HYPOINVERSE, 1, User's guide to versions 1, 2, 3, 4, U. S. Geol. Surv. Open File Rep., 78-694, 103 pp., 1978.
- Kong, L. S. L., R. S. Detrick, P. J. Fox, L. A. Mayer, and W. B. F. Ryan, The morphology and tectonics of the MARK area from Sea Beam and Sea MARC I observations (Mid-Atlantic Ridge 23°N), *Mar. Geophys. Res.*, *10*, 59-90, 1988.
- Kumazawa, M., and O. L. Anderson, Elasti moduli, pressure derivatives, and temperature derivatives of single-crystal olivine and single-crystal forsterite, *J. Geophys. Res.*, *74*, 5961-5972, 1969.
- Kuo, B-Y., D. W. Forsyth, and M. Wyssession, Lateral heterogeneity and azimuthal anisotropy in the North Atlantic determined from SS-S differential travel times, *J. Geophys. Res.*, *92*, 6421-6436, 1987.
- Lattimore, R. K., P. A. Rona, and O. E. DeWald, Magnetic anomaly sequence in the central North Atlantic, *J. Geophys. Res.*, *79*, 1207-1209, 1974.
- Lilwall, R. C., and R. Underwood, Seismic network bias maps, *Geophys. J. R. Astron. Soc.*, *20*, 335-339, 1970.
- Lilwall, R. C., T. J. G. Francis, and I. T. Porter, Ocean-bottom seismograph observations on the Mid-Atlantic Ridge near 45°N, *Geophys. J. R. Astron. Soc.*, *51*, 357-370, 1977.
- Lilwall, R. C., T. J. G. Francis, and I. T. Porter, Ocean-bottom seismograph observations on the Mid-Atlantic Ridge near 45°N - further results, *Geophys. J. R. Astron. Soc.*, *55*, 255-262, 1978.
- Lin, J., G. M. Purdy, H. Schouten, J. C. Sempere, and C. Zervas, Evidence from gravity data for focused magmatic accretion along the Mid-Atlantic Ridge, *Nature*, *344*, 627-632, 1990.
- Long, R. L., and M. G. Mitchell, Teleseismic P-wave delay time in Iceland, *Geophys. J. R. Astron. Soc.*, *20*, 41-48, 1970.
- McGregor, B. A., C. G. A. Harrison, J. W. Lavelle, and P. A. Rona, Magnetic anomaly pattern on the Mid-Atlantic Ridge crest at 26°N, *J. Geophys. Res.*, *82*, 231-238, 1977.
- McKenzie, D., The generation and compaction of partially molten rock, *J. Petrol.*, *25*, 713-765, 1984.

- Morris, G. B., R. W. Raitt, and G. G. Shor, Jr., Velocity anisotropy and delay-time maps of the mantle near Hawaii, *J. Geophys. Res.*, *74*, 4300-4316, 1969.
- Nabelek, J. L., Determination of earthquake source parameters from inversion of body waves, Ph.D Thesis, 346 pp., Mass. Inst. of Technol., Cambridge, 1984.
- Phillips, J. D., R. E. Needham, and R. M. Sheppard, Seismic ray tracing for relocating oceanic ridge earthquakes, in Seismic Discrimination, Semiannual Technical Summary, *Tech. Rep. ESD-TR-78-259*, pp. 7-14, Lincoln Lab., Mass. Inst. of Technol., Cambridge, 1979.
- Phipps Morgan, J., Melt migration beneath mid-ocean spreading centers, *Geophys. Res. Lett.*, *14*, 1238-1241, 1987.
- Purdy, G. M., and R. S. Detrick, The crustal structure of the Mid-Atlantic Ridge at 23°N from seismic refraction studies, *J. Geophys. Res.*, *91*, 3739-3762, 1986.
- Raleigh, C. B., Plastic deformation of upper mantle silicate minerals, *Geophys. J. R. Astron. Soc.*, *14*, 45-49, 1967.
- Rowlett, H., and D. Forsyth, Teleseismic P-wave delay times in a major oceanic fracture zone, *Geophys. Res. Lett.*, *6*, 273-276, 1979.
- Salisbury, M. H., and N. I. Christensen, The seismic velocity structure of a traverse through the Bay of Islands ophiolite complex, Newfoundland, an exposure of oceanic crust and upper mantle, *J. Geophys. Res.*, *83*, 805-817, 1978.
- Sclater, J. G., L. A. Lawver, and B. Parsons, Comparison of long-wavelength residual elevation and free air gravity anomalies in the North Atlantic and possible implications for the thickness of the lithospheric plate, *J. Geophys. Res.*, *80*, 1031-1052, 1975.
- Scott, D. R., and D. J. Stevenson, A self-consistent model of melting, magma migration and bouyancy-driven circulation beneath mid-ocean ridges, *J. Geophys. Res.*, *94*, 2973-2988, 1989.
- Sempere, J. C., G. M. Purdy, and H. Schouten, The segmentation of the Mid-Atlantic Ridge between the Kane and Atlantis fracture zones (abstract), *Eos Trans. AGU*, *70*, 455, 1989.
- Sheehan, A. F., and S. C. Solomon, SS-S differential travel time residuals in the vicinity of the Mid-Atlantic Ridge and Bermuda Rise (abstract), *Eos Trans. AGU*, *69*, 1328, 1988.
- Sheehan, A. F., and S. C. Solomon, Evidence from SS-S travel times for long wavelength variations in mantle structure beneath the north Atlantic (abstract), *Eos Trans. AGU*, *70*, 1227, 1989.
- Solomon, S. C., Shear wave attenuation and melting beneath the Mid-Atlantic Ridge, *J. Geophys. Res.*, *78*, 6044-6059, 1973.

- Solomon, S. C., and B. R. Julian, Seismic constraints on ocean-ridge mantle structure: Anomalous fault-plane solutions from first motions, *Geophys. J. R. Astron. Soc.*, *38*, 265-285, 1974.
- Steinmetz, L., R. B. Whitmarsh, and V. S. Moreira, Upper mantle structure beneath the Mid-Atlantic Ridge north of the Azores based on observations of compressional waves, *Geophys. J. R. Astron. Soc.*, *50*, 353-380, 1977.
- Toomey, D. R., S. C. Solomon, G. M. Purdy, and M. H. Murray, Microearthquakes beneath the median valley of the Mid-Atlantic Ridge near 23°N: Hypocenters and focal mechanisms, *J. Geophys. Res.*, *90*, 5443-5458, 1985.
- Toriumi, M. Preferred orientation of olivine in mantle-derived peridotites and stress in the lithosphere, *J. Phys. Earth*, *32*, 259-271, 1984.
- Tryggvason, E., Arrival times of P waves and upper mantle structure, *Bull. Seismol. Soc. Am.*, *54*, 727-736, 1964.
- Weidner, D. J., Rayleigh wave phase velocities in the Atlantic Ocean, *Geophys. J. R. Astron. Soc.*, *36*, 105-139, 1974.
- Weidner, D. J., and K. Aki, Focal depth and mechanism of mid-ocean ridge earthquakes, *J. Geophys. Res.*, *78*, 1818-1831, 1973.
- Woodward, R. L., and G. Masters, Global upper mantle structure from long period differential travel-times (abstract), *Eos Trans. AGU*, *69*, 1329, 1988.
- Woodward, R. L., and G. Masters, Global upper mantle structure from long-period differential travel-times, *J. Geophys. Res.*, in press, 1990.



## FIGURE CAPTIONS

- Figure 1. Sea Beam bathymetric map of the Mid-Atlantic Ridge near 26°N (0.25 km contour interval) [Sempere *et al.*, 1989]; areas shallower than 3 km are shown by diagonal hatching. Also shown are the locations of the local seismic network: numbered triangles are OBHs; numbered diamonds are OBSs. The locations of teleseismically-recorded earthquakes during the period 1964-1989 are shown as solid squares (epicenters of swarm events located by the OBH-OBS network), and circles (teleseismically relocated epicenters). The epicentroid for the large earthquakes is shown by a cross. Bathymetry is contoured at 0.25 km intervals. Inferred axes of *en echelon* ridge segments are shown by solid lines [from Sempere *et al.*, 1989].
- Figure 2. Examples of locally-recorded seismograms for two earthquakes, (a) 1939UT and (b) 2049UT, in the swarm. Starting times are the same for all traces. Instruments 1,2,3,4,5, and 6 are OBHs, and instrument 31 is an OBS (V=vertical, T=transverse channel). See Figure 1 for receiver locations. All records are plotted with equal maximum amplitudes. Low frequency, high amplitude waveforms following the P-wave arrival on OBHs 2, 5, and 6, and the S-wave arrival on OBS 31 indicate saturation.
- Figure 3. Typical seismograms showing P and S-wave arrivals recorded by OBS 31 (V=vertical, T=transverse) for swarm earthquakes occurring near 25°50'N. Traces are plotted with equal maximum amplitudes with V records amplified by a factor of 1.2 relative to transverse channel records. Amplitudes on the transverse channel following the S-wave arrival for the 1907UT and 1939UT earthquakes are saturated.
- Figure 4. Velocity models used to estimate hypocentral parameters. The median valley structure determined along the Mid-Atlantic Ridge at 23°N [Purdy and Detrick, 1986; Toomey *et al.*, 1985] is adopted for location with local data. The Herrin [1968] Earth model, which possesses a continental crustal structure, is used in the joint relocation of teleseismic data. Neither models contain low velocity zones in the upper mantle. The Jeffreys-Bullen [1940]

and isotropic PREM P and S-wave structures [Dziewonski and Anderson, 1981] are also considered as alternative average reference models.

- Figure 5. a) Change in locally-estimated epicenter with assumed focal depth for the 1854UT (circles) and 1907UT (squares) events. The 1939UT event is omitted for clarity. The average epicentral shift for all three events is  $1.1 \pm 0.6$  km along an azimuth of  $\sim N40^\circ E$  azimuth for each kilometer shoaling of depth. The hypocentroid of the teleseismically-estimated events (crossed circle) is used as the starting location for all runs, and  $V_p/V_s$  is taken to be 1.84. Increasing symbol sizes correspond to greater focal depths (7 to 1 km at 1 km intervals). Error ellipsoids (95%) are shown at a 6-km depth.
- b) Dependence of locally-estimated epicenter on starting trial epicenter. The maximum difference in epicenter between the hypocentroid starting location and other starting locations (ISC or relocated epicenters) is  $< 1$  km. A focal depth of 6.4 km beneath the seafloor and a  $V_p/V_s$  ratio of 1.84 are assumed. Each symbol corresponds to a starting and final location for each event. Error ellipsoids (95%) shown are for the locations obtained with the teleseismically relocated epicenter starting location (solid circles).
- c) Dependence of locally-estimated epicenter on assumed  $V_p/V_s$  ratio. The average change in epicenter is  $2.7 \pm 0.6$  km along an azimuth of  $\sim N40^\circ E$  for every 0.05 increase in the ratio. The teleseismically relocated epicenter (crossed circle) is used as the starting location, and a depth of 6.4 km beneath the seafloor is assumed. Error ellipsoids (95%) shown are for  $V_p/V_s = 1.85$ . Increasing symbol sizes correspond to decreasing  $V_p/V_s$  ratios (1.75 to 2.10 at 0.05 increments). The 1939UT event is omitted for clarity.

- Figure 6. Hypocentroid data importance. The large contribution from northern hemisphere stations results in a northward bias in the teleseismically-determined epicenter relative to the local estimate. Importance is plotted as a percentage contribution to the solution and binned according to station azimuth. Circles represent 10, 20, and 30% relative importance; azimuthal bins are  $30^\circ$  in width.

- Figure 7. Local (squares) and teleseismic (circles) estimates of earthquake locations. Teleseismically-determined epicenters are shown together with the principal axes of the 95% confidence ellipsoid; the largest symbols are for the 1854UT and 1907UT events. Solid triangle denotes the location of the closest recording ocean bottom instrument. Bathymetry, contoured at 0.25 km intervals, is from Figure 1. Lengths of major and minor axes for teleseismic earthquake location uncertainties are with respect to the hypocentroid (Figure 1).
- Figure 8. Origin time correction due to the northward bias in epicenter of the teleseismically-determined locations. The best estimate of origin time moves earlier since true epicenters are farther from the greatest concentration of seismic stations than indicated by the teleseismic location. The correction is linearly related to the magnitude of the bias in the northward direction of the teleseismically-determined epicenter relative to the local estimate. Open circles show the preferred corrections ( $V_p/V_s = 1.84$ ) for the *Herrin* [1968] Earth model.
- Figure 9. Comparison of observed (solid lines) and synthetic (dashed lines) long period P and SH waves for the 1854UT earthquake, with the focal mechanism solution obtained from waveform inversion. The source time function estimated by the inversion is also shown. Amplitudes are normalized to an instrument magnification of 1000 at  $\Delta = 40^\circ$ . Two vertical lines delimit the portion of the waveform (digitized at intervals of 0.5 s for WWSSN and 1.0 s for GDSN instruments) used in the inversion, with the first line showing the best fit arrival time. Open circles indicate dilatational P-wave arrivals. ANMO, BCAA, KONO, and LON (top seismogram) are GDSN stations; the remaining are WWSSN stations.
- Figure 10. Histogram showing the S-wave travel time residuals determined using an internally-consistent waveform fitting technique to pick arrival times, as compared with those calculated using arrival times reported by the ISC.

- Figure 11. Comparison of JB P and S-wave delays from this study (open symbols) with those from other Mid-Atlantic Ridge studies (all in s). The *Dorbath and Dorbath* [1981] value is an average between 12° and 20°N over a 200 km width about the ridge (diamond); the *Girardin* [1980] value is an average over the ages of 5-38 My (triangle). The delays of *Girardin and Poupinet* [1974] (square) and *Duschenes and Solomon* [1977] (solid circles) are from measured S-wave travel time residuals. See text for discussion.
- Figure 12. Observed variation in average PREM P and S-wave delays (PP-P or SS-S differential travel time residual divided by 2), corrected for age, versus latitude of the bounce point along the MAR between 21 and 31°N from *Woodward and Masters* [1990]. The delays at 26°N (square with associated uncertainty) are smaller than the means (dashed lines) for both P and S. Although the scatter in the P-wave residuals is 1-2 s, the data exhibit an along-axis minimum at 25-27°N. S residuals ( $\Delta = 55-85^\circ$ ) are also lower at these latitudes, but the latitude dependence is not robust. The residuals have been corrected for lithospheric age at the bounce point using an  $\text{age}^{1/2}$ -residual relation empirically determined from Atlantic data (PP-P from *Woodward and Masters* [1990], SS-S from *Kuo et al.* [1987]).
- Figure 13. a) Vertically-oriented mantle anisotropy may be caused by upwelling of mantle material beneath the ridge crest. Reorientation of olivine crystals, which display a high degree of compressional wave anisotropy (b), so that the a-axis is aligned with the upwelling direction, can result in a P-wave delay that is much smaller than predicted by an average isotropic mantle structure, and an S delay which is only slightly smaller. If the anisotropy is assumed to occur within the uppermost 200 km of mantle, a P wave velocities which are 7 % faster in the vertical direction are required. Mantle flow lines schematically shown are those predicted for spreading at the ridge axis (after *Phipps-Morgan*, 1987).
- b) Laboratory-measured velocities in the *a*, *b*, and *c* directions for single-crystal olivine, from *Kumazawa and Anderson* [1969]. Compressional wave velocities, much more than shear wave velocities, are highly dependent on the direction of propagation. S-wave velocity is an average for two waves with

mutually orthogonal particle motions propagating in each axial direction.  
Anisotropy may result from the physical alignment of olivine crystals.

TABLE 1: Hypocentral parameters determined by local and teleseismic seismic networks.

Date (m/d/yr)	Origin time	Latitude, °N	Longitude, °W	Error ellipse (95%)			Error (1- $\sigma$ ) in origin time, s	No. obs
				Major, km	Minor, km	Azi, major		
<u>From local network:</u>								
7 / 13 / 85	1854: 14.89	25.77117	45.05317	8.9 <sup>1</sup>	3.2 <sup>1</sup>	133°	0.19 <sup>1</sup>	8
7 / 13 / 85	1907: 02.93	25.83850	45.05883	7.9	2.2	136°	0.13	8
7 / 13 / 85	1939: 12.76	25.81800	45.05700	6.4	2.1	135°	0.12	7
<u>From teleseismic data:</u>								
	Hypocentroid	25.911	45.033	3.5	2.5	158°	0.07	1039
7 / 13 / 85	1854: 14.89	25.946	45.021	3.6 <sup>2</sup>	2.5 <sup>2</sup>	148°	0.07 <sup>2</sup>	183
7 / 13 / 85	1900: 20.51	25.905	45.012	9.3	6.2	128°	0.16	11
7 / 13 / 85	1907: 03.03	25.956	45.103	15.5	8.3	105°	0.29	7
7 / 13 / 85	1909: 20.04	25.981	45.044	3.6	2.6	154°	0.07	185
7 / 13 / 85	1939: 17.13	25.912	45.013	8.5	5.3	136°	0.14	16
11 / 29 / 66	503: 48.93	26.125	44.718	7.5	5.9	101°	0.15	28
7 / 11 / 67	16: 04.51	26.235	44.865	10.8	7.7	166°	0.21	12
1 / 5 / 73	338: 57.63	25.863	44.991	4.3	3.0	165°	0.08	85
2 / 15 / 76	0: 27.78	25.446	45.284	7.1	5.3	198°	0.15	25
3 / 4 / 77	2005: 11.47	26.240	44.887	7.5	5.3	169°	0.16	24
11 / 16 / 80	2157: 12.61	26.172	44.863	6.6	5.4	140°	0.12	13
1 / 29 / 82	2230: 20.30	25.547	45.339	9.7	6.1	133°	0.17	12
1 / 29 / 82	2232: 08.71	25.536	45.234	3.8	2.7	159°	0.07	160
6 / 18 / 85	436: 57.82	25.883	45.090	8.3	6.5	158°	0.15	10

<sup>1</sup> Errors calculated for  $V_p/V_s=1.84$ , which is assumed to be known.

<sup>2</sup> Standard error and lengths of semi-axes are for relative earthquake locations (which are determined with respect to the hypocentroid).

TABLE 2: Upper mantle P wave delay for 1854Z earthquake.

Uncorrected teleseismically-determined origin time:	$14.89 \pm 0.10$ s <sup>1</sup>
Correction to <i>Herrin</i> [1968] model for oceanic crustal thickness:	$+ 1.02 \pm 0.10$ s <sup>2</sup>
Correction for northward bias in global epicenter:	$- 0.73 \pm 0.15$ s <sup>3</sup>
<hr/>	
Corrected total origin time delay:	$15.18 \pm 0.21$ s <sup>4</sup>
Locally-determined origin time:	$14.89 \pm 0.19$ s
Uncertainty in local-network $V_p/V_s$ ratio:	$\pm 0.78$ s <sup>5</sup>
Upper mantle P wave delay:	$+ 0.29 \pm 0.83$ s <sup>4,6</sup>

<sup>1</sup> Error calculated by summation of estimated variances for hypocentroid and relative event locations.

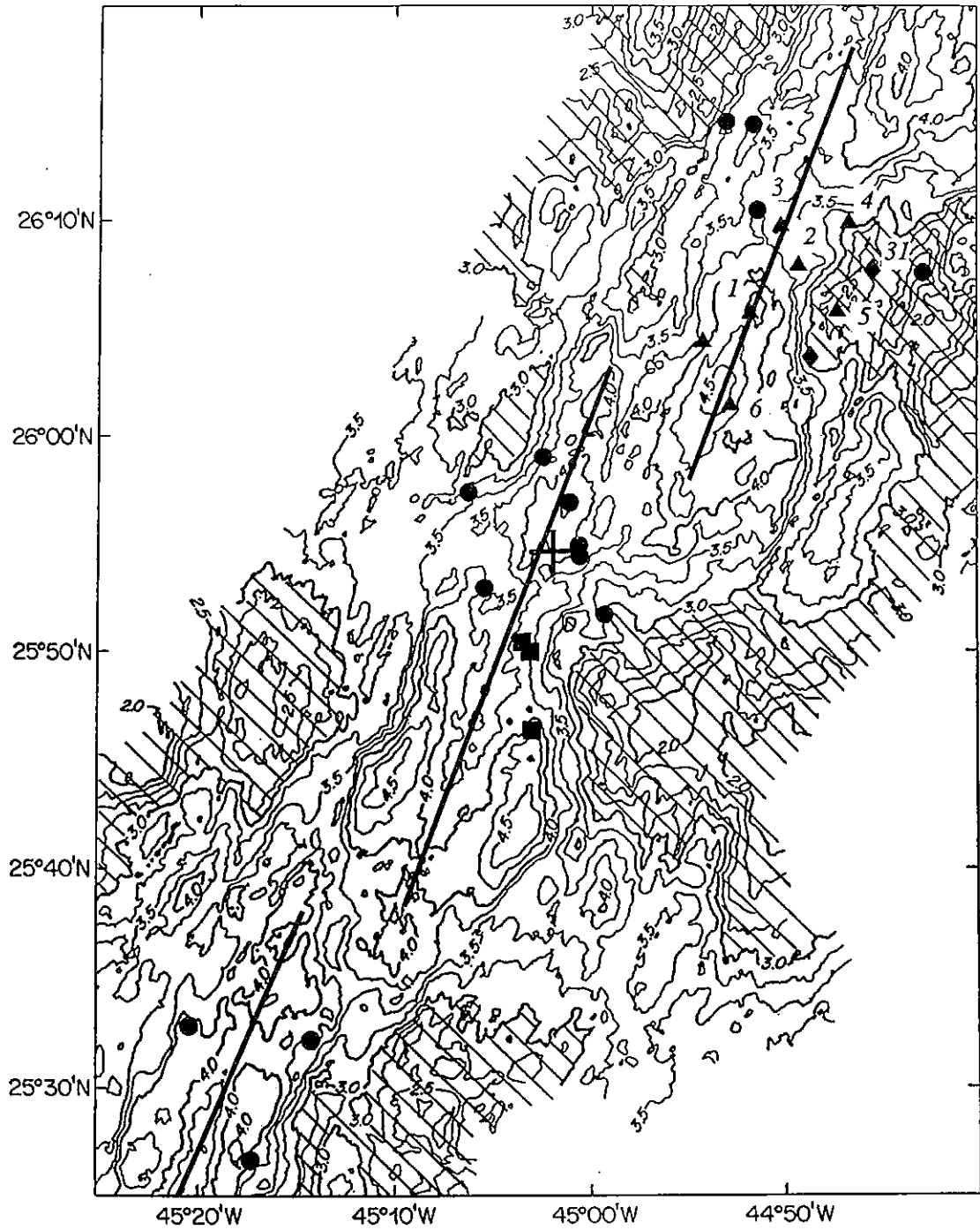
<sup>2</sup> Error represents range for rays at source incidence angles between 20 and 30°.

<sup>3</sup> Error based on uncertainty in local epicentral estimate ( $V_p/V_s = 1.84$ ).

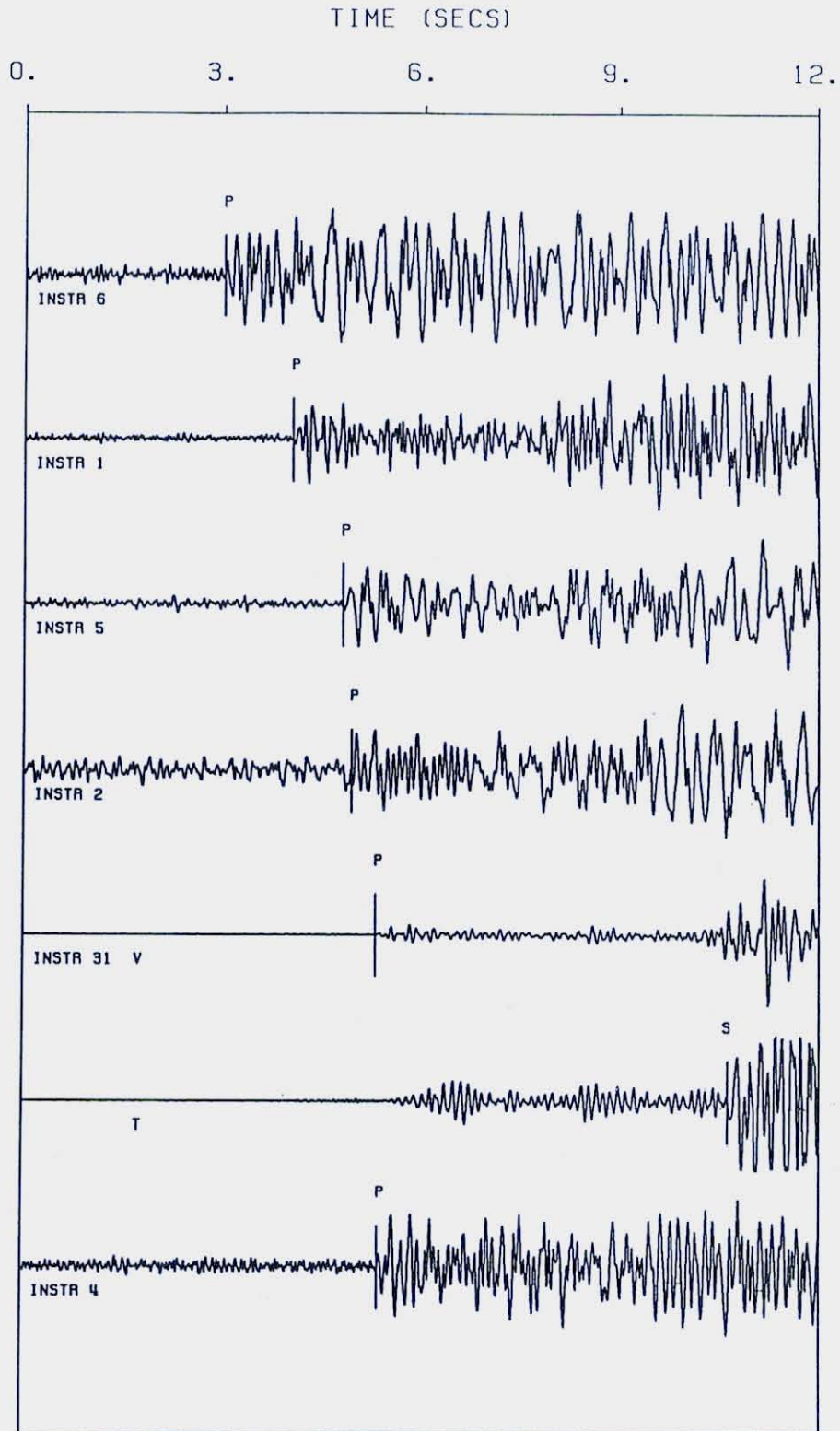
<sup>4</sup> Error calculated by summing above independently-estimated variances.

<sup>5</sup> Standard deviation around mean origin time for hypocenters estimated using  $V_p/V_s$  range of 1.78-1.99.

<sup>6</sup> Average delay with respect to a *Herrin* [1968] Earth model assuming a hypocenter given by the local network data.

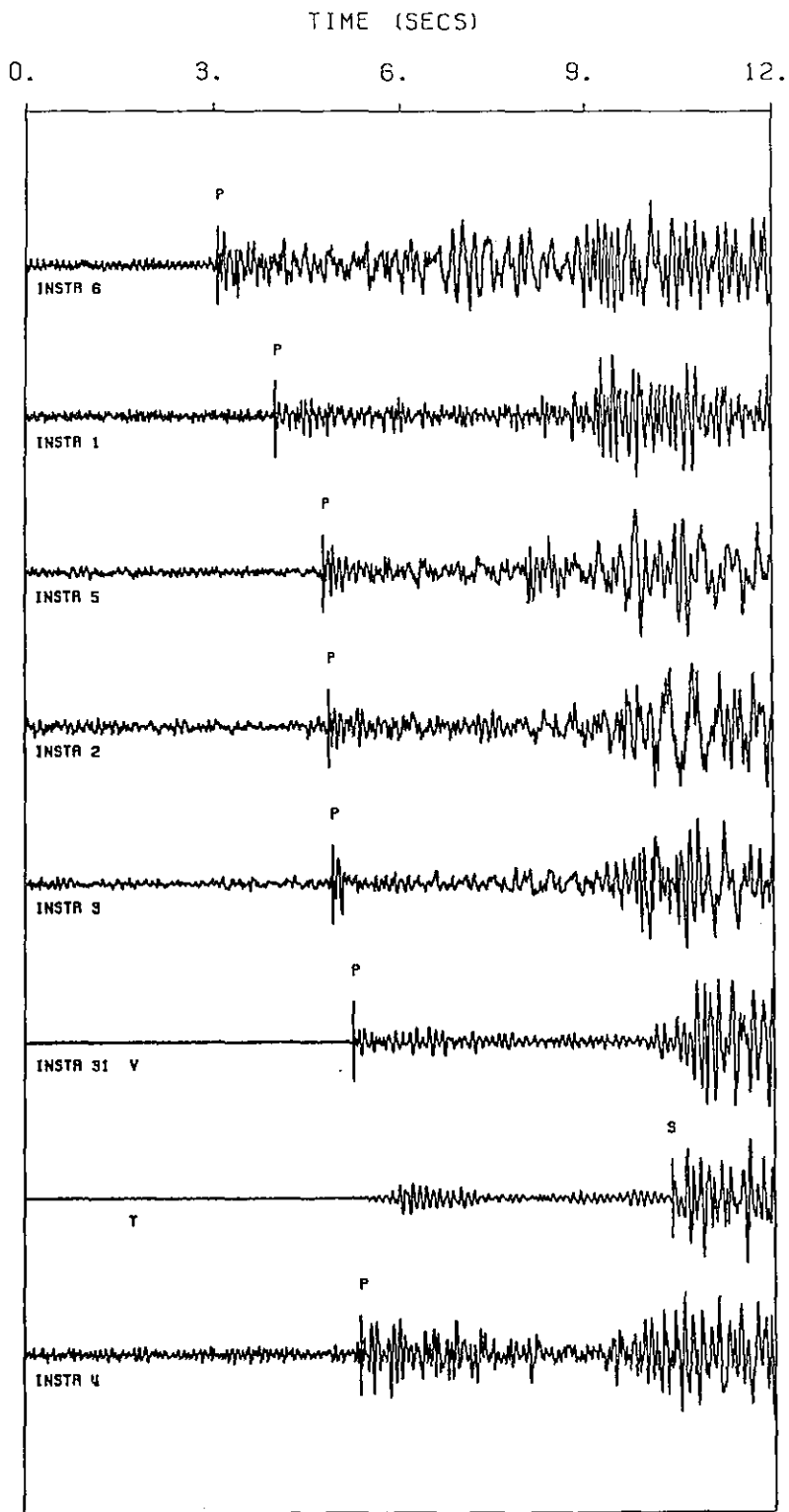
*Figure 1*





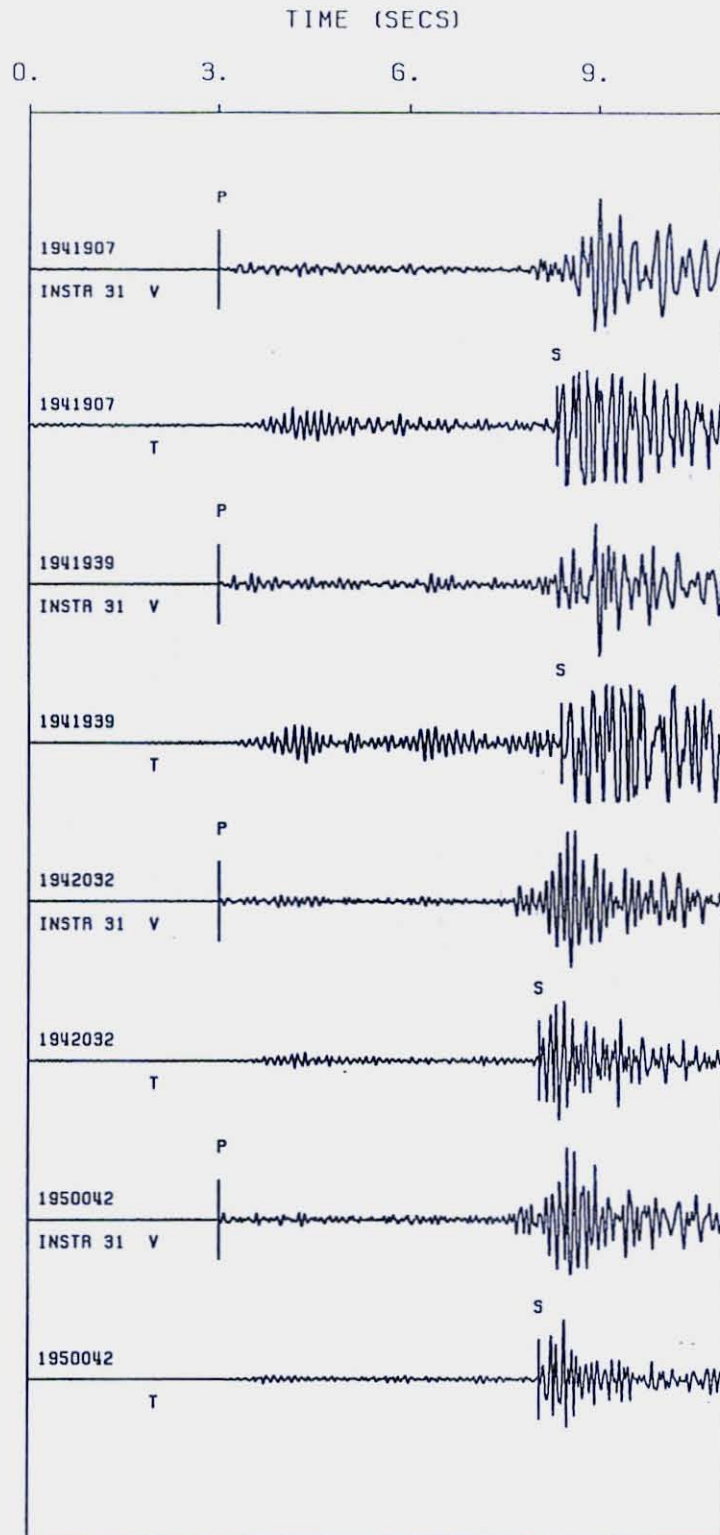
P,S-WAVE ARRIVALS FOR 1939UT EARTHQUAKE

*Figure 2 a*



P,S-WAVE ARRIVALS FOR 2049UT EARTHQUAKE

Figure 2b



JULY 1985 EARTHQUAKE SWARM

Figure 3

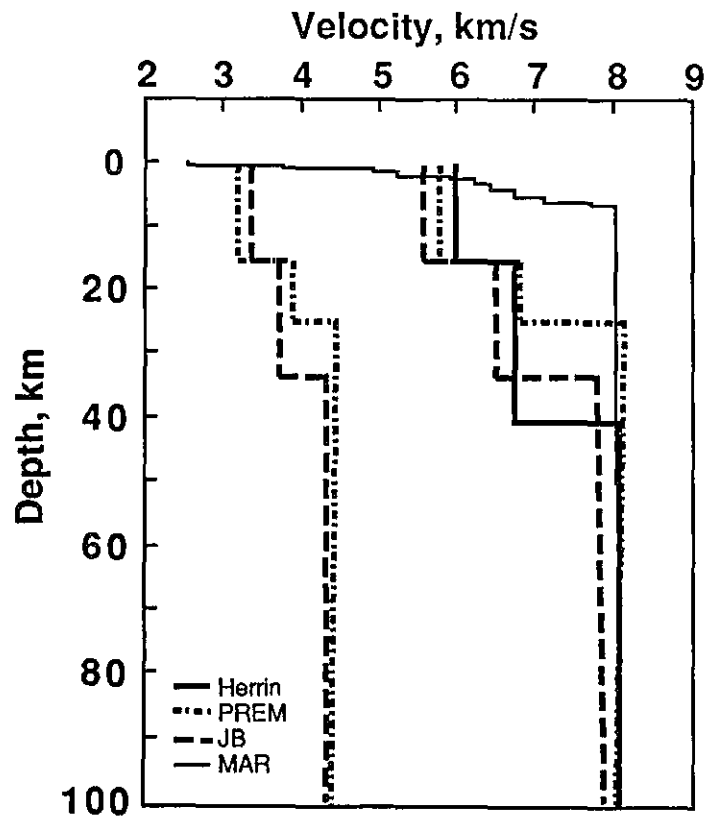


Figure 4

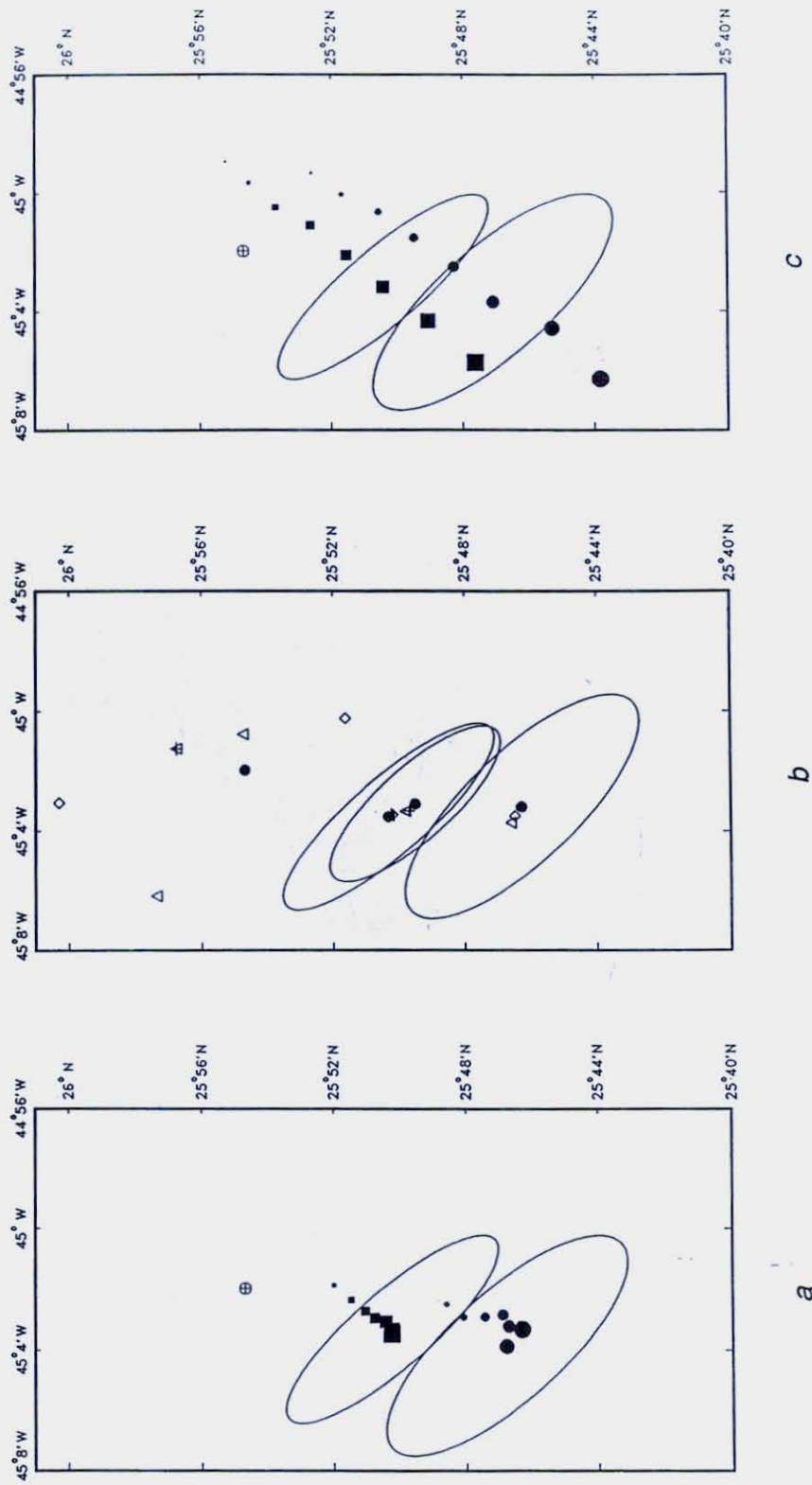
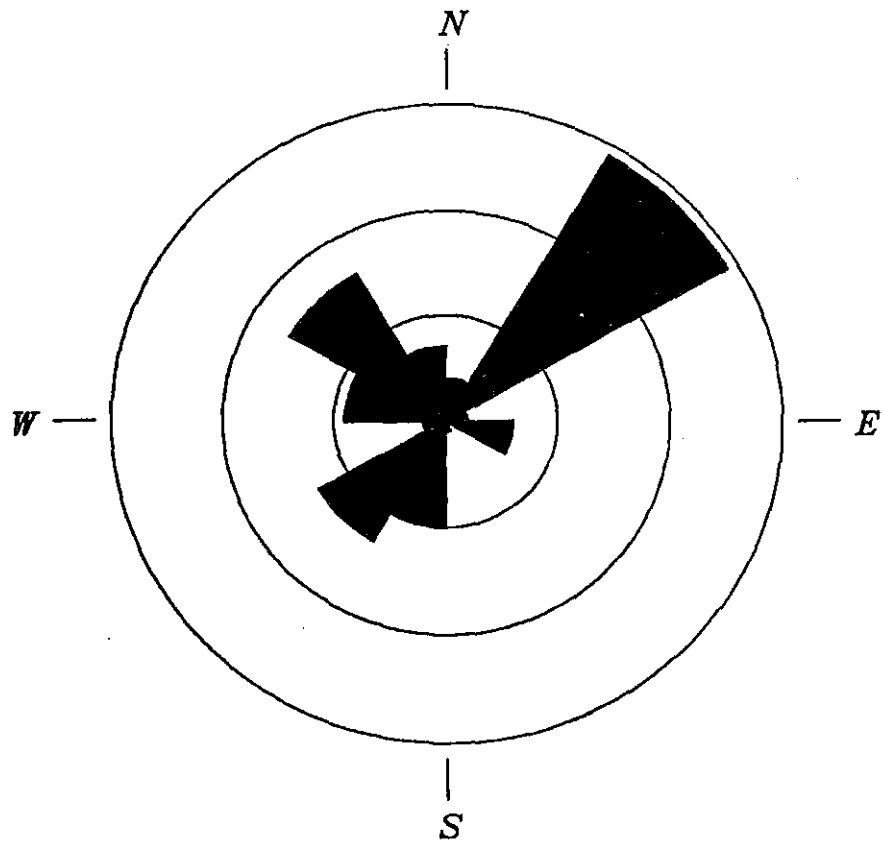
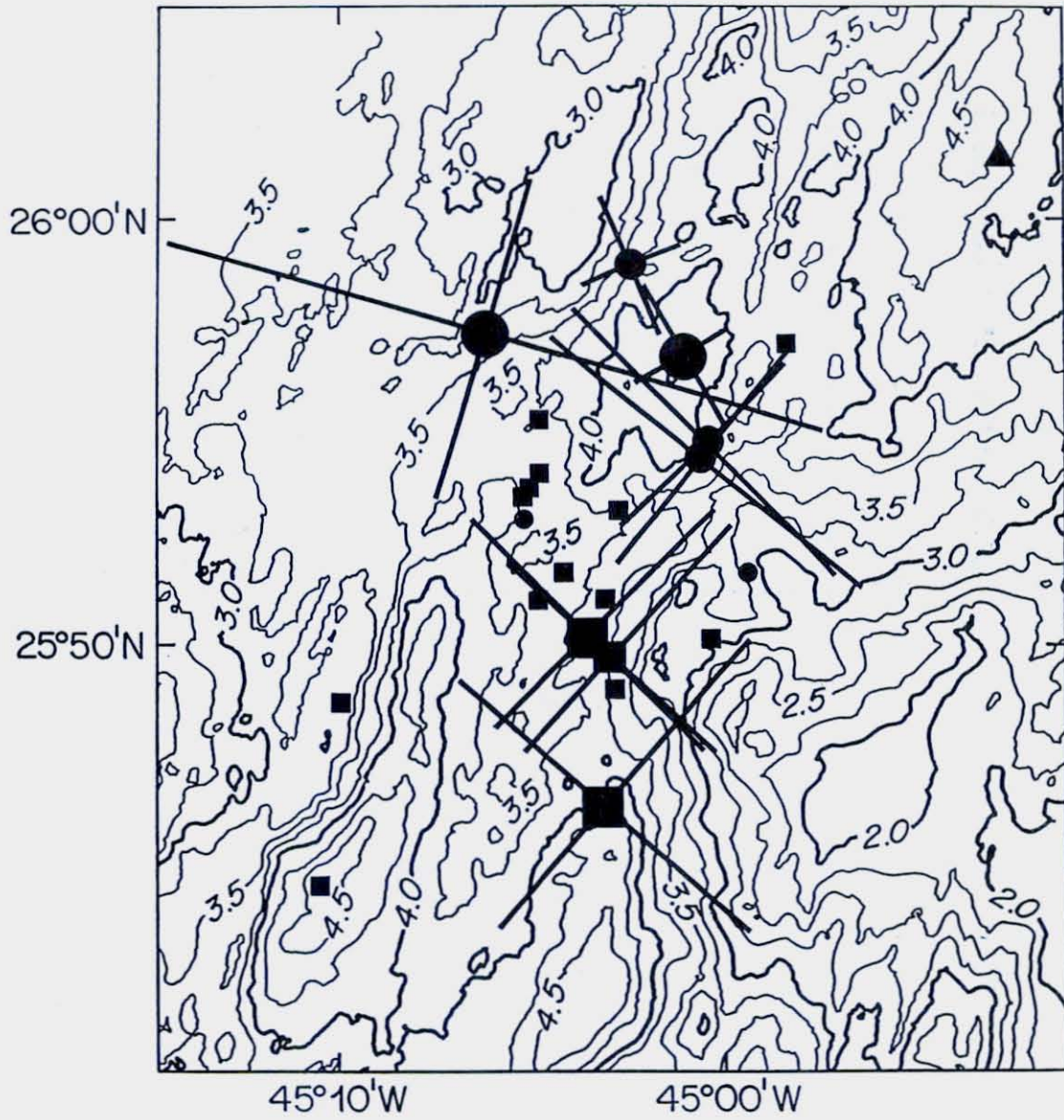


Figure 5

*Hypocentroid data importance**Figure 6*

*Figure 7*

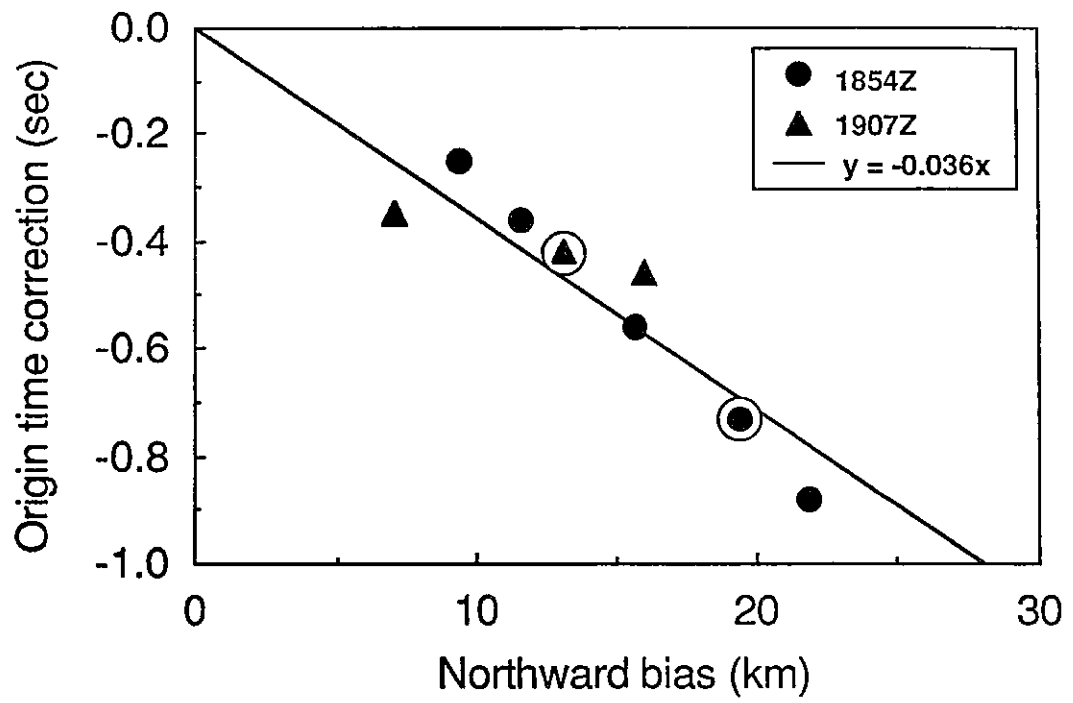


Figure 8



890612131650

# July 13, 1985 (1854)

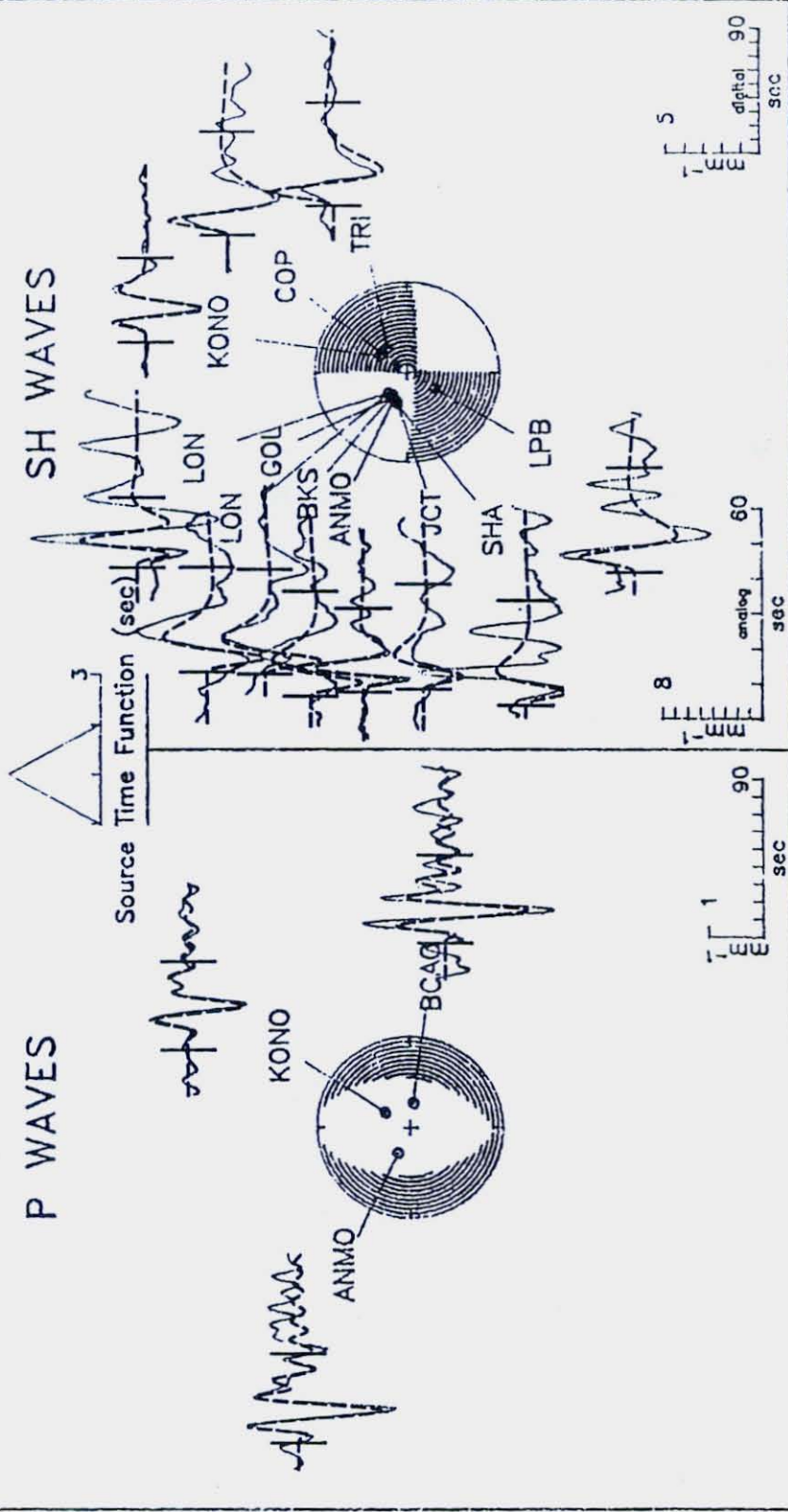
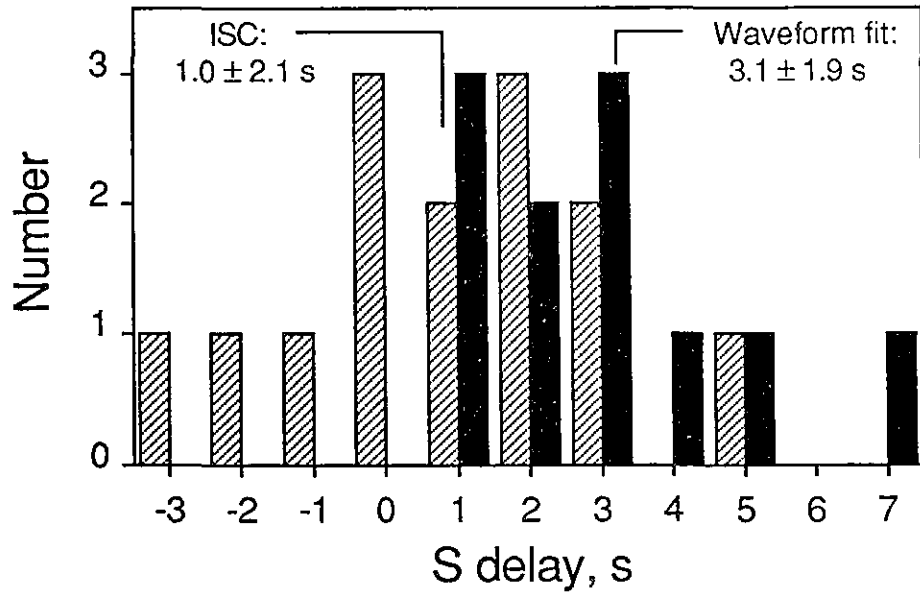
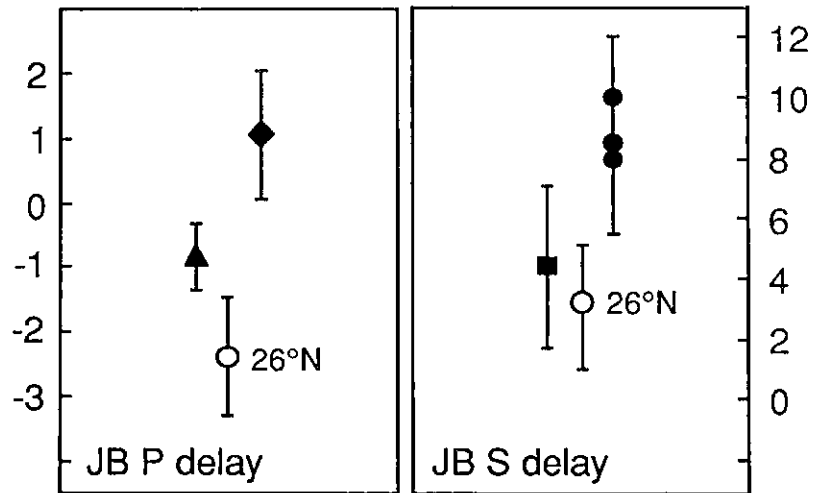


Figure 9

*Figure 10*

*Figure 11*

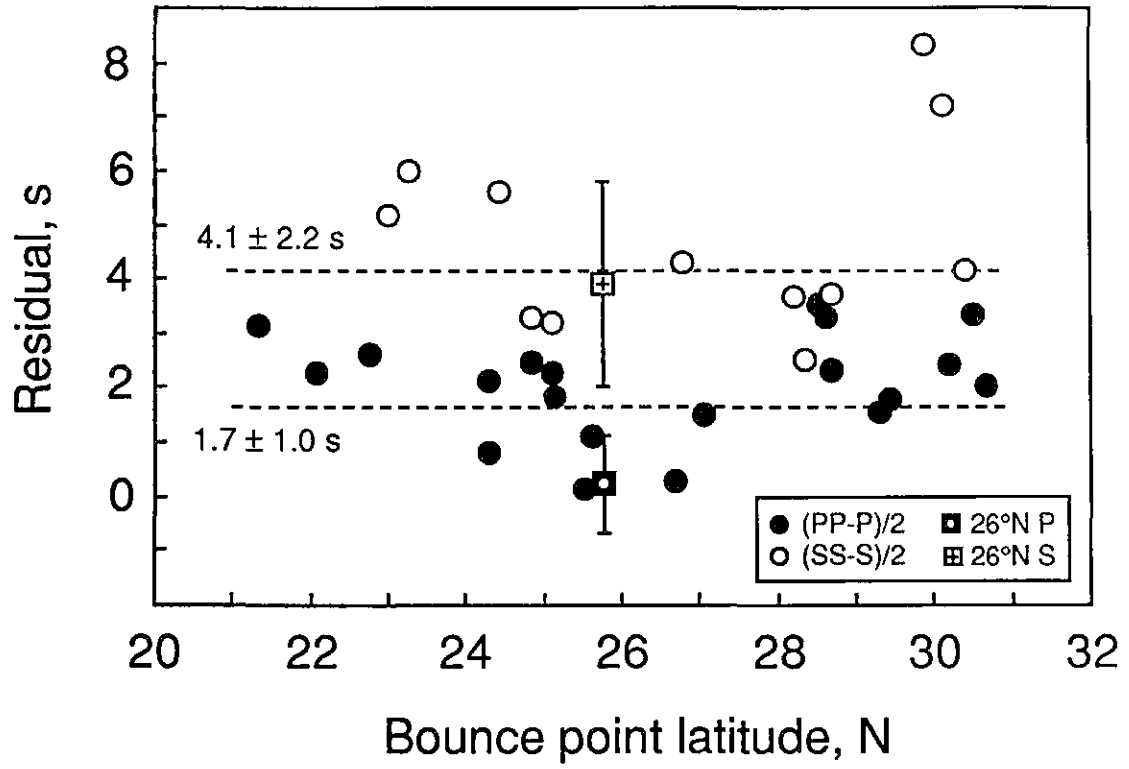


Figure 12

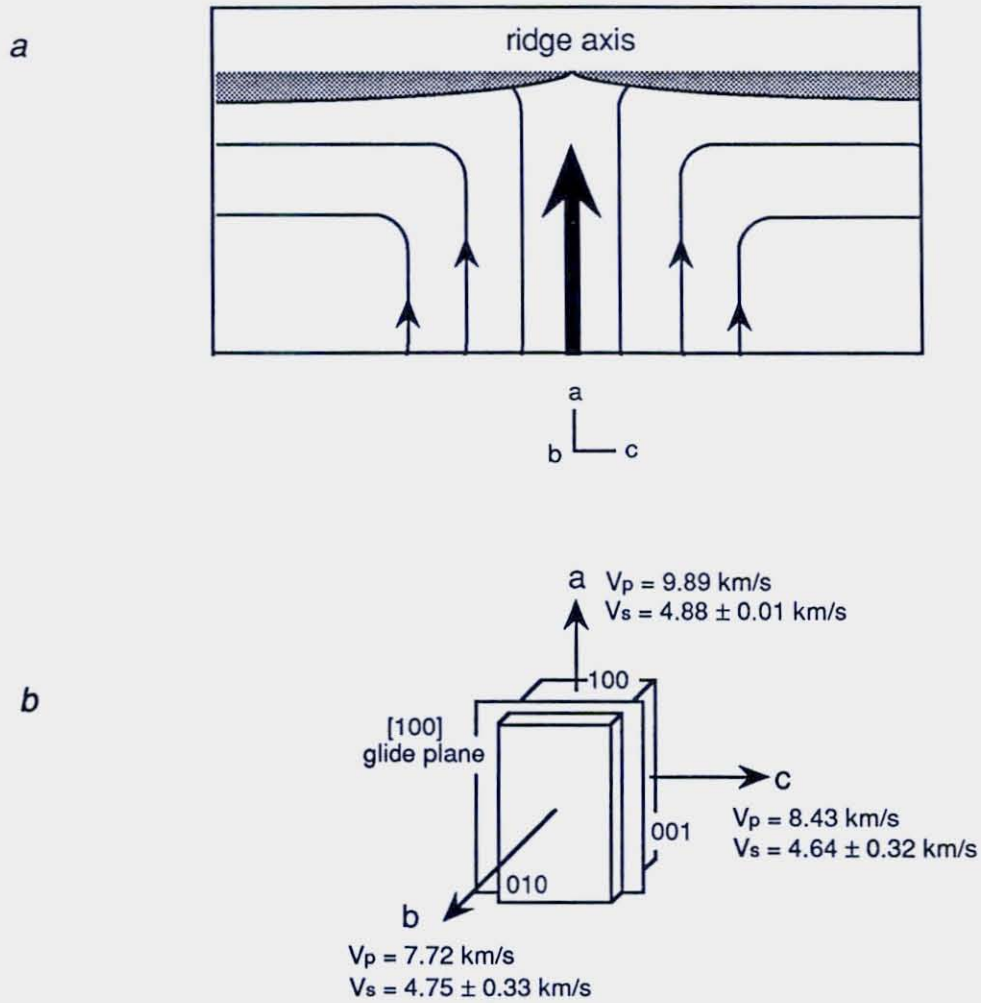


Figure 13



## CHAPTER 6. CONCLUSIONS

In this thesis, I have investigated the structure and tectonics within the median valley at two locales, 23°N and 26°N, along the Mid-Atlantic Ridge. The variability observed in the locations and morphologies of active volcanism and tectonism implies that the formation of oceanic crust at slow spreading centers is not a simple two-dimensional process in which crust is accreted uniformly both along the ridge axis and with time. Rather, the MAR appears to be divided into distinct *en echelon* segments, each characterized by different proportions of active magmatism and tectonism and in which the most vigorous volcanism occurs in the along-axis high region. Comparison of the seismic structures determined at 26°N with other MAR studies shows variability in the velocity-depth functions describing the inner floor along-axis high, however. The differences in structural and morphological heterogeneity documented within spreading cells at 23°N and 26°N suggests that the segments evolve independently to the interplay between extensional tectonism and episodic variations in magma production rates.

The conclusions of this thesis are based on seismic and side scan sonar observations of two geologically well-characterized portions of the Mid-Atlantic Ridge. Both areas have been investigated extensively by near-bottom surveys (camera, submersible, deeply-towed geochemical sensors), by surface geophysical experiments (seismic, magnetic, gravity), and by on- or in-bottom sampling programs (dredging, drilling and borehole logging of cores). The integration of Chapters 2-4 with the results from other studies has led to an exceptionally detailed description of variations in crustal accretion within a spreading cell. For example, although active high-temperature hydrothermal fields are found at locally high regions at both 23°N and 26°N, the geological settings for each are very different (neovolcanic ridge at 23°N, near eastern wall at 26°N).

The 100-km-length of ridge south of the Kane Fracture Zone consists of two *en echelon* spreading cells, each displaying different types and amounts of volcanism and tectonic fissuring, which overlap in a discordant zone lacking a well-developed median valley or neovolcanic zone (Chapter 2). The northern cell is dominated by a large constructional volcanic ridge atop which high-temperature hydrothermal activity has been mapped; analysis of hydrothermal fluids from the black smoker vents suggests a shallow heat source (~ 2 km) [Campbell *et al.*, 1988], though no magma chamber reflector (phase reversal) was observed in the seismic reflection data shot along the ridge crest [Detrick *et al.*, 1989]. The southern spreading cell is characterized by a NNE-trending band of

fissured and faulted small volcanos constructed upon older fissured and sediment-covered lavas; this cell is thought to be in a predominantly extensional phase (Chapter 2). The spreading cell interpretation is compatible with the results from a 120-km long refraction line shot along the median valley by *Purdy and Detrick* [1986], and with the inferences made by *Schulz et al.* [1988] from the magnetic anomaly data. Low seafloor velocities are associated with the shallowmost 1 km of crust beneath the along-axis high (22°55'N) of the southern cell [*Purdy and Detrick*, 1986; *Purdy*, 1987], and a zone of slightly lower velocities within layer 3, interpreted as the seismic remnants from the most recent magmatic pulse along the ridge, was found beneath the along-axis high [*Purdy and Detrick*, 1986].

From the analysis of microearthquakes (Chapter 3) and the tomographic inversion of P wave travel time residuals for two-dimensional along-axis structure beneath the median valley at 26°N (Chapter 4), it was inferred that the most recent locus of magmatic activity is concentrated at the along-axis high region where the hydrothermal field is located. The observed distribution of hypocenters and the diversity of faulting beneath the inner floor and walls are presumably a signature of lateral variations in the depth region over which brittle failure occurs, and are a consequence of along-axis changes in the thermal structure and state of stress; thermal stresses probably play a dominant role in determining the patterns of earthquake seismicity and source mechanisms. The shallowmost crust beneath the volcano and along-axis high is characterized by significantly higher velocities than are associated with the upper crust in the deepest portions of the median valley. A temporal variation is inferred to be a consequence of more recent volcanic activity in the along-axis high region (active accretion), as compared with the along-axis deep where tectonic fissuring has created a highly porous crust characterized by lower seafloor velocities (active tectonism).

The apparent lack of seismicity beneath the hydrothermal field, the absence of microearthquake activity greater than 4 km depth and the propagation of S waves through the crust beneath the volcano and along-axis high (Chapter 3), the location of hypocenters around a low P wave velocity zone, attenuation of P wave energy to instruments atop the high (Chapter 4), the higher b-values associated with the along-axis high region, and the observation of high-angle (or very low angle) normal and reverse faulting with variable nodal plane orientations for events beneath the inner floor along-axis high and the volcano, suggest that the low-velocity volume corresponds to a region of hot rock with no seismically-resolvable pockets of partial melt. The shallow velocity gradients describing



the low velocity volume appear to be characteristic of inferred zones of magmatic intrusion on the MAR.

The results from this thesis support the hypothesis that in the spreading cell model for slow spreading ridges, the most likely locale at which to find elevated crustal temperatures is at locally high regions of the inner floor. In contrast, tectonic forces appear to be dominant beneath along-axis deeps with volcanism much less energetic; fissuring and faulting of the uppermost crust results in high bulk permeabilities and low seafloor velocities at the ridge axis. Along-axis highs are approximately centered within each spreading cell. Comparison of the depth to the velocity inversion with the depths determined in other seismic studies at locally high regions along the MAR, the Juan de Fuca Ridge, and the East Pacific Rise reveals a correlation between lid thickness and spreading rate, suggesting that the amount of magma available at each location is spatially variable, or that the differences in lid thickness are describing the temporal evolution of magmatic intrusions beneath mid-ocean ridges.

## REFERENCES

- Campbell, A.C., M.R. Palmer, G.P. Klinkhammer, T.S. Bowers, J.M. Edmond, J.R. Lawrence, J.F. Casey, G. Thompson, S. Humphris, P. Rona and J.A. Karson, Chemistry of hot springs on the Mid-Atlantic Ridge, *Nature*, 335, 514-519, 1988.
- Detrick, R. S., J. C. Mutter, and P. Buhl, Multichannel seismic data across the Snake Pit hydrothermal field (Mid-Atlantic Ridge, 23°N): No evidence for a crustal magma chamber (abstract), *Eos Trans. AGU*, 70, 1325-1326, 1989.
- Purdy, G. M., New observations of the shallow seismic structure of young oceanic crust, *J. Geophys. Res.*, 92, 9351-9362, 1987.
- Purdy, G. M., and R. S. Detrick, The crustal structure of the Mid-Atlantic Ridge at 23°N from seismic refraction studies, *J. Geophys. Res.*, 91, 3739-3762, 1986.
- Schulz, N. J., R. S. Detrick, and S. P. Miller, Two and three-dimensional inversions of magnetic anomalies in the MARK area (Mid-Atlantic Ridge 23°N), *Mar. Geophys. Res.*, 10, 41-57, 1988.



## DOCUMENT LIBRARY

January 17, 1990

### *Distribution List for Technical Report Exchange*

Attn: Stella Sanchez-Wade  
Documents Section  
Scripps Institution of Oceanography  
Library, Mail Code C-075C  
La Jolla, CA 92093

Hancock Library of Biology &  
Oceanography  
Alan Hancock Laboratory  
University of Southern California  
University Park  
Los Angeles, CA 90089-0371

Gifts & Exchanges  
Library  
Bedford Institute of Oceanography  
P.O. Box 1006  
Dartmouth, NS, B2Y 4A2, CANADA

Office of the International  
Ice Patrol  
c/o Coast Guard R & D Center  
Avery Point  
Groton, CT 06340

NOAA/EDIS Miami Library Center  
4301 Rickenbacker Causeway  
Miami, FL 33149

Library  
Skidaway Institute of Oceanography  
P.O. Box 13687  
Savannah, GA 31416

Institute of Geophysics  
University of Hawaii  
Library Room 252  
2525 Correa Road  
Honolulu, HI 96822

Marine Resources Information Center  
Building E38-320  
MIT  
Cambridge, MA 02139

Library  
Lamont-Doherty Geological  
Observatory  
Columbia University  
Palisades, NY 10964

Library  
Serials Department  
Oregon State University  
Corvallis, OR 97331

Pell Marine Science Library  
University of Rhode Island  
Narragansett Bay Campus  
Narragansett, RI 02882

Working Collection  
Texas A&M University  
Dept. of Oceanography  
College Station, TX 77843

Library  
Virginia Institute of Marine Science  
Gloucester Point, VA 23062

Fisheries-Oceanography Library  
151 Oceanography Teaching Bldg.  
University of Washington  
Seattle, WA 98195

Library  
R.S.M.A.S.  
University of Miami  
4600 Rickenbacker Causeway  
Miami, FL 33149

Maury Oceanographic Library  
Naval Oceanographic Office  
Bay St. Louis  
NSTL, MS 39522-5001

Marine Sciences Collection  
Mayaguez Campus Library  
University of Puerto Rico  
Mayaguez, Puerto Rico 00708

Library  
Institute of Oceanographic Sciences  
Deacon Laboratory  
Wormley, Godalming  
Surrey GU8 5UB  
UNITED KINGDOM

The Librarian  
CSIRO Marine Laboratories  
G.P.O. Box 1538  
Hobart, Tasmania  
AUSTRALIA 7001

Library  
Proudman Oceanographic Laboratory  
Bidston Observatory  
Birkenhead  
Merseyside L43 7 RA  
UNITED KINGDOM

